An Experimental Study of Heat Transfer Deterioration at Supercritical Pressures

by

Nathan Kline

Thesis submitted to the Faculty of Graduate and Postdoctoral Studies
in partial fulfillment of the requirements for the degree of
MASTER OF APPLIED SCIENCE
in Mechanical Engineering

Ottawa-Carleton Institute for Mechanical and Aerospace Engineering
University of Ottawa
Ottawa, Canada

© Nathan Kline, Ottawa, Canada, 2017

Abstract

Convective heat transfer to CO_2 flowing upward in electrically heated vertical tubes at supercritical pressures was studied for wall heat fluxes q within ranges that included values corresponding to the onset of heat transfer deterioration (HTD). The inlet pressure was $P = 8.35$ MPa, the mass flux was in the range 200 kg/m^{2}s $\leq G \leq$ 1500 kg/m^{2}s, and the inlet temperature was in the range 0 °C $\leq T_{in} \leq$ 35 °C. Wall temperature measurements were collected in three tubular test sections, having inner diameters of $D = 4.6$, 8, and 22 mm. The abilities of three different HTD identification methods to separate the entire data set into deteriorated and normal heat transfer modes were tested. Two types of buoyancy parameters were tested as HTD detection methods, and correction factors for changes in mass flux were devised. The minimum heat flux at HTD onset was found to follow a power law of mass flux with the same exponent for all three sections and the same proportionality coefficient for the two smaller sections but a smaller one for the larger test section. For heat flux values that were larger than this minimum, HTD was found to occur only within a limited range of T_{in}, whose width increased with increasing heat flux. The heat transfer coefficient for normal heat transfer was expressed as an exponential function of the diameter.

Acknowledgements

I am very grateful to Professor Stavros Tavoularis for his support, deep academic knowledge and invaluable guidance during my graduate studies. His unwavering confidence in my academic abilities has been a crucial motivator.

I want to acknowledge the unconditional love and support from Deirdre, Quentin, and Asha throughout my studies.

The financial support of Natural Resources Canada (NRCAn), Natural Sciences and Engineering Research Council of Canada (NSERC), and Atomic Energy of Canada Limited (AECL) is greatly appreciated.

I also wish to thank Leo Denner for providing prompt and invaluable technical support throughout this project.

Contents

Abstract **ii**

Acknowledgements **iii**

1 Introduction **1**

1.1 Background 1

1.2 Heat transfer to supercritical fluids 2

1.3 Motivation and objectives 5

1.4 Plan of thesis 5

2 Literature review **7**

2.1 Detection methods of heat transfer deterioration 7

2.1.1 The occurrence of wall temperature spikes 7

2.1.2 Normalized heat transfer coefficient 8

2.1.3 Buoyancy parameter 9

2.1.4 Summary 11

2.2 Predicting the onset of HTD 19

2.2.1 Heat flux at HTD onset as a function of mass flux 19

2.2.2 Buoyancy parameter 20

2.2.3 Summary 21

3 Test facility and Instrumentation **24**

3.1 Experimental facility 24

3.1.1 Main flow circuit 24

3.1.2 CO_2 supply . . . 24
3.1.3 Pumps . . . 26
3.1.4 Preheater . . . 26
3.1.5 Heat exchangers . . . 26
3.1.6 Accumulators . . . 28
3.1.7 Test sections . . . 30
3.1.8 Power supply . . . 32
3.1.9 Safety features . . . 32
3.2 Instrumentation . . . 32
3.2.1 Data acquisition system (DAS) . . . 32
3.2.2 Mass flow rate . . . 33
3.2.3 Inlet and outlet fluid temperatures . . . 33
3.2.4 Wall temperature . . . 33
3.2.5 Power . . . 33
3.2.6 Absolute pressure . . . 34

4 Experimental procedures **35**
4.1 Loop operation procedure . . . 35
4.1.1 General procedure . . . 35
4.1.2 Mass flux adjustment . . . 36
4.1.3 Pressure adjustment . . . 36
4.1.4 Heat flux and inlet temperature adjustments . . . 37
4.2 Measurement procedures . . . 37
4.2.1 Heating power and heat flux measurements . . . 37
4.2.2 Measurement of the wall temperature and the heat transfer coefficient 39
4.2.3 Estimates of power imbalance . . . 40

5 Results and discussion **44**
5.1 Test matrix . . . 44
5.2 Comparisons with results in the literature . . . 45
5.3 Patterns of axial profiles of wall temperature . . . 47
5.4 Identification of HTD . . . 56

5.4.1 Identifying HTD from wall temperature spikes . . . 56
5.4.2 Identifying HTD by comparing measured Nusselt numbers with predictions of a correlation for normal heat transfer . . . 63
5.4.3 Identifying HTD using a buoyancy parameter . . . 71
5.4.4 Summary of HTD identification methods . . . 86
5.5 Onset of HTD . . . 87
5.5.1 HTD maps . . . 87
5.5.2 Minimum onset heat flux as a function of mass flux . . . 92
5.5.3 The buoyancy parameter as an HTD predictor . . . 95
5.6 Dependence of the HTC for normal heat transfer on the tube diameter . . . 101
5.7 Dependence of q_{onset} on the tube diameter . . . 105

6 Conclusion **107**
6.1 Summary of the results . . . 107
6.2 Main contributions . . . 109
6.3 Recommendations for future work . . . 110

A Measurements of wall temperature profiles **112**
A.1 4.6 mm test section . . . 113
A.2 8 mm test section . . . 153
A.3 22 mm test section . . . 210

B Comparisons of $\mathbf{Nu}_{exp}$ with $\mathbf{Nu}_{NHT}$ **249**
B.1 4.6 mm test section . . . 250
B.2 8 mm test section . . . 264

C Buoyancy parameter estimates **282**
C.1 4.6 mm test section . . . 283
C.2 8 mm test section . . . 301
C.3 22 mm test section . . . 326

D List of experimental conditions for all runs **343**

E Iteration method for evaluating $\mathbf{Nu}_{NHT}$ **352**

List of Tables

2.1 A summary of HTD detection methods 12
2.1 A summary of HTD detection methods (Cont'd) 13
2.1 A summary of HTD detection methods (Cont'd) 14
2.1 A summary of HTD detection methods (Cont'd) 15
2.1 A summary of HTD detection methods (Cont'd) 16
2.1 A summary of HTD detection methods (Cont'd) 17
2.1 A summary of HTD detection methods (Cont'd) 18
2.2 A summary of HTD onset correlations 22
2.2 A summary of HTD onset correlations (Cont'd) 23
3.1 Properties comparisons between Inconel® 600 and Sanicro® 70 31
4.1 Electrical properties of the 4.6, 8, and 22 mm test sections 38
4.2 Thermal conductivity of Sanicro® 70 alloy 40
5.1 Ranges of experimental conditions 44
5.2 Flow and heating comparison conditions 45
5.3 Conditions of normal heat transfer cases tested with the Nu_{NHT} correlation . 67
5.4 Fitted correlations between $q_{onset,min}$ and G for the present three test sections 94
5.5 List of normal HTC results for all three test sections 104
D.1 List of all measured conditions 344
D.1 List of all measured conditions (Cont'd) 345
D.1 List of all measured conditions (Cont'd) 346
D.1 List of all measured conditions (Cont'd) 347
D.1 List of all measured conditions (Cont'd) 348
D.1 List of all measured conditions (Cont'd) 349

D.1 List of all measured conditions (Cont'd) 350
D.1 List of all measured conditions (Cont'd) 351

List of Figures

1.1 Pressure-temperature diagram for CO_2 2
1.2 Thermophysical property changes with temperature 3
1.3 Temperature profiles showing normal, enhanced, and deteriorated heat transfer 4
3.1 Schematic diagram of the Supercritical University of Ottawa Loop 25
3.2 Schematic diagram of the heat exchanger flow configurations 27
3.3 A time history of pressure measurements 29
3.4 A time history of the pressure without power 29
3.5 Schematic diagrams of the test sections 30
4.1 Relative power error for different heating powers 41
4.2 Relative power error *vs.* the inlet and outlet specific enthalpies 42
4.3 Relative power error *vs.* the difference between h_{out} and h_{in}. 43
5.1 Temperature profile comparisons with results from literature 46
5.2 Classifications of HTD regimes by Kurganov et al. (2012, 2016) 48
5.3 Sample temperature profiles for $D = 8$ mm, $G = 200$ kg/m^{2}s 49
5.4 Sample temperature profiles for $D = 22$ mm, $G = 300$ kg/m^{2}s 50
5.5 Sample temperature profiles for $D = 4.6$ mm, $G = 300$ kg/m^{2}s 51
5.6 Sample temperature profiles for $D = 8$ mm, $G = 400$ kg/m^{2}s 52
5.7 Sample temperature profiles for $D = 4.6$ mm, $G = 400$ kg/m^{2}s 53
5.8 Sample temperature profiles for $D = 4.6$ mm, $G = 700$ kg/m^{2}s 54
5.9 Sample temperature profiles for $D = 8$ mm, $G = 1000$ kg/m^{2}s 55
5.10 Sample temperature profiles for $D = 8$ mm, $G = 200$ kg/m^{2}s, $T_{in} = 40$ °C . 56
5.11 Sample temperature profiles for $D = 4.6$ mm, $G = 300$ kg/m^{2}s 57
5.12 Sample temperature profiles for $D = 4.6$ mm, $G = 1000$ kg/m^{2}s 59

5.13 Sample temperature profiles for $D = 8$ mm, $G = 200$ kg/m^{2}s 60
5.14 Sample temperature profiles for $D = 8$ mm, $G = 700$ kg/m^{2}s 61
5.15 Sample of Nu predictions for $D = 4.6$ mm, $G = 500$ kg/m^{2}s, $q = 45$ kW/m^2 64
5.16 $\mathrm{Nu}_{exp}/\mathrm{Nu}_{NHT}$ for normal cases 68
5.17 Sample Nu_{NHT} comparisons for $D = 4.6$ mm and 8 mm for $G = 1000$ kg/m^{2}s 70
5.18 $T_{w_{exp}}$ and $T_{w_{NHT}}$ comparisons for $D = 8$ mm, $G = 1000$ kg/m^{2}s 71
5.19 Testing the $\overline{Bo_b}$ parameter 73
5.20 Testing the $Bo_{b_{VP}}$ parameter 75
5.21 Buoyancy parameter correction factor plot 76
5.22 $\overline{Bo_b}$ and $Bo_{b_{VP}}$ profiles for $D = 4.6$ mm, $G = 300$ kg/m^{2}s, $q = 18$ kW/m^2 . 77
5.23 $\overline{Bo_b}$ and $Bo_{b_{VP}}$ profiles for $D = 4.6$ mm, $G = 400$ kg/m^{2}s, $q = 33$ kW/m^2 . 78
5.24 $\overline{Bo_b}$ and $Bo_{b_{VP}}$ profiles for $D = 4.6$ mm, $G = 600$ kg/m^{2}s, $q = 83$ kW/m^2 . 79
5.25 $\overline{Bo_b}$ and $Bo_{b_{VP}}$ profiles for $D = 4.6$ mm, $G = 700$ kg/m^{2}s, $q = 125$ kW/m^2 . 79
5.26 $\overline{Bo_b}$ and $Bo_{b_{VP}}$ profiles for $D = 4.6$ mm, $G = 1000$ kg/m^{2}s, $q = 260$ kW/m^2 80
5.27 $\overline{Bo_b}$ and $Bo_{b_{VP}}$ profiles for $D = 8$ mm, $G = 200$ kg/m^{2}s, $q = 5$ kW/m^2 . . . 81
5.28 $\overline{Bo_b}$ and $Bo_{b_{VP}}$ profiles for $D = 8$ mm, $G = 400$ kg/m^{2}s, $q = 33$ kW/m^2 . . 82
5.29 $\overline{Bo_b}$ and $Bo_{b_{VP}}$ profiles for $D = 8$ mm, $G = 600$ kg/m^{2}s, $q = 83$ kW/m^2 . . 83
5.30 $\overline{Bo_b}$ and $Bo_{b_{VP}}$ profiles for $D = 8$ mm, $G = 700$ kg/m^{2}s, $q = 115$ kW/m^2 . . 83
5.31 $\overline{Bo_b}$ and $Bo_{b_{VP}}$ profiles for $D = 22$ mm, $G = 400$ kg/m^{2}s, $q = 35$ kW/m^2 . . 84
5.32 $\overline{Bo_b}$ and $Bo_{b_{VP}}$ profiles for $D = 22$ mm, $G = 600$ kg/m^{2}s, $q = 58$ kW/m^2 . . 85
5.33 $\overline{Bo_b}$ and $Bo_{b_{VP}}$ profiles for $D = 22$ mm, $G = 700$ kg/m^{2}s, $q = 90$ kW/m^2 . . 85
5.34 Effect of T_{in}, q, and G on the onset of HTD for the 22 mm test section. . . 89
5.35 Effect of T_{in}, q, and G on the onset of HTD for the 8 mm test section. . . . 90
5.36 Effect of T_{in}, q, and G on the onset of HTD for the 4.6 mm test section. . . 91
5.37 $T_{in,qmin}$ vs. G for all three test sections 92
5.38 A plot of $q_{onset,min}$ vs. G for all three test sections 93
5.39 Bo_b^* and T_w profiles for $D = 8$ mm, $G = 500$ kg/m^{2}s, $q = 55$ kW/m^2 96
5.40 Grouped Bo_b^* profiles for $D = 8$ mm, $G = 500$ kg/m^{2}s, $q = 55$ kW/m^2 . . . 97
5.41 Bo_b^* evaluated at $T_{in} = 21$ °C vs. q for $D = 22$ mm, ... 98
5.42 22 mm Bo_b^* results for all normal and deteriorated cases 99
5.43 Bo_b^* results for all deteriorated cases from all three test sections 100

5.44 Proposed function accounting for the effect of diameter on normal HTC . . 103
5.45 Proposed function accounting of the effect of diameter on $q_{onset,min}$ 106
A.1 Temperature profiles for $D = 4.6$ mm, $G = 300$ kg/m^{2}s, $q = 13$ kW/m^2 . . . 113
A.2 Temperature profiles for $D = 4.6$ mm, $G = 300$ kg/m^{2}s, $q = 15$ kW/m^2 . . . 114
A.3 Temperature profiles for $D = 4.6$ mm, $G = 300$ kg/m^{2}s, $q = 18$ kW/m^2 . . . 115
A.4 Temperature profiles for $D = 4.6$ mm, $G = 300$ kg/m^{2}s, $q = 20$ kW/m^2 . . . 116
A.5 Temperature profiles for $D = 4.6$ mm, $G = 400$ kg/m^{2}s, $q = 30$ kW/m^2 . . . 117
A.6 Temperature profiles for $D = 4.6$ mm, $G = 400$ kg/m^{2}s, $q = 33$ kW/m^2 . . . 118
A.7 Temperature profiles for $D = 4.6$ mm, $G = 400$ kg/m^{2}s, $q = 35$ kW/m^2 . . . 119
A.8 Temperature profiles for $D = 4.6$ mm, $G = 400$ kg/m^{2}s, $q = 38$ kW/m^2 . . . 120
A.9 Temperature profiles for $D = 4.6$ mm, $G = 400$ kg/m^{2}s, $q = 40$ kW/m^2 . . . 121
A.10 Temperature profiles for $D = 4.6$ mm, $G = 500$ kg/m^{2}s, $q = 45$ kW/m^2 . . . 122
A.11 Temperature profiles for $D = 4.6$ mm, $G = 500$ kg/m^{2}s, $q = 48$ kW/m^2 . . . 123
A.12 Temperature profiles for $D = 4.6$ mm, $G = 500$ kg/m^{2}s, $q = 50$ kW/m^2 . . . 124
A.13 Temperature profiles for $D = 4.6$ mm, $G = 500$ kg/m^{2}s, $q = 53$ kW/m^2 . . . 125
A.14 Temperature profiles for $D = 4.6$ mm, $G = 500$ kg/m^{2}s, $q = 55$ kW/m^2 . . . 126
A.15 Temperature profiles for $D = 4.6$ mm, $G = 600$ kg/m^{2}s, $q = 75$ kW/m^2 . . . 127
A.16 Temperature profiles for $D = 4.6$ mm, $G = 600$ kg/m^{2}s, $q = 80$ kW/m^2 . . . 128
A.17 Temperature profiles for $D = 4.6$ mm, $G = 600$ kg/m^{2}s, $q = 83$ kW/m^2 . . . 129
A.18 Temperature profiles for $D = 4.6$ mm, $G = 600$ kg/m^{2}s, $q = 85$ kW/m^2 . . . 130
A.19 Temperature profiles for $D = 4.6$ mm, $G = 700$ kg/m^{2}s, $q = 90$ kW/m^2 . . . 131
A.20 Temperature profiles for $D = 4.6$ mm, $G = 700$ kg/m^{2}s, $q = 95$ kW/m^2 . . . 132
A.21 Temperature profiles for $D = 4.6$ mm, $G = 700$ kg/m^{2}s, $q = 100$ kW/m^2 . . 133
A.22 Temperature profiles for $D = 4.6$ mm, $G = 700$ kg/m^{2}s, $q = 105$ kW/m^2 . . 134
A.23 Temperature profiles for $D = 4.6$ mm, $G = 700$ kg/m^{2}s, $q = 110$ kW/m^2 . . 135
A.24 Temperature profiles for $D = 4.6$ mm, $G = 700$ kg/m^{2}s, $q = 115$ kW/m^2 . . 136
A.25 Temperature profiles for $D = 4.6$ mm, $G = 700$ kg/m^{2}s, $q = 120$ kW/m^2 . . 137
A.26 Temperature profiles for $D = 4.6$ mm, $G = 700$ kg/m^{2}s, $q = 125$ kW/m^2 . . 138
A.27 Temperature profiles for $D = 4.6$ mm, $G = 1000$ kg/m^{2}s, $q = 225$ kW/m^2 . 139
A.28 Temperature profiles for $D = 4.6$ mm, $G = 1000$ kg/m^{2}s, $q = 230$ kW/m^2 . 140
A.29 Temperature profiles for $D = 4.6$ mm, $G = 1000$ kg/m^{2}s, $q = 240$ kW/m^2 . 141

A.30 Temperature profiles for $D = 4.6$ mm, $G = 1000$ kg/m^{2}s, $q = 245$ kW/m^2 . 142
A.31 Temperature profiles for $D = 4.6$ mm, $G = 1000$ kg/m^{2}s, $q = 250$ kW/m^2 . 143
A.32 Temperature profiles for $D = 4.6$ mm, $G = 1000$ kg/m^{2}s, $q = 260$ kW/m^2 . 144
A.33 Temperature profiles for $D = 4.6$ mm, $G = 1500$ kg/m^{2}s, $q = 380$ kW/m^2 . 145
A.34 Temperature profiles for $D = 4.6$ mm, $G = 1500$ kg/m^{2}s, $q = 390$ kW/m^2 . 146
A.35 Temperature profiles for $D = 4.6$ mm, $G = 1500$ kg/m^{2}s, $q = 400$ kW/m^2 . 147
A.36 Temperature profiles for $D = 4.6$ mm, $G = 1500$ kg/m^{2}s, $q = 410$ kW/m^2 . 148
A.37 Temperature profiles for $D = 4.6$ mm, $G = 1500$ kg/m^{2}s, $q = 420$ kW/m^2 . 149
A.38 Temperature profiles for $D = 4.6$ mm, $G = 1500$ kg/m^{2}s, $q = 430$ kW/m^2 . 150
A.39 Temperature profiles for $D = 4.6$ mm, $G = 1500$ kg/m^{2}s, $q = 440$ kW/m^2 . 151
A.40 Temperature profiles for $D = 4.6$ mm, $G = 1500$ kg/m^{2}s, $q = 450$ kW/m^2 . 152
A.41 Temperature profiles for $D = 8$ mm, $G = 200$ kg/m^{2}s, $q = 3$ kW/m^2 153
A.42 Temperature profiles for $D = 8$ mm, $G = 200$ kg/m^{2}s, $q = 5$ kW/m^2 154
A.43 Temperature profiles for $D = 8$ mm, $G = 200$ kg/m^{2}s, $q = 8$ kW/m^2 155
A.44 Temperature profiles for $D = 8$ mm, $G = 200$ kg/m^{2}s, $q = 10$ kW/m^2 156
A.45 Temperature profiles for $D = 8$ mm, $G = 200$ kg/m^{2}s, $q = 15$ kW/m^2 157
A.46 Temperature profiles for $D = 8$ mm, $G = 200$ kg/m^{2}s, $T_{in} = 40$ °C 158
A.47 Temperature profiles for $D = 8$ mm, $G = 300$ kg/m^{2}s, $q = 10$ kW/m^2 159
A.48 Temperature profiles for $D = 8$ mm, $G = 300$ kg/m^{2}s, $q = 13$ kW/m^2 160
A.49 Temperature profiles for $D = 8$ mm, $G = 300$ kg/m^{2}s, $q = 15$ kW/m^2 161
A.50 Temperature profiles for $D = 8$ mm, $G = 300$ kg/m^{2}s, $q = 18$ kW/m^2 162
A.51 Temperature profiles for $D = 8$ mm, $G = 300$ kg/m^{2}s, $q = 20$ kW/m^2 163
A.52 Temperature profiles for $D = 8$ mm, $G = 300$ kg/m^{2}s, $T_{in} = 38$ °C 164
A.53 Temperature profiles for $D = 8$ mm, $G = 400$ kg/m^{2}s, $q = 25$ kW/m^2 165
A.54 Temperature profiles for $D = 8$ mm, $G = 400$ kg/m^{2}s, $q = 30$ kW/m^2 166
A.55 Temperature profiles for $D = 8$ mm, $G = 400$ kg/m^{2}s, $q = 33$ kW/m^2 167
A.56 Temperature profiles for $D = 8$ mm, $G = 400$ kg/m^{2}s, $q = 35$ kW/m^2 168
A.57 Temperature profiles for $D = 8$ mm, $G = 400$ kg/m^{2}s, $q = 40$ kW/m^2 169
A.58 Temperature profiles for $D = 8$ mm, $G = 500$ kg/m^{2}s, $q = 50$ kW/m^2 170
A.59 Temperature profiles for $D = 8$ mm, $G = 500$ kg/m^{2}s, $q = 53$ kW/m^2 171
A.60 Temperature profiles for $D = 8$ mm, $G = 500$ kg/m^{2}s, $q = 55$ kW/m^2 172

A.61 Temperature profiles for $D = 8$ mm, $G = 500$ kg/m^{2}s, $q = 60$ kW/m^2 173
A.62 Temperature profiles for $D = 8$ mm, $G = 600$ kg/m^{2}s, $q = 65$ kW/m^2 174
A.63 Temperature profiles for $D = 8$ mm, $G = 600$ kg/m^{2}s, $q = 70$ kW/m^2 175
A.64 Temperature profiles for $D = 8$ mm, $G = 600$ kg/m^{2}s, $q = 73$ kW/m^2 176
A.65 Temperature profiles for $D = 8$ mm, $G = 600$ kg/m^{2}s, $q = 75$ kW/m^2 177
A.66 Temperature profiles for $D = 8$ mm, $G = 600$ kg/m^{2}s, $q = 78$ kW/m^2 178
A.67 Temperature profiles for $D = 8$ mm, $G = 600$ kg/m^{2}s, $q = 80$ kW/m^2 179
A.68 Temperature profiles for $D = 8$ mm, $G = 600$ kg/m^{2}s, $q = 83$ kW/m^2 180
A.69 Temperature profiles for $D = 8$ mm, $G = 600$ kg/m^{2}s, $q = 85$ kW/m^2 181
A.70 Temperature profiles for $D = 8$ mm, $G = 600$ kg/m^{2}s, $q = 90$ kW/m^2 182
A.71 Temperature profiles for $D = 8$ mm, $G = 700$ kg/m^{2}s, $q = 90$ kW/m^2 183
A.72 Temperature profiles for $D = 8$ mm, $G = 700$ kg/m^{2}s, $q = 95$ kW/m^2 184
A.73 Temperature profiles for $D = 8$ mm, $G = 700$ kg/m^{2}s, $q = 98$ kW/m^2 185
A.74 Temperature profiles for $D = 8$ mm, $G = 700$ kg/m^{2}s, $q = 100$ kW/m^2 . . . 186
A.75 Temperature profiles for $D = 8$ mm, $G = 700$ kg/m^{2}s, $q = 105$ kW/m^2 . . . 187
A.76 Temperature profiles for $D = 8$ mm, $G = 700$ kg/m^{2}s, $q = 110$ kW/m^2 . . . 188
A.77 Temperature profiles for $D = 8$ mm, $G = 700$ kg/m^{2}s, $q = 115$ kW/m^2 . . . 189
A.78 Temperature profiles for $D = 8$ mm, $G = 700$ kg/m^{2}s, $q = 120$ kW/m^2 . . . 190
A.79 Temperature profiles for $D = 8$ mm, $G = 1000$ kg/m^{2}s, $q = 190$ kW/m^2 . . 191
A.80 Temperature profiles for $D = 8$ mm, $G = 1000$ kg/m^{2}s, $q = 200$ kW/m^2 . . 192
A.81 Temperature profiles for $D = 8$ mm, $G = 1000$ kg/m^{2}s, $q = 210$ kW/m^2 . . 193
A.82 Temperature profiles for $D = 8$ mm, $G = 1000$ kg/m^{2}s, $q = 220$ kW/m^2 . . 194
A.83 Temperature profiles for $D = 8$ mm, $G = 1000$ kg/m^{2}s, $q = 225$ kW/m^2 . . 195
A.84 Temperature profiles for $D = 8$ mm, $G = 1000$ kg/m^{2}s, $q = 230$ kW/m^2 . . 196
A.85 Temperature profiles for $D = 8$ mm, $G = 1000$ kg/m^{2}s, $q = 235$ kW/m^2 . . 197
A.86 Temperature profiles for $D = 8$ mm, $G = 1000$ kg/m^{2}s, $q = 240$ kW/m^2 . . 198
A.87 Temperature profiles for $D = 8$ mm, $G = 1000$ kg/m^{2}s, $q = 245$ kW/m^2 . . 199
A.88 Temperature profiles for $D = 8$ mm, $G = 1000$ kg/m^{2}s, $q = 250$ kW/m^2 . . 200
A.89 Temperature profiles for $D = 8$ mm, $G = 1000$ kg/m^{2}s, $q = 260$ kW/m^2 . . 201
A.90 Temperature profiles for $D = 8$ mm, $G = 1500$ kg/m^{2}s, $q = 380$ kW/m^2 . . 202
A.91 Temperature profiles for $D = 8$ mm, $G = 1500$ kg/m^{2}s, $q = 390$ kW/m^2 . . 203

A.92 Temperature profiles for $D = 8$ mm, $G = 1500$ kg/m^{2}s, $q = 400$ kW/m^2 . . 204
A.93 Temperature profiles for $D = 8$ mm, $G = 1500$ kg/m^{2}s, $q = 410$ kW/m^2 . . 205
A.94 Temperature profiles for $D = 8$ mm, $G = 1500$ kg/m^{2}s, $q = 420$ kW/m^2 . . 206
A.95 Temperature profiles for $D = 8$ mm, $G = 1500$ kg/m^{2}s, $q = 430$ kW/m^2 . . 207
A.96 Temperature profiles for $D = 8$ mm, $G = 1500$ kg/m^{2}s, $q = 440$ kW/m^2 . . 208
A.97 Temperature profiles for $D = 8$ mm, $G = 1500$ kg/m^{2}s, $q = 450$ kW/m^2 . . 209
A.98 Temperature profiles for $D = 22$ mm, $G = 200$ kg/m^{2}s, $q = 2$ kW/m^2 210
A.99 Temperature profiles for $D = 22$ mm, $G = 200$ kg/m^{2}s, $q = 3$ kW/m^2 211
A.100 Temperature profiles for $D = 22$ mm, $G = 200$ kg/m^{2}s, $q = 3.5$ kW/m^2 . . . 212
A.101 Temperature profiles for $D = 22$ mm, $G = 200$ kg/m^{2}s, $q = 4$ kW/m^2 213
A.102 Temperature profiles for $D = 22$ mm, $G = 200$ kg/m^{2}s, $q = 5$ kW/m^2 214
A.103 Temperature profiles for $D = 22$ mm, $G = 200$ kg/m^{2}s, $q = 10$ kW/m^2 . . . 215
A.104 Temperature profiles for $D = 22$ mm, $G = 200$ kg/m^{2}s, $T_{in} = 40$ °C 216
A.105 Temperature profiles for $D = 22$ mm, $G = 300$ kg/m^{2}s, $q = 10$ kW/m^2 . . . 217
A.106 Temperature profiles for $D = 22$ mm, $G = 300$ kg/m^{2}s, $q = 13$ kW/m^2 . . . 218
A.107 Temperature profiles for $D = 22$ mm, $G = 300$ kg/m^{2}s, $q = 15$ kW/m^2 . . . 219
A.108 Temperature profiles for $D = 22$ mm, $G = 300$ kg/m^{2}s, $q = 20$ kW/m^2 . . . 220
A.109 Temperature profiles for $D = 22$ mm, $G = 300$ kg/m^{2}s, $T_{in} = 37$ °C 221
A.110 Temperature profiles for $D = 22$ mm, $G = 400$ kg/m^{2}s, $q = 20$ kW/m^2 . . . 222
A.111 Temperature profiles for $D = 22$ mm, $G = 400$ kg/m^{2}s, $q = 23$ kW/m^2 . . . 223
A.112 Temperature profiles for $D = 22$ mm, $G = 400$ kg/m^{2}s, $q = 25$ kW/m^2 . . . 224
A.113 Temperature profiles for $D = 22$ mm, $G = 400$ kg/m^{2}s, $q = 28$ kW/m^2 . . . 225
A.114 Temperature profiles for $D = 22$ mm, $G = 400$ kg/m^{2}s, $q = 30$ kW/m^2 . . . 226
A.115 Temperature profiles for $D = 22$ mm, $G = 400$ kg/m^{2}s, $q = 35$ kW/m^2 . . . 227
A.116 Temperature profiles for $D = 22$ mm, $G = 400$ kg/m^{2}s, $T_{in} = 37$ °C 228
A.117 Temperature profiles for $D = 22$ mm, $G = 500$ kg/m^{2}s, $q = 35$ kW/m^2 . . . 229
A.118 Temperature profiles for $D = 22$ mm, $G = 500$ kg/m^{2}s, $q = 38$ kW/m^2 . . . 230
A.119 Temperature profiles for $D = 22$ mm, $G = 500$ kg/m^{2}s, $q = 40$ kW/m^2 . . . 231
A.120 Temperature profiles for $D = 22$ mm, $G = 500$ kg/m^{2}s, $q = 43$ kW/m^2 . . . 232
A.121 Temperature profiles for $D = 22$ mm, $G = 500$ kg/m^{2}s, $q = 45$ kW/m^2 . . . 233
A.122 Temperature profiles for $D = 22$ mm, $G = 500$ kg/m^{2}s, $q = 48$ kW/m^2 . . . 234

A.123 Temperature profiles for $D = 22$ mm, $G = 500$ kg/m^{2}s, $q = 50$ kW/m^2 . . . 235
A.124 Temperature profiles for $D = 22$ mm, $G = 600$ kg/m^{2}s, $q = 55$ kW/m^2 . . . 236
A.125 Temperature profiles for $D = 22$ mm, $G = 600$ kg/m^{2}s, $q = 58$ kW/m^2 . . . 237
A.126 Temperature profiles for $D = 22$ mm, $G = 600$ kg/m^{2}s, $q = 60$ kW/m^2 . . . 238
A.127 Temperature profiles for $D = 22$ mm, $G = 600$ kg/m^{2}s, $q = 65$ kW/m^2 . . . 239
A.128 Temperature profiles for $D = 22$ mm, $G = 600$ kg/m^{2}s, $q = 70$ kW/m^2 . . . 240
A.129 Temperature profiles for $D = 22$ mm, $G = 700$ kg/m^{2}s, $q = 70$ kW/m^2 . . . 241
A.130 Temperature profiles for $D = 22$ mm, $G = 700$ kg/m^{2}s, $q = 73$ kW/m^2 . . . 242
A.131 Temperature profiles for $D = 22$ mm, $G = 700$ kg/m^{2}s, $q = 75$ kW/m^2 . . . 243
A.132 Temperature profiles for $D = 22$ mm, $G = 700$ kg/m^{2}s, $q = 78$ kW/m^2 . . . 244
A.133 Temperature profiles for $D = 22$ mm, $G = 700$ kg/m^{2}s, $q = 80$ kW/m^2 . . . 245
A.134 Temperature profiles for $D = 22$ mm, $G = 700$ kg/m^{2}s, $q = 83$ kW/m^2 . . . 246
A.135 Temperature profiles for $D = 22$ mm, $G = 700$ kg/m^{2}s, $q = 85$ kW/m^2 . . . 247
A.136 Temperature profiles for $D = 22$ mm, $G = 700$ kg/m^{2}s, $q = 90$ kW/m^2 . . . 248
B.1 Nu_{NHT} comparisons for $D = 4.6$ mm, $G = 1000$ kg/m^{2}s, $q = 225$ kW/m^2 . . 250
B.2 Nu_{NHT} comparisons for $D = 4.6$ mm, $G = 1000$ kg/m^{2}s, $q = 230$ kW/m^2 . . 251
B.3 Nu_{NHT} comparisons for $D = 4.6$ mm, $G = 1000$ kg/m^{2}s, $q = 240$ kW/m^2 . . 252
B.4 Nu_{NHT} comparisons for $D = 4.6$ mm, $G = 1000$ kg/m^{2}s, $q = 250$ kW/m^2 . . 253
B.5 Nu_{NHT} comparisons for $D = 4.6$ mm, $G = 1000$ kg/m^{2}s, $q = 260$ kW/m^2 . . 254
B.6 Nu_{NHT} comparisons for $D = 4.6$ mm, $G = 1000$ kg/m^{2}s, $q = 290$ kW/m^2 . . 255
B.7 Nu_{NHT} comparisons for $D = 4.6$ mm, $G = 1500$ kg/m^{2}s, $q = 380$ kW/m^2 . . 256
B.8 Nu_{NHT} comparisons for $D = 4.6$ mm, $G = 1500$ kg/m^{2}s, $q = 390$ kW/m^2 . . 257
B.9 Nu_{NHT} comparisons for $D = 4.6$ mm, $G = 1500$ kg/m^{2}s, $q = 400$ kW/m^2 . . 258
B.10 Nu_{NHT} comparisons for $D = 4.6$ mm, $G = 1500$ kg/m^{2}s, $q = 410$ kW/m^2 . . 259
B.11 Nu_{NHT} comparisons for $D = 4.6$ mm, $G = 1500$ kg/m^{2}s, $q = 420$ kW/m^2 . . 260
B.12 Nu_{NHT} comparisons for $D = 4.6$ mm, $G = 1500$ kg/m^{2}s, $q = 430$ kW/m^2 . . 261
B.13 Nu_{NHT} comparisons for $D = 4.6$ mm, $G = 1500$ kg/m^{2}s, $q = 440$ kW/m^2 . . 262
B.14 Nu_{NHT} comparisons for $D = 4.6$ mm, $G = 1500$ kg/m^{2}s, $q = 450$ kW/m^2 . . 263
B.15 Nu_{NHT} comparisons for $D = 8$ mm, $G = 1000$ kg/m^{2}s, $q = 200$ kW/m^2 . . . 264
B.16 Nu_{NHT} comparisons for $D = 8$ mm, $G = 1000$ kg/m^{2}s, $q = 210$ kW/m^2 . . . 265
B.17 Nu_{NHT} comparisons for $D = 8$ mm, $G = 1000$ kg/m^{2}s, $q = 220$ kW/m^2 . . . 266

B.18 Nu_{NHT} comparisons for $D = 8$ mm, $G = 1000$ kg/m^{2}s, $q = 225$ kW/m^2 . . . 267
B.19 Nu_{NHT} comparisons for $D = 8$ mm, $G = 1000$ kg/m^{2}s, $q = 230$ kW/m^2 . . . 268
B.20 Nu_{NHT} comparisons for $D = 8$ mm, $G = 1000$ kg/m^{2}s, $q = 235$ kW/m^2 . . . 269
B.21 Nu_{NHT} comparisons for $D = 8$ mm, $G = 1000$ kg/m^{2}s, $q = 240$ kW/m^2 . . . 270
B.22 Nu_{NHT} comparisons for $D = 8$ mm, $G = 1000$ kg/m^{2}s, $q = 245$ kW/m^2 . . . 271
B.23 Nu_{NHT} comparisons for $D = 8$ mm, $G = 1000$ kg/m^{2}s, $q = 250$ kW/m^2 . . . 272
B.24 Nu_{NHT} comparisons for $D = 8$ mm, $G = 1000$ kg/m^{2}s, $q = 260$ kW/m^2 . . . 273
B.25 Nu_{NHT} comparisons for $D = 8$ mm, $G = 1500$ kg/m^{2}s, $q = 380$ kW/m^2 . . . 274
B.26 Nu_{NHT} comparisons for $D = 8$ mm, $G = 1500$ kg/m^{2}s, $q = 380$ kW/m^2 . . . 275
B.27 Nu_{NHT} comparisons for $D = 8$ mm, $G = 1500$ kg/m^{2}s, $q = 400$ kW/m^2 . . . 276
B.28 Nu_{NHT} comparisons for $D = 8$ mm, $G = 1500$ kg/m^{2}s, $q = 410$ kW/m^2 . . . 277
B.29 Nu_{NHT} comparisons for $D = 8$ mm, $G = 1500$ kg/m^{2}s, $q = 420$ kW/m^2 . . . 278
B.30 Nu_{NHT} comparisons for $D = 8$ mm, $G = 1500$ kg/m^{2}s, $q = 430$ kW/m^2 . . . 279
B.31 Nu_{NHT} comparisons for $D = 8$ mm, $G = 1500$ kg/m^{2}s, $q = 440$ kW/m^2 . . . 280
B.32 Nu_{NHT} comparisons for $D = 8$ mm, $G = 1500$ kg/m^{2}s, $q = 450$ kW/m^2 . . . 281
C.1 $\overline{Bo_b}$ and $Bo_{b_{VP}}$ profiles for $D = 4.6$ mm, $G = 300$ kg/m^{2}s, $q = 15$ kW/m^2 . 283
C.2 $\overline{Bo_b}$ and $Bo_{b_{VP}}$ profiles for $D = 4.6$ mm, $G = 300$ kg/m^{2}s, $q = 18$ kW/m^2 . 283
C.3 $\overline{Bo_b}$ and $Bo_{b_{VP}}$ profiles for $D = 4.6$ mm, $G = 300$ kg/m^{2}s, $q = 20$ kW/m^2 . 284
C.4 $\overline{Bo_b}$ and $Bo_{b_{VP}}$ profiles for $D = 4.6$ mm, $G = 400$ kg/m^{2}s, $q = 30$ kW/m^2 . 284
C.5 $\overline{Bo_b}$ and $Bo_{b_{VP}}$ profiles for $D = 4.6$ mm, $G = 400$ kg/m^{2}s, $q = 33$ kW/m^2 . 285
C.6 $\overline{Bo_b}$ and $Bo_{b_{VP}}$ profiles for $D = 4.6$ mm, $G = 400$ kg/m^{2}s, $q = 35$ kW/m^2 . 285
C.7 $\overline{Bo_b}$ and $Bo_{b_{VP}}$ profiles for $D = 4.6$ mm, $G = 400$ kg/m^{2}s, $q = 38$ kW/m^2 . 286
C.8 $\overline{Bo_b}$ and $Bo_{b_{VP}}$ profiles for $D = 4.6$ mm, $G = 500$ kg/m^{2}s, $q = 50$ kW/m^2 . 286
C.9 $\overline{Bo_b}$ and $Bo_{b_{VP}}$ profiles for $D = 4.6$ mm, $G = 500$ kg/m^{2}s, $q = 53$ kW/m^2 . 287
C.10 $\overline{Bo_b}$ and $Bo_{b_{VP}}$ profiles for $D = 4.6$ mm, $G = 500$ kg/m^{2}s, $q = 55$ kW/m^2 . 287
C.11 $\overline{Bo_b}$ and $Bo_{b_{VP}}$ profiles for $D = 4.6$ mm, $G = 600$ kg/m^{2}s, $q = 80$ kW/m^2 . 288
C.12 $\overline{Bo_b}$ and $Bo_{b_{VP}}$ profiles for $D = 4.6$ mm, $G = 600$ kg/m^{2}s, $q = 80$ kW/m^2 . 288
C.13 $\overline{Bo_b}$ and $Bo_{b_{VP}}$ profiles for $D = 4.6$ mm, $G = 600$ kg/m^{2}s, $q = 83$ kW/m^2 . 289
C.14 $\overline{Bo_b}$ and $Bo_{b_{VP}}$ profiles for $D = 4.6$ mm, $G = 600$ kg/m^{2}s, $q = 85$ kW/m^2 . 289
C.15 $\overline{Bo_b}$ and $Bo_{b_{VP}}$ profiles for $D = 4.6$ mm, $G = 700$ kg/m^{2}s, $q = 110$ kW/m^2 . 290
C.16 $\overline{Bo_b}$ and $Bo_{b_{VP}}$ profiles for $D = 4.6$ mm, $G = 700$ kg/m^{2}s, $q = 110$ kW/m^2 . 290

C.17 $\overline{Bo_b}$ and $Bo_{b_{VP}}$ profiles for $D = 4.6$ mm, $G = 700$ kg/m^{2}s, $q = 110$ kW/m^2 . 291
C.18 $\overline{Bo_b}$ and $Bo_{b_{VP}}$ profiles for $D = 4.6$ mm, $G = 700$ kg/m^{2}s, $q = 110$ kW/m^2 . 291
C.19 $\overline{Bo_b}$ and $Bo_{b_{VP}}$ profiles for $D = 4.6$ mm, $G = 700$ kg/m^{2}s, $q = 110$ kW/m^2 . 292
C.20 $\overline{Bo_b}$ and $Bo_{b_{VP}}$ profiles for $D = 4.6$ mm, $G = 700$ kg/m^{2}s, $q = 115$ kW/m^2 . 292
C.21 $\overline{Bo_b}$ and $Bo_{b_{VP}}$ profiles for $D = 4.6$ mm, $G = 700$ kg/m^{2}s, $q = 120$ kW/m^2 . 293
C.22 $\overline{Bo_b}$ and $Bo_{b_{VP}}$ profiles for $D = 4.6$ mm, $G = 700$ kg/m^{2}s, $q = 125$ kW/m^2 . 293
C.23 $\overline{Bo_b}$ and $Bo_{b_{VP}}$ profiles for $D = 4.6$ mm, $G = 1000$ kg/m^{2}s, $q = 240$ kW/m^2 294
C.24 $\overline{Bo_b}$ and $Bo_{b_{VP}}$ profiles for $D = 4.6$ mm, $G = 1000$ kg/m^{2}s, $q = 240$ kW/m^2 294
C.25 $\overline{Bo_b}$ and $Bo_{b_{VP}}$ profiles for $D = 4.6$ mm, $G = 1000$ kg/m^{2}s, $q = 240$ kW/m^2 295
C.26 $\overline{Bo_b}$ and $Bo_{b_{VP}}$ profiles for $D = 4.6$ mm, $G = 1000$ kg/m^{2}s, $q = 250$ kW/m^2 295
C.27 $\overline{Bo_b}$ and $Bo_{b_{VP}}$ profiles for $D = 4.6$ mm, $G = 1000$ kg/m^{2}s, $q = 260$ kW/m^2 296
C.28 $\overline{Bo_b}$ and $Bo_{b_{VP}}$ profiles for $D = 4.6$ mm, $G = 1000$ kg/m^{2}s, $q = 290$ kW/m^2 296
C.29 $\overline{Bo_b}$ and $Bo_{b_{VP}}$ profiles for $D = 4.6$ mm, $G = 1500$ kg/m^{2}s, $q = 380$ kW/m^2 297
C.30 $\overline{Bo_b}$ and $Bo_{b_{VP}}$ profiles for $D = 4.6$ mm, $G = 1500$ kg/m^{2}s, $q = 390$ kW/m^2 297
C.31 $\overline{Bo_b}$ and $Bo_{b_{VP}}$ profiles for $D = 4.6$ mm, $G = 1500$ kg/m^{2}s, $q = 400$ kW/m^2 298
C.32 $\overline{Bo_b}$ and $Bo_{b_{VP}}$ profiles for $D = 4.6$ mm, $G = 1500$ kg/m^{2}s, $q = 410$ kW/m^2 298
C.33 $\overline{Bo_b}$ and $Bo_{b_{VP}}$ profiles for $D = 4.6$ mm, $G = 1500$ kg/m^{2}s, $q = 420$ kW/m^2 299
C.34 $\overline{Bo_b}$ and $Bo_{b_{VP}}$ profiles for $D = 4.6$ mm, $G = 1500$ kg/m^{2}s, $q = 430$ kW/m^2 299
C.35 $\overline{Bo_b}$ and $Bo_{b_{VP}}$ profiles for $D = 4.6$ mm, $G = 1500$ kg/m^{2}s, $q = 440$ kW/m^2 300
C.36 $\overline{Bo_b}$ and $Bo_{b_{VP}}$ profiles for $D = 4.6$ mm, $G = 1500$ kg/m^{2}s, $q = 450$ kW/m^2 300
C.37 $\overline{Bo_b}$ and $Bo_{b_{VP}}$ profiles for $D = 8$ mm, $G = 200$ kg/m^{2}s, $q = 3$ kW/m^2 . . . 301
C.38 $\overline{Bo_b}$ and $Bo_{b_{VP}}$ profiles for $D = 8$ mm, $G = 200$ kg/m^{2}s, $q = 3$ kW/m^2 . . . 301
C.39 $\overline{Bo_b}$ and $Bo_{b_{VP}}$ profiles for $D = 8$ mm, $G = 200$ kg/m^{2}s, $q = 8$ kW/m^2 . . . 302
C.40 $\overline{Bo_b}$ and $Bo_{b_{VP}}$ profiles for $D = 8$ mm, $G = 200$ kg/m^{2}s, $q = 3$ kW/m^2 . . . 302
C.41 $\overline{Bo_b}$ and $Bo_{b_{VP}}$ profiles for $D = 8$ mm, $G = 200$ kg/m^{2}s, $q = 15$ kW/m^2 . . 303
C.42 $\overline{Bo_b}$ and $Bo_{b_{VP}}$ profiles for $D = 8$ mm, $G = 300$ kg/m^{2}s, $q = 15$ kW/m^2 . . 303
C.43 $\overline{Bo_b}$ and $Bo_{b_{VP}}$ profiles for $D = 8$ mm, $G = 300$ kg/m^{2}s, $q = 15$ kW/m^2 . . 304
C.44 $\overline{Bo_b}$ and $Bo_{b_{VP}}$ profiles for $D = 8$ mm, $G = 300$ kg/m^{2}s, $q = 20$ kW/m^2 . . 304
C.45 $\overline{Bo_b}$ and $Bo_{b_{VP}}$ profiles for $D = 8$ mm, $G = 400$ kg/m^{2}s, $q = 30$ kW/m^2 . . 305
C.46 $\overline{Bo_b}$ and $Bo_{b_{VP}}$ profiles for $D = 8$ mm, $G = 400$ kg/m^{2}s, $q = 33$ kW/m^2 . . 305
C.47 $\overline{Bo_b}$ and $Bo_{b_{VP}}$ profiles for $D = 8$ mm, $G = 400$ kg/m^{2}s, $q = 35$ kW/m^2 . . 306

C.48 $\overline{Bo_b}$ and $Bo_{b_{VP}}$ profiles for $D = 8$ mm, $G = 400$ kg/m^{2}s, $q = 40$ kW/m^2 . . 306
C.49 $\overline{Bo_b}$ and $Bo_{b_{VP}}$ profiles for $D = 8$ mm, $G = 500$ kg/m^{2}s, $q = 53$ kW/m^2 . . 307
C.50 $\overline{Bo_b}$ and $Bo_{b_{VP}}$ profiles for $D = 8$ mm, $G = 500$ kg/m^{2}s, $q = 55$ kW/m^2 . . 307
C.51 $\overline{Bo_b}$ and $Bo_{b_{VP}}$ profiles for $D = 8$ mm, $G = 500$ kg/m^{2}s, $q = 60$ kW/m^2 . . 308
C.52 $\overline{Bo_b}$ and $Bo_{b_{VP}}$ profiles for $D = 8$ mm, $G = 600$ kg/m^{2}s, $q = 65$ kW/m^2 . . 308
C.53 $\overline{Bo_b}$ and $Bo_{b_{VP}}$ profiles for $D = 8$ mm, $G = 600$ kg/m^{2}s, $q = 70$ kW/m^2 . . 309
C.54 $\overline{Bo_b}$ and $Bo_{b_{VP}}$ profiles for $D = 8$ mm, $G = 600$ kg/m^{2}s, $q = 73$ kW/m^2 . . 309
C.55 $\overline{Bo_b}$ and $Bo_{b_{VP}}$ profiles for $D = 8$ mm, $G = 600$ kg/m^{2}s, $q = 75$ kW/m^2 . . 310
C.56 $\overline{Bo_b}$ and $Bo_{b_{VP}}$ profiles for $D = 8$ mm, $G = 600$ kg/m^{2}s, $q = 78$ kW/m^2 . . 310
C.57 $\overline{Bo_b}$ and $Bo_{b_{VP}}$ profiles for $D = 8$ mm, $G = 600$ kg/m^{2}s, $q = 80$ kW/m^2 . . 311
C.58 $\overline{Bo_b}$ and $Bo_{b_{VP}}$ profiles for $D = 8$ mm, $G = 600$ kg/m^{2}s, $q = 83$ kW/m^2 . . 311
C.59 $\overline{Bo_b}$ and $Bo_{b_{VP}}$ profiles for $D = 8$ mm, $G = 600$ kg/m^{2}s, $q = 85$ kW/m^2 . . 312
C.60 $\overline{Bo_b}$ and $Bo_{b_{VP}}$ profiles for $D = 8$ mm, $G = 600$ kg/m^{2}s, $q = 90$ kW/m^2 . . 312
C.61 $\overline{Bo_b}$ and $Bo_{b_{VP}}$ profiles for $D = 8$ mm, $G = 700$ kg/m^{2}s, $q = 90$ kW/m^2 . . 313
C.62 $\overline{Bo_b}$ and $Bo_{b_{VP}}$ profiles for $D = 8$ mm, $G = 700$ kg/m^{2}s, $q = 95$ kW/m^2 . . 313
C.63 $\overline{Bo_b}$ and $Bo_{b_{VP}}$ profiles for $D = 8$ mm, $G = 700$ kg/m^{2}s, $q = 98$ kW/m^2 . . 314
C.64 $\overline{Bo_b}$ and $Bo_{b_{VP}}$ profiles for $D = 8$ mm, $G = 700$ kg/m^{2}s, $q = 100$ kW/m^2 . . 314
C.65 $\overline{Bo_b}$ and $Bo_{b_{VP}}$ profiles for $D = 8$ mm, $G = 700$ kg/m^{2}s, $q = 105$ kW/m^2 . . 315
C.66 $\overline{Bo_b}$ and $Bo_{b_{VP}}$ profiles for $D = 8$ mm, $G = 700$ kg/m^{2}s, $q = 110$ kW/m^2 . . 315
C.67 $\overline{Bo_b}$ and $Bo_{b_{VP}}$ profiles for $D = 8$ mm, $G = 700$ kg/m^{2}s, $q = 115$ kW/m^2 . . 316
C.68 $\overline{Bo_b}$ and $Bo_{b_{VP}}$ profiles for $D = 8$ mm, $G = 700$ kg/m^{2}s, $q = 120$ kW/m^2 . . 316
C.69 $\overline{Bo_b}$ and $Bo_{b_{VP}}$ profiles for $D = 8$ mm, $G = 1000$ kg/m^{2}s, $q = 200$ kW/m^2 . 317
C.70 $\overline{Bo_b}$ and $Bo_{b_{VP}}$ profiles for $D = 8$ mm, $G = 1000$ kg/m^{2}s, $q = 210$ kW/m^2 . 317
C.71 $\overline{Bo_b}$ and $Bo_{b_{VP}}$ profiles for $D = 8$ mm, $G = 1000$ kg/m^{2}s, $q = 220$ kW/m^2 . 318
C.72 $\overline{Bo_b}$ and $Bo_{b_{VP}}$ profiles for $D = 8$ mm, $G = 1000$ kg/m^{2}s, $q = 225$ kW/m^2 . 318
C.73 $\overline{Bo_b}$ and $Bo_{b_{VP}}$ profiles for $D = 8$ mm, $G = 1000$ kg/m^{2}s, $q = 235$ kW/m^2 . 319
C.74 $\overline{Bo_b}$ and $Bo_{b_{VP}}$ profiles for $D = 8$ mm, $G = 1000$ kg/m^{2}s, $q = 235$ kW/m^2 . 319
C.75 $\overline{Bo_b}$ and $Bo_{b_{VP}}$ profiles for $D = 8$ mm, $G = 1000$ kg/m^{2}s, $q = 240$ kW/m^2 . 320
C.76 $\overline{Bo_b}$ and $Bo_{b_{VP}}$ profiles for $D = 8$ mm, $G = 1000$ kg/m^{2}s, $q = 240$ kW/m^2 . 320
C.77 $\overline{Bo_b}$ and $Bo_{b_{VP}}$ profiles for $D = 8$ mm, $G = 1000$ kg/m^{2}s, $q = 250$ kW/m^2 . 321
C.78 $\overline{Bo_b}$ and $Bo_{b_{VP}}$ profiles for $D = 8$ mm, $G = 1000$ kg/m^{2}s, $q = 260$ kW/m^2 . 321

C.79 $\overline{Bo_b}$ and $Bo_{b_{VP}}$ profiles for $D = 8$ mm, $G = 1500$ kg/m^{2}s, $q = 380$ kW/m^2 . 322
C.80 $\overline{Bo_b}$ and $Bo_{b_{VP}}$ profiles for $D = 8$ mm, $G = 1500$ kg/m^{2}s, $q = 390$ kW/m^2 . 322
C.81 $\overline{Bo_b}$ and $Bo_{b_{VP}}$ profiles for $D = 8$ mm, $G = 1500$ kg/m^{2}s, $q = 400$ kW/m^2 . 323
C.82 $\overline{Bo_b}$ and $Bo_{b_{VP}}$ profiles for $D = 8$ mm, $G = 1500$ kg/m^{2}s, $q = 410$ kW/m^2 . 323
C.83 $\overline{Bo_b}$ and $Bo_{b_{VP}}$ profiles for $D = 8$ mm, $G = 1500$ kg/m^{2}s, $q = 420$ kW/m^2 . 324
C.84 $\overline{Bo_b}$ and $Bo_{b_{VP}}$ profiles for $D = 8$ mm, $G = 1500$ kg/m^{2}s, $q = 430$ kW/m^2 . 324
C.85 $\overline{Bo_b}$ and $Bo_{b_{VP}}$ profiles for $D = 8$ mm, $G = 1500$ kg/m^{2}s, $q = 440$ kW/m^2 . 325
C.86 $\overline{Bo_b}$ and $Bo_{b_{VP}}$ profiles for $D = 8$ mm, $G = 1500$ kg/m^{2}s, $q = 450$ kW/m^2 . 325
C.87 $\overline{Bo_b}$ and $Bo_{b_{VP}}$ profiles for $D = 22$ mm, $G = 200$ kg/m^{2}s, $q = 2$ kW/m^2 . . 326
C.88 $\overline{Bo_b}$ and $Bo_{b_{VP}}$ profiles for $D = 22$ mm, $G = 200$ kg/m^{2}s, $q = 3$ kW/m^2 . . 326
C.89 $\overline{Bo_b}$ and $Bo_{b_{VP}}$ profiles for $D = 22$ mm, $G = 200$ kg/m^{2}s, $q = 3.5$ kW/m^2 . 327
C.90 $\overline{Bo_b}$ and $Bo_{b_{VP}}$ profiles for $D = 22$ mm, $G = 200$ kg/m^{2}s, $q = 4$ kW/m^2 . . 327
C.91 $\overline{Bo_b}$ and $Bo_{b_{VP}}$ profiles for $D = 22$ mm, $G = 200$ kg/m^{2}s, $q = 5$ kW/m^2 . . 328
C.92 $\overline{Bo_b}$ and $Bo_{b_{VP}}$ profiles for $D = 22$ mm, $G = 200$ kg/m^{2}s, $q = 10$ kW/m^2 . . 328
C.93 $\overline{Bo_b}$ and $Bo_{b_{VP}}$ profiles for $D = 22$ mm, $G = 300$ kg/m^{2}s, $q = 10$ kW/m^2 . . 329
C.94 $\overline{Bo_b}$ and $Bo_{b_{VP}}$ profiles for $D = 22$ mm, $G = 300$ kg/m^{2}s, $q = 13$ kW/m^2 . . 329
C.95 $\overline{Bo_b}$ and $Bo_{b_{VP}}$ profiles for $D = 22$ mm, $G = 300$ kg/m^{2}s, $q = 15$ kW/m^2 . . 330
C.96 $\overline{Bo_b}$ and $Bo_{b_{VP}}$ profiles for $D = 22$ mm, $G = 300$ kg/m^{2}s, $q = 20$ kW/m^2 . . 330
C.97 $\overline{Bo_b}$ and $Bo_{b_{VP}}$ profiles for $D = 22$ mm, $G = 400$ kg/m^{2}s, $q = 23$ kW/m^2 . . 331
C.98 $\overline{Bo_b}$ and $Bo_{b_{VP}}$ profiles for $D = 22$ mm, $G = 400$ kg/m^{2}s, $q = 25$ kW/m^2 . . 331
C.99 $\overline{Bo_b}$ and $Bo_{b_{VP}}$ profiles for $D = 22$ mm, $G = 400$ kg/m^{2}s, $q = 28$ kW/m^2 . . 332
C.100 $\overline{Bo_b}$ and $Bo_{b_{VP}}$ profiles for $D = 22$ mm, $G = 400$ kg/m^{2}s, $q = 30$ kW/m^2 . . 332
C.101 $\overline{Bo_b}$ and $Bo_{b_{VP}}$ profiles for $D = 22$ mm, $G = 400$ kg/m^{2}s, $q = 35$ kW/m^2 . . 333
C.102 $\overline{Bo_b}$ and $Bo_{b_{VP}}$ profiles for $D = 22$ mm, $G = 500$ kg/m^{2}s, $q = 38$ kW/m^2 . . 333
C.103 $\overline{Bo_b}$ and $Bo_{b_{VP}}$ profiles for $D = 22$ mm, $G = 500$ kg/m^{2}s, $q = 40$ kW/m^2 . . 334
C.104 $\overline{Bo_b}$ and $Bo_{b_{VP}}$ profiles for $D = 22$ mm, $G = 500$ kg/m^{2}s, $q = 43$ kW/m^2 . . 334
C.105 $\overline{Bo_b}$ and $Bo_{b_{VP}}$ profiles for $D = 22$ mm, $G = 500$ kg/m^{2}s, $q = 45$ kW/m^2 . . 335
C.106 $\overline{Bo_b}$ and $Bo_{b_{VP}}$ profiles for $D = 22$ mm, $G = 500$ kg/m^{2}s, $q = 48$ kW/m^2 . . 335
C.107 $\overline{Bo_b}$ and $Bo_{b_{VP}}$ profiles for $D = 22$ mm, $G = 500$ kg/m^{2}s, $q = 50$ kW/m^2 . . 336
C.108 $\overline{Bo_b}$ and $Bo_{b_{VP}}$ profiles for $D = 22$ mm, $G = 600$ kg/m^{2}s, $q = 55$ kW/m^2 . . 336
C.109 $\overline{Bo_b}$ and $Bo_{b_{VP}}$ profiles for $D = 22$ mm, $G = 600$ kg/m^{2}s, $q = 58$ kW/m^2 . . 337

C.110 $\overline{Bo_b}$ and $Bo_{b_{VP}}$ profiles for $D = 22$ mm, $G = 600$ kg/m^{2}s, $q = 60$ kW/m^2 . . 337
C.111 $\overline{Bo_b}$ and $Bo_{b_{VP}}$ profiles for $D = 22$ mm, $G = 600$ kg/m^{2}s, $q = 65$ kW/m^2 . . 338
C.112 $\overline{Bo_b}$ and $Bo_{b_{VP}}$ profiles for $D = 22$ mm, $G = 600$ kg/m^{2}s, $q = 70$ kW/m^2 . . 338
C.113 $\overline{Bo_b}$ and $Bo_{b_{VP}}$ profiles for $D = 22$ mm, $G = 700$ kg/m^{2}s, $q = 70$ kW/m^2 . . 339
C.114 $\overline{Bo_b}$ and $Bo_{b_{VP}}$ profiles for $D = 22$ mm, $G = 700$ kg/m^{2}s, $q = 75$ kW/m^2 . . 339
C.115 $\overline{Bo_b}$ and $Bo_{b_{VP}}$ profiles for $D = 22$ mm, $G = 700$ kg/m^{2}s, $q = 78$ kW/m^2 . . 340
C.116 $\overline{Bo_b}$ and $Bo_{b_{VP}}$ profiles for $D = 22$ mm, $G = 700$ kg/m^{2}s, $q = 80$ kW/m^2 . . 340
C.117 $\overline{Bo_b}$ and $Bo_{b_{VP}}$ profiles for $D = 22$ mm, $G = 700$ kg/m^{2}s, $q = 83$ kW/m^2 . . 341
C.118 $\overline{Bo_b}$ and $Bo_{b_{VP}}$ profiles for $D = 22$ mm, $G = 700$ kg/m^{2}s, $q = 85$ kW/m^2 . . 341
C.119 $\overline{Bo_b}$ and $Bo_{b_{VP}}$ profiles for $D = 22$ mm, $G = 700$ kg/m^{2}s, $q = 90$ kW/m^2 . . 342

Nomenclature

A	area, m^2
Bo	buoyancy parameter
Bo^*	modified buoyancy parameter
C_p	specific heat, J/kgK
D	test section inner diameter, mm, m
e_Q	power imbalance error, %
E	internal energy, W
F_D	function of diameter
F_P	function of pressure
g	gravitational acceleration, m/s^2
G	mass flux, kg/m^2s
Gr	Grashof number
h	specific enthalpy, kJ/kg
HTC	heat transfer coefficient, W/m^2K
I	electric current, A
k	thermal conductivity, W/m°C
L	length, m
$\dot{m}$	mass flow rate, kg/s
M	molecular mass, g/mol
N	number of samples
Nu	Nusselt number

P	pressure, kPa, MPa
Pr	Prandtl number
q	heat flux, kW/m^2
q_{loss}	heat loss, W
Q	heating power, W
r	radius, m
R	electric resistance, Ω
Ra	Rayleigh number
Re	Reynolds number
t	time, s
T	temperature, °C, K
v	velocity, m/s
V	electric voltage, V
x	variable
z	axial location, m

Greek Letters

β	volumetric thermal expansion coefficient, K^{-1}
Δ	differential
μ	dynamic viscosity, kg/ms; arithmetic mean
ν	kinematic viscosity, m^2/s
ρ	density, kg/m^3
ρ_e	electrical resistivity, $\Omega \cdot$ m
σ	standard deviation

Subscripts

4.6	4.6 mm test section
8	8 mm test section
22	22 mm test section
ave	time averaged

b	bulk
B	buoyancy
c	critical
cs	cross section
DB	Dittus-Boelter
e	electric
exp	experimental
h	heated
hy	hydraulic
i	inner, index
in	inlet
max	maximum value
min	minimum value
NHT	normal heat transfer
o	outer
out	outlet
pc	pseudocritical
ref	reference
rms	root mean square
w	wall
VP	variable properties

Superscripts

V	volumetric
$*$	modified

Overbar

$\overline{}$	averaged over a temperature range

Abbreviations

AECL	Atomic Energy of Canada Limited
DAS	Data acquisition system
EG	Ethylene glycol
CO_2	Carbon dioxide
HE	Heat exchanger
HTD	Heat transfer deterioration
I.D.	Inner diameter
PT	Pressure transducer
RTD	Resistance temperature detector
SC	Supercritical
SCHT	Supercritical heat transfer
SCUOL	Supercritical University of Ottawa Loop
SCWR	Supercritical water-cooled reactor
V	valve
Vt	vent

Chapter 1

Introduction

1.1 Background

Advanced designs of nuclear power plants are being considered for future development. The main design goals for Generation IV nuclear reactor concepts are to improve economics, enhance safety, extend sustainability, and strengthen proliferation resistance (Aksan et al., 2014). A large number of potential designs were developed as a result of the Generation IV initiative and among them, six concepts were selected. The only concept among the chosen six that have evolved from the current generation of water cooled reactors is the supercritical water cooled reactor (SCWR). Two of the main advantages for using supercritical water in nuclear reactors are the increased efficiency and decreased costs which are achieved by the simplification of plant components, systems, and layout (i.e., eliminating heat exchangers, steam generators, steam dryers, and moisture separator reheaters). There is, however, a need for qualified experimental data on the heat transfer characteristics for supercritical fluid flow in rod bundles and straight pipes to be used in support of the safety analyses for SCWRs.

Atomic Energy of Canada (AECL) is designing the Canadian SCWR concept, which has evolved from the well-established pressure tube type CANDU reactor. The Canadian SCWR is designed to produce electricity as the main product, but it is also designed to produce process heat, hydrogen, industrial isotopes, and drinking water (through desalination processes) as supplementary products (Aksan et al., 2014). A national program has been established in Canada to support R&D studies for the Canadian SCWR design and covers key areas

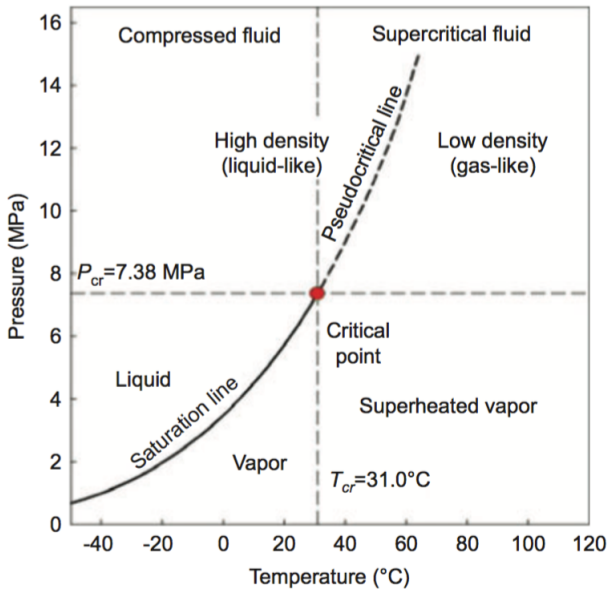


Figure 1.1: Pressure-temperature diagram for CO_2 (Pioro et al., 2011).

of interest (including thermalhydraulics, safety, materials, and chemistry) to participants in the Generation-IV SCWR designs. The supercritical heat transfer research group at the University of Ottawa, which is supported by this program, focuses on a range of thermohydraulics topics, including heat transfer, turbulence and the construction of a look-up table. The Supercritical University of Ottawa Loop (SCUOL), a state-of-the-art facility designed and constructed by the group, was used to collect the data used for the present thesis. The results and discussions from the analysis of these experiments can be found in later chapters.

1.2 Heat transfer to supercritical fluids

At supercritical pressures, a fluid does not undergo phase change with a change in temperature, even though its thermophysical properties change significantly near the pseudocritical line, which is the locus of points with temperatures corresponding to the maximum value of the specific heat. The pseudocritical line for CO_2 is shown in Fig. 1.1, whereas corresponding changes of density, thermal conductivity, specific heat, and viscosity at a fixed supercritical pressure are shown in Fig. 1.2.

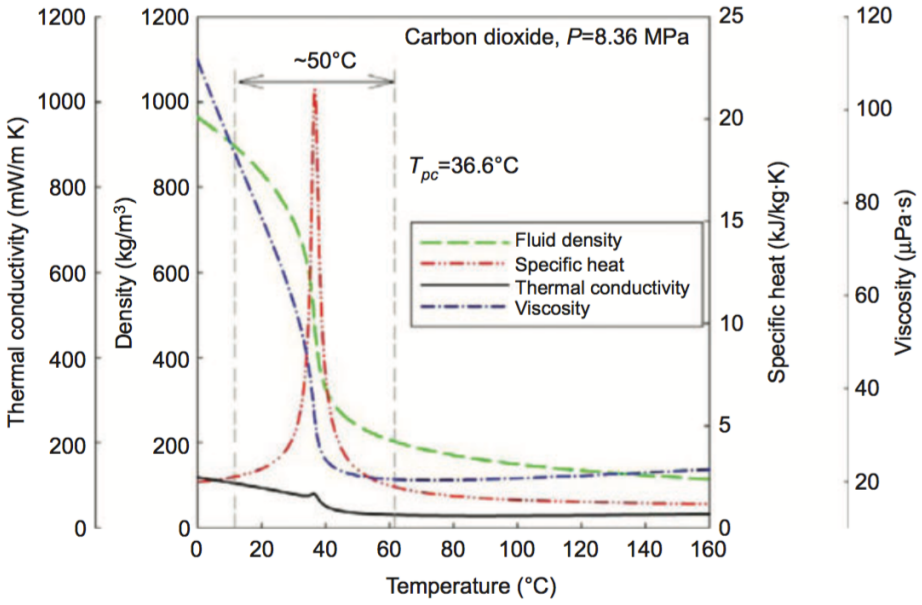


Figure 1.2: Changes of thermophysical properties of CO_2 with increasing temperature at $P = 8.36$ MPa (Pioro et al., 2011).

In general, crossing the pseudocritical line from left to right is quite similar to crossing the saturation line from liquid to vapour. However, changes in thermophysical properties near the pseudocritical temperature are gradual, whereas such changes across the saturation temperature are abrupt. Therefore, supercritical fluids behave as single-phase substances, although they may be distinguished into liquid-like and gas-like fluids, depending on whether their temperature is lower or higher than the pseudocritical value.

In general, three major heat transfer regimes have been observed at supercritical pressures:

1. Normal heat transfer
2. Enhanced heat transfer
3. Deteriorated heat transfer.

Heat transfer deterioration (HTD) is commonly detected by the presence of localized wall temperature spikes, in contrast to the monotonically rising wall temperatures along the test

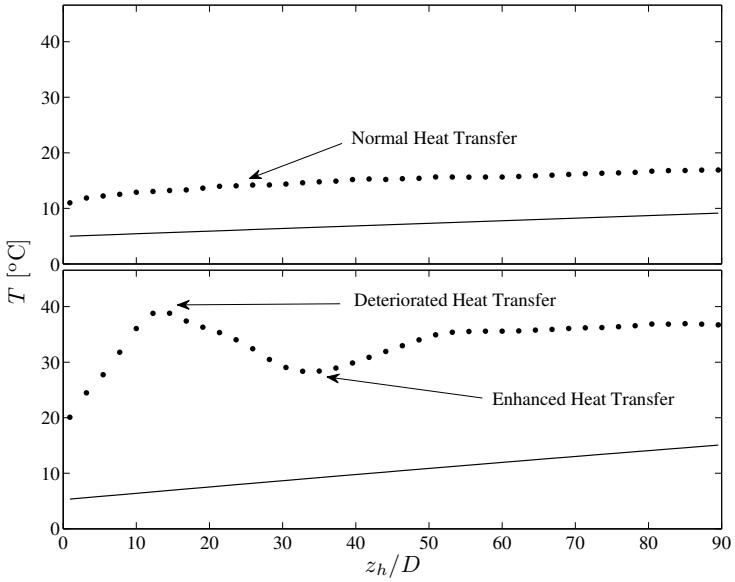


Figure 1.3: Wall temperature profiles along a heated tube showing normal, enhanced, and deteriorated heat transfer; solid line represents the bulk temperature.

section that characterize the normal heat transfer regime. HTD usually occurs in tubes at relatively large wall heat fluxes and relatively low mass fluxes. Early experiments by Jackson and Hall (1978) demonstrated that localized temperature spikes appeared under certain conditions only in upward and not in downward flows under the same conditions, which led to the hypothesis that buoyancy forces were playing a role. Later experiments at high heat fluxes showed, however, that temperature spikes occurred in both upward and downward flows, which led to a second hypothesis that flow acceleration rather than buoyancy forces was causing this phenomenon to occur (Jackson, 2013). Enhanced heat transfer is commonly detected by the presence of localized wall temperature drops and often occurs immediately downstream of a wall temperature spike. Examples of the three supercritical heat transfer (SCHT) regimes are presented in Fig. 1.3.

1.3 Motivation and objectives

One of the most important requirements for accurate operation and safety analyses of future supercritical nuclear power plants is an understanding and a predictive ability of the deteriorated heat transfer regime, because of the adverse effects HTD can have on reactor efficiency and safety. Results from heat transfer experiments using fluids at supercritical pressures in vertical passages have shown, that, under certain conditions, unusual behaviour can occur at locations where heat transfer is severely deteriorated. This unusual behaviour manifests itself in the form of sharp or broad temperature spikes at various locations along the heated channel for upward, downward, or even horizontal flows. This phenomenon was first observed in the 1960s but a reliable method for its prediction has yet to be established.

The main objectives of this thesis are to collect and analyse heat transfer measurements in three vertical tubular test sections (I.D. = 4.6, 8, and 22 mm) at heating and flow conditions near those at the onset of HTD. Moreover, the results of these tests will be compared to published analyses in an effort to improve HTD detection methods and HTD onset correlations.

1.4 Plan of thesis

This thesis is organized into six chapters. Chapter 1 provides a description of the SCWR concept and some background information on heat transfer to fluids at supercritical pressures. The motivations and objectives of this work are also described in this chapter. Chapter 2 contains a literature review on different methods of identifying heat transfer deterioration used by past researchers. The literature review also summarizes previous research work concerning the onset of heat transfer deterioration. Chapter 3 describes the Supercritical University of Ottawa Loop, on which the experiments were performed. Information about the test sections used and the accompanying instrumentation are also presented. Chapter 4 provides a detailed description of the measurement procedures and the calculations carried out for data analyses. Chapter 5 is an extensive chapter presenting and discussing the results obtained from the experiments and the analyses performed, including comparisons to the literature when possible. A complete collection of plots which display the entire data set

and plots displaying the results of the various analyses performed are included at the end of corresponding section. Chapter 6 is the concluding chapter where all of the findings of this study are summarized and recommendations for future work are outlined.

Chapter 2

Literature review

2.1 Detection methods of heat transfer deterioration

2.1.1 The occurrence of wall temperature spikes

The vast majority of authors have detected heat transfer deterioration by observing the occurrence of wall temperature spikes along the test section. Many qualitative observations have been documented, which categorize these temperature spikes by describing them as sharp peaks or broad peaks and also in terms of whether they occurred near the heated test section inlet or far downstream from it. Although this definition applies to most HTD cases observed, it does not include cases in which the temperature spike was very broad, or even spanned the entire test section. Moreover, there is no established criterion for the amplitude of a spike that is appropriate for the heat transfer to be classified as deteriorated.

Some early observations by Goldman (1961) on water at supercritical pressures identified two distinct heat transfer modes, one of which (the "unusual" mode) showed temperature spikes near the end of the test section. In addition, the observed temperature spikes were accompanied by a distinct "whistling" noise coming from the tube, which was similar to noises commonly heard during boiling at subcritical pressures. Heat transfer impairment was described by Shitsman (1963) as temperature "jumps" in the temperature profile and it was observed that these jumps would occur at bulk enthalpies larger than 1630 kJ/kg for water at supercritical pressures. Ackerman (1970) described an unpredictable heat transfer

mode occurring when the wall temperature peaked while the pseudo-critical temperature was between the bulk and the wall temperatures. There were a number of works (Glushchenko et al., 1972; Yamagata et al., 1972; Grabezhnaya and Kirillov, 2006), which defined HTD as temperature spikes in the temperature profile and then used this information to establish a heat flux limit as a function of the mass flux in order to predict the onset of HTD. Protopopov and Sharma (1976) performed an investigation using carbon dioxide at supercritical pressures and observed local temperature spikes, which they related to the Rayleigh number. Yamashita et al. (2003) performed experiments on heat transfer and pressure drop of HCFC22 at supercritical pressures and defined HTD by the presence of temperature spikes; they observed that broad peaks formed over a wide range of bulk fluid enthalpies below the pseudocritical point and sharp peaks formed at lower flow rates. Papers by Song et al. (2008) and Kim et al. (2007) explored the criterion on the similarity of heat transfer of supercritical fluid flows in tubes with different diameters and also defined HTD by observing spikes in the temperature profile. A recent article by Kurganov et al. (2012) identified six different categories of heat transfer deterioration, based on various observations which took into consideration the shapes of the peaks, the position of the peaks along the test section, the effect of heat flux on the position of the peaks, and the occurrence of the peaks in terms of the inlet enthalpy value with respect to the pseudocritical enthalpy value. Each of the six groups was assigned a number from one to six and these were related to a potential parameter describing the effect of Archimedes forces, which could be used to predict the onset of heat transfer deterioration. The same authors mentioned that each category would occur when the heating load, defined as q/G, reached a certain value, but did not specify these values.

2.1.2 Normalized heat transfer coefficient

Another common method for defining heat transfer deterioration is with the use of a normalised heat transfer coefficient $HTC_{experimental}/HTC_{predicted}$ or a normalised Nusselt number $\mathrm{Nu}_{experimental}/\mathrm{Nu}_{predicted}$, where $HTC_{predicted}$ and $\mathrm{Nu}_{predicted}$ are the predictions of a trusted correlation for heat transfer under non-deteriorated conditions. Early work by Shiralkar and Griffith (1969) developed a safe versus unsafe plot in terms of the mass flux and

the "allowable" heat flux for supercritical carbon dioxide flowing upward and downward in vertical tubes. The allowable heat flux was such that the ratio of $\mathrm{Nu}_{experimental}/\mathrm{Nu}_{predicted}$ (see Table 2.1) was not less than the prescribed value of 0.5. Heat transfer to supercritical helium flowing in a vertical tube was investigated by Giarratano and Jones (1975), who defined HTD by normalizing the heat transfer coefficient using a Dittus-Boelter type correlation containing an additional parameter defined as the ratio between the wall and bulk temperatures (see Table 2.1). There was no specific value given to the normalized heat transfer coefficient to define HTD, but this value was compared to a non-dimensional parameter which divided the heat per unit mass by the difference in pseudocritical and inlet enthalpies. Observations were made for conditions which produced $HTC_{experimental}/HTC_{predicted} < 1$, thus indicating a deteriorated heat transfer mode. Schatte et al. (2016) examined data from 14 independent references, using water as the cooling fluid, and determined that $HTC_{experimental}/HTC_{predicted} < 0.3$ was the most frequently used method for defining HTD.

2.1.3 Buoyancy parameter

In an early work, Hall and Jackson (1969) postulated that the localized HTD to fluids flowing upward in heated pipes was due to the reduction of the level of shear stress in the wall layer region caused by fluid buoyancy, which led to a diminution of the turbulence production component and to impaired diffusion of heat by turbulent actions. It was suggested that the laminarisation process depended on the value of the group $\frac{\mathrm{Gr}'}{\mathrm{Re}^{2.7}}\left(\frac{\nu_w}{\nu_b}\right)^3\left(\frac{\rho_w}{\rho_b}\right)^{0.5}$, where $\mathrm{Gr}' = \left(\frac{\rho_b-\rho_w}{\rho_w}\right)\frac{gD^3}{\nu_w^2}$, and would occur when this group had a value of about 10^{-4}. Alferov et al. (1969) stated that under certain conditions heat transfer in heated vertical tubes was governed not only by the mechanism of forced convective turbulent heat transfer, but also by the influence of gravitational forces governing free convection. Tests were carried out using water at supercritical pressures and it was confirmed that, when $HTC_{forced}/HTC_{free} > 2.5-3$ (see Table 2.1 for definitions), free convection did not cause an appreciable deterioration of the heat transfer coefficient. Jackson and Hall (1978) later stated that these findings were in agreement with their modified criterion for the onset of buoyancy effects, defined as

$$\overline{Bo}_b = \frac{\overline{\mathrm{Gr}}_b}{\mathrm{Re}_b^{2.7}\mathrm{Pr}_b^{0.5}} \quad , \tag{2.1}$$

where

$$\overline{\mathrm{Gr}}_b = \frac{(\rho_b - \overline{\rho})gD^3}{\rho_b \nu_b^2} \quad , \tag{2.2}$$

and the integrated density calculated as $\overline{\rho} = \frac{1}{(T_w - T_b)} \int_{T_b}^{T_w} \rho_b \, dT$. Jackson and Hall (1978) suggested that $\overline{Bo}_b \geq 10^{-5}$ for a reduction of HTC to be greater than 5%, which was verified by identifying HTD using $\mathrm{Nu}_{experimental}/\mathrm{Nu}_{predicted} < 1$ (see Table 2.1). Polyakov (1975) examined the effect of thermogravitational forces and local acceleration of flow due to a change in the density on turbulent momentum transfer at supercritical coolant using available experimental data on the local impairment of heat transfer in the case of the flow of water, carbon dioxide, and helium. Based on observed temperature spikes, the suggested parameter was tested and was deemed to describe well the limits of the local impairment of the heat transfer in all cases examined (see Table 2.1). Watts and Chou (1982) tested $\overline{Bo}_b$ using experimental results from flowing water in vertical heated tubes. It was concluded, from observed temperature spikes, that the heat transfer was affected by buoyancy when $\overline{Bo}_b \geq 10^{-5}$, which was in agreement with Jackson and Hall (1978). Bae et al. (2010) carried out experiments of heat transfer to carbon dioxide flowing upward and downward in a vertical tube and determined that HTD occurs when $\overline{Bo}_b = \frac{\overline{\mathrm{Gr}}_b}{\mathrm{Re}_b^{2.7}} \geq 2 \times 10^{-5}$. This criterion was verified by identifying HTD using $Nu_{experimental}/Nu_{predicted} < 1$ (see Table 2.1). In a more recent work, Jackson (2013) revised the buoyancy criterion and suggested a number of correction factors which better described the effect of buoyancy on heat transfer in the presence of significant non-uniformity of fluid properties as

$$Bo_{b_{VP}} = C_B Bo_b F_{VP_1} F_{VP_2} F_{VP_3}, \tag{2.3}$$

where $F_{VP_1} = \left(\frac{\overline{\mu}}{\mu_b}\right)\left(\frac{\overline{\rho}}{\rho_b}\right)^{-0.5}$, $F_{VP_2} = \left(\frac{\overline{\mathrm{Pr}}}{\mathrm{Pr}_b}\right)^{-0.4}$, $F_{VP_3} = \frac{(\rho_b - \overline{\rho})}{(\rho_b - \rho_w)}$, and $C_B = 4600$. The buoyancy parameter Bo_b was also changed slightly to

$$Bo_b = \frac{\mathrm{Gr}_b}{\mathrm{Re}_b^{2.7}\mathrm{Pr}_b^{0.4}} \quad , \tag{2.4}$$

where

$$\mathrm{Gr}_b = \frac{(\rho_b - \rho_w)gD^3}{\rho_b \nu_b^2} \quad . \tag{2.5}$$

It was suggested that when $Bo_{b_{VP}} \geq 0.04$, the effect of buoyancy on heat transfer should be greater than 5%. This criterion was verified by detecting HTD using $\mathrm{Nu}_{experimental}/\mathrm{Nu}_{predicted} < 1$ (see Table 2.1).

2.1.4 Summary

In order to attempt to establish a reliable correlation for predicting the onset of the heat transfer deterioration at supercritical pressures, one must first establish a reliable detection method. The most common methods used by the authors discussed in the previous section can be found in Table 2.1.

Table 2.1: A summary of HTD detection methods for heat transfer to fluids at supercritical pressures

Author(s)	**Fluid**	P/P_{cr}	q [kW/m^2]	G [kg/m^{2}s]	D [mm]	**HTD Detection Methods**
Goldman (1961)	Water	1.56	315 - 946	2034 - 5425	1.27 & 1.91	Observed temperature spikes
Shitsman (1963)	Water	1.06 - 1.15	≤ 1163	300 - 1500	10	Observed temperature spikes
Vikrev and Lokshin (1964)	Water	1.02 - 1.33	349 - 699	400 - 1000	10	Observed temperature spikes
Hall and Jackson (1969)	CO_2	1.03	34 - 455	148 - 4304	5 & 8	$\frac{\mathrm{Gr}'}{\mathrm{Re}^{2.7}}\left(\frac{\nu_w}{\nu_b}\right)^3\left(\frac{\rho_w}{\rho_b}\right)^{0.5} \geq 10^{-4}$, where $\mathrm{Gr}' = \left(\frac{\rho_b-\rho_w}{\rho_w}\right)\frac{gD^3}{\nu_w^2}$
Alferov et al. (1969)	Water	0.69 - 1.38	174 - 698	250 -1000	14 & 20	$\left(\frac{HTC_{forced}}{HTC_{free}}\right)_{in} \leq 1.6$ where $HTC_{forced} = 0.023\left(\frac{k_b}{D}\right)\mathrm{Re}_b^{0.8}\mathrm{Pr}_b^{0.4}$, $HTC_{free} = 0.135\frac{\overline{k_b}}{D}(\overline{\mathrm{Gr}}_b^*\overline{\mathrm{Pr}}_b)^{1/3}$, $\overline{\mathrm{Gr}}_b^* = \frac{\overline{\beta_b} g D^3}{\overline{\nu_b}^2}(T_w - T_{in})$, $T_w \approx T_{in} + \frac{q}{(HTC_{forced})_{in}}$

Table 2.1: A summary of HTD detection methods for heat transfer to fluids at supercritical pressures (Cont'd)

Author(s)	**Fluid**	P/P_{cr}	q [$\mathbf{kW/m^2}$]	G [$\mathbf{kg/m^2s}$]	D [mm]	**HTD Detection Methods**
Bourke et al. (1970); Bourke and Pulling (1972)	CO_2	1.01 - 1.40	8 - 350	311 - 1654	22.8	Observed temperature spikes. Velocity profiles were also measured using hot-wires, but only plots were generated with no quantitative relations to deterioration
Shiralkar and Griffith (1970)	CO_2	1.03 - 1.40	5 - 454	1288 - 4069	3.18 & 6.35	$\frac{\mathrm{Nu}_{experimental}}{\mathrm{Nu}_{predicted}} < 0.5$ where $\mathrm{Nu}_{predicted} = 0.023\mathrm{Re}_b^{0.8}\mathrm{Pr}_b^{0.4}$
Ackerman (1970)	Water	1.03 - 1.87	126 - 1735	135 - 2170	9.4 - 24.4	Observed temperature spikes
Glushchenko et al. (1972)	Water	1.02 - 1.33	≤ 3000	500 - 3000	3 - 8	Observed temperature spikes
Yamagata et al. (1972)	Water	1.02 - 1.33	116 - 930	310 - 1830	10	Observed temperature spikes

Table 2.1: A summary of HTD detection methods for heat transfer to fluids at supercritical pressures (Cont'd)

Author(s)	**Fluid**	$\boldsymbol{P/P_{cr}}$	$\boldsymbol{q}$ **[kW/m²]**	$\boldsymbol{G}$ **[kg/m²s]**	$\boldsymbol{D}$ **[mm]**	**HTD Detection Methods**
Giarratano and Jones (1975)	Helium	1.11	0.08 - 7.13	70 - 220	2.13	$\frac{HTC_{experimental}}{HTC_{predicted}} < 1$ where $HTC_{predicted} = 0.0259\left(\frac{T_b}{T_w}\right)^{0.716}\frac{G^{0.8}}{D^{0.2}}k^{0.6}\frac{C_{p_b}^{0.4}}{\mu_b^{0.4}}$ OR $\frac{4zq''}{(h_{pc}-h_{in})GD} > 0.3$
Polyakov (1975)	Water, CO_2, and Helium	> 1	n.a.	n.a.	n.a.	$\frac{(J\pm\overline{\mathrm{Gr}}_b^*)}{\Phi} \leq 5$ where $\overline{\mathrm{Gr}}_b^* = \frac{g\overline{\beta}qD^4}{k_b\nu_b^2}$ $J = \frac{4\mathrm{Re}_b}{\overline{\mathrm{Pr}}}\left(\frac{qD}{k_b}\overline{\beta}\frac{\rho_b}{\overline{\rho}}\right)^2$ $\Phi = 10^{-4}\overline{\mathrm{Pr}}\mathrm{Re}_b^{2.8}\frac{\mathrm{Re}_b^{0.1}+1.8(\overline{\mathrm{Pr}}^{2/3}-1)}{log(\mathrm{Re}_b)+1.15log(1+5\overline{\mathrm{Pr}})+0.5\overline{\mathrm{Pr}}-1.8}$ $\overline{\rho}$ is evaluated using $T = \frac{(T_w+T_b)}{2}$ $\overline{\beta} = (1/\overline{\rho})(\rho_b - \rho_w)(T_w - T_b)$ $\overline{\mathrm{Pr}} = \frac{(h_w-h_b)}{(T_w-T_b)}\left(\frac{\mu_b}{k_b}\right)$

Table 2.1: A summary of HTD detection methods for heat transfer to fluids at supercritical pressures (Cont'd)

Author(s)	**Fluid**	P/P_{cr}	q [kW/m^2]	G [kg/m^{2}s]	D [mm]	**HTD Detection Methods**
Protopopov and Sharma (1976)	CO_2	1.02 - 1.36	3.5 - 110	Only expressed in terms of Ra = 1×10^7 – 1.4×10^{15}	8.18 & 19.6	Observed temperature spikes and some observations in terms of the Rayleigh number: $\mathrm{Ra}_b \approx 10^{10} - 5\times10^{10}$ for $T_b < T_{pc}$ at low heat flux $\mathrm{Ra}_b \approx 10^9$ for $T_b < T_{pc}$ at high heat flux $\mathrm{Ra}_b \approx 5\times10^8 - 5\times10^{10}$ for $T_b \geq T_{pc}$
Jackson and Hall (1978)	CO_2	0.99 - 1.03	2.56 - 455	205 - 3245	5 - 19	$\overline{Bo}_b = \frac{\overline{\mathrm{Gr}}_b}{\mathrm{Re}_b^{2.7}\mathrm{Pr}_b^{0.5}} > 10^{-5}$ where $\overline{Gr}_b = \frac{(\rho_b-\overline{\rho})gD^3}{\rho_b\nu_b^2}$ $\overline{Bo}_b$ was verified using $\mathrm{Nu}_{experimental}/\mathrm{Nu}_{predicte} < 1$ where $\mathrm{Nu}_{predicted} = 0.0183\mathrm{Re}_b^{0.82}\mathrm{Pr}_b^{0.5}$
Watts and Chou (1982)	Water	1.13	175 - 440	106 - 1060	25.4 & 32.2	$\frac{\overline{\mathrm{Gr}}_b}{\mathrm{Re}_b^{2.7}\overline{\mathrm{Pr}}_b^{0.5}} > 10^{-5}$ where $\overline{\mathrm{Gr}}_b = \frac{(\rho_b-\overline{\rho})gD^3}{\rho_b\nu_b^2}$

Table 2.1: A summary of HTD detection methods for heat transfer to fluids at supercritical pressures (Cont'd)

Author(s)	**Fluid**	P/P_{cr}	q [$\mathbf{kW/m^2}$]	G [$\mathbf{kg/m^2s}$]	D [mm]	**HTD Detection Methods**
Yamashita et al. (2003)	HCFC22	1.1	10 - 170	400 - 2000	4.4 - 13	Observed temperature spikes in relation to estimated frictional pressure drop across heated test section. Only qualitative observations were provided due to large error estimates for pressure drop.
Grabezhnaya and Kirillov (2006)	Water and CO_2	1.02 - 1.55	290 - 4830	400 - 2500	2 - 20	Observed temperature spikes
Song et al. (2008)	CO_2	1.1	30 & 50	400 & 1200	4.4 & 9	Observed temperature spikes
Kim et al. (2008)	CO_2	1.1	30 & 50	400 & 1200	4.4 & 9	Observed temperature spikes

Table 2.1: A summary of HTD detection methods for heat transfer to fluids at supercritical pressures (Cont'd)

Author(s)	**Fluid**	P/P_{cr}	q [kW/m^2]	G [kg/m^{2}s]	D [mm]	**HTD Detection Methods**
Bae et al. (2010)	CO_2	1.05 & 1.1	30 - 170	285 - 1200	6.32	$\overline{Bo}_b = \frac{\overline{\mathrm{Gr}}_b}{\mathrm{Re}_b^{2.7}} > 2 \times 10^{-5}$ where $\overline{\mathrm{Gr}}_b = \frac{\rho_b(\rho_b - \overline{\rho})gD^3}{\mu_b^2}$ $\overline{Bo}_b$ was verified using $\frac{\mathrm{Nu}_{experimental}}{\mathrm{Nu}_{predicted}} < 1$ where $\mathrm{Nu}_{predicted} = 0.021\mathrm{Re}_b^{0.8}\mathrm{Pr}_b^{0.5}\left(\frac{\rho_w}{\rho_b}\right)^{0.3}\left(\frac{\overline{C_p}}{C_{p_b}}\right)^n$
Kurganov et al. (2012, 2016)	> 1	n.a.	n.a.	n.a.	n.a.	Observed temperature spikes

Table 2.1: A summary of HTD detection methods for heat transfer to fluids at supercritical pressures (Cont'd)

Author(s)	**Fluid**	$\boldsymbol{P/P_{cr}}$	$\boldsymbol{q}$ **[kW/m²]**	$\boldsymbol{G}$ **[kg/m²s]**	$\boldsymbol{D}$ **[mm]**	**HTD Detection Methods**
Jackson (2013, 2015)	CO_2	0.99 - 1.03	2.56 - 455	205 - 3245	5 - 19	$Bo_{VP} = C_B Bo_b F_{VP1} F_{VP2} F_{VP3} > 0.04$ where $C_B = 4600$ $Bo_b = \frac{\mathrm{Gr}_b}{\mathrm{Re}_b^{2.625}\mathrm{Pr}_b^{0.4}}$, $\mathrm{Gr}_b = \frac{(\rho_b - \rho_w) g D^3}{\rho_b \nu_b^2}$ $F_{VP1} = \left(\frac{\overline{\mu}}{\mu_b}\right)\left(\frac{\overline{\rho}}{\rho_b}\right)^{-0.5}$ $F_{VP2} = \left(\frac{\overline{\mathrm{Pr}}}{\mathrm{Pr}_b}\right)^{-0.4}$ $F_{VP3} = \frac{(\rho_b - \overline{\rho})}{(\rho_b - \rho_w)}$ Bo_{VP} was verified using $\mathrm{Nu}_{experimental}/\mathrm{Nu}_{predicted} < 1$ where $\mathrm{Nu}_{predicted} = 0.0183\mathrm{Re}_b^{0.82}\mathrm{Pr}_b^{0.5}\left(\frac{\rho_w}{\rho_b}\right)^{0.3}$
Schatte et al. (2016)	Water	1.02 - 1.36	166 - 1650	200 - 2000	7.6 - 38	$HTC_{experimental}/HTC_{predicted} < 0.3$ where $HTC_{predicted} = \left(\frac{k_b}{D}\right) 0.023\mathrm{Re}_b^{0.8}\mathrm{Pr}_b^{0.4}$

2.2 Predicting the onset of HTD

2.2.1 Heat flux at HTD onset as a function of mass flux

Numerous studies have proposed correlations for the prediction of the heat flux q_{onset} that corresponds to the onset of HTD. Most of the correlations define q_{onset} as a power function of mass flux G, namely as $q_{onset} = mG^n$. Although there seems to be much agreement that power laws provide good estimates, different authors have suggested different values for the coefficient m and exponent n for various fluids and channel shapes. Other variations of this correlation defined the relationship between q_{onset} and G as a linear function or multiplied the power function by parameters which depended on the tube diameter and the pressure.

Early heat transfer experiments using water flowing upward in a heated vertical tube were performed by Vikhrev et al. (1967); in these experiments, temperature spikes were produced in various locations along the test section. It was proposed that one should distinguish between two types of HDT, with the first appearing in the initial tube section and the second appearing at any section of the tube, but within a certain enthalpy region. Vikhrev et al. (1967) suggested that the occurrence of both of these types of deteriorated heat transfer is caused by relatively high heat fluxes, so that $q > 0.4G$. Yamagata et al. (1972) also described a limit heat flux above which HTD occurs to vertically flowing water at supercritical pressures. Although it was observed that the limit heat flux increased somewhat with an increase in pressure, the limit heat flux could be related to the mass flux as $q_{onset} = 0.2G^{1.2}$. Glushchenko et al. (1972) performed experiments with water flowing upward and downward in heated vertical tubes with four different inner diameters and one annular channel at supercritical pressures. It was found that the influence of the main operational parameters on the conditions of occurrence of HTD in tubes with different diameters and annular channels to be mainly the same at $q/G > 0.5-1.0$, where the lower values refer to higher temperatures at the inlet. Cheng et al. (2009) analyzed the onset of HTD for supercritical water using existing data from the literature and proposed a correction factor accounting for the effect of pressure. The resulting correlation $q = 1.354 \times 10^{-3} \left(\frac{C_{p,pc}}{\beta_{pc}}\right) G$ was found to agree well with the Yamagata et al. (1972) correlation with additional variation due to the effect of pressure by raising the onset limit as the pressure increased. In an article by Mokry et al. (2011), an analysis of heat transfer to supercritical water in bare vertical tubes was performed using

a large set of experimental data obtained from Russia. As part of the study, an empirical correlation, defined as $q_{onset} = -58.97 + 0.745G$, was proposed for calculating the minimum heat flux at which the HTD appears. It became evident to Schatte et al. (2016) that there was room for the development of a more accurate correlation for predicting the heat flux to water flowing in tubes at supercritical pressures causing the onset of HTD. It was made a requirement that the correlation should contain all relevant design parameters, including pressure, inner diameter and mass flux. The suggested correlation was $q_{onset} = mF_DF_PG^n$, where $m = 1.942 \times 10^{-6}$, $n = 0.795$, $F_D = (30 - D)^{0.339}$, and $F_P = \left(\frac{C_{p,pc}}{\beta_{pc}}\right)^{2.065}$.

Grabezhnaya and Kirillov (2006) analyzed and compared the heat transfer deterioration boundary using experimental data obtained for different coolants, including water, carbon dioxide and Refrigerant 12 (R12). It was determined that the best agreement with the data for determining the onset of HTD for water in tubes was $q_{onset} = 0.6G$. It was also found that the boundary of the onset for CO_2 was considerably lower for specific enthalpies between 0.2 and 0.3 kJ/kg. Even smaller values were determined for R12 at specific enthalpies below 0.1 kJ/kg. Grabezhnaya and Kirillov (2006) analyzed the effect of molecular masses of coolants on the relations determining the onset of deteriorated heat transfer by substituting the reduced value of the heat flux as $q_{reduced} = \frac{M}{M_{H_2O}}q$, where M and M_{H_2O} represent the molar mass of the coolant and water respectively, for the experimental value of the heat flux. It was concluded that the lower boundary of the regimes with deteriorated heat transfer for the coolants could be defined by $q_{onset} = 0.6\frac{M_{H_2O}}{M}G$. Bae et al. (2010) performed supercritical heat transfer experiments using CO_2 as a coolant for upward and downward flows in a circular tube. After testing four different criteria for the onset of HTD, it was determined that a criterion based on water cannot be applied directly to other fluids. Bae et al. (2010) tested the criterion proposed by Grabezhnaya and Kirillov (2006) and concluded that this generalized criterion overestimated the boundary of onset and that the onset heat flux for upward flowing CO_2 in tubes is best predicted using $q_{onset} = 2 \times 10^{-4}G^{2.0}$.

2.2.2 Buoyancy parameter

A buoyancy parameter that contains only bulk fluid properties and not properties at wall temperature would potentially be suitable as a criterion for predicting HTD onset conditions.

Such a buoyancy parameter is defined as

$$Bo_b^* = \frac{\mathrm{Gr_b^*}}{\mathrm{Re}_b^{3.425}\mathrm{Pr}_b^{0.8}}, \tag{2.6}$$

where

$$\mathrm{Gr}_b^* = \frac{g\beta_b D^4 q}{k_b \nu_b^2}, \tag{2.7}$$

and

$$\mathrm{Re}_b = \frac{GD}{\mu_b}. \tag{2.8}$$

In an article by Jackson et al. (1989), the buoyancy parameter Bo_b^* was considered for predicting the onset of HTD in vertical pipe flows of water and air at atmospheric pressure. It was determined that the value $Bo_b^* \approx 6\times10^{-6}$ was a fair estimate of a lower threshold for HTD in vertical circular tubes. McEligot and Jackson (2004) extended this HTD onset criterion for convective heat transfer to gas flows through non-circular ducts. It was determined that the values of Bo_b^* for HTD onset conditions in circular tubes, annuli, and annular ducts would be different, however, it was confirmed that the value $Bo_b^* \approx 6 \times 10^{-6}$ was a good approximation for circular tubes. Li et al. (2010) performed an experimental investigation of convection heat transfer of CO_2 at supercritical pressures in a vertical tube. The buoyancy parameter Bo_b^* was tested and it was found that, for upward flow, the heat transfer rate decreased with increasing buoyancy parameter in the range $2 \times 10^{-7} < Bo_b^* < 6 \times 10^{-7}$, followed by recovery of the heat transfer for $6 \times 10^{-7} < Bo_b^* < 2 \times 10^{-5}$ and improved heat transfer for $Bo_b^* > 2 \times 10^{-5}$.

2.2.3 Summary

As shown in Table 2.2, most onset correlations define q_{onset} as a function of G in the form of a power law with coefficients and exponents that differ from one research study to another. The coefficients and exponents seem to differ the most between experimental data using different cooling fluids, whereas there is good agreement between authors for each fluid. A number of authors also introduced correction factors to the power law function in an effort to account for the effects of pressure, tube diameter, and fluid type (see Table 2.2).

The Bo_b^* parameter was also used to provide an estimate for conditions which would cause the onset of HTD. As can be seen in Table 2.2, there is a range of threshold values suggested in the literature.

Table 2.2: A summary of HTD onset correlations for fluids at supercritical pressures

Author(s)	**Fluid**	P/P_{cr}	q [kW/m^2]	G [kg/m^{2}s]	D [mm]	**HTD Onset Correlations**
Vikhrev et al. (1967)	Water	1.11	565 - 630	485 - 510	7.85	$q_{onset} = 0.4G$
Glushchenko et al. (1972)	Water	1.02 - 1.33	≤ 3000	500 - 3000	3 - 8	$q_{onset} = mG$ where $m = 0.5 - 1.0$ note: $m = 0.5$ for low inlet temperatures
Yamagata et al. (1972)	Water	1.02 - 1.33	116 - 930	310 - 1830	10	$q_{onset} = 0.2G^{1.2}$
Jackson et al. (1989), McEligot and Jackson (2004)	Water and Air	Atm.	n.a.	n.a.	n.a.	$Bo_b^* > 6 \times 10^{-6}$ where $Bo_b^* = \frac{\mathrm{Gr}_b^*}{\mathrm{Re}^{3.425}\mathrm{Pr}_b^{0.8}}$ $\mathrm{Gr}_b^* = \frac{g\beta_b D^4 q}{k_b \nu_b^2}$
Grabezhnaya and Kirillov (2006)	Water, CO_2, and R-12	1.02 - 1.55	290 - 4830	400 - 2500	2 - 20	$q_{onset} = 0.6\frac{M_{H_2O}}{M}G$, where M=molecular mass

Table 2.2: A summary of HTD onset correlations for fluids at supercritical pressures (Cont'd)

Author(s)	**Fluid**	P/P_{cr}	q [kW/m^2]	G [kg/m^{2}s]	D [mm]	**HTD Onset Correlations**
Cheng et al. (2009)	Water	1.02 - 1.13	300 - 2000	700 - 3500	10 & 20	$q_{onset} = 1.354 \times 10^{-3} F_P G$ where $F_P = \left(\frac{C_{p,pc}}{\beta_{pc}}\right)$
Bae et al. (2010)	CO_2	1.05 & 1.1	30 - 170	285 - 1200	6.32	$q_{onset} = 2 \times 10^{-4} G^{2.0}$
Li et al. (2010)	CO_2	1.06 - 1.29	6.5 - 52	expressed as Re = 3800 – 20000	2	$2 \times 10^{-7} < Bo_b^* < 2 \times 10^{-5}$ Where $Bo_b^* = \frac{\mathrm{Gr}_b^*}{\mathrm{Re}_b^{3.425}\mathrm{Pr}_b^{0.8}}$ $\mathrm{Gr}_b^* = \frac{g\beta D^4 q}{k_b \nu_b^2}$
Mokry et al. (2011)	Water	1.08	70 - 1250	200 - 1500	10	$q_{onset} = -58.97 + 0.745G$
Schatte et al. (2016)	Water	1.02 - 1.36	166 - 1650	200 - 2000	7.6 - 38	$q_{onset} = 1.942 \times 10^{-6} F_D F_P G^{0.795}$ where $F_D = (30 - D)^{0.339}$ $F_P = \left(\frac{C_{p,pc}}{\beta_{pc}}\right)^{2.065}$

Chapter 3

Test facility and Instrumentation

3.1 Experimental facility

3.1.1 Main flow circuit

The Supercritical University of Ottawa Loop (SCUOL) was designed to operate with different fluids, including carbon dioxide and a refrigerant, such as R134a, at a maximum operating pressure of 10 MPa. A schematic diagram of the loop can be seen in Fig. 3.1. A more detailed description of the components, dimensions, material compatibility, and thermal insulation was given by Jiang (2015).

3.1.2 CO_2 supply

A high pressure cylinder of CO_2 (Linde Canada, Mississauga, Ontario, Canada) with a purity of 99.998% (Grad 4.8) was connected to the loop using a pressure regulator (TESCOM Model 44-1812-24, Emerson Process Management, a division of Emerson Electric Company, Ferguson, Missouri, USA), installed at the outlet of the cylinder. For increasing the pressure of its content, the cylinder could be heated by an insulated cylinder warmer (Omega GCW Series Model GCW-951-150-240, Spectris Canada, Quebec, Canada), equipped with self-regulating grounded heating elements and designed to maintain the bottom of the cylinder at 54 °C and the top of the cylinder at 49 °C, while not exceeding a surface temperature of 66 °C. The cylinder warmer was capable of raising the cylinder pressure from approximately

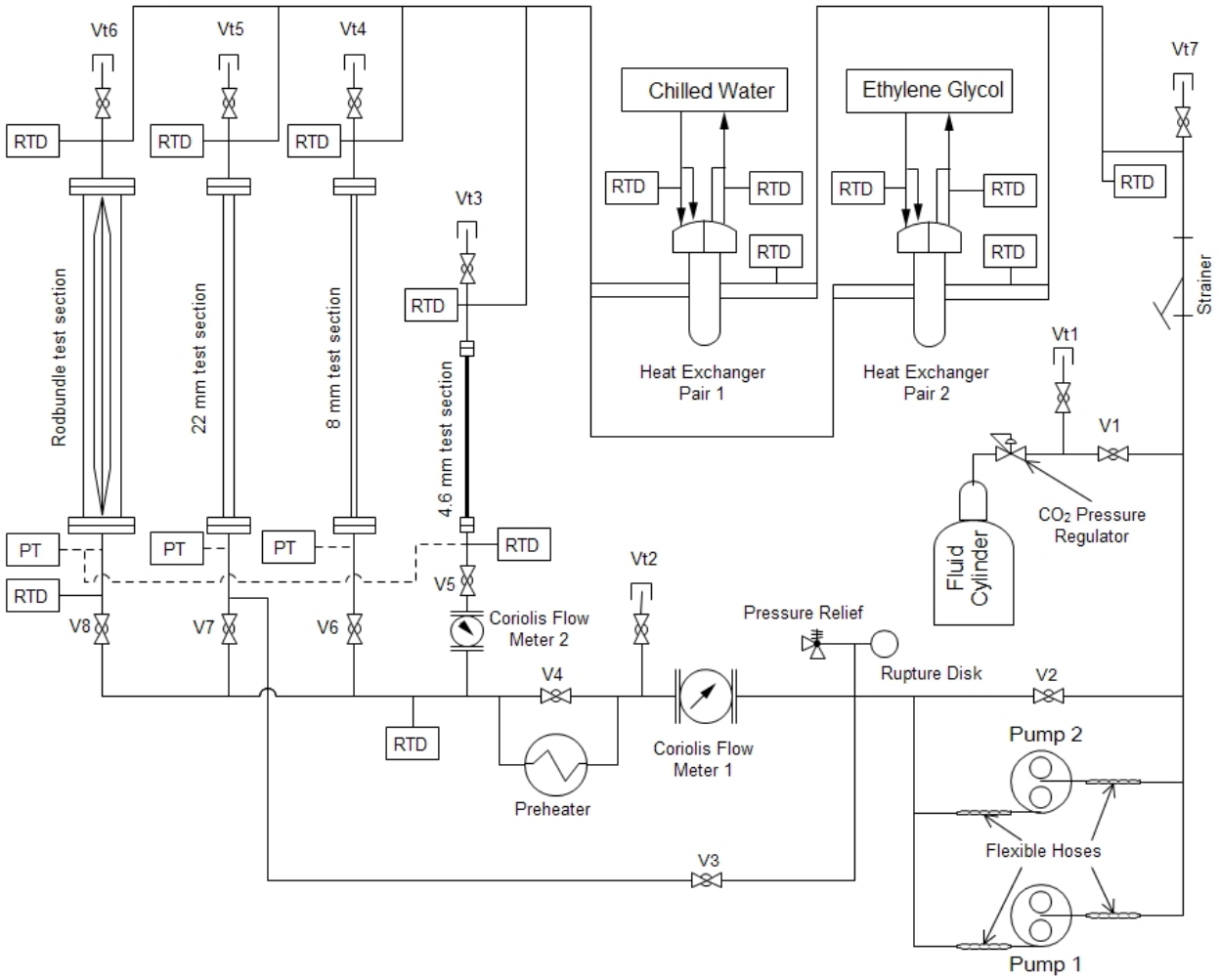


Figure 3.1: A schematic diagram of the Supercritical University of Ottawa Loop (SCUOL); RTD represents location of Resistance Temperature Sensor; PT represents location of Pressure Transducer; V represents valve; Vt represents vent.

6.2 MPa to 9.0 MPa when the cylinder was full and had reached its steady state maximum temperature.

3.1.3 Pumps

The cooling fluid was circulated through the loop using one or two gear pumps (Micro Pump Model GL-H23.JFS.E-M2N1CH15), depending on the desired flow rate, connected in parallel (see Fig. 3.1). The main bypass valve (V2 in Fig. 3.1) was installed as a safety precaution ensuring that fluid was always circulating through the pump(s) in the event that all test section isolation valves (V6 - V9 in Fig. 3.1) were closed. Always leaving V2 partially open prevented possible overheating and pump failure. More details about the pump power, seals, coupling, and pressure limitations can be found in Jiang (2015).

3.1.4 Preheater

An electric preheater (CAST-X 3000 circulation heater, Part Number BX17E6G300U-WTT, Cast Aluminum Solutions, Batavia, Illinois, USA) provided temperature adjustment and control of the fluid entering the test section within a wide range of inlet bulk temperatures T_{in}. The preheater (Fig. 3.1) could maintain the inlet temperature to any of the test sections within 2 °C of the desired temperature, provided enough time was allowed for steady state to be reached. More details concerning the construction, electrical specifications, and pressure limitations of the preheater can be found in Jiang (2015).

3.1.5 Heat exchangers

Two pairs of heat exchangers (Model FXF-6223U, Sentry Equipment Corp, Oconomowoc, Wisconsin, USA), with, respectively, chilled water and cooled ethylene glycol as secondary fluids, were installed upstream from the pumps, as shown in Fig. 3.1, to ensure the fluid was cooled to a liquid-like state before entering the pumps. The heat exchangers were installed in a parallel configuration, which meant that the CO_2 flow was split into four equal streams before entering the heat exchangers, as shown in Fig. 3.2. The chilled water, supplied from the University at 9 °C in the summer and at 14 °C in the winter, could be cut off from

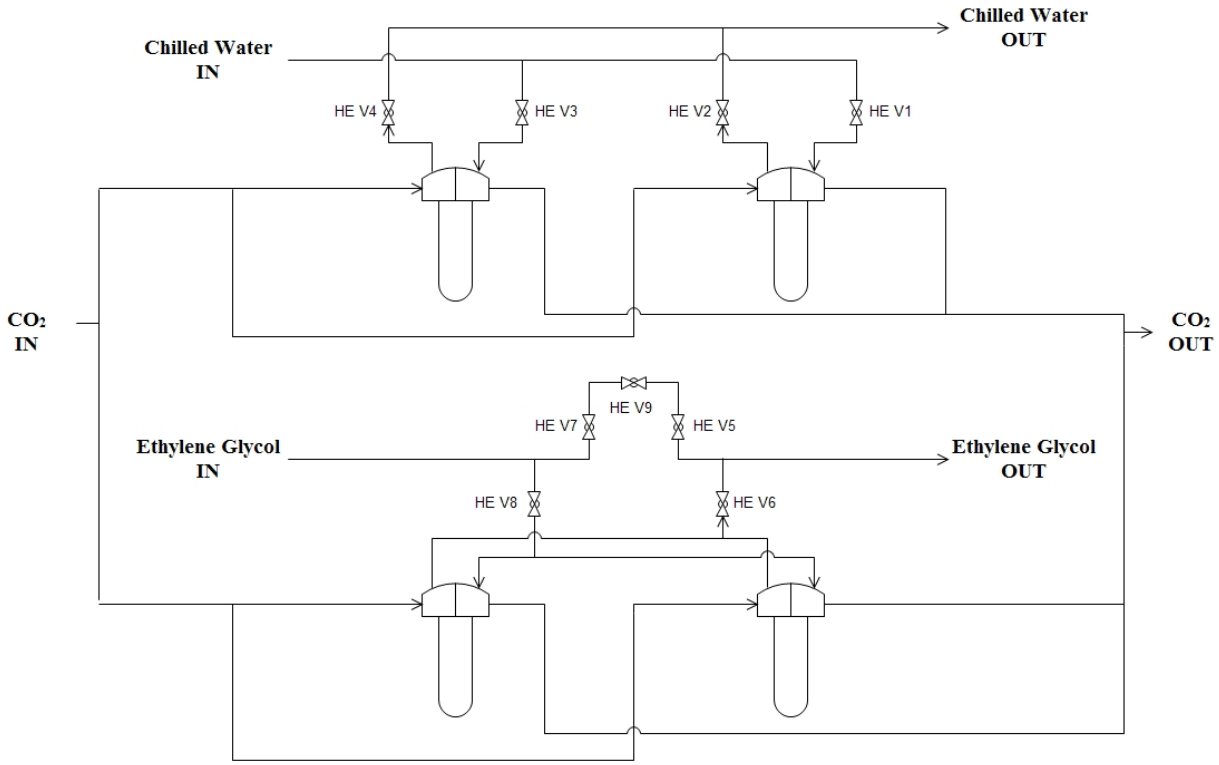


Figure 3.2: A schematic diagram of the heat exchanger flow configurations for the chilled water, ethylene glycol, and CO_2; HE represents heat exchanger; V represents valve.

flowing through either of the chilled water heat exchangers using valves HE V1 and HE V3 in Fig. 3.2, which made a substantial adjustment to the cooling load.

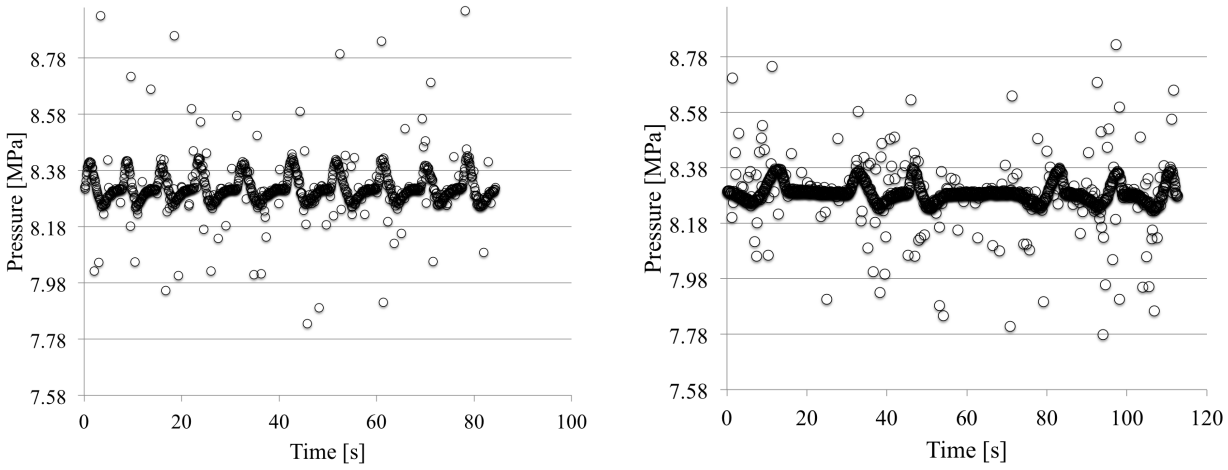
The ethylene glycol was chilled inside a large walk-in freezer equipped with separate temperature settings, one for the freezer chamber and the other for the ethylene glycol fluid. There were two pumps installed in the cooling system. One pump was for circulating the ethylene glycol through the heat exchangers and the other pump was for circulating the ethylene glycol through the freezer chamber. Changes to the cooling load were achieved by adjusting the ethylene glycol temperature using the control system and/or by adjusting the flow rate of the ethylene glycol through both heat exchangers by either using the set of bypass valves (HE V5, HE V7, and HE V9 in Fig. 3.2) or by changing the ethylene glycol pump frequency. More details regarding the heat exchanger construction and pressure and temperature limits as well as information on the construction of the freezer can be found in Jiang (2015).

3.1.6 Accumulators

Accumulators were used by previous users of the loop in order to dampen pressure variations and to make small adjustments to the pressure. These devices were disconnected from the main loop because leaks through the internal stainless steel baffles separating the pressurized nitrogen chamber from the CO_2 supply were discovered. Measurements were repeated after the accumulators were disconnected to see how the pressure would behave. Figure 3.3 shows a time history comparison of the pressure before and after the accumulators were disconnected at the same flow and heating conditions. It can be seen that the accumulators actually had little affect on the pressure oscillations and it was determined that the accumulators did not need to be repaired and reconnected for this purpose.

Furthermore, for any tests that were conducted with only the pumps and the preheater turned on, the pressure did not fluctuate as long as the power supply was turned off, as shown in Fig. 3.4. Based on the previous observations, it was concluded that electromagnetic interference from the power supply was causing the fluctuations in the pressure measurements rather than physical phenomena causing actual pressure fluctuations.

To replace the pressure adjustment function of the accumulators, an additional bypass



(a) with accumulators

(b) without accumulators

Figure 3.3: A time history of pressure measurements taken before and after the accumulators were disconnected for $D = 8$ mm, $G = 300$ kg/m^{2}s, $q = 15$ kW/m^2, $T_{in} = 14$ °C.

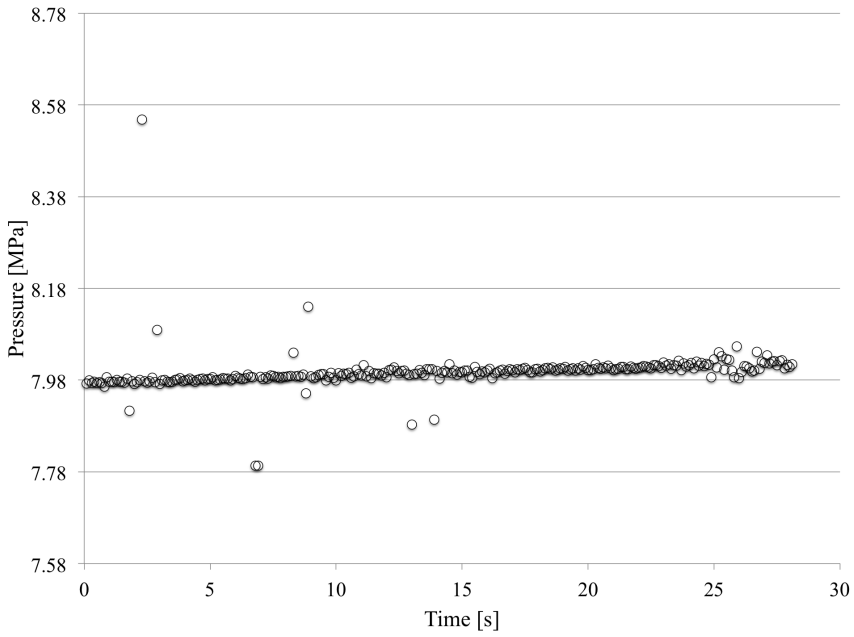
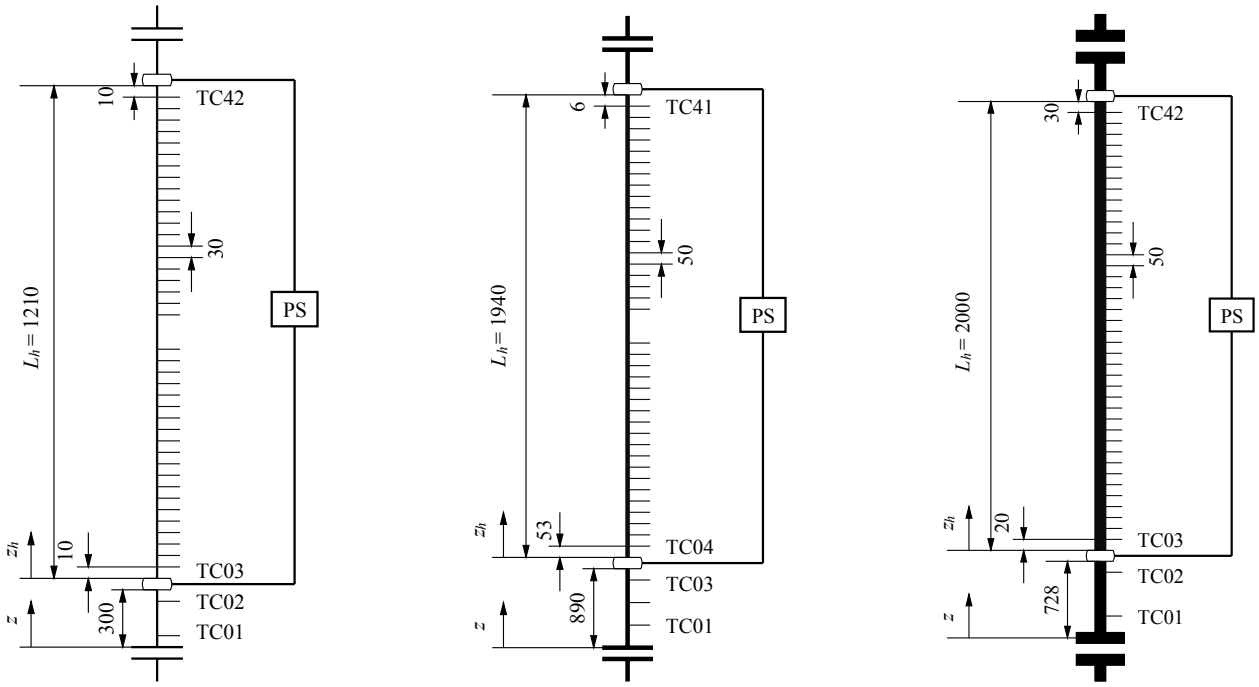


Figure 3.4: A time history of the pressure when the power supply is turned off for $D = 8$ mm, $G = 775$ kg/m^{2}s, $q = 0$ kW/m^2, $T_{in} = 25$ °C.



(a) 4.6 mm I.D. (b) 8 mm I.D. (c) 22 mm I.D.

Figure 3.5: Schematic diagrams of the test sections, showing the locations of the thermocouples; PS: power supply; dimensions in mm.

was installed (V3 in Fig. 3.1) to provide a quick and easy means to adjust the loop pressure, when using the 8 mm, 4.6 mm, or three-rod bundle test sections, by changing the flow rate of CO_2 passing through the heat exchangers. When using the 22 mm test section, it was necessary to keep a heated full cylinder of CO_2 connected to the loop in case it was necessary to recover some pressure and one of the vents was used to decrease the pressure.

3.1.7 Test sections

The test sections used in the present experiments consisted of three heated circular tubes oriented vertically for upward flow, as seen in Fig. 3.5, with inner diameters $D = 4.57(\approx 4.6)$, 8.0, and 22.0 mm, heated lengths $L_h = 1200, 1940$, and 2000 mm, and wall thicknesses of 0.89, 1.00, and 1.50 mm, respectively. The 8 mm and 22 mm test sections were made of Inconel® 600 and Inconel® 625 (Special Metals Corporation of Huntington, West Virginia,

Table 3.1: Material, thermal, and electrical properties comparisons between Inconel® 600 and Sanicro® 70

Property	Value	
	Inconel® 600	Sanicro® 70
Density [kg/m^3]	8470	8400
Thermal Conductivity (@ 20 °C) [W/m°C]	14.9	13
Electrical Resistivity (@ 20 °C) [$\mu\Omega \cdot$ m]	1.03	1.05

USA), respectively. The 4.6 mm test section was made of Sanicro® 70 (Sandvik Canada Inc., Mississauga, Ontario, Canada), which was very similar to Inconel® 600. Comparisons between material, thermal, and electrical properties can be found in Table 3.1.

The 4.6 mm test section was installed at a later stage of the experiments. It was connected to the loop using two pairs of ANSI 1500 flanges equipped with 1/2 inch Swagelok® pipe fittings (Model SS-810-F8-1500, Swagelok Central Ontario, Ontario, Canada) and sealed with dielectric flange gasket kits (Model ETTFG7DWG7N0051500, Corrpro, Quebec, Canada), which were constructed with PTFE (Teflon™) sealing rings. Power clamps, made of Alloy 101 copper blocks, ordered from McMaster Carr supply company, were machined at the University of Ottawa mechanical engineering machine shop for connecting the power cables coming from the power supply to the test section. Detailed information on the construction of the 8 and 22 mm test sections can be found in Jiang (2015).

All three test sections were thermally insulated with three layers of insulating materials. High temperature tape (Fiberglass-Reinforced Foil Tape, McMaster Carr, Ohio, USA), rated to 315 °C, was wrapped around each thermocouple individually to ensure that the self-adhesive silicone pad containing the thermocouple measurement tip was pressed securely to the outer surface of the test section. The next layer was made of fibreglass cloth ribbon wrapped around the test section from bottom to top for added protection of the thermocouples from the outer layer of insulation. The outer layer provided the bulk of the insulation and was constructed of 40 mm thick fibreglass pipe insulation (Rigid High-Temperature Fiberglass Pipe Insulation, McMaster Carr, Ohio, USA) rated to 450 °C.

3.1.8 Power supply

Electric power for the heating of the test sections was provided by a rectified power supply, rated at a maximum voltage of 60 V and a maximum current of approximately 3000 A. It drew power from the university's 380 V, 60 Hz, 3-Phase AC power grid and outputed rectified current at 360 Hz. The local temperature of the test section walls could not follow the high frequency of voltage fluctuations and was essentially steady. Thick cables from the power supply were bolted onto copper blocks machined to clamp onto the top and bottom of each test section forming the limits of the heated section.

3.1.9 Safety features

A high-volume air ventilation system and an oxygen depletion sensor (Osyguard®, OxyGuard International A/S, Farum, Denmark) ensured that the room's oxygen had not been displaced by enough CO_2 to cause asphyxiation. A high pressure relief valve (Swagelok® SS-R4S8, Swagelok Central Ontario, Ontario, Canada) was installed, set to approximately 9.65 MPa (1400 psia), to relieve excessive pressure build-up caused by unforeseen accidents. As a last line of defence against loop over-pressurization, a rupture disc (25.4 mm PolySD Bolted Type Series, Fike Canada Inc., Burlington, Ontario, Canada) was installed in the loop, where a set pressure of 10.3 MPa (1500 psia) would rupture the disc inside the holder releasing the loop pressure. More detailed safety information can be found in Jiang (2015).

3.2 Instrumentation

3.2.1 Data acquisition system (DAS)

A dedicated computerized data acquisition system (National Instruments of Austin, Texas, USA) was used for monitoring and controlling the facility as well as logging experimental results. Each type of DAS module used for measuring the various properties of interest, listed in the following sections, is described in Jiang (2015).

3.2.2 Mass flow rate

The coolant mass flow rate in the 8 and 22 mm test sections was measured with a Coriolis flow meter (Micro Motion ELITE CFM050M320N0A2E2ZZ), having an uncertainty of 0.05% for liquid flow. The coolant mass flow rate in the 4.6 mm test section was measured with a smaller Coriolis flow meter (Micro Motion ELITE CFMS015M319N0A2E2ZZ), having an uncertainty of 0.1% for liquid flow.

3.2.3 Inlet and outlet fluid temperatures

The bulk fluid temperatures at the inlet and outlet of each test section was measured with ultra-precise immersion RTD sensors (Omega P-M-1/10-1/8-5-1/2-G-15), having an uncertainty of 0.35 K within the temperature range of 0 to 100 ^{o}C.

3.2.4 Wall temperature

Wall temperature measurements were taken using T-type thermocouples (Omega SA1XL-T-SRTC), having an uncertainty of 0.5 K and a time constant of less than 0.15 s. Approximately 40 thermocouples were attached to the exterior wall of each test section using a silicone-based adhesive and reinforced with an additional fibreglass reinforced high-temperature tape rated to a maximum temperature of 315 ^{o}C.

3.2.5 Power

The voltage drop across the heated test section was measured directly from the copper blocks which are connected to a 24-bit digital voltage measurement module (National Instrument NI 9225), having a range of $\pm$300 V and an uncertainty of 0.034 V. The electrical power was calculated from the measured RMS voltage and the electrical resistance of the test section, which was estimated using the Inconel® resistivity values provided by Special Metals and the Sancro® resistivity values provided by Sandvik.

3.2.6 Absolute pressure

The 8 mm test section inlet absolute pressure was measured by a pressure transducer (Omega PX01C1-3KA5T) with an uncertainty of 21 kPa, whereas the 4.6 and 22 mm test section inlet absolute pressures were measured by a different pressure transducer (Rosemount 3051TG4M2B21AM5C6Q4), calibrated in the range from 101 to 27580 kPa with a maximum uncertainty of 7.8 kPa.

Chapter 4

Experimental procedures

4.1 Loop operation procedure

4.1.1 General procedure

All tests were planned carefully to ensure efficient data collection and economic use of the resources. The loop was filled with CO_2 at the desired pressure from a CO_2 cylinder, which was usually heated externally so that its contents reached a pressure above the value at ambient temperature. It was found that, for an efficient day of tests, it was best to maintain the loop pressure and mass flux fixed for all runs and perform tests using three or four different values of the wall heat flux, for each of which the inlet temperature was set to span the typical range from 0 °C to 36 °C in increments of 2 or 3 °C. To avoid having to supply additional CO_2 to the loop in order to recover the required pressure level between runs, the runs were arranged to start with the lowest inlet temperature and end with the highest inlet temperature. Heating to a higher inlet temperature caused the loop pressure to exceed somewhat the desired value, which was recovered by the venting of a small quantity of CO_2 to the ambient through any one of the test section vent valves (Vt4, Vt5, Vt6, or Vt8 in Fig. 3.1). The following subsections provide more detailed explanations on the techniques that were used for adjusting the values of different parameters.

4.1.2 Mass flux adjustment

To get sufficient traction in order to start circulating still fluid in the loop (namely, while fluid in the pumps is at room temperature), the pumps must contain liquid or liquid-like CO_2. For this reason, before the pumps were started, the loop was pressurized sufficiently for the fluid to be in a liquid-like state at room temperature. The loop permits the adjustment of mass flux in three different ways: a) by adjusting the bypass valve V2 (Fig. 3.1); this bypass branch not only ensures that some fluid always circulates through the pumps, but also permits a substantial portion of the flow to be diverted away from the test section without a significant change of the loop pressure; b) by adjusting the pump motor rotational speed ("frequency"); for a typical set of measurements at a fixed flow rate, the bypass valve V2 was fixed at one position and small adjustments to the mass flux were made by changing the pump frequency using the DAS; c) for very low mass flux values, the test section isolation valve (V6 - V9 in Fig. 3.1) was used to restrict the flow through the test section. Although an adjustment of the bypass valve V3 would also change the mass flux through the 4.6 and 8 mm test sections, this would also change significantly the loop pressure and, for this reason, such adjustment was avoided for this purpose.

4.1.3 Pressure adjustment

A full cylinder provided sufficiently high pressure when heated, but after only a few experiments the pressure of a fully heated cylinder often dropped below the required loop operating pressure. In order to extract as much CO_2 from a cylinder as possible, we started the daily tests by cooling the fluid in the loop as much as possible. For this purpose, the freezer room and the ethylene glycol temperatures were typically set at $-30\,^{\circ}\mathrm{C}$ and $-20\,^{\circ}\mathrm{C}$, respectively. For runs with the 4.6 or 8 mm test sections, bypass valve V3 (Fig. 3.1) was fully opened in order to maximize the flow rate through the heat exchangers. As the temperature of the fluid in the loop dropped, the pressure dropped, which allowed more CO_2 to be charged from the cylinder. This procedure of dropping the fluid temperature and adding CO_2 was repeated until the fluid in the loop reached a sufficiently low steady state temperature. At that time, power to the test section and the preheater were turned on and gradually increased to the lowest settings for the planned test matrix of the day. Adding heat to the loop increased the

pressure; the amount of CO_2 that was added to the loop during the initial cooling procedure was empirically adjusted so that the pressure rose approximately to the desired level at steady state. Small adjustments to the pressure were further made by adjusting the bypass valve V3, which changed the CO_2 flow rate through the heat exchangers. Larger adjustments to the pressure were achieved by adjusting the ethylene glycol temperature, however, this approach took a longer time for the pressure to return to steady state.

4.1.4 Heat flux and inlet temperature adjustments

Measurements were recorded only after the operating conditions reached the desired steady state values. It was found that the system reached a steady state much faster following a heat flux adjustment than an inlet temperature adjustment. For example, after a small adjustment to the inlet temperature, loop conditions took as long as 10 min before reaching a steady state, whereas this time was reduced to about 1 min after a small adjustment to the heat flux. For this reason, a series of runs were performed by keeping the inlet temperature constant and changing the heat flux, from lowest to highest within the test matrix range. Additional runs were performed after incrementing the inlet temperature to the next value within the test matrix. A typical series of measurements would be recorded for a fixed inlet temperature and 3-4 values of heat flux, with each run typically requiring small adjustments to the pressure and the mass flux with sufficient time between adjustments for a steady state to be reached. For the next series of runs, the heat flux was turned down to the lowest value and the inlet temperature was increased. Additional series of runs were performed until data for all heat fluxes and inlet temperatures in the test matrix were recorded.

4.2 Measurement procedures

4.2.1 Heating power and heat flux measurements

The electric power supplied to a test section can be determined from measurements of the voltage and current through the test section. Although labelled a DC power supply, the custom-designed, high current power supply used produced a rectified AC voltage output. Accordingly, the Joule power of the test section was proportional to the root mean square

voltage V_{rms}, measured at the clamps that provided power to the test section. The voltage time series was measured very accurately by a dedicated high frequency computer module and V_{rms} was calculated by an rms function within the LabView program. The current could be measured directly across an installed shunt, but it was observed that this method was subjected to erratic fluctuations (Jiang, 2015). To avoid a substantial uncertainty, we computed the heating power as

$$Q_e = \frac{V_{rms}^2}{R}, \tag{4.1}$$

where the test section electric resistance R was calculated as

$$R = \frac{\rho_e L_h}{A_{cs}}. \tag{4.2}$$

In this expression, ρ_e is the electrical resistivity of the test section wall material, L_h is the heated length and A_{cs} is the cross-sectional area of the test section wall. The values of these parameters, including values presented by Jiang (2015), are listed in Table 4.1.

Table 4.1: Electrical properties of the 4.6, 8, and 22 mm test sections

Test Section (Material)	ρ_e [$\mu\Omega \cdot$ m]	L_h [m]	A_{cs} [m^2]	R [Ω]
4.6 mm tube (Sanicro® 70)	1.05	1.21	1.525×10^{-5}	0.0833
8 mm tube (Inconel® 600)	1.03	1.94	2.827×10^{-5}	0.0707
22 mm tube (Inconel® 625)	1.29	2.00	1.107×10^{-4}	0.0233

The heat flux from the test section wall to the fluid was calculated as

$$q = \frac{Q_e}{\pi D L_h}, \tag{4.3}$$

under the assumption that there were no heat losses to the environment or axial heat conduction to the unheated sections.

4.2.2 Measurement of the wall temperature and the heat transfer coefficient

The thermocouples that were attached to the test section walls measured the local outer wall temperature $T_{w,o}$. The inner wall temperature T_w was estimated from the axisymmetric heat diffusion equation with uniform internal energy generation as

$$T_w = T_{w,o} + \frac{2q_{loss}r_o - q^V r_o^2}{2k} ln\frac{r_o}{r_i} + (r_o^2 - r_i^2)\frac{q^V}{4k}, \tag{4.4}$$

where q_{loss} is the heat loss to the surroundings (neglected in this analysis), q^V is the volumetric heat generation, calculated as

$$q^V = \frac{Q_e}{\pi(r_o^2 - r_i^2)L_h}, \tag{4.5}$$

and r_o and r_i are the tube outer and inner radii, respectively. The thermal conductivity k of the test section material was evaluated at the local $T_{w,o}$, rather than being given a fixed value. This is because the temperature along the heated test sections varied from approximately 20 °C to 300 °C, depending on the experimental conditions, and the thermal conductivities k of Inconel® and Sanicro® alloys had measurable variations within that range, although these were relatively small by comparison to variations of the thermal conductivities of other metals and alloys. The local k was evaluated for each specified temperature with the use of linear expressions that were fitted to data supplied by the manufacturers. Jiang (2015) determined the expressions

$$k = 0.0146T + 14.509\ , \quad \text{for Inconel® 600 and} \tag{4.6}$$

$$k = 0.0145T + 9.503\ , \ \text{for Inconel® 625,} \tag{4.7}$$

where T is specified in °C. The manufacturer of Sanicro® 70 provided values of k at different temperatures that appeared to be rounded to two significant digits (Table 4.2). The linear fit to these data was

$$k = 0.0149T + 12.691. \tag{4.8}$$

Table 4.2: Thermal conductivity of Sanicro® 70 alloy

Temperature [°C]	Manufacturer's Value [W/m°C]	Value from Linear Fit [W/m°C]	% Difference
20	13	12.99	0.08
100	14	14.18	1.29
200	16	15.67	2.06
300	17	17.16	0.94

The bulk fluid specific enthalpy along the heated test section was calculated from the simplified energy equation as

$$h_b = h_{in} + \frac{Q_e}{\dot{m}} \frac{z_h}{L_h}, \tag{4.9}$$

where h_{in} is the specific enthalpy at the inlet, $\dot{m}$ is the mass flow rate (measured by the Coriolis flow meter), and z_h is the axial distance along the heated test section. The corresponding local bulk fluid temperature T_b and the thermophysical properties of carbon dioxide were calculated from tables constructed by NIST (Lemmon et al., 2002). Finally, the local heat transfer coefficient was calculated as

$$HTC = \frac{q}{T_w - T_b}. \tag{4.10}$$

4.2.3 Estimates of power imbalance

As a measure of the combined inaccuracies of the measurement procedures and the effect of heat losses that were neglected in the analysis, we computed the imbalance between our estimates of the heating power Q_e and the power Q_t given to the fluid, under the assumption of steady state conditions. An application of the steady energy equation provides this imbalance as

$$\Delta Q = Q_e - Q_t = Q_e - \dot{m} \left[\left(h + \frac{v^2}{2} + gz \right)_{out} - \left(h + \frac{v^2}{2} + gz \right)_{in} \right]. \tag{4.11}$$

In this expression, the specific enthalpies at inlet h_{in} and outlet h_{out} of the test sections were evaluated from linked NIST property tables at the temperature measured by the corresponding RTDs. The flow velocities v_{in} and v_{out} were calculated from the mass flow rate $\dot{m}$, flow

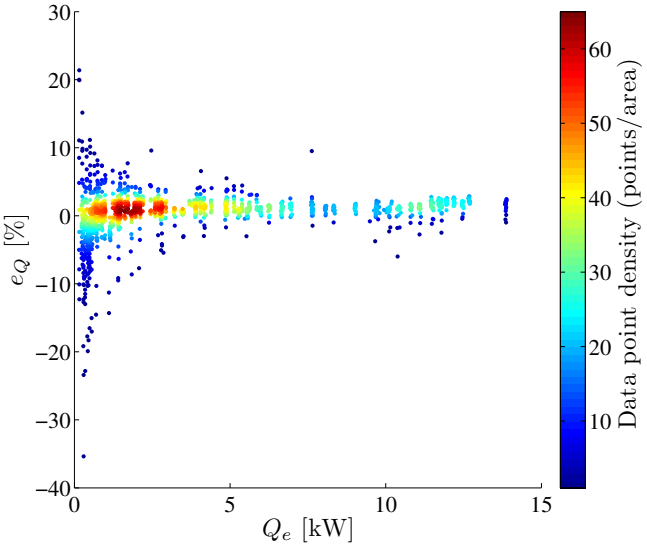


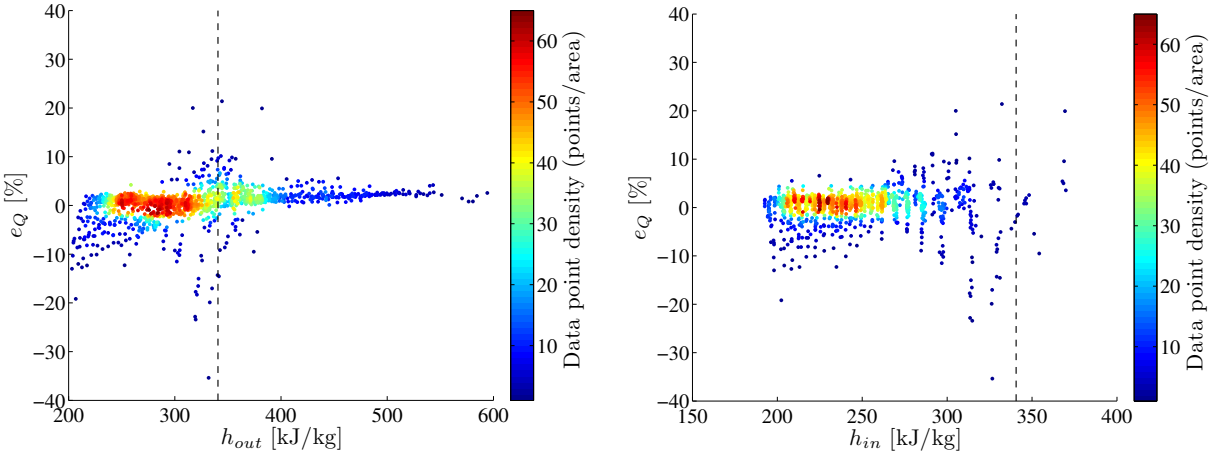
Figure 4.1: Relative power error for different heating powers.

area, and density values evaluated at the inlet and outlet temperatures. The elevations of the inlet and outlet planes, z_{in} and z_{out}, were specified. The relative error in power measurement was calculated as

$$e_Q = \frac{\Delta Q}{Q_e} \times 100. \tag{4.12}$$

Fig. 4.1 shows the relative error for all tests performed. One may see that for 91% of the measurements $\mid e_Q \mid$ was less than 5%. The same figure also shows that the vast majority of the 9% of the tests that produced a higher than 5% heat balance error were at very low power. Because heat losses to the environment would be relatively low at very low heating powers, we may conclude that the bulk of the observed errors was not due to heat losses. The near symmetry of the error distributions also indicates that heat losses were not a significant source of error and that imbalances were mainly of the precision (random) type, rather than biases.

When bulk inlet or outlet temperatures are near to the pseudo-critical temperature, specific enthalpy calculations using NIST tables become very sensitive to small changes in temperature and small errors in these values could introduce large power imbalances. Figure 4.2 shows the relative power error plotted versus h_{in} and h_{out}. One can clearly see that most



(a) h_{out} (b) h_{in}

Figure 4.2: Relative power error *vs.* the inlet and outlet specific enthalpies; dashed line represents the pseudo-critical specific enthalpy h_{pc}.

of the large errors occurred when $h_{in} \approx h_{pc}$ or $h_{out} \approx h_{pc}$. As shown in Fig. 4.3, the observed relative power error distributions had long tails when the difference $\Delta h = h_{out} - h_{in}$ was small, which helps to explain why there were large power imbalance errors at low heating powers.

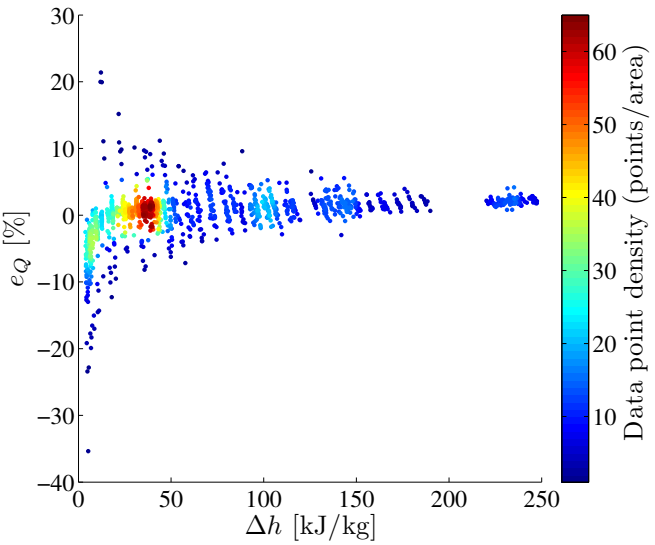


Figure 4.3: Relative power error *vs.* the difference between h_{out} and h_{in}.

Chapter 5

Results and discussion

5.1 Test matrix

Extensive measurements were made in vertical upward flows of CO_2 through each of the three test sections, having IDs $D = 4.6, 8$ and 22 mm. The ranges of experimental conditions are listed in Table 5.1. In all cases, the reduced pressure was $P/P_c \approx 1.13$. The mass flux G was incremented by increments of $100\,\mathrm{kg/m^2s}$ up to $G = 700$ kg/m^{2}s, with measurements also taken in the 4.6 and 8 mm test sections for $G = 1000$ and 1500 kg/m^{2}s. For each G, measurements were taken for three or four different heat fluxes q at levels slightly below and above the corresponding value at HTD onset. For each of the mass flux and heat flux combinations, tests were performed for inlet temperatures in the range $0\,^\circ\mathrm{C} \lesssim T_{in} \lesssim 36\,^\circ\mathrm{C}$, with increments of approximately $3\,^\circ\mathrm{C}$.

Table 5.1: Ranges of experimental conditions

Parameter	Test Section Parameter Ranges		
	$D = 4.6$ mm	$D = 8$ mm	$D = 22$ mm
P/P_c [–]	1.13	1.13	1.13
G [kg/m^{2}s]	300 - 1500	200 - 1500	200 - 700
q [kW/m^2]	10 - 450	3 - 450	2 - 100
T_{in} [°C]	0 - 36	0 - 36	0 - 36

The procedure for choosing the experimental heat flux range for each value of mass flux was such as to allow the determination of the heat flux at HTD onset, which was one of the main objectives of this research. After the mass flux was set at the desired value, but before any measurements were recorded, the heat flux was gradually increased from zero up to a value for which the axial profile of the test section wall temperature, displayed in real time on the monitor, showed a spike, which was evidence of HTD. Then, all other conditions were readjusted and allowed to settle at the desired levels and measurements were recorded for heat flux values slightly lower and slightly higher than the previous value over a full range of inlet temperatures. These measurements included cases with normal temperature profiles and cases with deteriorated temperature profiles. This method allowed for detailed mapping of the onset of HTD for all mass fluxes examined over as wide a range of inlet temperatures as possible.

5.2 Comparisons with results in the literature

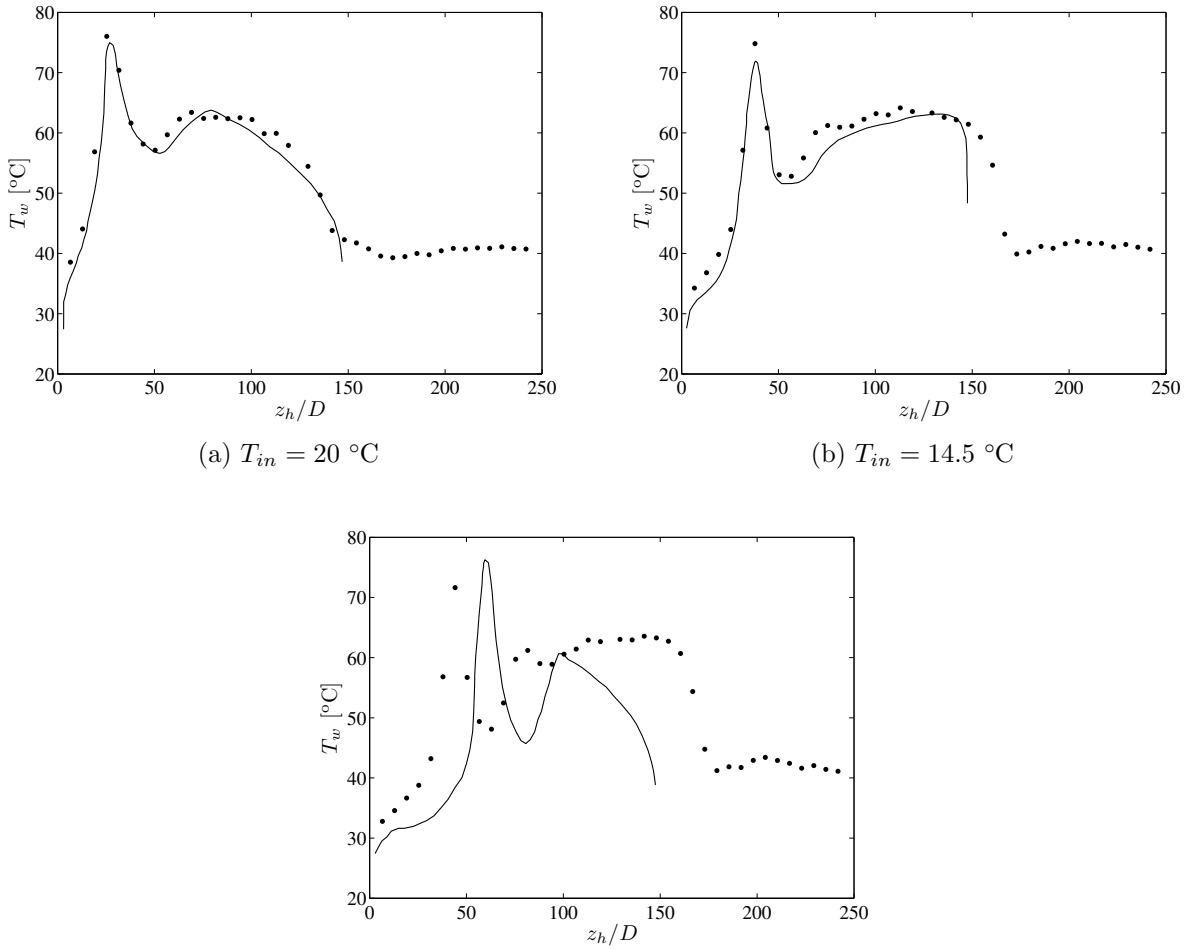
To investigate the reproducibility of our experimental results, we performed some tests under HTD conditions that approximated those in some of the tests by Fewster and Jackson (2004). As Table 5.2 shows, the agreement between the corresponding sets of conditions was good, but not perfect.

Table 5.2: Experimental conditions in selected present experiments and corresponding tests by Fewster and Jackson (2004)

Author	D [mm]	L_h [m]	P [kPa]	G [kg/m^{2}s]	q [kW/m^2]	T_{in} [°C]
Fewster and Jackson (2004)	8	1.185	7580	398	33.6	11, 14.5, 20
present	8	1.94	7588	380	33.6	11.5
present	8	1.94	7561	380	33.7	14.4
present	8	1.94	7498	379	33.5	20.0

Figure 5.1 shows plots of our wall temperature profiles alongside data from Fewster and

Jackson (2004).



(a) $T_{in} = 20$ °C

(b) $T_{in} = 14.5$ °C

(c) $T_{in} = 11$ °C

Figure 5.1: Temperature profile comparisons with results from literature for $D = 8$ mm, $P/P_c \approx 1.03$, $G \approx 400$ kg/m^{2}s, $q \approx 34$ kW/m^2; black dots represent present results; solid lines represent digitized results from Fewster and Jackson (2004).

The agreement between corresponding sets of data was remarkably good, especially considering the differences in the lengths of the test sections and the loop designs, sensitivity of HTD to test conditions and measurement uncertainties in both experiments. We found that the present temperature profiles came closer to the Fewster and Jackson profiles, especially

those at higher inlet temperatures, when we set the mass flux to values that were slightly lower than those in the previous tests. In the case of the lowest inlet temperature tested, the two temperature profiles no longer lined up, but appeared to be slightly shifted with respect to each other. Additional comparisons between results from SCUOL and the literature were presented by Zahlan et al. (2015).

5.3 Patterns of axial profiles of wall temperature

In this subsection, we present selected plots of wall temperature profiles along all three test sections as examples of the observed types of patterns of axial profiles of temperature. Complete sets of plots have been included in Appendix A, organized by different combinations of G and q, with all T_{in} measurements grouped together in one plot. Plots for selected T_{in} values are also organized in groups, which provide one the opportunity to view pertinent temperature profiles individually.

Kurganov et al. (2012, 2016) analyzed data from literature on supercritical heat transfer experiments and identified six different deteriorated heat transfer regimes. Figure 5.2 (Kurganov et al., 2012) shows examples of the observed wall temperature patterns in each of these regimes. In the following, we will show that some patterns in the presently measured temperature profiles are similar to patterns seen in Figure 5.2.

Present wall temperature profiles at the lowest mass flux of $G = 200$ kg/m^{2}s for the 8 mm and 22 mm test sections (the 4.6 mm test section was not tested at this mass flux) developed small temperature spikes near the inlet when the heat flux exceeded certain value and T_{in} was within a certain range. A representative example for the 8mm test section is shown in Figure 5.3, where small temperature spikes appear near the inlet for $q = 5$ kW/m^2 and and even closer to the inlet for $q = 15$ kW/m^2. This behaviour is consistent with the description of Group 1 of Kurganov et al. (2012, 2016), who stated that in this regime weak inlet peaks appeared in upward flows and disappeared with further increase in heat load. Within the presently examined range of q, the data showed no evidence that the peaks would disappear at high heat loads, however, we observed a trend of diminishing peaks, which moved closer to the inlet as the heat flux was increased.

For the mass flux of $G = 300$ kg/m^{2}s in the 8 mm and 22 mm test sections, prominent

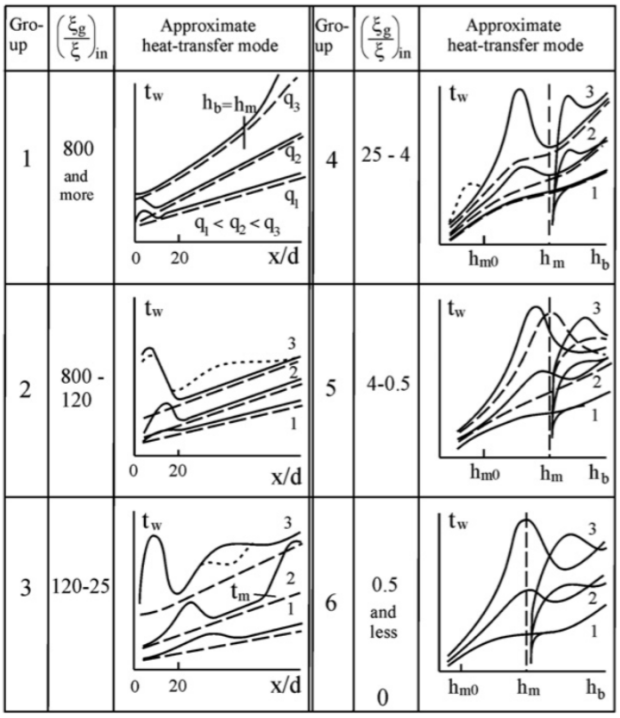
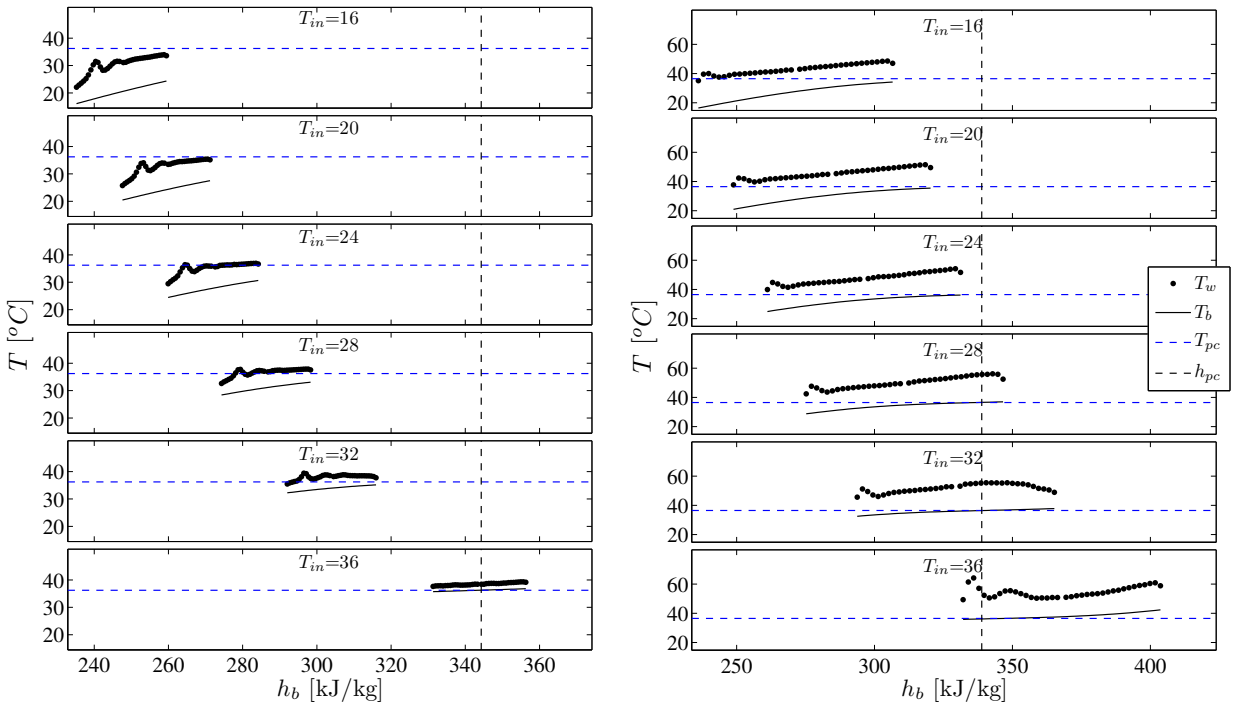


Figure 5.2: Schematic presentation of six different HTD regimes proposed by Kurganov et al. (2012, 2016); solid lines represent upward flow; dotted lines represent possible version of upward flow; dashed lines represent downward flow; $h_m = h_{pc}$.

temperature spikes appeared suddenly near the inlet at a certain heat flux over a range of inlet temperatures. A representative example for the 22 mm test section is shown in Figure 5.4, where temperature spikes are visible near the inlet for $q = 13$ kW/m^2 and even closer to the inlet for $q = 20$ kW/m^2. This behaviour is consistent with the description of Group 2 of Kurganov et al. (2012, 2016), who stated that inlet peaks appeared in upward flow within the heated inlet section and shifted to the very inlet with an increase in heat flux. These authors also mention that, in some cases, a second, more extended, region of elevated temperature formed downstream of the first peak. Figure 5.4 also shows that, at the higher heat flux of $q = 20$ kW/m^2, the inlet peaks appeared closer to the inlet than the those for $q = 13$ kW/m^2, while a second, relatively broad and mild, bump appeared downstream of the first spike in the temperature profile (this bump was most noticeable for $T_{in} = 30$ °C). We further observed that the proximity of the temperature spikes to the inlet for all three

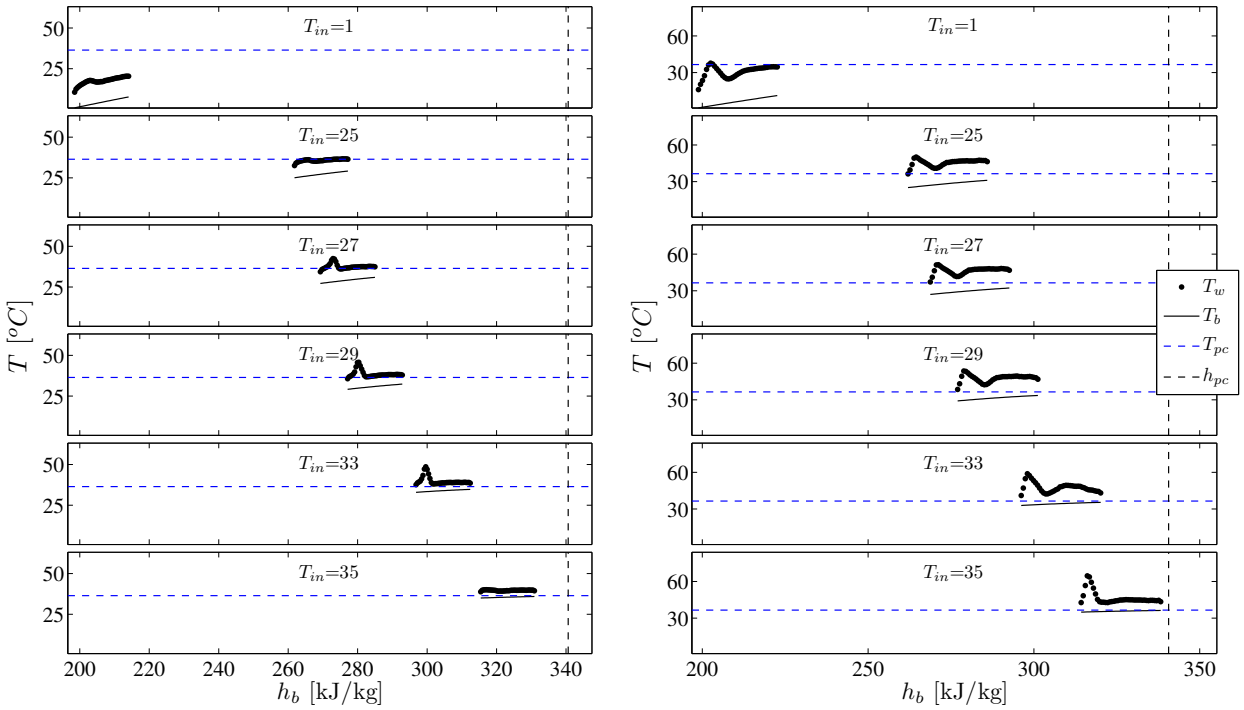


(a) $q = 5$ kW/m^2 (b) $q = 15$ kW/m^2

Figure 5.3: Sample temperature profiles for $P/P_c = 1.13$, $D = 8$ mm, $G = 200$ kg/m^{2}s and two heat fluxes; T_{in} is in °C.

test sections depended not only on q, but also on T_{in}, with the spikes moving closer to the inlet as T_{in} was increased; this dependence on T_{in} was not discussed by Kurganov et al. (2012, 2016).

In contrast to those in the two larger test sections, temperature profiles for $G = 300$ kg/m^{2}s in the 4.6 mm test section did not match the description for Group 2. Figure 5.5 shows that temperature spikes formed at the end of the test section at low T_{in} and moved toward the inlet as T_{in} was increased. None of the groups described by Kurganov et al. (2012, 2016) have peaks at the very end of the test section. The presence of peaks near the end of the test section introduces the possibility that peaks may have appeared in a longer test section for even lower T_{in} values. On the other hand, some of the profiles in the 4.6 mm tube show the formation of a second elevated temperature region, which is consistent with

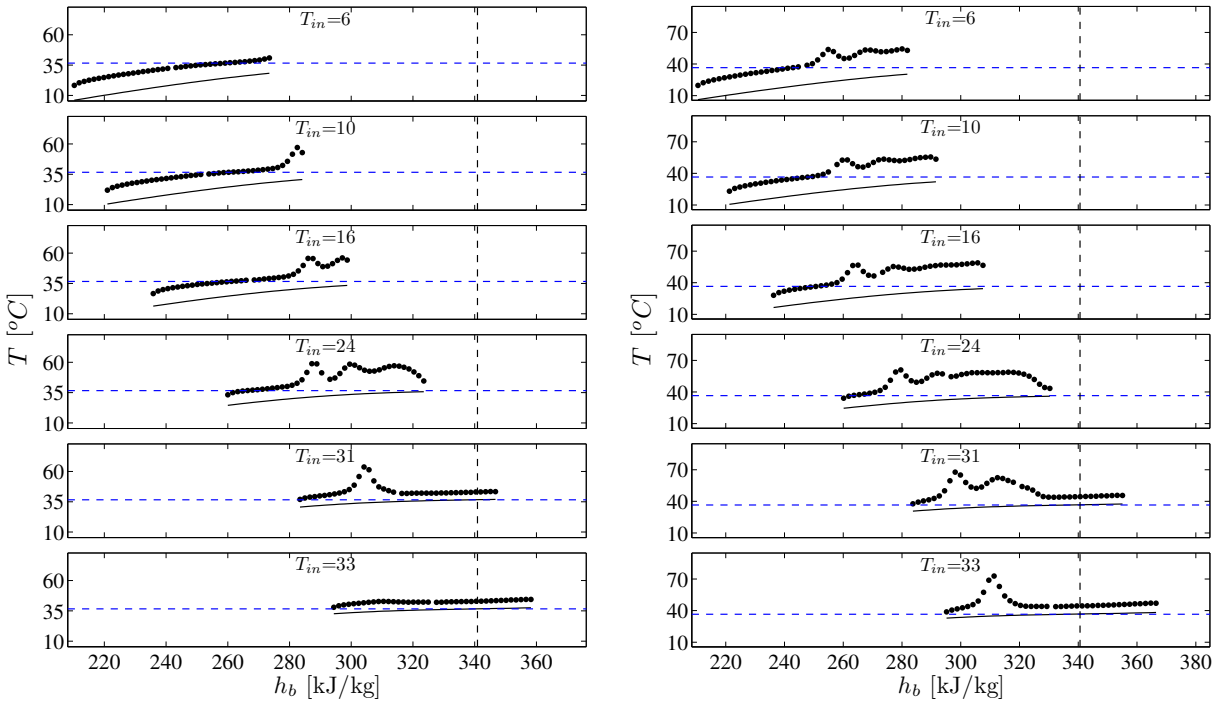


(a) $q = 13$ kW/m^2 (b) $q = 20$ kW/m^2

Figure 5.4: Sample temperature profiles for $P/P_c = 1.13$, $D = 22$ mm, $G = 300$ kg/m^{2}s and two heat fluxes; T_{in} is in °C.

patterns in the two larger test sections for the same G and those in Group 2.

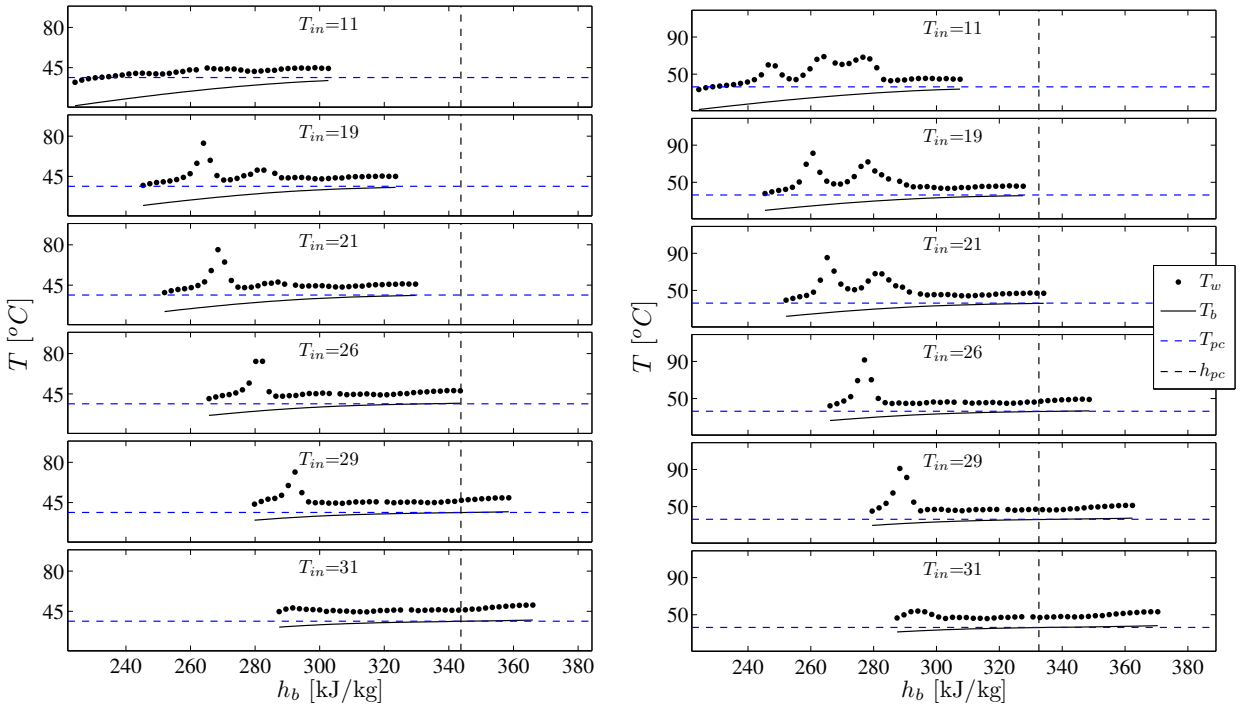
For mass fluxes in the range $400\,\mathrm{kg/m^2s} \leq G \leq 600\,\mathrm{kg/m^2s}$ in the 8 mm and 22 mm test sections, large temperature spikes appeared initially at axial locations that were a little farther away from the inlet than spikes observed at the lower mass fluxes and also depended on T_{in}. Moreover, at high enough heat fluxes, and over a limited T_{in} range, a second region of elevated temperature appeared in the form of a bump, peak, or plateau. This behaviour is consistent with Group 3 of Kurganov et al. (2012, 2016), in which inlet peaks formed away from the inlet and shifted towards the inlet with an increase in heat flux; some temperature profiles in this group also showed a second, and even a third, peak under certain conditions. Representative examples for the 8 mm test section are shown in Figure 5.6. The temperature



(a) $q = 18$ kW/m^2 (b) $q = 20$ kW/m^2

Figure 5.5: Sample temperature profiles for $P/P_c = 1.13$, $D = 4.6$ mm, $G = 300$ kg/m^{2}s and two heat fluxes; T_{in} is in °C.

profiles shown in this figure have qualitative similarities with those in Group 3. At the higher heat flux of $q = 35$ kW/m^2, at least one secondary peak appeared over a range of T_{in}. In the 22 mm test section, secondary peaks were observed for $G = 500$ kg/m^{2}s and $G = 600$ kg/m^{2}s and relatively high heat fluxes. In the 8 mm test section, no distinct secondary peaks were observed for $G = 600$ kg/m^{2}s. However, secondary bumps appeared in the profile for the highest heat flux examined and it is possible that, for even higher heat fluxes, these bumps would turn into more substantial secondary peaks or plateaus. Temperature profiles in the 4.6 mm test section over the same mass flux range, shown in Figure 5.7, had a feature that was never observed in the larger sections: a peak formed at some distance from the inlet when T_{in} dropped below some value and moved towards the end of the test section as T_{in} was

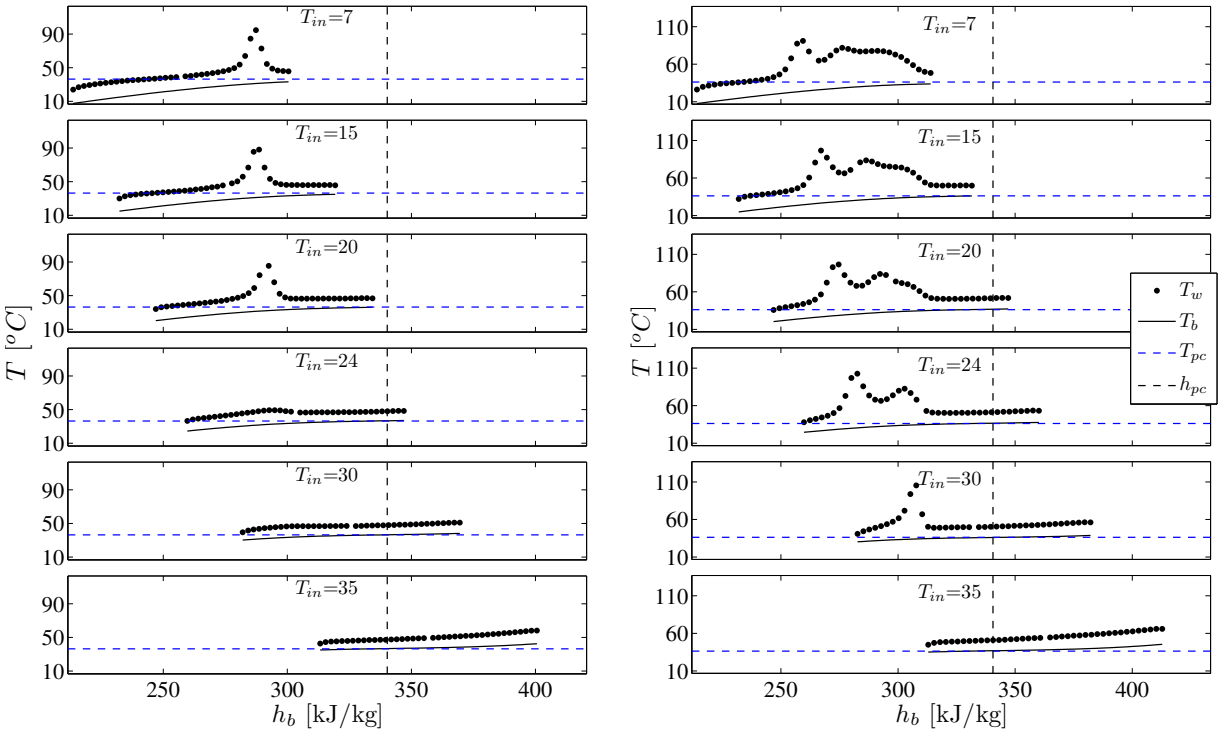


(a) $q = 33$ kW/m^2 (b) $q = 35$ kW/m^2

Figure 5.6: Sample temperature profiles for $P/P_c = 1.13$, $D = 8$ mm, $G = 400$ kg/m^{2}s and two heat fluxes; T_{in} is in °C.

further decreased. If one follows this trend, it is possible that, for even lower T_{in}, there would have been no peak observed (so the heat transfer would appear to be normal throughout) but HTD might have occurred in a longer test section. The fact that spikes occurred near the end of the test section only in the 4.6 mm tube, but not in the larger tubes, seems to indicate that there are HTD patterns in small tubes that may not be possible in large tubes. An explanation of these and other possible differences in supercritical heat transfer in small *vs.* large tubes may be related to differences in the relevance of bulk properties: large tubes have core regions in which the temperature is near the bulk value, whereas small tubes may have a significant radial temperature gradient throughout, so that bulk values would not apply to any significant region of the flow. Besides this peculiarity, all other heat transfer patterns in the 4.6 mm tube were similar to those in the larger tubes. One or more

secondary peaks appeared at higher heat fluxes and all peaks were shifted towards the inlet as q and/or T_{in} were increased. Although secondary peaks were not observed in the 4.6 mm test section for $G = 500$ and $G = 600$ kg/m^{2}s within the heat flux range examined, it seems possible that they might have appeared at even higher q.

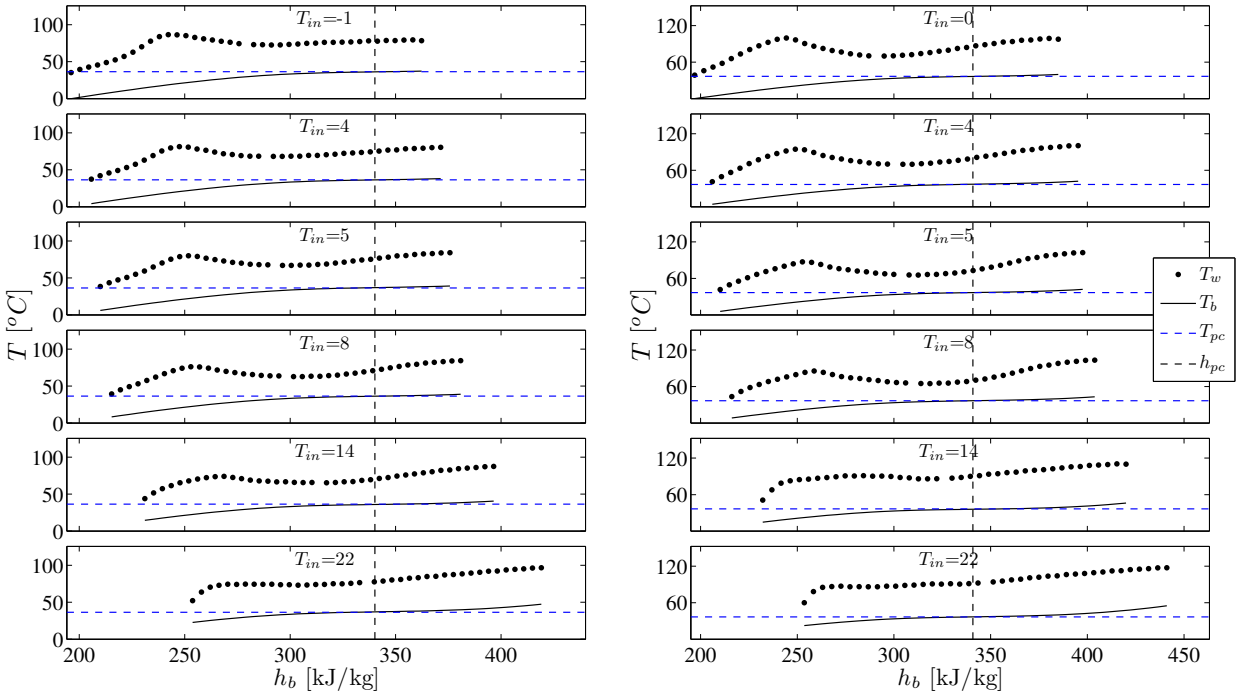


(a) $q = 33$ kW/m^2 (b) $q = 38$ kW/m^2

Figure 5.7: Sample temperature profiles for $P/P_c = 1.13$, $D = 4.6$ mm, $G = 400$ kg/m^{2}s and two heat fluxes; T_{in} is in °C.

For $G = 700$ kg/m^{2}s, broad peaks formed away from the inlet at some q, and gradually increased in magnitude and moved toward the inlet with increasing q. This behaviour was observed in all three test sections. A representative example for the 4.6 mm test section can be seen in Figure 5.8. This behaviour seems to be consistent with the description of Group 4.

For $G = 1000$ and 1500 kg/m^{2}s, broad humps appeared in the temperature profiles near

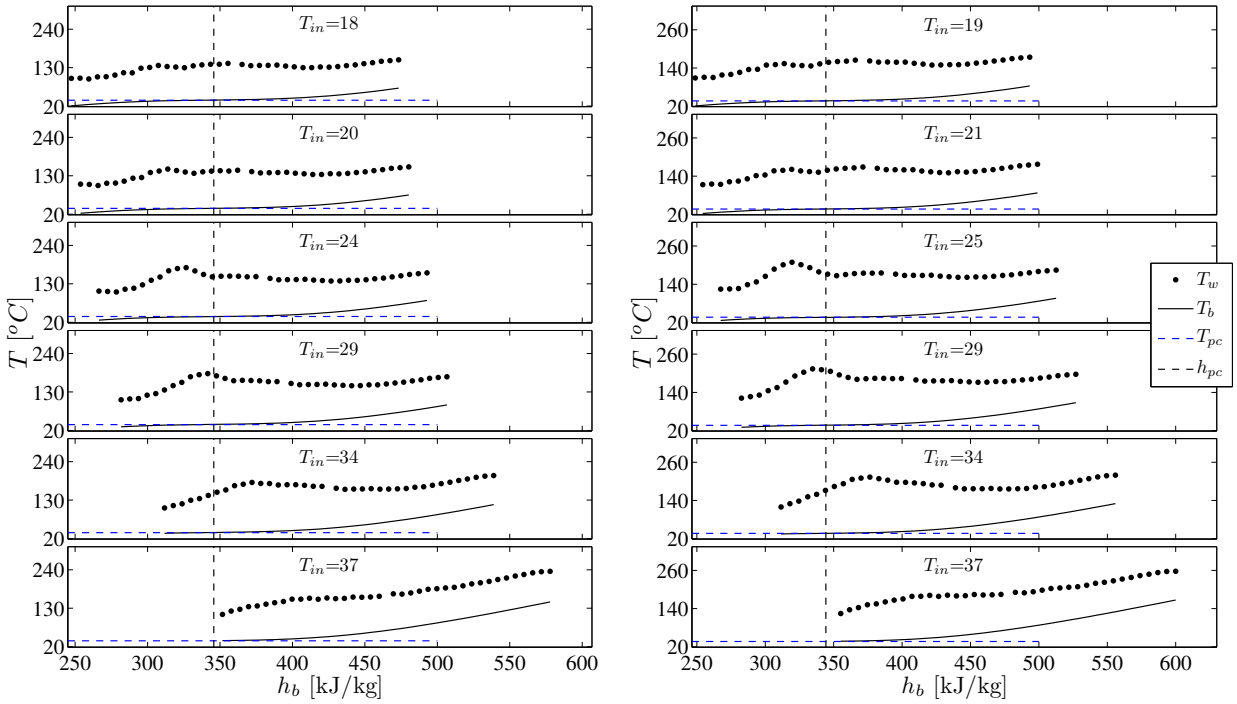


(a) $q = 110$ kW/m^2 (b) $q = 125$ kW/m^2

Figure 5.8: Sample temperature profiles for $P/P_c = 1.13$, $D = 4.6$ mm, $G = 700$ kg/m^{2}s and two heat fluxes; T_{in} is in °C.

the pseudocritical enthalpy, with locations and magnitudes that depended on q and T_{in}. This behaviour was observed in the 4.6 mm and 8 mm test sections, whereas no tests were performed in the 22 mm test section at $G > 700$ kg/m^{2}s. For the same conditions, the bumps in the 4.6 mm test section were farther downstream from the inlet than those in the 8 mm test section. A representative example for the 8 mm test section can be seen in Figure 5.9. This behaviour seems to be consistent with the description of Group 5 in Figure 5.2. Kurganov et al. (2012, 2016) stated that a wide region of elevated temperature appeared in wall temperature profiles in this group, with a peak located in the vicinity of h_{pc}, regardless of flow direction. The present temperature profiles had mild bumps that did not change significantly in shape or magnitude over the heat flux range examined, but we cannot exclude the possibility that these bumps might have developed substantial peaks had

q been increased further.



(a) $q = 240$ kW/m^2 (b) $q = 260$ kW/m^2

Figure 5.9: Sample temperature profiles for $P/P_c = 1.13$, $D = 8$ mm, $G = 1000$ kg/m^{2}s and two heat fluxes; T_{in} is in °C.

Although the vast majority of tests were performed by setting $T_{in} < T_{pc}$, a small number of measurements were taken in the 8 and 22 mm test sections for $T_{in} > T_{pc}$. Such measurements were collected for $G = 200$, 300, and 400 kg/m^{2}s and different q. It was found that, in cases with sufficiently large q, HTD occurred near the inlet, as evidenced by the emergence of spikes in the representative wall temperature profiles shown in Figure 5.10. Similar temperature spikes in the region with $h_b > h_{pc}$ can be seen for Groups 4-6 in Figure 5.2, but their significance was not discussed by Kurganov et al. (2012, 2016). We found, that, in both the 8 and 22 mm test sections, q_{onset} was much higher when $T_{in} > T_{pc}$ than when $T_{in} < T_{pc}$. In particular, the ratio of the two values of q_{onset} was about 10 for $G = 200$ kg/m^{2}s in both test sections and about 4 for $G = 300$ kg/m^{2}s in both test sections as well

as for $G = 400$ kg/m^{2}s in the 22 mm test section, which was the only test section in which HTD was produced in our facility for this G. A complete collection of temperature profiles in the 8 and 22 mm test sections, showing spikes for $T_{in} > T_{pc}$ can be found in Appendix A, Figures A.46, A.52, A.104, A.109 and A.116. The analysis in the following sections will not include these cases, as their type of HTD would likely be quite different from those in the cases with $T_{in} < T_{pc}$.

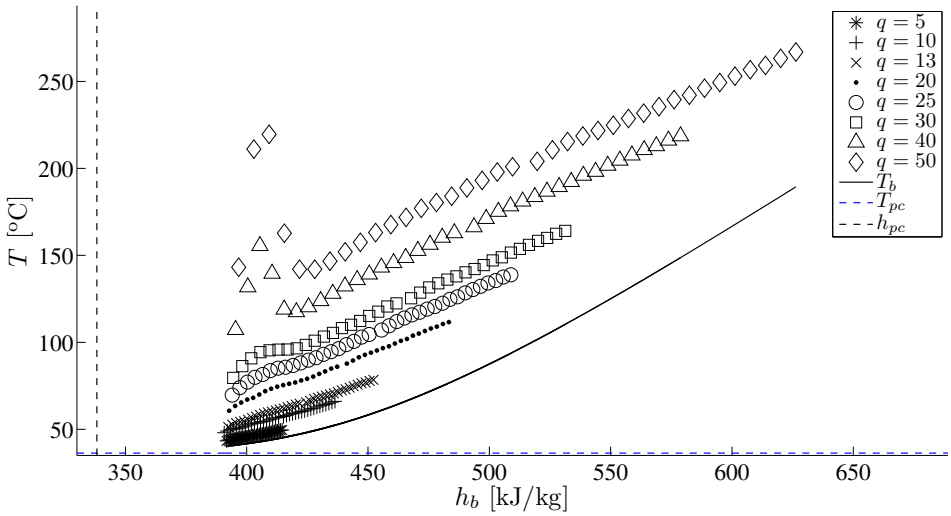


Figure 5.10: Sample temperature profiles for $P/P_c = 1.13$, $D = 8$ mm, $G = 200$ kg/m^{2}s, and $T_{in} = 40$ °C; q is in kW/m^2.

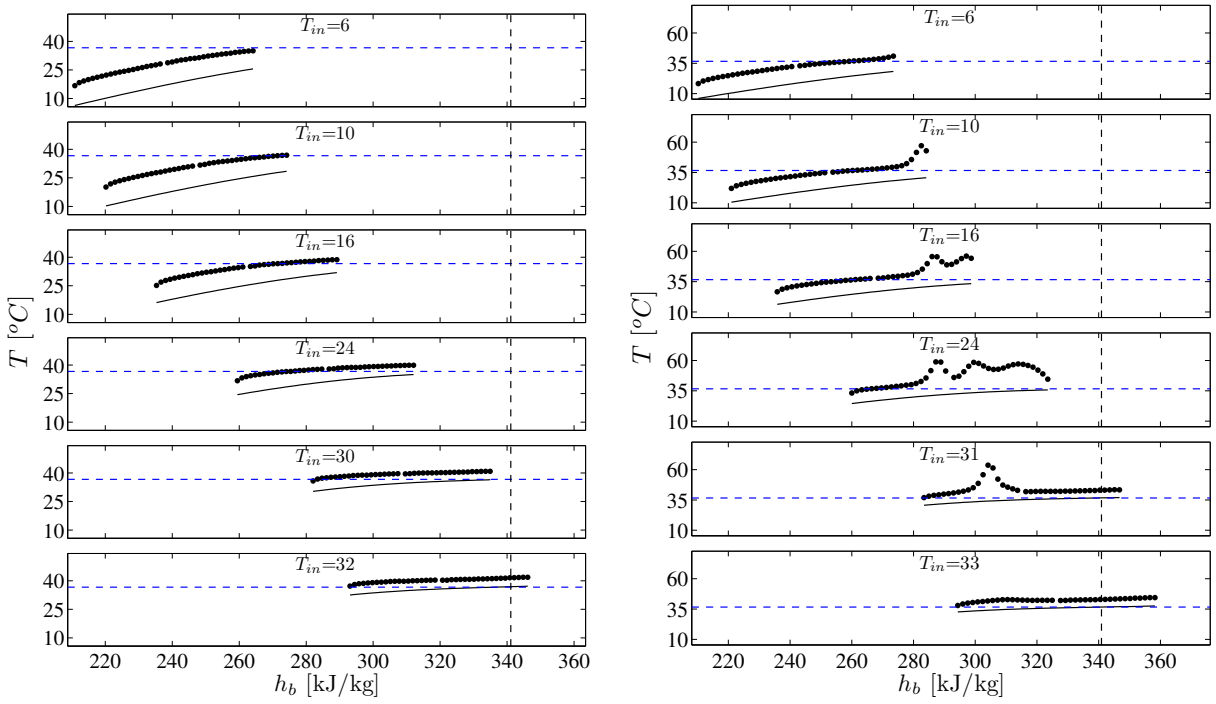
5.4 Identification of HTD

5.4.1 Identifying HTD from wall temperature spikes

The appearance of spikes in a wall temperature profile is generally reliable evidence for the occurrence of local HTD. In many cases, observation of the profiles permitted us to determine cases for which heat transfer can be considered to be normal and cases for which heat transfer was clearly deteriorated. Nevertheless, for a number of cases this approach was not sufficient for identifying HTD.

4.6 mm Test Section Temperature Profiles

For the 4.6 mm test section and with a mass flux in the range $300\,\mathrm{kg/m^2s} \leq G \leq 600\,\mathrm{kg/m^2s}$, the presence of temperature spikes in the axial temperature profiles clearly distinguishes the deteriorated heat transfer cases from the normal ones. An example is shown in Figure 5.11, where $G = 300$ kg/m^{2}s; for $q = 15$ kW/m^2, temperature spikes do not appear for any of the measured T_{in} values, whereas, for the slightly larger $q = 18$ kW/m^2, such spikes are visible for $10\,^\circ\mathrm{C} \leq T_{in} \leq 31\,^\circ\mathrm{C}$. It is also possible to see in Figure 5.11b that, for $G = 300$ kg/m^{2}s and



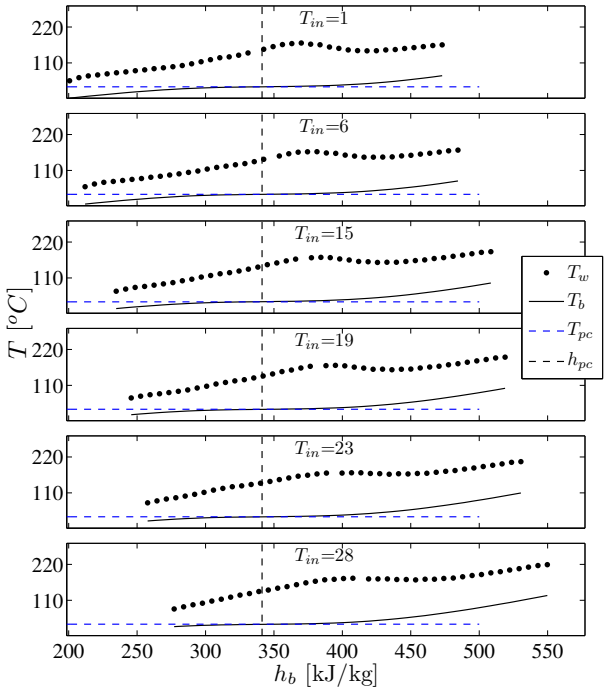
(a) $q = 15$ kW/m^2 (b) $q = 18$ kW/m^2

Figure 5.11: Sample temperature profiles for $P/P_c = 1.13$, $D = 4.6$ mm, $G = 300$ kg/m^{2}s showing the sudden growth of distinct temperature spikes at a certain q over a limited T_{in} range; units of T_{in} are °C.

$q = 18$ kW/m^2, HTD can be identified only for inlet temperatures in the range $10\,^\circ\mathrm{C} \leq T_{in} \leq 31\,^\circ\mathrm{C}$, while profiles at lower and higher inlet temperatures do not show any temperature

spikes. Some caution must be exercised, however, when observing these plots. The trends in the data indicate that a wall temperature spike might have appeared far downstream for the $T_{in} = 6\,^{\circ}\mathrm{C}$ case, if the heated test section were longer, as discussed in Section 5.3. Moreover, the wall temperature profile for the highest inlet temperature considered ($T_{in} = 33\,^{\circ}\mathrm{C}$) contained a smooth bump, which likely indicates a tendency towards a mild form of deterioration. For the present study, however, only cases that showed relatively large temperature spikes were considered as deteriorated, whereas those that had small bumps in the temperature profile were classified as normal. The same clear distinction between normal and deteriorated heat transfer was observed for the $G = 400$, 500 and $600\,\mathrm{kg/m^2s}$ cases, for which temperature spikes did not appear for any T_{in} in the test range for q lower than 33, 53 and $80\,\mathrm{kW/m^2}$, respectively. A complete collection of temperature profiles for measurements taken in the 4.6 mm test section for mass fluxes in the range $300\,\mathrm{kg/m^2s} \leq G \leq 600\,\mathrm{kg/m^2s}$ is presented in Appendix A, Figures A.1 to A.18.

For mass fluxes $G = 700$, 1000, and 1500 $\mathrm{kg/m^2s}$, the axial wall temperature profiles at sufficiently large q contained smooth bumps, which, however, did not turn into sharp spikes at higher heat fluxes. For example, Figure 5.12 shows temperature profiles for $G = 1000$ $\mathrm{kg/m^2s}$ at the highest heat flux examined; none of these profiles had a sharp spike and so the occurrence or not of HTD could not be based reliably on this criterion. Because of experimental limitations of SCUOL at the time of these tests, it was not possible to increase q further in order to investigate the possibility of temperature spike appearances. Whether HTD characteristics at higher G are different from those at lower G requires additional experiments under wider ranges of conditions. A complete collection of temperature profiles for measurements taken in the 4.6 mm test section for $G = 700$, 1000, and $1500\,\mathrm{kg/m^2s}$ is presented in Appendix A, Figures A.19 to A.40.

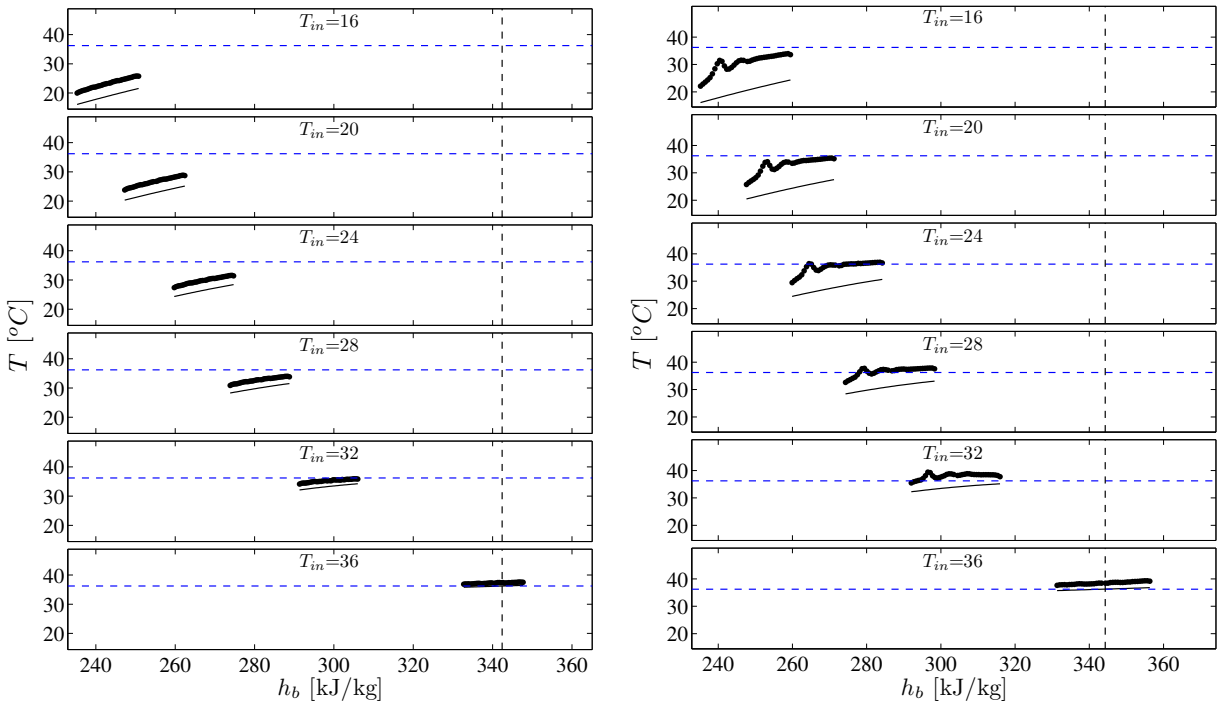


(a) $q = 260$ kW/m^2

Figure 5.12: Sample temperature profiles for $P/P_c = 1.13$, $D = 4.6$ mm, $G = 1000$ kg/m^{2}s showing the gradual growth of temperature bumps for the lowest and highest q examined; units of T_{in} are °C.

8 mm Test Section Temperature Profiles

As shown in Figure 5.13, for the low mass flux of $G = 200$ kg/m^{2}s, temperature spikes did not appear in the 8 mm test section for heat fluxes lower than 5 kW/m^2. It can also be seen in Figure 5.13b that the temperature spikes were sharp and distinct, but they are small, which sets them apart qualitatively from the temperatures spikes that were observed at higher mass fluxes, as discussed in Section 5.3. A complete collection of temperature profiles for measurements taken in the 8 mm test section for $G = 200$ kg/m^{2}s has been included in Appendix A, Figures A.41 to A.45.

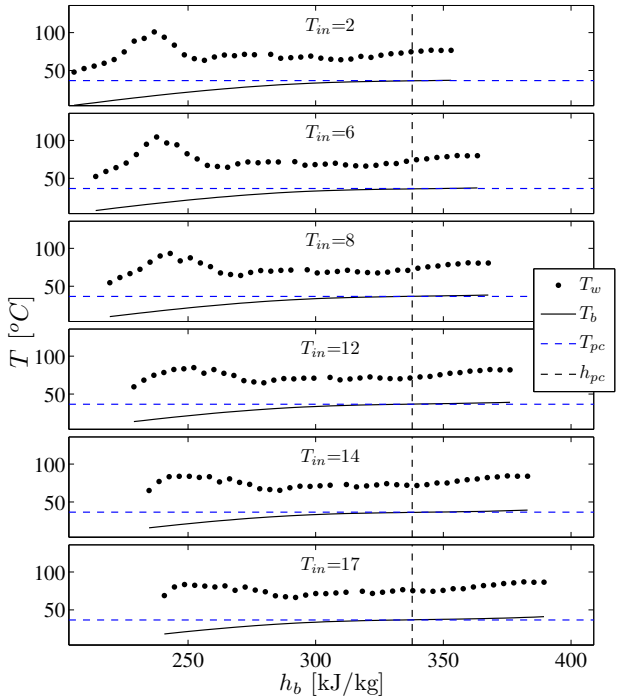


(a) $q = 3$ kW/m^2 (b) $q = 5$ kW/m^2

Figure 5.13: Sample temperature profiles for $P/P_c = 1.13$, $D = 8$ mm, $G = 200$ kg/m^{2}s showing the sudden growth of small distinct temperature spikes at a certain q over a limited T_{in} range; units of T_{in} are °C.

For mass fluxes in the range $300\,\text{kg/m}^2\text{s} \leq G \leq 600\,\text{kg/m}^2\text{s}$, the temperature profiles generally developed large distinct temperature spikes as soon as the heat flux exceeded a certain value. This behaviour is very similar to the one for the same mass flux range in the 4.6 mm test section (see Figure 5.11). It was found that HTD occurred for $q \geq 18$, 33, 55, and 80 kW/m^2, when $G = 300$, 400, 500, and 600 kg/m^{2}s, respectively. As q was increased, mild bumps developed in the profile and grew larger, eventually turning into sharp temperature spikes, which were clear visual identifiers for HTD. A complete collection of temperature profiles for measurements taken in the 8 mm test section for the mass flux range of $300\,\text{kg/m}^2\text{s} \leq G \leq 600\,\text{kg/m}^2\text{s}$ is shown in Appendix A, Figures A.47 to A.51 and A.53 to A.70.

For the case with $G = 700$ kg/m^{2}s, temperature spikes were also observed under certain conditions. However, they did not appear suddenly when q exceeded a certain threshold, but developed gradually from relatively broad bumps with a gradual increase in q. In consequence, it is difficult to identify a value of q at HTD onset. A representative example is shown in Figure 5.14. This example also shows a gradual transformation of a bump to a spike, as T_{in} was increased; although HTD is apparent for $T_{in} = 2$ and 6 °C, it is less obvious for $T_{in} = 17$ °C. A complete collection of temperature profiles for measurements taken in the 8 mm test section for $G = 700$ kg/m^{2}s can be found in Appendix A, Figures A.71 to A.78.



(a) $q = 110$ kW/m^2

Figure 5.14: Sample temperature profiles for $P/P_c = 1.13$, $D = 8$ mm, $G = 700$ kg/m^{2}s showing the gradual growth of large temperature spikes as q increases over a limited T_{in} range; units of T_{in} are °C.

In a manner that was very similar to the examples shown in Figure 5.12 for the 4.6 mm test section, temperature profiles for cases with $G = 1000$ and 1500 kg/m^{2}s in the 8 mm

test section exhibited mild and broad bumps, which gradually increased in amplitude as the heat flux was increased, but did not develop into sharp spikes, even for the highest q that was possible in our setup. There were no conditions for which HTD could be identified from observation of the temperature profiles exclusively. A complete collection of temperature profiles for measurements taken in the 8 mm test section for $G = 1000$ and 1500 kg/m^{2}s can be found in Appendix A, Figures A.79 to A.97.

22 mm test section temperature profiles

For $G = 200$ kg/m^{2}s in the 22 mm test section, temperature spikes formed when $q \geq 3.5$ kW/m^2. The temperature spikes were similar qualitatively to those in the 8 mm test section at the same mass flux; they appeared near to the entrance of the heated test section and they were not very large in amplitude, when compared to temperature spikes observed at higher mass fluxes (see Figure 5.13, as an example). A complete collection of temperature profiles for measurements taken in the 22 mm test section for $G = 200$ kg/m^{2}s can be found in Appendix A, Figures A.98 to A.103.

The behaviour of HTD in the 22 mm test section for mass fluxes in the range 300 kg/m^{2}s $\leq G \leq$ 600 kg/m^{2}s was similar to that in the 4.6 mm and 8 mm test sections over the same mass flux range (see Figure 5.11 as an example). Within a certain T_{in} range, bumps initially appeared in the temperature profiles at lower q; when q reached a certain threshold, the bumps turned into distinct sharp temperature spikes, which permitted one to confidently identify HTD. The heat flux values at the onset of HTD were $q = 13$, 25, 40, and 58 kW/m^2 for $G = 300$, 400, 500, and 600 kg/m^{2}s, respectively. A complete collection of temperature profiles for measurements taken in the 22 mm test section for 300 kg/m^{2}s $\leq G \leq$ 600 kg/m^{2}s can be found in Appendix A, Figures A.105 to A.108, A.110 to A.115 and A.117 to A.128.

Temperature profiles for $G = 700$ kg/m^{2}s in the 22 mm test section were qualitatively similar to those in the 4.6 and 8 mm test sections for the same mass flux. At lower heat fluxes, bumps formed in the profiles and then, as q was increased, these bumps gradually evolved into spikes (see Figure 5.14 as an example), which made it difficult to identify a specific q at HTD onset. A complete collection of temperature profiles for measurements taken in the 22 mm test section for $G = 700$ kg/m^{2}s can be found in Appendix A, Figures A.129 to A.136.

Summary

Temperature profiles for conditions near those at the onset of HTD were found to be qualitatively similar for all three test sections. Under certain conditions, these profiles contained temperature spikes, which were distinguished into three types for the purpose of HTD identification. For $G = 200$ kg/m^{2}s, the spikes were sharp and distinct, but had small amplitude and only formed near the inlet of the test section over a limited range of T_{in}. For G in the range from 300 to 600 kg/m^{2}s, a large sharp spike formed away from the inlet, sometimes near the end of the test section and possibly further downstream if the heated section were longer; this was also observed for a limited range of T_{in}. In this range of G, temperature profiles often developed low-amplitude, broad bumps as q was increased but remained relatively small, which turned into large distinct spikes abruptly at some higher q. At the higher mass flux of $G = 700$ kg/m^{2}s, significant temperature spikes evolved gradually from bumps, without any sudden changes, as the heat flux was increased. For the even higher mass flux of $G = 1000$ and 1500 kg/m^{2}s, the temperature profiles had broad bumps, which grew very slightly as q was increased but did not turn into spikes even for the highest heat flux examined. The shape of wall temperature profiles at higher G makes it difficult to positively identify HTD.

5.4.2 Identifying HTD by comparing measured Nusselt numbers with predictions of a correlation for normal heat transfer

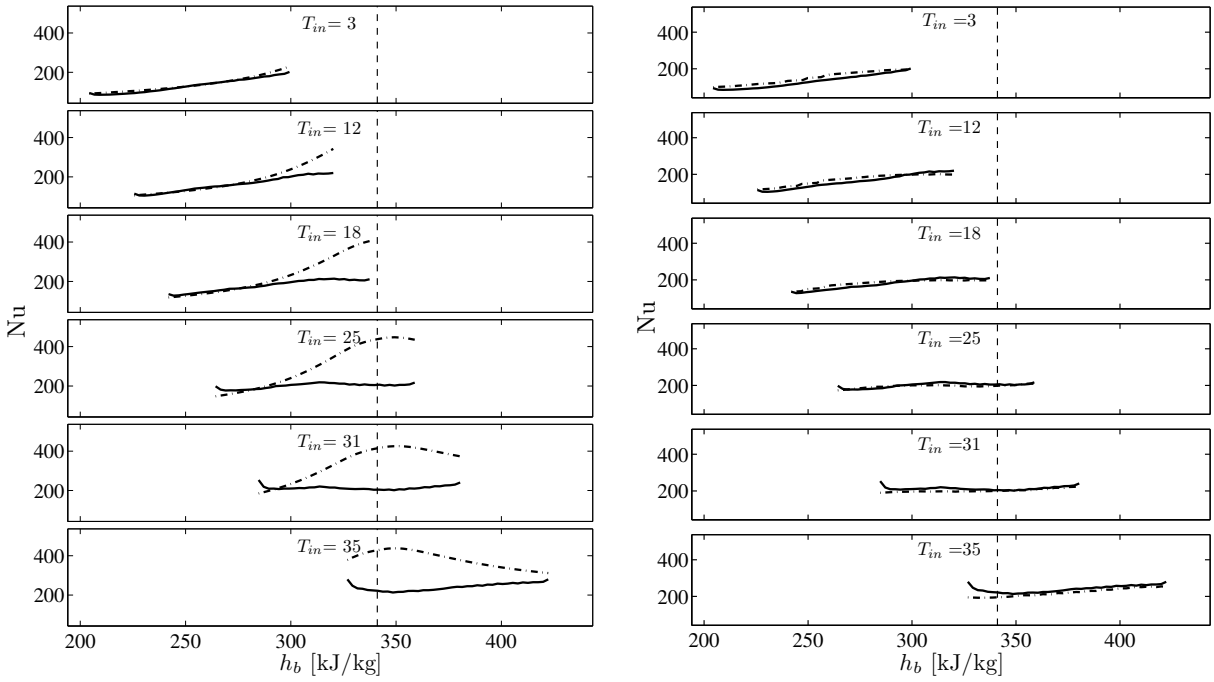
Selection of a normal heat transfer correlation

Several authors have identified the occurrence of HTD by comparing the measured heat transfer coefficient HTC, or Nusselt number Nu, with predictions of different correlations for normal heat transfer. As can be seen in Table 2.1, most of the available normal heat transfer correlations are based on the Dittus and Boelter (1930) correlation

$$\mathrm{Nu}_{DB} = 0.023 \mathrm{Re}_b^{0.8} \mathrm{Pr}_b^{0.4} \quad . \tag{5.1}$$

Figure 5.15a shows some representative comparisons of predictions of this correlation and present measurements for normal heat transfer. It can be seen that predictions and measurements were in good agreement as long as the bulk enthalpy h_b was significantly lower

of higher than the pseudo-critical value h_{pc}. In contrast, within a range of h_b that was centrered at h_{pc}, the Dittus-Boelter correlation greatly over-predicted the measurements, with the maximum discrepancy occurring at bulk specific enthalpies slightly higher than h_{pc}. This was found to apply consistently to all normal heat transfer measurements in all three test sections.



(a) Nu_{DB} predictions

(b) Nu_{NHT} predictions

Figure 5.15: Comparisons between Nu_{exp} and predicted Nu for $P/P_c = 1.13$, $D = 4.6$ mm, $G = 500$ kg/m^{2}s, $q = 45$ kW/m^2; solid lines represent Nu_{exp}; dashed-dotted lines represent predicted Nu; vertical dashed lines represent h_{pc}; units of T_{in} are °C.

A well-known limitation of the Dittus-Boelter correlation (and other correlations that are based on bulk properties) for pipe flows with a strong radial temperature gradient is that it does not account for a possible cross-sectional variation of thermophysical properties. This would indeed be the case in a pipe flow at a supercritical pressure, in which the wall temperature was near the pseudo-critical value whereas the bulk temperature was

well below it. Then the values of thermophysical properties, particularly the specific heat, would change drastically across the test section, which in turn would have a strong impact on the heat transfer coefficient. Because the near-wall specific heat would be higher than the bulk value, heat transfer would appear to be enhanced compared to an estimate based on bulk temperature. To account for this effect, several authors have introduced corrections to bulk-based correlations that include the evaluation of properties at both wall and bulk temperatures, and sometimes at intermediate ones as well. The earliest example is the work by Krasnoshchekov and Protopopov (1966). These authors started with the bulk-based correlation

$$\mathrm{Nu}_o = \frac{\zeta}{8}\mathrm{Re}_b\mathrm{Pr}_b\frac{1}{12.7\sqrt{\frac{\zeta}{8}}\left(\mathrm{Pr}_b^{2/3}-1\right)+1.07} \quad ,$$

where

$$\zeta = \frac{1}{\left(1.82log(\mathrm{Re}_b)-1.64\right)^2} \quad .$$

Then, they introduced correction factors to compensate for changes in thermophysical properties over the cross section of the flow, as follows

$$\mathrm{Nu}_{Kras} = \mathrm{Nu}_o\left(\frac{\rho_w}{\rho_b}\right)^{0.3}\left(\frac{\overline{C_p}}{C_{p_b}}\right)^n \quad . \tag{5.2}$$

In this expression, the exponent n was evaluated as

$$\begin{aligned}
n = 0.4 \quad &\text{for} \quad T_b < T_w < T_{pc} \qquad \text{and for} \quad 1.2T_{pc} < T_b < T_w \\
n = 0.4 + 0.2\left(\tfrac{T_w}{T_{pc}}-1\right) \quad &\text{for} \quad T_b < T_{pc} < T_w \\
n = 0.4 + 0.2\left(\tfrac{T_w}{T_{pc}}-1\right)\left[1-5\left(\tfrac{T_b}{T_{pc}}-1\right)\right] \quad &\text{for} \quad T_{pc} < T_b < 1.2T_{pc} \quad \text{and} \quad T_b < T_w
\end{aligned}$$

and $\overline{C_p}$ was defined as

$$\overline{C_p} = \frac{h_w - h_b}{T_w - T_b} \; . \tag{5.3}$$

The same correction relationship (5.2) was recently adopted by Jackson (2013), who, however, instead of Nu_o, used the bulk-based correlation of Kays (1966)

$$\mathrm{Nu}_K = 0.0183\mathrm{Re}_b^{0.82}\mathrm{Pr}_b^{0.5} \quad . \tag{5.4}$$

Jackson (2013) reported that predictions of the Nusselt number for normal heat transfer in carbon dioxide were 98% of the time within ±25% of the measured value. He also stated,

albeit without presenting any evidence, that the performance of this correlation would have been virtually the same, if Nu_{DB} were used instead of Nu_K.

Because Nu_{DB} is more widely used than other bulk-based correlations, as well as fitting well to the present normal heat transfer data at far-from-pseudo-critical conditions, we decided to assess the occurrence of HTD by comparison of our measurements to predictions of the following normal heat transfer correlation

$$\mathrm{Nu}_{NHT} = \mathrm{Nu}_{DB} \left(\frac{\rho_w}{\rho_b}\right)^{0.3} \left(\frac{\overline{C_p}}{C_{p_b}}\right)^n \quad , \tag{5.5}$$

where the exponent n is evaluated in the same way as for Eq. (5.2).

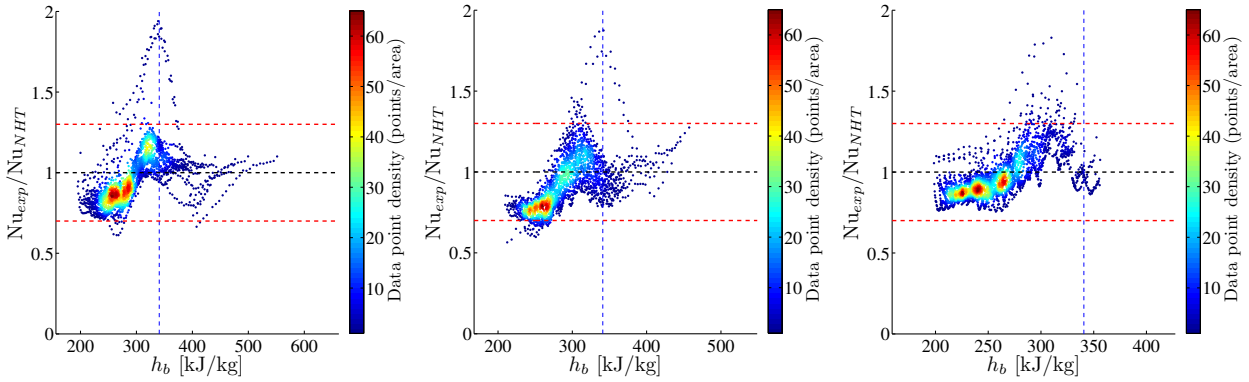
Testing of the selected correlation against normal heat transfer data

We computed the prediction of the selected correlation by means of an iterative process (see Appendix E for details) and tested its accuracy against our normal heat transfer data in all three test sections, for cases with conditions listed in Table 5.3. As shown for a representative case in Figure 5.15b, the predictions of this correlation near the pseudo-critical bulk enthalpy were much better than those of the Dittus-Boelter correlation. In fact, we found Nu_{NHT} to be fairly accurate for the vast majority of tested cases, as illustrated in Figure 5.16. Predictions of Nu_{NHT} were within $\pm 30\%$ of the measured values for 98%, 94%, and 98% of the data points collected in the 4.6 mm, 8 mm, and 22 mm test sections, respectively. Figure 5.16 also shows that a great portion of data points that differed significantly (up to 100%) from the predictions of Nu_{NHT} were taken at near-pseudo-critical conditions. The uncertainties of both measurements and predictions are expected to be elevated under such conditions, for which the values of thermophysical properties would be very sensitive to errors in the recorded values of temperature, pressure *etc.* and even values computed from the NIST tables could have higher uncertainty.

In summary, it has been shown that the use of Nu_{NHT} or similar normal heat transfer correlations as a basis for HTD identification may lead to occasional misdiagnoses, especially for cases with specific bulk enthalpies near to h_{pc}. Even so, as will be demonstrated in the following, this approach is capable of providing additional insight for cases for which HTD identification based on the shape of a measured wall temperature profile is inconclusive.

Table 5.3: Conditions of normal heat transfer cases tested with the Nu_{NHT} correlation

D [mm]	P/P_c [–]	G [kg/m^{2}s]	q [kW/m^2]	T_{in} [°C]
4.6	1.13	300	13	8, 10, 12, 16, 20, 24, 27, 30, 32, 35
4.6	1.13	400	30	0, 3, 7, 12, 15, 17, 20, 22, 24, 26, 30, 35
4.6	1.13	500	45	-1, 3, 5, 9, 12, 14, 18, 20, 23, 25, 30, 35
4.6	1.13	600	75	-1, 4, 7, 10, 12, 14, 16, 18, 20, 22, 24, 26, 30, 35
4.6	1.13	700	110	26, 34
4.6	1.13	1000	230	15, 23, 35
8	1.13	300	13	14, 16, 18, 20, 22, 24, 28, 31, 33, 35
8	1.13	400	30	6, 9, 11, 13, 15, 17, 19, 21, 23, 25, 26, 27, 28, 31, 33
8	1.13	500	50	5, 7, 9, 11, 13, 15, 17, 19, 21, 23, 25, 27, 29, 31
8	1.13	600	80	4, 6, 8, 10, 12, 14, 16, 18, 20
8	1.13	700	100	25, 29, 34
8	1.13	1000	235	4, 14
22	1.13	300	10	1, 3, 5, 7, 9, 11, 13, 15, 17, 19, 21, 23, 25, 27, 29, 31, 33, 35, 36
22	1.13	400	20	13, 15, 17, 19, 21, 23, 25, 27, 29, 31, 33, 35, 36
22	1.13	500	35	3, 5, 7, 9, 11, 13, 15, 17, 19, 21, 23, 25, 27
22	1.13	600	55	3, 5, 7, 9, 11, 13, 15, 17, 19, 21, 23, 25, 27, 29, 31
22	1.13	700	70	2, 5, 7, 31, 33, 35



(a) 4.6 mm test section (b) 8 mm test section (c) 22 mm test section

Figure 5.16: Plots of $\mathrm{Nu}_{exp}/\mathrm{Nu}_{NHT}$ for normal heat transfer cases; blue dashed line represents h_{pc}; black dashed line represents $\mathrm{Nu}_{exp}/\mathrm{Nu}_{NHT} = 1$; red dashed lines represent $\mathrm{Nu}_{exp}/\mathrm{Nu}_{NHT} = \pm 30\%$.

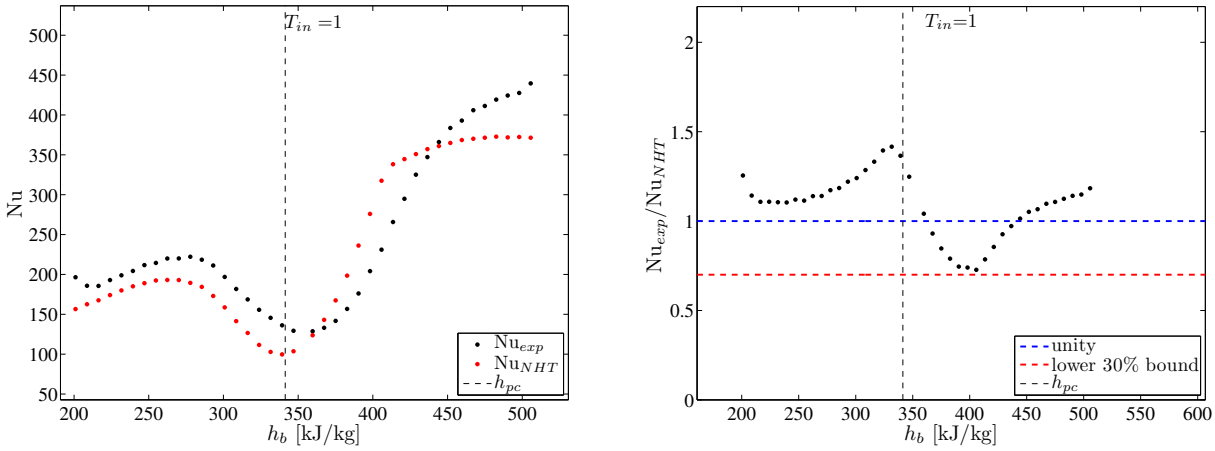
HTD identification from a normal heat transfer correlation

As discussed in Section 5.4.1, under certain conditions, wall temperature profiles contained sharp spikes, which were clear indications of local HTD occurrence. Under different conditions, however, such profiles contained broad and mild bumps, which did not evolve into spikes even for the highest heat flux examined. This was, for example, the case for $G = 1000$ and 1500 kg/m^{2}s in the 4.6 and 8 mm test sections, for which observation of the temperature profiles did not lead into a positive identification of either HTD or normal heat transfer. To test the suitability of Nu_{NHT} for use in HTD identification, we have plotted together the measured and predicted Nusselt numbers, as well as their ratio in separate plots, for all cases with $G = 1000$ and 1500 kg/m^{2}s in the 4.6 and 8 mm test sections (see Appendix B, Figures B.1 to B.14 for the 4.6 mm test section and Figures B.15 to B.32 for the 8 mm test section). A representative example for each test section is shown in Figure 5.17. In these plots we can see that Nu_{NHT} never deviated significantly from Nu_{exp}; in certain regions the former was larger than the latter and in others the reverse was true. These examples seem to indicate that, in general, $\mathrm{Nu}_{exp}/\mathrm{Nu}_{NHT} > 1$ in the near-pseudo-critical region. This does not

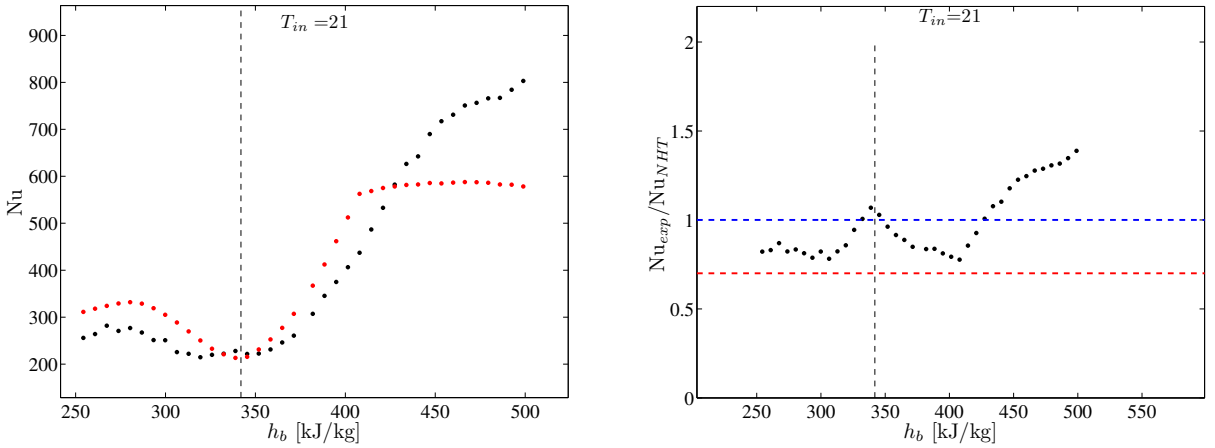
necessarily indicate that heat transfer was enhanced, but more likely that Nu_{NHT} underestimated the normal Nu in this region, as already demonstrated by Figure 5.16. One may also notice a region with $\mathrm{Nu}_{exp}/\mathrm{Nu}_{NHT} < 1$ at a location around the bump in the temperature profile. Nevertheless, values of this ratio never dropped below 0.7, which means that heat transfer could well be normal, according to the criterion used for constructing Figure 5.16.

By comparing $T_{w_{exp}}$ to $T_{w_{NHT}}$ over a wide range of T_{in} and different q (see Figure 5.18), it can be seen that deterioration indeed occurred at sufficiently large q. Although the predicted wall temperature was not very close to the measured values for some cases, especially near to h_{pc}, grouping sets of $T_{w_{exp}}$ and $T_{w_{NHT}}$ over wide ranges of conditions allowed a confident identification of HTD, even for cases that were individually unclear, as those for $G = 1000$ and 1500 kg/m^{2}s in both test sections. A complete set of $T_{w_{exp}}$ and $T_{w_{NHT}}$ for all three test sections can be found in Appendix C. These results will be used to identify HTD for cases with gradually developing, mild temperature bumps.

In summary, comparison of the measured Nu_{exp} with the normal heat transfer correlation Nu_{NHT} did not indicate that there was significant HTD in the 4.6 and 8 mm test sections for $G = 1000$ and 1500 kg/m^{2}s and q in the tested range. However, when comparing $T_{w_{exp}}$ to $T_{w_{NHT}}$ by grouping large sets of data together, it was possible to identify the occurrence of HTD with some confidence. The results also seem to indicate that further empirical adjustment of the correction factors to the Dittus-Boelter correlation might produce a correlation that accounts more accurately for a radial variation of thermophysical properties.

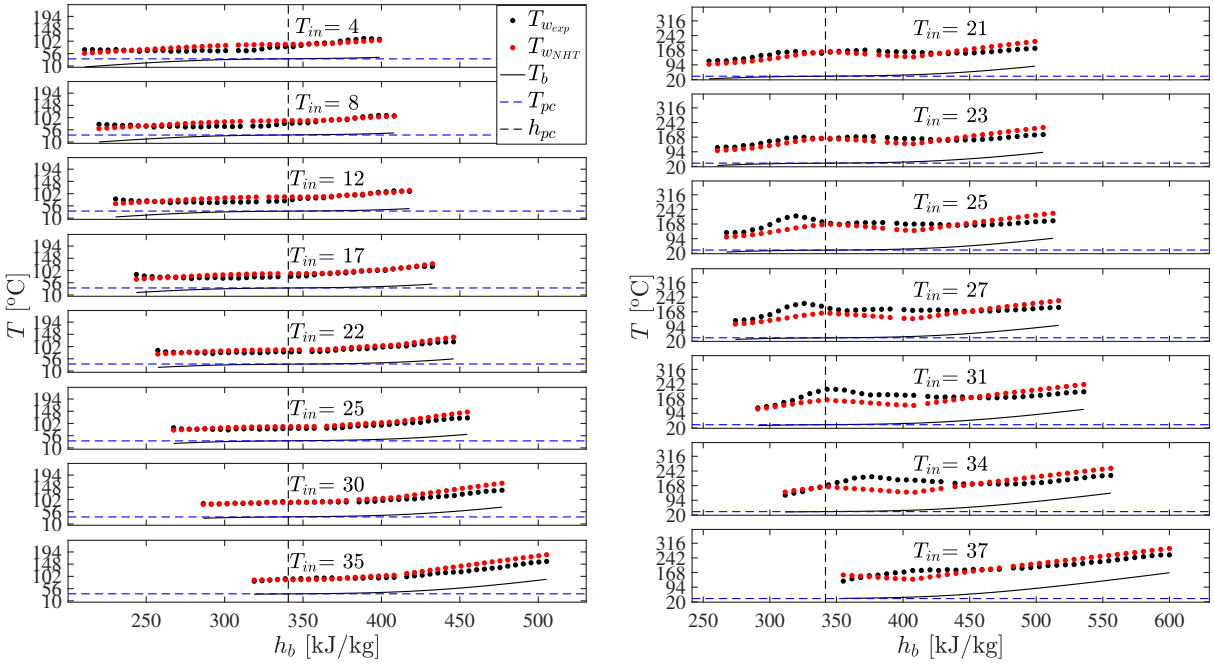


(a) 4.6 mm Test Section



(b) 8 mm Test Section

Figure 5.17: Axial profiles of Nu_{exp}, Nu_{NHT} and their ratio. In all cases, $P/P_c = 1.13$ and $G = 1000$ kg/m^{2}s. a) 4.6 mm test section with $q = 260$ kW/m^2; b) 8 mm test section with $q = 290$ kW/m^2; T_{in} is in °C.



(a) $q = 200$ kW/m^2 (b) $q = 260$ kW/m^2

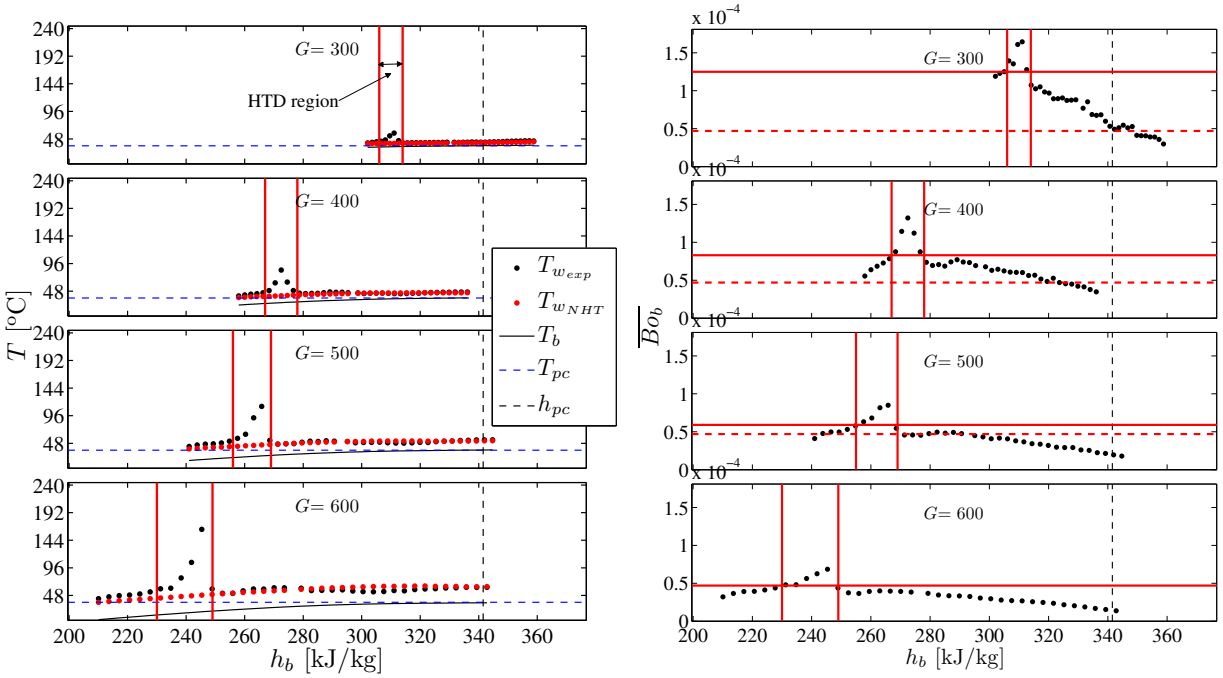
Figure 5.18: Comparisons between $T_{w_{exp}}$ and $T_{w_{NHT}}$ for $P/P_c = 1.13$, $D = 8$ mm, $G = 1000$ kg/m^{2}s.

5.4.3 Identifying HTD using a buoyancy parameter

As mentioned in Section 2.1.3, Jackson and Hall (1978) introduced a buoyancy parameter $\overline{Bo_b}$ (Equation 2.1) and estimated that HTD would be significant (*i.e.*, the HTC would be reduced by at least 5% by comparison to the normal case) when $\overline{Bo_b}$ exceeded 10^{-5}. Since its introduction, numerous authors have evaluated the buoyancy parameter from experimental data and have suggested different threshold values for HTD occurrence (see Table 2.1). Modifications to the original buoyancy parameter have also been suggested and tested, but in all cases success has been limited. The present database, compiled following a dense test matrix, provides an opportunity for a detailed evaluation of previously suggested buoyancy parameters and the possible introduction of additional corrections.

First, we tested the original hypothesis that there is a universal threshold of $\overline{Bo_b}$ for the

occurrence of HTD. We selected a few cases for which spikes appeared in the wall temperature profiles, thus providing unmistakable evidence of HTD, whereas large parts of the same profiles were in the normal heat transfer mode. Such profiles for a few mass fluxes in the 8 mm test section are shown in Figure 5.19a, where measured values $T_{w_{exp}}$ are compared with predictions $T_{w_{NHT}}$ using Nu_{NHT}. Regions of significant HTD can be confidently identified in all profiles. Figure 5.19b shows profiles of the corresponding $\overline{Bo_b}$ and demonstrates that evident spikes also appeared in these profiles, which qualifies the buoyancy parameter as a qualitative indicator of HTD. On the other hand, the spikes in $\overline{Bo_b}$ diminished in amplitude as G was increased, in sharp contrast to spikes in $T_{w_{exp}}$, which became more accentuated with increasing G. This observation indicates that spikes in $\overline{Bo_b}$ would likely become a less sensitive qualitative indicator of HTD than spikes in $T_{w_{exp}}$ as G is increased. The main interest in $\overline{Bo_b}$, however, is not as a qualitative HTD indicator, but rather a quantitative one. In each of the four plots in Figure 5.19b, we have drawn a horizontal solid line that intersects the $\overline{Bo_b}$ profile at the approximated boundaries of its HTD region, as determined from the edges of the spikes in the wall temperature profile. Each of these lines defines a threshold $\overline{Bo_{b,HTD}}$ for HTD occurrence for the particular case considered. A comparison of the different thresholds shows clearly that their value decreased from about 1.3×10^{-4} for the lowest G considered to 0.5×10^{-4} for the highest G, which was only twice as high as the lowest G in these tests. The use of a low–G threshold would miss HTD entirely in some high–G cases, whereas the use of a high–G threshold would misidentify extensive regions of normal heat transfer in low–G cases as HTD regions. This discussion has demonstrated that the use of a fixed threshold of $\overline{Bo_b}$ as HTD identifier would lead to misdiagnoses for wide ranges of conditions.



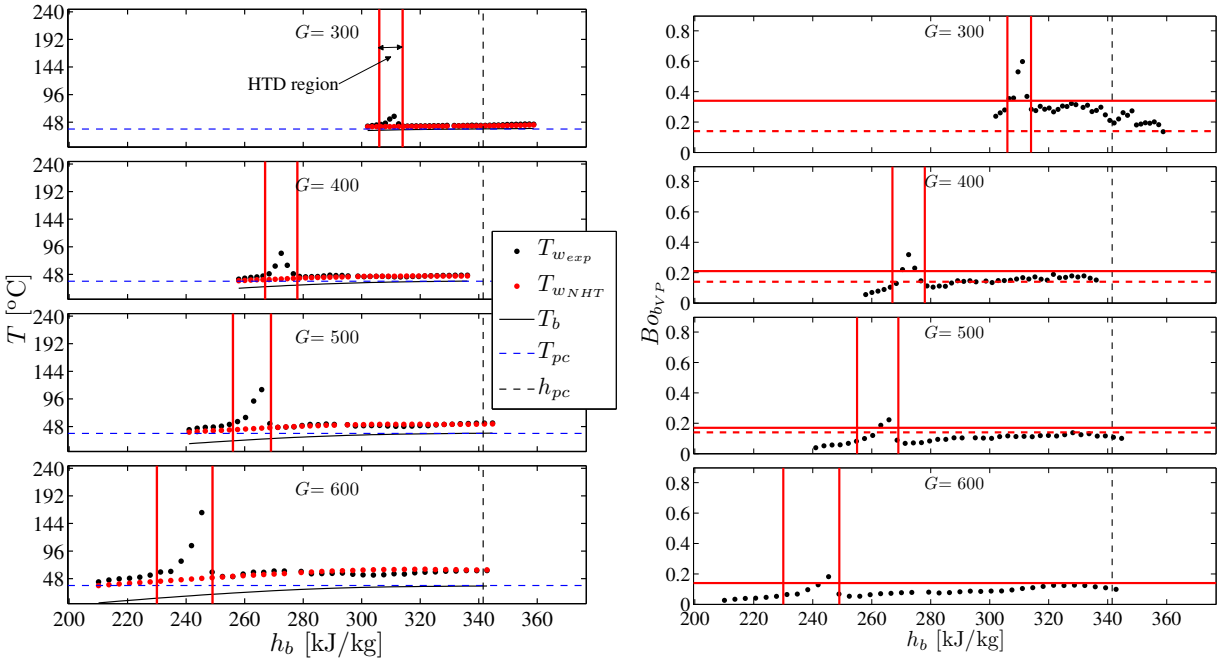
(a) T_w profiles

(b) $\overline{Bo_b}$ profiles

Figure 5.19: a) Axial profiles of the wall temperature for different mass fluxes G (in units of kg/m^{2}s) for the 8 mm test section; b) axial profiles of the corresponding $\overline{Bo_b}$; solid red lines represent the HTD threshold for the particular G, whereas dashed red line represent the threshold for the highest G.

A corrected version $Bo_{b_{VP}}$ of the buoyancy parameter (Section 2.1.3, Equation 2.3) was proposed by Jackson (2013). This parameter incorporates several correction factors to account for the effect of buoyancy on heat transfer in the presence of significant non-uniformity of fluid properties and also includes a coefficient C_B, which is proportional to the dimensionless buffer layer thickness δ^+. Further assuming that $\delta^+ \approx 30$, Jackson (2013) estimated the value $C_B \approx 4600$ and suggested that buoyancy would decrease the HTC by at least 5%, when $Bo_{b_{VP}} \geq 0.04$. Although the use of a universal proportionality coefficient is of no consequence in the determination of a threshold, we will retain this value of C_B in our analysis for consistency with the literature. In the following, we will test the accuracy of the modified buoyancy parameter as HTD identifier against our data.

Axial profiles of the modified buoyancy parameter have been plotted next to corresponding wall temperature profiles in Figure 5.20 for the same conditions as those used in Figure 5.19. Qualitatively, the $Bo_{b_{VP}}$ profiles seem to resemble the corresponding T_w profiles closer than $\overline{Bo_b}$ profiles do. Both $Bo_{b_{VP}}$ and $\overline{Bo_b}$ have peaks at the locations of T_w peaks, but $\overline{Bo_b}$ drops significantly at higher h_b, whereas $Bo_{b_{VP}}$ maintains fairly high values, in resemblance to the T_w profiles. For the purposes of HTD identification, however, this is not a desirable feature, because it introduces the possibility that values of $Bo_{b_{VP}}$ at high h_b, which clearly correspond to normal heat transfer, may be higher than its value at the peak, which presumably corresponds to HTD. As for the $\overline{Bo_b}$ plots, we fitted the $Bo_{b_{VP}}$ plots with thresholds $Bo_{b_{VP,HTD}}$ separating regions of NHT and HTD. It can be readily seen in Figure 5.20 that these thresholds did not have a universal value, but decreased with increasing mass flux. It is also evident that, as a consequence of the exclusion of NHT regions at high h_b, the use of $Bo_{b_{VP,HTD}}$ severely restricts the extent of HTD regions, whereas the use $\overline{Bo_{b,HTD}}$ poses a lesser restriction in this respect. Further comparison between the profiles of the two buoyancy parameters indicates once more that the modified parameter offers no advantage in separating regions of NHT and HTD, because the magnitudes of the peaks of these parameters are slightly smaller than those of the original buoyancy parameter. Although our observations have demonstrated that $Bo_{b_{VP}}$ may be a more problematic HTD indicator than $\overline{Bo_b}$ is, we will pursue the testing of both parameters in order to enhance our understanding of their significance.



(a) T_w profiles

(b) $Bo_{b_{VP}}$ profiles

Figure 5.20: a) Axial profiles of the wall temperature for different mass fluxes G (in units of kg/m^{2}s) for the 8 mm test section; b) axial profiles of the corresponding $Bo_{b_{VP}}$; solid red lines represent the HTD threshold for the particular G, whereas dashed red line represent the threshold for the highest G.

Having noticed the clear dependence of the HTD thresholds $\overline{Bo_{b_{HTD}}}$ and $Bo_{b_{VP,HTD}}$ of both buoyancy parameters upon the mass flux, we will next develop correction factors $C_{G,\overline{Bo_b}}$ and $C_{G,Bo_{b_{VP}}}$ for this dependence. Each threshold from Figures 5.19b and 5.20b, normalised by the corresponding reference value $\overline{Bo_{b_{HTD,ref}}} = 0.47 \times 10^{-4}$ or $Bo_{b_{VP,HTD,ref}} = 0.14$ at $G_{ref} = 600$ kg/m^{2}s, has been plotted in Figure 5.21 *vs.* G/G_{ref} and using log-log scales. It can be seen that the two sets of values can be fitted well by the power functions

$$\frac{\overline{Bo_{b_{HTD}}}}{\overline{Bo_{b_{HTD,ref}}}} = \left(\frac{G}{G_{ref}}\right)^{-1.4} \equiv \left(C_{G,\overline{Bo_b}}\right)^{-1} \tag{5.6}$$

and

$$\frac{Bo_{b_{VP,HTD}}}{Bo_{b_{VP,HTD,ref}}} = \left(\frac{G}{G_{ref}}\right)^{-1.2} \equiv \left(C_{G,Bo_{b_{VP}}}\right)^{-1} . \tag{5.7}$$

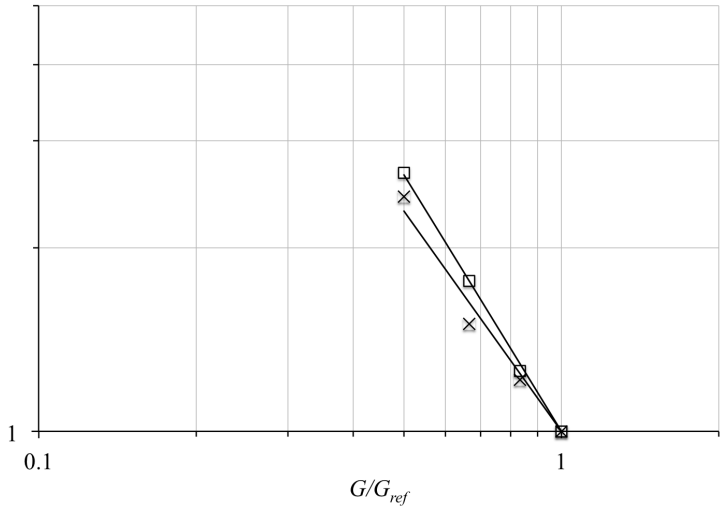


Figure 5.21: Plots of $\overline{Bo_{b_{HTD}}}/\overline{Bo_{b_{HTD,ref}}}$ (□) and $Bo_{b_{VP,HTD}}/\overline{Bo_{b_{VP,HTD,ref}}}$ (×) *vs.* G/G_{ref}, where $G_{ref} = 600$ kg/m^{2}s; black lines represent fitted power functions.

In the remainder of this section, we will evaluate the appropriateness of the two corrected buoyancy parameters as HTD identifiers in our tests. More specifically, we will examine whether wall temperature profiles with clearly visible spikes, and only these, satisfy the conditions

$$C_{G,\overline{Bo_b}}\overline{Bo_b} \geq 0.47 \times 10^{-4} \tag{5.8}$$

and

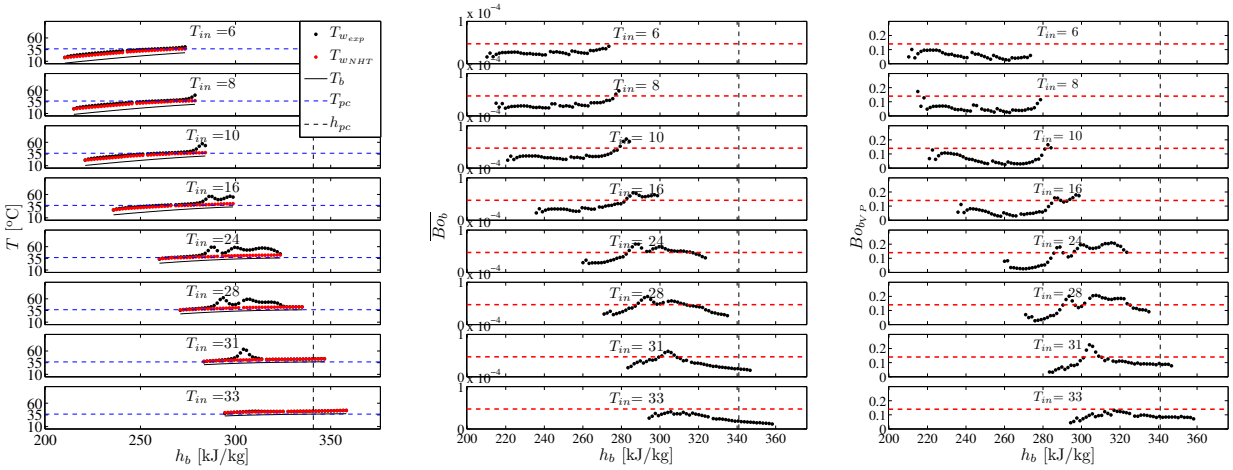
$$C_{G,Bo_{b_{VP}}} Bo_{b_{VP}} \geq 0.14 . \tag{5.9}$$

We will present axial profiles of the two corrected buoyancy parameters next to profiles of wall temperature, which were our main basis for HTD identification.

Tests of corrected buoyancy parameters against data in the 4.6 mm test section

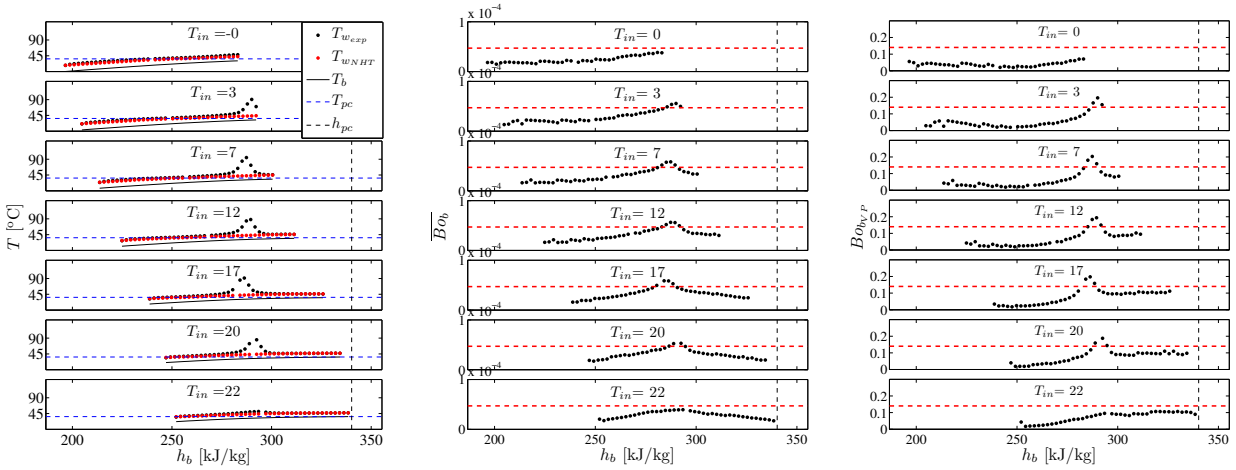
As shown in Figure 5.22, for $G = 300$ kg/m^{2}s, the profiles of both buoyancy parameters were choppy and had discontinuities, which were not present in the temperature profiles.

These discontinuities are attributed to discontinuities in the calculation of thermophysical properties from the NIST tables. Although they should have no significance on the occurrence of HTD, in one case ($T_{in} = 8$ °C) they were large enough to trigger a false indication of HTD. Excluding this case, both parameters identified HTD correctly, with their primary and secondary peaks rising above the thresholds. For $G = 400$ (Figure 5.23) and 500 kg/m^{2}s (not shown here), both buoyancy parameters also predicted HTD correctly, although peaks in the $\overline{Bo_b}$ profiles were in some cases not as well defined as those in the $Bo_{b_{VP}}$ profiles.



(a) T_w profiles (b) $\overline{Bo_b}$ profiles (c) $Bo_{b_{VP}}$ profiles

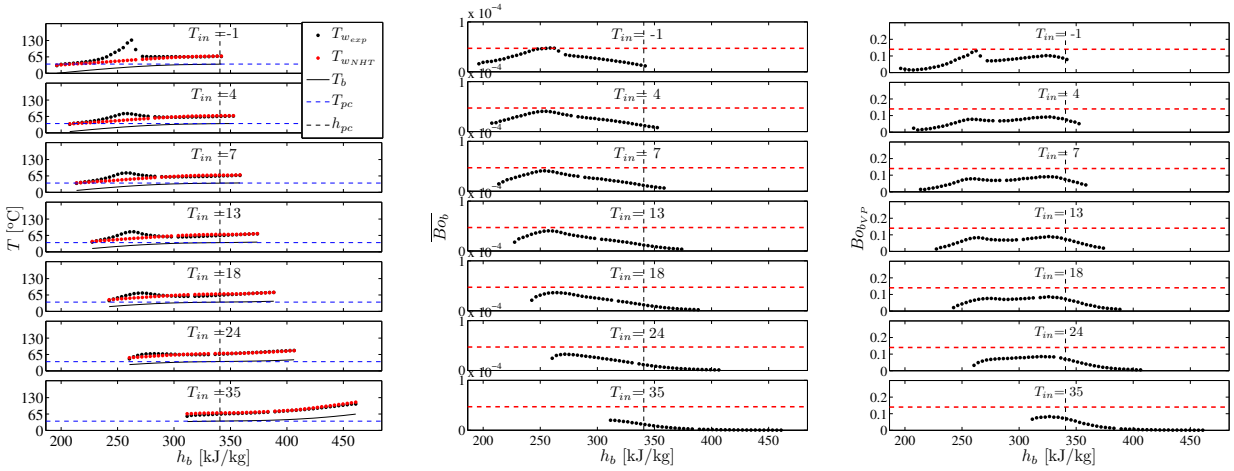
Figure 5.22: $\overline{Bo_b}$, $Bo_{b_{VP}}$, and T_w profiles for $P/P_c = 1.13$, $D = 4.6$ mm, $G = 300$ kg/m^{2}s, $q = 18$ kW/m^2; dashed red lines represent suggested thresholds; T_{in} is in °C.



(a) T_w profiles (b) $\overline{Bo_b}$ profiles (c) $Bo_{b_{VP}}$ profiles

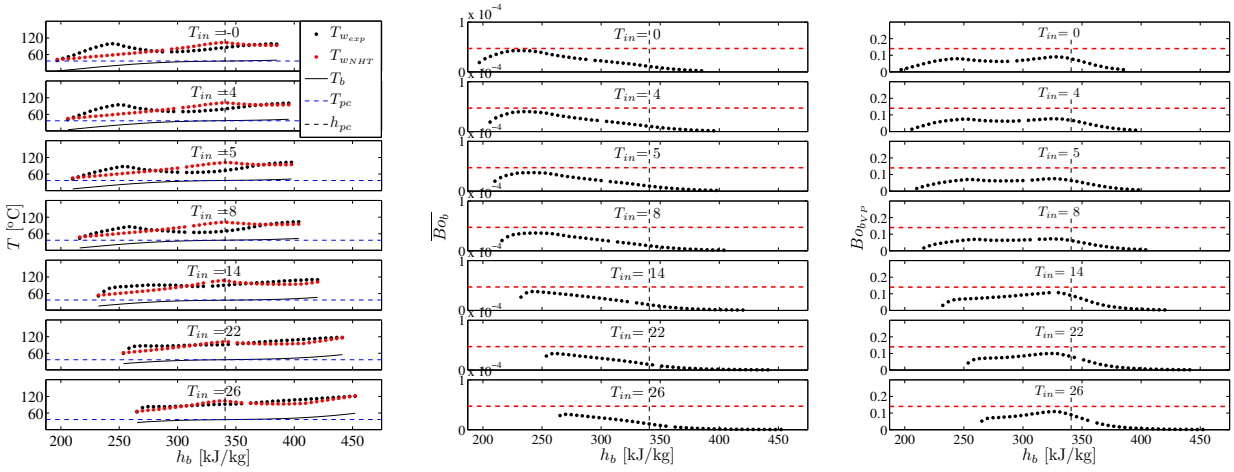
Figure 5.23: $\overline{Bo_b}$, $Bo_{b_{VP}}$, and T_w profiles for $P/P_c = 1.13$, $D = 4.6$ mm, $G = 400$ kg/m^{2}s, $q = 33$ kW/m^2; dashed red lines represent suggested thresholds; T_{in} is in °C.

In contrast to the lower G cases, when the mass flux was increased to $G = 600$ kg/m^{2}s (Figure 5.24), both of the buoyancy parameters missed some HTD cases or barely reached the threshold. With further increase of G to 700 kg/m^{2}s (Figure 5.25), none of the $\overline{Bo_b}$ and $Bo_{b_{VP}}$ profiles crossed the HTD threshold, even for cases with strong T_w bumps. In these cases, $\overline{Bo_b}$ seems to outperform $Bo_{b_{VP}}$ by producing bumps that came closer to the threshold and, unlike $Bo_{b_{VP}}$, by not showing a second large rise near h_{pc} that is not reflected in the temperature profile and could potentially trigger a false identification of HTD. In general, it seems that the performance of both parameters for the 4.6 mm test section decreased as the mass flux was increased.



(a) T_w profiles (b) $\overline{Bo_b}$ profiles (c) $Bo_{b_{VP}}$ profiles

Figure 5.24: $\overline{Bo_b}$, $Bo_{b_{VP}}$, and T_w profiles for $P/P_c = 1.13$, $D = 4.6$ mm, $G = 600$ kg/m^{2}s, $q = 83$ kW/m^2; dashed red lines represent suggested thresholds; T_{in} is in °C.

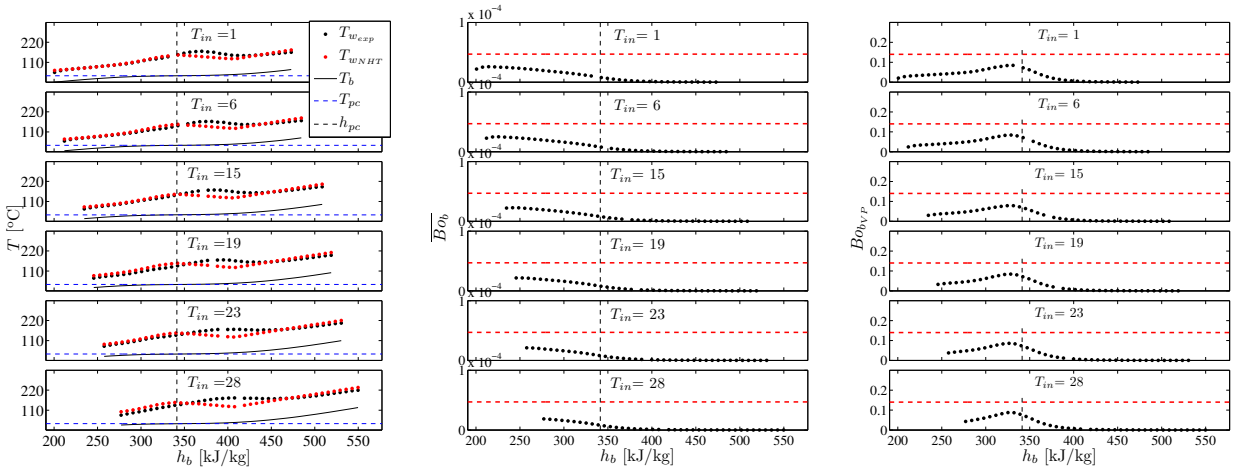


(a) T_w profiles (b) $\overline{Bo_b}$ profiles (c) $Bo_{b_{VP}}$ profiles

Figure 5.25: $\overline{Bo_b}$, $Bo_{b_{VP}}$, and T_w profiles for $P/P_c = 1.13$, $D = 4.6$ mm, $G = 700$ kg/m^{2}s, $q = 125$ kW/m^2; dashed red lines represent suggested thresholds; T_{in} is in °C.

For the highest mass fluxes $G = 1000$ and 1500 kg/m^{2}s (Figure 5.26), neither buoyancy

parameter indicated the presence of HTD in any of the cases; this may be an incorrect prediction because some of the temperature profiles in these cases contained small bumps. Nevertheless, the $Bo_{b_{VP}}$ profiles showed a bump near h_{pc} which does not correspond to a bump in the temperature profiles, whereas the $\overline{Bo_b}$ profiles did not show such bumps. The trend in T_w indicates that HTD would likely have been more distinct if q were increased sufficiently, but the values of the buoyancy parameters at the estimated location of the temperature peak do not seem likely to exceed the threshold levels following a moderate increase in q. A more extensive collection of axial profiles of the two corrected buoyancy parameters next to profiles of wall temperature for the 4.6 mm test section can be found in Appendix C, Figures C.1 to C.36.



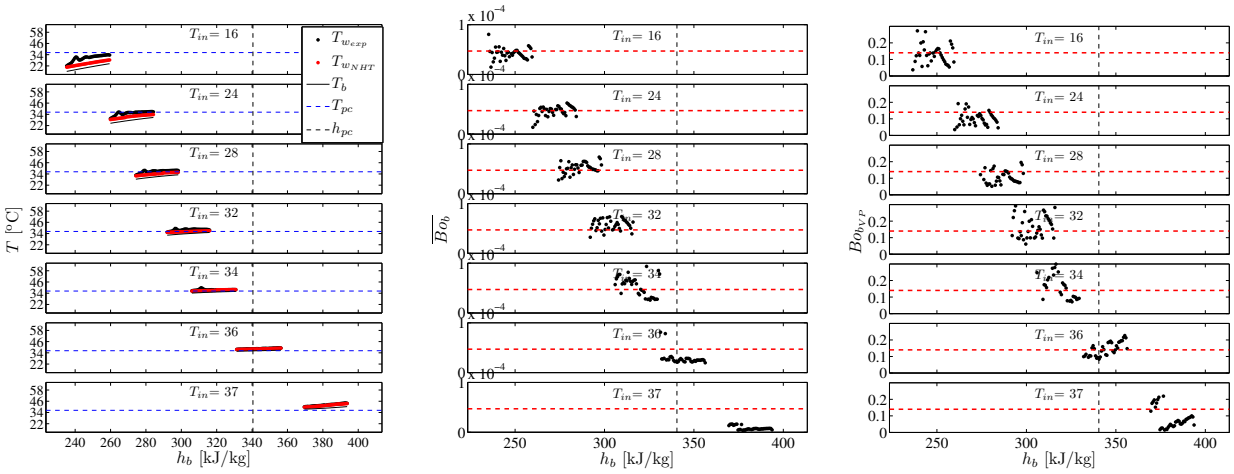
(a) T_w profiles (b) $\overline{Bo_b}$ profiles (c) $Bo_{b_{VP}}$ profiles

Figure 5.26: $\overline{Bo_b}$, $Bo_{b_{VP}}$, and T_w profiles for $P/P_c = 1.13$, $D = 4.6$ mm, $G = 1000$ kg/m^{2}s, $q = 260$ kW/m^2; dashed red lines represent suggested thresholds; T_{in} is in °C.

Tests of corrected buoyancy parameters against data in the 8 mm test section

For the lowest G tested of 200 kg/m^{2}s (Figure 5.27), the $\overline{Bo_b}$ and $Bo_{b_{VP}}$ profiles were very erratic and choppy to the point that they cannot be trusted. In fact, both parameters sporadically exceeded their HTD thresholds, in contradiction to the T_w profiles, which were smooth and indicated normal heat transfer. The $\overline{Bo_b}$ and $Bo_{b_{VP}}$ profiles for $G = 300$ kg/m^{2}s

were also choppy, especially at lower heat fluxes, but did not exceed the thresholds, which is a behaviour very similar to the one observed in the 4.6 mm test section (see Figure 5.22).

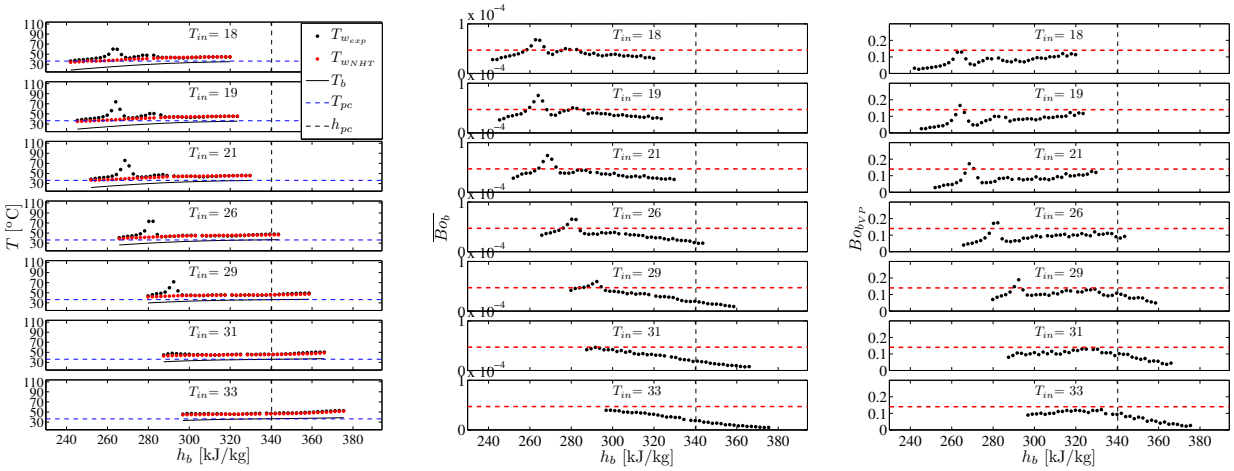


(a) T_w profiles (b) $\overline{Bo_b}$ profiles (c) $Bo_{b_{VP}}$ profiles

Figure 5.27: $\overline{Bo_b}$, $Bo_{b_{VP}}$, and T_w profiles for $P/P_c = 1.13$, $D = 8$ mm, $G = 200$ kg/m^{2}s, $q = 5$ kW/m^2; dashed red lines represent suggested thresholds; T_{in} is in °C.

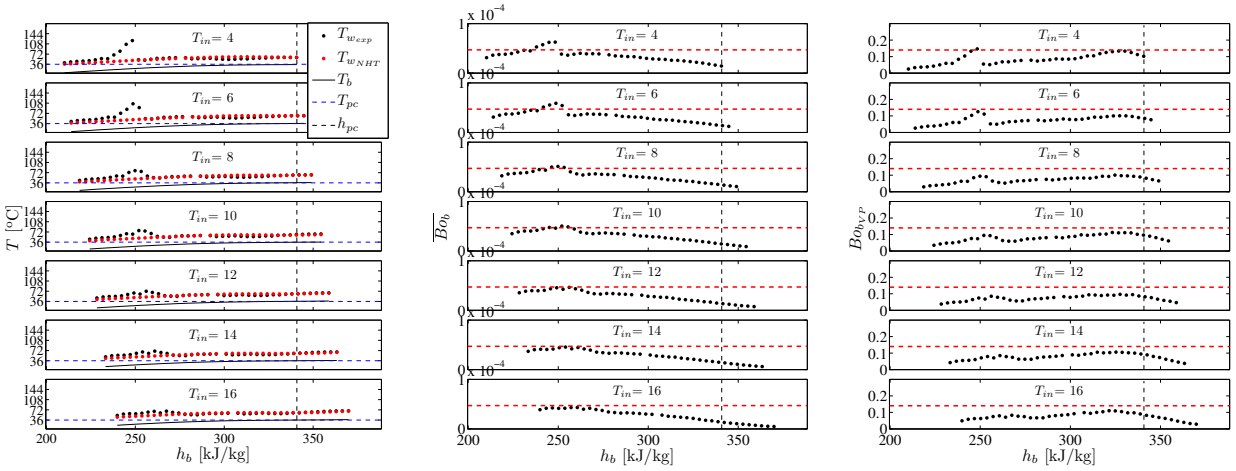
For $G = 400\,\text{kg/m}^2\text{s}$ (Figure 5.28), the profiles of both buoyancy parameter contained spikes, and even secondary bumps, that corresponded to spikes and bumps in the temperature profiles. $\overline{Bo_b}$ was generally successful in separating HTD and NHT cases, with even its secondary bumps often exceeding the threshold. $Bo_{b_{VP}}$ also had some success in identifying HTD, but missed the HTD case for $T_{in} = 18$ °C. Moreover, the profiles of $Bo_{b_{VP}}$ continued to rise downstream of the primary spike, in contrast to the temperature profiles. This prevented us from setting the threshold any lower in an effort to identify HTD more accurately. For $G = 500$ (not shown here), 600 (Figure 5.29) and $700\,\text{kg/m}^2\text{s}$ (Figure 5.30) $Bo_{b_{VP}}$ continued to perform well in nearly all cases (a possible exception is the $T_{in} = 17$ °C case in Figure 5.30, in which HTD is detected only marginally), while the performance of $Bo_{b_{VP}}$ continued to deteriorate to the point that it missed all HTD cases for the higher G. For $G = 1000$ and 1500 kg/m^{2}s, the performances of the two buoyancy parameters were similar to those observed in the 4.6 mm test section for the same G (Figure 5.26). $\overline{Bo_b}$ did not detect any HTD and did not produce a bump in the profile near h_{pc}. $Bo_{b_{VP}}$ profiles, however, contained

large bumps forming near h_{pc}, which grew in magnitude with increasing heat flux, although never exceeding the HTD threshold. A more extensive collection of axial profiles of the two corrected buoyancy parameters next to profiles of wall temperature for the 8 mm test section can be found in Appendix C, Figures C.37 to C.86.



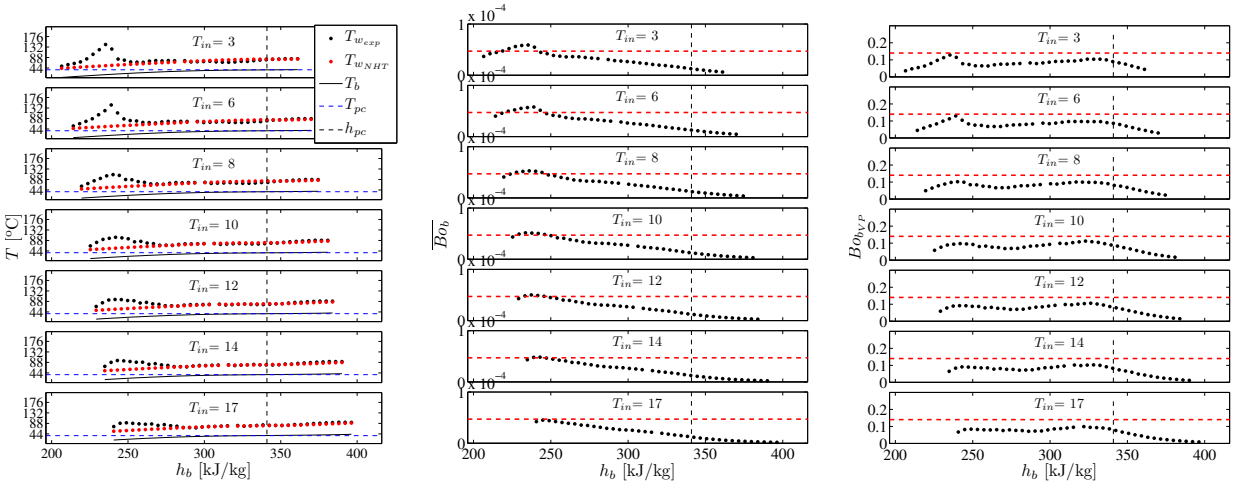
(a) T_w profiles (b) $\overline{Bo_b}$ profiles (c) $Bo_{b_{VP}}$ profiles

Figure 5.28: $\overline{Bo_b}$, $Bo_{b_{VP}}$, and T_w profiles for $P/P_c = 1.13$, $D = 8$ mm, $G = 400$ kg/m^{2}s, $q = 33$ kW/m^2; dashed red lines represent suggested thresholds; T_{in} is in °C.



(a) T_w profiles (b) $\overline{Bo_b}$ profiles (c) $Bo_{b_{VP}}$ profiles

Figure 5.29: $\overline{Bo_b}$, $Bo_{b_{VP}}$, and T_w profiles for $P/P_c = 1.13$, $D = 8$ mm, $G = 600$ kg/m^{2}s, $q = 83$ kW/m^2; dashed red lines represent suggested thresholds; T_{in} is in °C.

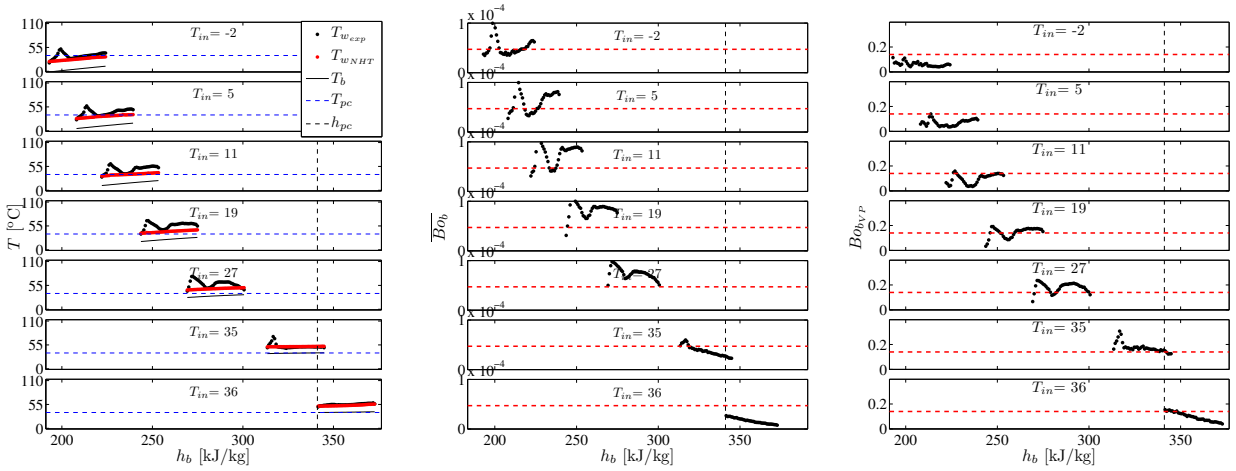


(a) T_w profiles (b) $\overline{Bo_b}$ profiles (c) $Bo_{b_{VP}}$ profiles

Figure 5.30: $\overline{Bo_b}$, $Bo_{b_{VP}}$, and T_w profiles for $P/P_c = 1.13$, $D = 8$ mm, $G = 700$ kg/m^{2}s, $q = 115$ kW/m^2; dashed red lines represent suggested thresholds; T_{in} is in °C.

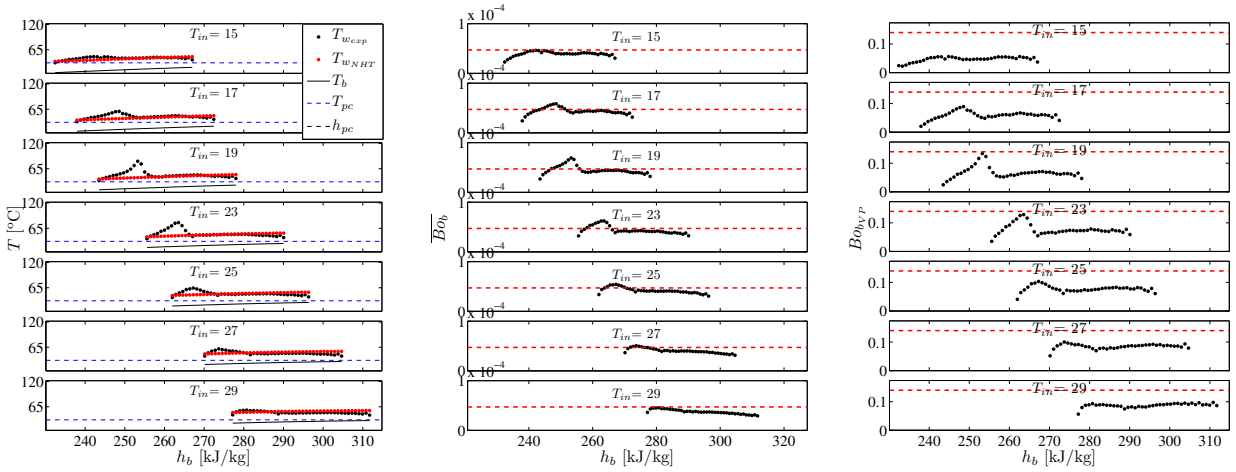
Tests of corrected buoyancy parameters against data in the 22 mm test section

The performances of the two corrected buoyancy parameters as HTD identifiers in the 22 mm test section were generally similar to those in the two smaller test sections at the same G. The profiles of both parameters for $G = 200$ and $300\,\mathrm{kg/m^2s}$ were choppy and could not be trusted to provide reliable HTD identification. For $G = 400$ (Figure 5.31), 500, 600 (Figure 5.32) and 700 $\mathrm{kg/m^2s}$ (Figure 5.33), $\overline{Bo_b}$ identified correctly all HTD cases. In some cases with high heat flux, however, some $\overline{Bo_b}$ profiles had very large peaks and were entirely above the threshold, in contrast with the corresponding temperature profiles, which indicated that HTD was localised. $Bo_{b_{VP}}$ suffered from the same problems as in the smaller test sections, altogether missing many HTD cases and having elevated values in the high enthalpy region, which could be potentially misidentified as HTD. A more extensive collection of axial profiles of the two corrected buoyancy parameters next to profiles of wall temperature for the 22 mm test section can be found in Appendix C, Figures C.87 to C.119.



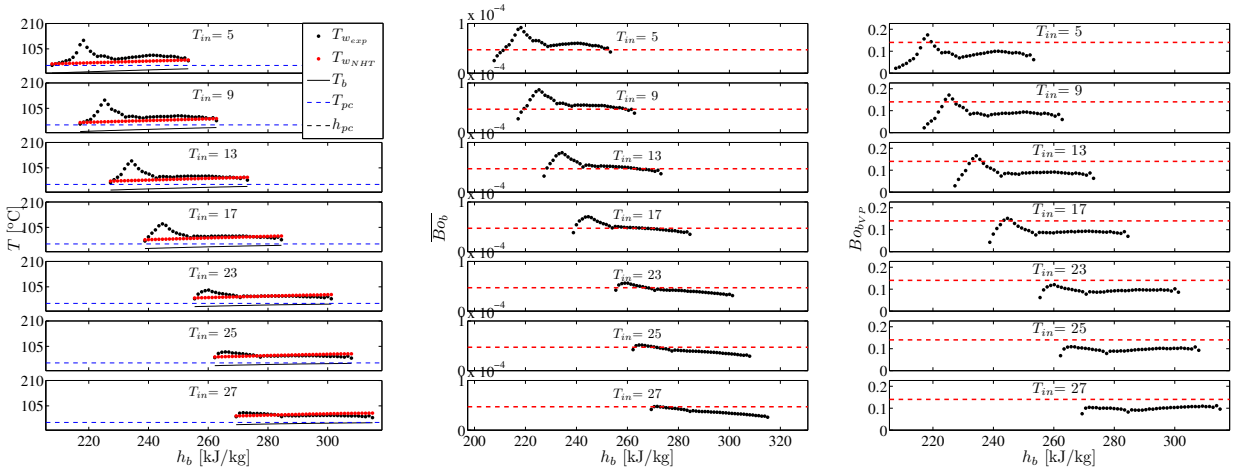
(a) T_w profiles (b) $\overline{Bo_b}$ profiles (c) $Bo_{b_{VP}}$ profiles

Figure 5.31: $\overline{Bo_b}$, $Bo_{b_{VP}}$, and T_w profiles for $P/P_c = 1.13$, $D = 22$ mm, $G = 400\ \mathrm{kg/m^2s}$, $q = 35\ \mathrm{kW/m^2}$; dashed red lines represent suggested thresholds; T_{in} is in °C.



(a) T_w profiles (b) $\overline{Bo_b}$ profiles (c) $Bo_{b_{VP}}$ profiles

Figure 5.32: $\overline{Bo_b}$, $Bo_{b_{VP}}$, and T_w profiles for $P/P_c = 1.13$, $D = 22$ mm, $G = 600$ kg/m^{2}s, $q = 58$ kW/m^2; dashed red lines represent suggested thresholds; T_{in} is in °C.



(a) T_w profiles (b) $\overline{Bo_b}$ profiles (c) $Bo_{b_{VP}}$ profiles

Figure 5.33: $\overline{Bo_b}$, $Bo_{b_{VP}}$, and T_w profiles for $P/P_c = 1.13$, $D = 22$ mm, $G = 700$ kg/m^{2}s, $q = 90$ kW/m^2; dashed red lines represent suggested thresholds; T_{in} is in °C.

5.4.4 Summary of HTD identification methods

Table D.1 in Appendix D contains a complete list of test conditions, with all identified HTD cases marked with the use of red font. HTD was identified by the observation of temperature spikes in the temperature profiles, complemented by a comparison of measured wall temperature values and those predicted by a normal heat transfer correlation. Despite being qualitative and subjective, this method was found to be the most reliable and, for the vast majority of cases at near–HTD–onset conditions, gave unambiguous results. In general, temperature spikes were distinct and sharp and appeared suddenly as the wall heat flux was increased gradually, making HTD onset clearly distinguishable from normal heat transfer behaviour. In some cases, however, temperature rises appeared gradually in the form of mild bumps in the profile as conditions were changed, so that the conditions for HTD onset were hard to identify precisely. In these cases, it was useful to compare the measured temperature profiles to predicted ones, using a newly suggested Nu_{NHT} correlation, on a case-by-cases basis. When differences in the corresponding values were significant near the peak of a bump, HTD was considered to have occurred. Because of the approximate nature of this approach and the wide ranges of conditions and profile shapes encountered, we considered it futile to attempt to quantify, even less automate, HTD detection based on temperature profiles.

An extensive analysis of the buoyancy parameters $\overline{Bo_b}$ and $Bo_{b_{VP}}$ was conducted for our data in three test sections, operating under widely ranging and closely incremented conditions, in order to assess the performance of these parameters as quantitative HTD identifiers. It was first found that correction factors were required for both parameters to account for shifting thresholds for HTD occurrence as the mass flux was increased or decreased. The corrected threshold for $\overline{Bo_b}$ identified correctly HTD in the majority of cases examined, although it missed a few HTD cases, especially in the 4.6 mm test section. Additional fine tuning of the $\overline{Bo_b}$ threshold and its correction factor seems to be worthwhile for establishing this parameter as HTD identifier under specified ranges of conditions. On the contrary, $Bo_{b_{VP}}$ did not perform very well in any test section and it seems that some or all of the suggested correction factors overcompensated the parameter for different influences. Because of its serious limitations, we do not see much value in incorporating small improvements to this parameters.

In closing, we would like to acknowledge some benefits from the use of a normal heat

transfer correlation and a buoyancy parameter threshold as unified and quantitative means for identifying HTD in a set of measurements. On the other hand, we found that these approaches are prone to misdiagnoses and can not be trusted blindly. Wall temperature measurements are, in any case, necessary for evaluating these parameters and so we see no reason to adopt either of these at the exclusion of direct observation of spikes in temperature profiles.

5.5 Onset of HTD

5.5.1 HTD maps

Following the three methods described in Section 5.4, we were able to classify each set of measurements as either a deteriorated or a normal heat transfer (NHT) case. This permitted us to illustrate the regions occupied by each heat transfer mode in maps having the experimental conditions D, T_{in}, q and G as parameters. To avoid clutter, we separated these maps according to the values of D and G and then plotted the regions occupied by each of the two heat transfer modes against axes corresponding to q and T_{in}. The results for the three test sections are shown in Figures 5.34 to 5.36. The maps shown in these figures have red regions that correspond to HTD and blue regions that correspond to NHT. Let us first make some general observations that apply to all results.

For a fixed value of T_{in}, we could observe NHT when $q < q_{onset}(D, G, T_{in})$ and HTD when $q \geq q_{onset}(D, G, T_{in})$. By exception, for a range of T_{in} values just below T_{pc}, NHT occurred even for the highest q considered, although we cannot exclude the possibility of HTD for even higher q. The lowest among all values of q_{onset} will be denoted as $q = q_{onset,min}(D, G)$; it represents the highest q for which HTD did not occur for any value of T_{in} within the present test range. To determine $q = q_{onset,min}$, we extrapolated by eye the HTD regions toward the low-q side and then marked the approximate location of $q_{onset,min}$ in each plot by a vertical red solid line. A comparison among the values of $q_{onset,min}$ for different G in each test section, makes it evident that they increased monotonically with increasing G, in agreement with past literature.

When T_{in} was increased gradually, while q was fixed, the heat transfer mode followed one

of two possible paths, depending on the values of D, G and q. When q had a sufficiently low value, NHT occurred for the entire range of T_{in} considered. For higher values of q, however, HTD occurred when T_{in} was within a subrange of the test range and NHT occurred when T_{in} was outside this subrange. In some cases, this subrange extended to the lowest considered values of T_{in}, whereas in others the HTD subrange was an intermediate one, with NHT regions appearing between the lower HTD boundary and the lowest T_{in} of the tests, as well as between the upper HTD boundary and T_{pc}. For the latter type of cases, and only for these, it was possible to identify an apex of the extrapolated HTD region, with coordinates $q = q_{onset,min}$ and $T_{in,qmin}$. At these conditions, HTD occurred only for an essentially isolated value of T_{in} and not for any other, higher or lower, values. For the cases for which it existed, $T_{in,qmin}$ was marked in the plots by a horizontal red solid line. Among the six cases with different G that were considered for each test section, clear identification of an HTD region apex was possible for $G = 300, 400, 500, 600$ and $700\,\mathrm{kg/m^2s}$ for the 22 mm tube, $G = 400$ and $500\,\mathrm{kg/m^2s}$ for the 8 mm tube, and possibly $G = 300$ and $400\,\mathrm{kg/m^2s}$ for the 4.6 mm tube. This confirms previous observations that larger tubes are more prone to HTD than smaller ones. For those cases, the width of the HTD region clearly increased with increasing q. The $G = 200\,\mathrm{kg/m^2s}$ cases in the two larger test sections (tests in the 4.6 mm tube were difficult to perform at this low G) seem to indicate that $q_{onset,min}$ may correspond to a range, rather than a single value, of T_{in}, which may put these cases in a different category from the others. For the high–G cases without an HTD region apex, it seems possible that $T_{in,qmin}$ could not be observed because it was lower than the lowest T_{in} examined.

Figure 5.37 shows $T_{in,qmin}$ *vs.* G for the three test sections. Uncertainty bars, estimated intuitively from the plots, were added to the points. The general trend in all three test sections was that $T_{in,qmin}$ shifted to lower values as G increased up to 700 $\mathrm{kg/m^2s}$, however, the 8 mm results show that the $T_{in,qmin}$ shifted to higher values from $G = 1000$ to 1500 $\mathrm{kg/m^2s}$. It can also be seen in Figure 5.37 that $T_{in,qmin}$ for a fixed G increased with increasing tube diameter. The cause and significance of this observation require further investigation.

The present results have confirmed some previous findings concerning the onset of HTD, but have also introduced some novel observations, notably the existence of a limited range of T_{in} for the occurrence of HTD for each D, G and q and not simply an onset heat flux that applies to all T_{in}. This observation was possible because of the dense test matrix we adopted.

Although the ranges of conditions in our tests were insufficient for all HTD phenomena to be observed in all test sections, they were sufficient to demonstrate the general dependence of HTD onset on the values of the various parameters.

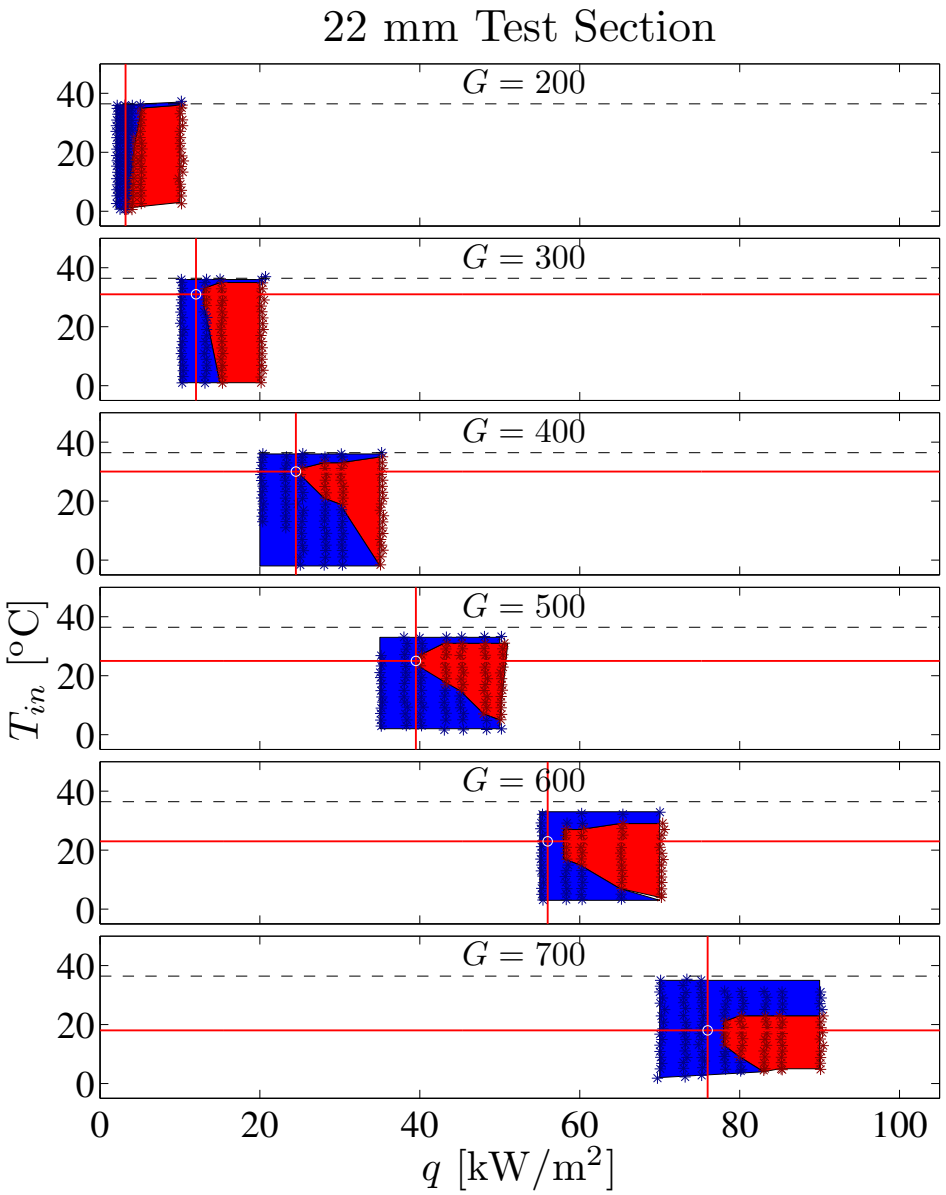


Figure 5.34: Effect of T_{in}, q, and G on the onset of HTD for the 22 mm test section.

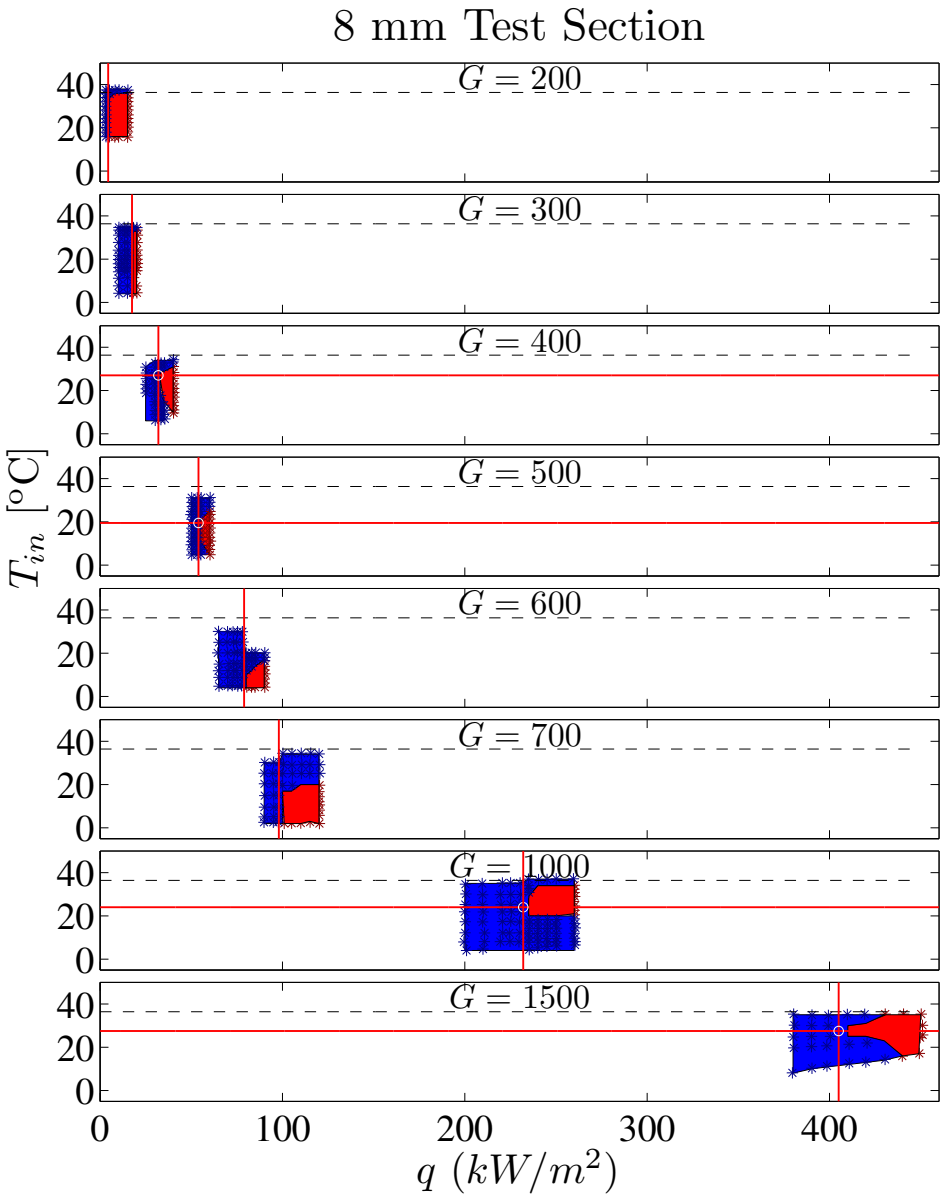


Figure 5.35: Effect of T_{in}, q, and G on the onset of HTD for the 8 mm test section.

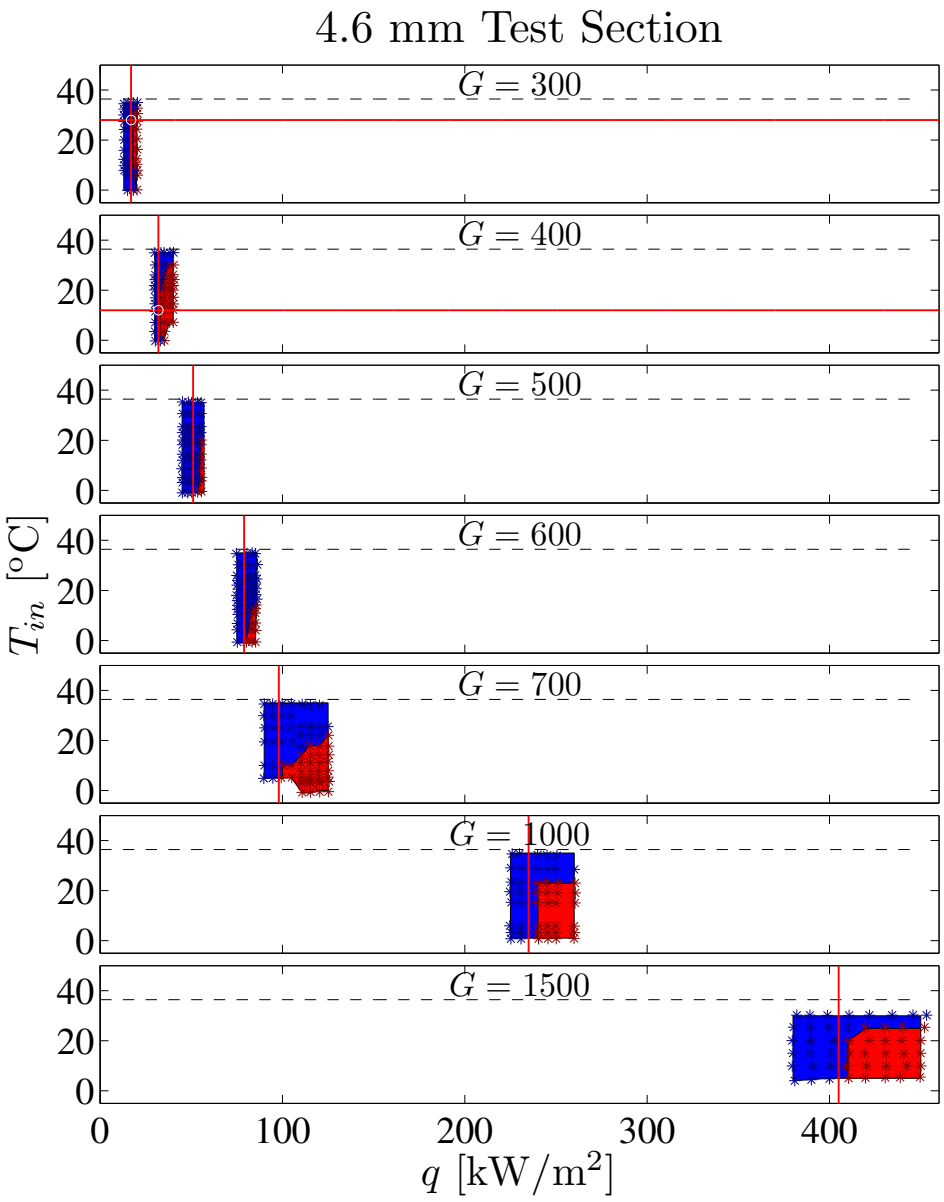


Figure 5.36: Effect of T_{in}, q, and G on the onset of HTD for the 4.6 mm test section.

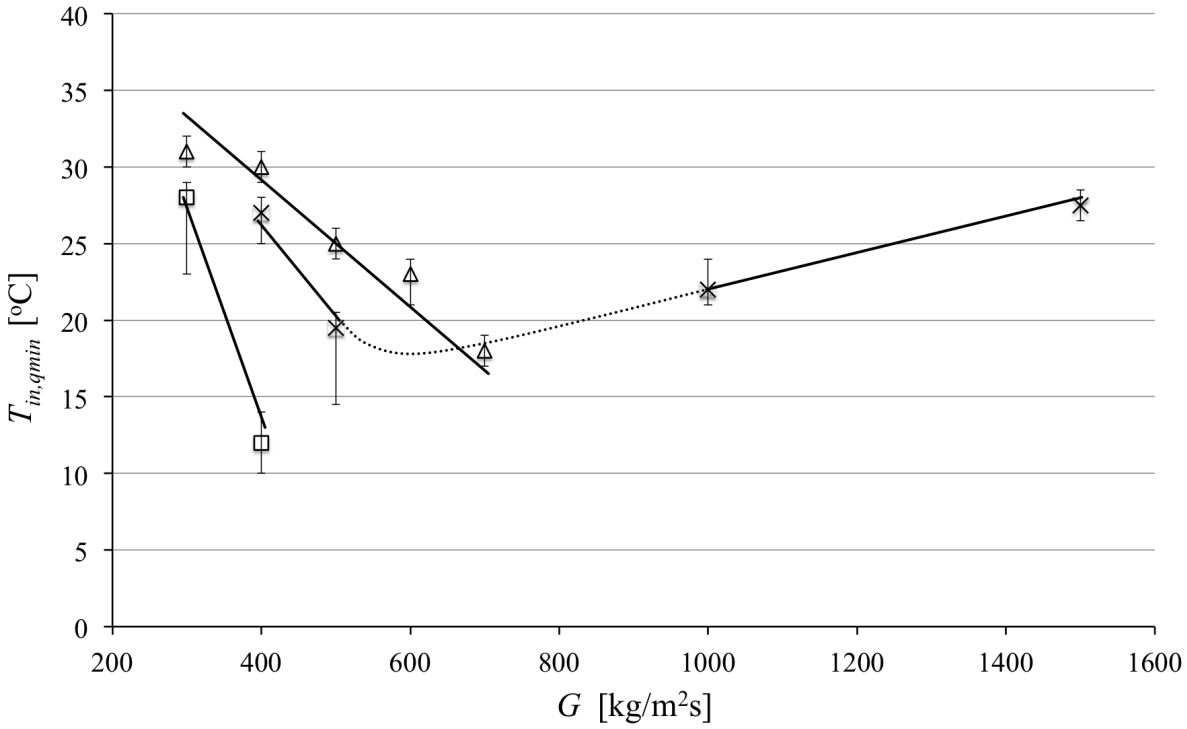


Figure 5.37: $T_{in,qmin}$ vs. G for the 22 mm (△), 8 mm (×) and 4.6 mm (□) test sections; solid lines have been fitted roughly to the data as a family; dotted line connects the 8 mm families.

5.5.2 Minimum onset heat flux as a function of mass flux

A common approach in the HTD literature has been to express q_{onset} in a given cross section as a function of G. Such assertions were based on experiments for which T_{in} was fixed or varied within a narrow range. Our tests, however, which spanned wide ranges of T_{in} for each q, proved that q_{onset} was also sensitive to T_{in}. We have already noted that, depending on the value of T_{in}, both normal and deteriorated cases occurred for each value of q above some threshold $q_{onset,min}$, below which HTD was never observed for any value of inlet temperature. In fact, normal heat transfer was observed for values of q that were up to 40% higher than $q_{onset,min}$ over an inlet temperature range of $5\,°\text{C} \leq T_{in} \leq 30\,°\text{C}$. Our results permitted us to estimate, for each tube diameter and each mass flux, this heat flux threshold, which hereafter will be referred to as the *minimum onset heat flux*.

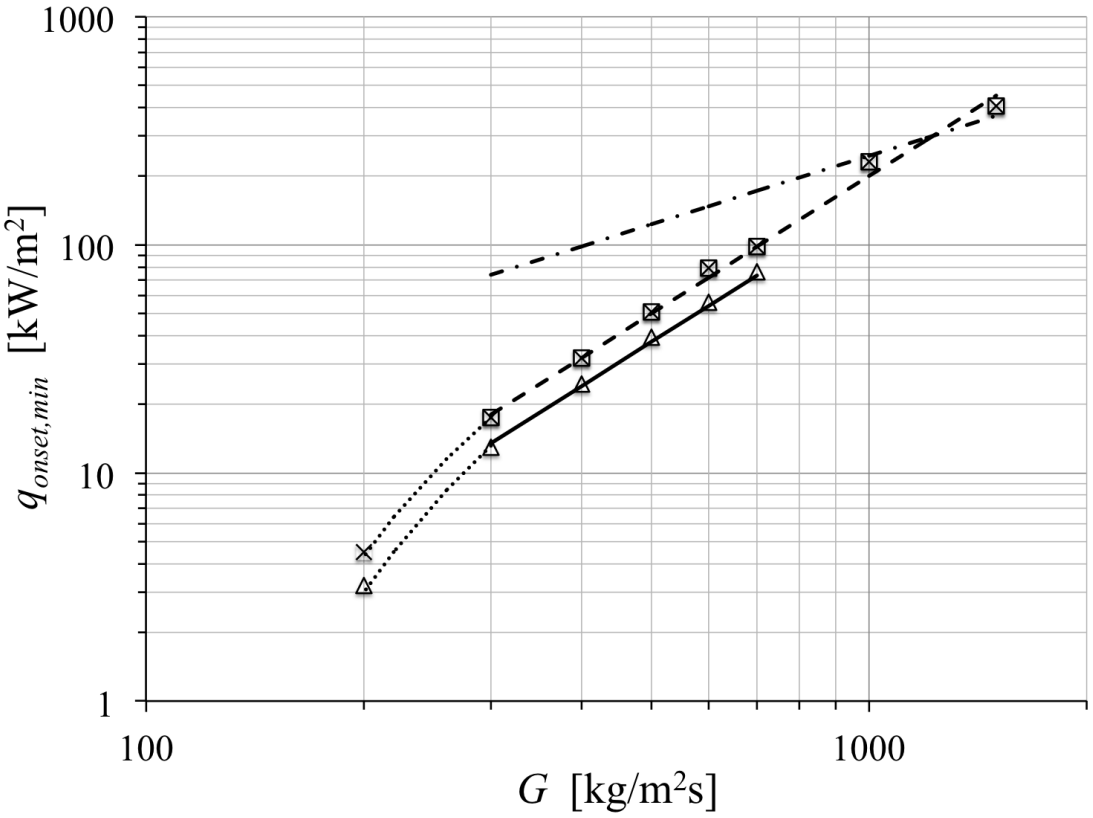


Figure 5.38: A log-log plot of $q_{onset,min}$ *vs.* G for the 4.6 (□), 8 (×) and 22 mm (△) test sections; solid line represents fitted power function (see Table 5.4); dotted-line connects the fitted correlations to the corresponding lowest–G points; dashed-dotted line represents the Grabezhnaya and Kirillov (2006) correlation and dashed line represents the Bae et al. (2010) correlation.

All estimated values of $q_{onset,min}$ in the present tests have been plotted *vs.* G in log-log scales in Figure 5.38. One may observe that the corresponding values for the 4.6 and 8 mm test sections essentially coincided, whereas the values for the 22 mm test section were lower by nearly 30%. The data in the range 300 kg/m^{2}s $\leq G \leq$ 1500 kg/m^{2}s for the 4.6 and 8 mm test sections could be fitted well by a power function and the data in the range 300 kg/m^{2}s $\leq G \leq$ 700 kg/m^{2}s for the 22 mm test section could also be fitted well by a different power function. The two functions have been drawn as a dashed line and a solid line, respectively, in the figure and are listed in Table 5.4. The power functions for all three sections had the

Table 5.4: Fitted correlations between $q_{onset,min}$ and G for the present three test sections

D [mm]	$q_{onset,min}(G)$ [kW/m^2]	G range [kg/m^{2}s]	Comments
4.6	$q_{onset,min} = 2.0 \times 10^{-4} G^2$	300 - 1500	insufficient data to provide q_{onset} for a wide T_{in} range
8	$q_{onset,min} = 2.0 \times 10^{-4} G^2$	300 - 1500	insufficient data to provide q_{onset} for a wide T_{in} range
22	$q_{onset,min} = 1.5 \times 10^{-4} G^2$	300 - 700	sufficient data to provide q_{onset} for a wide T_{in} range

same exponent 2.0, but the proportionality coefficient was lower for the 22 mm results than those for the other two, which were equal. The values of $q_{onset,min}$ for $G = 200$ kg/m^{2}s were nearly 40% lower than predictions of the corresponding power functions, extrapolated to lower G.

The present findings will be compared to predictions of two previous correlations, which have been selected among several others proposed by different authors mostly for water flows but also for other fluids. The first one is the correlation of Grabezhnaya and Kirillov (2006), which was based on literature data for three different fluids and contains a scaling parameter to accommodate the fluid type. These authors have not specified how the onset of HTD was identified and so it is not clear whether the heat flux in this correlation is equivalent to our own $q_{onset,min}$. The second correlation is the one by Bae et al. (2010), which was fitted to their own CO_2 data in a vertical heated tube with an ID of 6.32 mm. Bae et al. (2010) presented an analysis of their data in the context of developing a new heat transfer correlation, but did not explain how they determined HTD onset conditions. In summary, our work is the first study that attempts to define unambiguously HTD onset and its relationship to the experimental conditions. The two previous correlations have been plotted together with our results in Figure 5.38. It can be seen that the Grabezhnaya and Kirillov (2006) correlation, with the scaling parameter adjusted for CO_2, predicted much higher q_{onset} than the present ones, especially at lower mass fluxes; the exponent in the power function of this correlation was also significantly lower than the one we found presently. On the other hand, predictions

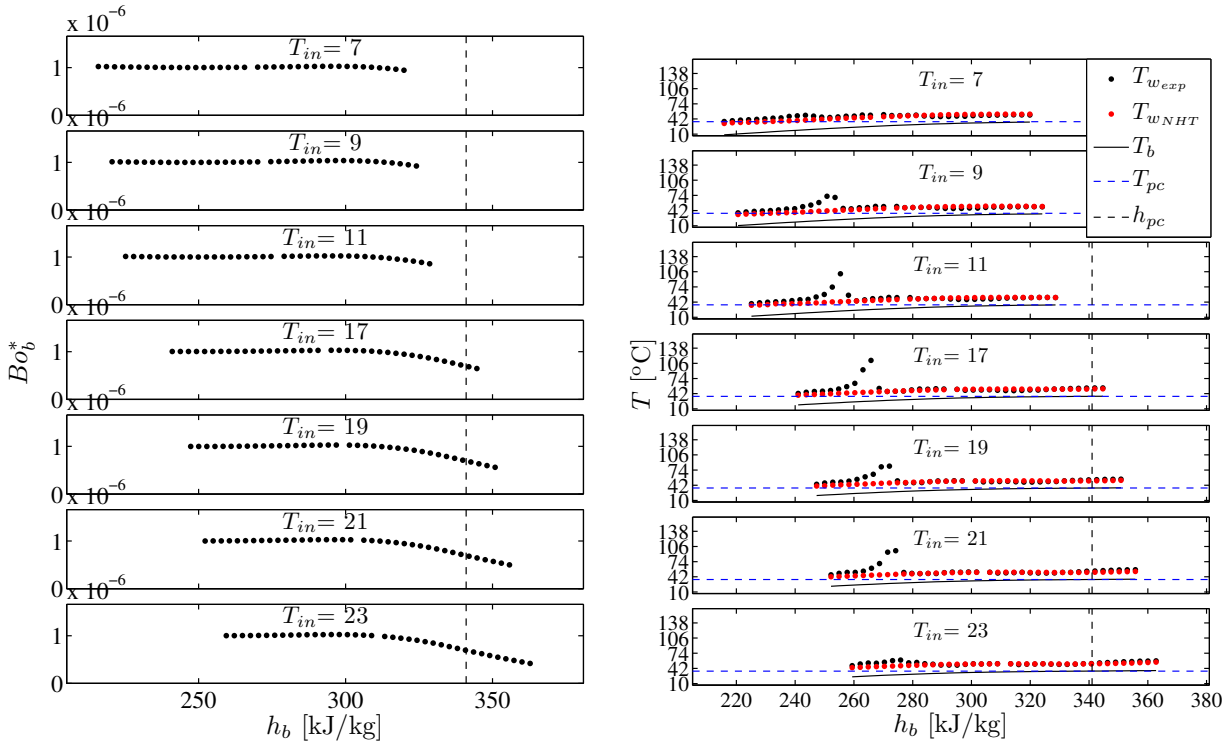
of the Bae et al. (2010) correlation coincide with the present results in the 4.6 and 8 mm tubes, which supports the accuracy of the correlation and our observation that $q_{onset,min}$ was insensitive to tube diameter within the range 4.6 to 8 mm.

5.5.3 The buoyancy parameter as an HTD predictor

Previous researchers (Jackson et al., 1989; McEligot and Jackson, 2004; Li et al., 2010) have proposed that the onset of HTD is related to the value of a buoyancy parameter Bo_b^* (Eq. 2.6), which contains a Grashof number Gr_b^* that depends only on q and local bulk fluid properties, as discussed in Section 2.2.2. In the following, we will investigate the sensitivity of this buoyancy parameter to some properties that affect HTD.

Sensitivity to wall temperature and bulk enthalpy

Representative Bo_b^* profiles for normal and deteriorated cases in the 8 mm test section are presented in Fig. 5.39, together with the measured wall temperature profiles and predictions of wall temperature by the normal heat transfer correlation Nu_{NHT} (Eq. 5.5). Although HTD cases are easy to identify by the presence of spikes in the measured T_w profiles, the corresponding Bo_b^* profiles show no difference between deteriorated and normal cases. This is not surprising, because Bo_b^* was evaluated from properties at bulk temperature and had no contribution by any parameter at wall temperature. Another observation that can be made is that Bo_b^* was insensitive to the value of specific enthalpy within a wide range of h_b and decreased with increasing h_b only in the vicinity of the pseudo-critical value. The present findings seem to suggest that a buoyancy parameter that takes into account local wall temperature might be more successful than Bo_b^* as an HTD indicator. Of course, because wall temperature is generally not known in advance, the usefulness of such parameter for predicting HTD onset might be limited.



(a) Bo_b^* profiles

(b) T_w profiles

Figure 5.39: Bo_b^* and T_w profiles for $P/P_c = 1.13$, $D = 8$ mm, $G = 500$ kg/m^{2}s, $q = 55$ kW/m^2; units of T_{in} are °C

Sensitivity to inlet temperature

As shown in Fig. 5.40, Bo_b^* at any given h_b was insensitive to changes in T_{in} over the entire range of T_{in} values tested. Moreover, over a wide range of h_b below h_{pc}, Bo_b^* was nearly constant, although it acquired a strong downward slope in the vicinity of h_{pc} and beyond. Therefore, for low h_b cases, it would be sufficient to evaluate Bo_b^* at T_{in}, rather than the local bulk temperature.

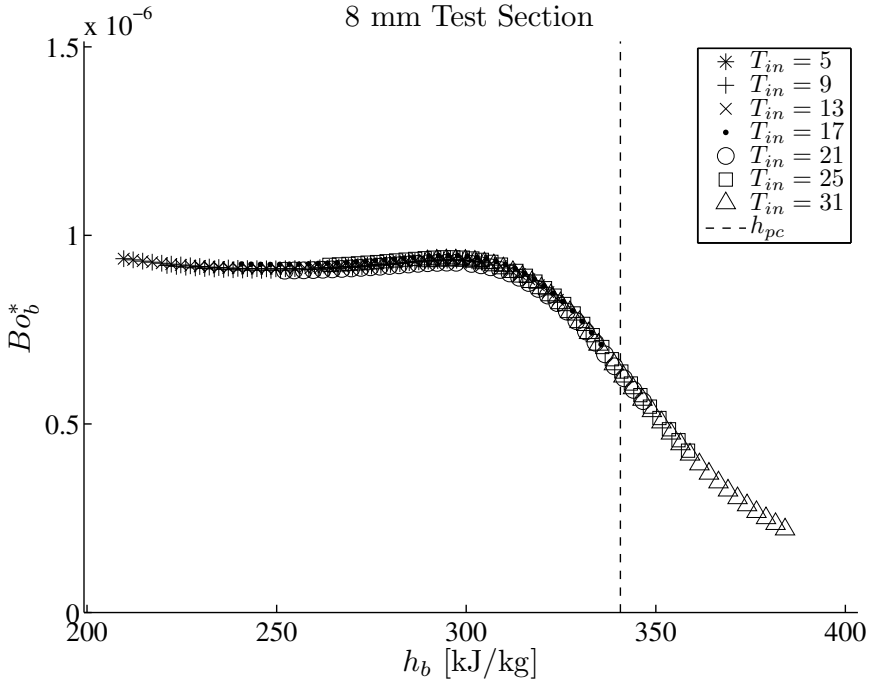


Figure 5.40: Bo_b^* profiles for $P/P_c = 1.13$, $G = 500$ kg/m^{2}s, $q = 55$ kW/m^2; units of T_{in} are °C.

Sensitivity to mass flux and heat flux

The sensitivity of Bo_b^* to mass flux changes could be tested with the use of our results in the 22 mm test section, which had overlapping ranges of q and T_{in} for different values of the mass flux. Among these results, we selected cases for which the bulk conditions remained well below the pseudo-critical values in the entire test section. Figure 5.41 shows some representative findings. It is evident in this figure that an increase in heat flux, with all other conditions kept constant, resulted in a proportional increase in Bo_b^*. The sensitivity of this parameter to q decreased markedly with increasing G, as demonstrated by the decreasing slopes of the heat flux isolines. Figure 5.41 also shows that, if G were increased by 100 kg/m^{2}s while all other conditions were kept unchanged, Bo_b^* would drop by a very large percentage of its value, which, however, decreased with increasing G. It appears that this sensitivity of Bo_b^* can be accounted for with a use of a correction factor for G, in a manner similar to the one that was applied to $\overline{Bo_b}$ and $Bo_{b_{VP}}$ (see Section 5.4.3).

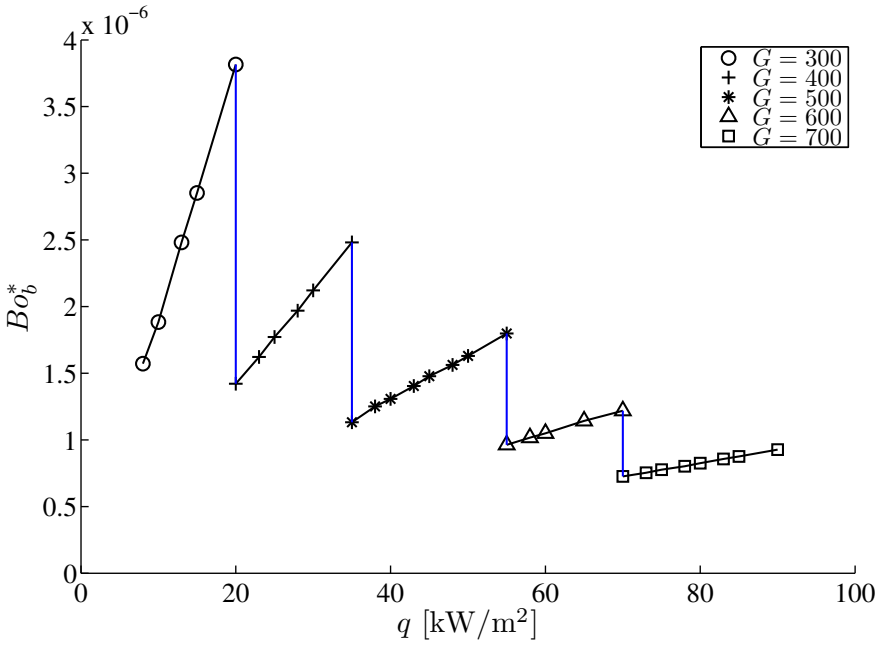


Figure 5.41: Bo_b^* evaluated at $T_{in} = 21$ °C and plotted versus q for $D = 22$ mm, $P/P_c = 1.13$; black lines represent heat flux isolines; blue lines represent mass flux isolines; units of G are kg/m^{2}s.

Overview of Bo_b^* for all three test sections

It has been suggested that Bo_b^* may be usable for predicting significant HTD due to its lack of dependence on wall temperature. The previous discussion has shown, however, that this parameter has some sensitivity to q at higher G and a high sensitivity to G for all q tested. Figure 5.42 shows plots of all normal and deteriorated heat transfer cases in the 22 mm test section, with Bo_b^* evaluated at T_{in} for each case. It can be seen that Bo_b^* values for NHT and HTD overlapped considerably, especially for $G \geq 600$ kg/m^{2}s. This overlap is attributed to the sensitivity of this parameter to q and makes it impossible to establish a single Bo_b^* threshold that would separate the normal and deteriorated zones, therefore we have limited the analysis to the highest mass flux of $G = 700$ kg/m^{2}s. We have, however, drawn a line that is the locus of the smallest values of Bo_b^* for which HTD was observed. In doing so, we have disregarded the data for $G = 200$ kg/m^{2}s, as it was demonstrated previously that properties calculated from NIST tables for these cases were erratic. It must be emphasized

that the benefit from using this threshold for identifying HTD is small, because several values of Bo_b^* for NHT were larger than this threshold and those that were not were only slightly lower. Such "threshold" lines for all three test sections have been drawn in Figure 5.43. These results show that this threshold decreased rapidly with both increasing G and decreasing tube diameter. Although we may have easily devised corrections for these effects, we did not do so because of the poor performance of Bo_b^* in separating NHT and HTD cases.

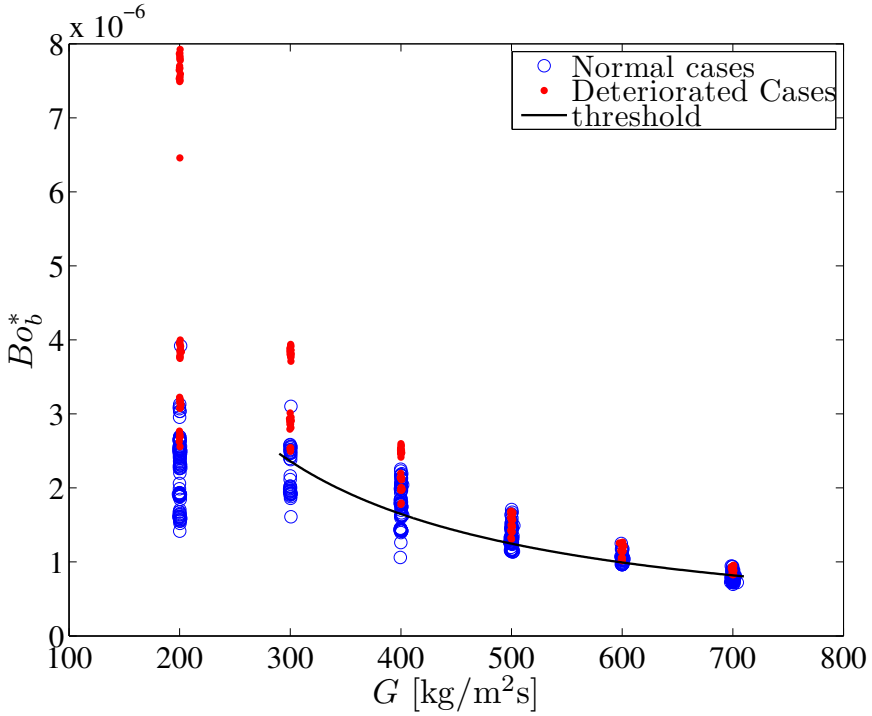


Figure 5.42: Plot of Bo_b^* values, evaluated at T_{in} conditions, vs G for all normal and deteriorated cases from the 22 mm test section

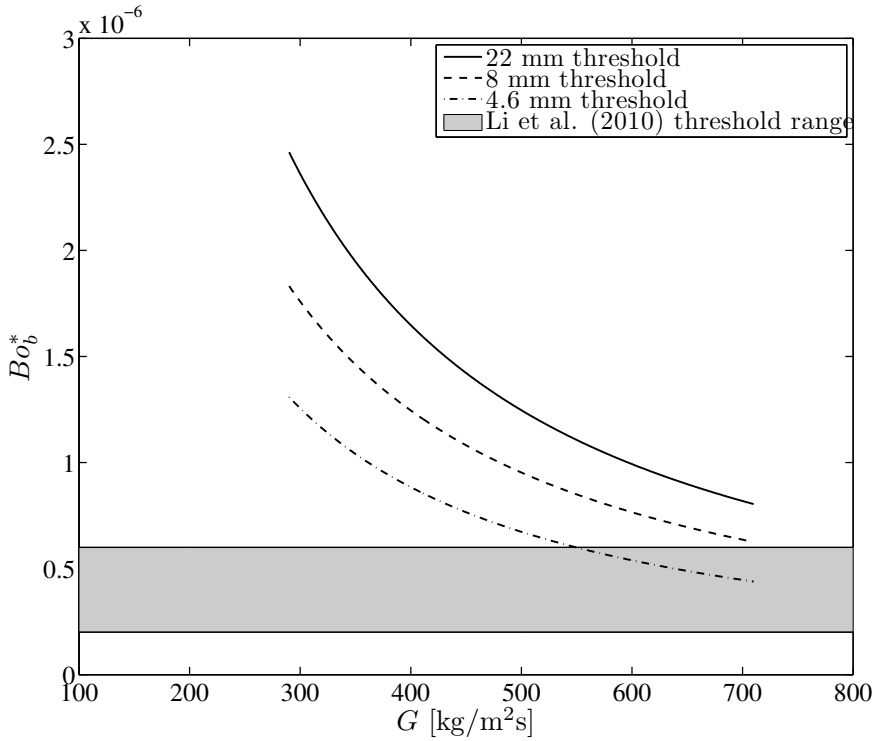


Figure 5.43: Plot of Bo_b^* values, evaluated at T_{in} conditions, vs G for all deteriorated cases from all three test sections

In closing, it seems worthwhile to compare the levels of Bo_b^* thresholds for the present experiments and those suggested by previous authors. Jackson et al. (1989) and McEligot and Jackson (2004) suggested the value $Bo_b^* > 6 \times 10^{-6}$ as a lower limit for HTD to occur. This value is much higher than any of the three thresholds shown in Figure 5.43, but this comparison may not be meaningful because the values suggested by Jackson et al. (1989) and McEligot and Jackson (2004) were determined from experiments in water and air at atmospheric pressure, in which property variations across the flow would have been much weaker than at supercritical pressures. Li et al. (2010) considered data in supercritical upward flows of CO_2 in a 2 mm tube and suggested that the buoyancy parameter threshold for HTD would be in the range $2 \times 10^{-7} \leq Bo_b^* \leq 6 \times 10^{-7}$. Although these values are lower than the present ones for $G \leq 500$ kg/m^{2}s, they seem to agree well for higher mass fluxes, especially when considering the presently found decrease of this threshold with decreasing

tube diameter.

5.6 Dependence of the *HTC* for normal heat transfer on the tube diameter

The existing literature on the effect of tube diameter on supercritical heat transfer was reviewed recently by Yildiz and Groeneveld (2014), who concluded that, in general, the HTC for normal heat transfer would decrease with increasing tube diameter, if all other conditions were kept the same. The exact dependence of HTC on D has not yet been established, but some authors (Bae et al., 2010) adopted the power law $D^{-0.2}$, which is consistent dimensionally with the Dittus-Boelter correlation Nu_{DB} for normal heat transfer in tubes at low subcritical pressures. An obvious limitation of a simple power law is that it would lead to counter-intuitive predictions, if extrapolated in either direction. If D were increased indefinitely, the predicted HTC would tend to vanish, rather than settling at the value for a plane wall, whereas, if D were diminished indefinitely, HTC would tend towards infinity, which is impossible. Moreover, we have shown in Section 5.4.2 that Nu_{DB} did not describe well the present normal heat transfer experimental data when the specific enthalpy was near the pseudo-critical value.

The availability of data obtained in test sections with three different diameters, but otherwise under comparable conditions, offers us an opportunity to revisit the dependence of the heat transfer coefficient on tube diameter. HTC values in the three tubes were compared for various combinations of conditions within the following ranges: a single pressure, $P/P_c = 1.13$; three different inlet temperatures, namely $T_{in} = 10$, 20, and 30 °C; mass fluxes in the range from 300 to 700 kg/m^{2}s, at increments of 100 kg/m^{2}s; a single value of q for each G, for which heat transfer was normal in all three test sections; and a narrow range (having a width of 5 kg/kJ) of bulk specific enthalpy h_b. The choices of h_b ranges among all available normal heat transfer measurements were such as to provide data under comparable conditions in all three test sections.

Figure 5.44 shows normalised HTC measurements *vs.* the normalised tube diameter for three different h_b ranges. Because many symbols in the plot overlap and are difficult to

distinguish, we have listed all symbol types and experimental values in Table 5.5. The tube diameter was normalised by $D_{ref} = 8$ mm, whereas the HTC was normalized by reference values HTC_{ref} in the 8 mm tube. The data presented a lot of scatter, but showed a clear decrease of HTC/HTC_{ref} with increasing D/D_{ref}. The power law

$$\frac{HTC}{HTC_{ref}} = \left(\frac{D}{D_{ref}}\right)^{-0.2} \quad , \tag{5.10}$$

actually represented well the average trend, although it could not distinguish among cases with different G and h_b, besides leading to physical impossibilities if extrapolated to smaller and larger D. For these reasons, we put effort into developing a more suitable correction factor that describes diameter effects on the HTC. A careful examination of the data showed that the HTC values in a given test section generally tended to increase systematically with increasing G and so we decided to include G as a parameter in our new correlation. Instead of a monotonically decreasing function of D, we decided to use a function that would approach a constant asymptote as $D \to \infty$. After testing several different types of functions, we chose the expression

$$\frac{HTC}{HTC_{ref}} = \frac{A}{1-(1-A)^{D/D_{ref}}} \quad , \tag{5.11}$$

where

$$A = -(G/G_{ref})^2 + 0.1(G/G_{ref}) + 1 \quad , \tag{5.12}$$

and $G_{ref} = 1380$ kg/m^{2}s. This correlation would also predict unrealistically large HTC as $D \to 0$ and so it should not be used for tubes with diameters much smaller than 4.6 mm. Although not precise and only based on data in relatively narrow ranges of conditions, this correction factor is in our opinion preferable to the simple power law. The selected G_{ref} applies to flows of CO_2. For use with water or other fluids, we suggest that this reference value is scaled following an established fluid-to-fluid scaling law for normal heat transfer (Zahlan et al., 2014).

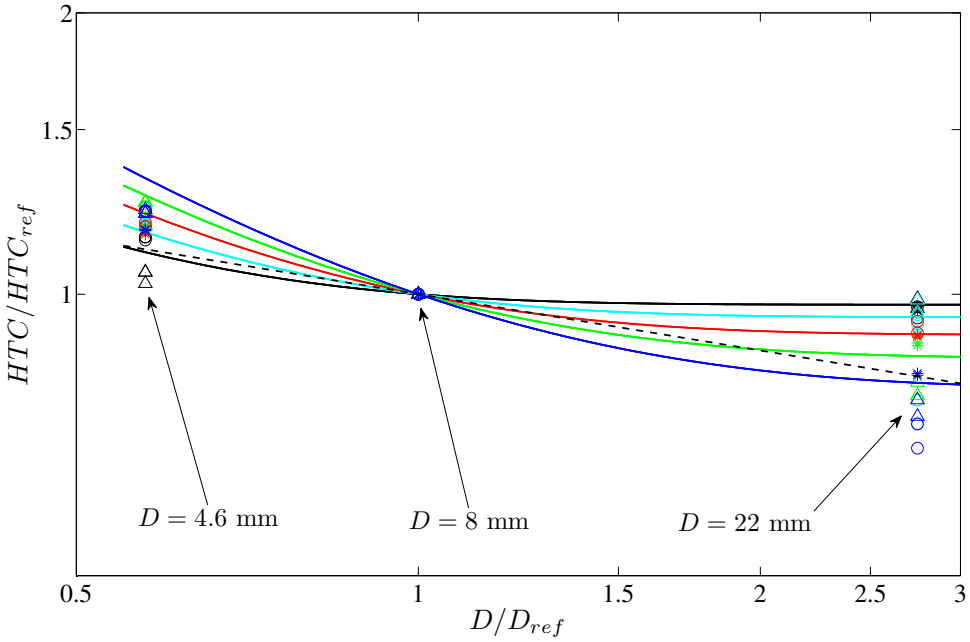


Figure 5.44: A log-log plot of HTC/HTC_{ref} *vs.* D/D_{ref}; symbols are listed in Table 5.5; $D_{ref} = 8$ mm and HTC_{ref} represents values measured in the 8 mm test section; the dashed line is a plot of the power law, Eq. 5.10; black, turquoise, red, green and blue solid lines are, respectively, plots of Eq. 5.11 for $G = 300$, 400, 500, 600, 700 kg/m^{2}s.

Table 5.5: List of normal HTC results for all three test sections

	D [mm]	G [kg/m^{2}s]	q [kW/m^2]	h_b [kJ/kg]	HTC [kW/m^{2}K]
∗	4.6	300	10	230 - 235	1.38
○	4.6	300	10	255 - 260	1.51
△	4.6	300	10	295 - 300	1.73
∗	8	300	10	230 - 235	1.17
○	8	300	10	255 - 260	1.26
△	8	300	10	295 - 300	1.41
∗	22	300	10	230 - 235	1.13
○	22	300	10	255 - 260	1.28
△	22	300	10	295 - 300	1.52
∗	4.6	400	20	230 - 235	1.91
○	4.6	400	20	255 - 260	2.10
△	4.6	400	20	295 - 300	2.39
∗	8	400	20	230 - 235	1.60
○	8	400	20	255 - 260	1.79
△	8	400	20	295 - 300	2.10
∗	22	400	20	230 - 235	1.46
○	22	400	20	255 - 260	1.72
△	22	400	20	295 - 300	2.14
∗	4.6	500	35	230 - 235	2.36
○	4.6	500	35	255 - 260	2.75
∗	8	500	35	230 - 235	2.02
○	8	500	35	255 - 260	2.54
∗	22	500	35	230 - 235	1.82
○	22	500	35	255 - 260	2.33
∗	4.6	600	55	230 - 235	2.83
○	4.6	600	55	255 - 260	3.56
△	4.6	600	55	295 - 300	4.74
∗	8	600	55	230 - 235	2.40
○	8	600	55	255 - 260	2.95
△	8	600	55	295 - 300	3.82
∗	22	600	55	230 - 235	2.13
○	22	600	55	255 - 260	2.67
△	22	600	55	295 - 300	3.55
∗	4.6	700	70	230 - 235	3.33
○	4.6	700	70	255 - 260	4.18
△	4.6	700	70	295 - 300	5.53
∗	8	700	70	230 - 235	2.84
○	8	700	70	255 - 260	3.53
△	8	700	70	295 - 300	4.63
∗	22	700	70	230 - 235	2.33
○	22	700	70	255 - 260	2.95
△	22	700	70	295 - 300	3.93

5.7 Dependence of q_{onset} on the tube diameter

In Section 5.5.2, it was shown that the minimum onset heat flux could be defined as a function of G in the form of a power law. Results were analyzed for three different test section diameters and it was found that the resulting $q_{onset,min}$ expressions had the same exponent, but a proportionality coefficient that was substantially lower for the 22 mm tube than the 4.6 and 8 mm tubes, which had a common value. To quantify the relative effect of diameter, we normalised the measured values of $q_{onset,min}$ in the mass flux range of 300 kg/m^{2}s $\leq G \leq$ 1500 kg/m^{2}s by the corresponding reference value $q_{onset,min,ref}$ for the 8 mm tube. The resulting ratios are shown in Figure 5.45. For convenience of future users, we fitted the three experimental points with an S-shape function of diameter that also preserved plausible experimental trends when interpolated or extrapolated with respect to the data points. This function was

$$F_D = \frac{q_{onset,min}}{q_{onset,min,ref}} = 0.7 + \frac{(1-0.7)}{1+e^{4(D/D_{ref}-2.35)}} \quad , \tag{5.13}$$

where $q_{onset,min,ref} = 2.0{\times}10^{-4}G^2$ and $D_{ref} = 8$ mm. This expression has an upper asymptote for small D, which is consistent with the near coincidence of estimated values of $q_{onset,min}$ in the two smaller tubes. This upper asymptote may not apply to tubes with extremely small diameters, which may not have a distinct thermal boundary layer and may not be subjected to HTD. This function also has a lower asymptote for large G. We did not measure directly the value of this asymptote, but we intuitively set it to correspond to a $q_{onset,min}$ that was slightly lower than the value in the largest test section we examined. Our belief in the existence of a lower asymptote was based on the rationale that $q_{onset,min}$ cannot decrease indefinitely as the diameter grows towards infinity, because the thermal boundary layer thickness would eventually approach the value it would have along a plane wall (in other words, wall curvature would be too small to have any influence on heat transfer). Expression 5.13 can be easily incorporated as a correction factor for diameter effects into the following general power law for the onset of HTD in tubes

$$q_{onset,min} = 2.0 \times 10^{-4} F_D G^2 \quad . \tag{5.14}$$

It is reminded that this law has been validated only for diameters from 4.6 to 22 mm, mass fluxes from 300 to 1500 kg/m^{2}s and a reduced pressure of $P/P_c = 1.13$.

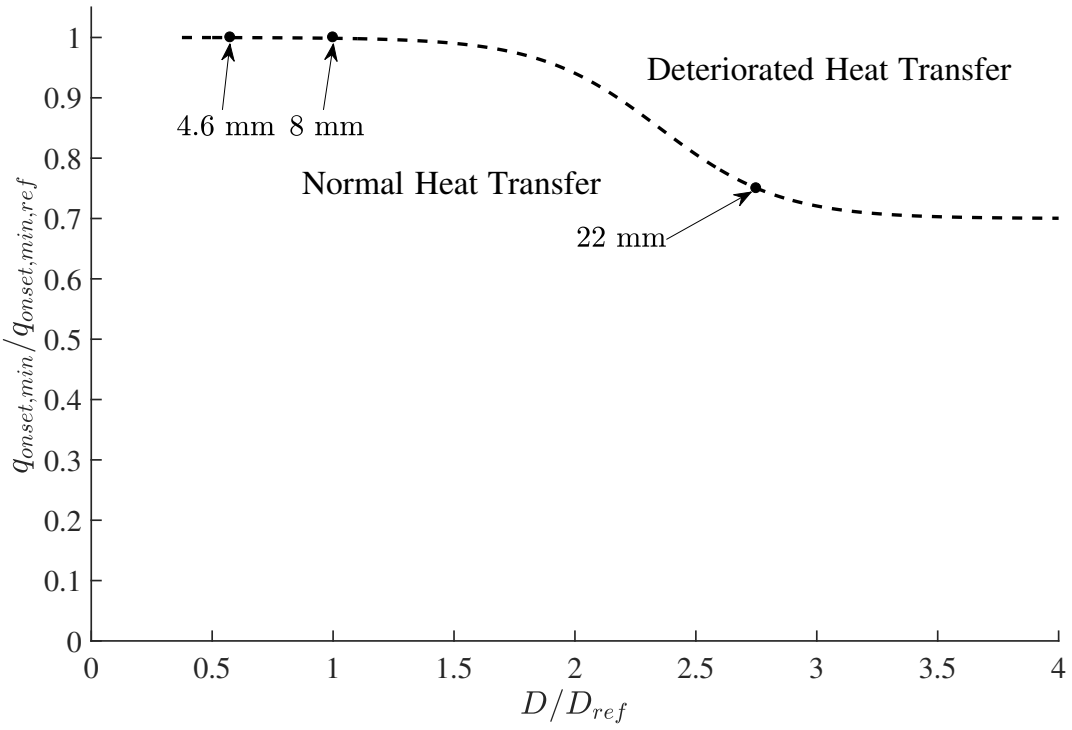


Figure 5.45: Dependence of normalised heat flux at HTD onset on tube diameter; the dashed line represents Equation 5.13.

Chapter 6

Conclusion

6.1 Summary of the results

The first part of this study was focused on methods for identifying HTD in flows in heated tubes at supercritical pressures. Three main HTD identification methods have been used by previous researchers, but in most experimental studies HTD seems to have been treated as an obvious phenomenon, as authors did not find it necessary to explain their identification method. This ambiguity may introduce inconsistencies in comparisons among HTD results from different sources. The most straightforward criterion for HTD occurrence is the presence of spikes in axial profiles of wall temperature. The second method is to compare the measured heat transfer coefficient and one predicted by a normal heat transfer correlation and assume that HTD occurs when the ratio of these HTC drops below an empirical threshold. The third method is to consider the value of a buoyancy parameter, computed with the use of values of thermophysical properties evaluated at both bulk and wall temperatures, and assume that HTD occurs when this parameter exceeds an empirical threshold. A detailed examination of all three methods led to the following conclusions.

- A comparison of wall temperature profiles for different heat fluxes and inlet temperatures, but grouped together in single graphs or organized in a series of individual plots, was generally a reliable method of distinguishing deteriorated cases from normal cases.
- HTD could be identified confidently in single temperature profiles that contained

abrupt spikes. Such spikes were observed for mass fluxes in the range $200 \leq G \leq 600$ kg/m^{2}s.

- A new normal heat transfer correlation was within $\pm 30\%$ of the measurements for 95% of our data in three test sections. Comparisons of measured HTC with predictions of this correlation was useful for identifying HTD on a case-by-case basis, when observation of a temperature profile had an inconclusive outcome.

- Comparison of a previously suggested buoyancy parameter, corrected empirically for the effect of mass flux, with a fixed threshold separated deteriorated and normal heat transfer cases successfully for most, but not all, present tests.

- A modified buoyancy parameter, also suggested in the literature and corrected for mass flux effects, was found to be inferior to the original buoyancy parameter for the purpose of HTD identification.

The second part of this study was to examine the onset of HTD for different combinations of values of the parameters D, T_{in}, q, and G. Two methods for determining the onset of HTD were identified in the literature. The most common method was to devise an empirical relationship between q_{onset} and G in the form of a power function. The second method was to determine a threshold for a buoyancy parameter, defined as a function of q and bulk fluid properties but without the need for wall temperature values. A thorough examination of both methods, taking into consideration the effects of T_{in} and D, led to the following conclusions.

- With D and G fixed, HTD occurred only when q exceeded a minimum $q_{onset,min}$. Within the G range from 300 to 1500 kg/m^{2}s, this minimum was expressed as a power function of G, which was the same for the 4.6 mm and 8 mm test sections but had a smaller proportionality coefficient for the 22 mm test section. Our findings agreed with literature results under comparable conditions.

- For fixed values of D and G, and $q > q_{onset,min}$, HTD occurred only when T_{in} was within a limited range, which became wider as q was increased.

- For the range of conditions examined, HTD was not observed when T_{in} was near T_{pc}. Some tests demonstrated that HTD was also possible for $T_{in} > T_{pc}$, but required extremely large q.

- A bulk buoyancy parameter threshold could be fitted to our data for HTD onset in each test section. Correction factors for this threshold for the effects of G and D seem to be possible, but were not suggested because such a threshold could not separate a large number of normal heat transfer cases from those with HTD.

The third part of this study was to examine the effects of diameter on the onset of HTD and on the HTC for normal heat transfer. Our main findings were as follows.

- An S-shaped correction factor was developed to account for diameter effects on $q_{onset,min}$.

- Although the previously suggested normal heat transfer relationship $HTC \propto D^{-0.2}$ was compatible with the present experimental results, we suggested a more complex function of G and D, which fitted our data better and also satisfied the expectation that the diameter effect would weaken with further increase in D.

6.2 Main contributions

Although following several decades of work on similar topics by many authors worldwide, this is one of the most systematic, thorough and well documented experimental studies and analyses of results on the identification and onset of HTD in tubes and on the effects of tube diameter. Among the original contributions of this work, we can mention the following ones.

- It reports an experimental database on the onset of HTD in CO_2 that was compiled with the densest so far test matrix.

- It is the first in-depth comparison of all HTD criteria.

- It introduced an improved normal heat transfer correlation, which further contains a new correction factor for the effect of tube diameter.

- It introduced new correction factors for the buoyancy parameters.

- It is the first mapping of HTD and NHT regions with respect to D, T_{in}, q, and G for CO_2.
- It proposed a new correlation for predicting HTD onset, which includes a correction factor for tube diameter effects.

6.3 Recommendations for future work

The present work may be readily continued to extend the ranges of of experimental conditions and to cover additional topics related to HTD in supercritical flows. The following list of recommendations for future work only includes tasks which are within the capabilities of the present facility.

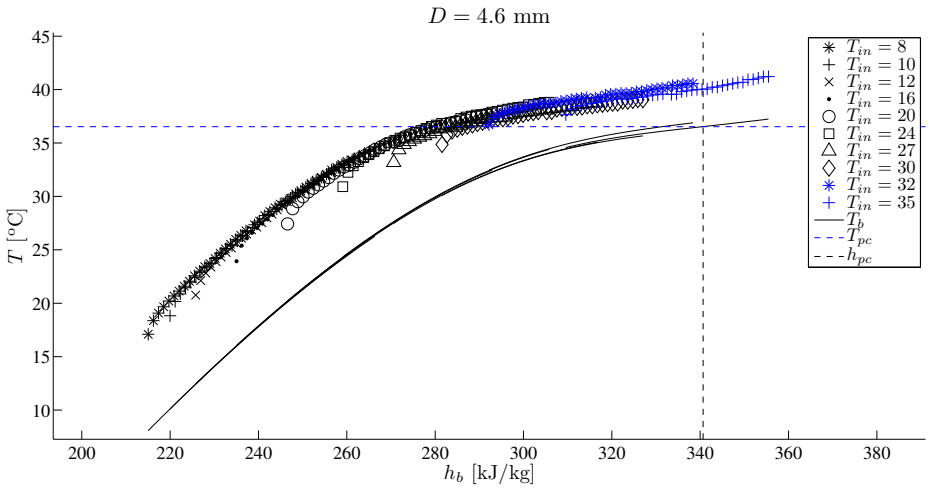
- The current analysis is based on data taken at one pressure and it would be valuable to extend this analysis using data taken at a different pressure. In fact, some measurements at a lower supercritical pressure have already been collected for the 8 mm test section by a visiting intern.
- It would be valuable to extend the ranges of heat flux from the present near–onset region to higher values. Some of this work has also been performed by the same visiting intern, following small modifications of the thermocouple mounting procedure to extend the range of acceptable wall temperatures in the loop.
- The present database and analyses would benefit from additional tests at higher mass fluxes. For the larger test section, this would require the connection of one or two additional pumps in parallel with the present ones.
- Measurements and analyses like the present ones could be repeated for a different modelling fluid. Such work with Refrigerant 134a is currently in progress as part of a different M.A.Sc. thesis research. These results can be compared to the present ones for an evaluation and possible improvement of supercritical fluid-to-fluid scaling laws for normal heat transfer and for the onset of HTD.

- The present results can be used for the validation of numerical simulations of supercritical flows. Such work has been initiated by another student as part of a Ph.D. thesis research.

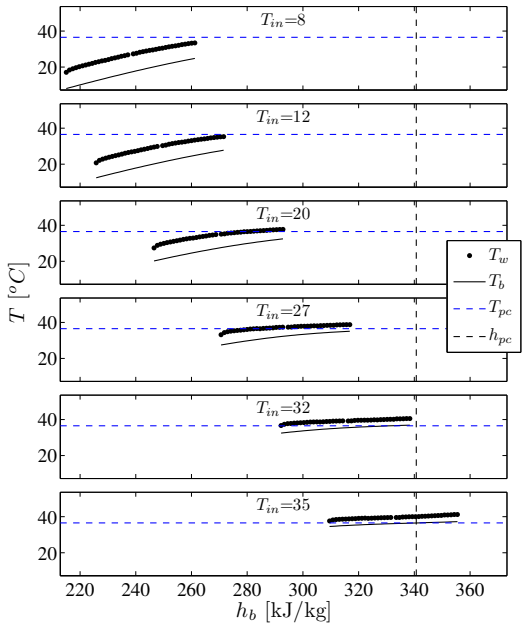
Appendix A

Measurements of wall temperature profiles

A.1 4.6 mm test section

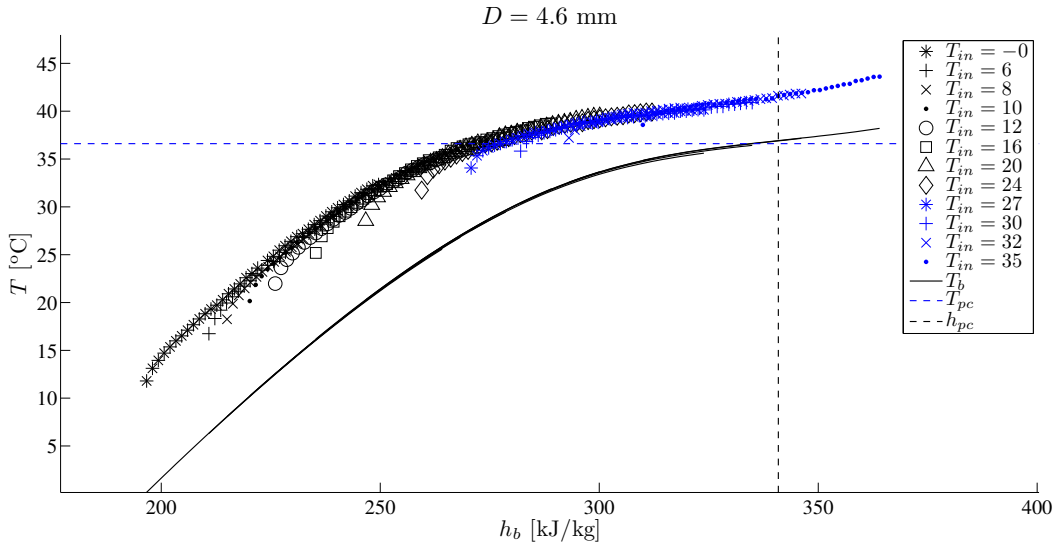


(a) All cases

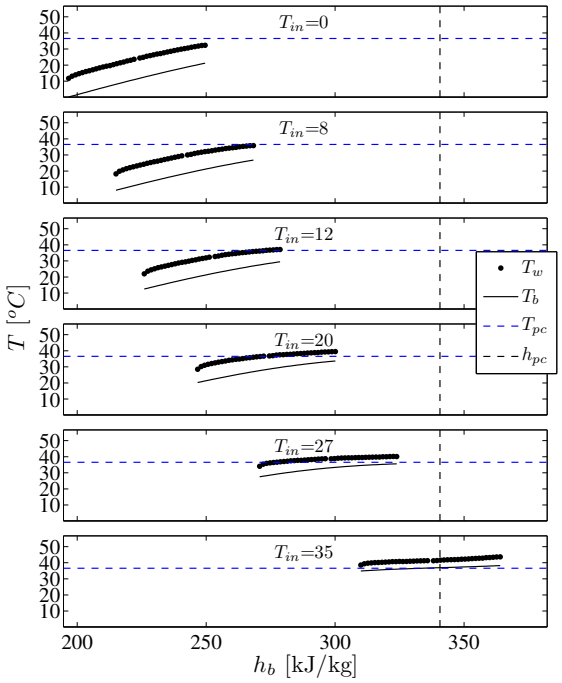


(b) Select cases

Figure A.1: Temperature profiles for $P/P_c = 1.13$, $G = 300$ kg/m^{2}s, $q = 13$ kW/m^2; units of T_{in} are °C.

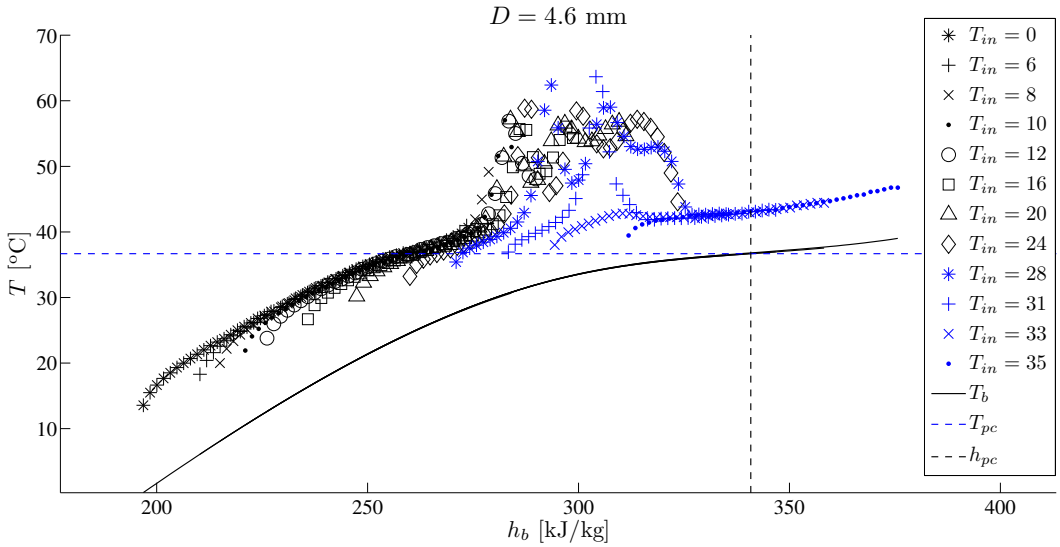


(a) All cases

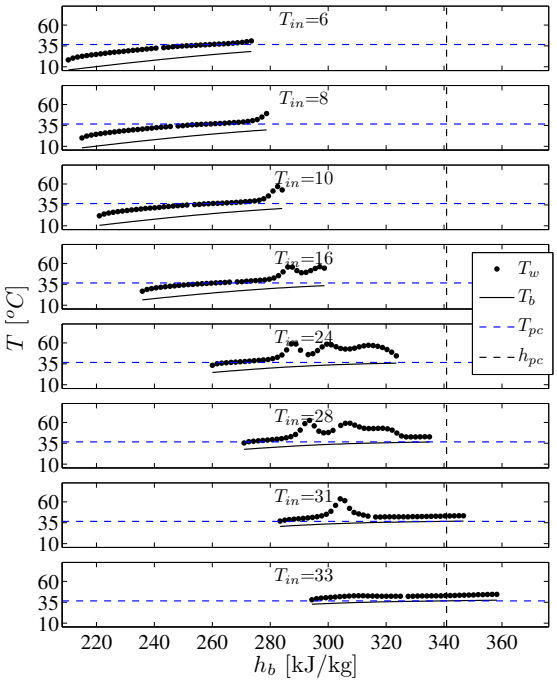


(b) Select cases

Figure A.2: Temperature profiles for $P/P_c = 1.13$, $G = 300$ kg/m^{2}s, $q = 15$ kW/m^2; units of T_{in} are °C.

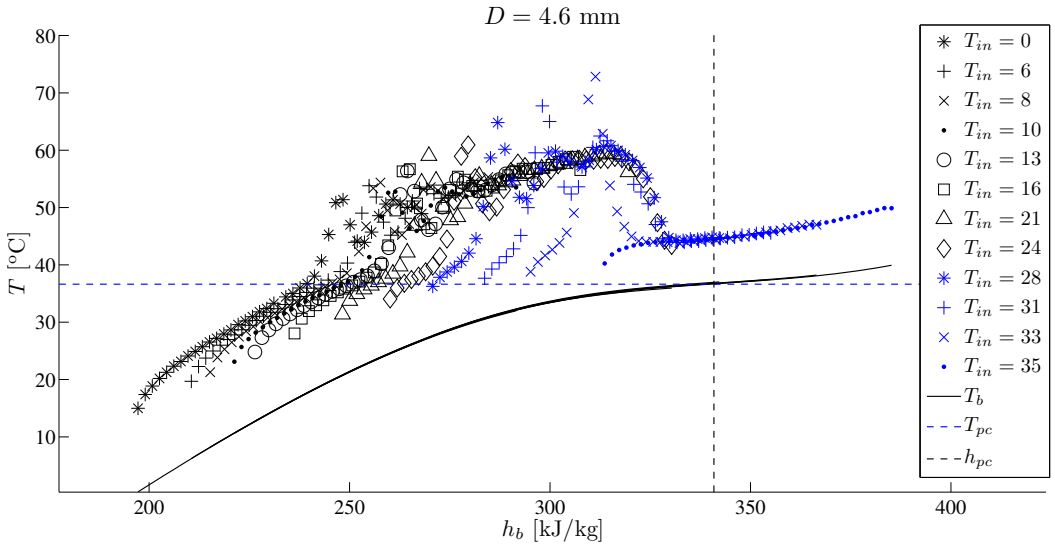


(a) All cases

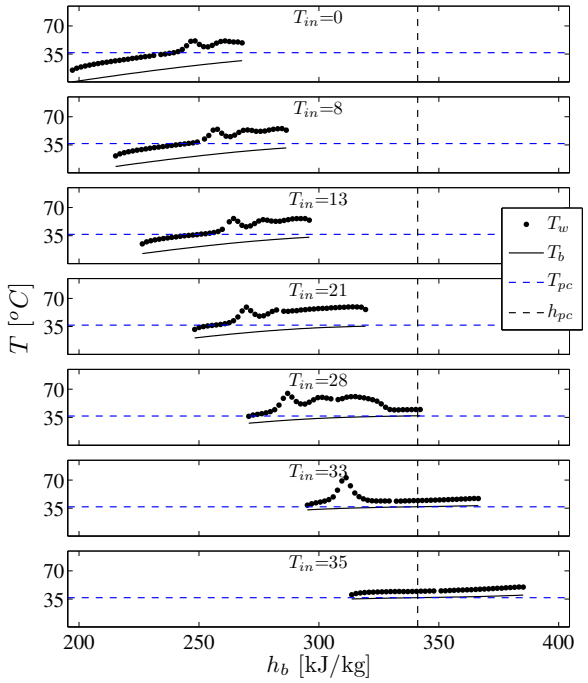


(b) Select cases

Figure A.3: Temperature profiles for $P/P_c = 1.13$, $G = 300$ kg/m^{2}s, $q = 18$ kW/m^2; units of T_{in} are °C.

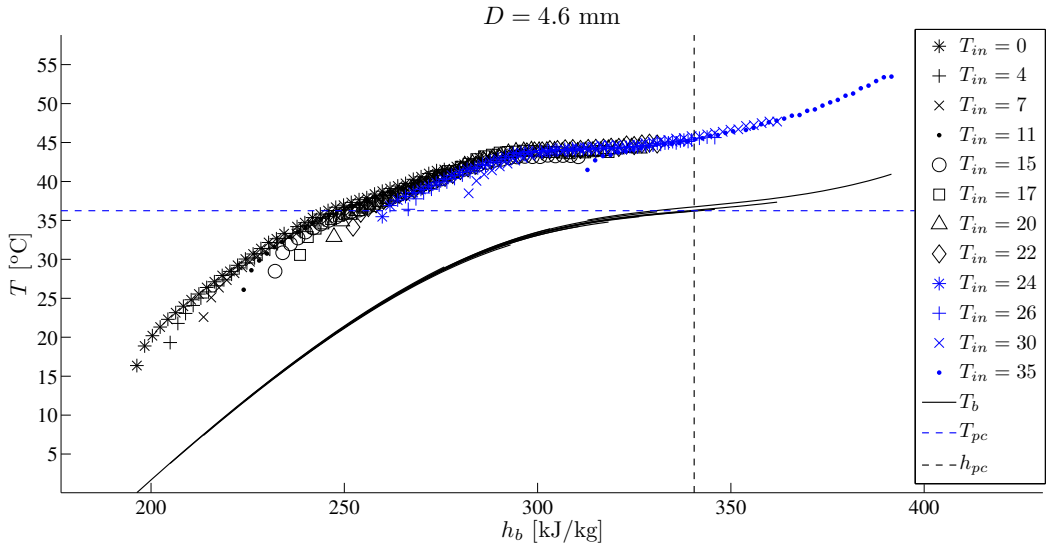


(a) All cases

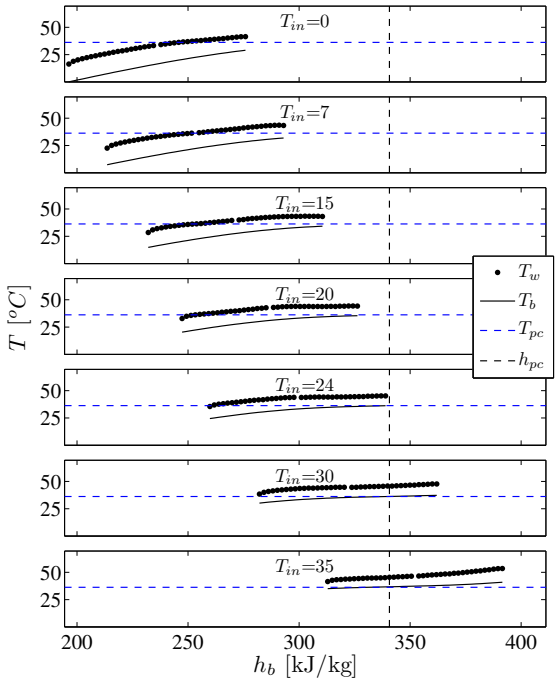


(b) Select cases

Figure A.4: Temperature profiles for $P/P_c = 1.13$, $G = 300$ kg/m^{2}s, $q = 20$ kW/m^2; units of T_{in} are °C.

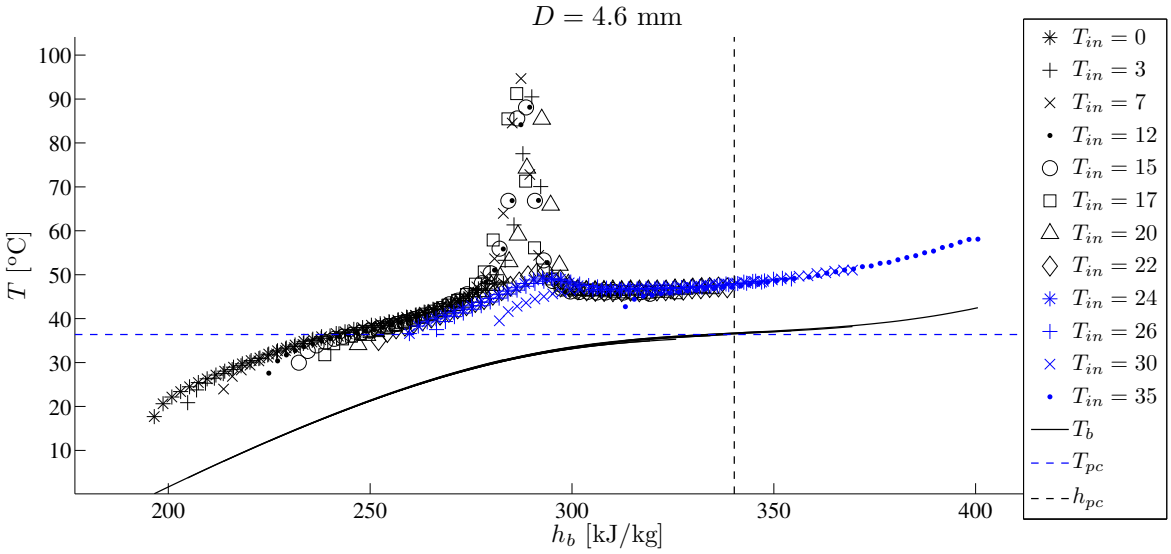


(a) All cases

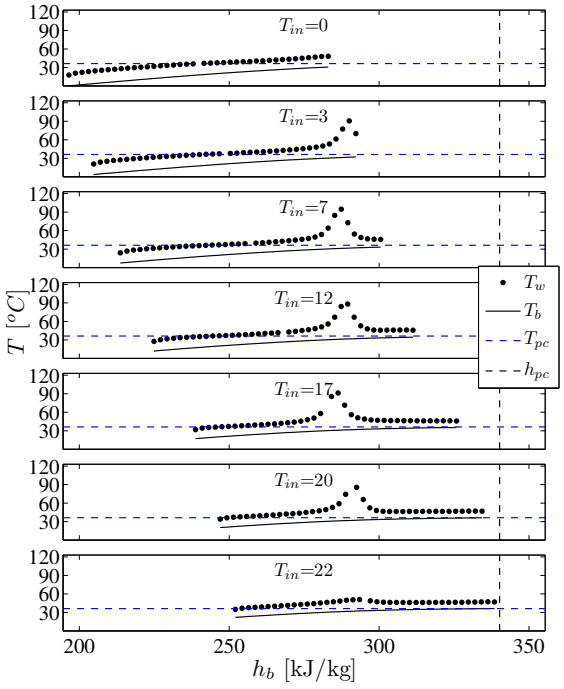


(b) Select cases

Figure A.5: Temperature profiles for $P/P_c = 1.13$, $G = 400$ kg/m^{2}s, $q = 30$ kW/m^2; units of T_{in} are °C.

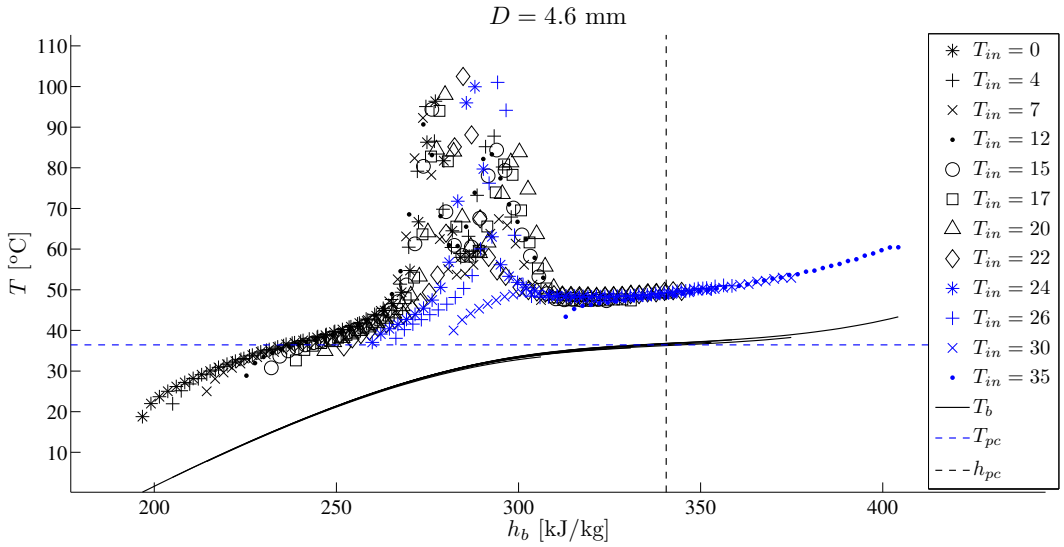


(a) All cases

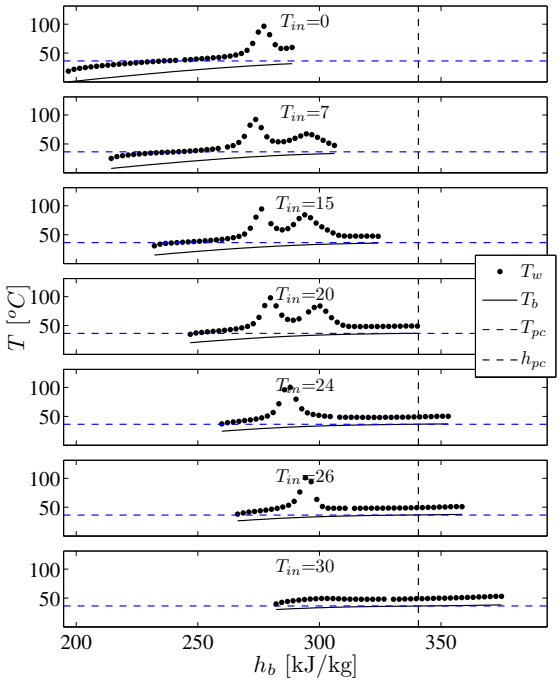


(b) Select cases

Figure A.6: Temperature profiles for $P/P_c = 1.13$, $G = 400$ kg/m^{2}s, $q = 33$ kW/m^2; units of T_{in} are °C.

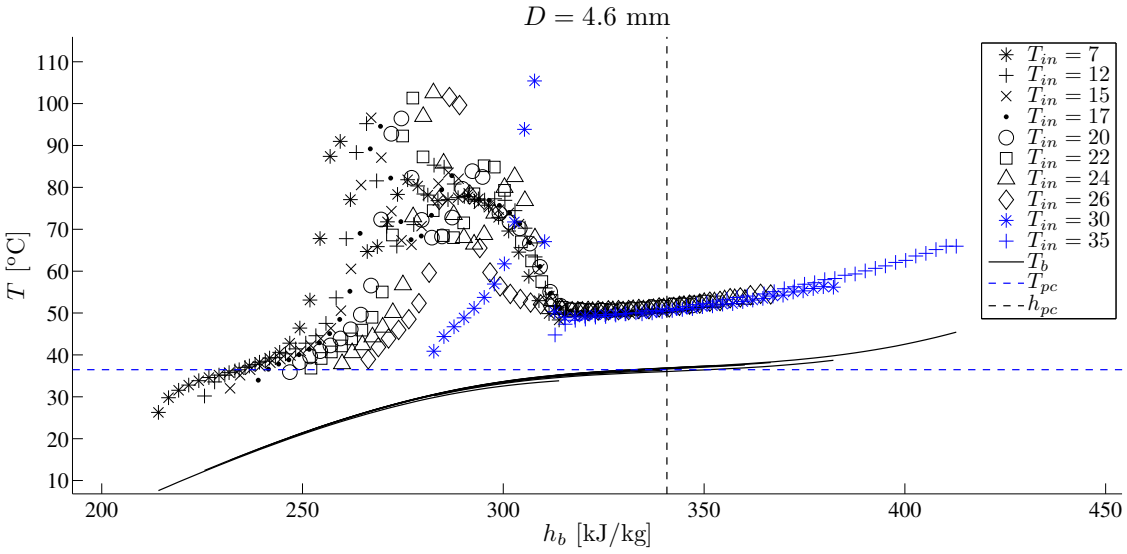


(a) All cases

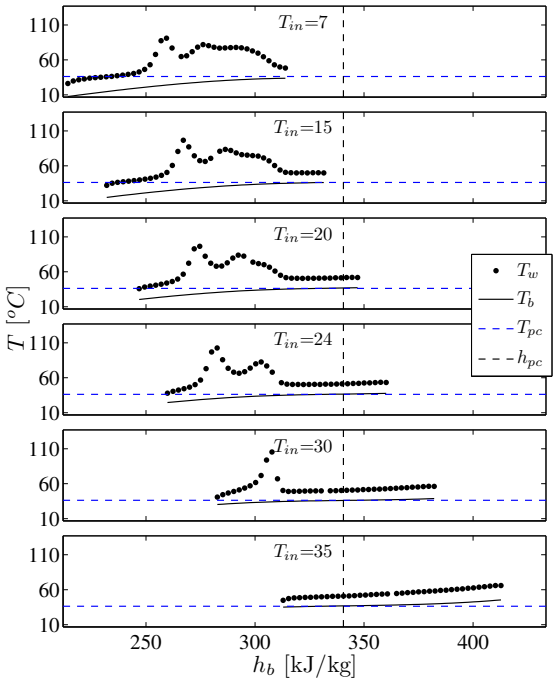


(b) Select cases

Figure A.7: Temperature profiles for $P/P_c = 1.13$, $G = 400$ kg/m^{2}s, $q = 35$ kW/m^2; units of T_{in} are °C.

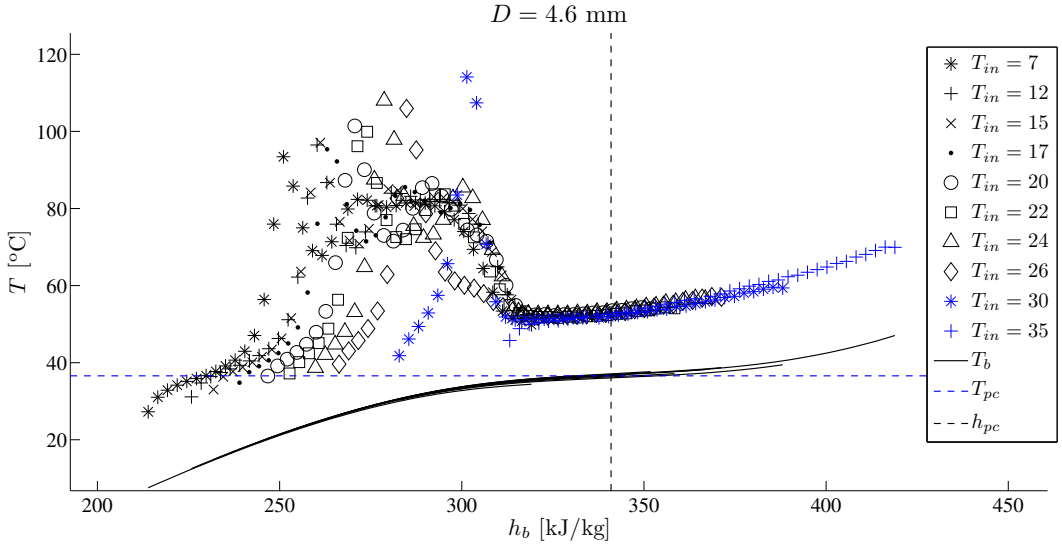


(a) All cases

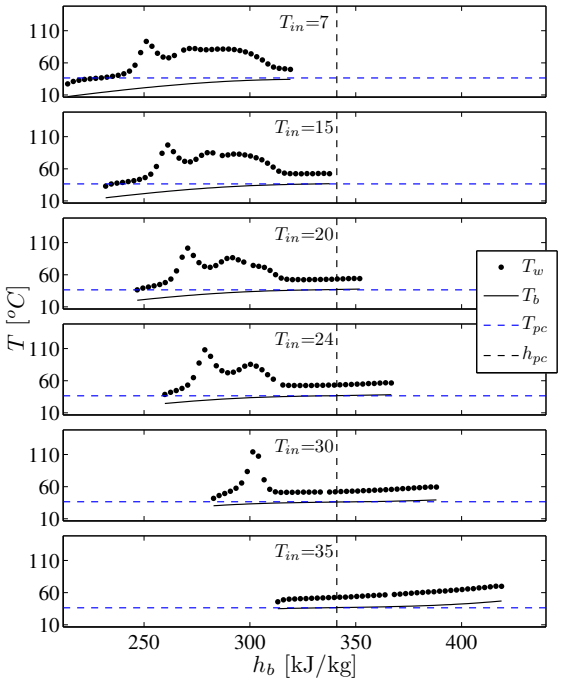


(b) Select cases

Figure A.8: Temperature profiles for $P/P_c = 1.13$, $G = 400$ kg/m^{2}s, $q = 38$ kW/m^2; units of T_{in} are °C.

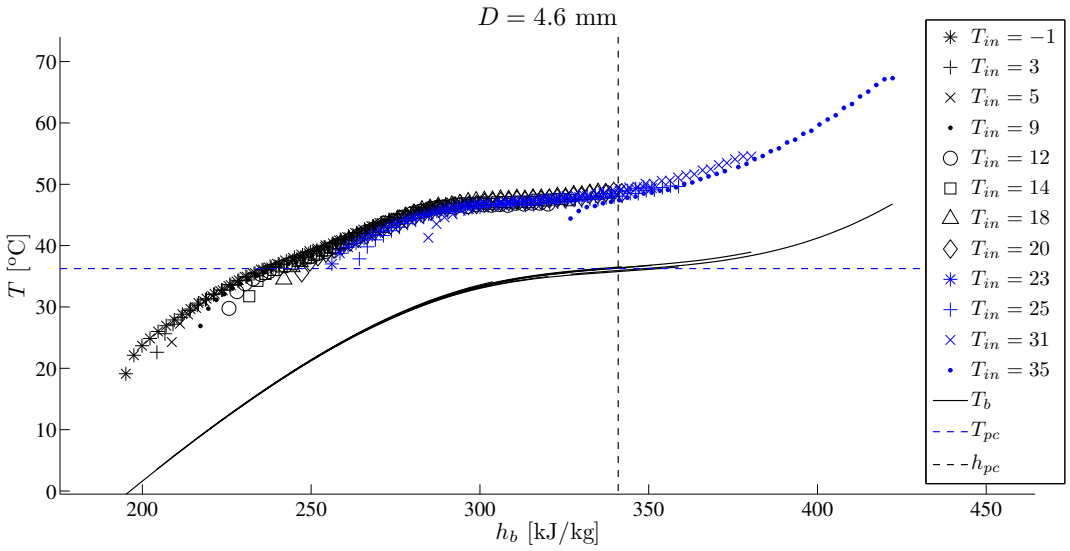


(a) All cases

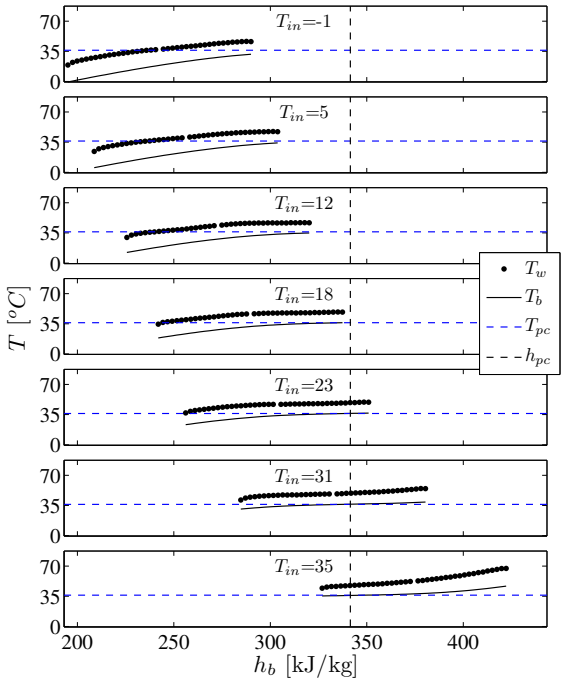


(b) Select cases

Figure A.9: Temperature profiles for $P/P_c = 1.13$, $G = 400$ kg/m^{2}s, $q = 40$ kW/m^2; units of T_{in} are °C.

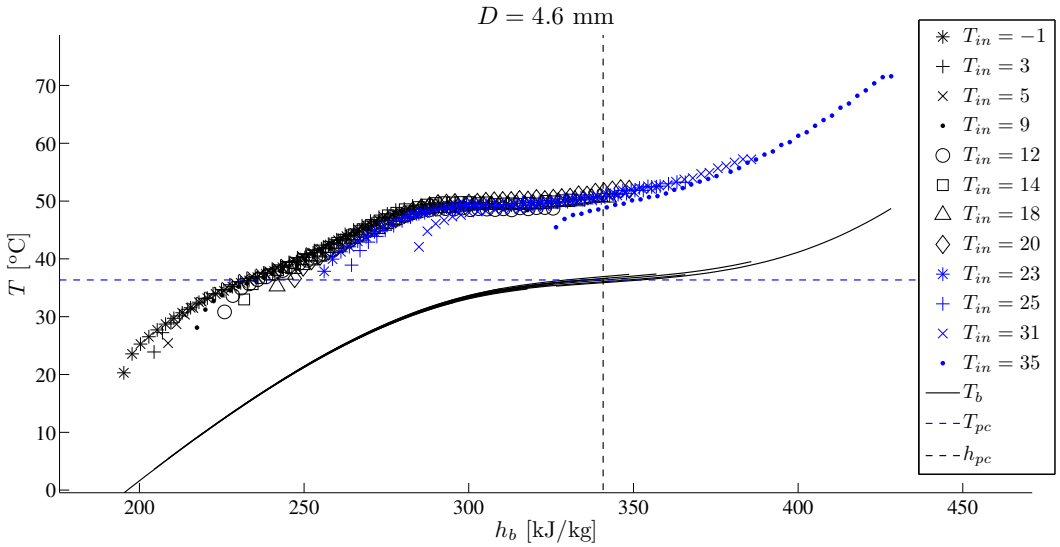


(a) All cases

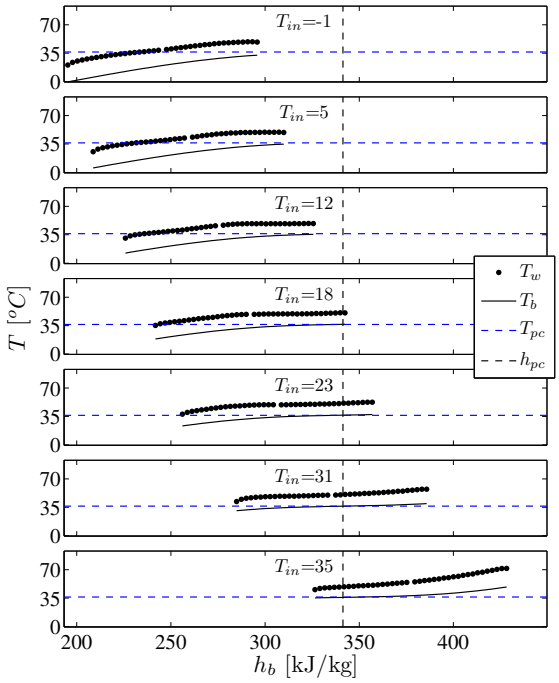


(b) Select cases

Figure A.10: Temperature profiles for $P/P_c = 1.13$, $G = 500$ kg/m^{2}s, $q = 45$ kW/m^2; units of T_{in} are °C.

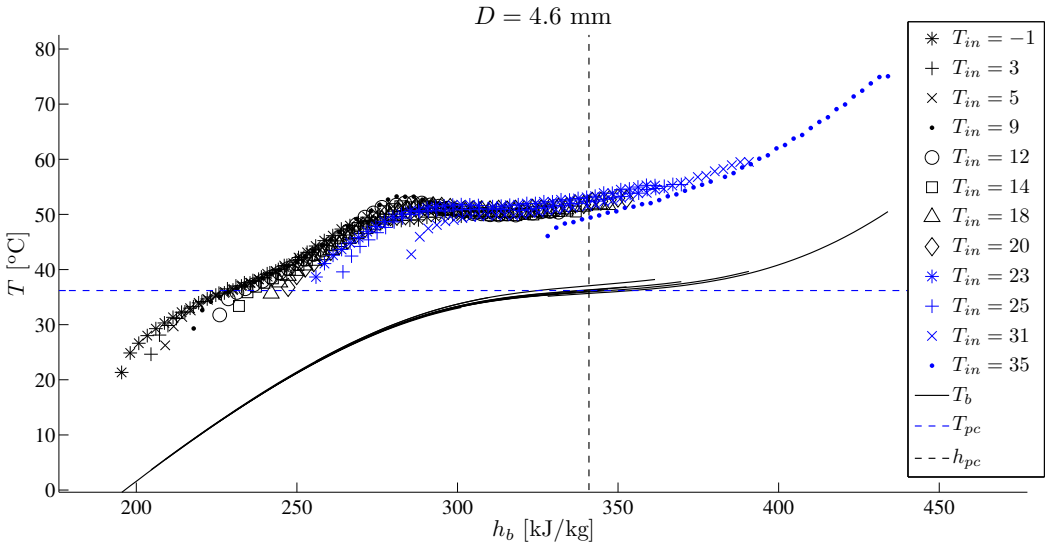


(a) All cases

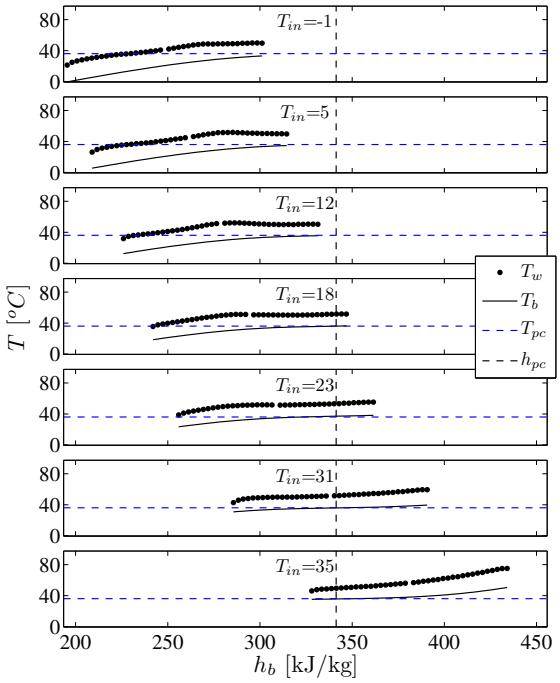


(b) Select cases

Figure A.11: Temperature profiles for $P/P_c = 1.13$, $G = 500$ kg/m^{2}s, $q = 48$ kW/m^2; units of T_{in} are °C.

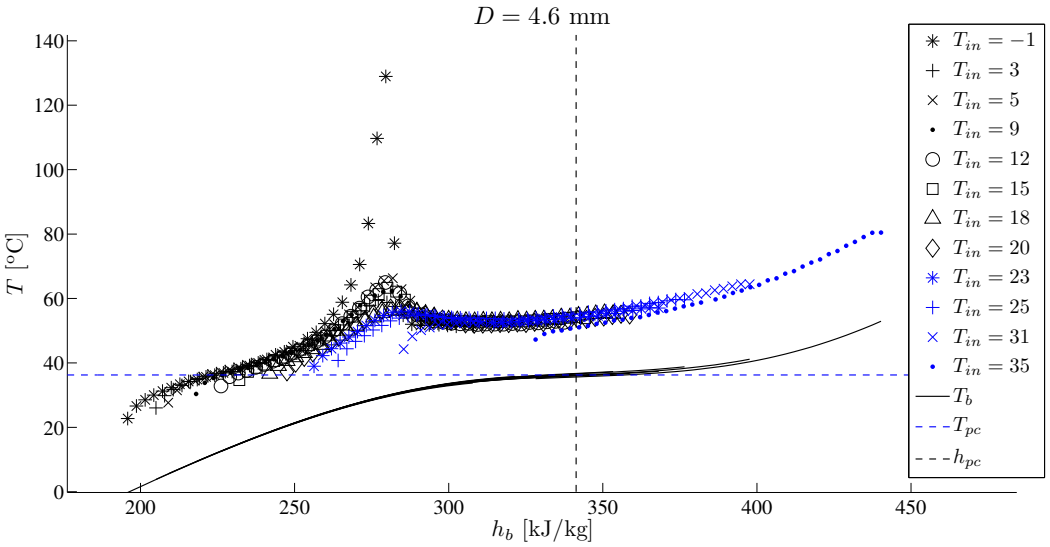


(a) All cases

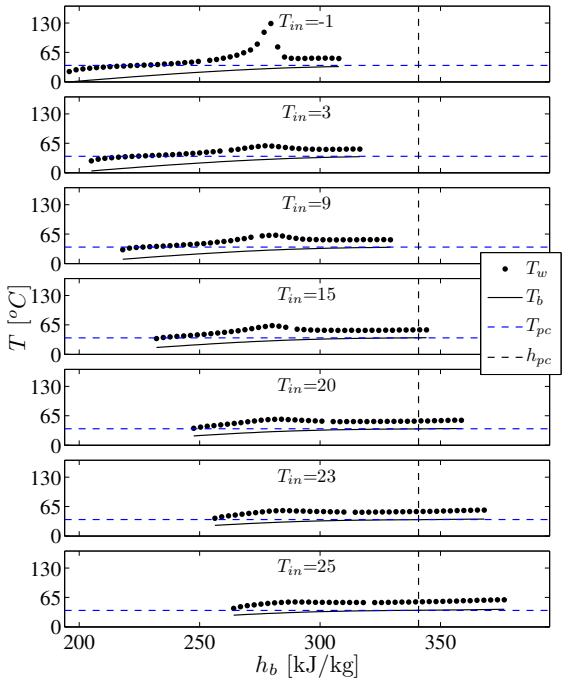


(b) Select cases

Figure A.12: Temperature profiles for $P/P_c = 1.13$, $G = 500$ kg/m^{2}s, $q = 50$ kW/m^2; units of T_{in} are °C.

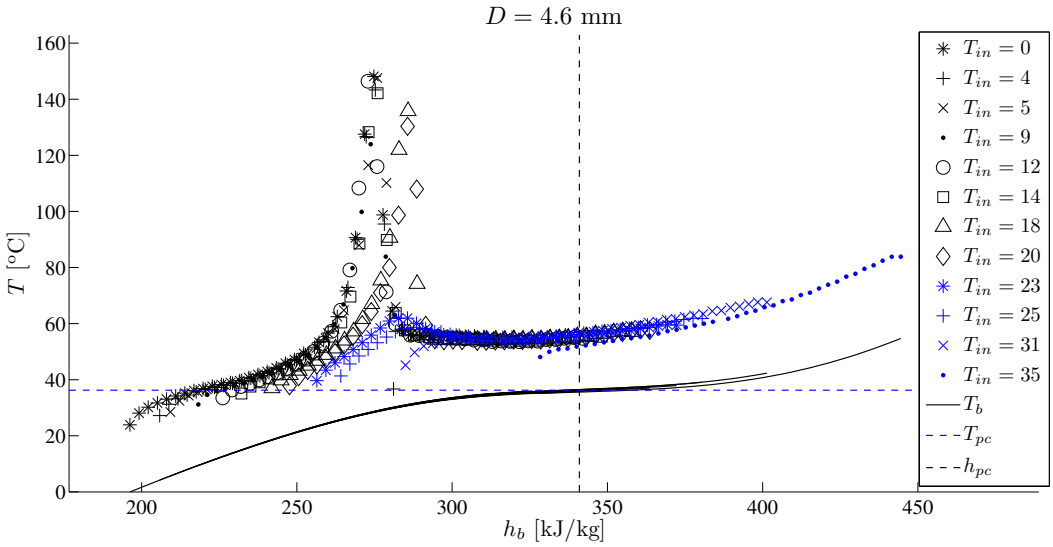


(a) All cases

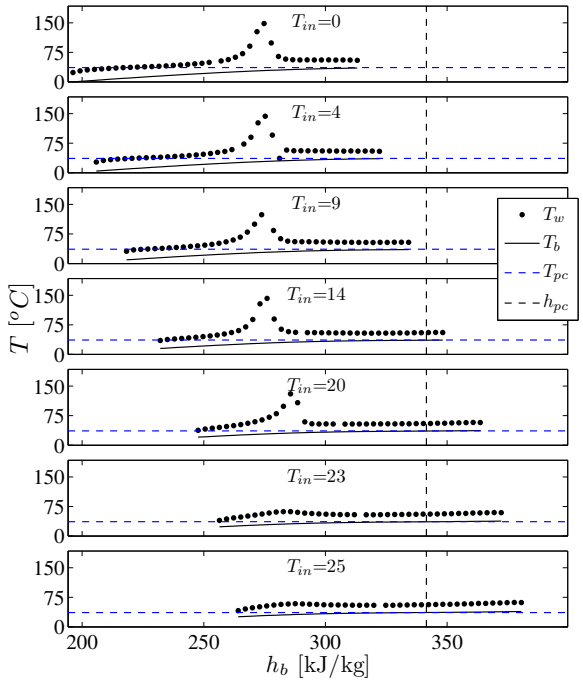


(b) Select cases

Figure A.13: Temperature profiles for $P/P_c = 1.13$, $G = 500$ kg/m^{2}s, $q = 53$ kW/m^2; units of T_{in} are °C.

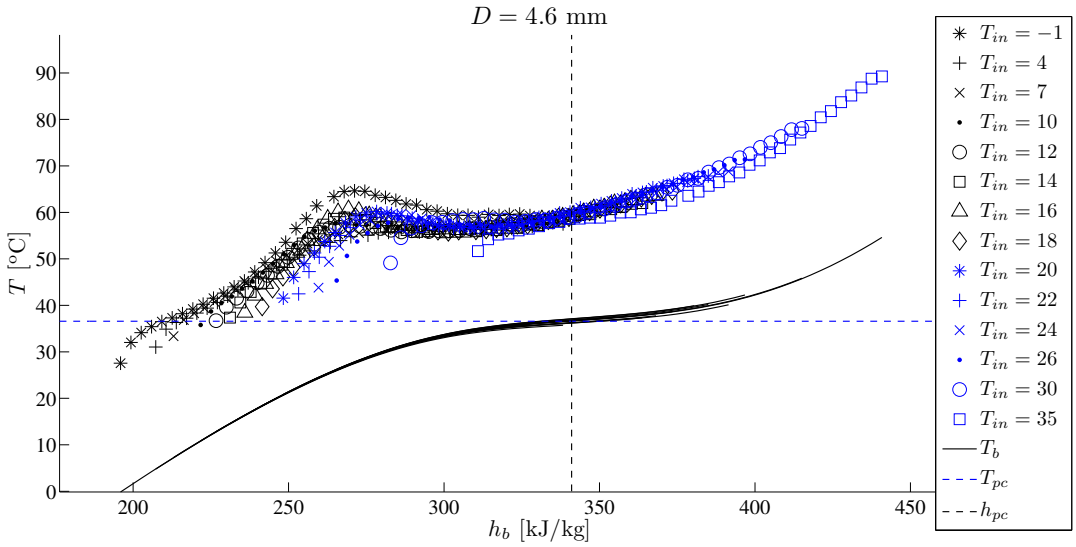


(a) All cases

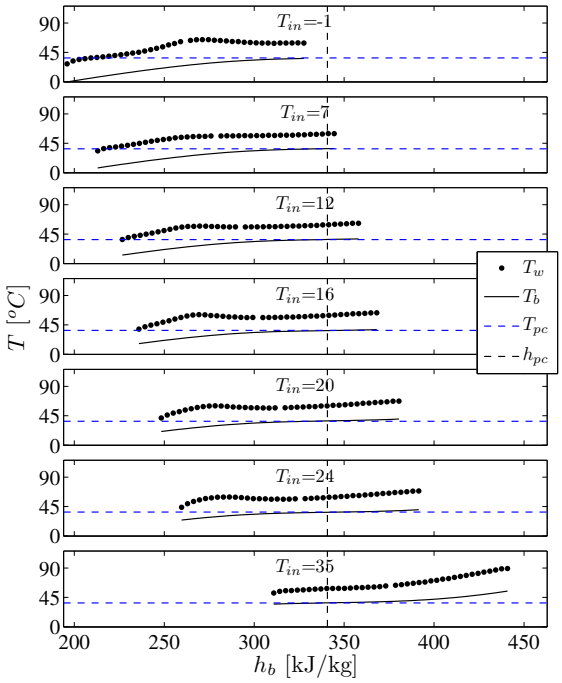


(b) Select cases

Figure A.14: Temperature profiles for $P/P_c = 1.13$, $G = 500$ kg/m^{2}s, $q = 55$ kW/m^2; units of T_{in} are °C.

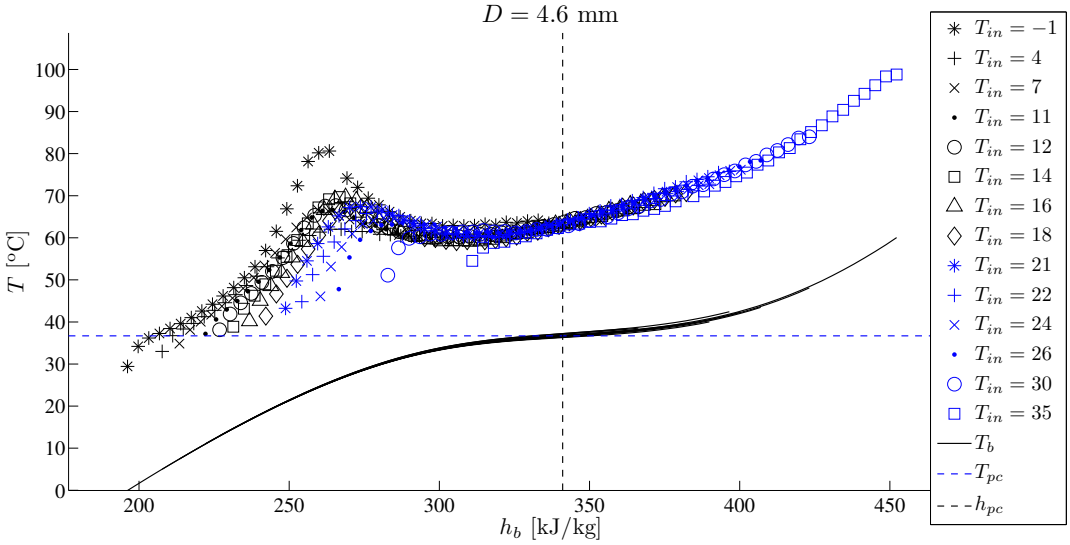


(a) All cases

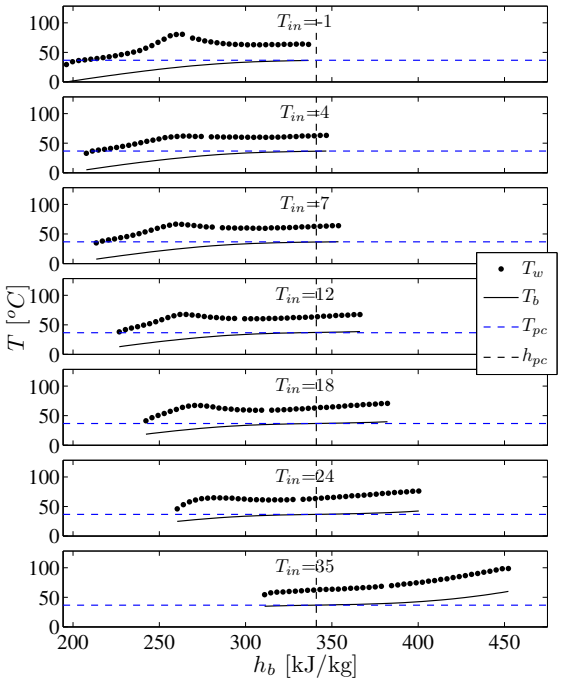


(b) Select cases

Figure A.15: Temperature profiles for $P/P_c = 1.13$, $G = 600$ kg/m^{2}s, $q = 75$ kW/m^2; units of T_{in} are °C.

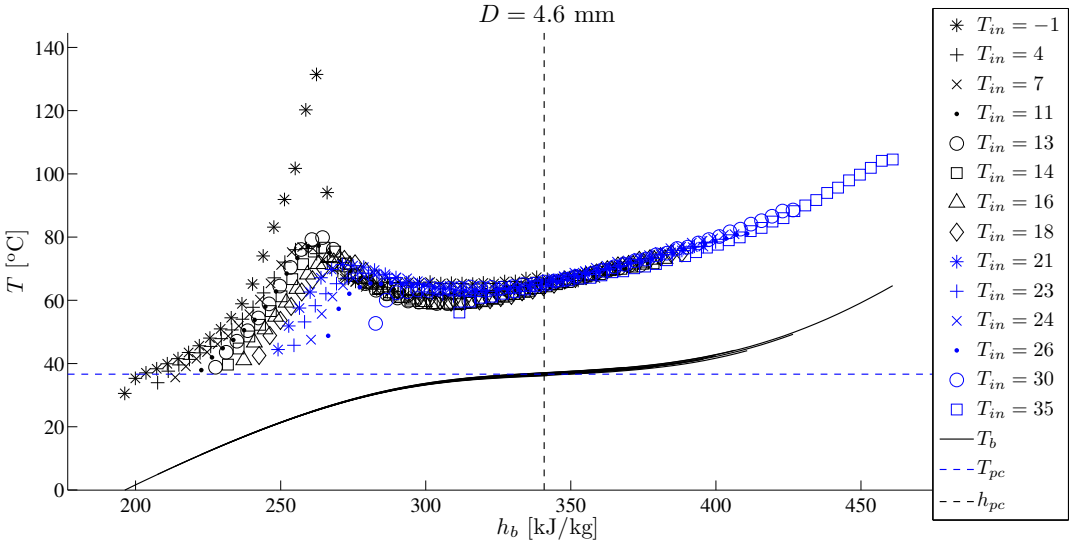


(a) All cases

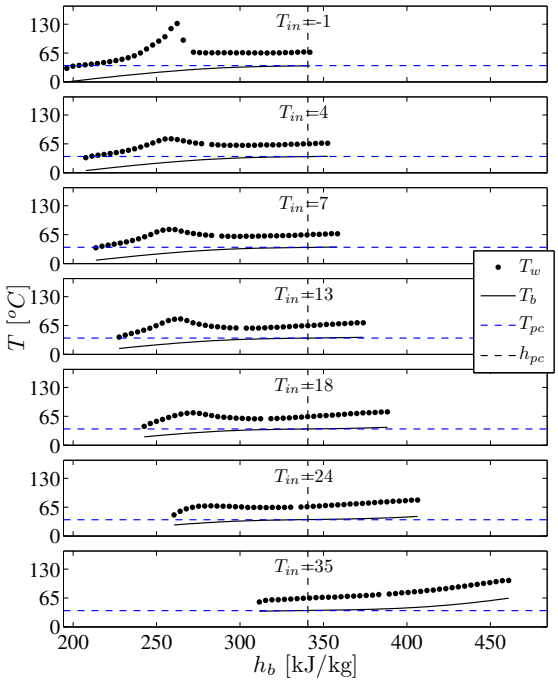


(b) Select cases

Figure A.16: Temperature profiles for $P/P_c = 1.13$, $G = 600$ kg/m^{2}s, $q = 80$ kW/m^2; units of T_{in} are °C.

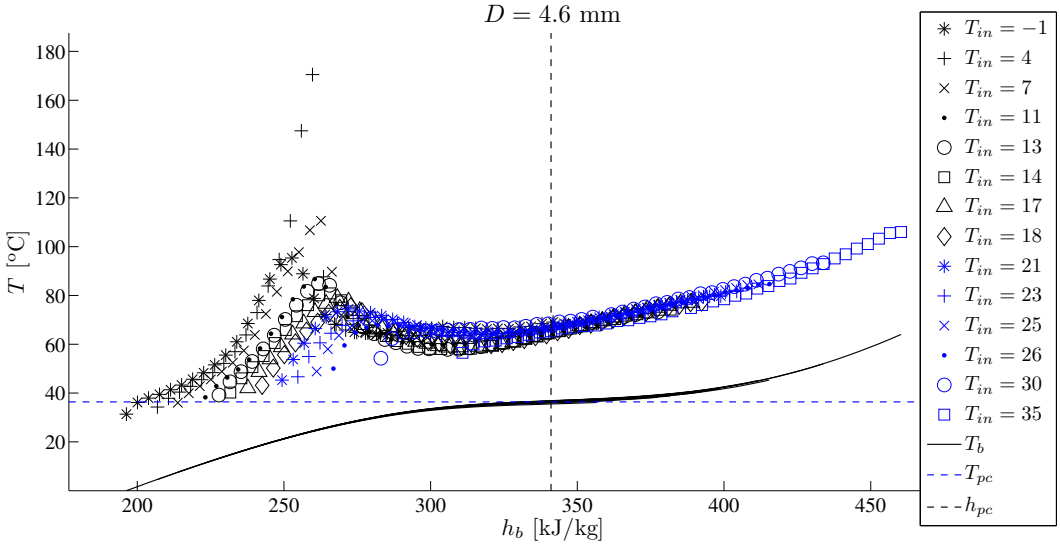


(a) All cases

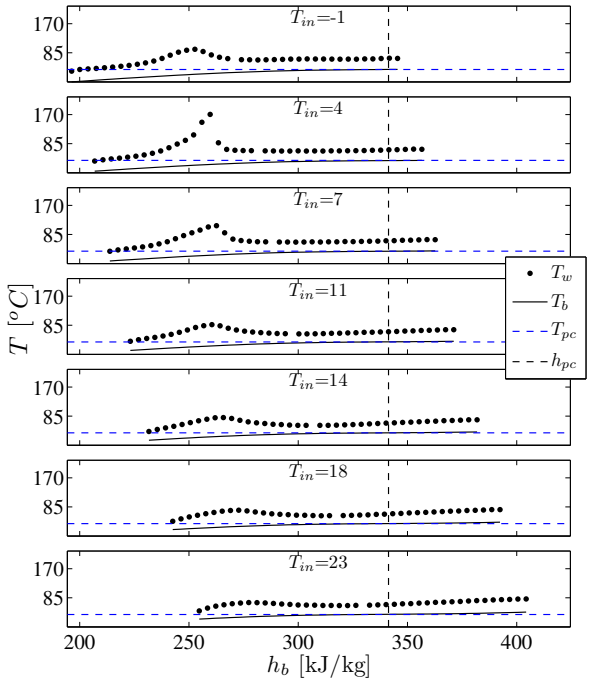


(b) Select cases

Figure A.17: Temperature profiles for $P/P_c = 1.13$, $G = 600$ kg/m^{2}s, $q = 83$ kW/m^2; units of T_{in} are °C.

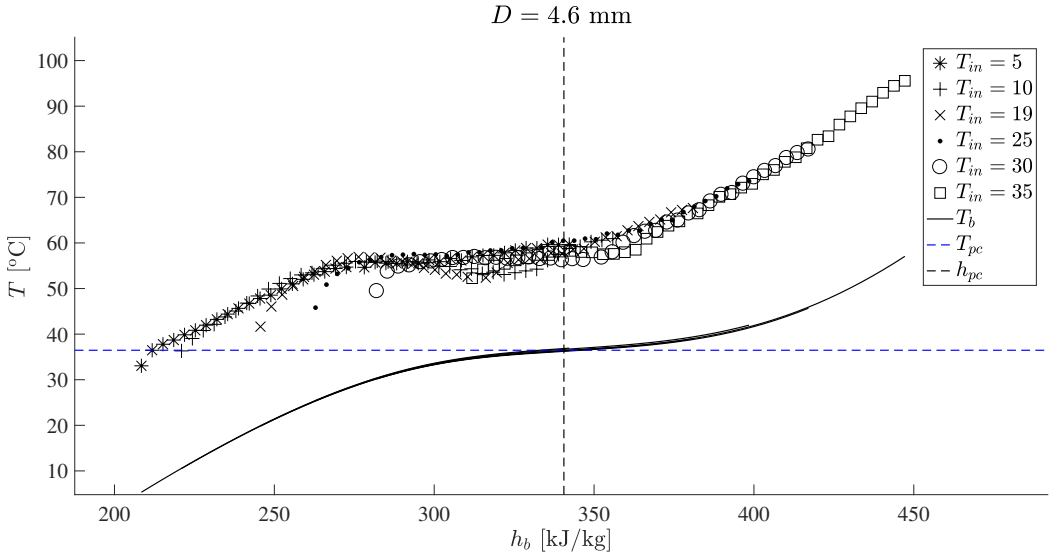


(a) All cases

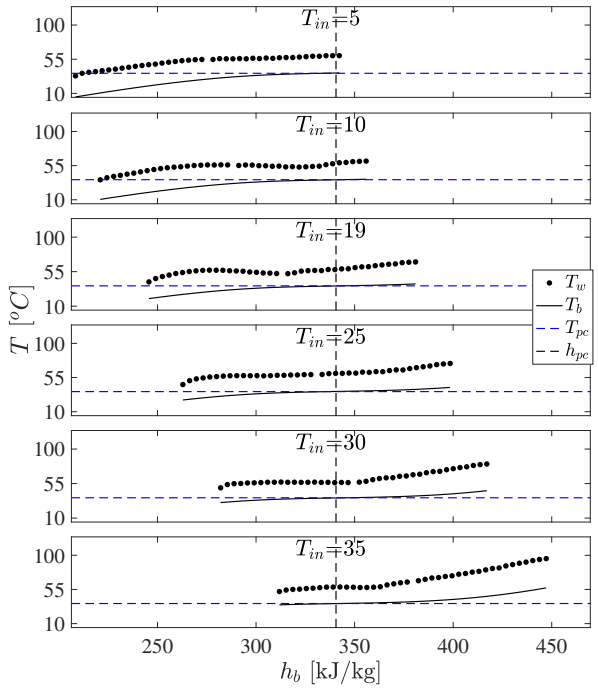


(b) Select cases

Figure A.18: Temperature profiles for $P/P_c = 1.13$, $G = 600$ kg/m^{2}s, $q = 85$ kW/m^2; units of T_{in} are °C.

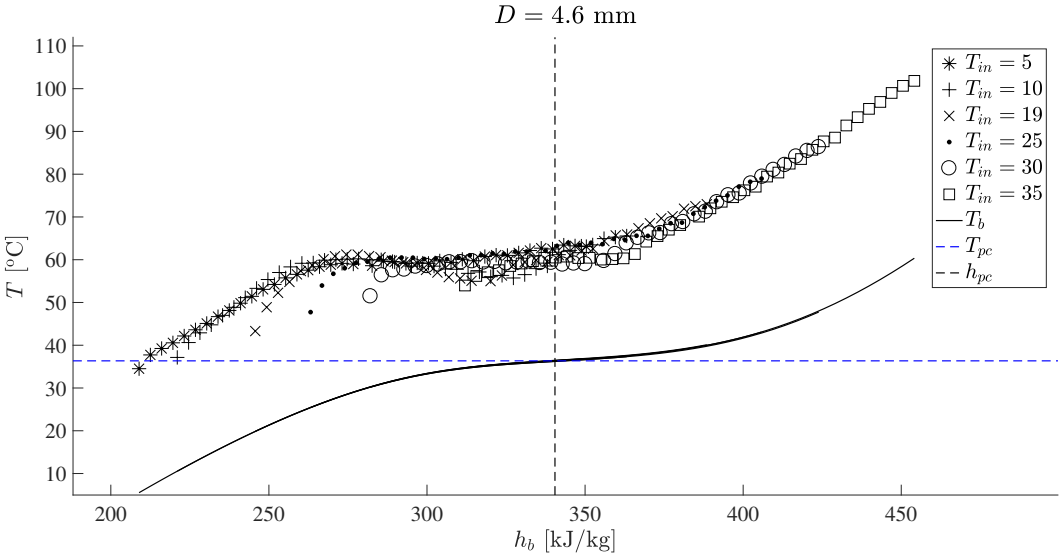


(a) All cases

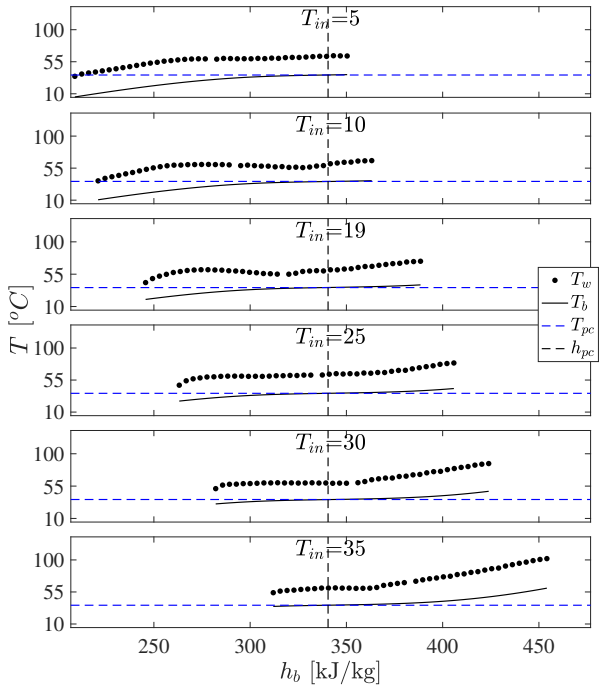


(b) Select cases

Figure A.19: Temperature profiles for $P/P_c = 1.13$, $G = 700$ kg/m^{2}s, $q = 90$ kW/m^2; units of T_{in} are °C.

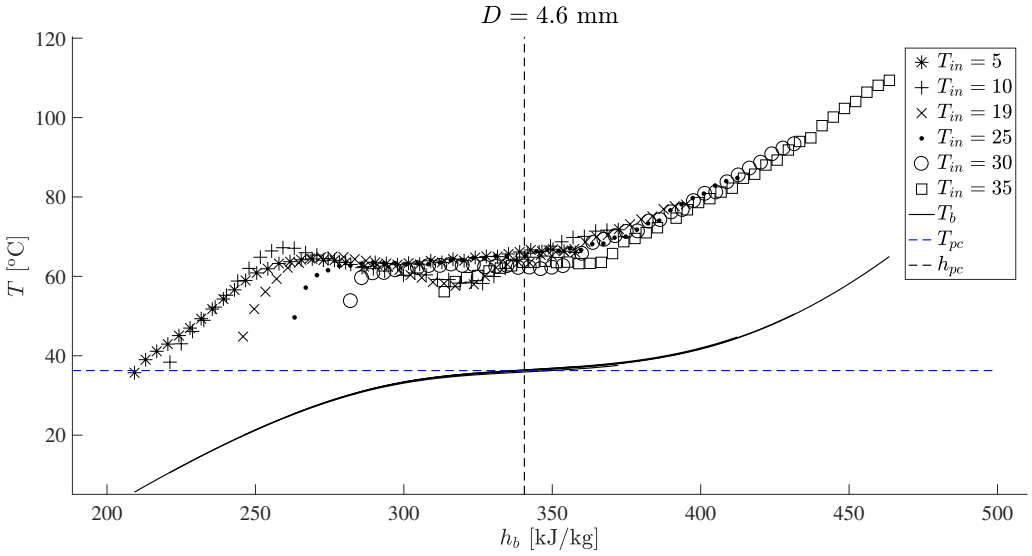


(a) All cases

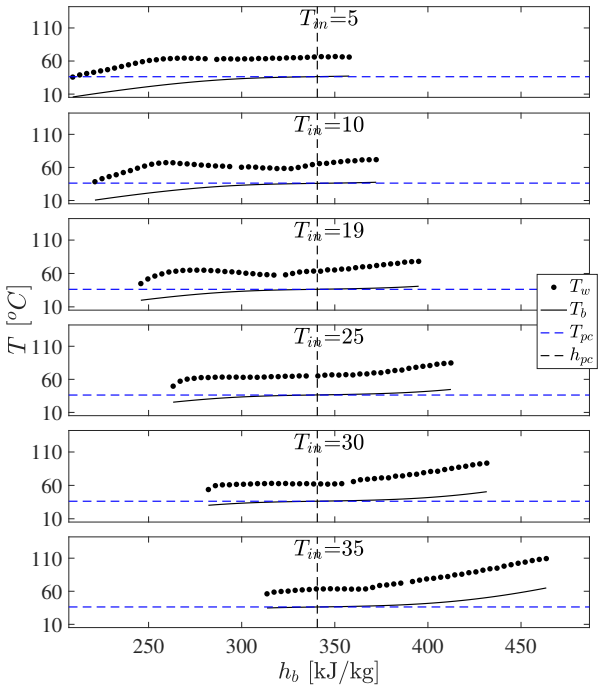


(b) Select cases

Figure A.20: Temperature profiles for $P/P_c = 1.13$, $G = 700$ kg/m^{2}s, $q = 95$ kW/m^2; units of T_{in} are °C.

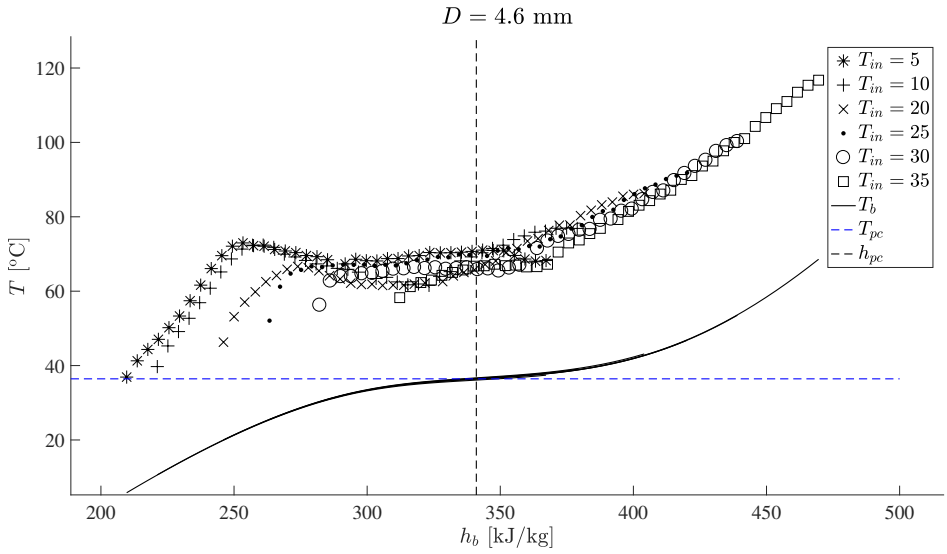


(a) All cases

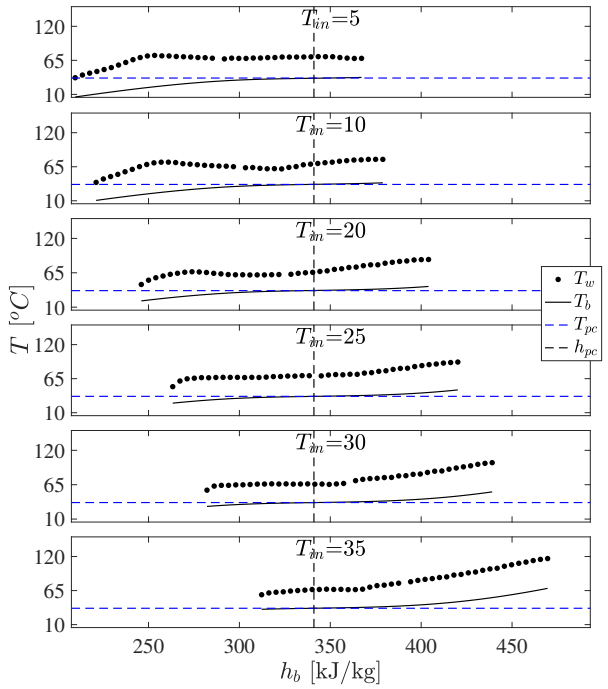


(b) Select cases

Figure A.21: Temperature profiles for $P/P_c = 1.13$, $G = 700$ kg/m^{2}s, $q = 100$ kW/m^2; units of T_{in} are °C.

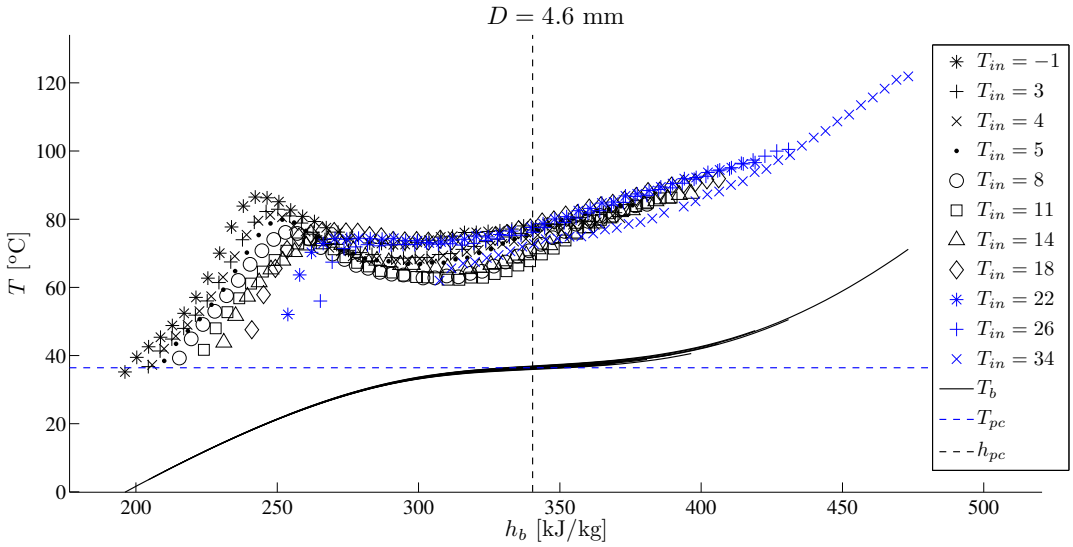


(a) All cases

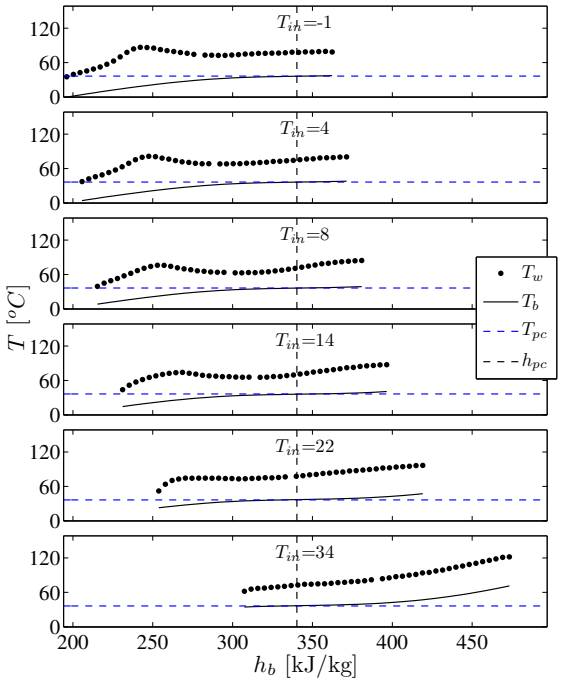


(b) Select cases

Figure A.22: Temperature profiles for $P/P_c = 1.13$, $G = 700$ kg/m^{2}s, $q = 105$ kW/m^2; units of T_{in} are °C.

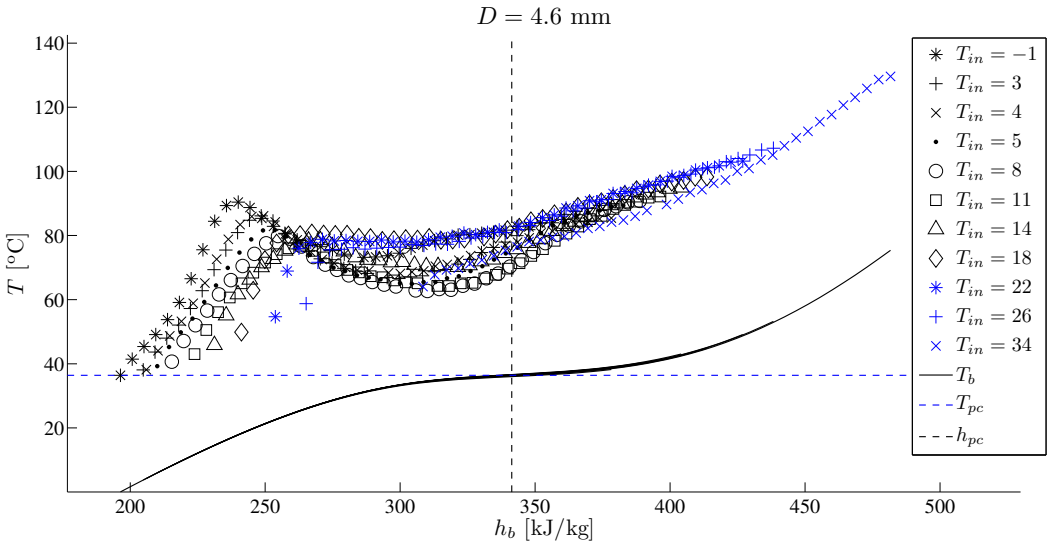


(a) All cases

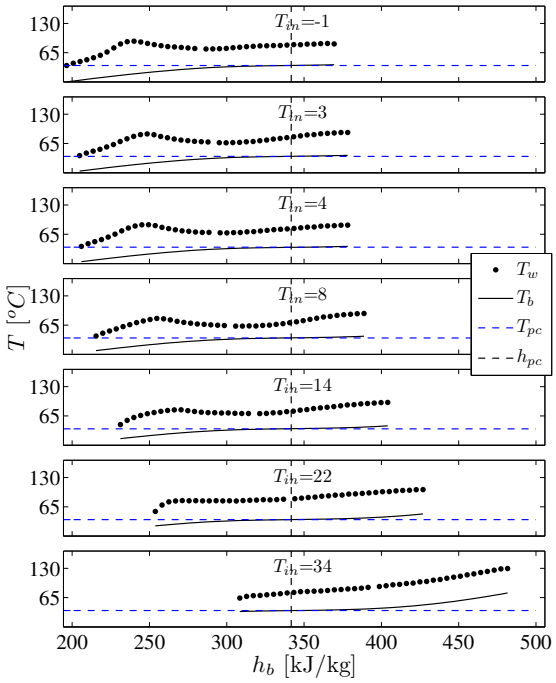


(b) Select cases

Figure A.23: Temperature profiles for $P/P_c = 1.13$, $G = 700$ kg/m^{2}s, $q = 110$ kW/m^2; units of T_{in} are °C.

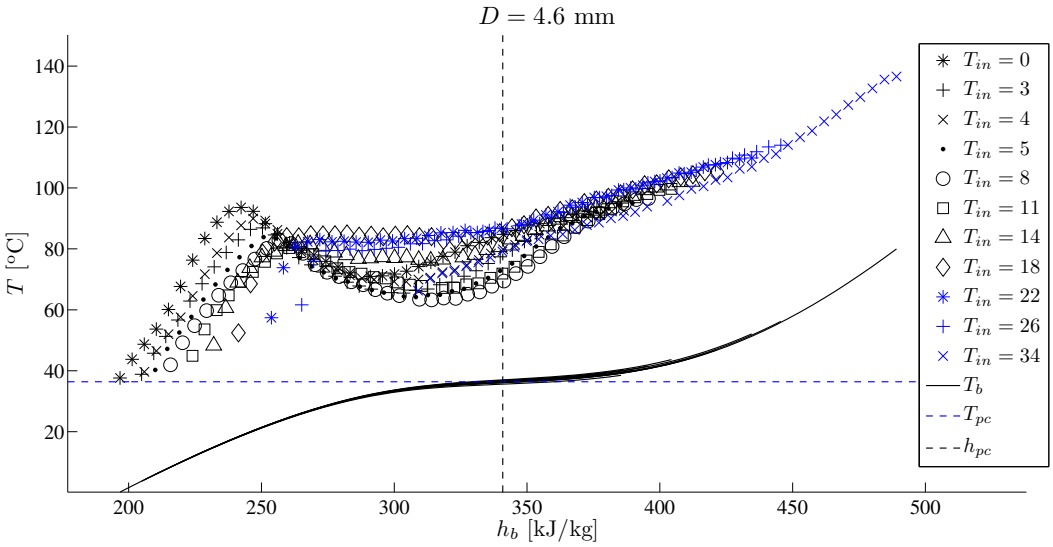


(a) All cases

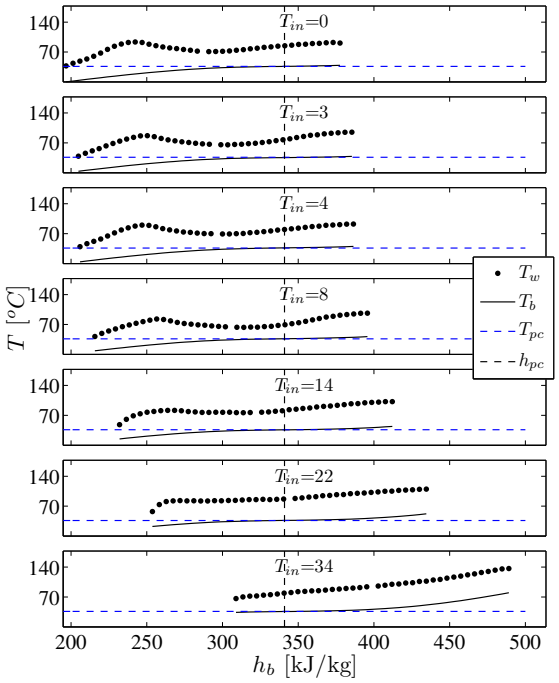


(b) Select cases

Figure A.24: Temperature profiles for $P/P_c = 1.13$, $G = 700$ kg/m^{2}s, $q = 115$ kW/m^2; units of T_{in} are °C.

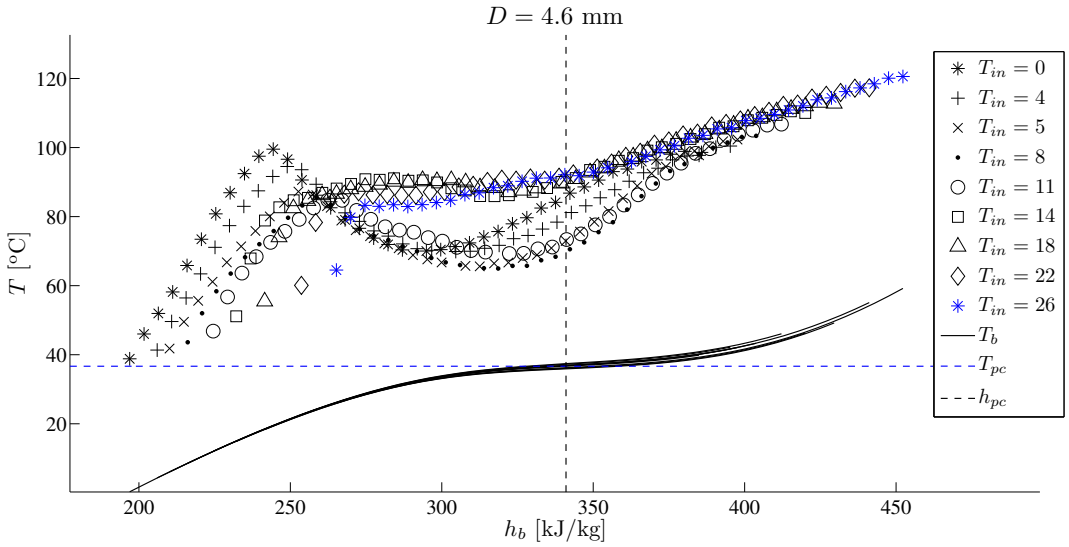


(a) All cases

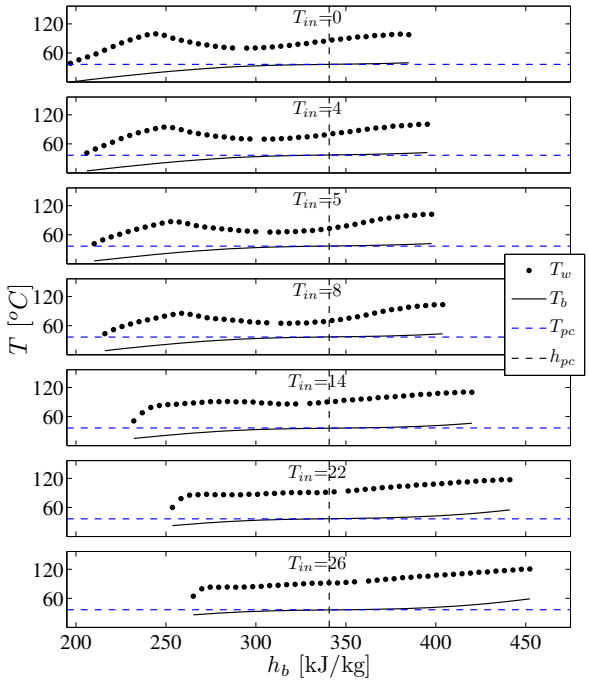


(b) Select cases

Figure A.25: Temperature profiles for $P/P_c = 1.13$, $G = 700$ kg/m^{2}s, $q = 120$ kW/m^2; units of T_{in} are °C.

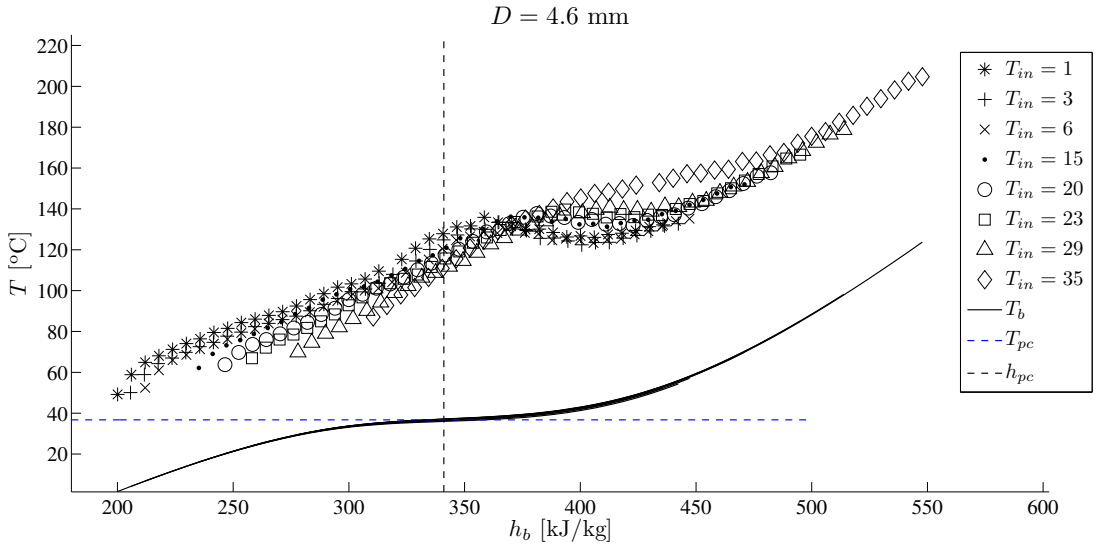


(a) All cases

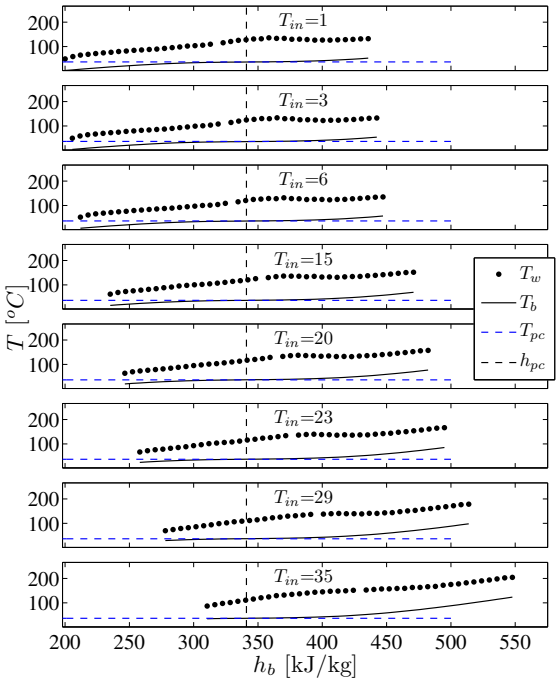


(b) Select cases

Figure A.26: Temperature profiles for $P/P_c = 1.13$, $G = 700$ kg/m^{2}s, $q = 125$ kW/m^2; units of T_{in} are °C.

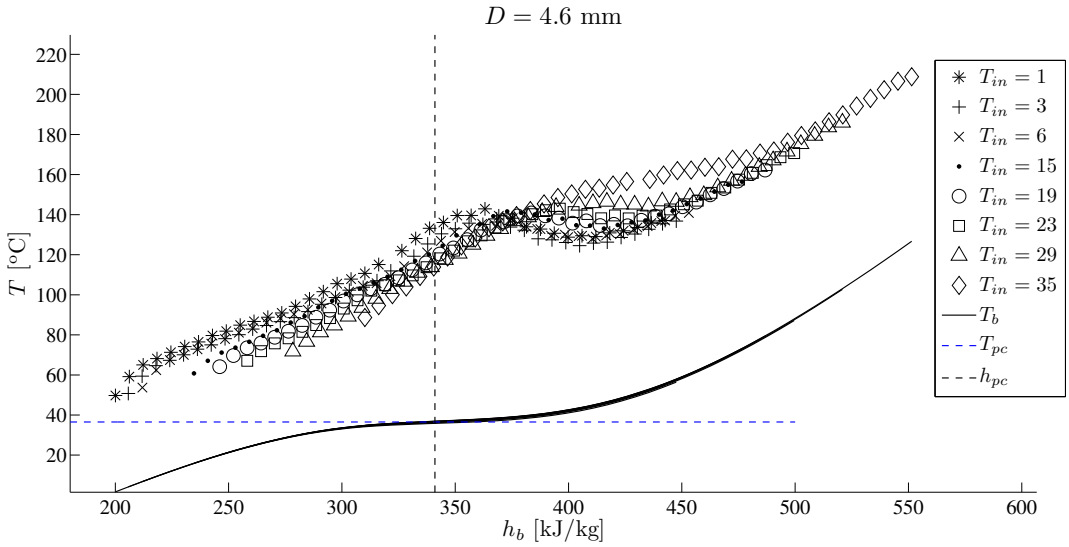


(a) All cases

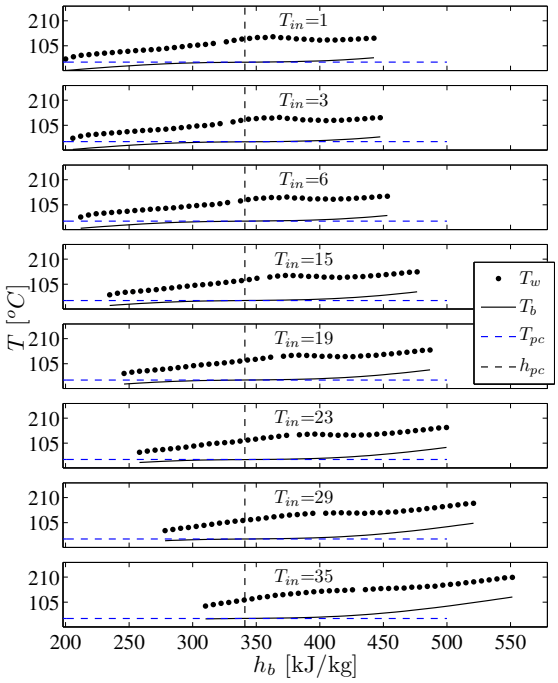


(b) Select cases

Figure A.27: Temperature profiles for $P/P_c = 1.13$, $G = 1000$ kg/m^{2}s, $q = 225$ kW/m^2; units of T_{in} are °C.

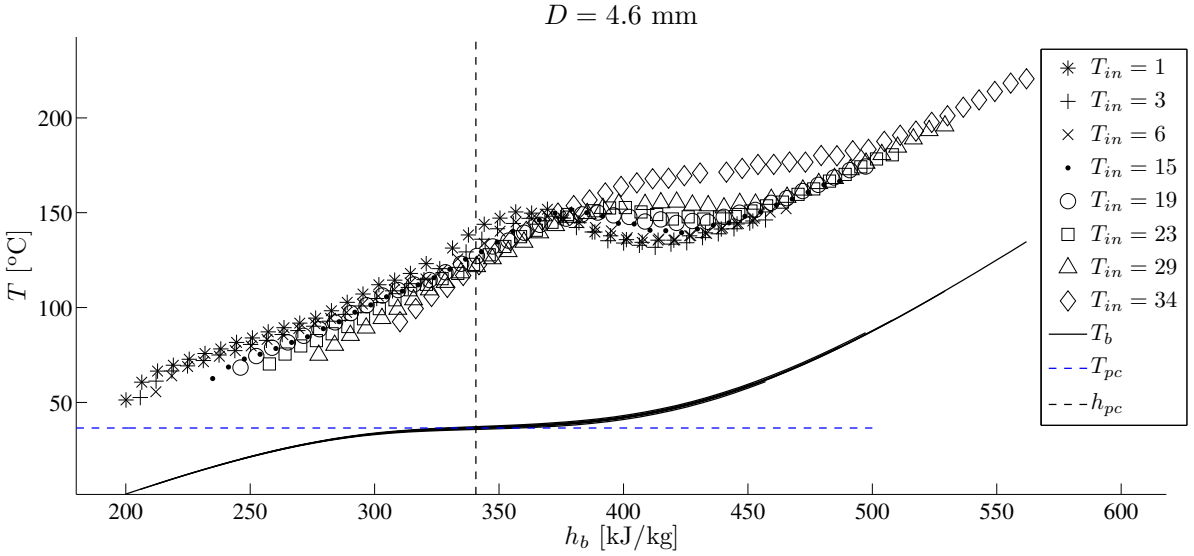


(a) All cases

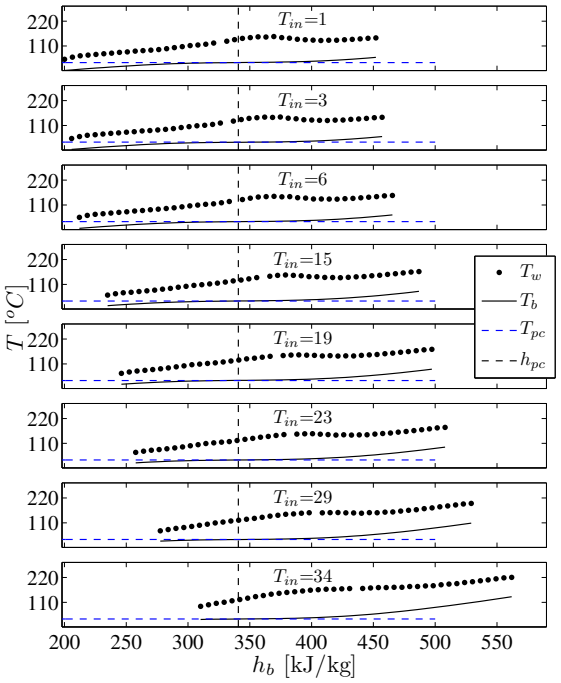


(b) Select cases

Figure A.28: Temperature profiles for $P/P_c = 1.13$, $G = 1000$ kg/m^{2}s, $q = 230$ kW/m^2; units of T_{in} are °C.

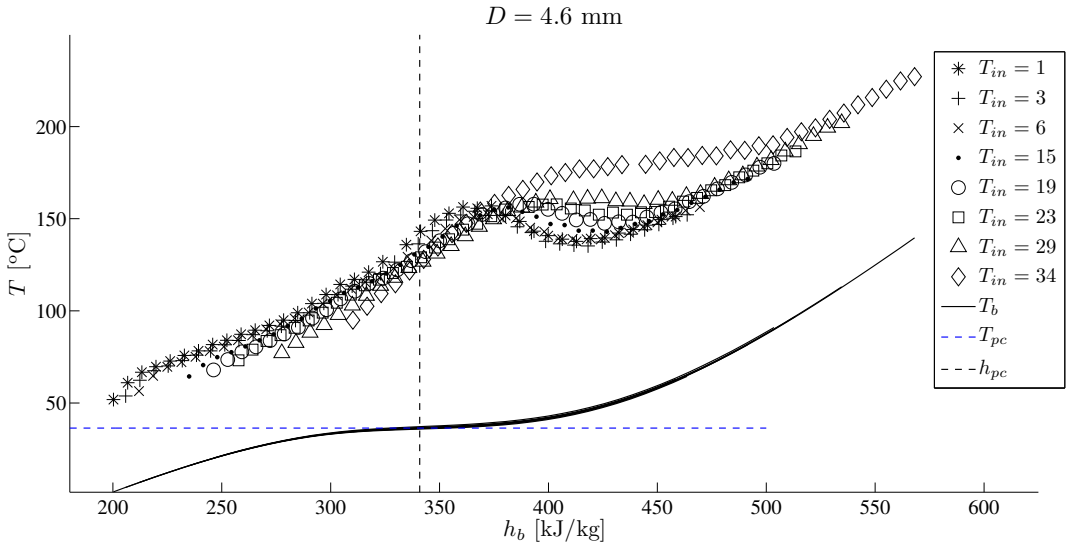


(a) All cases

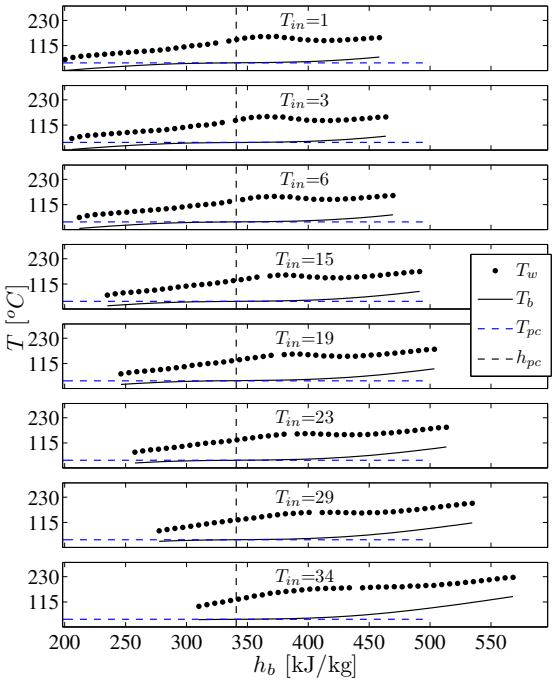


(b) Select cases

Figure A.29: Temperature profiles for $P/P_c = 1.13$, $G = 1000$ kg/m^{2}s, $q = 240$ kW/m^2; units of T_{in} are °C.

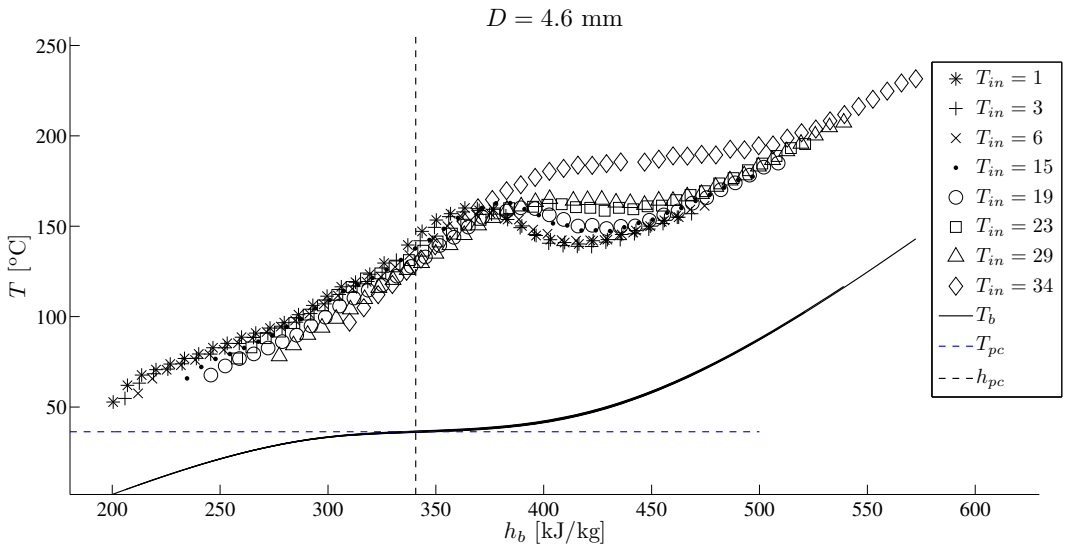


(a) All cases

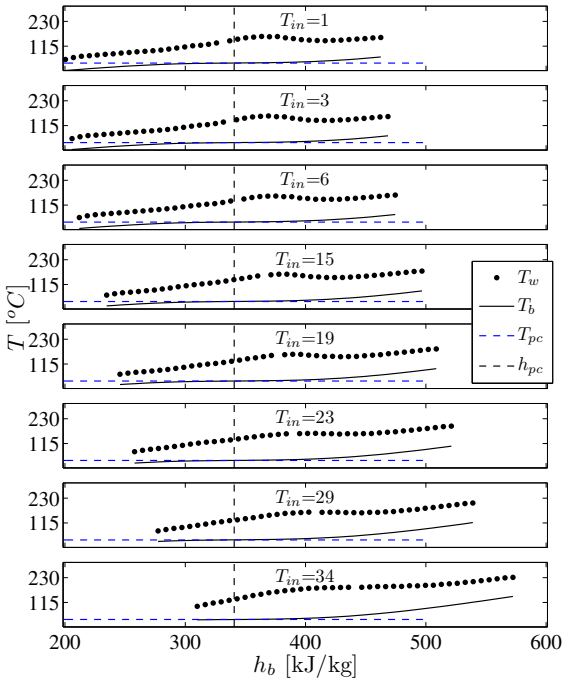


(b) Select cases

Figure A.30: Temperature profiles for $P/P_c = 1.13$, $G = 1000$ kg/m^{2}s, $q = 245$ kW/m^2; units of T_{in} are °C.

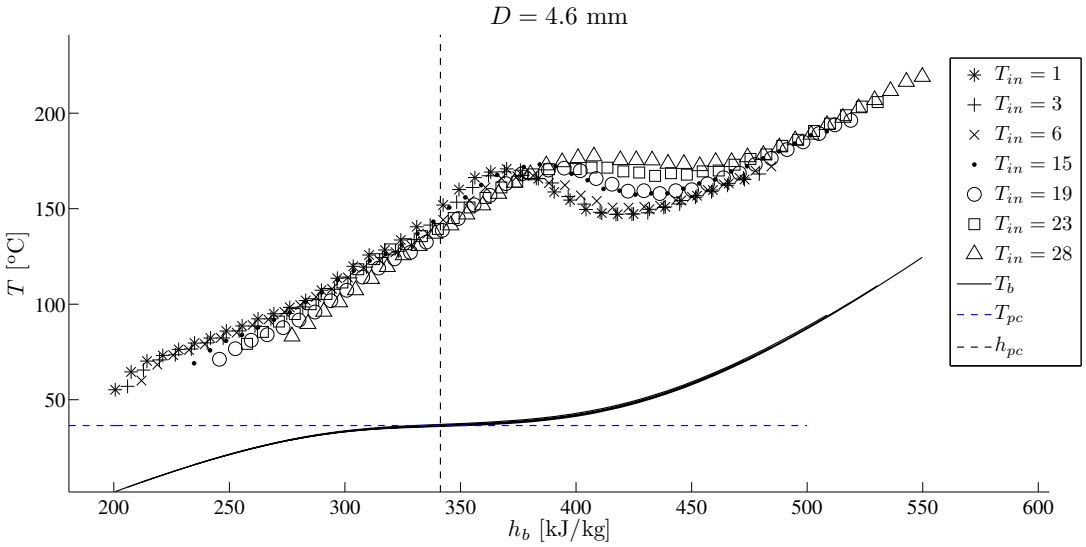


(a) All cases

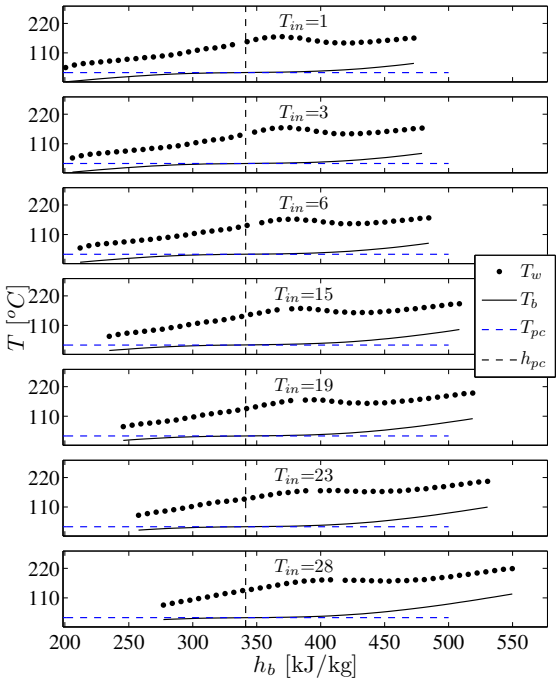


(b) Select cases

Figure A.31: Temperature profiles for $P/P_c = 1.13$, $G = 1000$ kg/m^{2}s, $q = 250$ kW/m^2; units of T_{in} are °C.

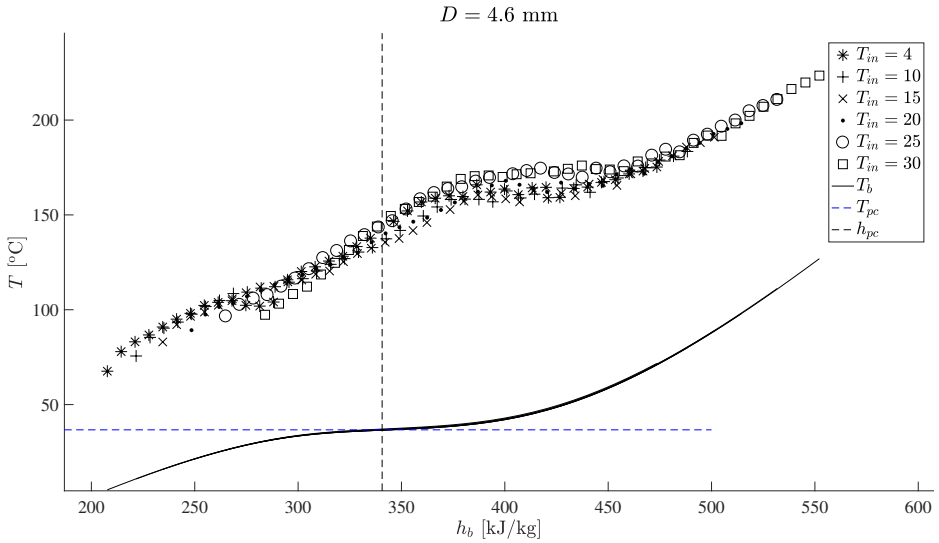


(a) All cases

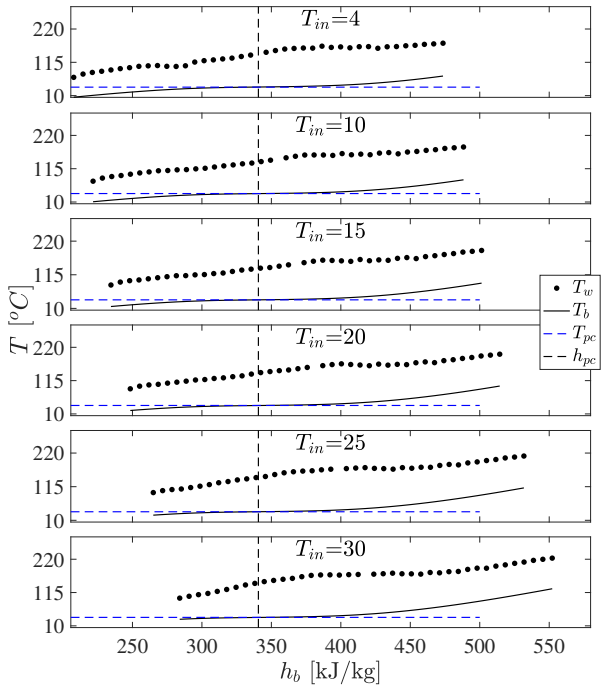


(b) Select cases

Figure A.32: Temperature profiles for $P/P_c = 1.13$, $G = 1000$ kg/m^{2}s, $q = 260$ kW/m^2; units of T_{in} are °C.

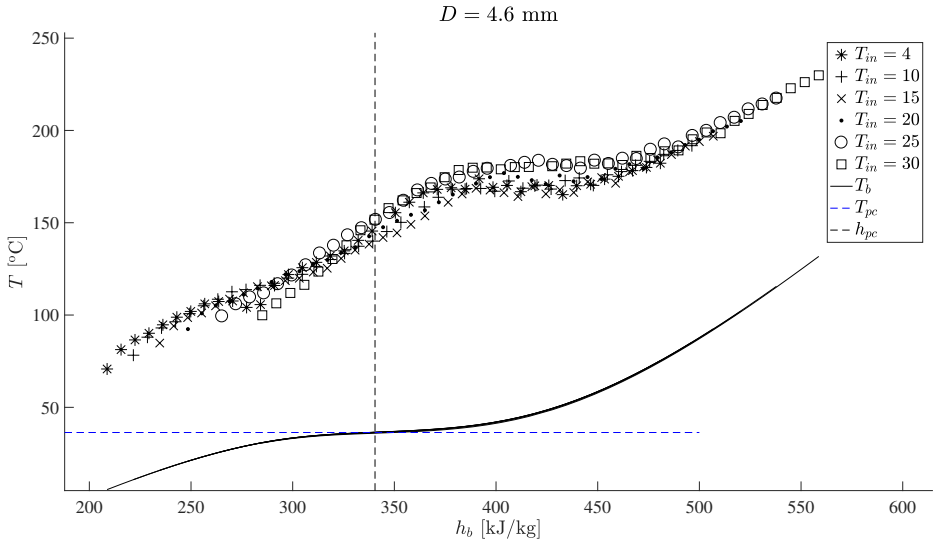


(a) All cases

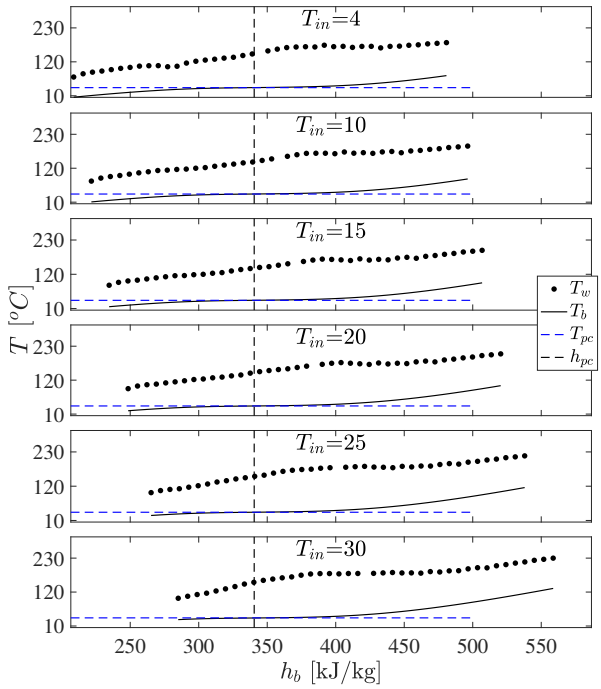


(b) Select cases

Figure A.33: Temperature profiles for $P/P_c = 1.13$, $G = 1500$ kg/m^{2}s, $q = 380$ kW/m^2; units of T_{in} are °C.

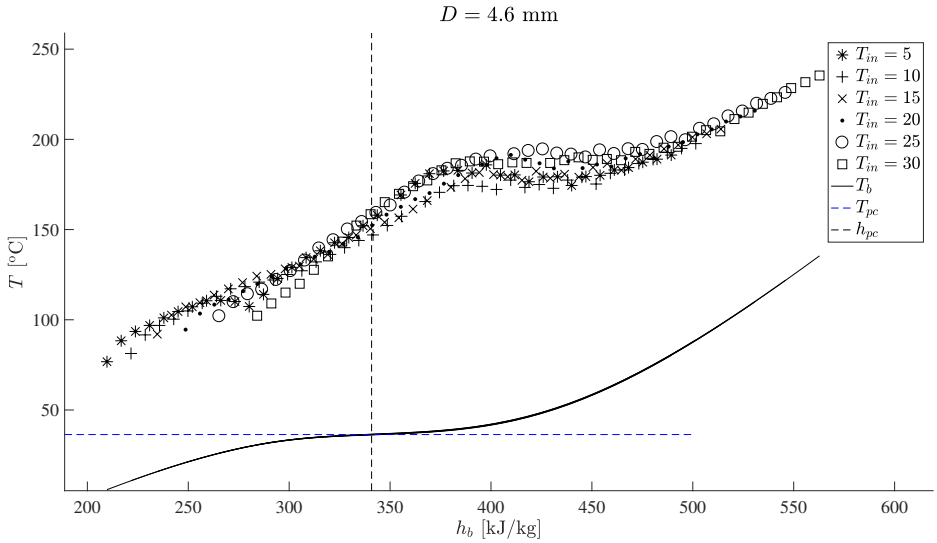


(a) All cases

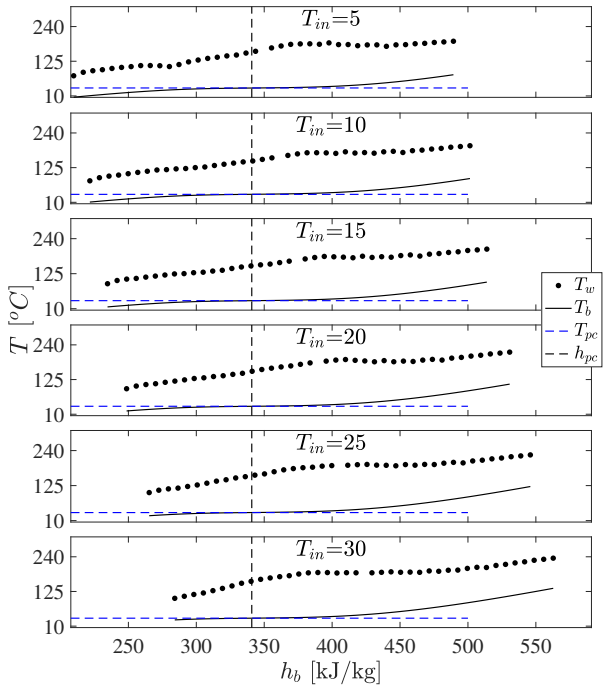


(b) Select cases

Figure A.34: Temperature profiles for $P/P_c = 1.13$, $G = 1500$ kg/m^{2}s, $q = 390$ kW/m^2; units of T_{in} are °C.

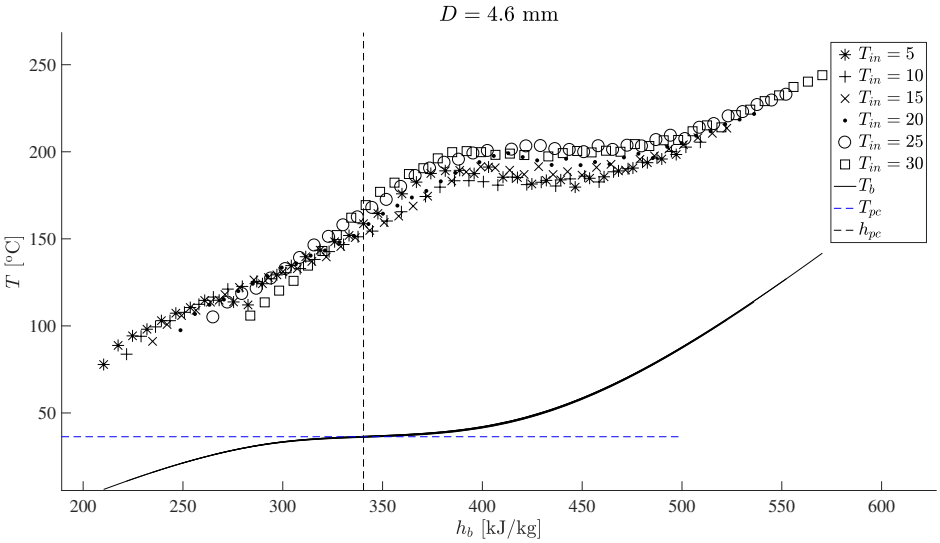


(a) All cases

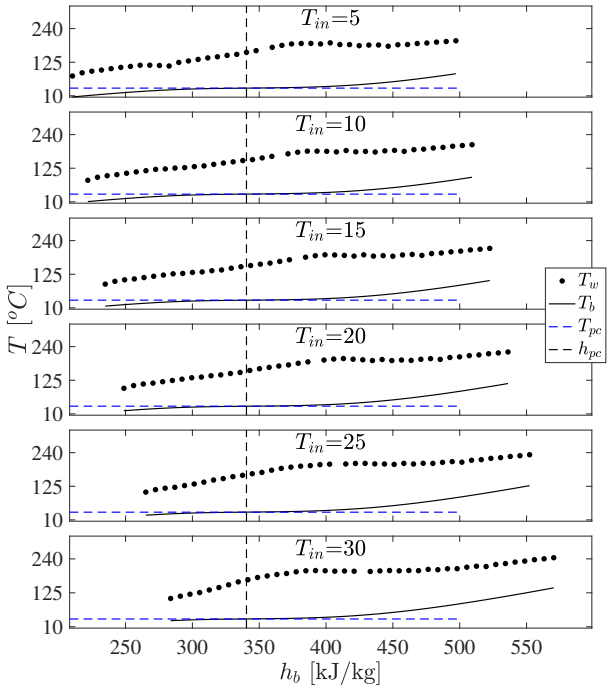


(b) Select cases

Figure A.35: Temperature profiles for $P/P_c = 1.13$, $G = 1500$ kg/m^{2}s, $q = 400$ kW/m^2; units of T_{in} are °C.

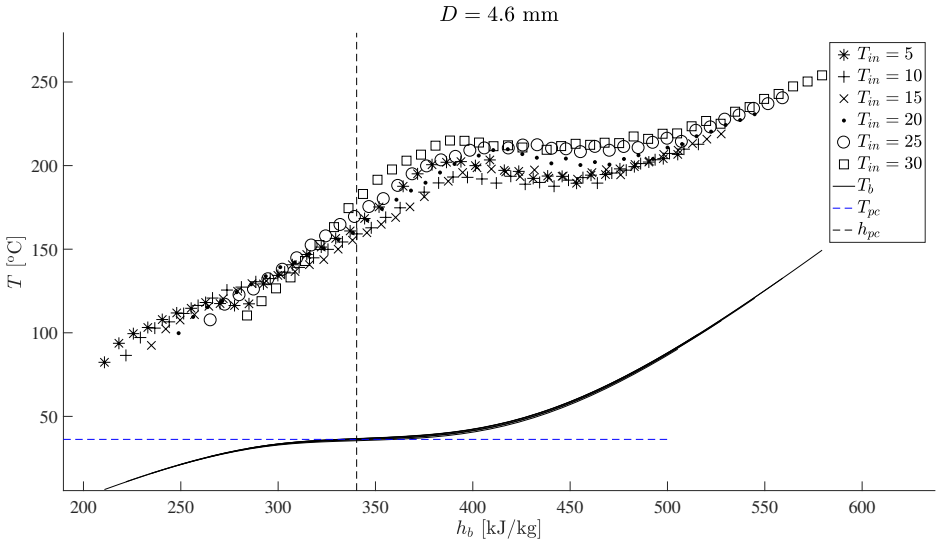


(a) All cases

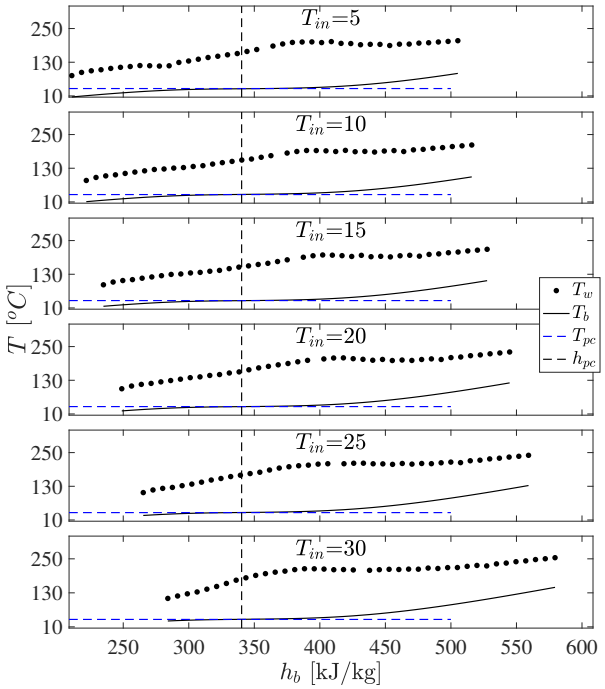


(b) Select cases

Figure A.36: Temperature profiles for $P/P_c = 1.13$, $G = 1500$ kg/m^{2}s, $q = 410$ kW/m^2; units of T_{in} are °C.

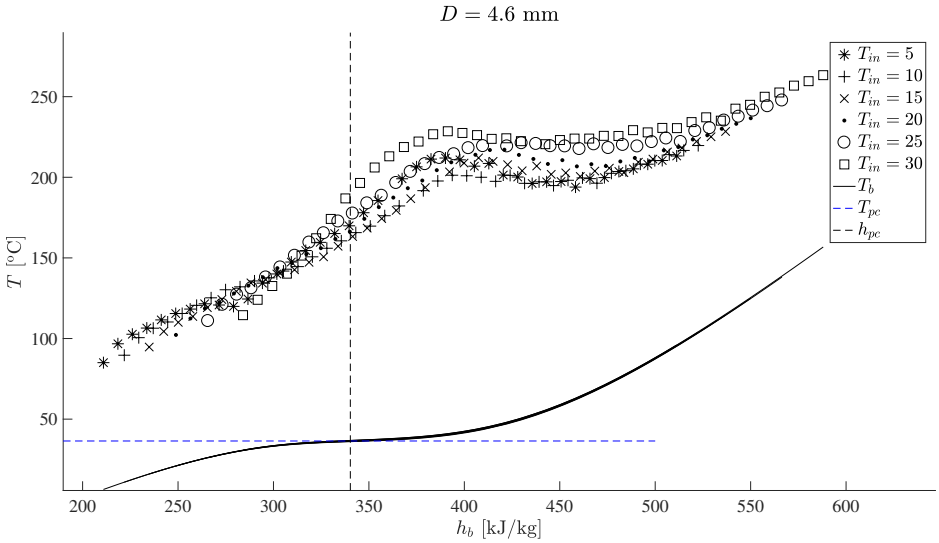


(a) All cases

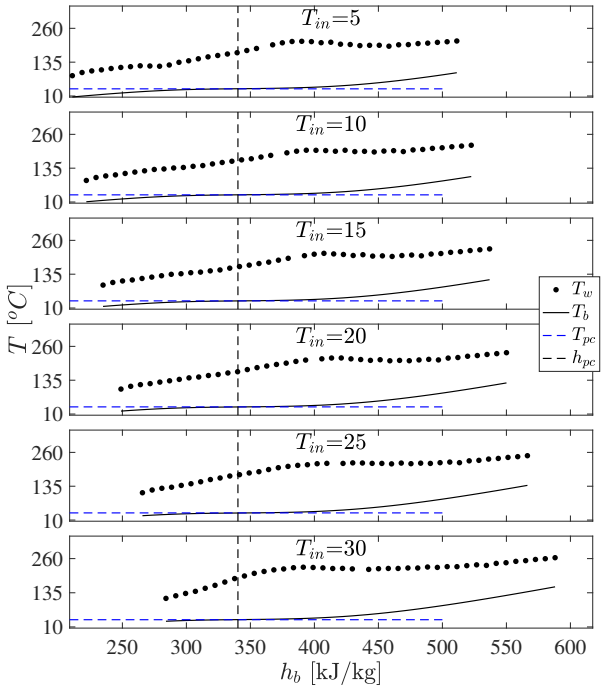


(b) Select cases

Figure A.37: Temperature profiles for $P/P_c = 1.13$, $G = 1500$ kg/m^{2}s, $q = 420$ kW/m^2; units of T_{in} are °C.

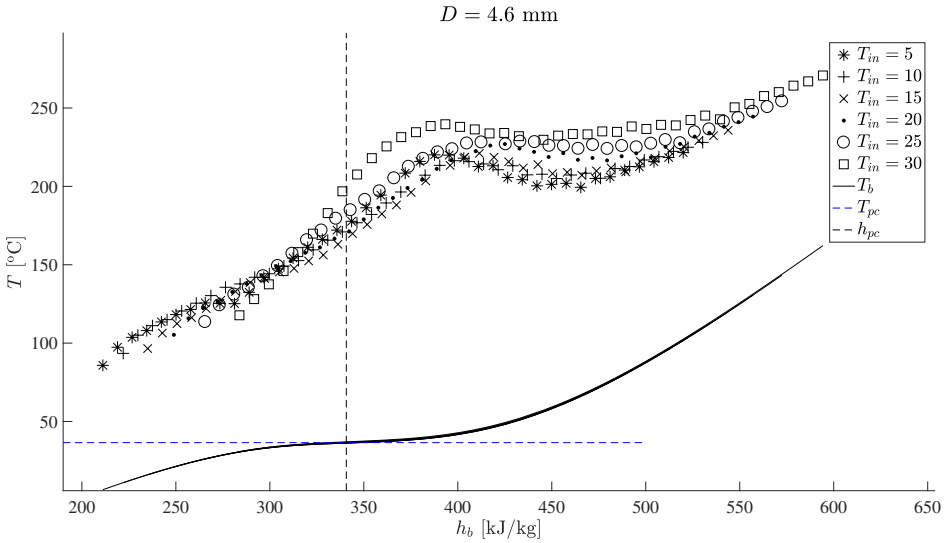


(a) All cases

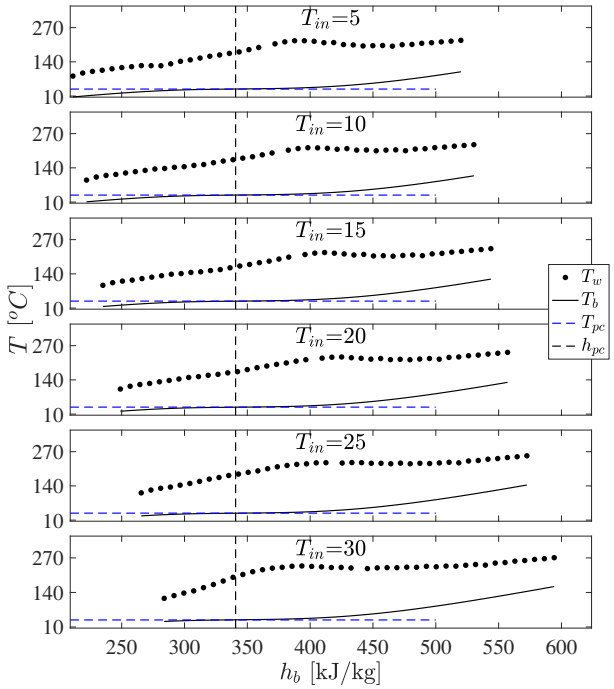


(b) Select cases

Figure A.38: Temperature profiles for $P/P_c = 1.13$, $G = 1500$ kg/m^{2}s, $q = 430$ kW/m^2; units of T_{in} are °C.

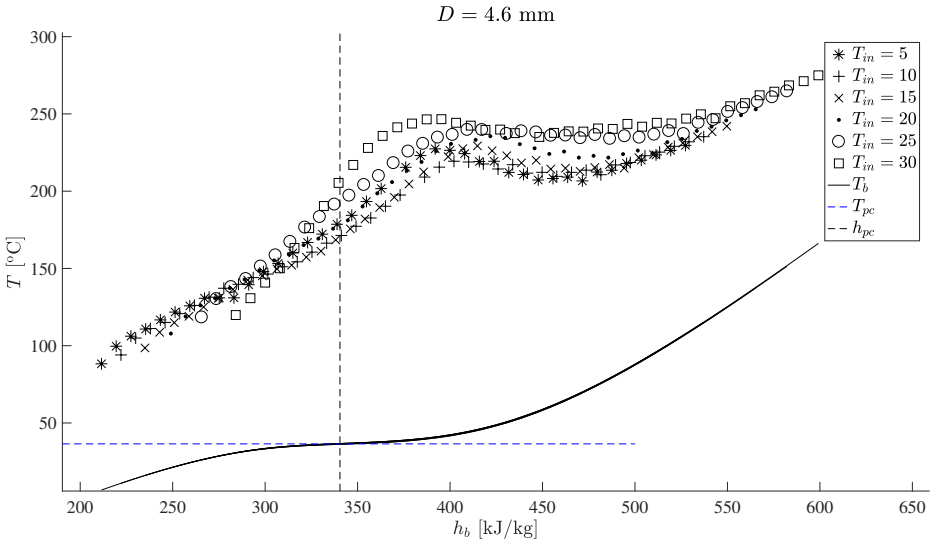


(a) All cases

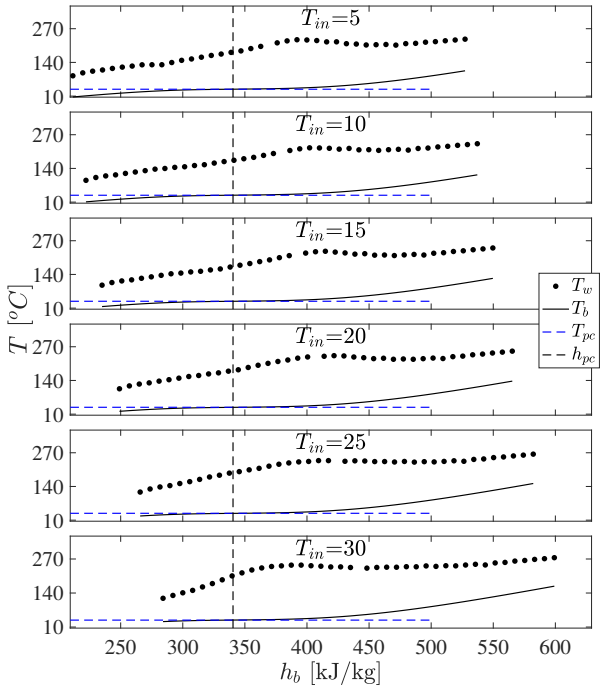


(b) Select cases

Figure A.39: Temperature profiles for $P/P_c = 1.13$, $G = 1500$ kg/m^{2}s, $q = 440$ kW/m^2; units of T_{in} are °C.



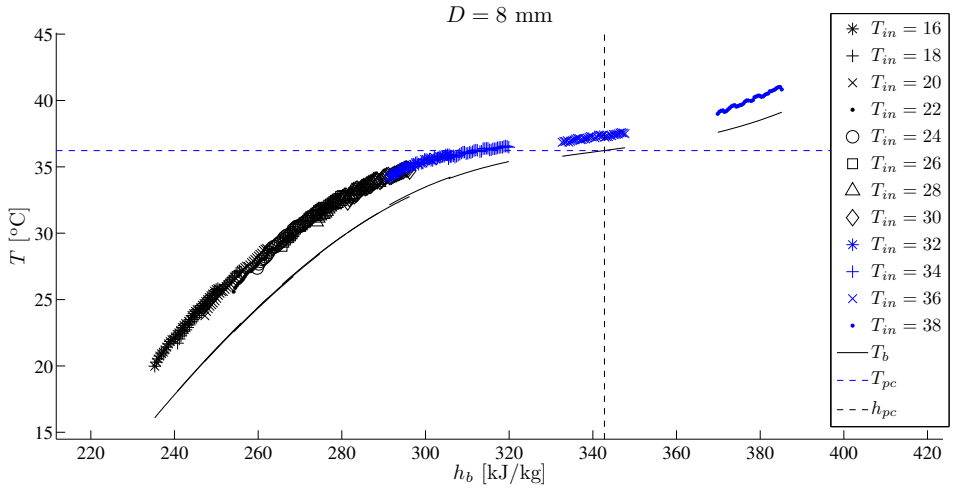
(a) All cases



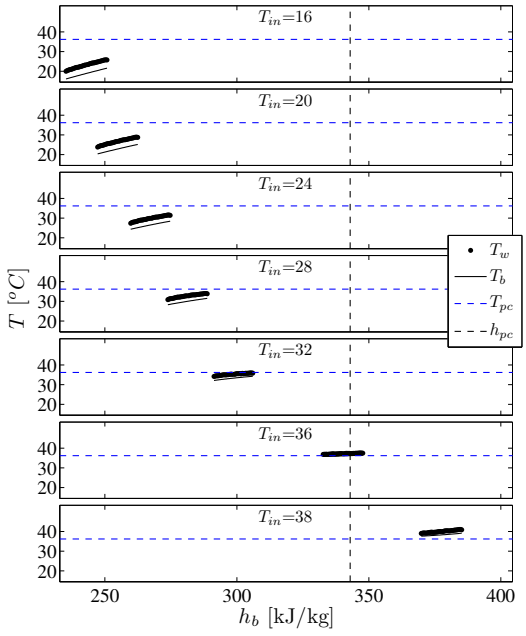
(b) Select cases

Figure A.40: Temperature profiles for $P/P_c = 1.13$, $G = 1500$ kg/m^{2}s, $q = 450$ kW/m^2; units of T_{in} are °C.

A.2 8 mm test section

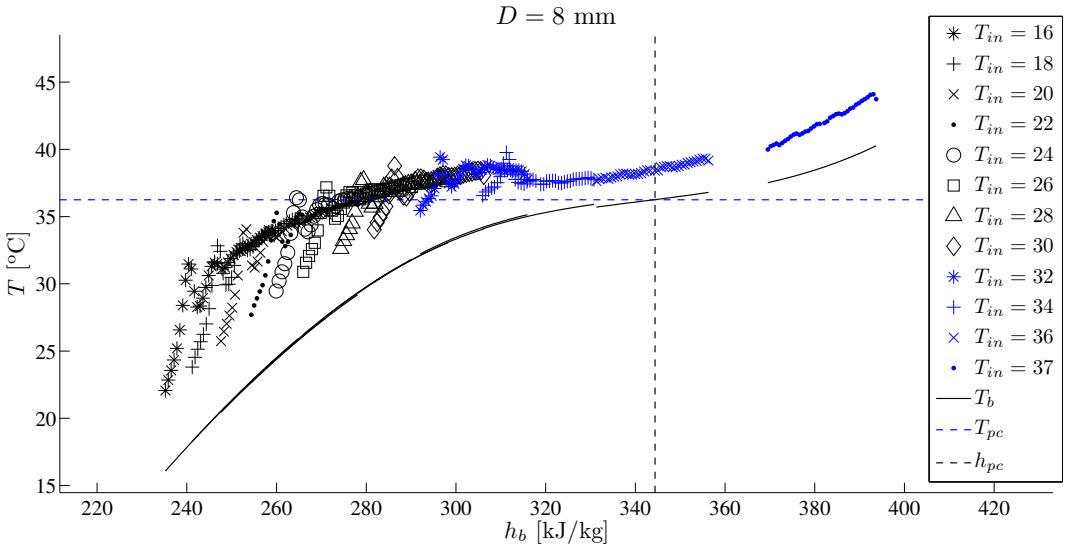


(a) All cases

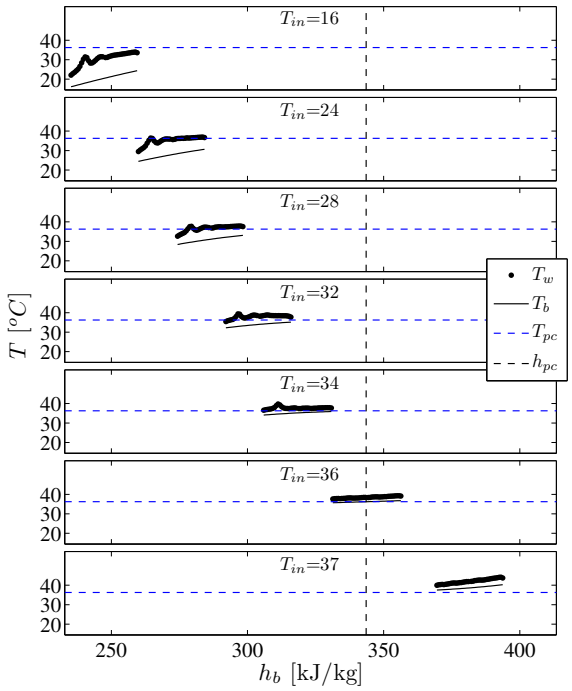


(b) Select cases

Figure A.41: Temperature profiles for $P/P_c = 1.13$, $G = 200$ kg/m^{2}s, $q = 3$ kW/m^2; units of T_{in} are °C.

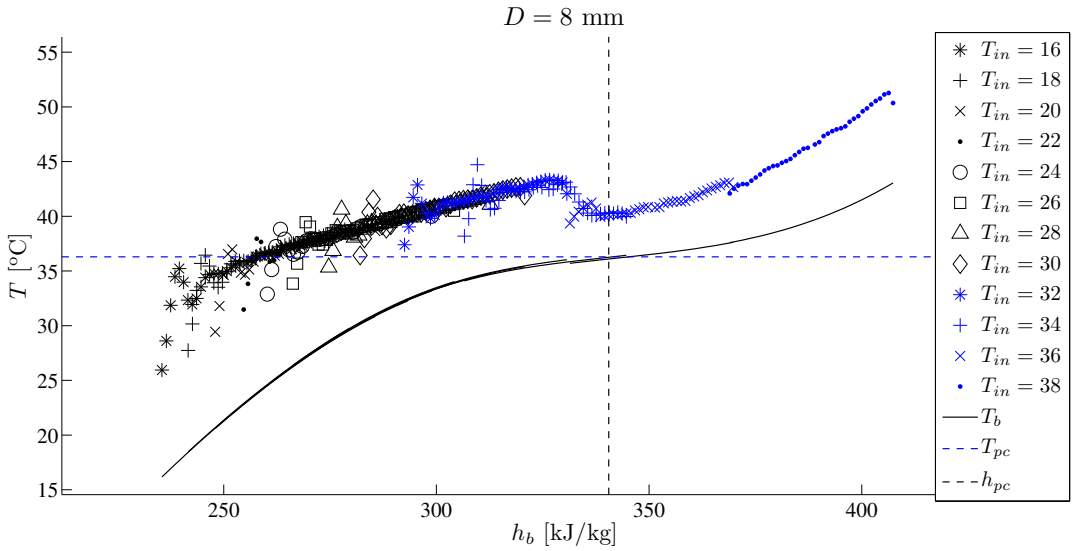


(a) All cases

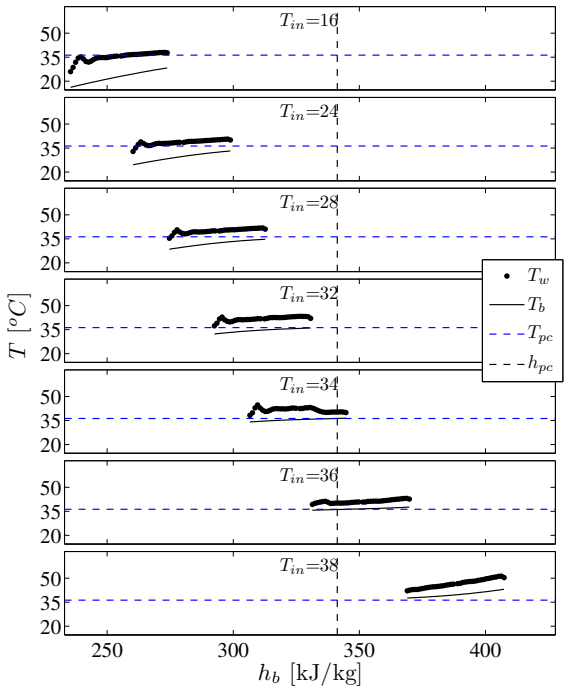


(b) Select cases

Figure A.42: Temperature profiles for $P/P_c = 1.13$, $G = 200$ kg/m^{2}s, $q = 5$ kW/m^2; units of T_{in} are °C.

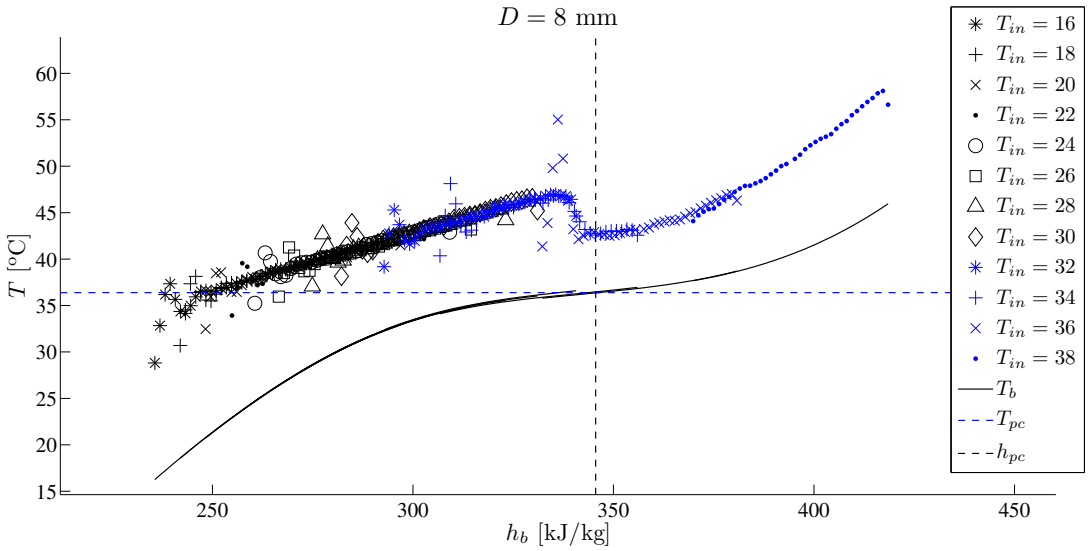


(a) All cases

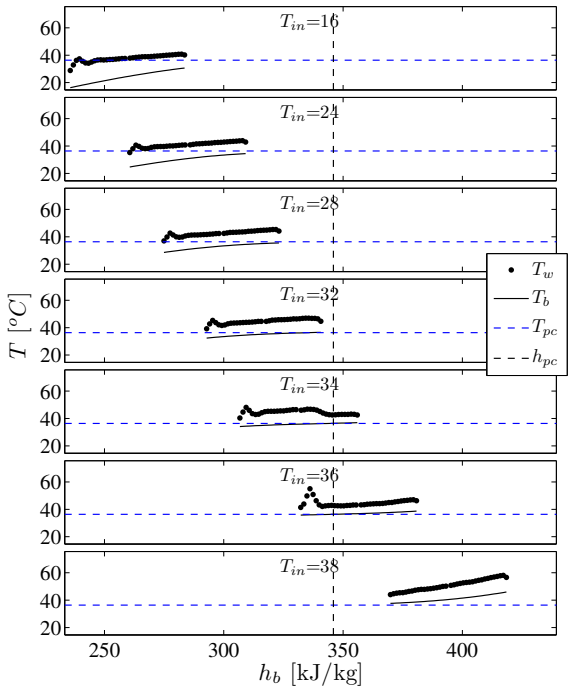


(b) Select cases

Figure A.43: Temperature profiles for $P/P_c = 1.13$, $G = 800$ kg/m^{2}s, $q = 8$ kW/m^2; units of T_{in} are °C.

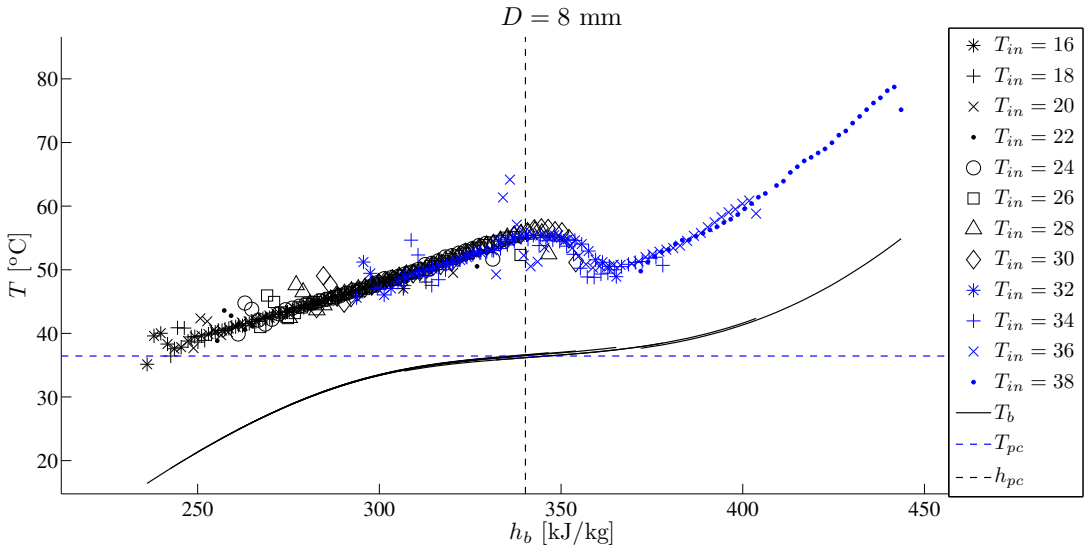


(a) All cases

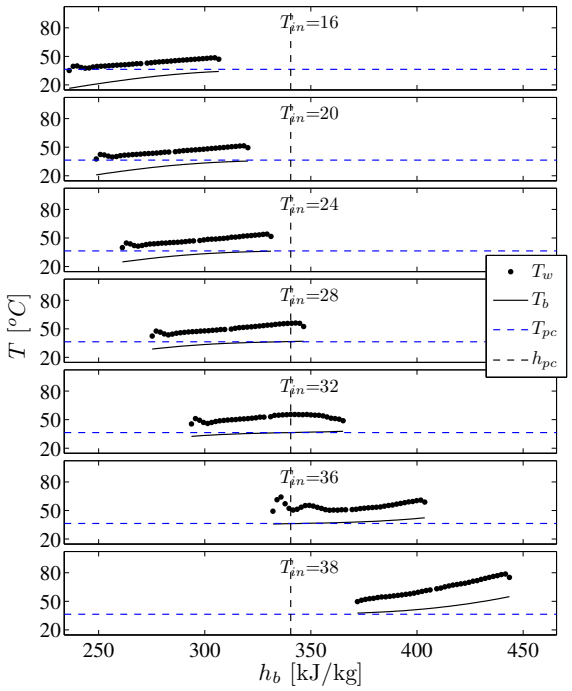


(b) Select cases

Figure A.44: Temperature profiles for $P/P_c = 1.13$, $G = 200$ kg/m^{2}s, $q = 10$ kW/m^2; units of T_{in} are °C.



(a) All cases



(b) Select cases

Figure A.45: Temperature profiles for $P/P_c = 1.13$, $G = 200$ kg/m^{2}s, $q = 15$ kW/m^2; units of T_{in} are °C.

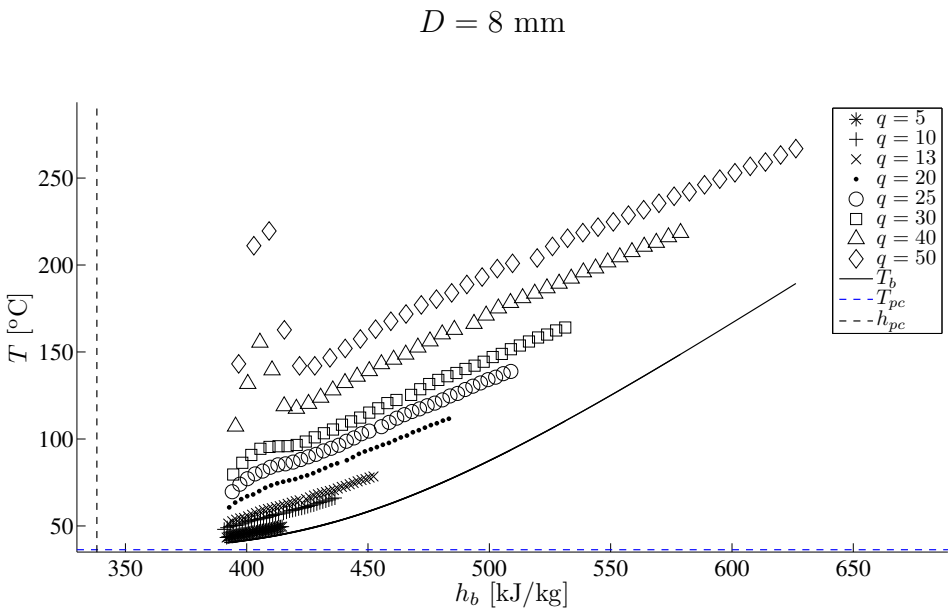
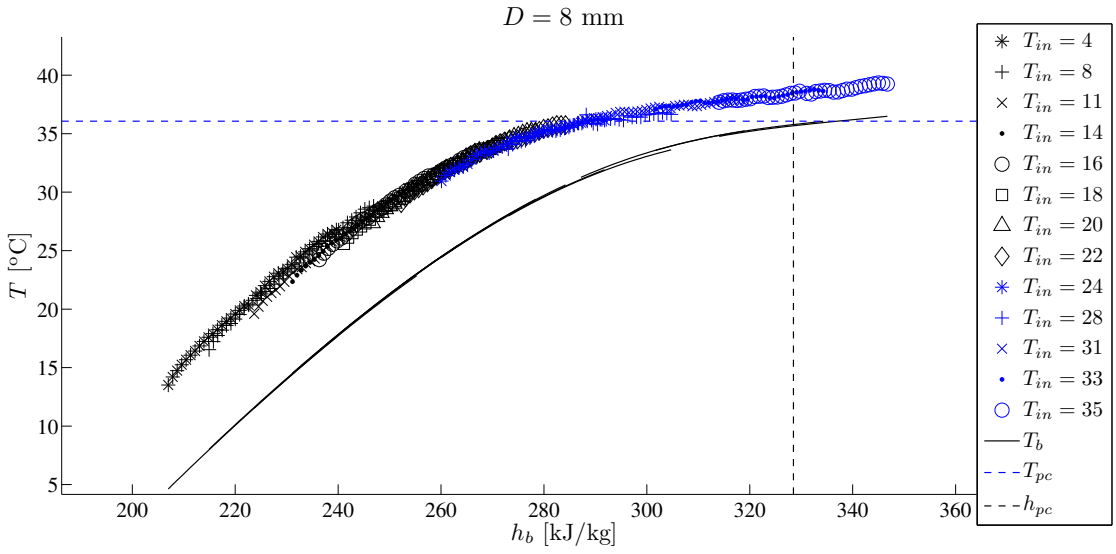
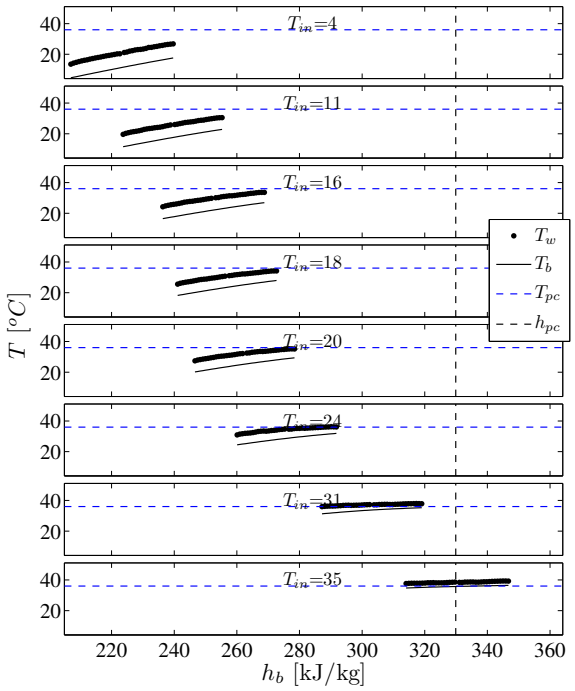


Figure A.46: Temperature profiles for $P/P_c = 1.13$, $G = 200$ kg/m^{2}s, $T_{in} = 40$ °C; units of q are kW/m^2.

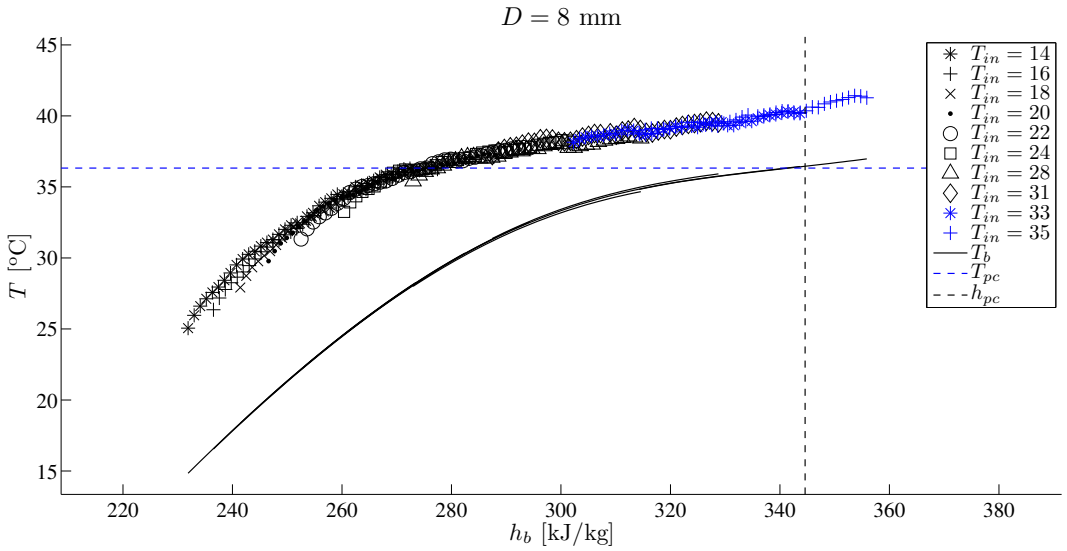


(a) All cases

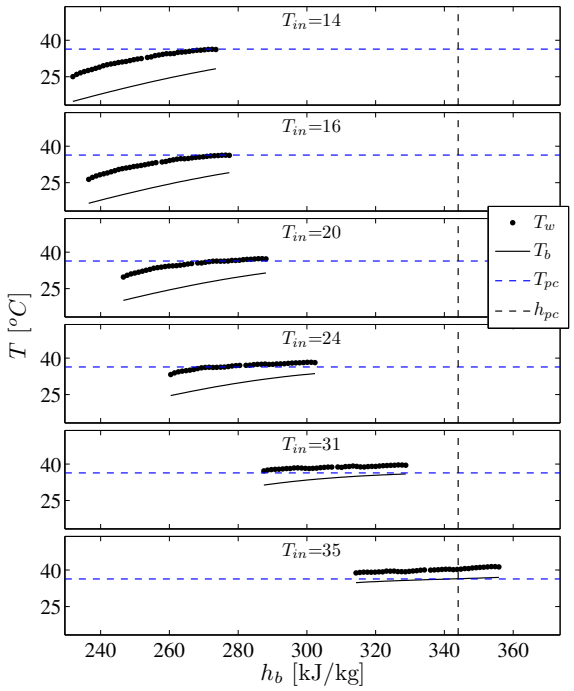


(b) Select cases

Figure A.47: Temperature profiles for $P/P_c = 1.13$, $G = 300$ kg/m^{2}s, $q = 10$ kW/m^2; units of T_{in} are °C.

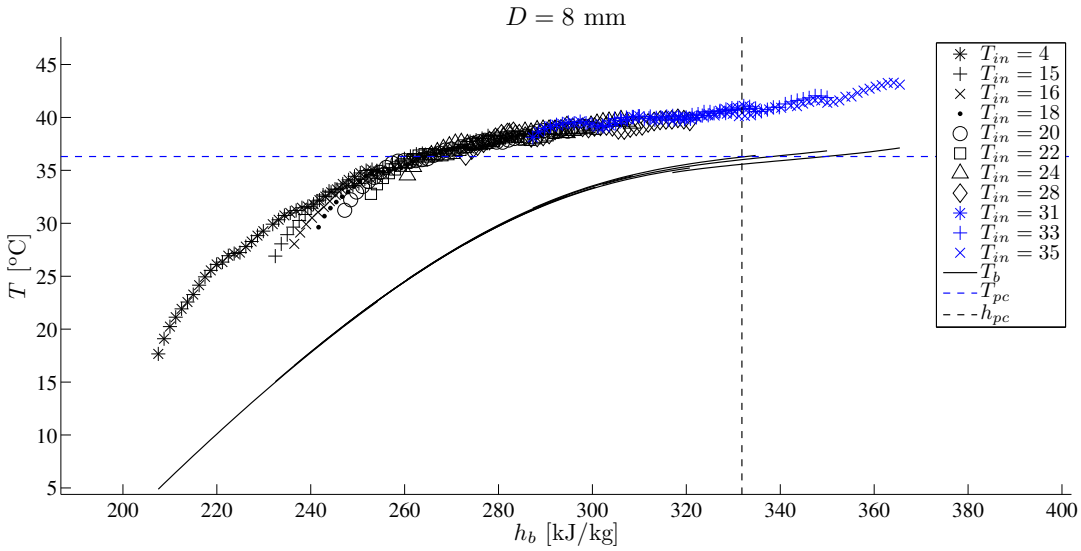


(a) All cases

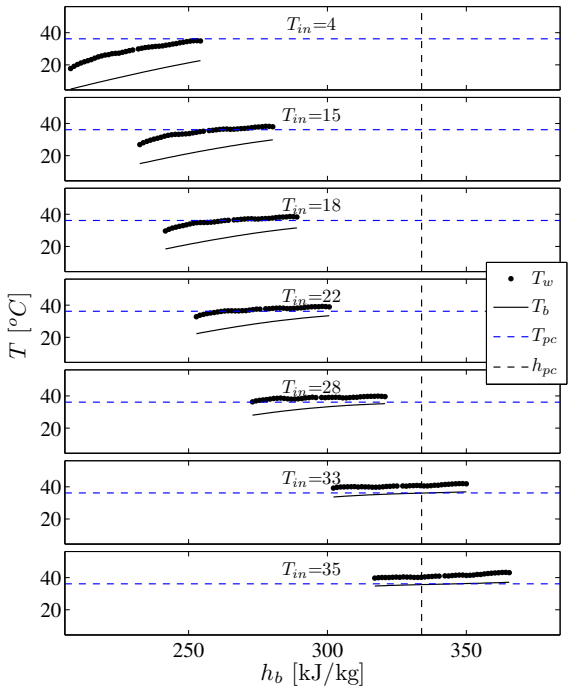


(b) Select cases

Figure A.48: Temperature profiles for $P/P_c = 1.13$, $G = 300$ kg/m^{2}s, $q = 13$ kW/m^2; units of T_{in} are °C.

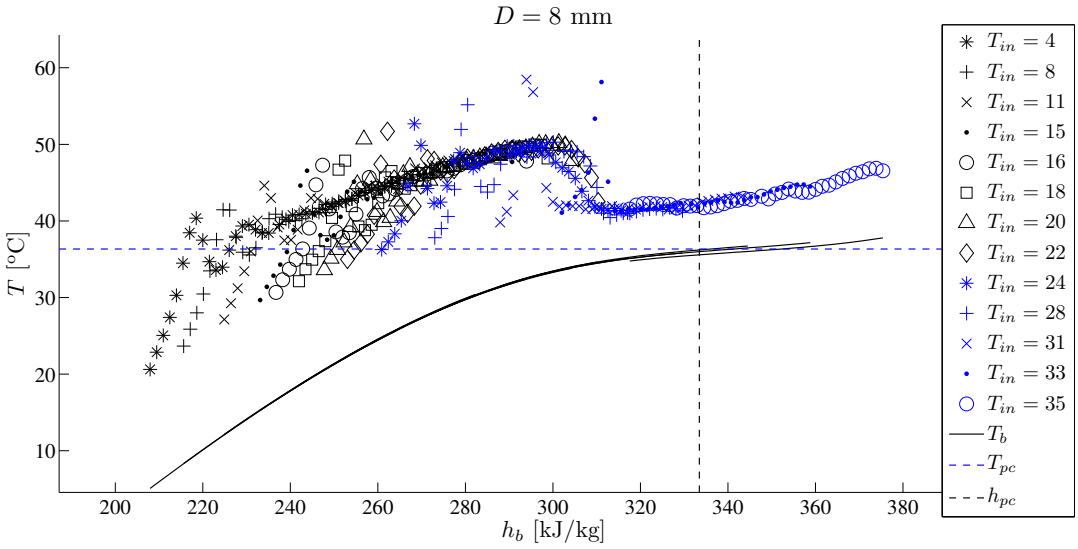


(a) All cases

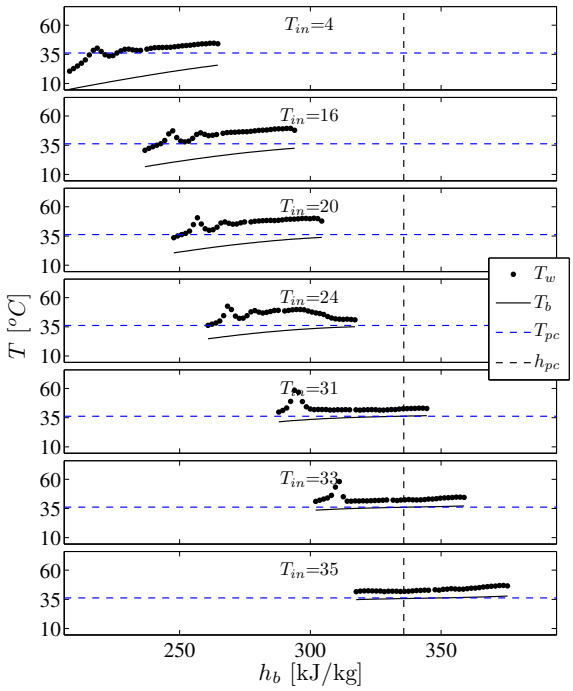


(b) Select cases

Figure A.49: Temperature profiles for $P/P_c = 1.13$, $G = 300$ kg/m^{2}s, $q = 15$ kW/m^2; units of T_{in} are °C.

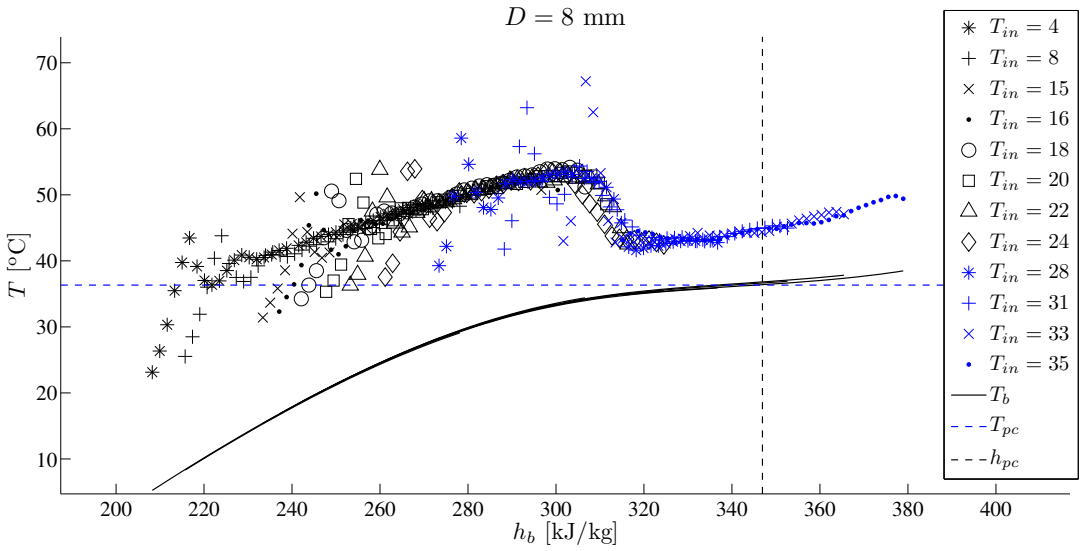


(a) All cases

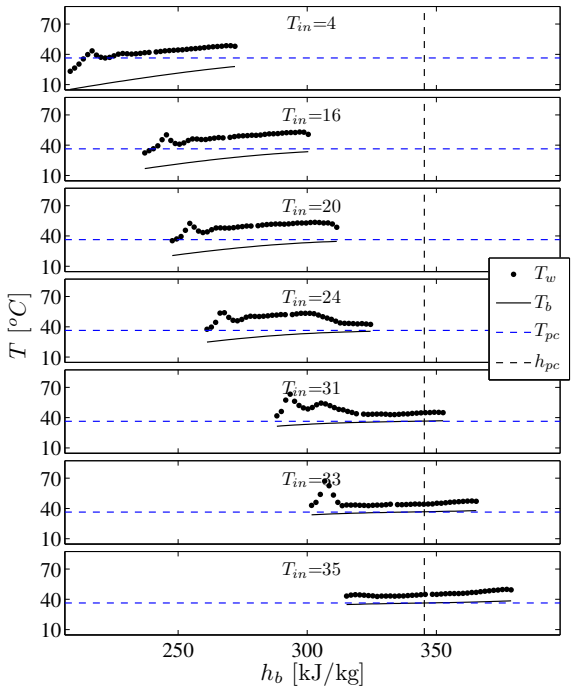


(b) Select cases

Figure A.50: Temperature profiles for $P/P_c = 1.13$, $G = 300$ kg/m^{2}s, $q = 18$ kW/m^2; units of T_{in} are °C.



(a) All cases



(b) Select cases

Figure A.51: Temperature profiles for $P/P_c = 1.13$, $G = 300$ kg/m^{2}s, $q = 20$ kW/m^2; units of T_{in} are °C.

$D = 8$ mm

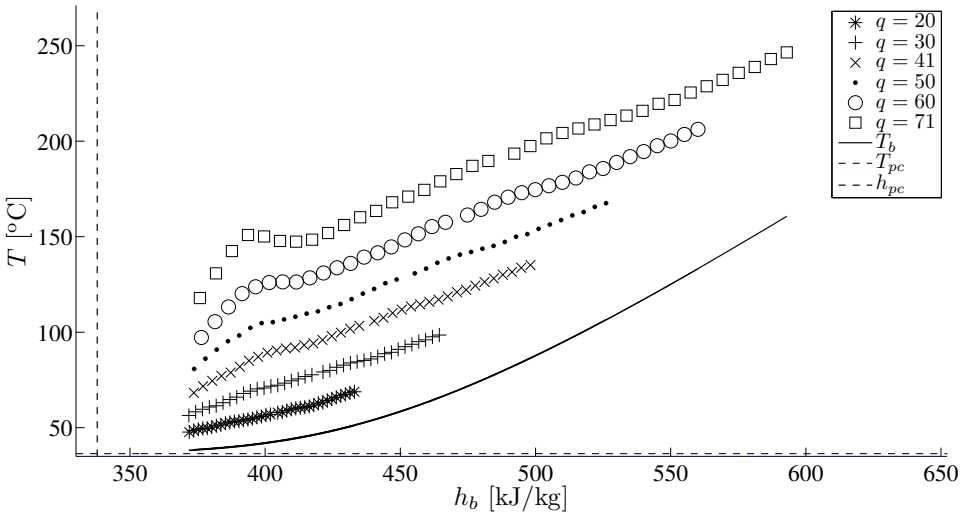
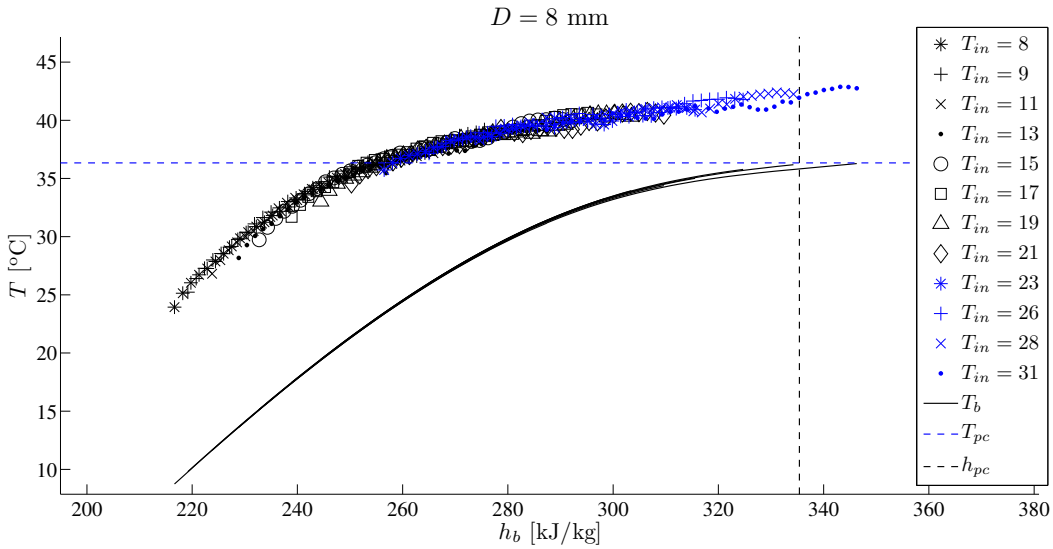
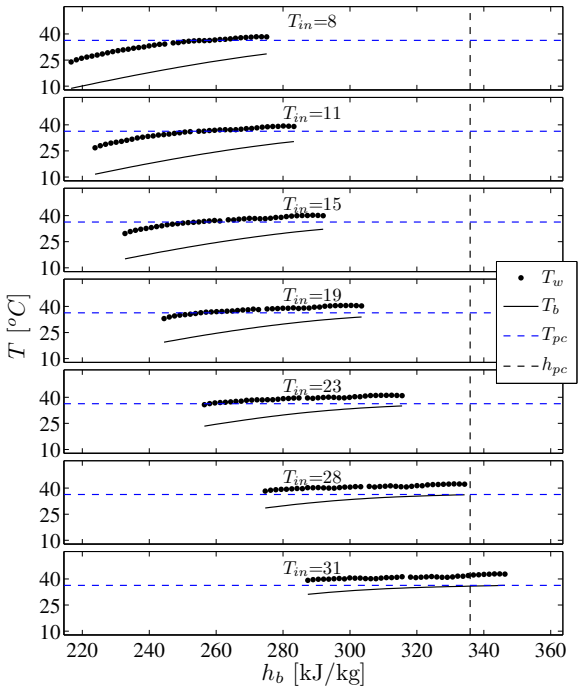


Figure A.52: Temperature profiles for $P/P_c = 1.13$, $G = 300$ kg/m^{2}s, $T_{in} = 38$ °C; units of q are kW/m^2.

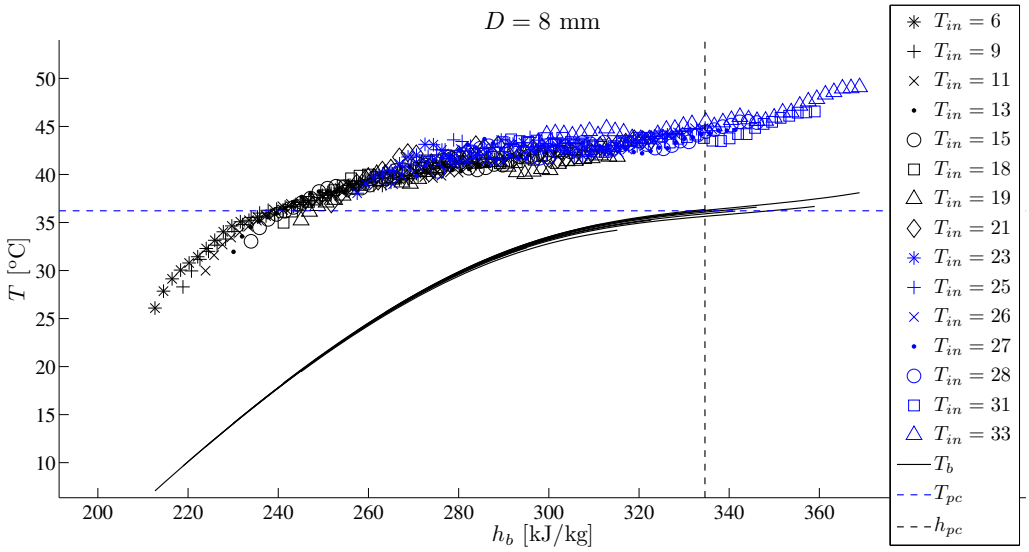


(a) All cases

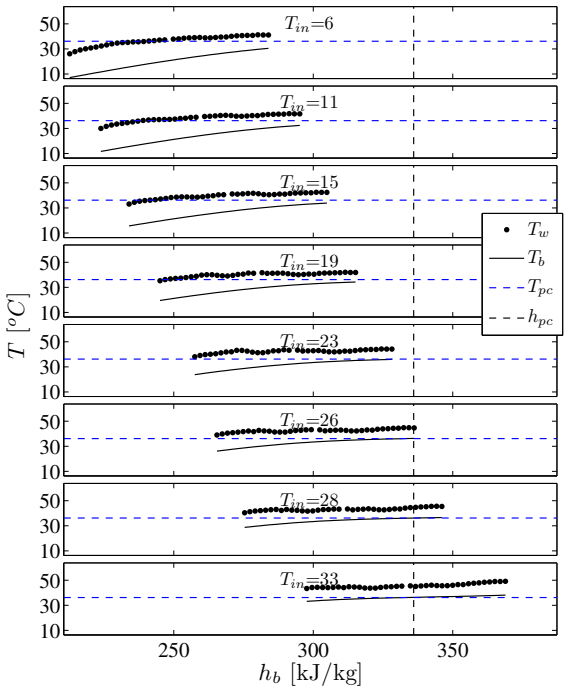


(b) Select cases

Figure A.53: Temperature profiles for $P/P_c = 1.13$, $G = 400$ kg/m^{2}s, $q = 25$ kW/m^2; units of T_{in} are °C.

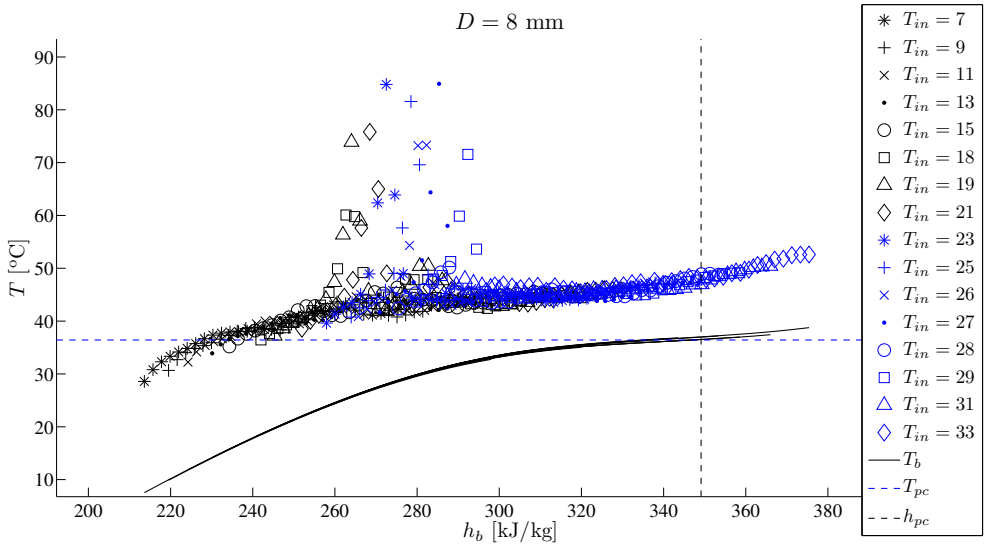


(a) All cases

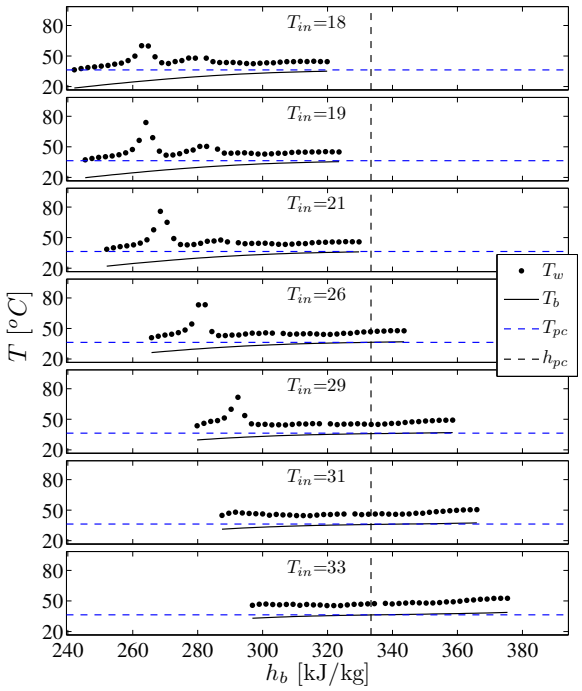


(b) Select cases

Figure A.54: Temperature profiles for $P/P_c = 1.13$, $G = 400$ kg/m^{2}s, $q = 30$ kW/m^2; units of T_{in} are °C.

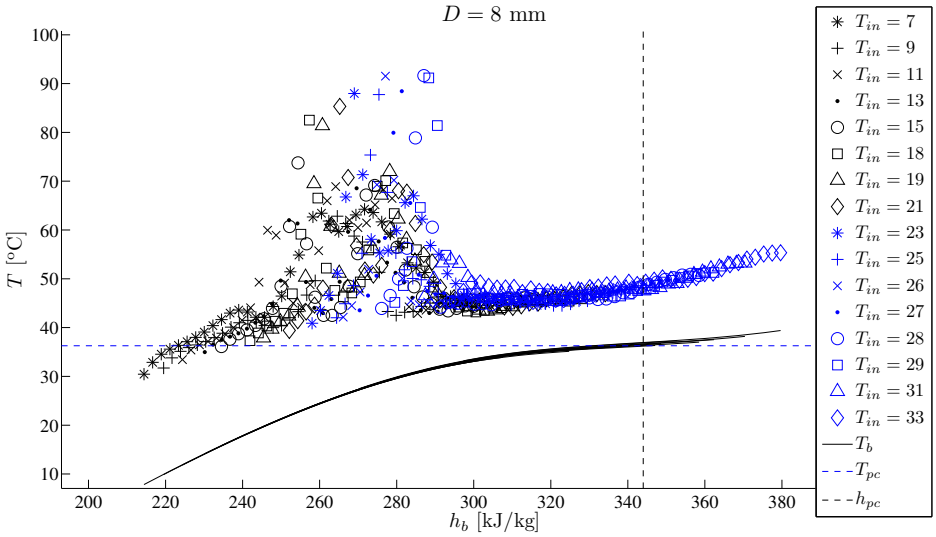


(a) All cases

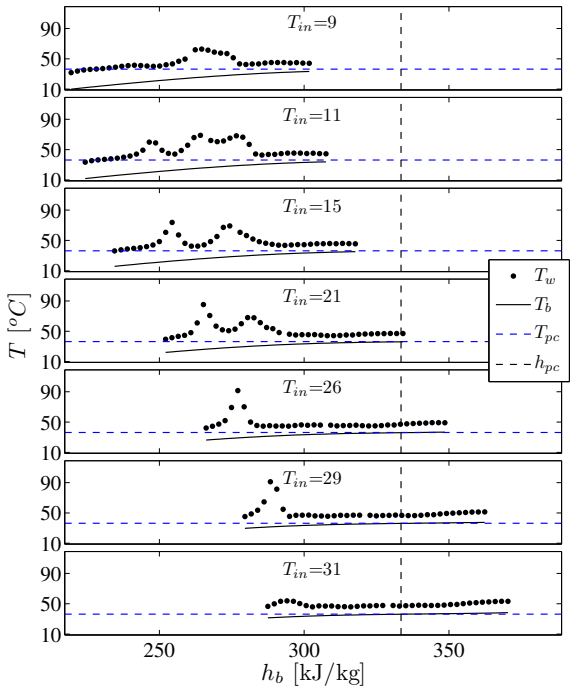


(b) Select cases

Figure A.55: Temperature profiles for $P/P_c = 1.13$, $G = 400$ kg/m^{2}s, $q = 33$ kW/m^2; units of T_{in} are °C.

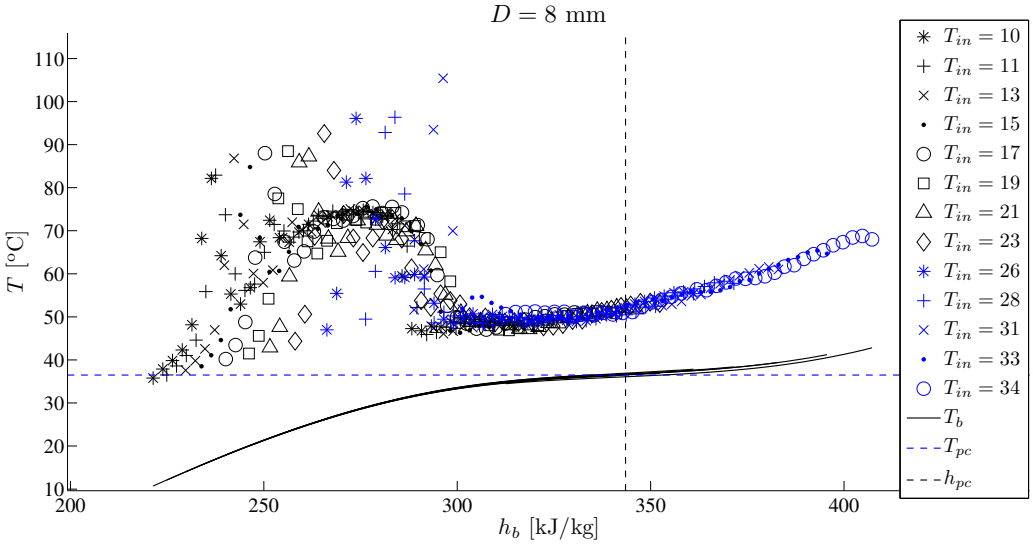


(a) All cases

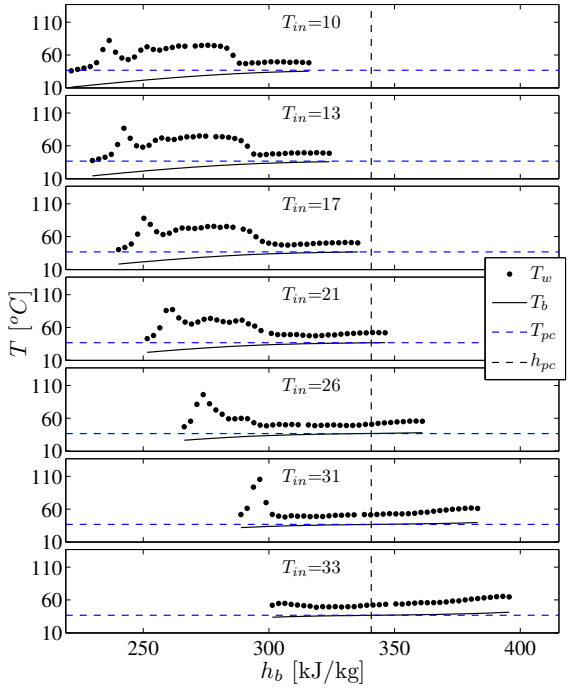


(b) Select cases

Figure A.56: Temperature profiles for $P/P_c = 1.13$, $G = 400$ kg/m^{2}s, $q = 35$ kW/m^2; units of T_{in} are °C.

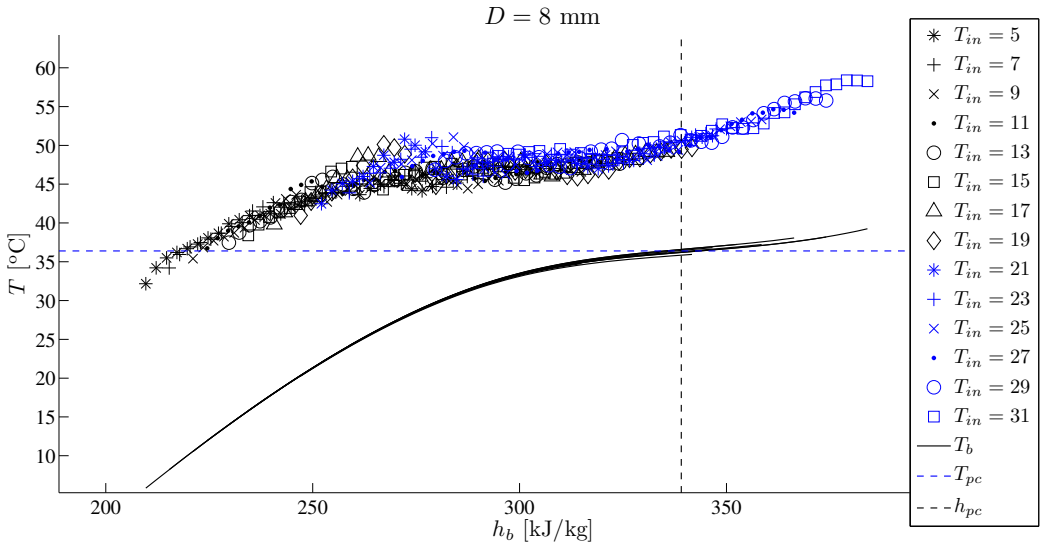


(a) All cases

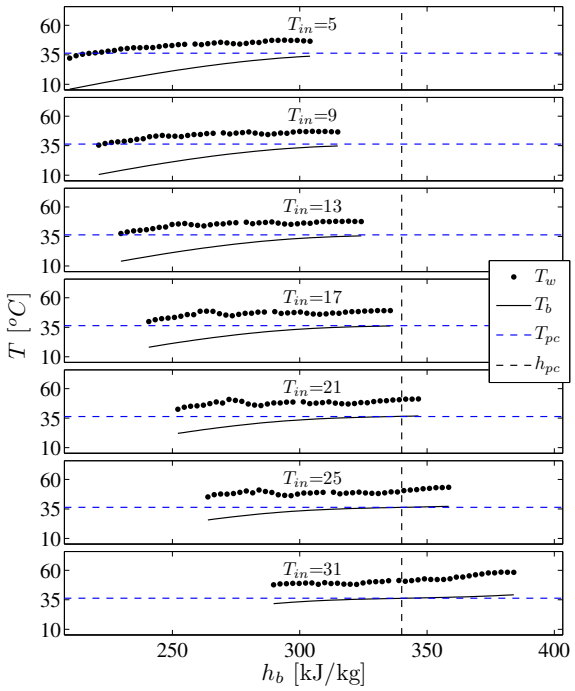


(b) Select cases

Figure A.57: Temperature profiles for $P/P_c = 1.13$, $G = 400$ kg/m^{2}s, $q = 40$ kW/m^2; units of T_{in} are °C.

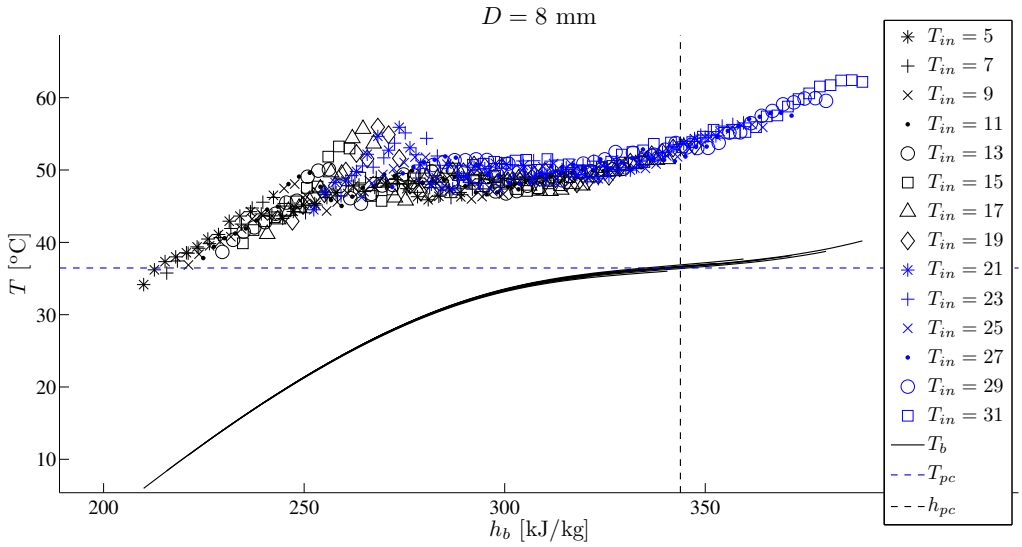


(a) All cases

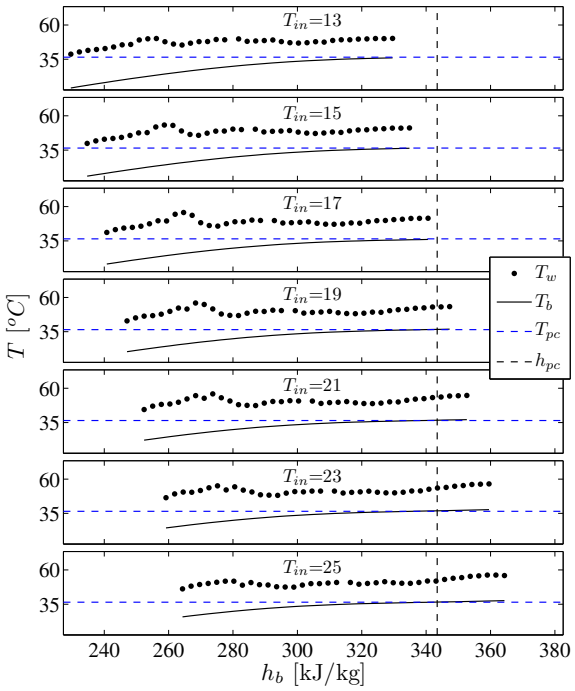


(b) Select cases

Figure A.58: Temperature profiles for $P/P_c = 1.13$, $G = 500$ kg/m^{2}s, $q = 50$ kW/m^2; units of T_{in} are °C.

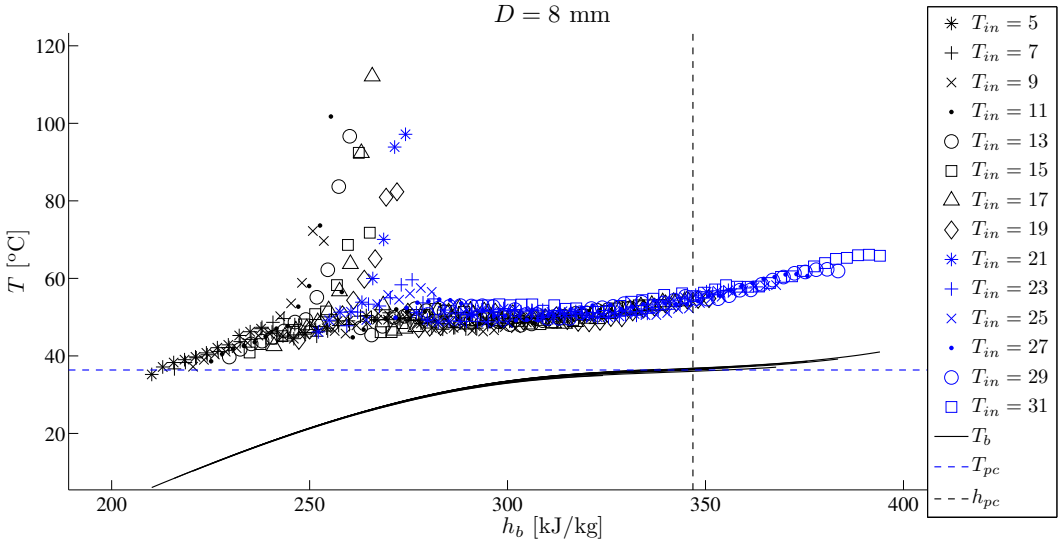


(a) All cases

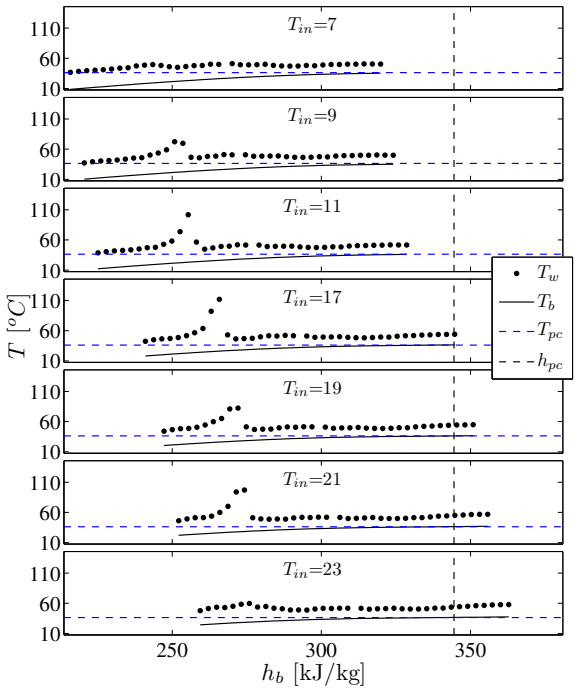


(b) Select cases

Figure A.59: Temperature profiles for $P/P_c = 1.13$, $G = 500$ kg/m^{2}s, $q = 53$ kW/m^2; units of T_{in} are °C.

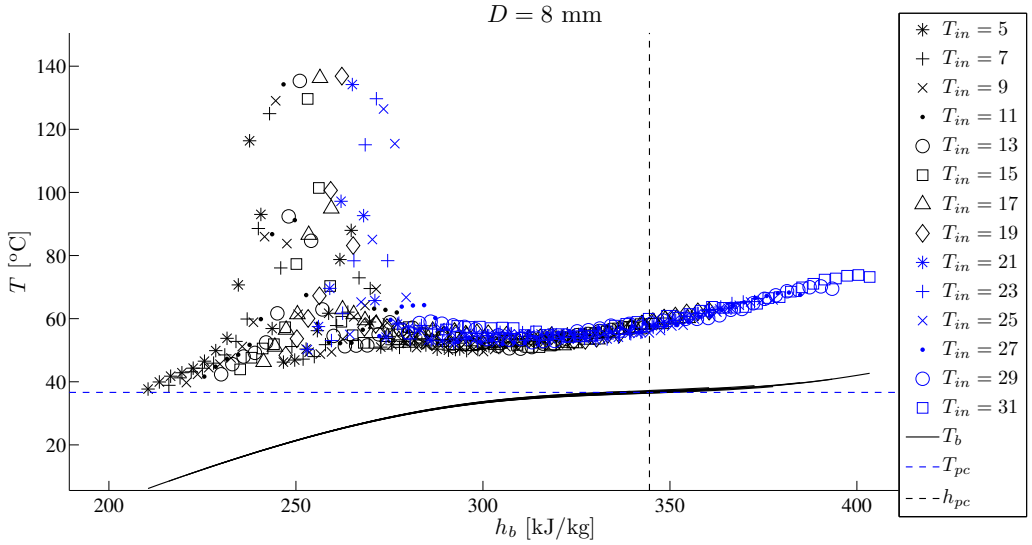


(a) All cases

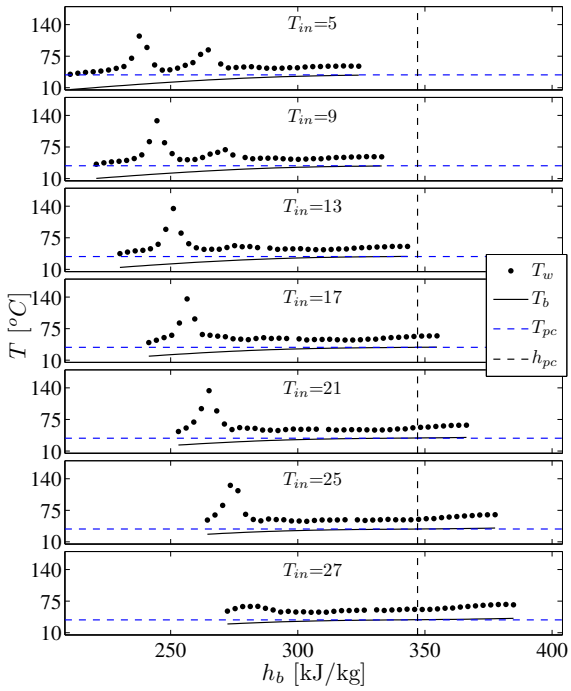


(b) Select cases

Figure A.60: Temperature profiles for $P/P_c = 1.13$, $G = 500$ kg/m^{2}s, $q = 55$ kW/m^2; units of T_{in} are °C.

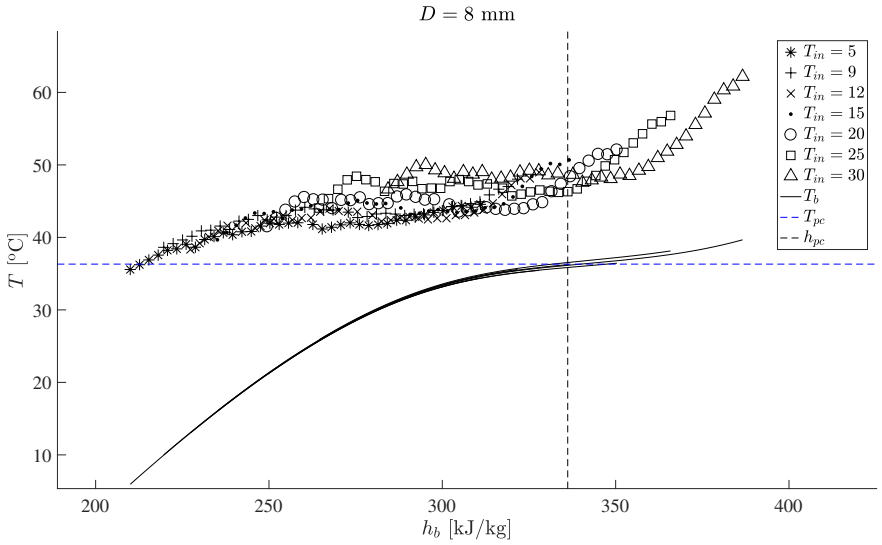


(a) All cases

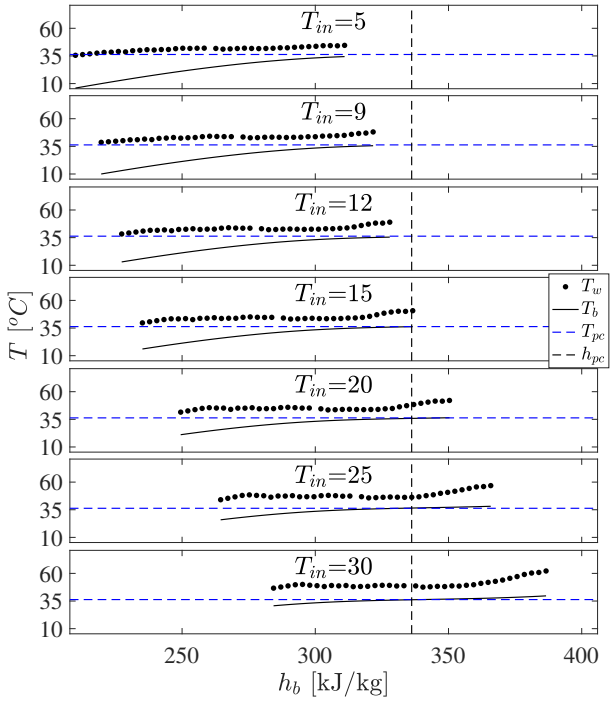


(b) Select cases

Figure A.61: Temperature profiles for $P/P_c = 1.13$, $G = 500$ kg/m^{2}s, $q = 60$ kW/m^2; units of T_{in} are °C.

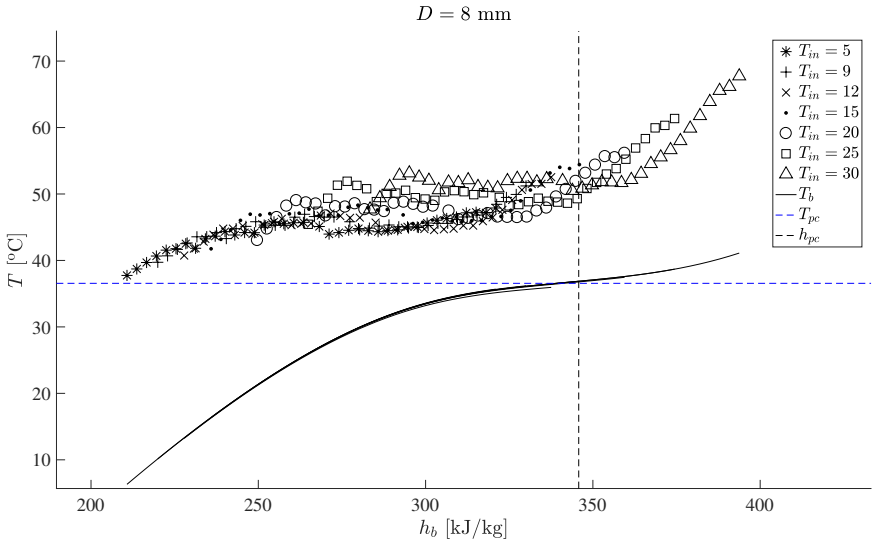


(a) All cases

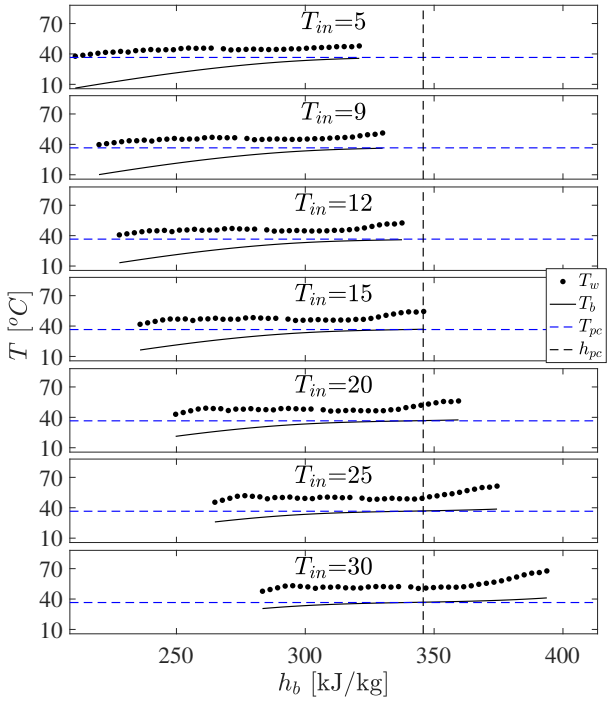


(b) Select cases

Figure A.62: Temperature profiles for $P/P_c = 1.13$, $G = 600$ kg/m^{2}s, $q = 65$ kW/m^2; units of T_{in} are °C.

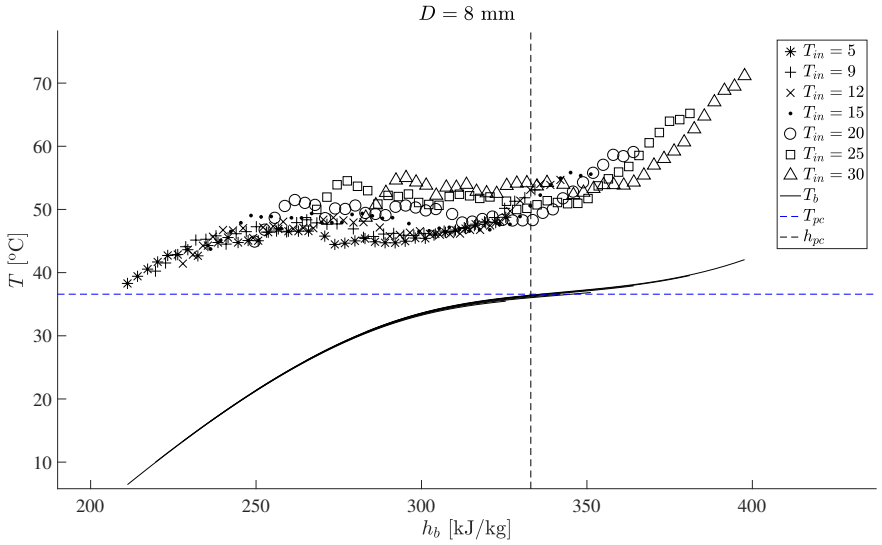


(a) All cases

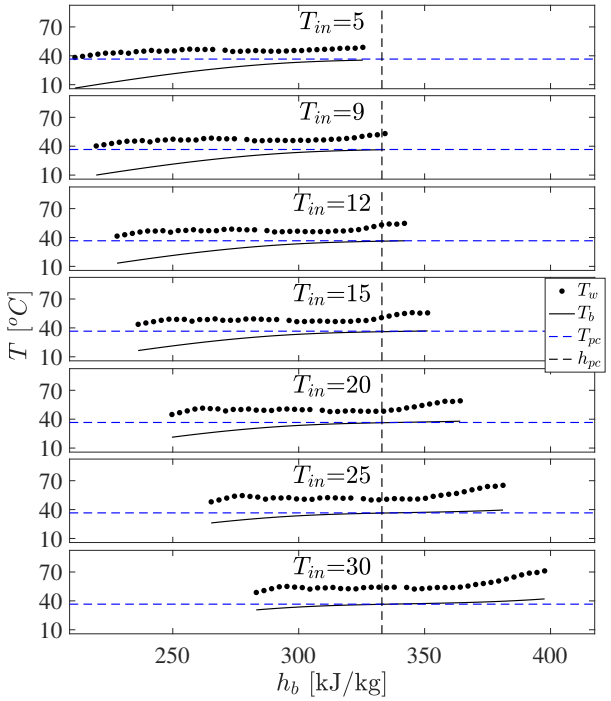


(b) Select cases

Figure A.63: Temperature profiles for $P/P_c = 1.13$, $G = 600$ kg/m^{2}s, $q = 70$ kW/m^2; units of T_{in} are °C.

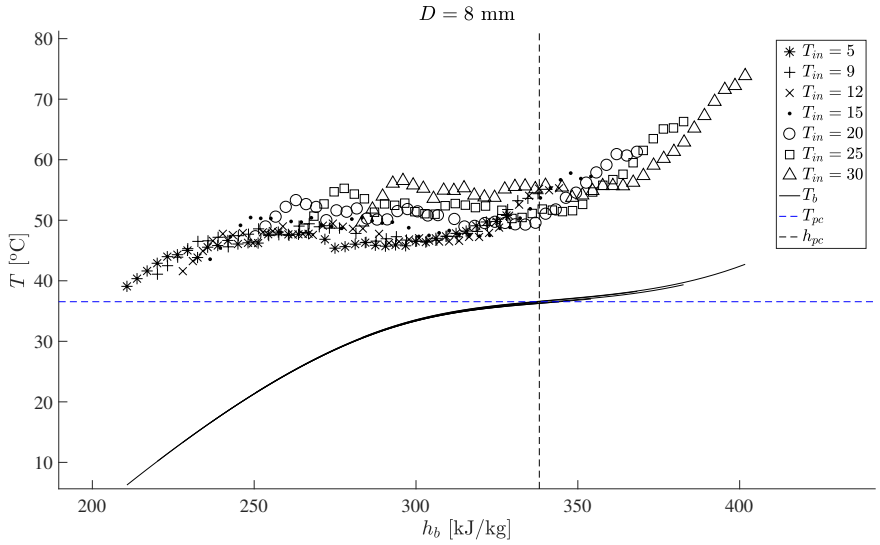


(a) All cases

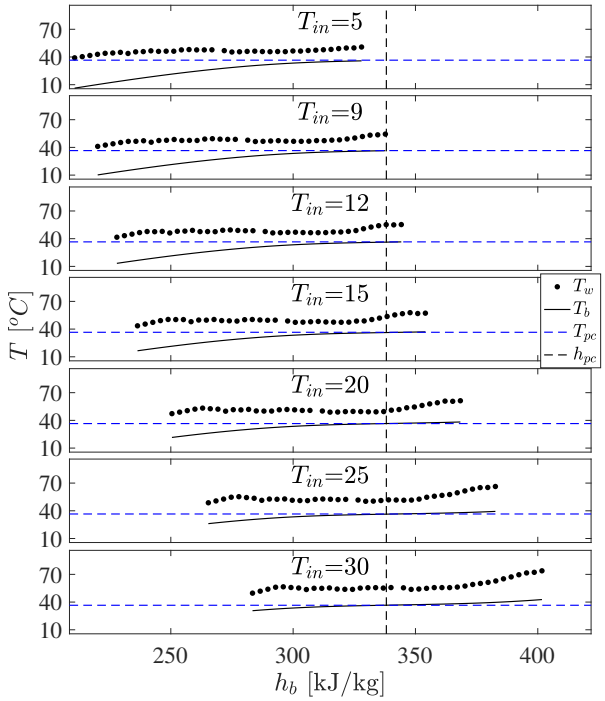


(b) Select cases

Figure A.64: Temperature profiles for $P/P_c = 1.13$, $G = 600$ kg/m^{2}s, $q = 73$ kW/m^2; units of T_{in} are °C.

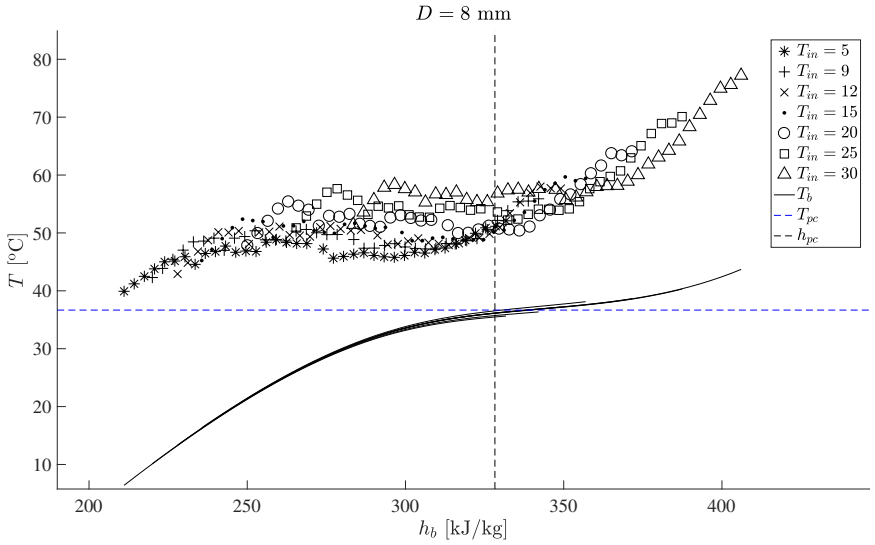


(a) All cases

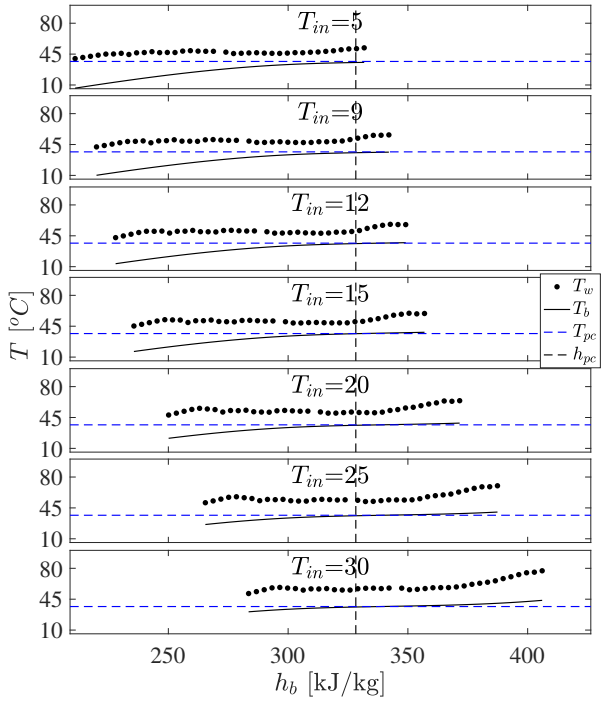


(b) Select cases

Figure A.65: Temperature profiles for $P/P_c = 1.13$, $G = 600$ kg/m^{2}s, $q = 75$ kW/m^2; units of T_{in} are °C.

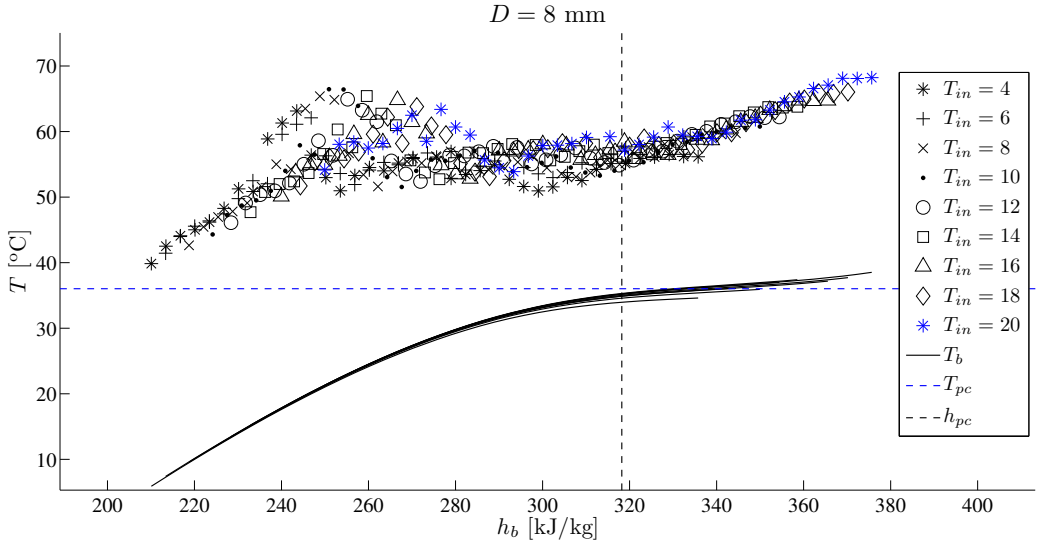


(a) All cases

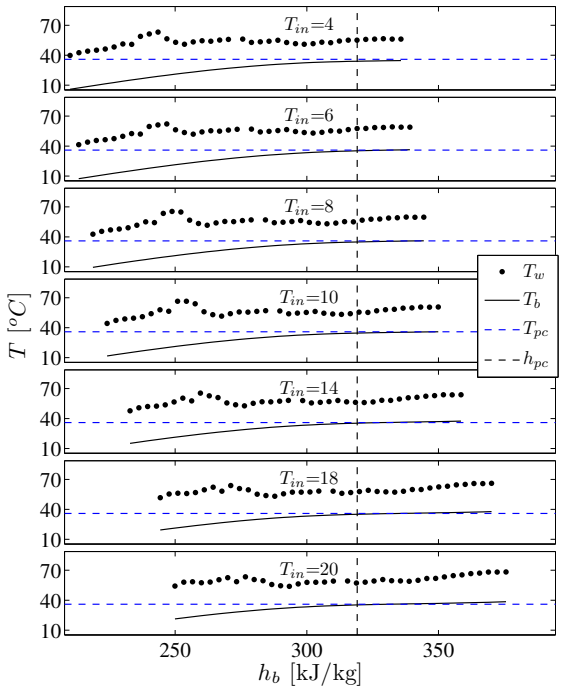


(b) Select cases

Figure A.66: Temperature profiles for $P/P_c = 1.13$, $G = 600$ kg/m^{2}s, $q = 78$ kW/m^2; units of T_{in} are °C.

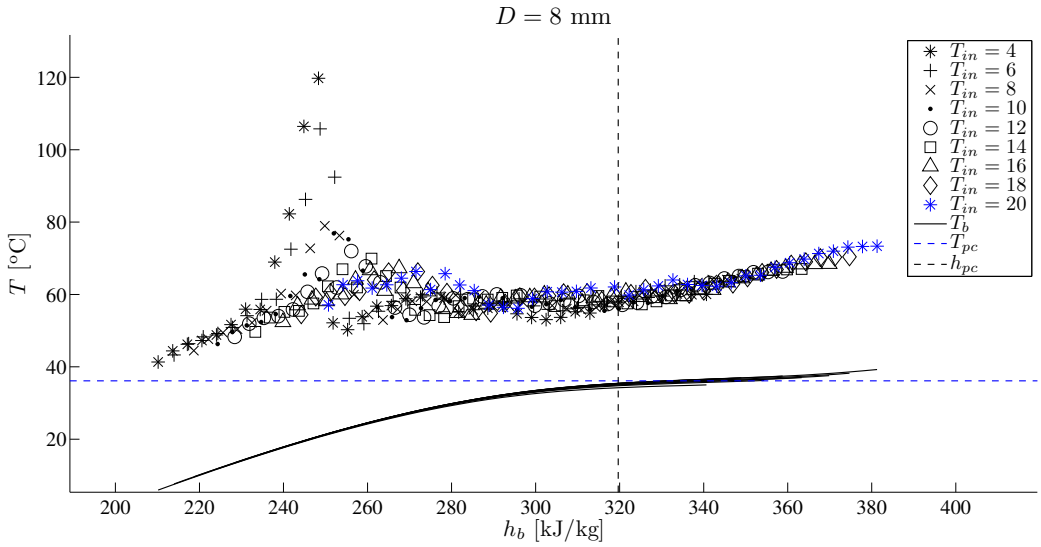


(a) All cases

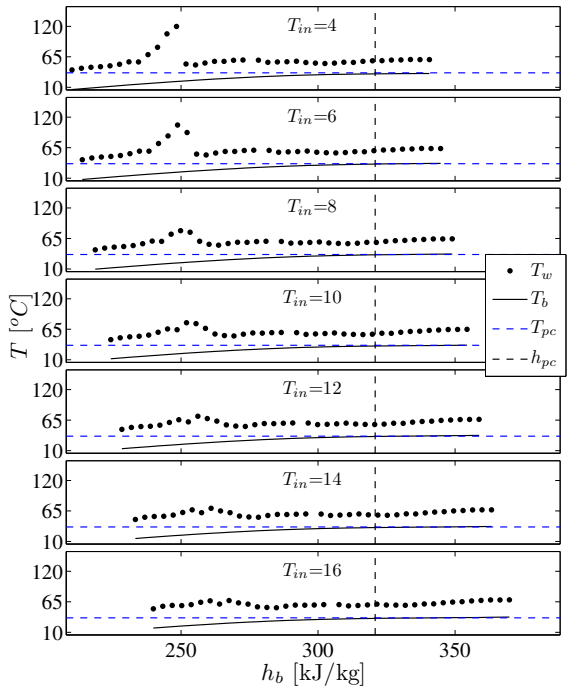


(b) Select cases

Figure A.67: Temperature profiles for $P/P_c = 1.13$, $G = 600$ kg/m^{2}s, $q = 80$ kW/m^2; units of T_{in} are °C.

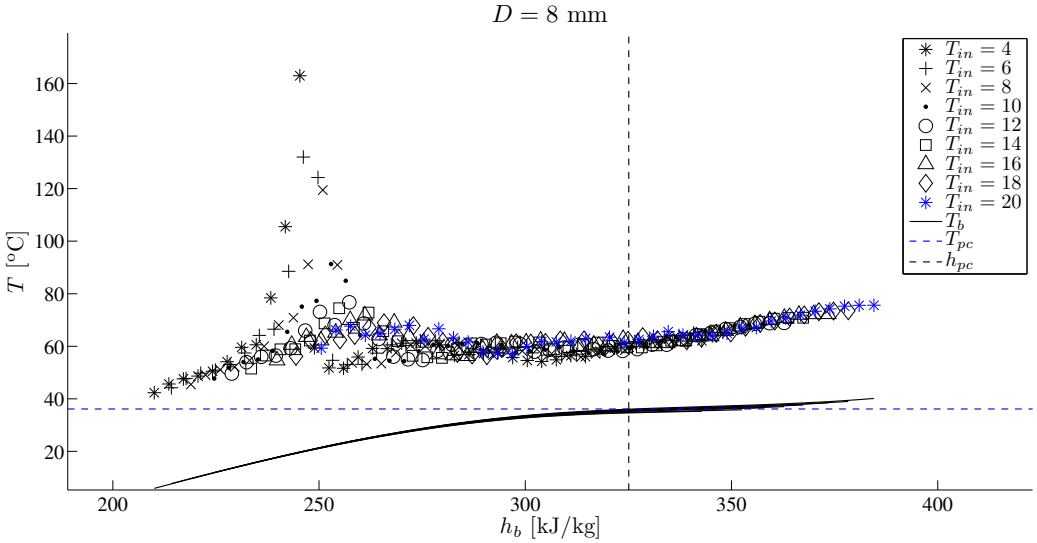


(a) All cases

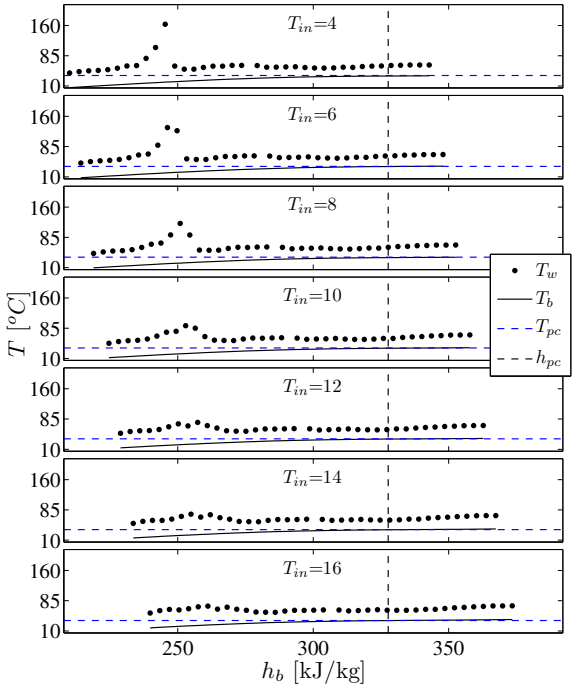


(b) Select cases

Figure A.68: Temperature profiles for $P/P_c = 1.13$, $G = 600$ kg/m^{2}s, $q = 83$ kW/m^2; units of T_{in} are °C.

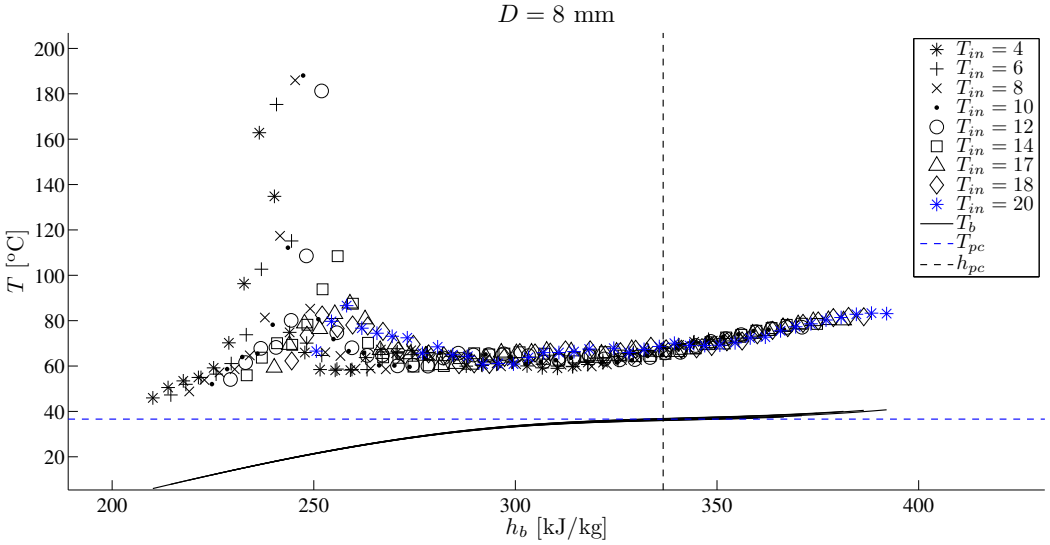


(a) All cases

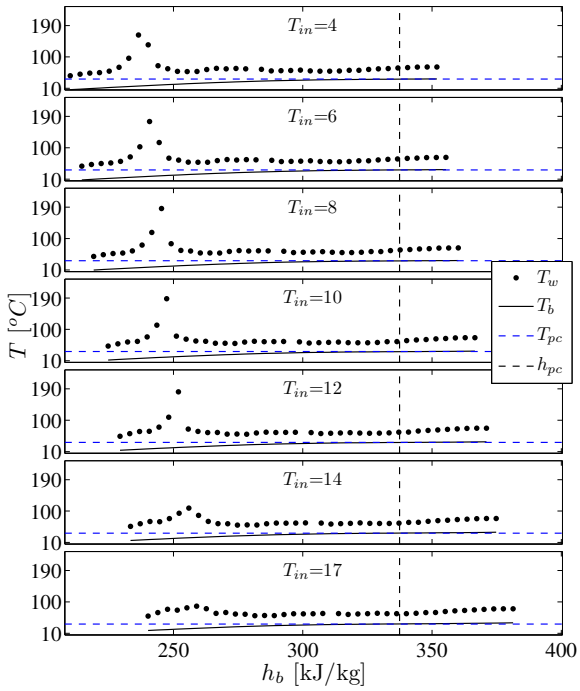


(b) Select cases

Figure A.69: Temperature profiles for $P/P_c = 1.13$, $G = 600$ kg/m^{2}s, $q = 85$ kW/m^2; units of T_{in} are °C.

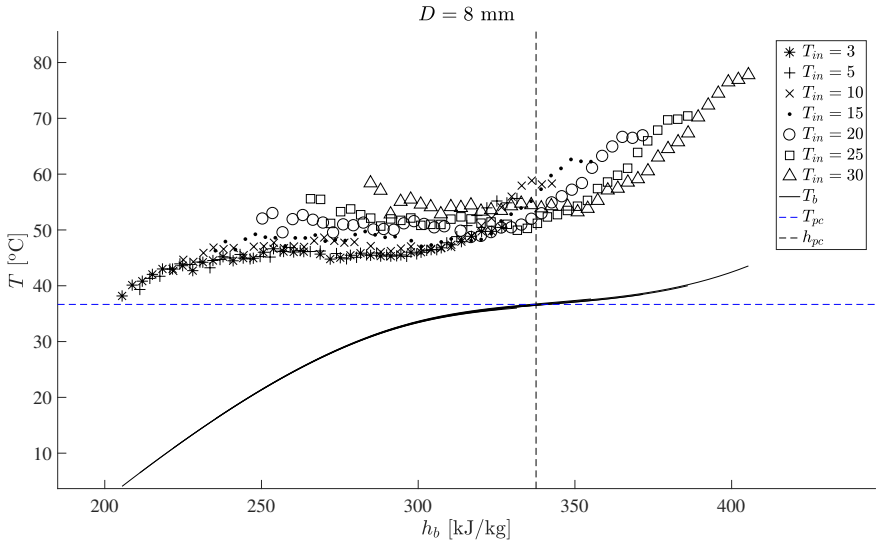


(a) All cases

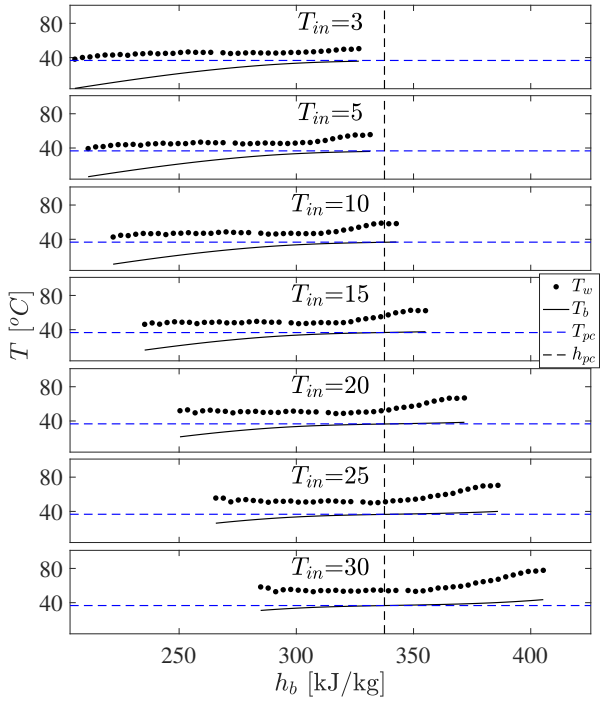


(b) Select cases

Figure A.70: Temperature profiles for $P/P_c = 1.13$, $G = 600$ kg/m^{2}s, $q = 90$ kW/m^2; units of T_{in} are °C.

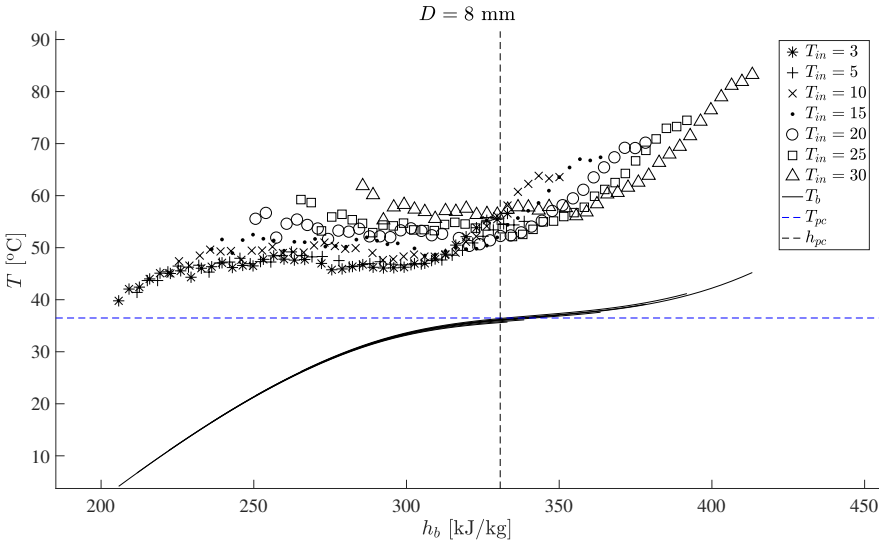


(a) All cases

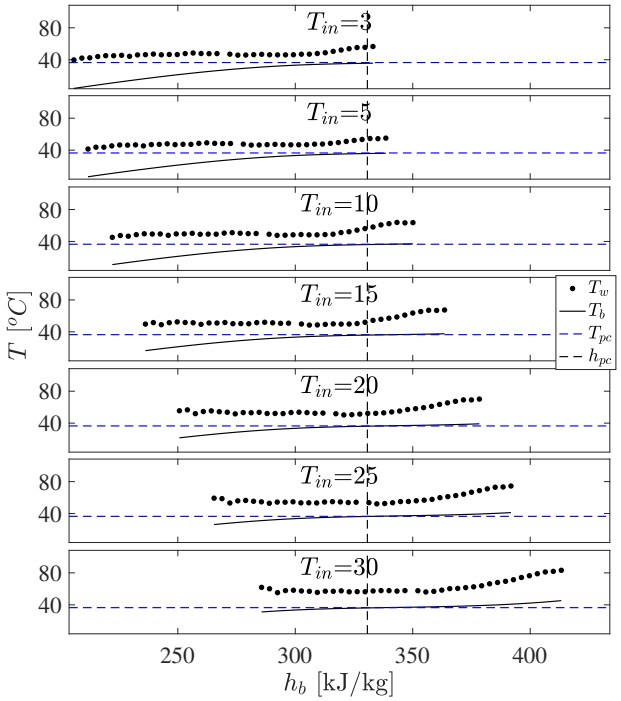


(b) Select cases

Figure A.71: Temperature profiles for $P/P_c = 1.13$, $G = 700$ kg/m^{2}s, $q = 90$ kW/m^2; units of T_{in} are °C.

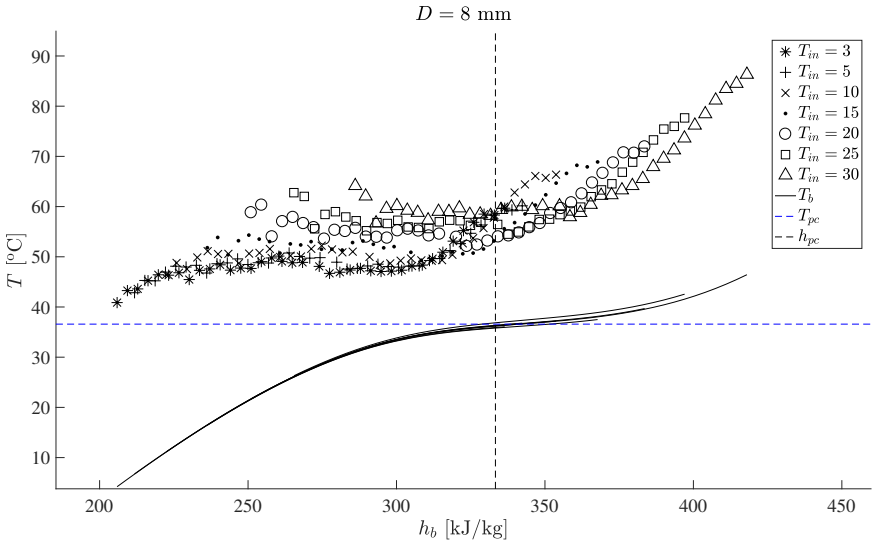


(a) All cases

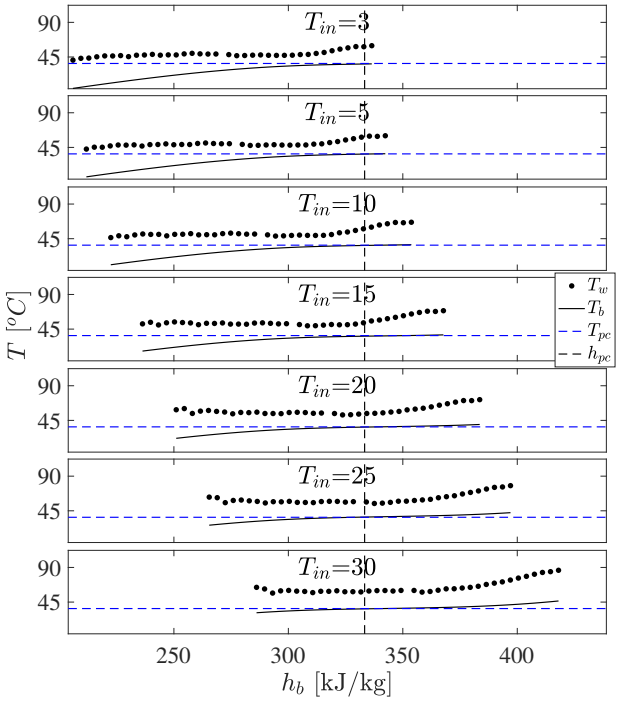


(b) Select cases

Figure A.72: Temperature profiles for $P/P_c = 1.13$, $G = 700$ kg/m^{2}s, $q = 95$ kW/m^2; units of T_{in} are °C.

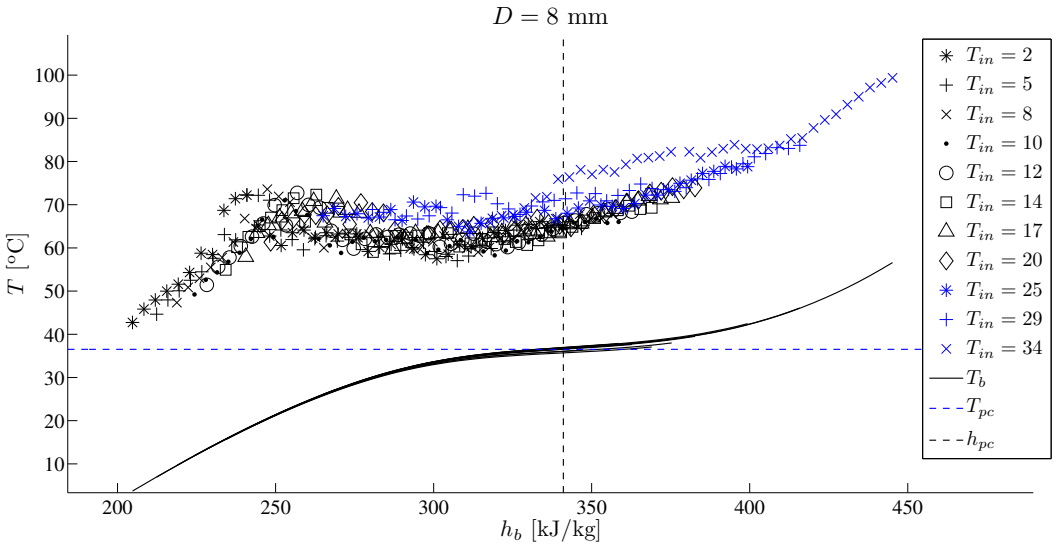


(a) All cases

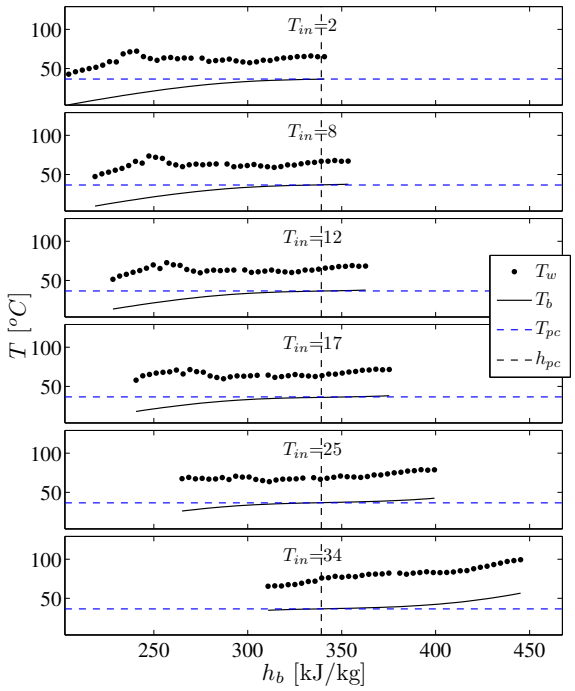


(b) Select cases

Figure A.73: Temperature profiles for $P/P_c = 1.13$, $G = 700$ kg/m^{2}s, $q = 98$ kW/m^2; units of T_{in} are °C.

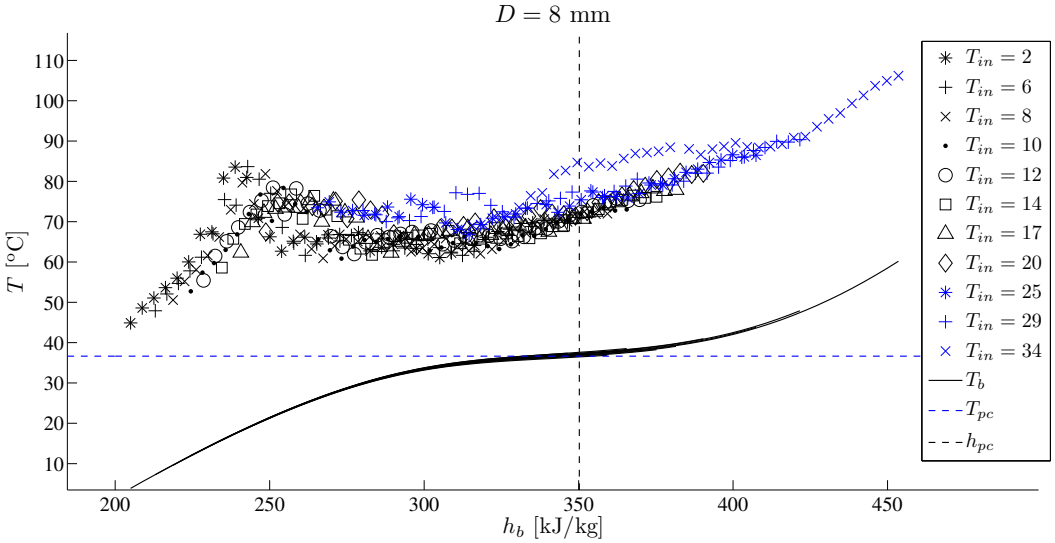


(a) All cases

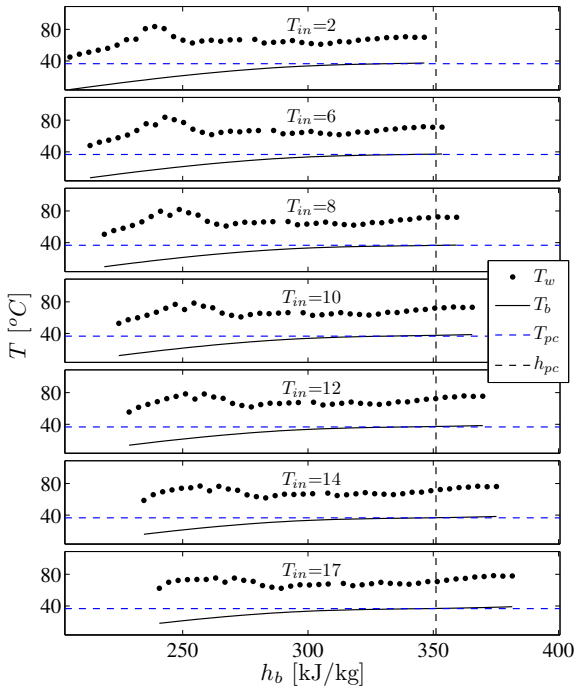


(b) Select cases

Figure A.74: Temperature profiles for $P/P_c = 1.13$, $G = 700$ kg/m^{2}s, $q = 100$ kW/m^2; units of T_{in} are °C.

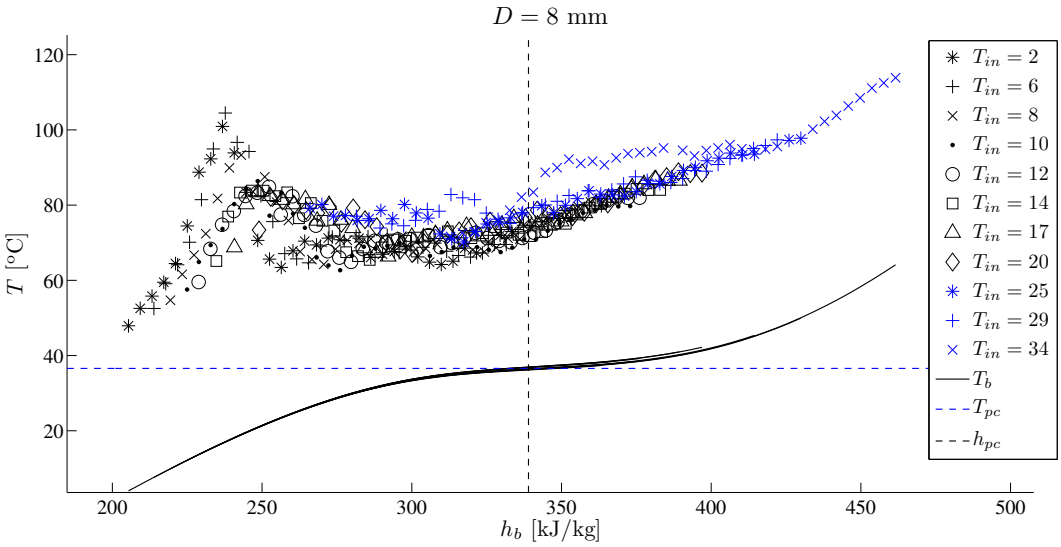


(a) All cases

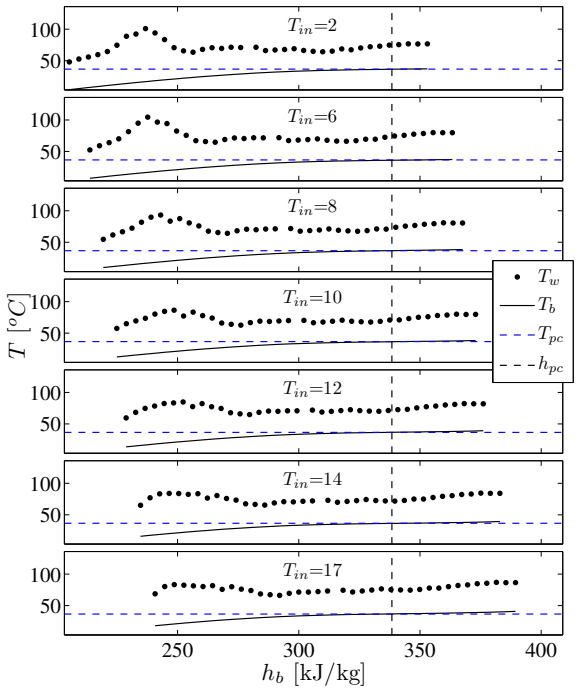


(b) Select cases

Figure A.75: Temperature profiles for $P/P_c = 1.13$, $G = 700$ kg/m^{2}s, $q = 105$ kW/m^2; units of T_{in} are °C.

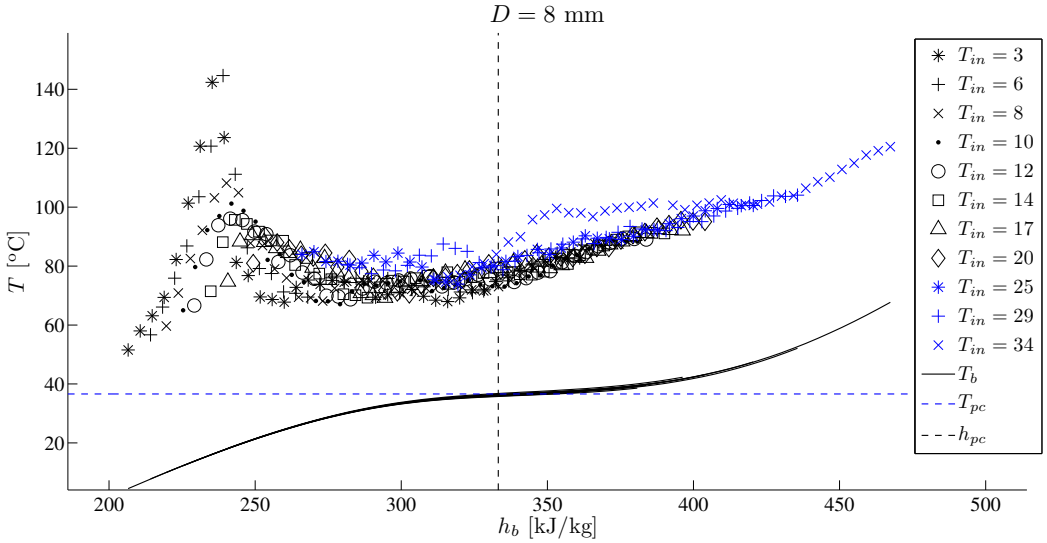


(a) All cases

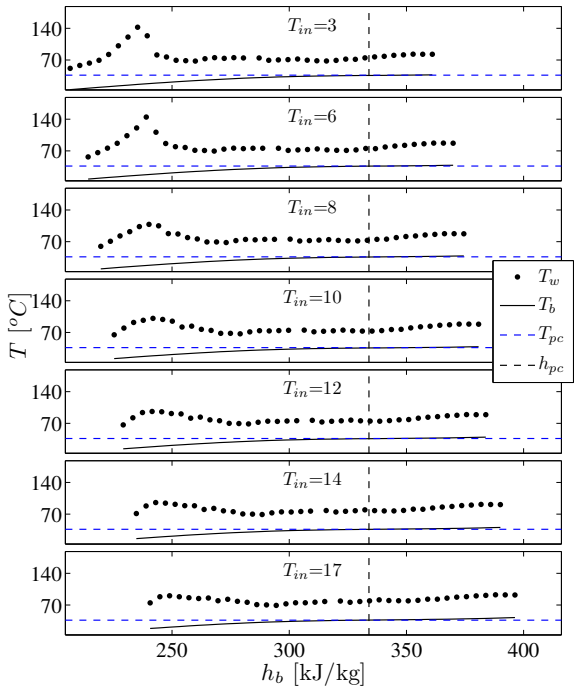


(b) Select cases

Figure A.76: Temperature profiles for $P/P_c = 1.13$, $G = 700$ kg/m^{2}s, $q = 110$ kW/m^2; units of T_{in} are °C.

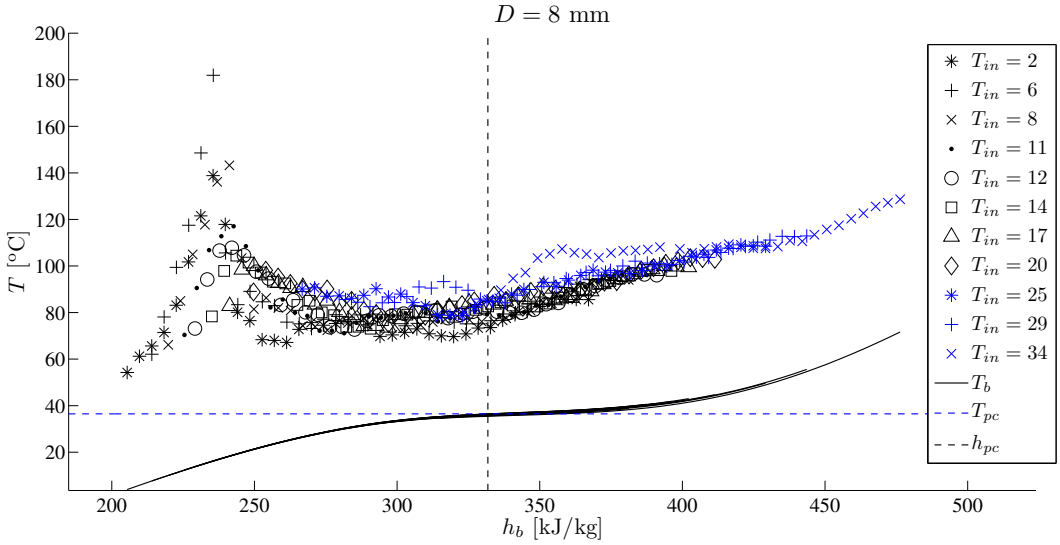


(a) All cases

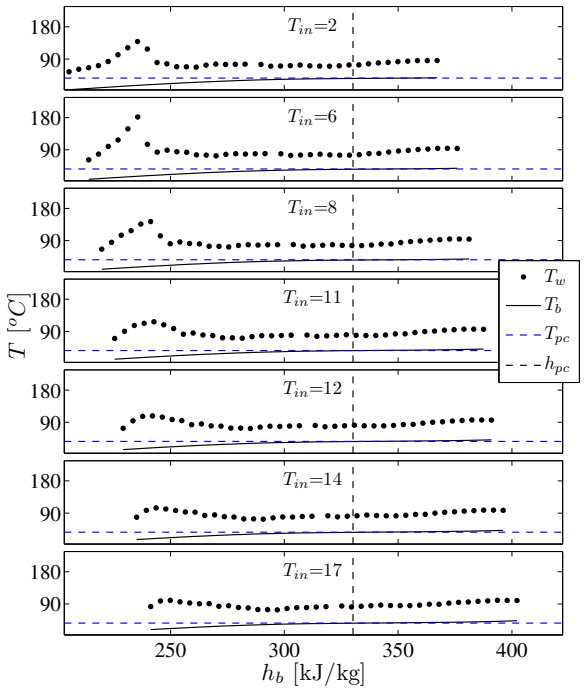


(b) Select cases

Figure A.77: Temperature profiles for $P/P_c = 1.13$, $G = 700$ kg/m^{2}s, $q = 115$ kW/m^2; units of T_{in} are °C.

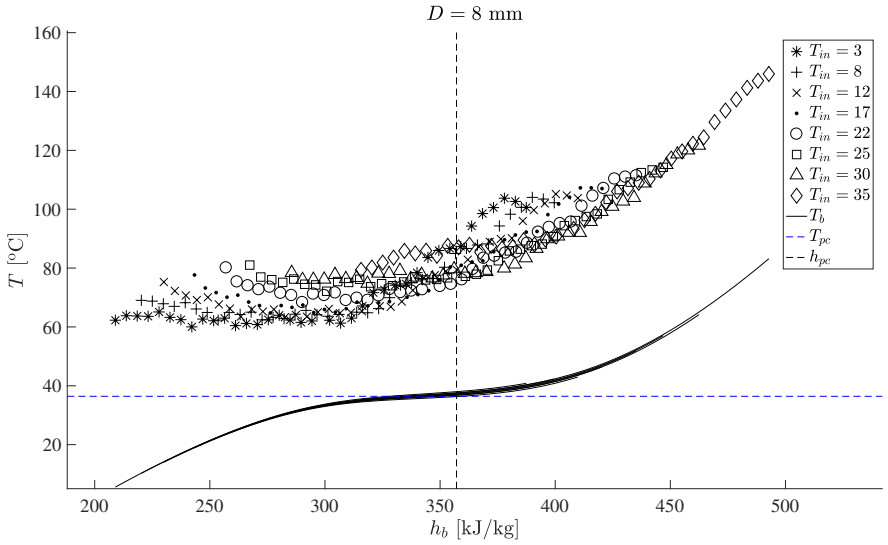


(a) All cases

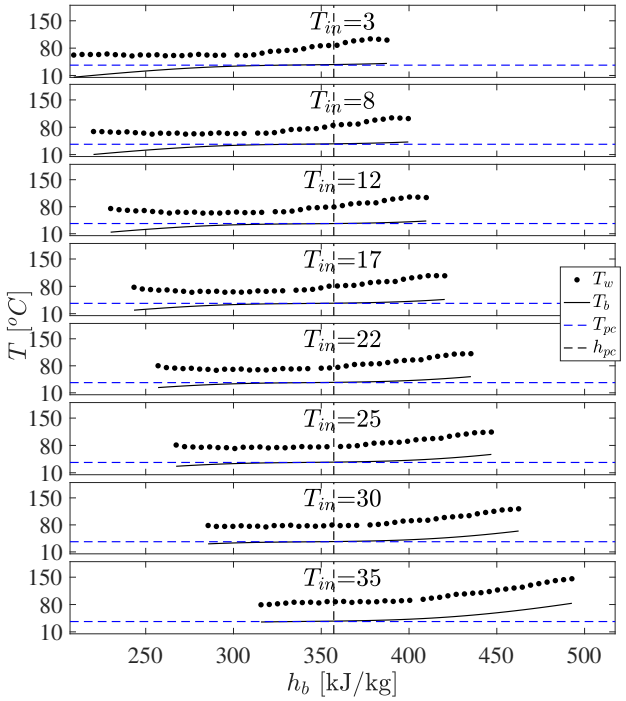


(b) Select cases

Figure A.78: Temperature profiles for $P/P_c = 1.13$, $G = 700$ kg/m^{2}s, $q = 120$ kW/m^2; units of T_{in} are °C.

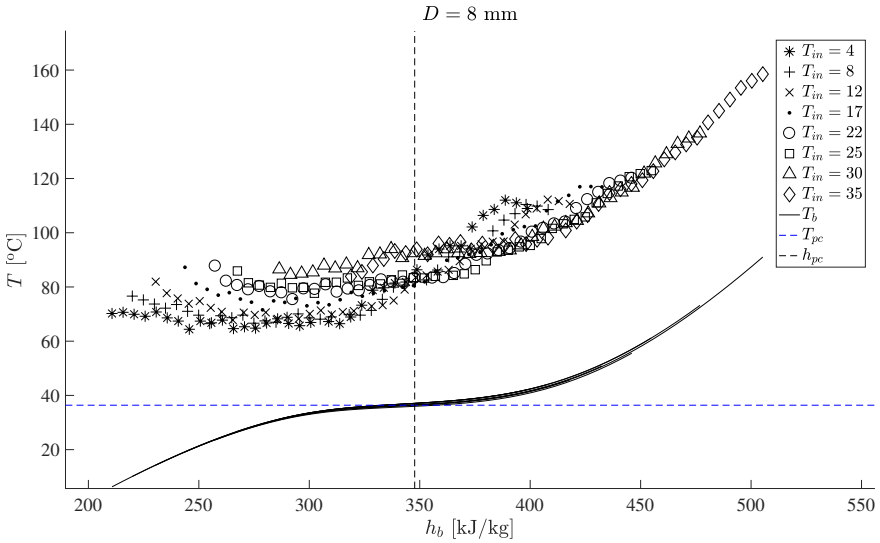


(a) All cases

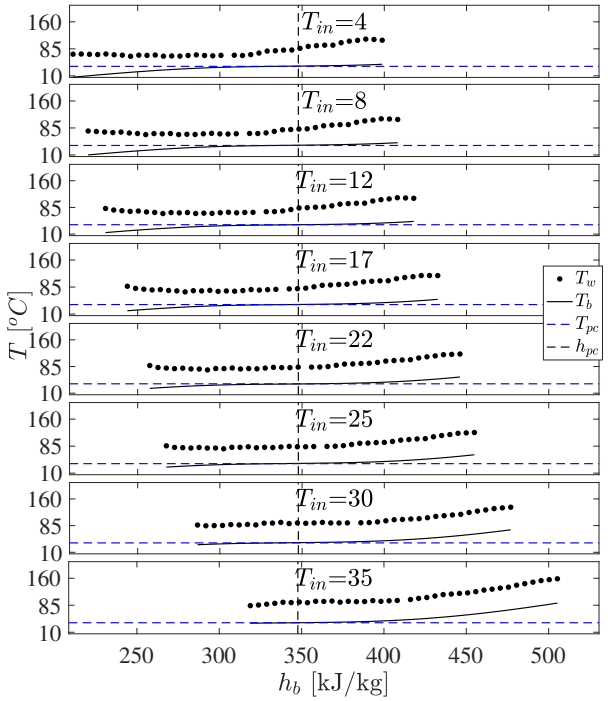


(b) Select cases

Figure A.79: Temperature profiles for $P/P_c = 1.13$, $G = 1000$ kg/m^{2}s, $q = 190$ kW/m^2; units of T_{in} are °C.

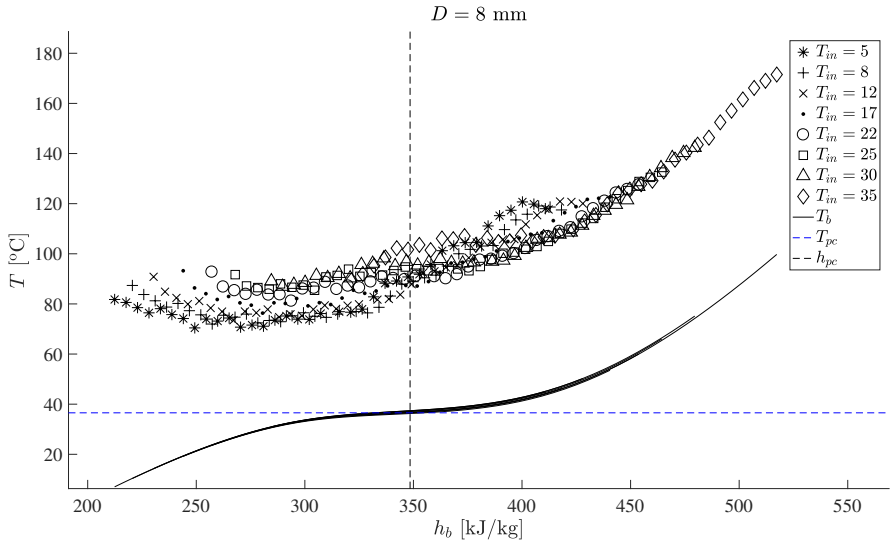


(a) All cases

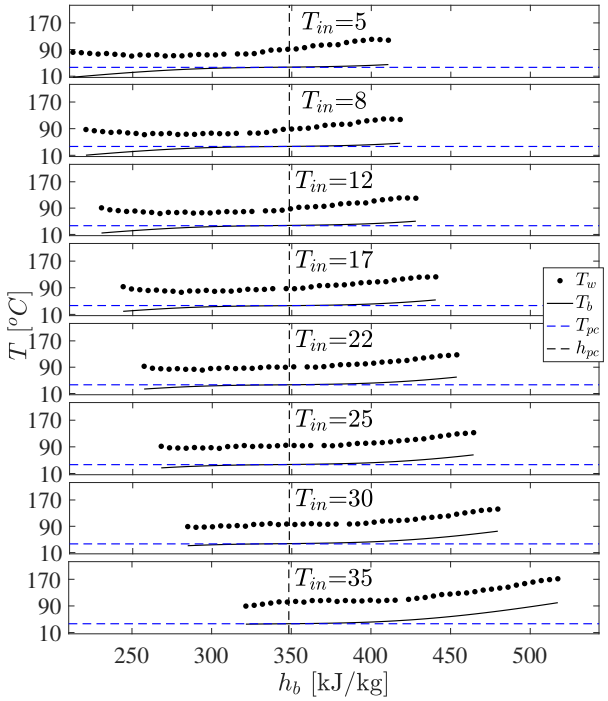


(b) Select cases

Figure A.80: Temperature profiles for $P/P_c = 1.13$, $G = 1000$ kg/m^{2}s, $q = 200$ kW/m^2; units of T_{in} are °C.

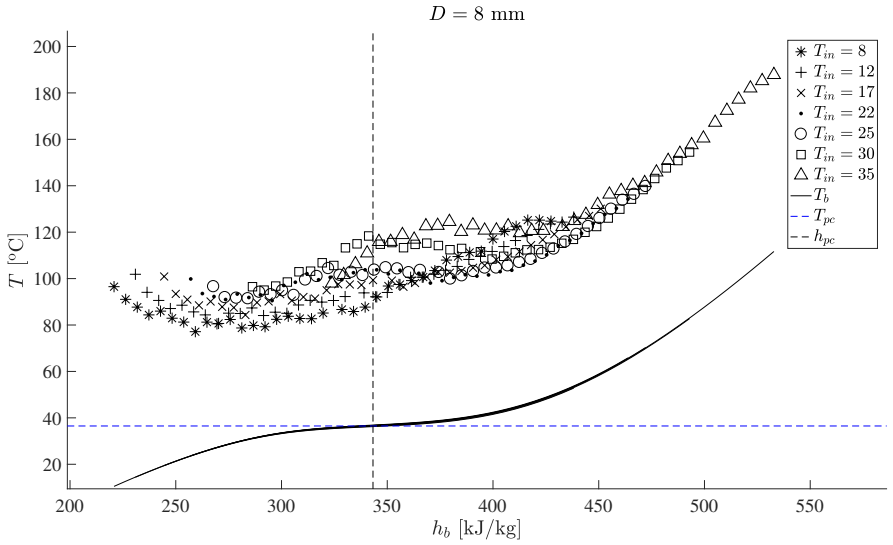


(a) All cases

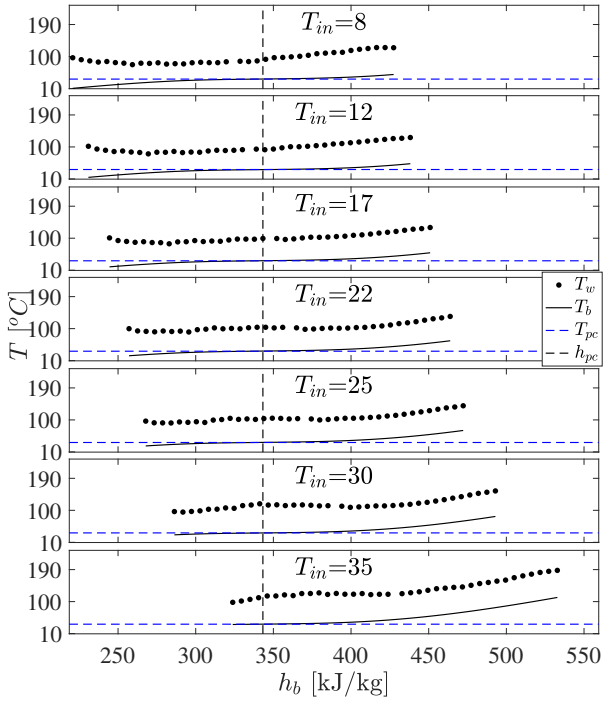


(b) Select cases

Figure A.81: Temperature profiles for $P/P_c = 1.13$, $G = 1000$ kg/m^{2}s, $q = 210$ kW/m^2; units of T_{in} are °C.

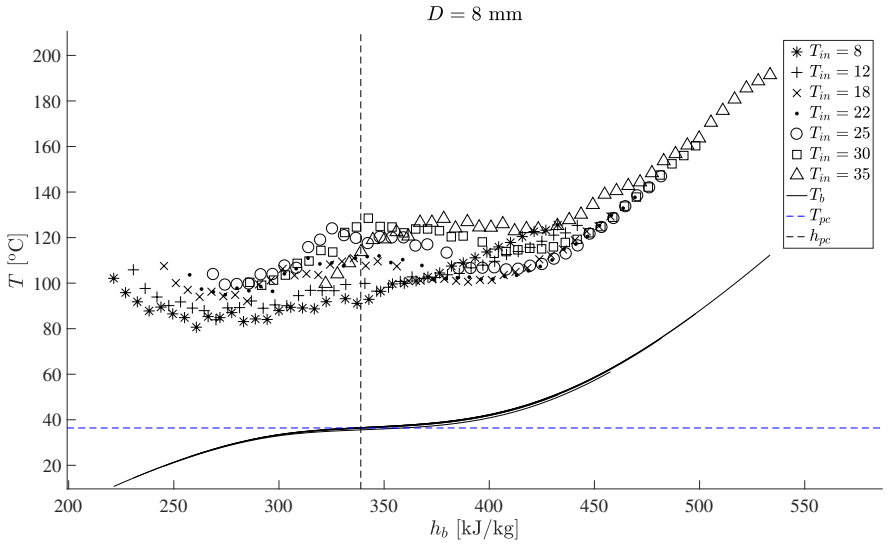


(a) All cases

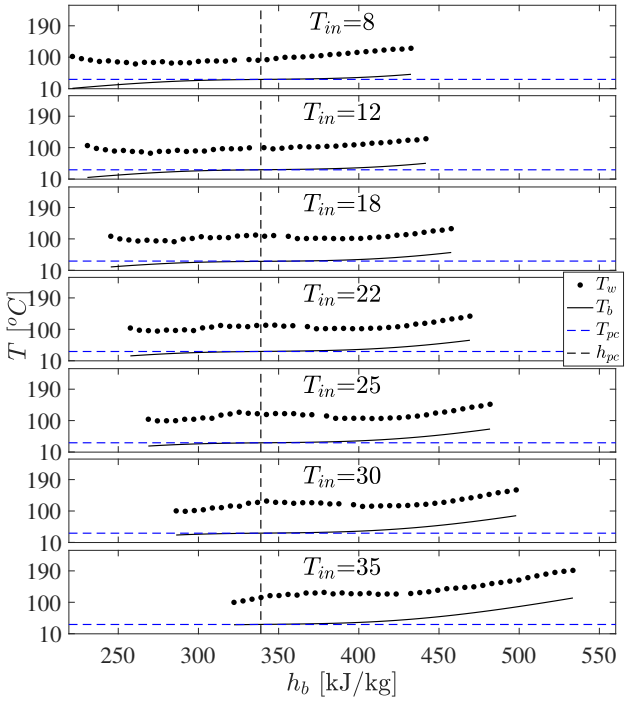


(b) Select cases

Figure A.82: Temperature profiles for $P/P_c = 1.13$, $G = 1000$ kg/m^{2}s, $q = 220$ kW/m^2; units of T_{in} are °C.

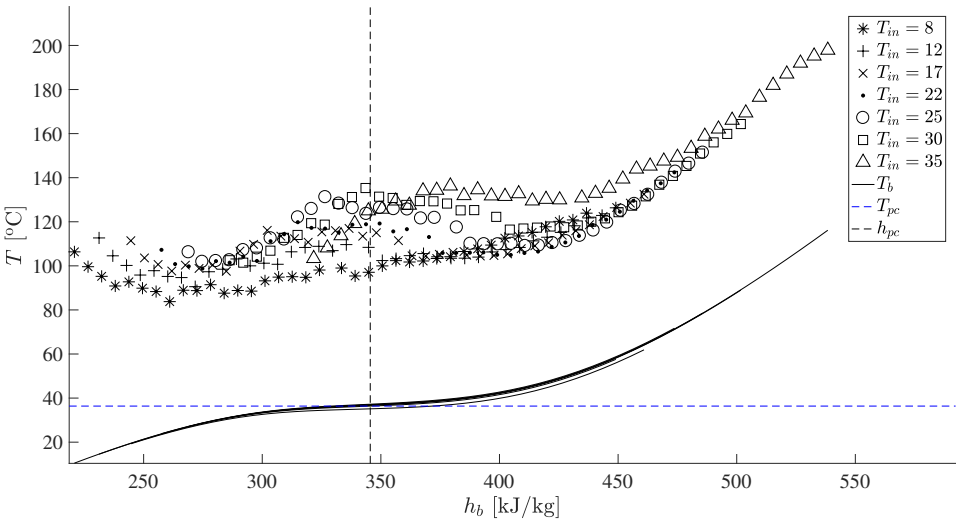


(a) All cases

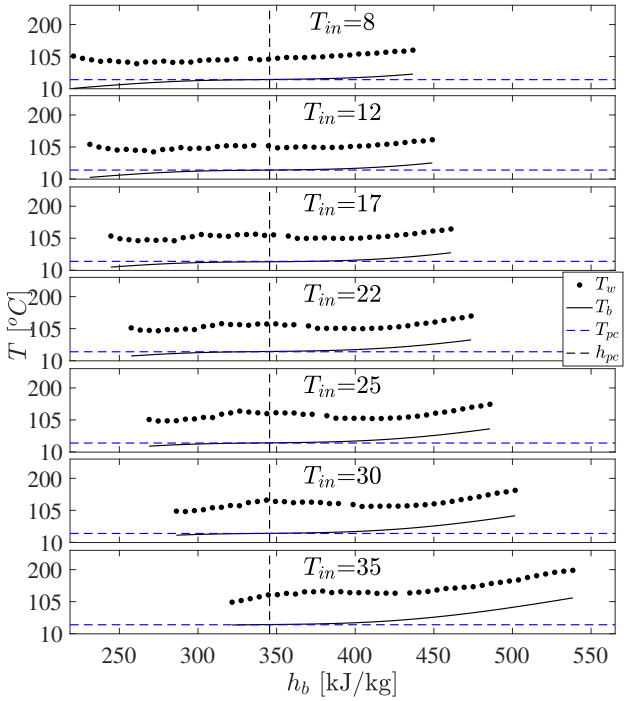


(b) Select cases

Figure A.83: Temperature profiles for $P/P_c = 1.13$, $G = 1000$ kg/m^{2}s, $q = 225$ kW/m^2; units of T_{in} are °C.

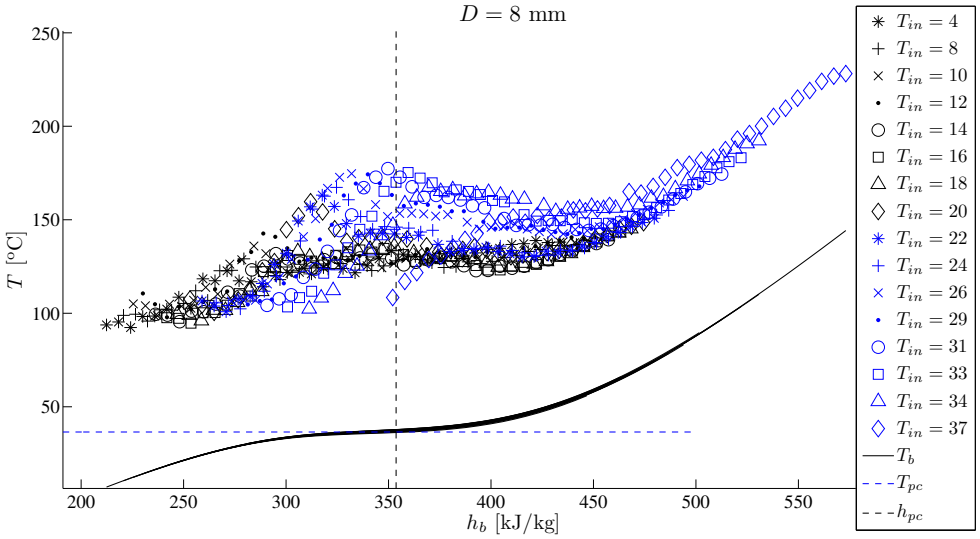


(a) All cases

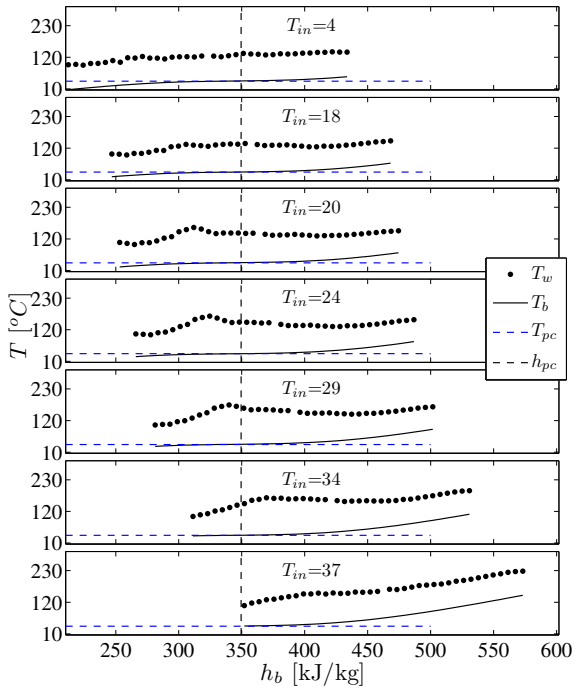


(b) Select cases

Figure A.84: Temperature profiles for $P/P_c = 1.13$, $G = 1000$ kg/m^{2}s, $q = 230$ kW/m^2; units of T_{in} are °C.

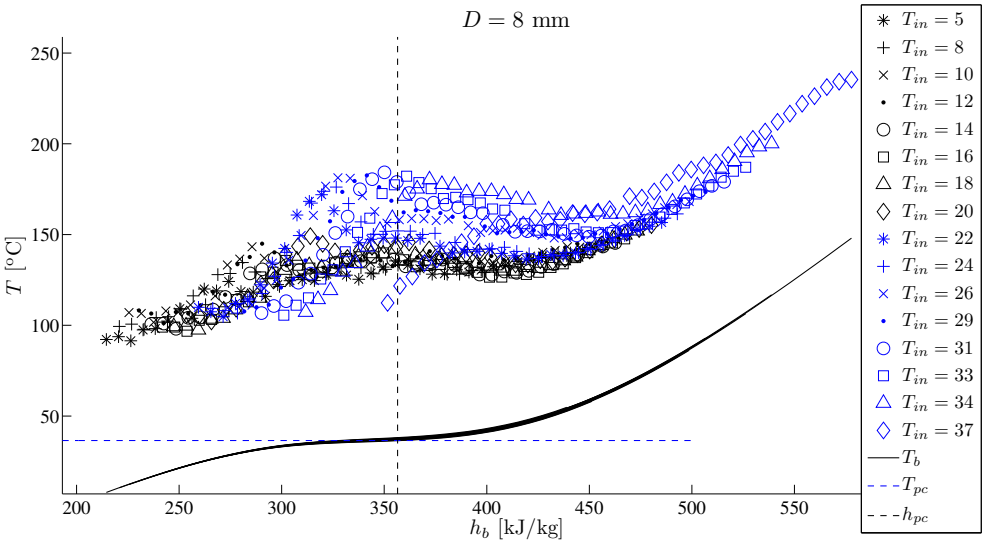


(a) All cases

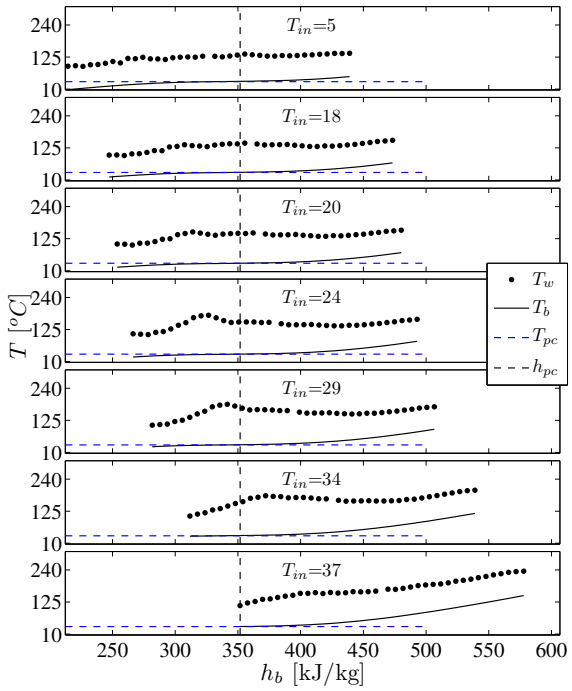


(b) Select cases

Figure A.85: Temperature profiles for $P/P_c = 1.13$, $G = 1000$ kg/m^{2}s, $q = 235$ kW/m^2; units of T_{in} are °C.

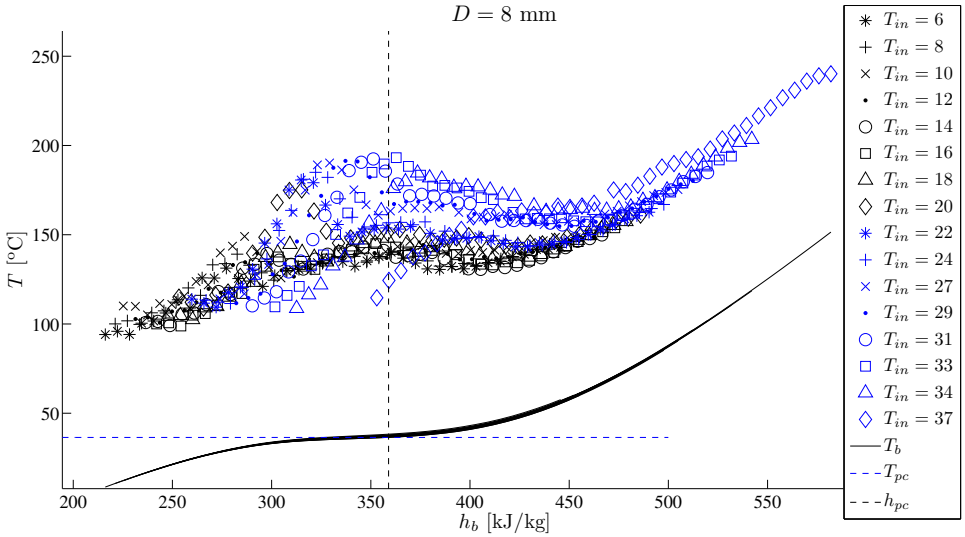


(a) All cases

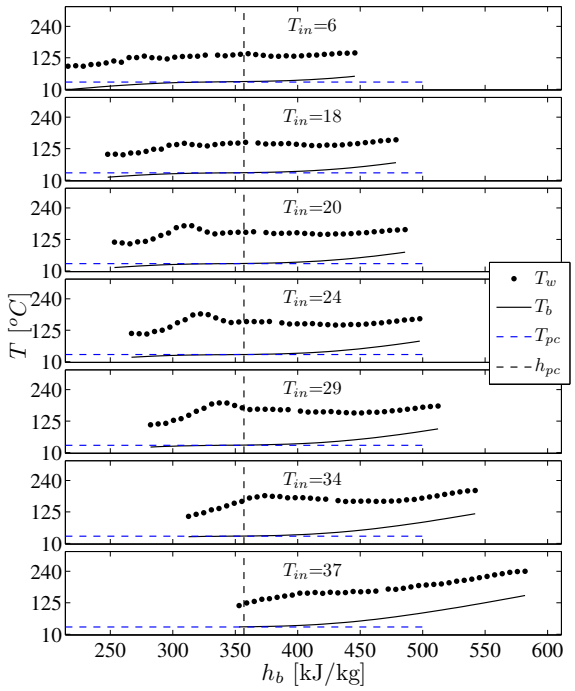


(b) Select cases

Figure A.86: Temperature profiles for $P/P_c = 1.13$, $G = 1000$ kg/m^{2}s, $q = 240$ kW/m^2; units of T_{in} are °C.

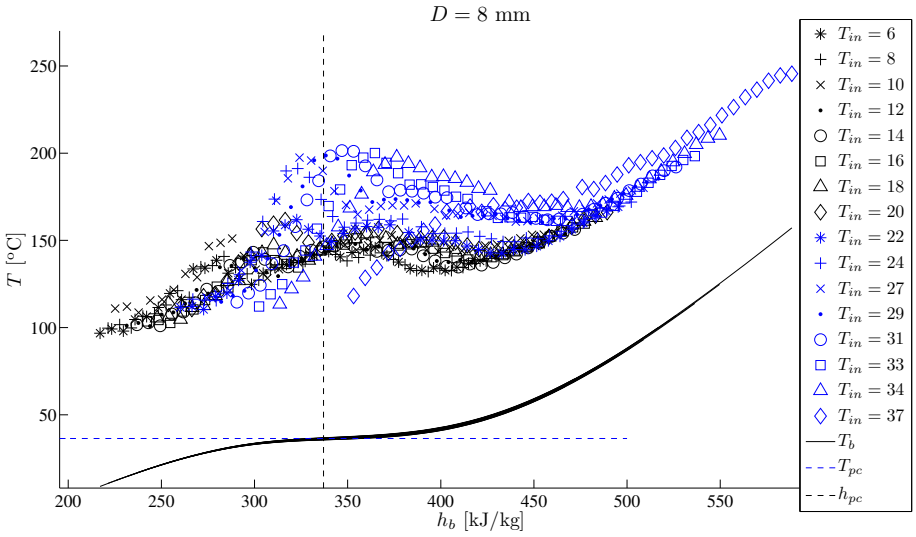


(a) All cases

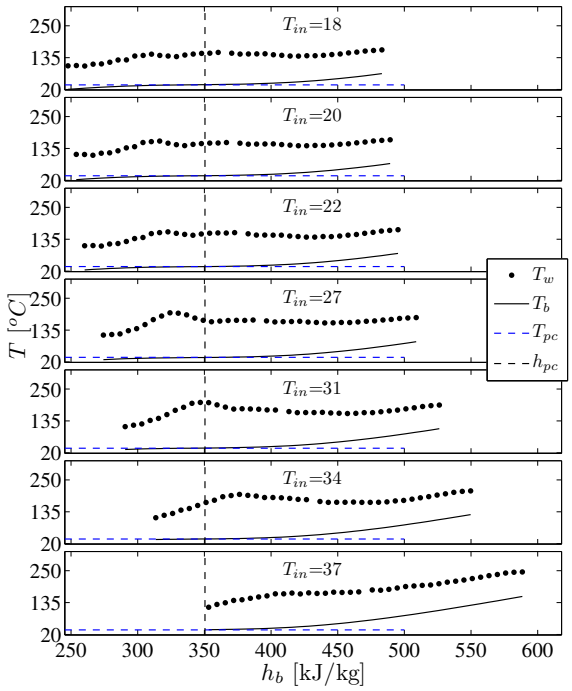


(b) Select cases

Figure A.87: Temperature profiles for $P/P_c = 1.13$, $G = 1000$ kg/m^{2}s, $q = 245$ kW/m^2; units of T_{in} are °C.

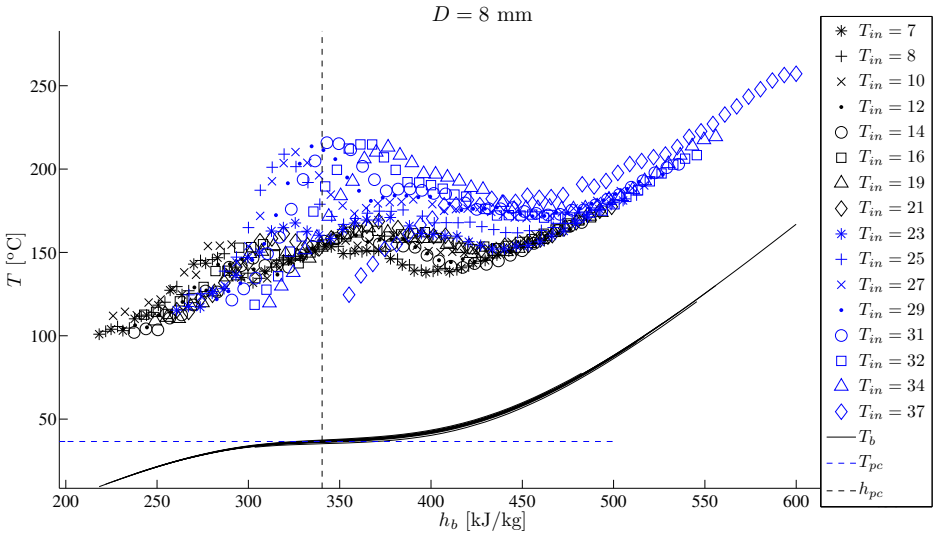


(a) All cases

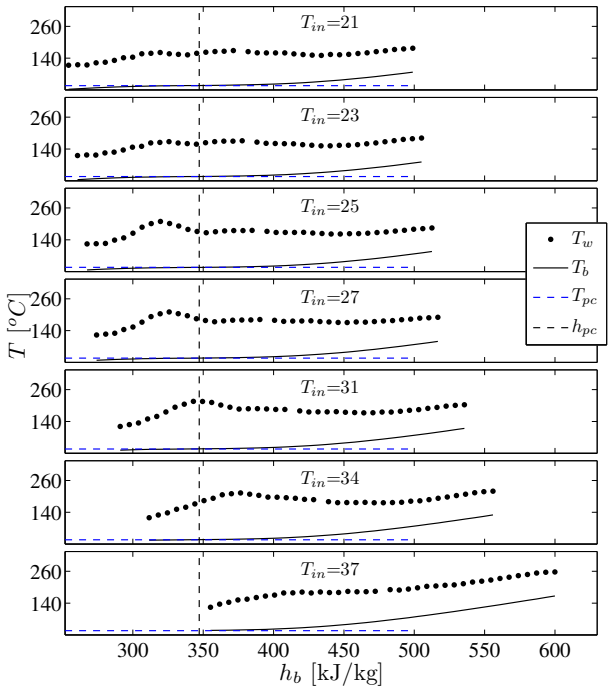


(b) Select cases

Figure A.88: Temperature profiles for $P/P_c = 1.13$, $G = 1000$ kg/m^{2}s, $q = 250$ kW/m^2; units of T_{in} are °C.

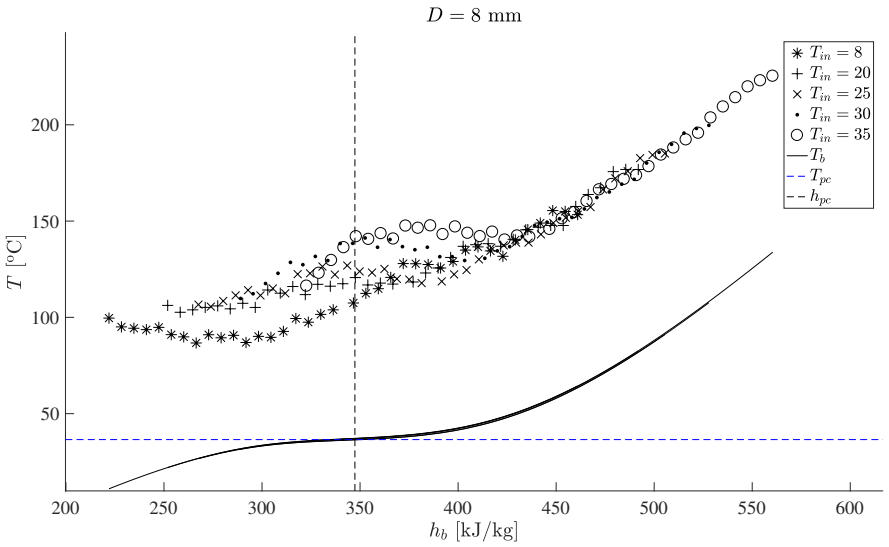


(a) All cases

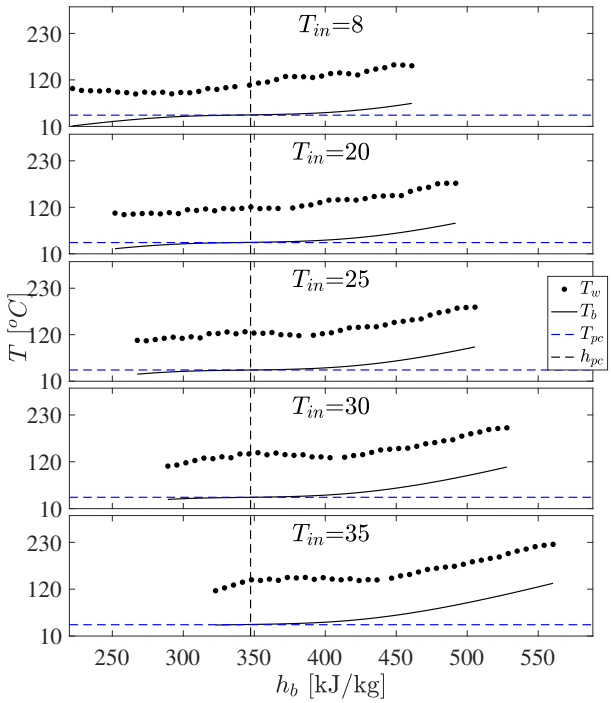


(b) Select cases

Figure A.89: Temperature profiles for $P/P_c = 1.13$, $G = 1000$ kg/m^{2}s, $q = 260$ kW/m^2; units of T_{in} are °C.

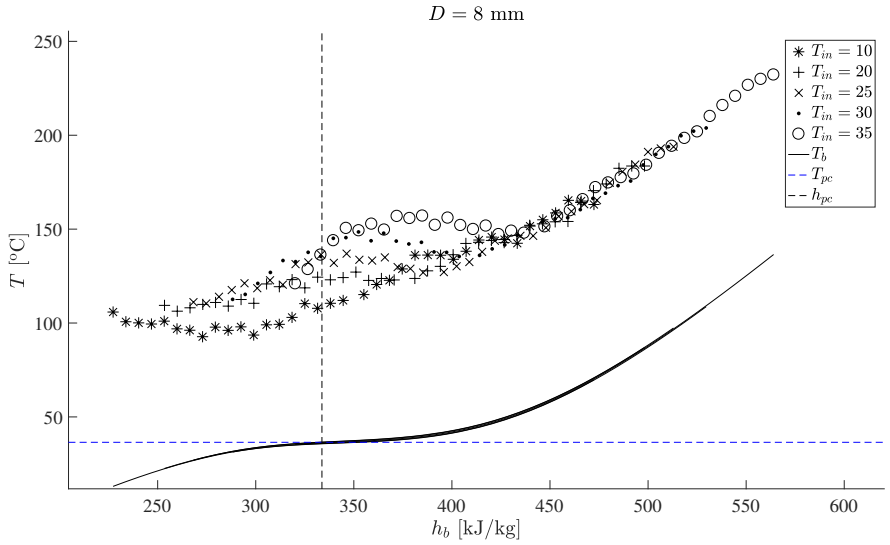


(a) All cases

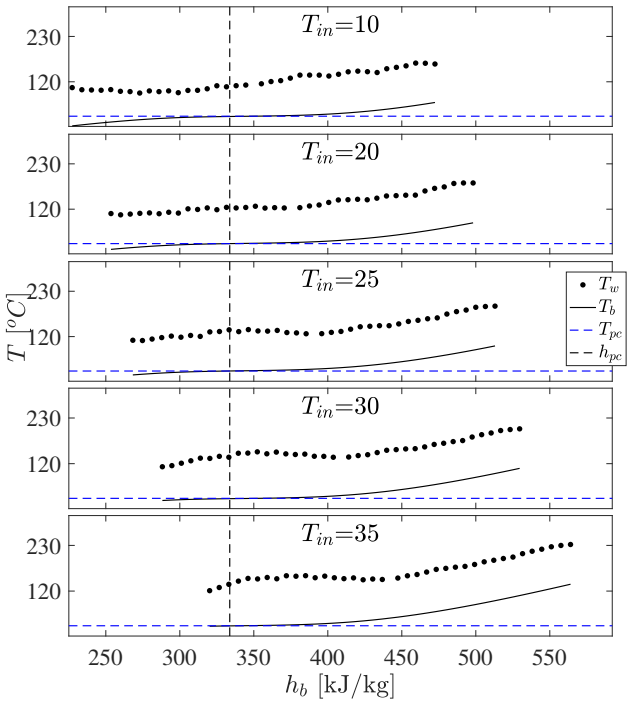


(b) Select cases

Figure A.90: Temperature profiles for $P/P_c = 1.13$, $G = 1500$ kg/m^{2}s, $q = 380$ kW/m^2; units of T_{in} are °C.

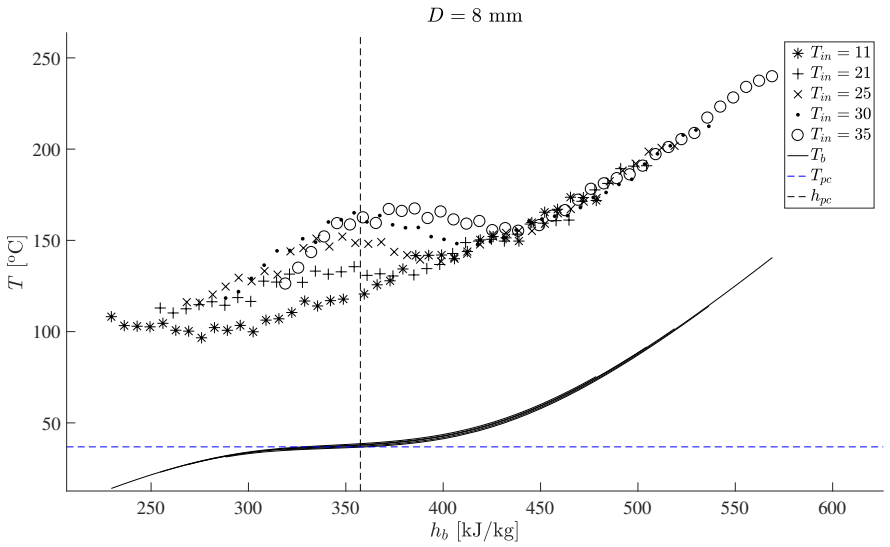


(a) All cases

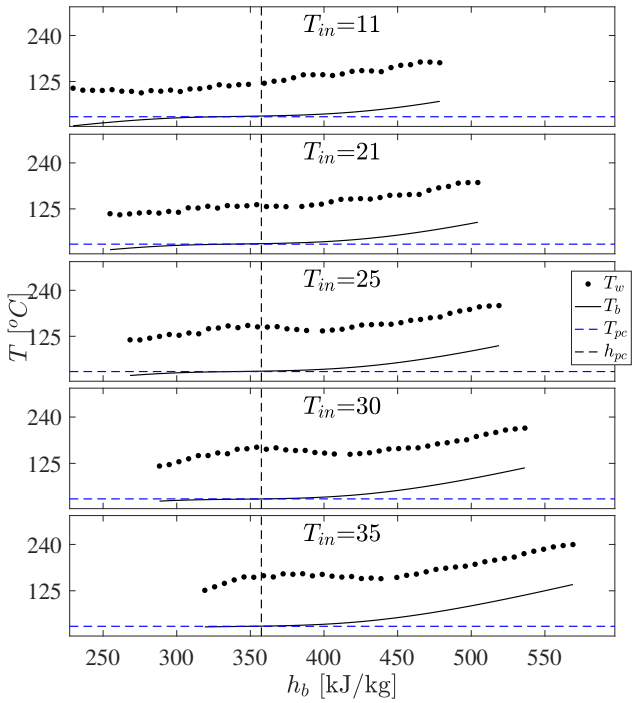


(b) Select cases

Figure A.91: Temperature profiles for $P/P_c = 1.13$, $G = 1500$ kg/m^{2}s, $q = 390$ kW/m^2; units of T_{in} are °C.

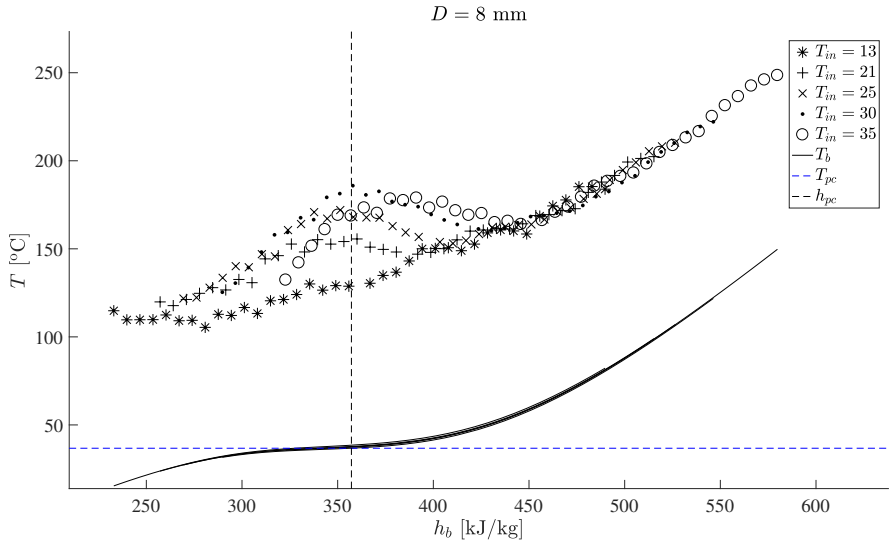


(a) All cases

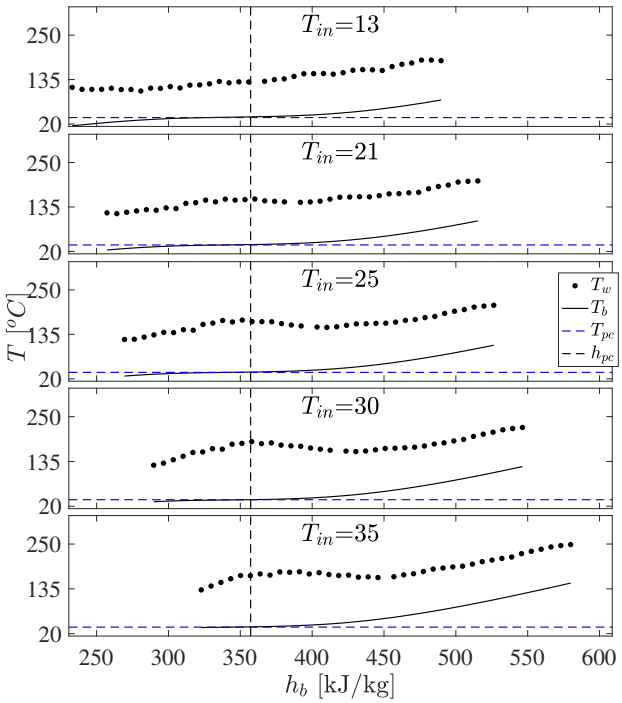


(b) Select cases

Figure A.92: Temperature profiles for $P/P_c = 1.13$, $G = 1500$ kg/m^{2}s, $q = 400$ kW/m^2; units of T_{in} are °C.

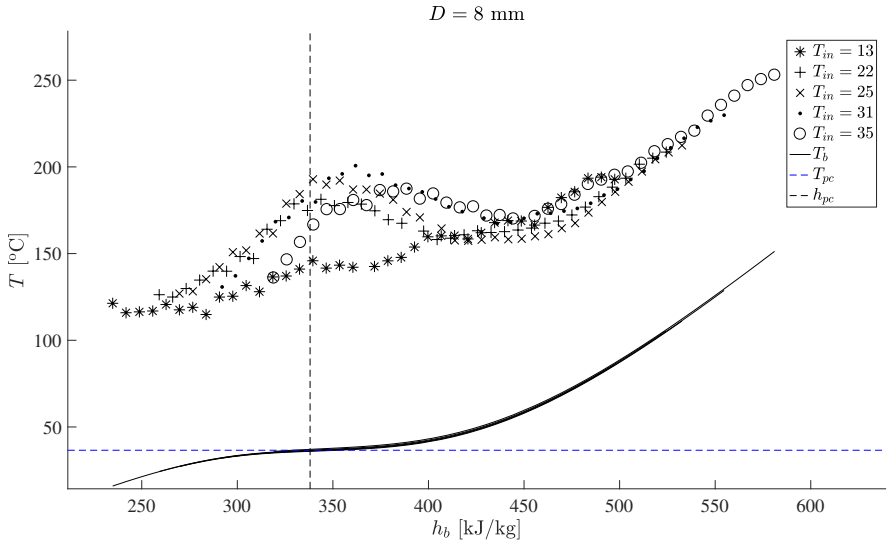


(a) All cases

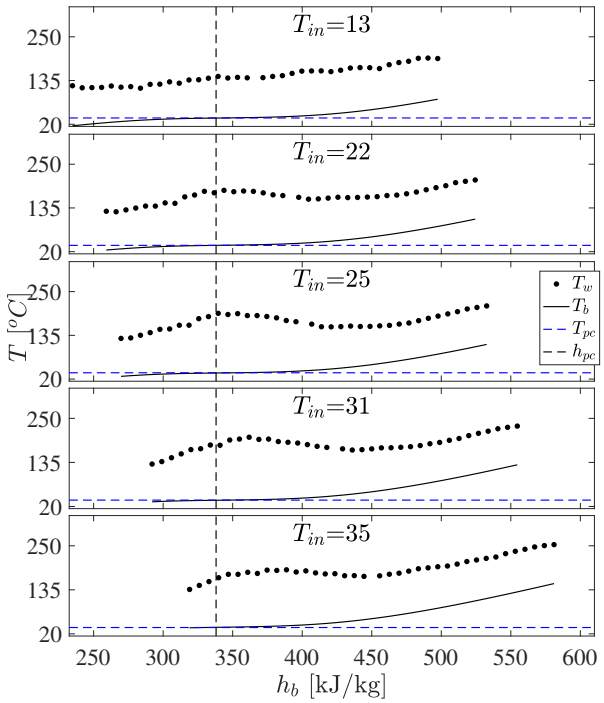


(b) Select cases

Figure A.93: Temperature profiles for $P/P_c = 1.13$, $G = 1500$ kg/m^{2}s, $q = 410$ kW/m^2; units of T_{in} are °C.

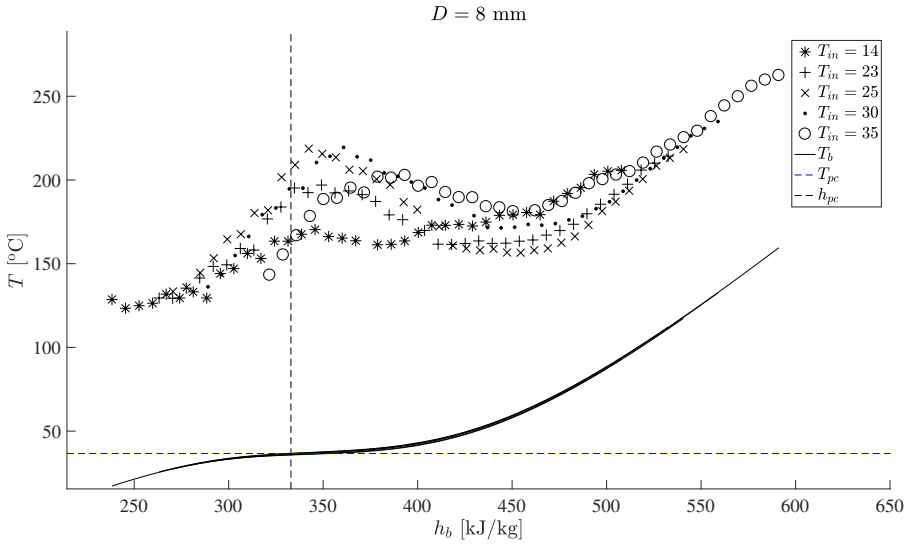


(a) All cases

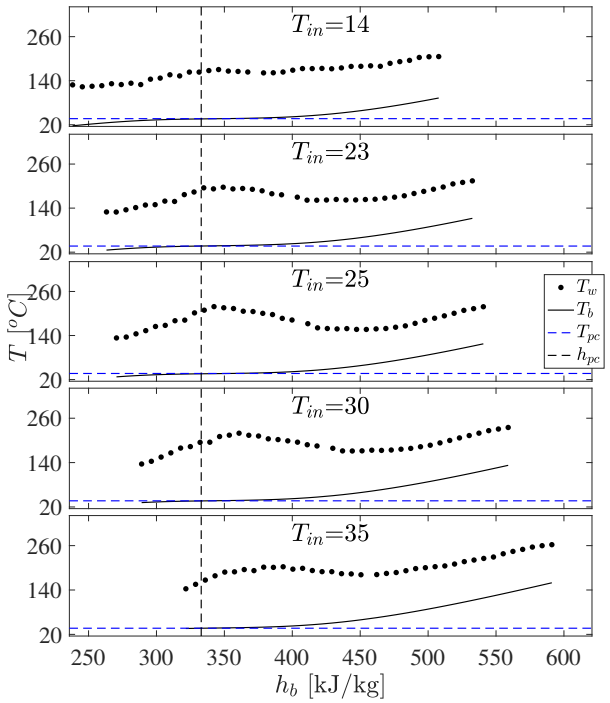


(b) Select cases

Figure A.94: Temperature profiles for $P/P_c = 1.13$, $G = 1500$ kg/m^{2}s, $q = 420$ kW/m^2; units of T_{in} are °C.

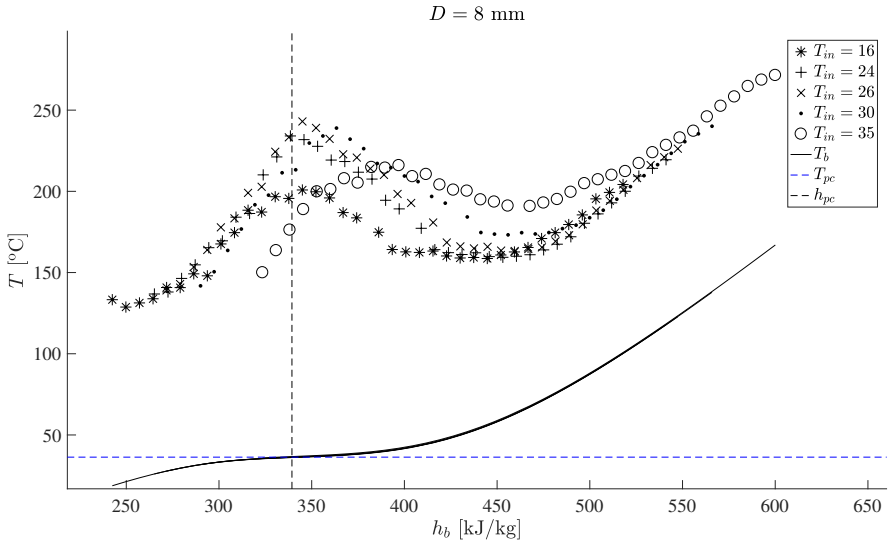


(a) All cases

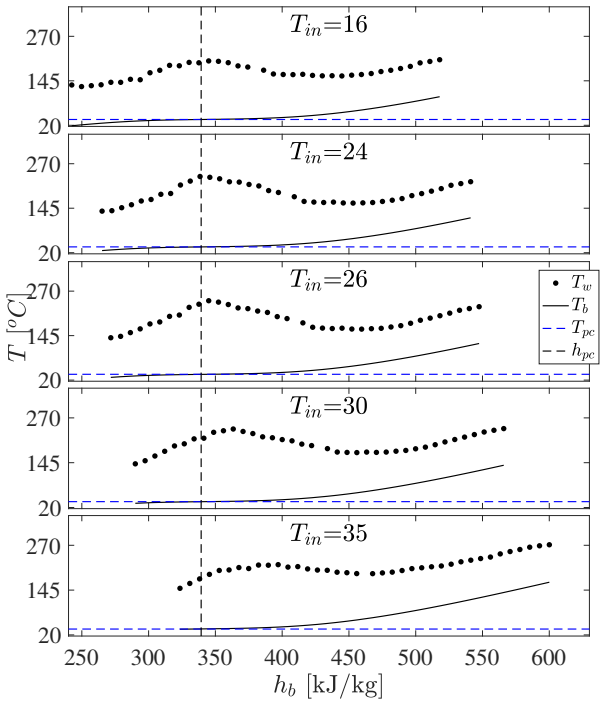


(b) Select cases

Figure A.95: Temperature profiles for $P/P_c = 1.13$, $G = 1500$ kg/m^{2}s, $q = 430$ kW/m^2; units of T_{in} are °C.

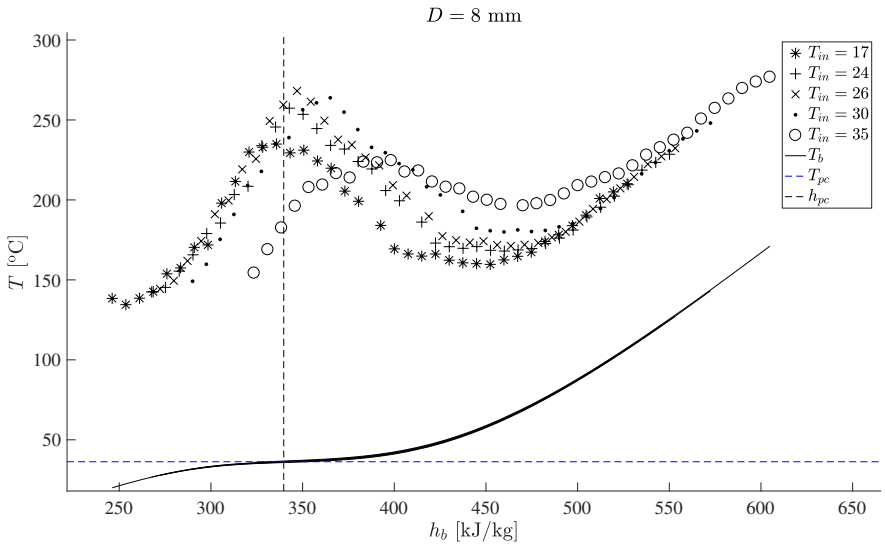


(a) All cases

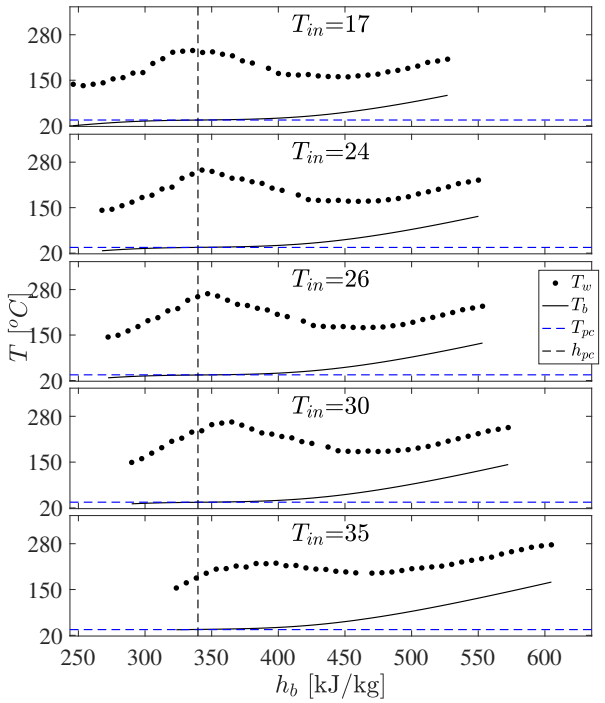


(b) Select cases

Figure A.96: Temperature profiles for $P/P_c = 1.13$, $G = 1500$ kg/m^{2}s, $q = 440$ kW/m^2; units of T_{in} are °C.



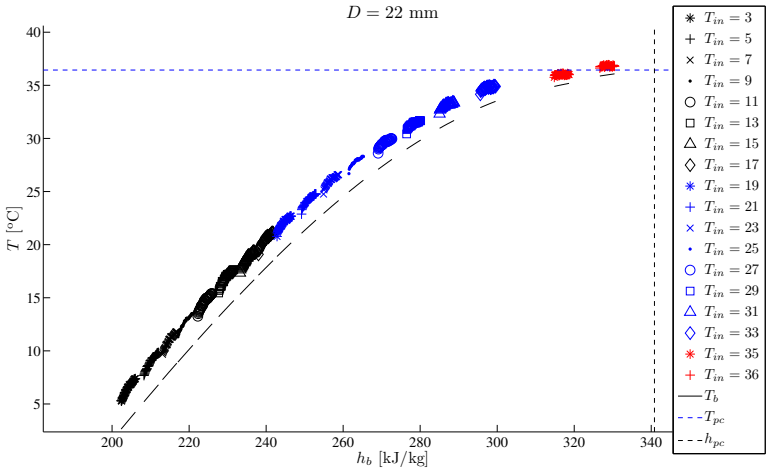
(a) All cases



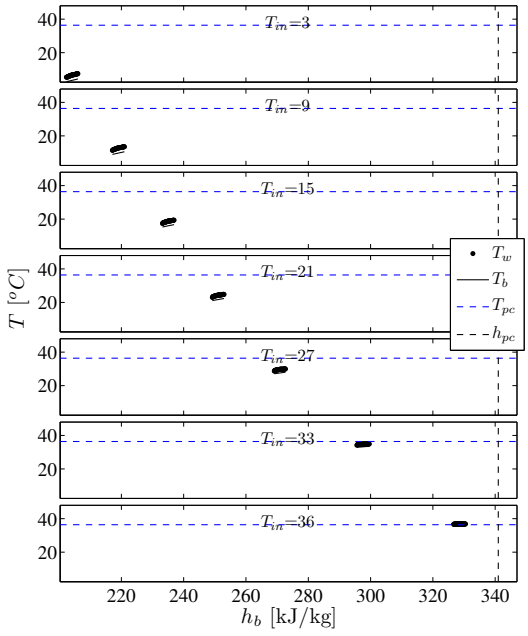
(b) Select cases

Figure A.97: Temperature profiles for $P/P_c = 1.13$, $G = 1500$ kg/m^{2}s, $q = 450$ kW/m^2; units of T_{in} are °C.

A.3 22 mm test section

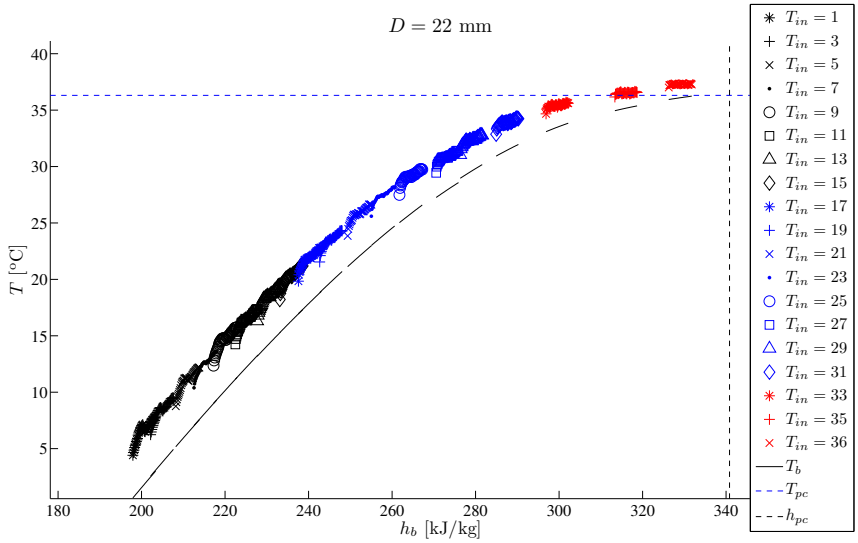


(a) All cases

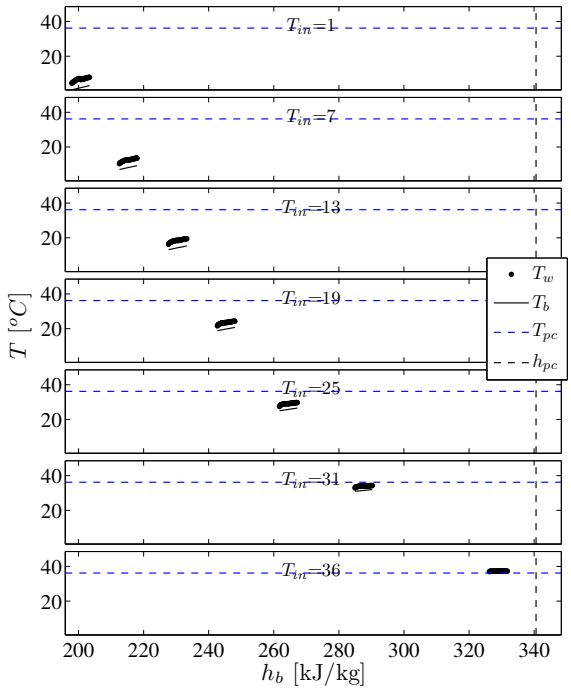


(b) Select cases

Figure A.98: Temperature profiles for $P/P_c = 1.13$, $G = 200$ kg/m^{2}s, $q = 2$ kW/m^2; units of T_{in} are °C.

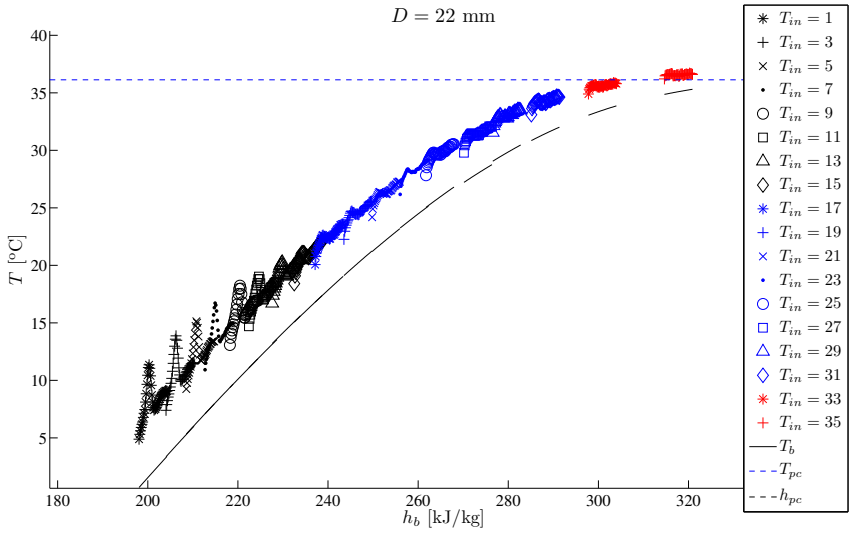


(a) All cases

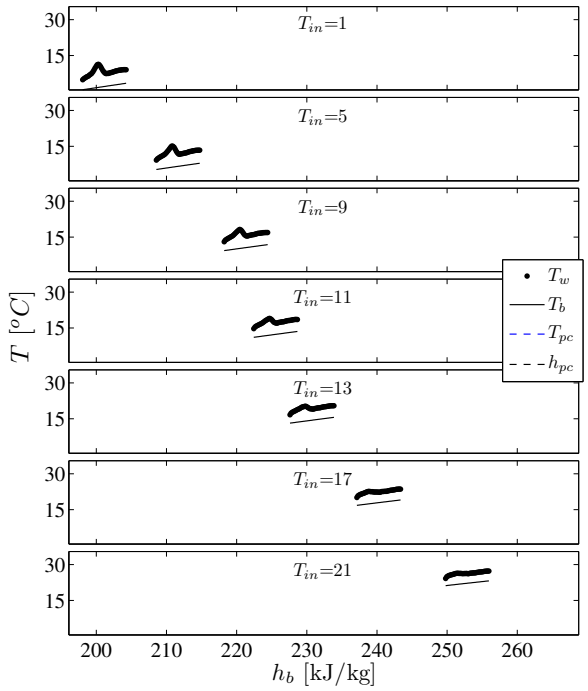


(b) Select cases

Figure A.99: Temperature profiles for $P/P_c = 1.13$, $G = 200$ kg/m^{2}s, $q = 3$ kW/m^2; units of T_{in} are °C.

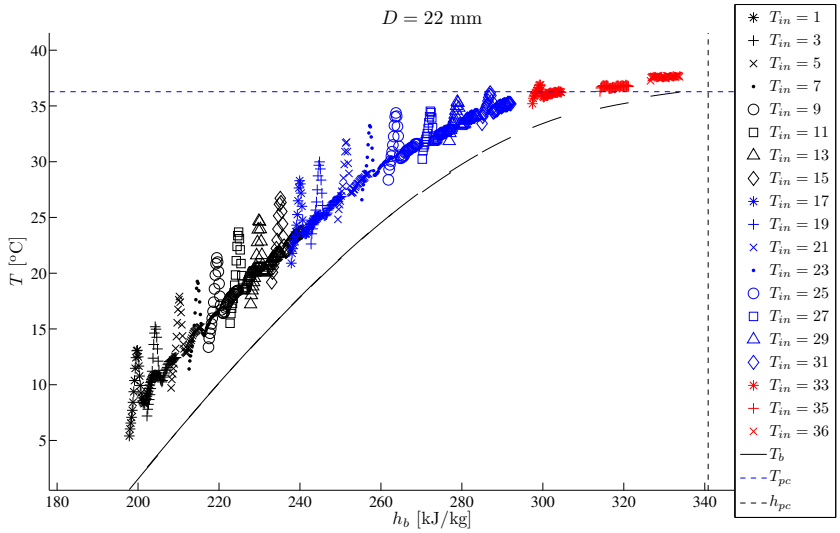


(a) All cases

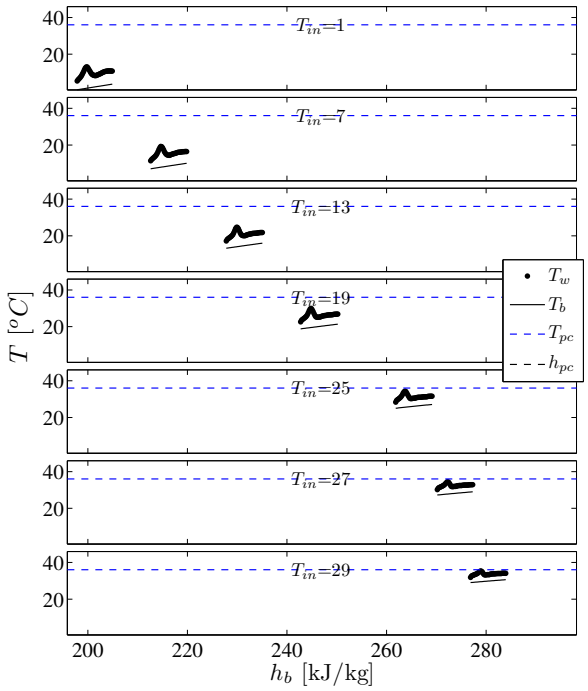


(b) Select cases

Figure A.100: Temperature profiles for $P/P_c = 1.13$, $G = 200$ kg/m^{2}s, $q = 3.5$ kW/m^2; units of T_{in} are °C.

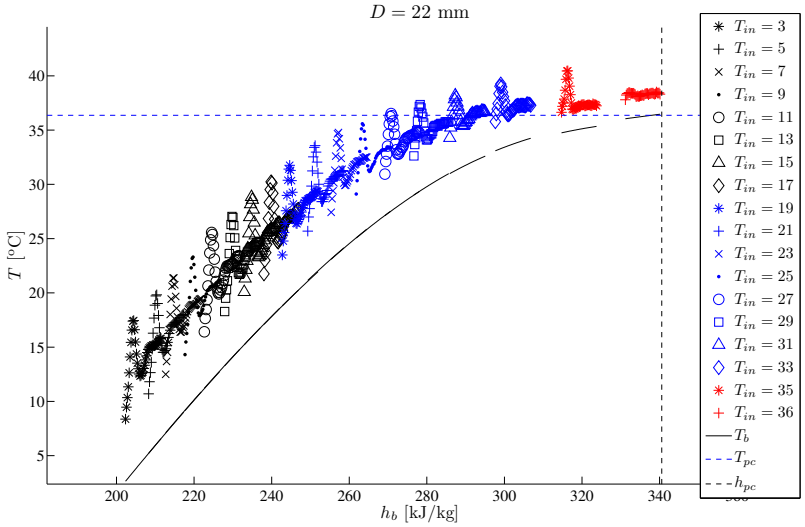


(a) All cases

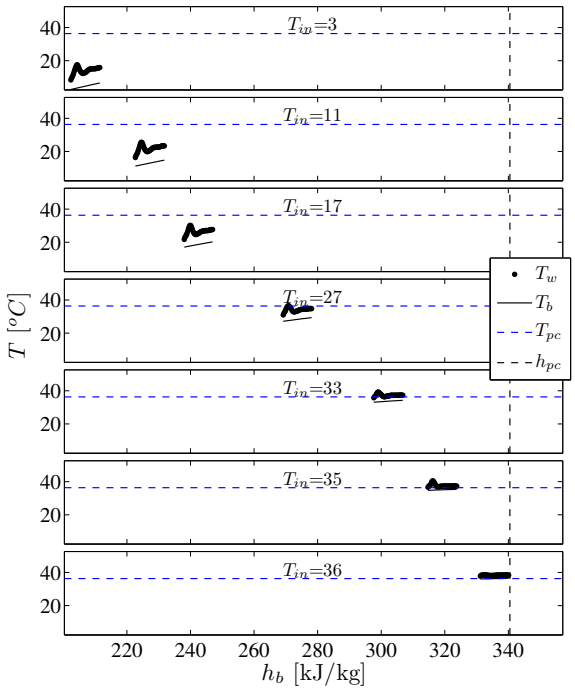


(b) Select cases

Figure A.101: Temperature profiles for $P/P_c = 1.13$, $G = 200$ kg/m^{2}s, $q = 4$ kW/m^2; units of T_{in} are °C.

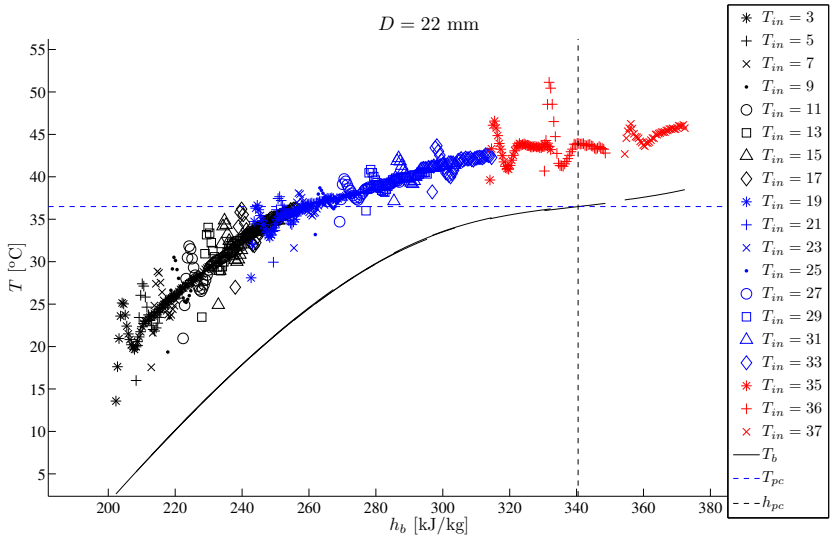


(a) All cases

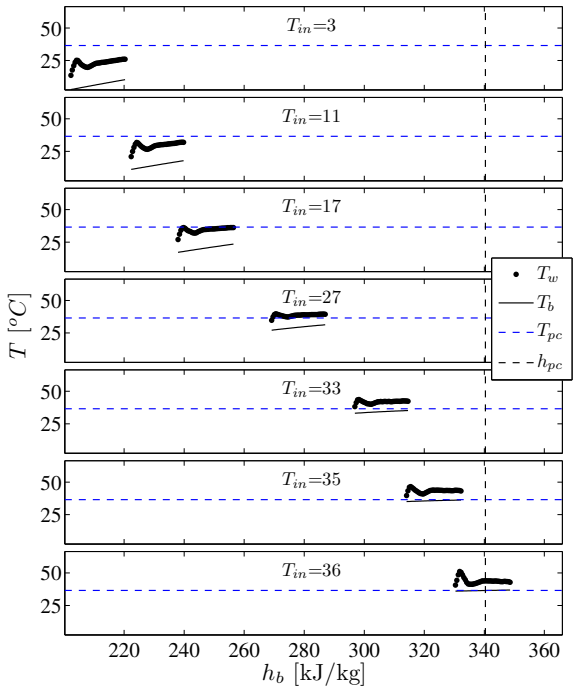


(b) Select cases

Figure A.102: Temperature profiles for $P/P_c = 1.13$, $G = 200$ kg/m^{2}s, $q = 5$ kW/m^2; units of T_{in} are °C.



(a) All cases



(b) Select cases

Figure A.103: Temperature profiles for $P/P_c = 1.13$, $G = 200$ kg/m^{2}s, $q = 10$ kW/m^2; units of T_{in} are °C.

$D = 22$ mm

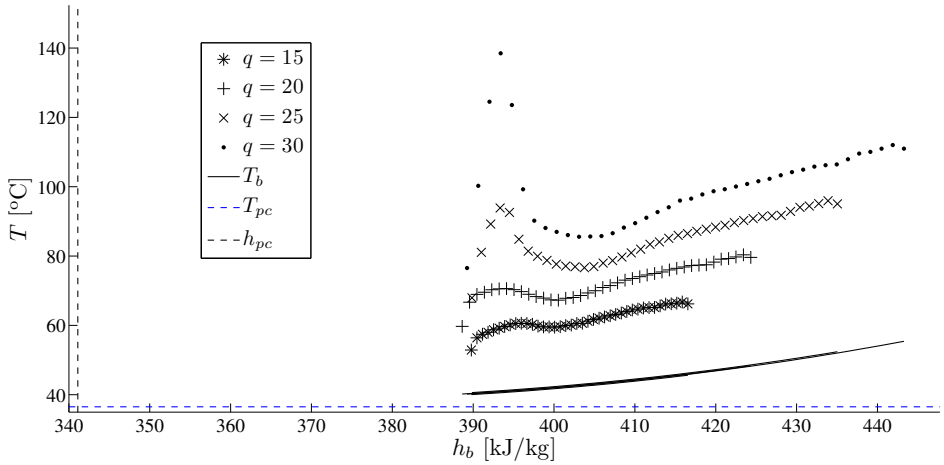
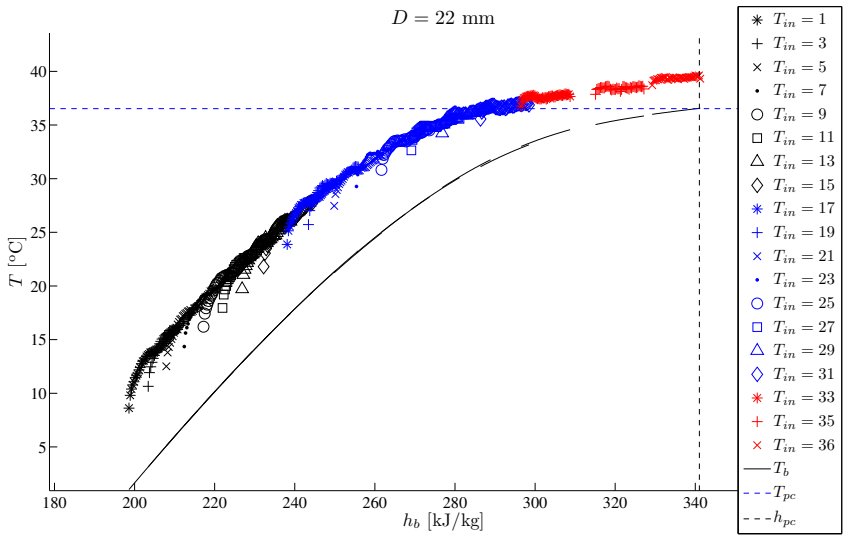
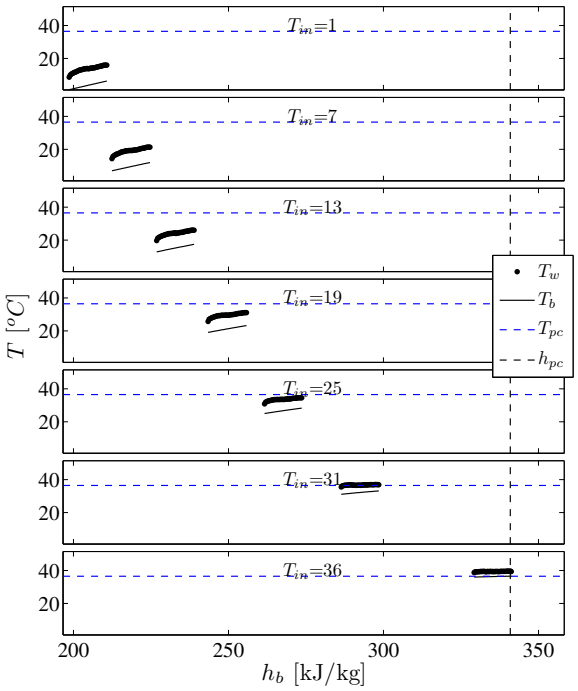


Figure A.104: Temperature profiles for $P/P_c = 1.13$, $G = 200$ kg/m^{2}s, $T_{in} = 40$ °C; units of q are kW/m^2.

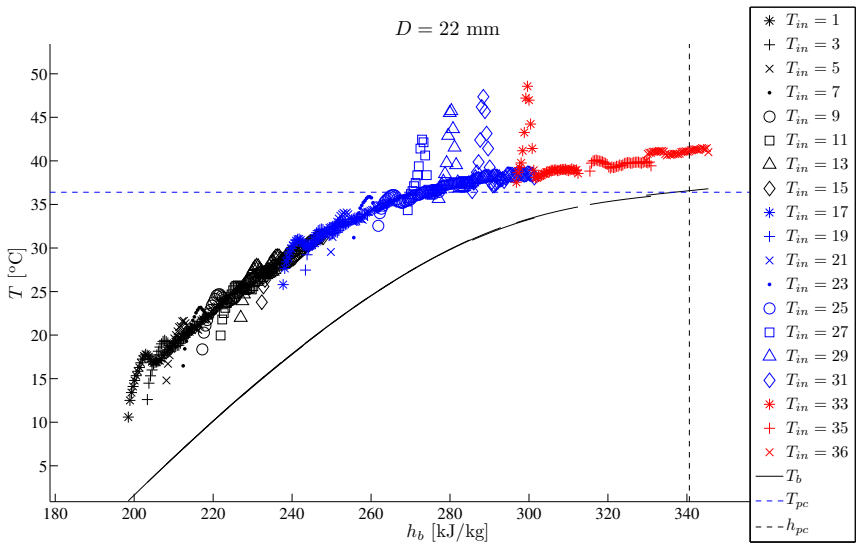


(a) All cases

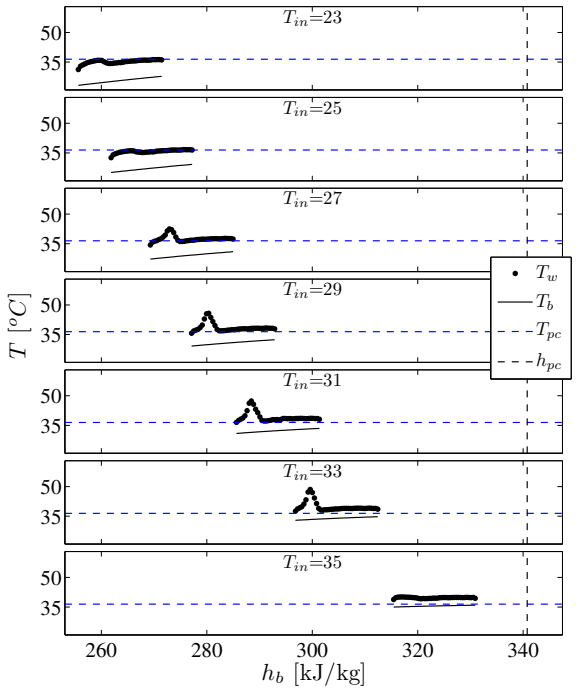


(b) Select cases

Figure A.105: Temperature profiles for $P/P_c = 1.13$, $G = 300$ kg/m^{2}s, $q = 10$ kW/m^2; units of T_{in} are °C.

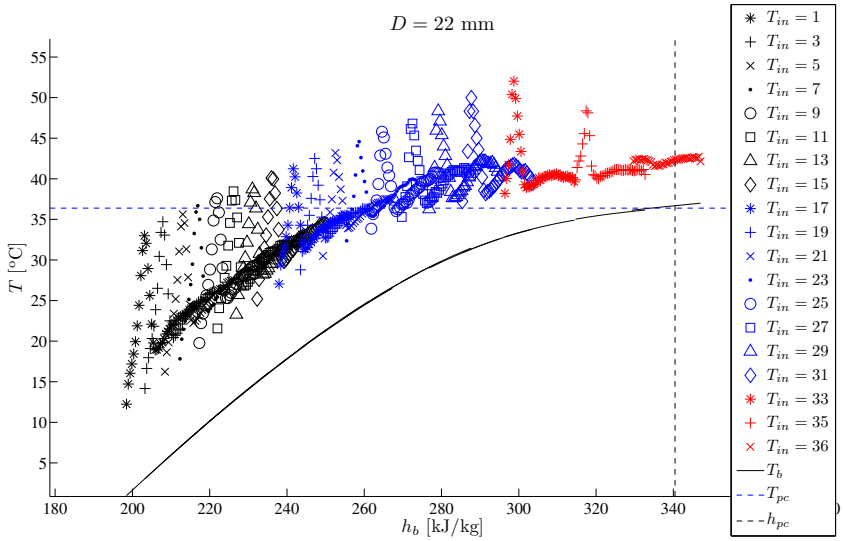


(a) All cases

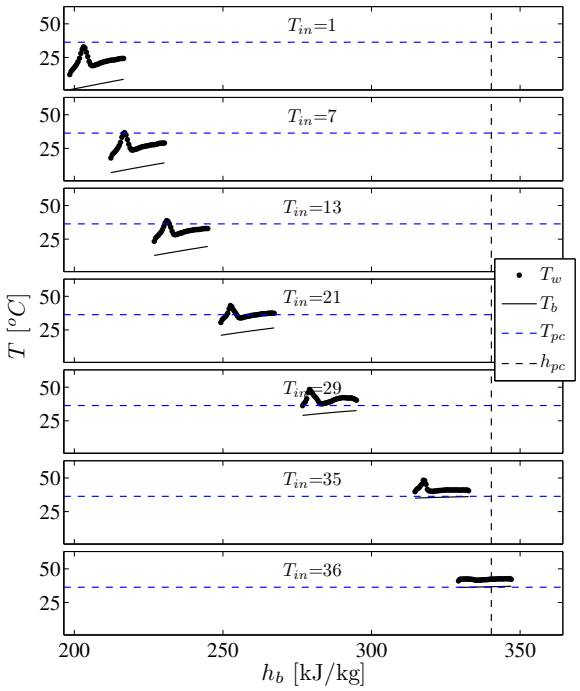


(b) Select cases

Figure A.106: Temperature profiles for $P/P_c = 1.13$, $G = 300$ kg/m^{2}s, $q = 13$ kW/m^2; units of T_{in} are °C.

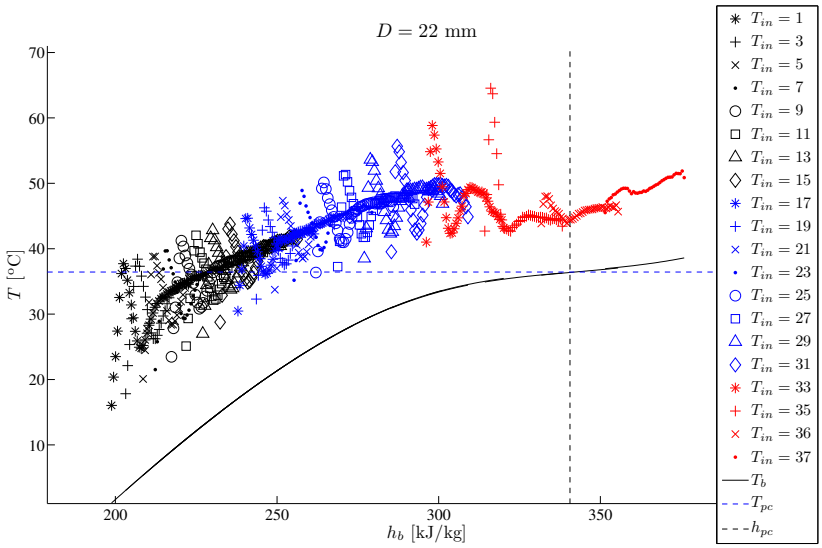


(a) All cases

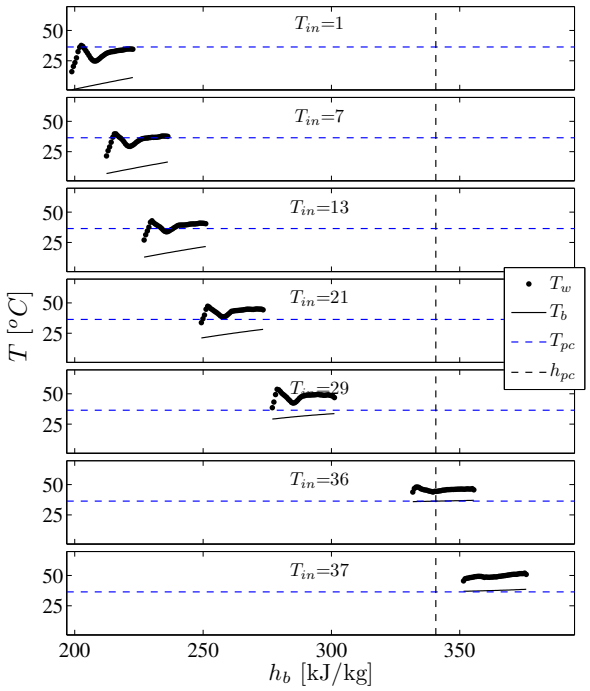


(b) Select cases

Figure A.107: Temperature profiles for $P/P_c = 1.13$, $G = 300$ kg/m^{2}s, $q = 15$ kW/m^2; units of T_{in} are °C.



(a) All cases



(b) Select cases

Figure A.108: Temperature profiles for $P/P_c = 1.13$, $G = 300$ kg/m^{2}s, $q = 20$ kW/m^2; units of T_{in} are °C.

$D = 22$ mm

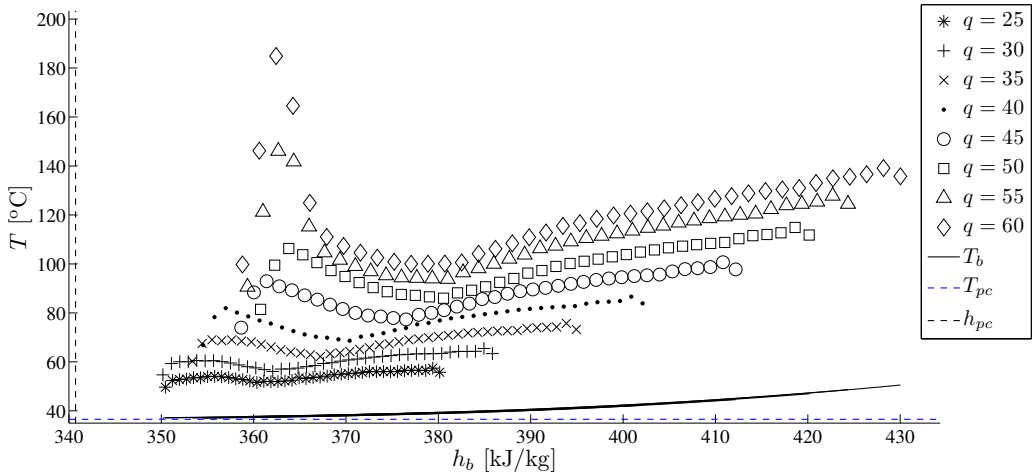
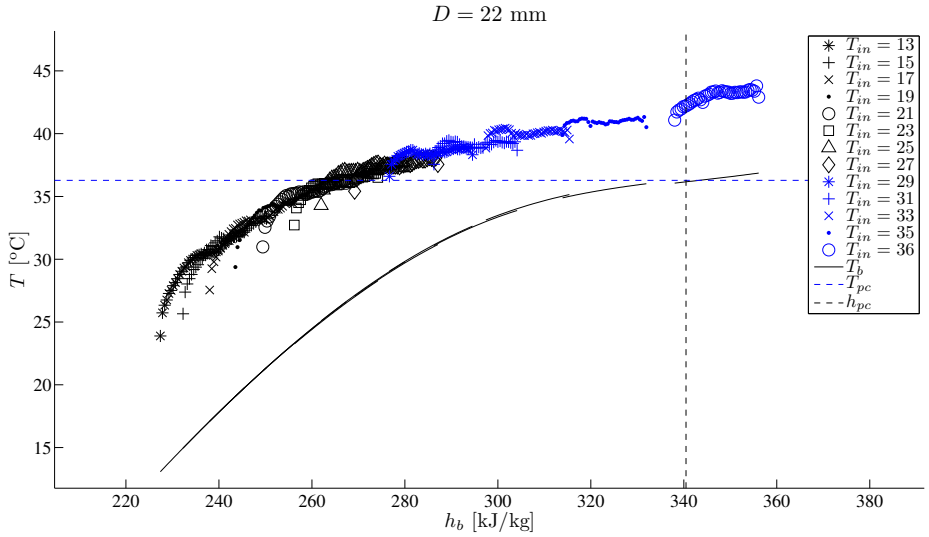
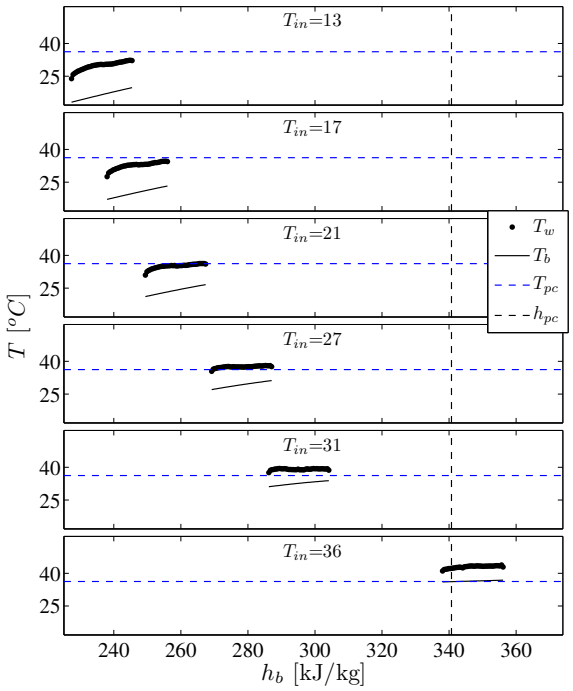


Figure A.109: Temperature profiles for $P/P_c = 1.13$, $G = 300$ kg/m^{2}s, $T_{in} = 37$ °C; units of q are kW/m^2.

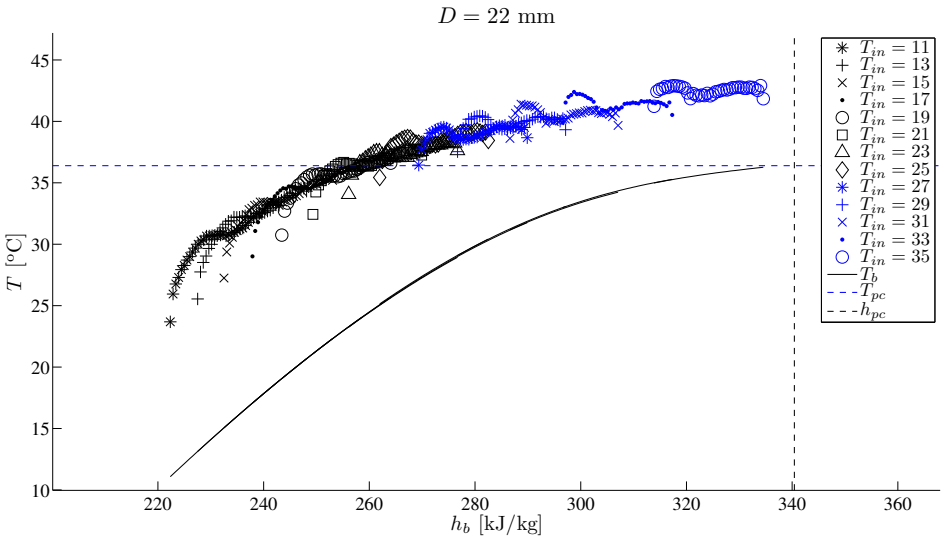


(a) All cases

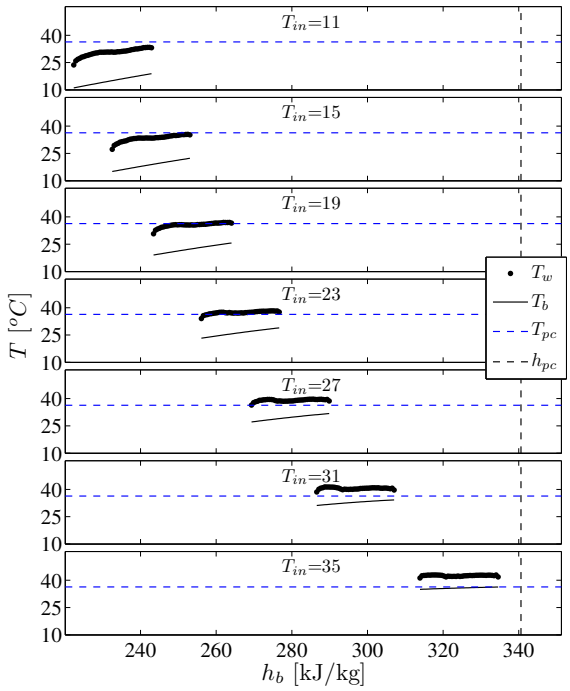


(b) Select cases

Figure A.110: Temperature profiles for $P/P_c = 1.13$, $G = 400$ kg/m^{2}s, $q = 20$ kW/m^2; units of T_{in} are °C.

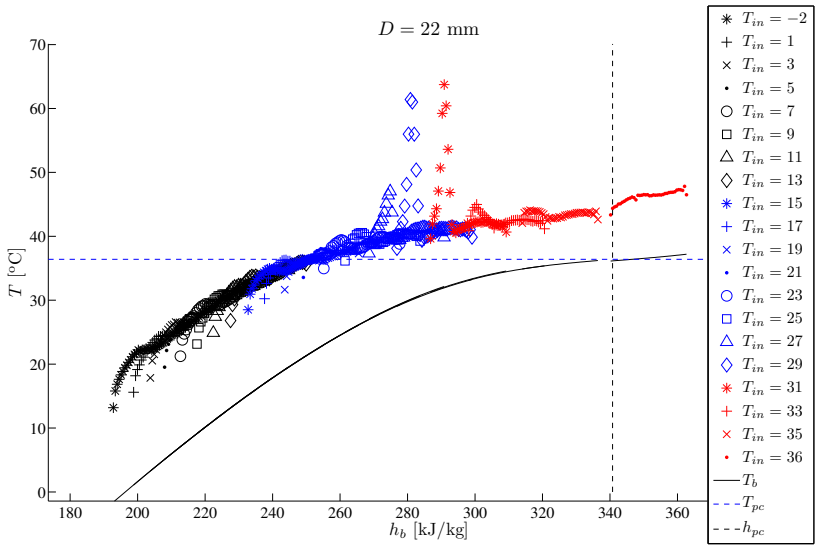


(a) All cases

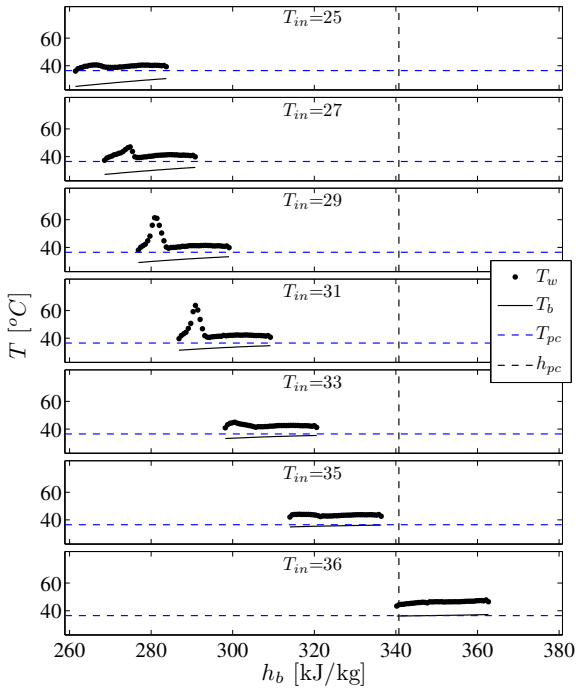


(b) Select cases

Figure A.111: Temperature profiles for $P/P_c = 1.13$, $G = 400$ kg/m^{2}s, $q = 23$ kW/m^2; units of T_{in} are °C.

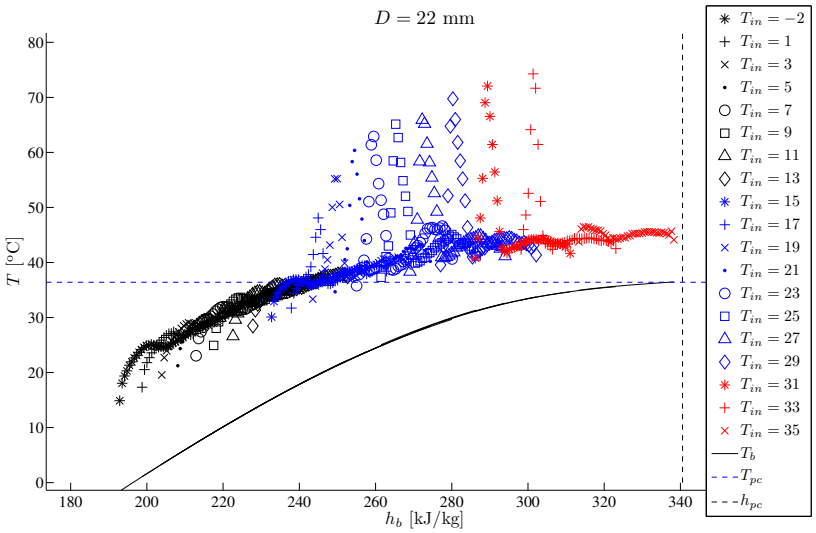


(a) All cases

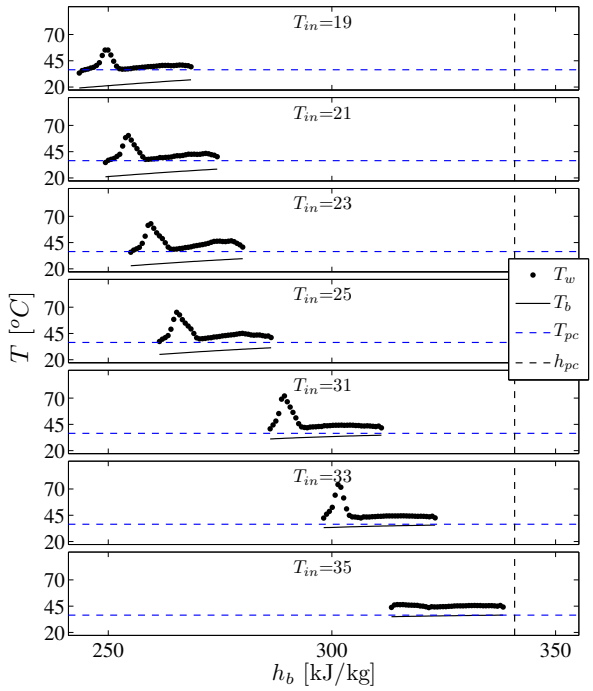


(b) Select cases

Figure A.112: Temperature profiles for $P/P_c = 1.13$, $G = 400$ kg/m^{2}s, $q = 25$ kW/m^2; units of T_{in} are °C.

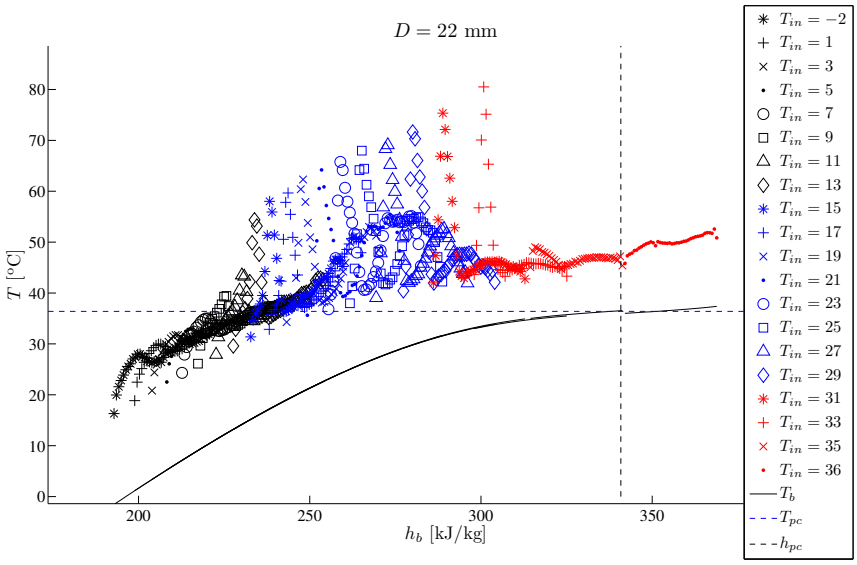


(a) All cases

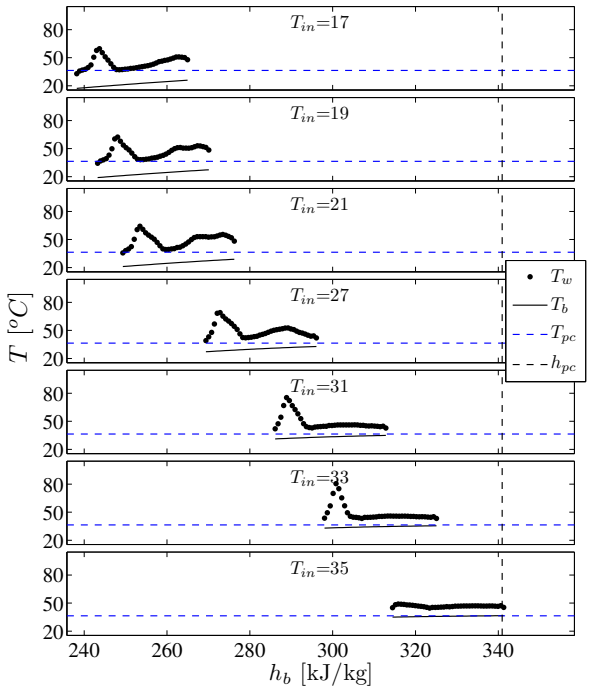


(b) Select cases

Figure A.113: Temperature profiles for $P/P_c = 1.13$, $G = 400$ kg/m^{2}s, $q = 28$ kW/m^2; units of T_{in} are °C.

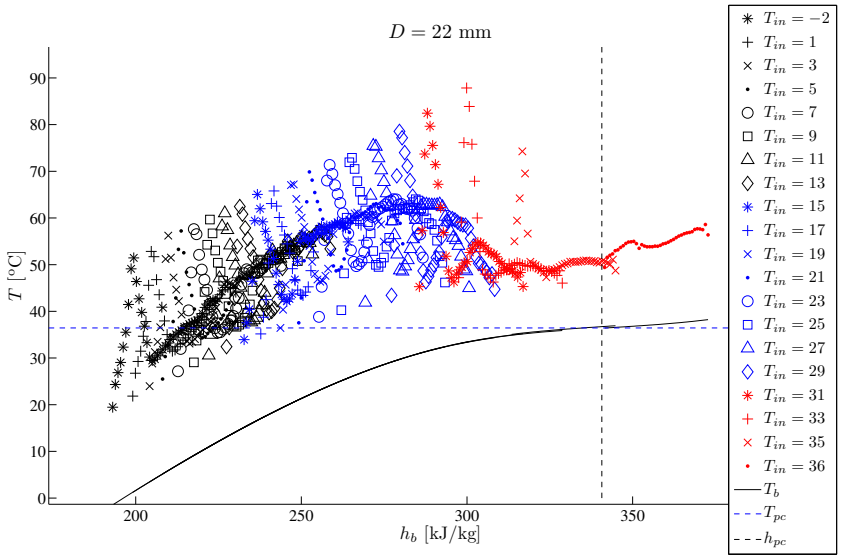


(a) All cases

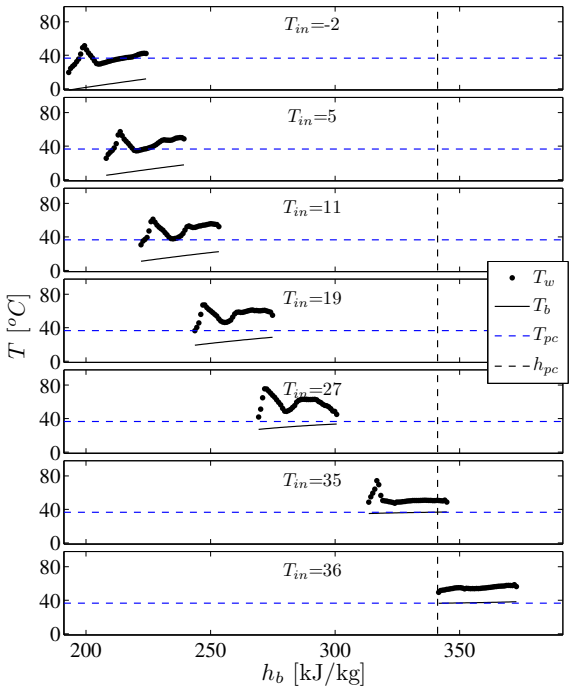


(b) Select cases

Figure A.114: Temperature profiles for $P/P_c = 1.13$, $G = 400$ kg/m^{2}s, $q = 30$ kW/m^2; units of T_{in} are °C.



(a) All cases



(b) Select cases

Figure A.115: Temperature profiles for $P/P_c = 1.13$, $G = 400$ kg/m^{2}s, $q = 35$ kW/m^2; units of T_{in} are °C.

$D = 22$ mm

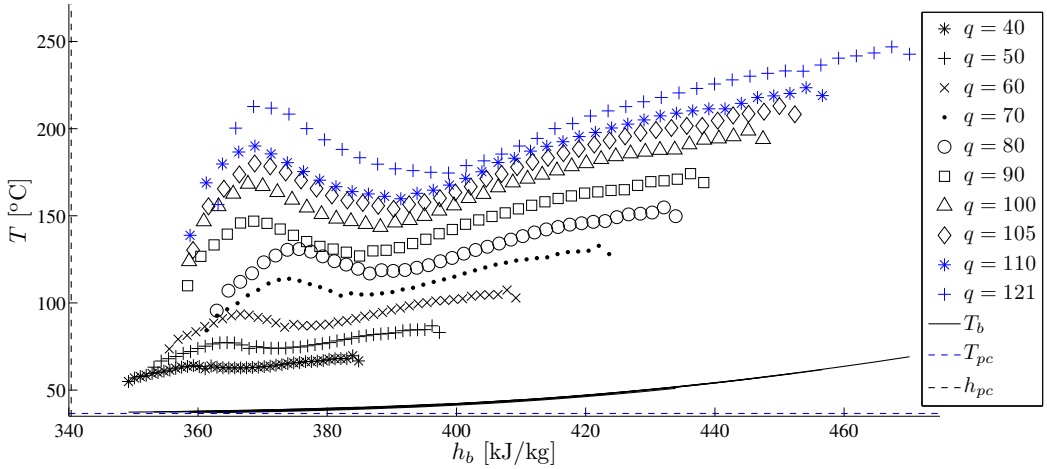
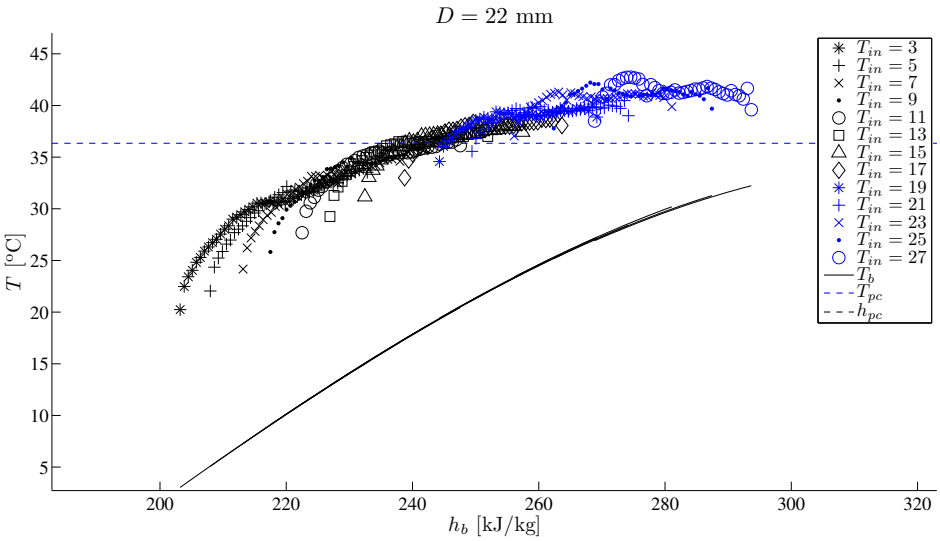
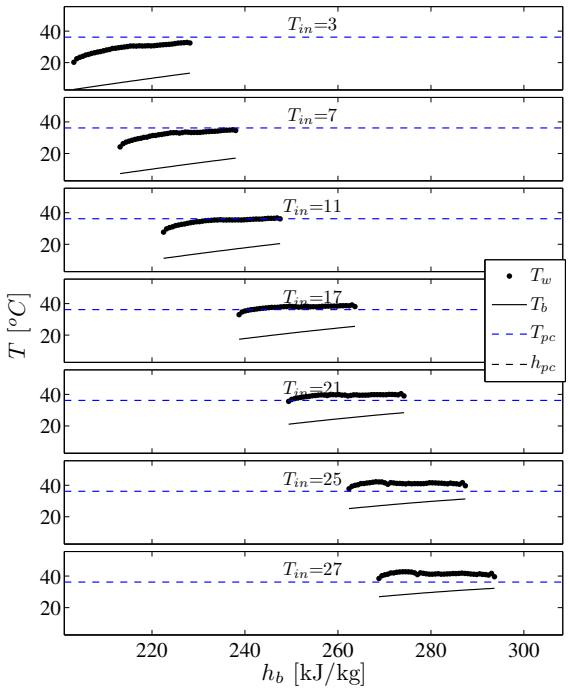


Figure A.116: Temperature profiles for $P/P_c = 1.13$, $G = 400$ kg/m^{2}s, $T_{in} = 37$ °C; units of q are kW/m^2.

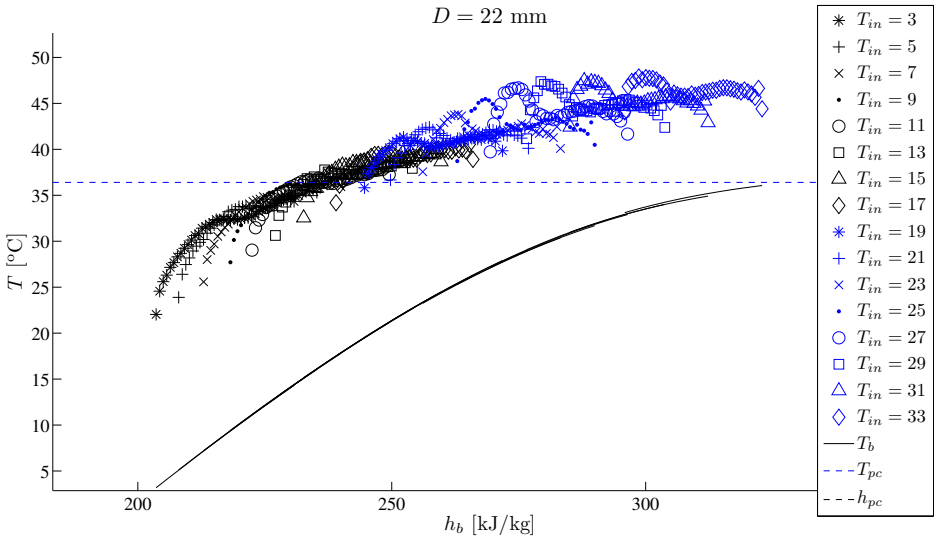


(a) All cases

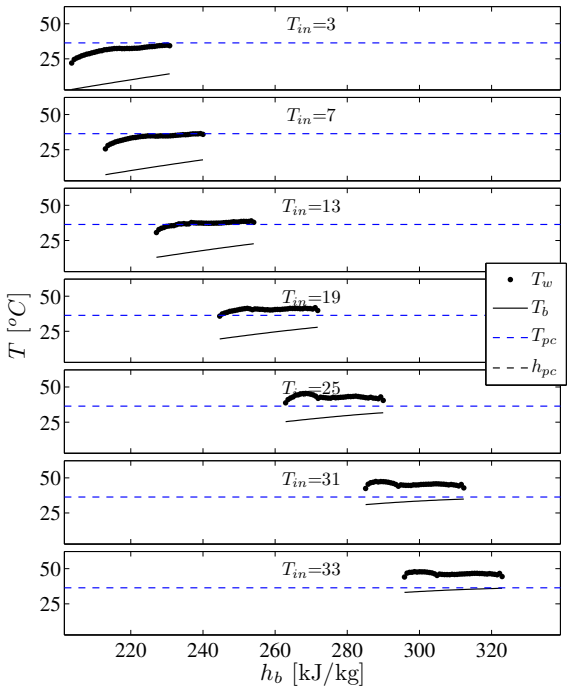


(b) Select cases

Figure A.117: Temperature profiles for $P/P_c = 1.13$, $G = 500$ kg/m^{2}s, $q = 35$ kW/m^2; units of T_{in} are °C.

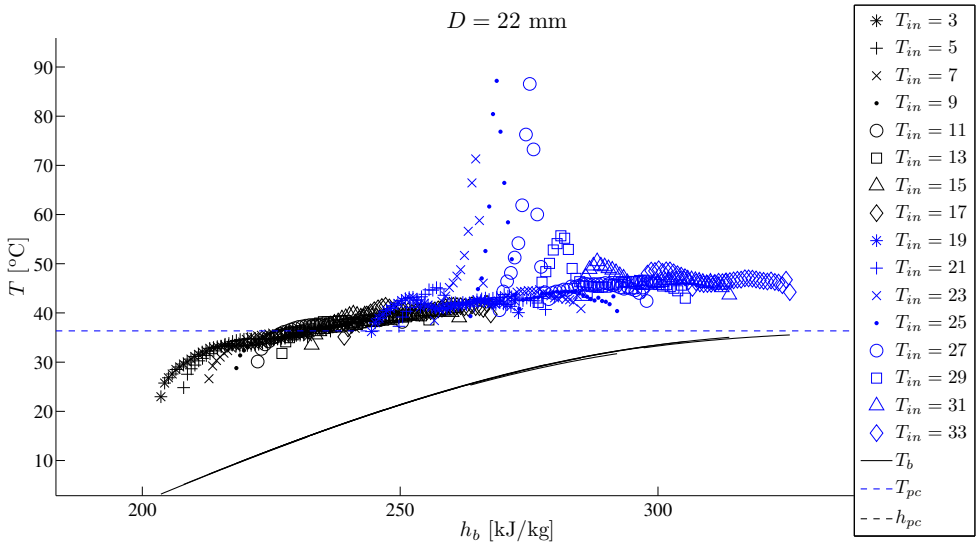


(a) All cases

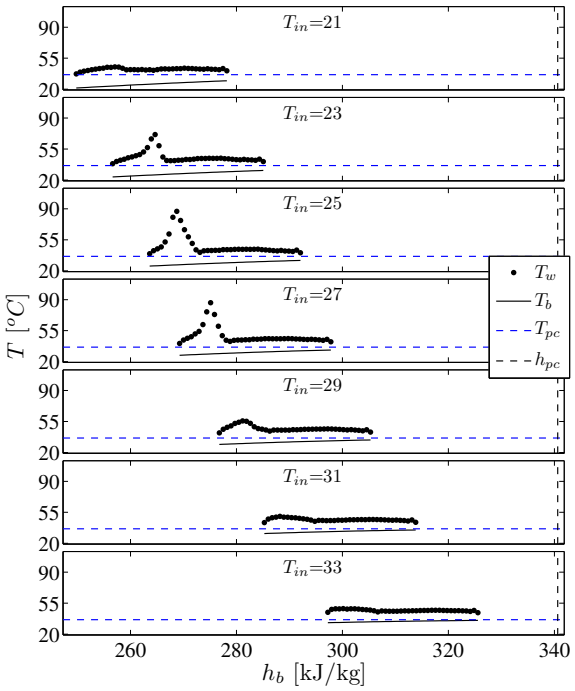


(b) Select cases

Figure A.118: Temperature profiles for $P/P_c = 1.13$, $G = 500$ kg/m^{2}s, $q = 38$ kW/m^2; units of T_{in} are °C.

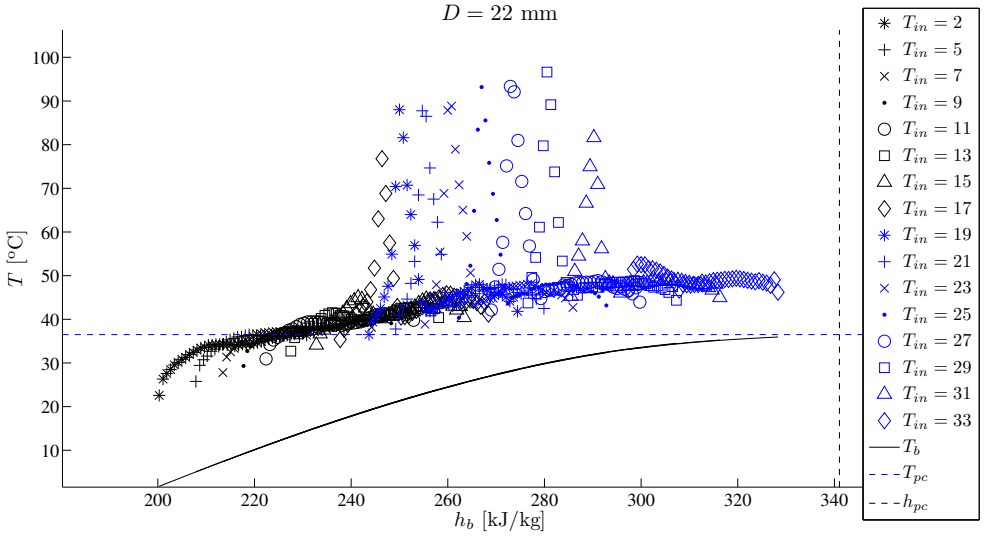


(a) All cases

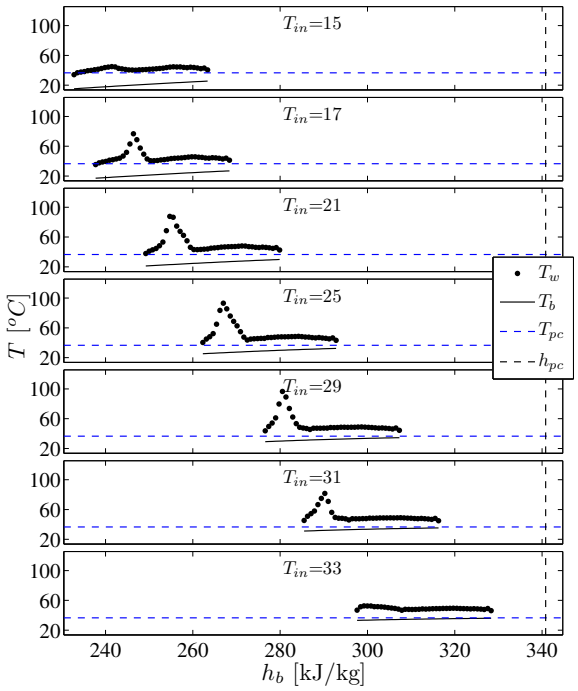


(b) Select cases

Figure A.119: Temperature profiles for $P/P_c = 1.13$, $G = 500$ kg/m^{2}s, $q = 40$ kW/m^2; units of T_{in} are °C.

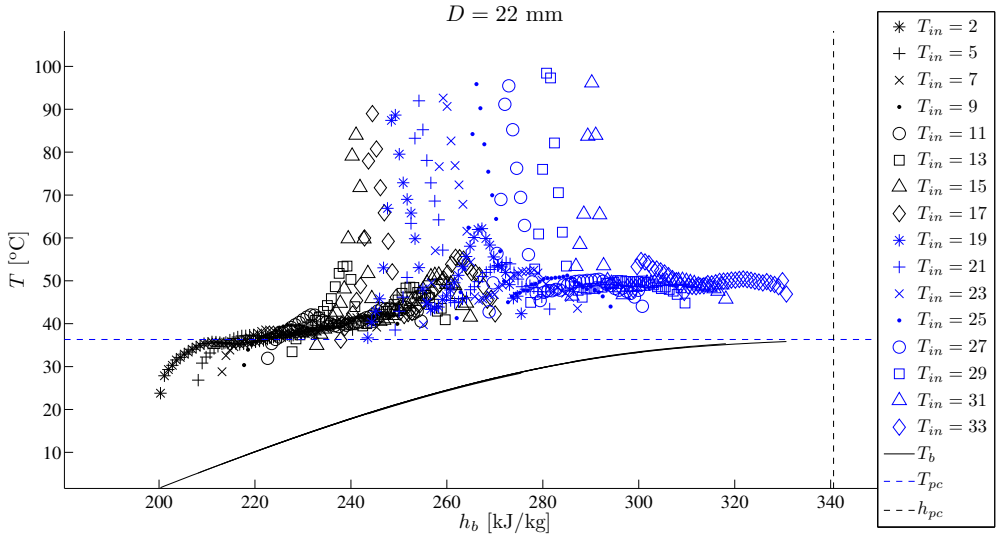


(a) All cases

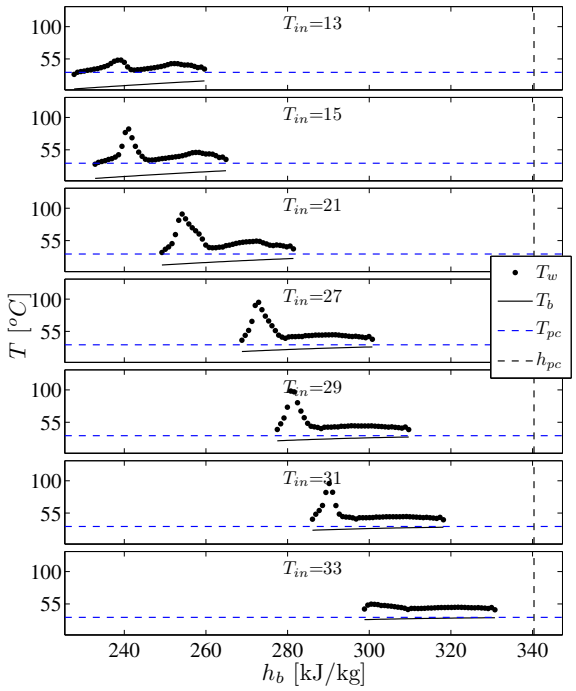


(b) Select cases

Figure A.120: Temperature profiles for $P/P_c = 1.13$, $G = 500$ kg/m^{2}s, $q = 43$ kW/m^2; units of T_{in} are °C.

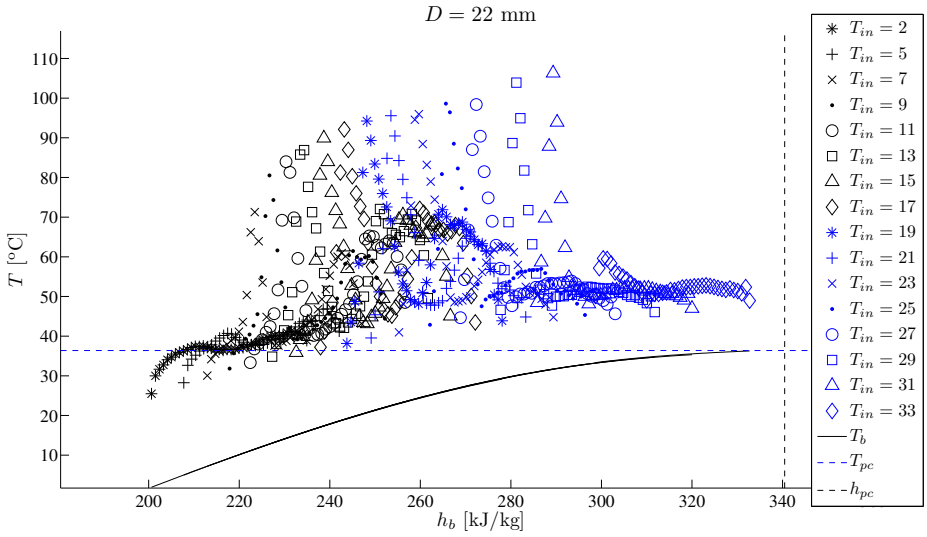


(a) All cases

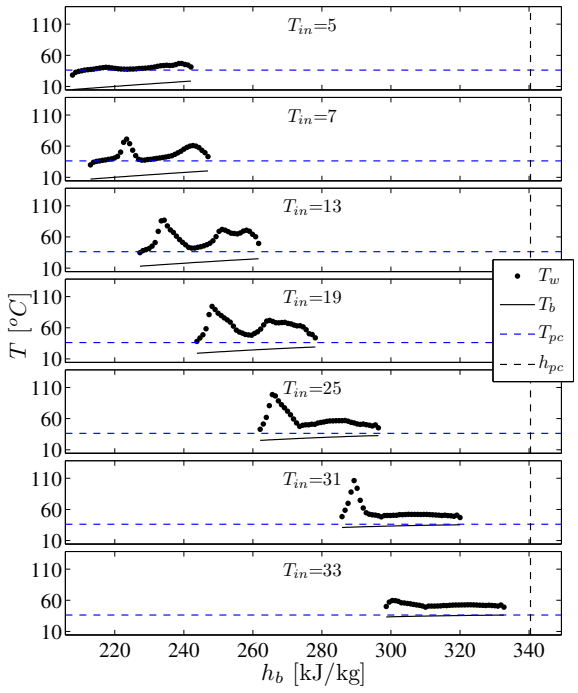


(b) Select cases

Figure A.121: Temperature profiles for $P/P_c = 1.13$, $G = 500$ kg/m^{2}s, $q = 45$ kW/m^2; units of T_{in} are °C.

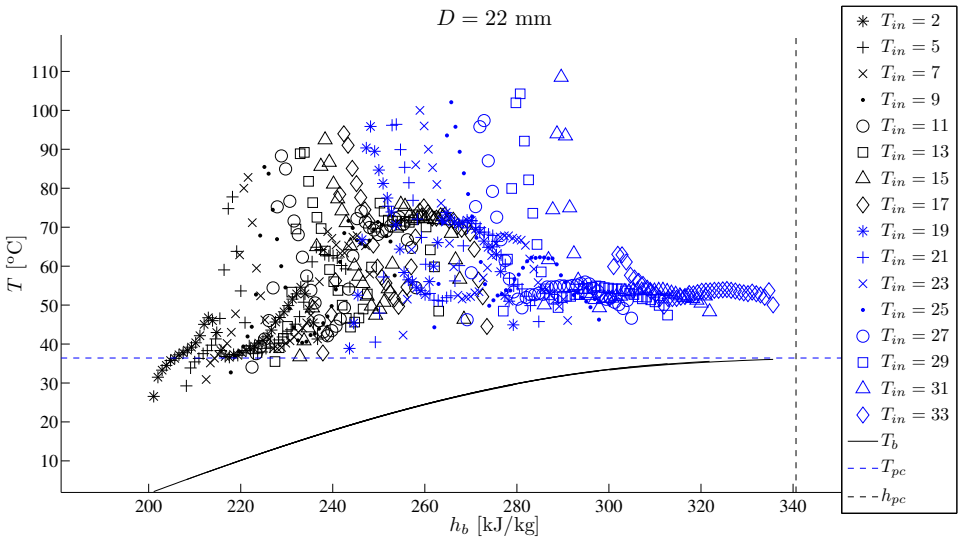


(a) All cases

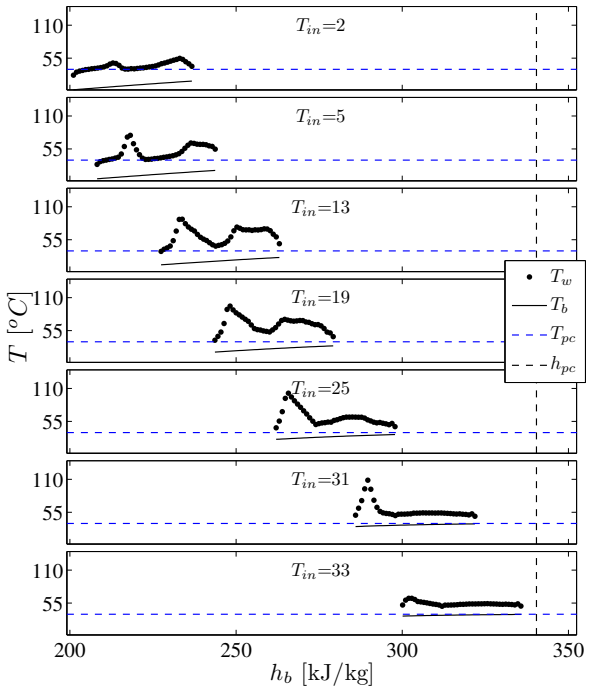


(b) Select cases

Figure A.122: Temperature profiles for $P/P_c = 1.13$, $G = 500$ kg/m^{2}s, $q = 48$ kW/m^2; units of T_{in} are °C.

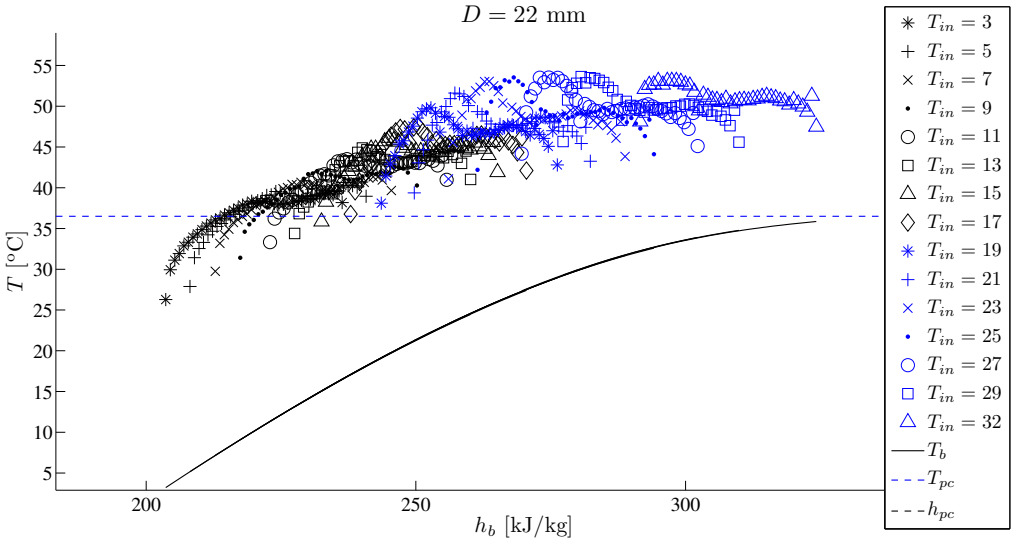


(a) All cases

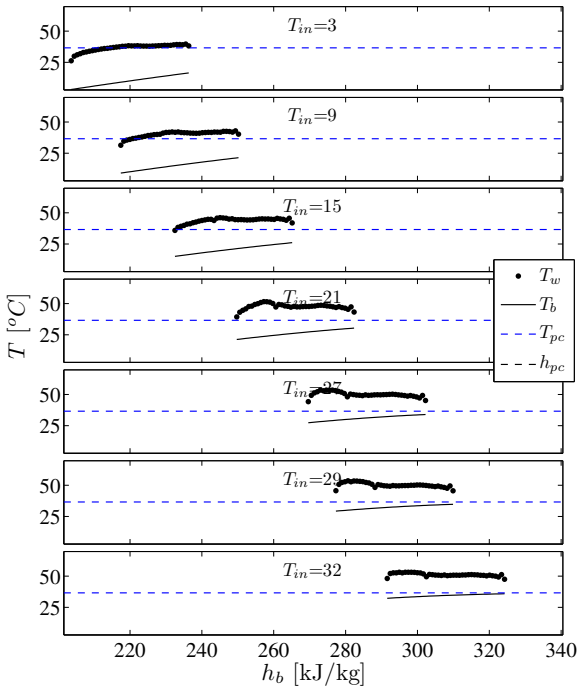


(b) Select cases

Figure A.123: Temperature profiles for $P/P_c = 1.13$, $G = 500$ kg/m^{2}s, $q = 50$ kW/m^2; units of T_{in} are °C.

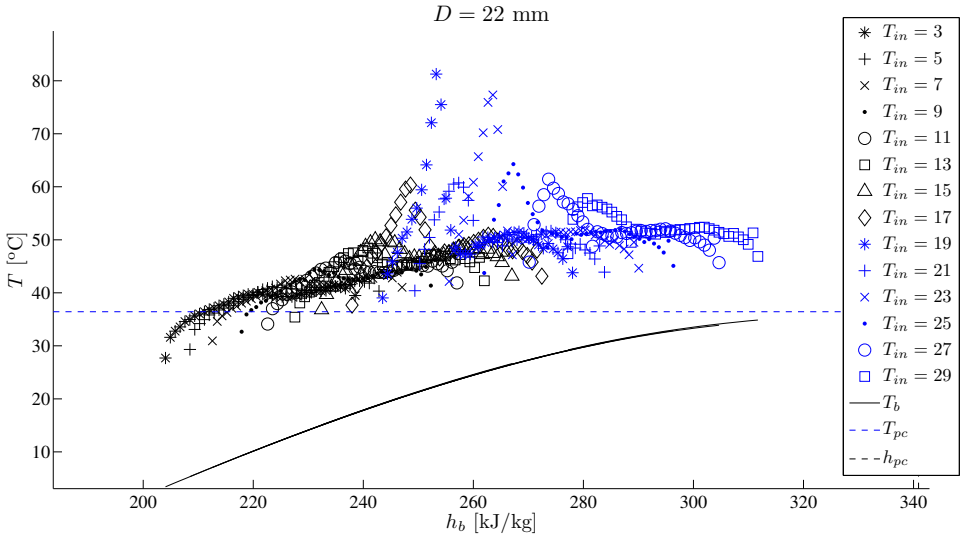


(a) All cases

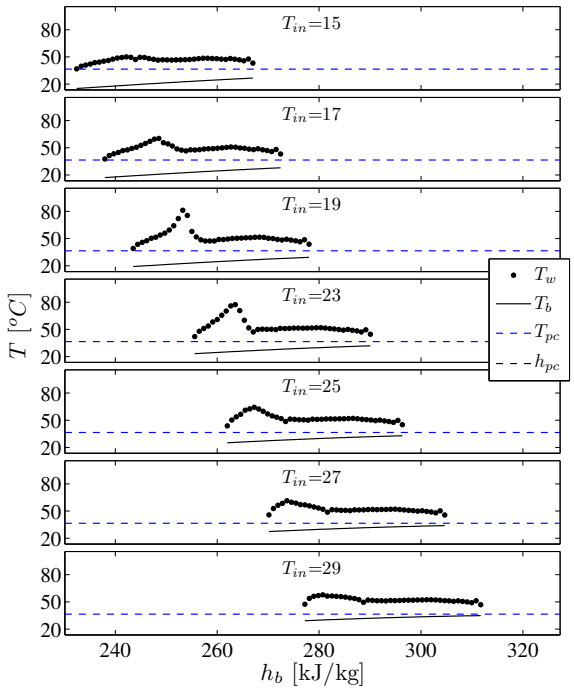


(b) Select cases

Figure A.124: Temperature profiles for $P/P_c = 1.13$, $G = 600$ kg/m^{2}s, $q = 55$ kW/m^2; units of T_{in} are °C.

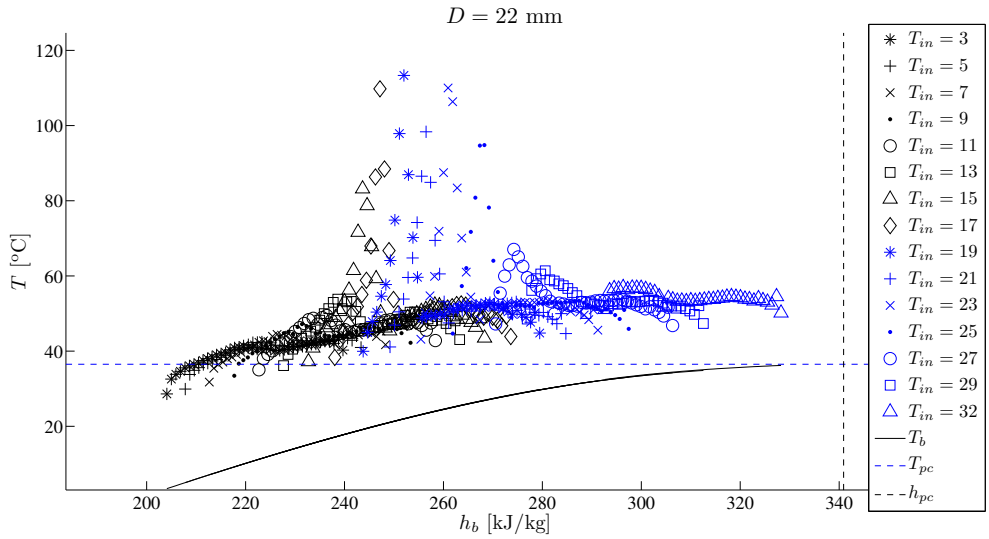


(a) All cases

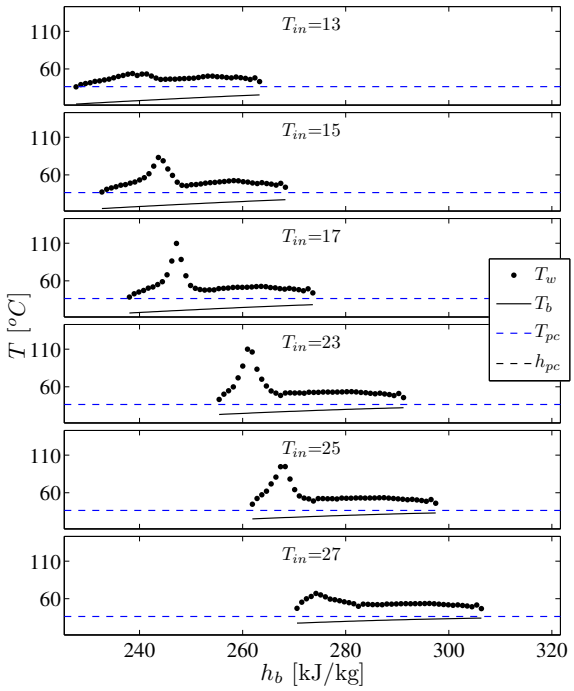


(b) Select cases

Figure A.125: Temperature profiles for $P/P_c = 1.13$, $G = 600$ kg/m^{2}s, $q = 58$ kW/m^2; units of T_{in} are °C.

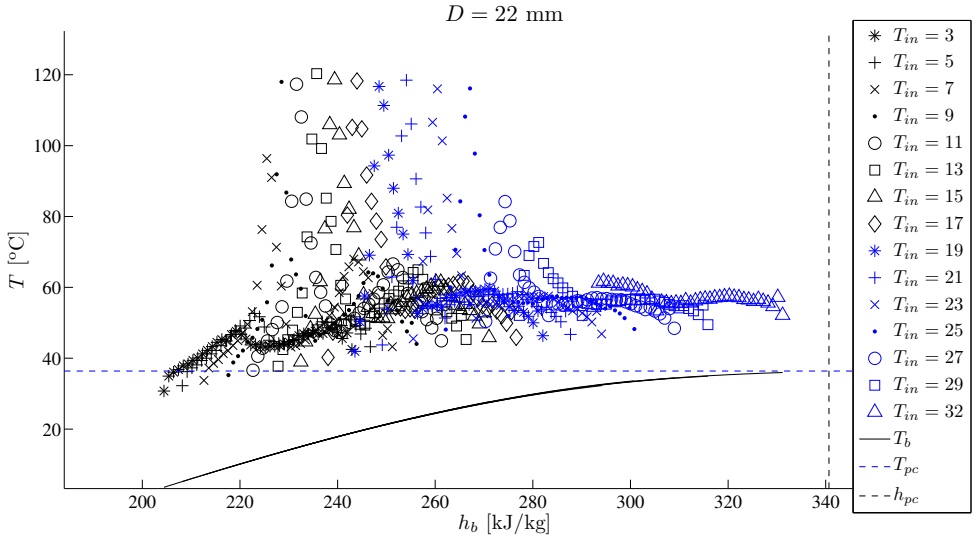


(a) All cases

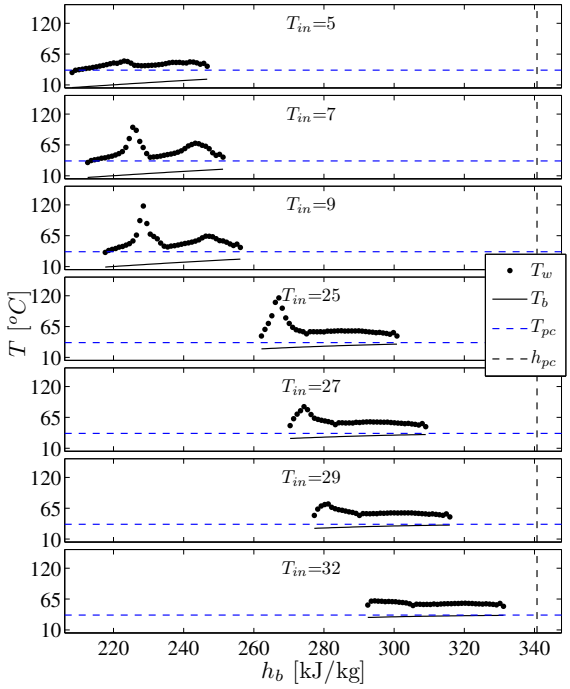


(b) Select cases

Figure A.126: Temperature profiles for $P/P_c = 1.13$, $G = 600$ kg/m^{2}s, $q = 60$ kW/m^2; units of T_{in} are °C.

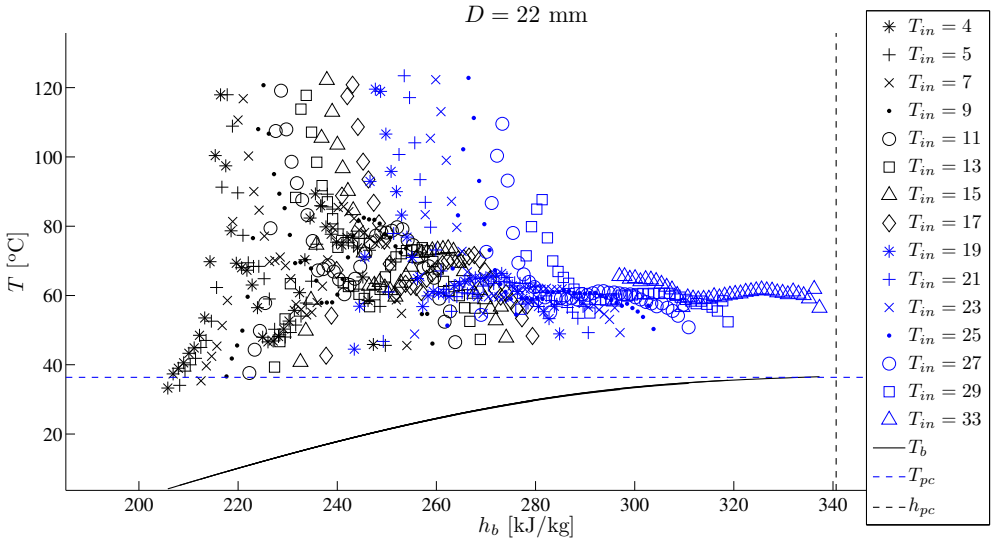


(a) All cases

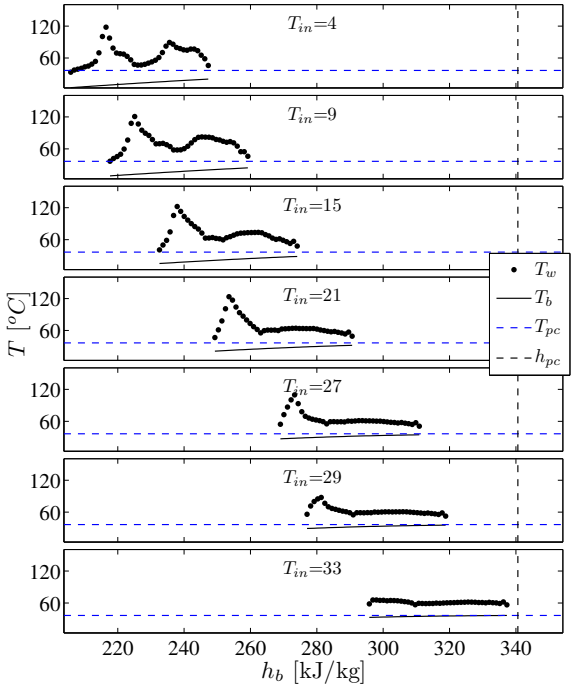


(b) Select cases

Figure A.127: Temperature profiles for $P/P_c = 1.13$, $G = 600$ kg/m^{2}s, $q = 65$ kW/m^2; units of T_{in} are °C.

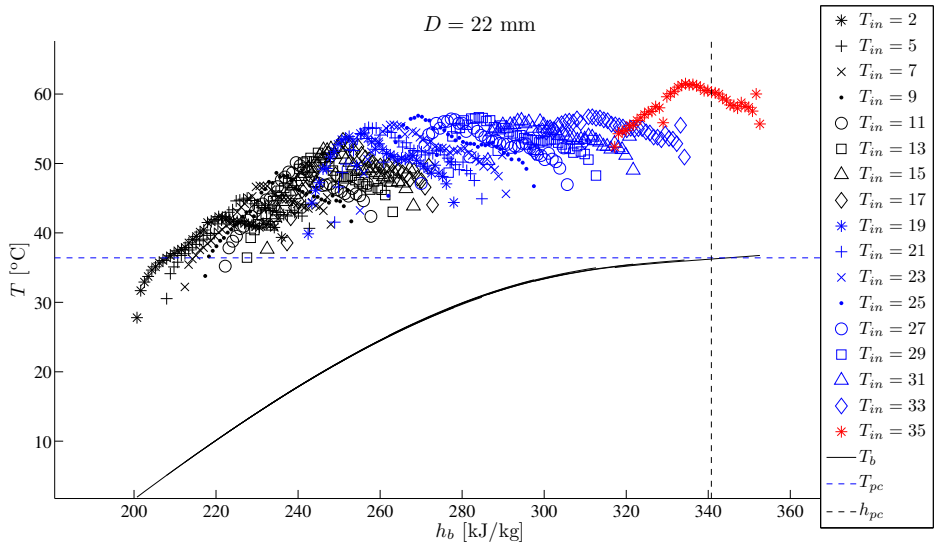


(a) All cases

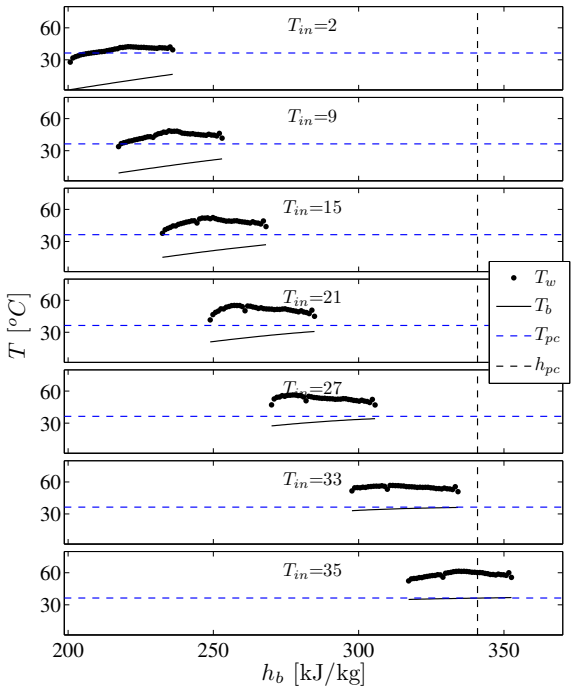


(b) Select cases

Figure A.128: Temperature profiles for $P/P_c = 1.13$, $G = 600$ kg/m^{2}s, $q = 70$ kW/m^2; units of T_{in} are °C.

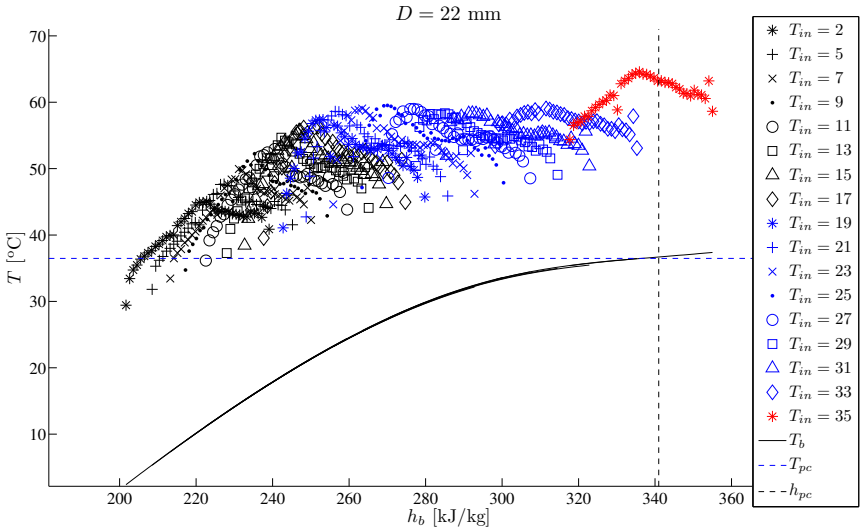


(a) All cases

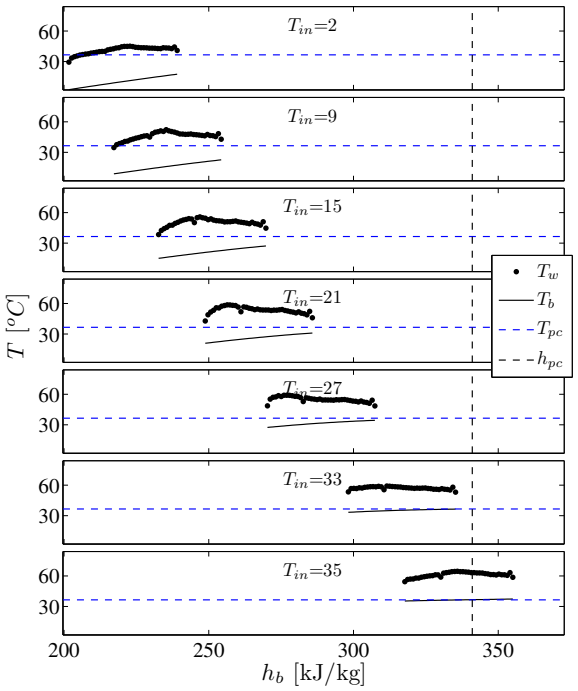


(b) Select cases

Figure A.129: Temperature profiles for $P/P_c = 1.13$, $G = 700$ kg/m^{2}s, $q = 70$ kW/m^2; units of T_{in} are °C.

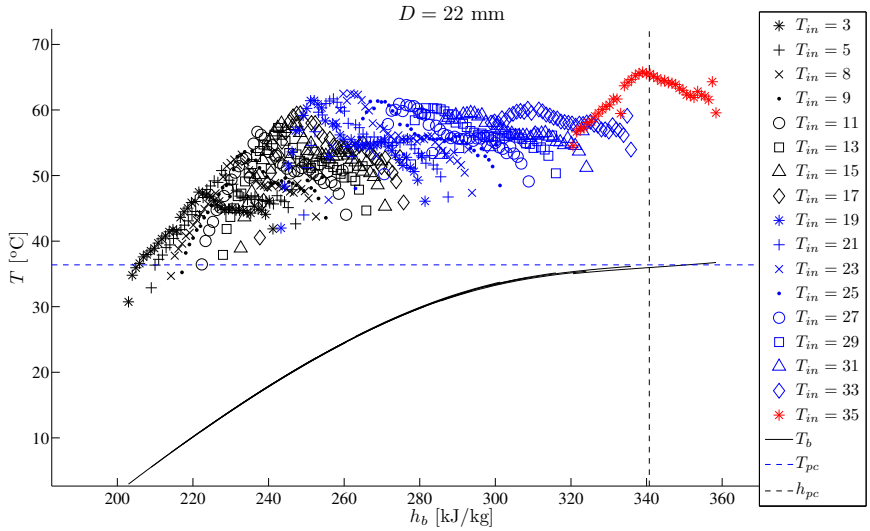


(a) All cases

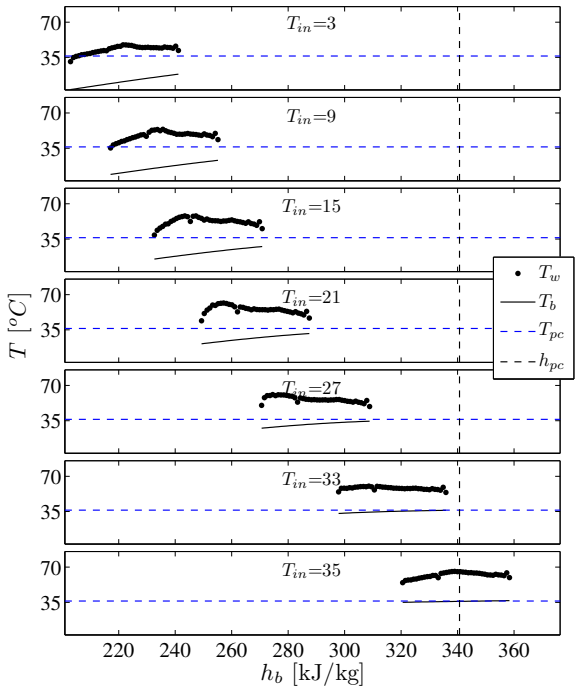


(b) Select cases

Figure A.130: Temperature profiles for $P/P_c = 1.13$, $G = 700$ kg/m^{2}s, $q = 73$ kW/m^2; units of T_{in} are °C.

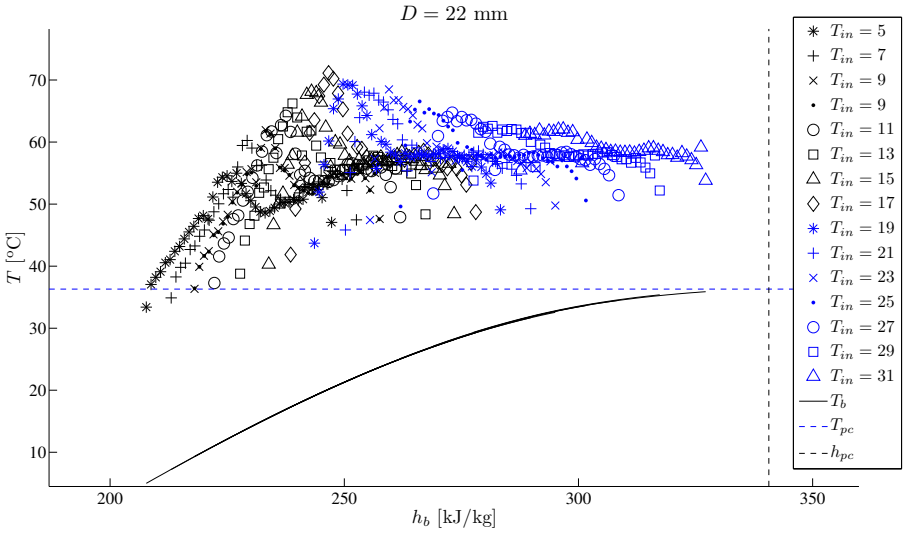


(a) All cases

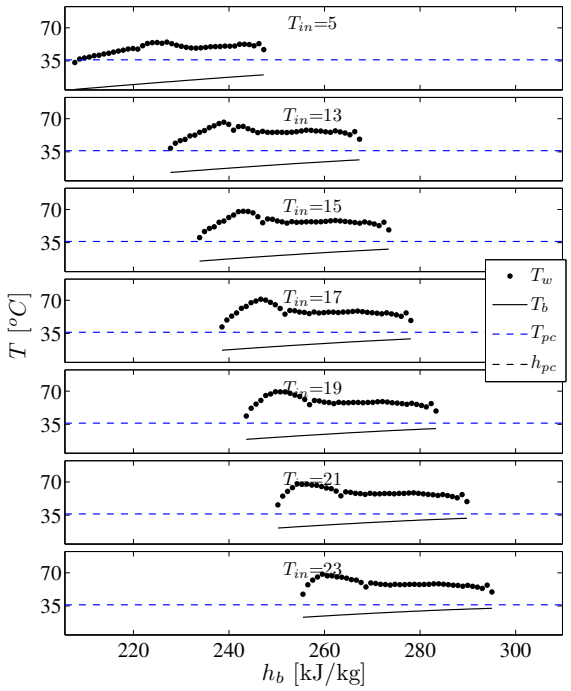


(b) Select cases

Figure A.131: Temperature profiles for $P/P_c = 1.13$, $G = 700$ kg/m^{2}s, $q = 75$ kW/m^2; units of T_{in} are °C.

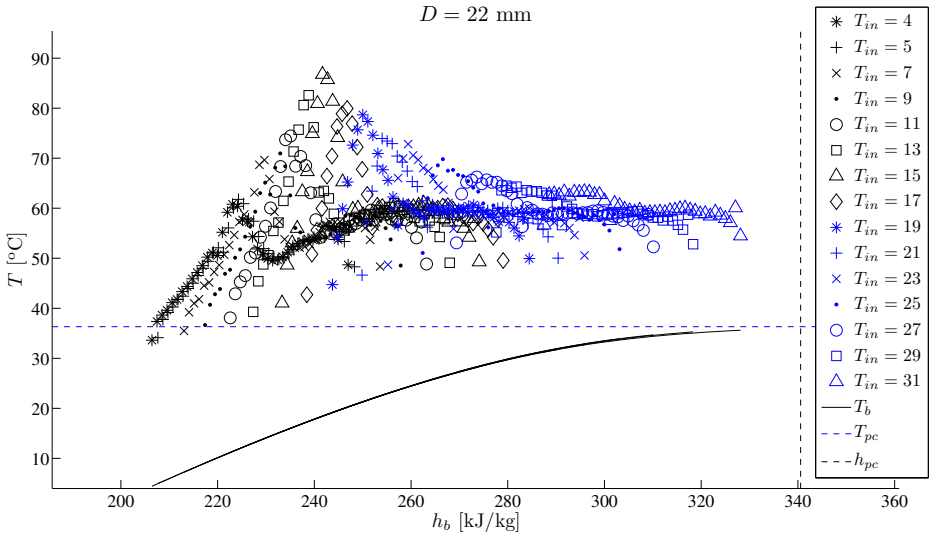


(a) All cases

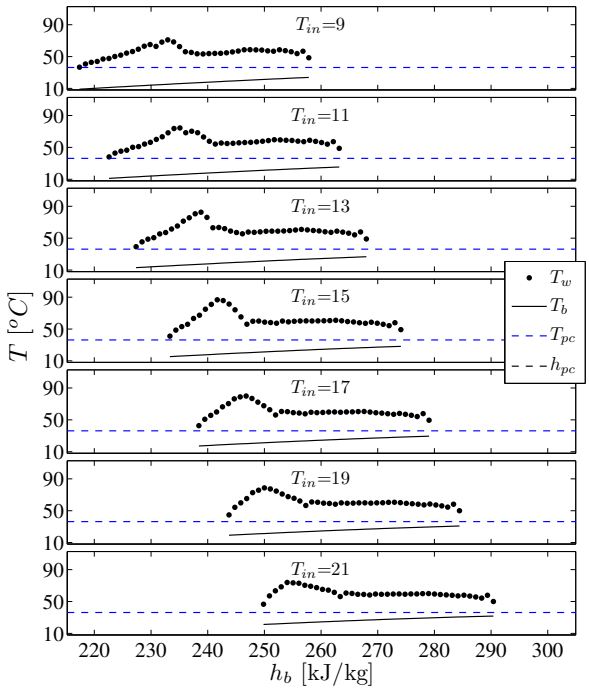


(b) Select cases

Figure A.132: Temperature profiles for $P/P_c = 1.13$, $G = 700$ kg/m^{2}s, $q = 78$ kW/m^2; units of T_{in} are °C.

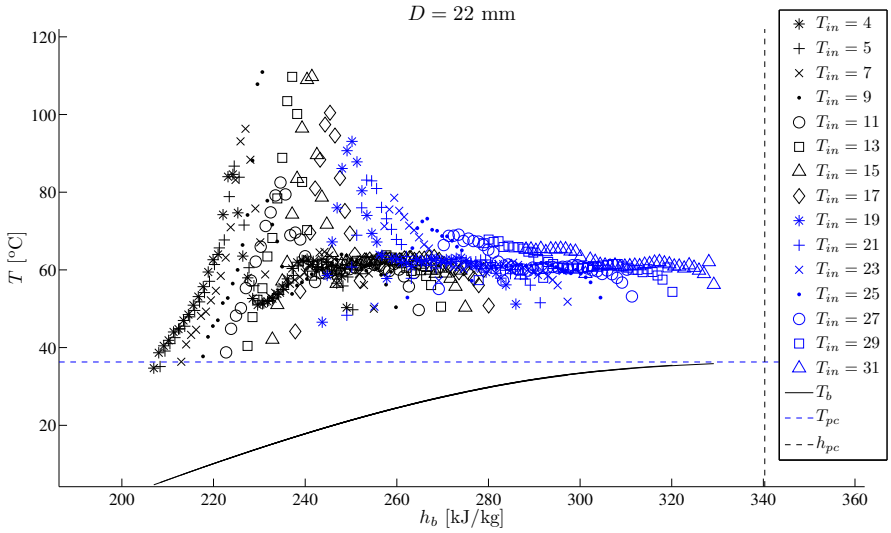


(a) All cases

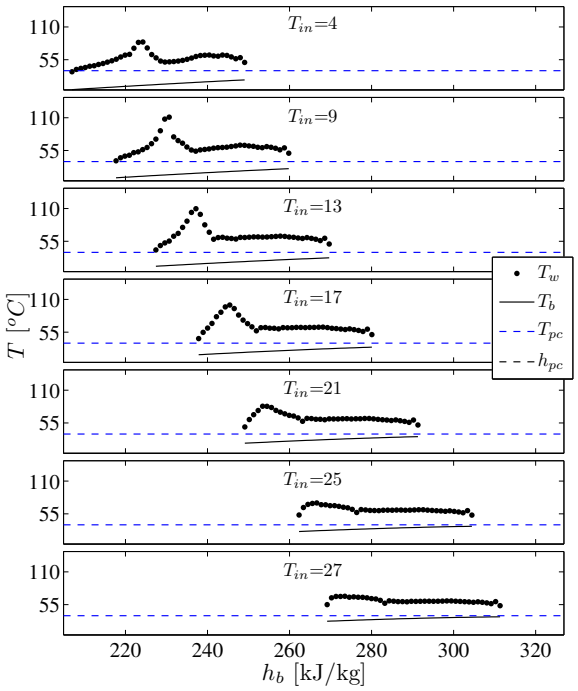


(b) Select cases

Figure A.133: Temperature profiles for $P/P_c = 1.13$, $G = 700$ kg/m^{2}s, $q = 80$ kW/m^2; units of T_{in} are °C.

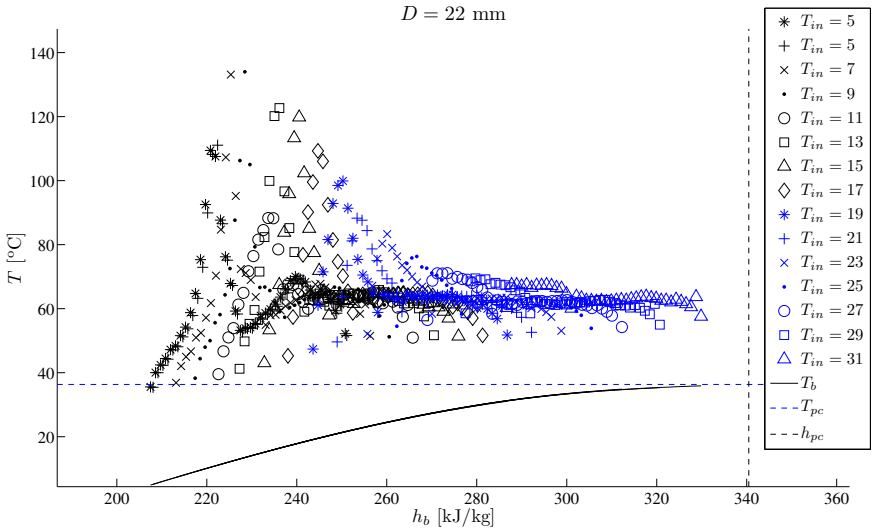


(a) All cases

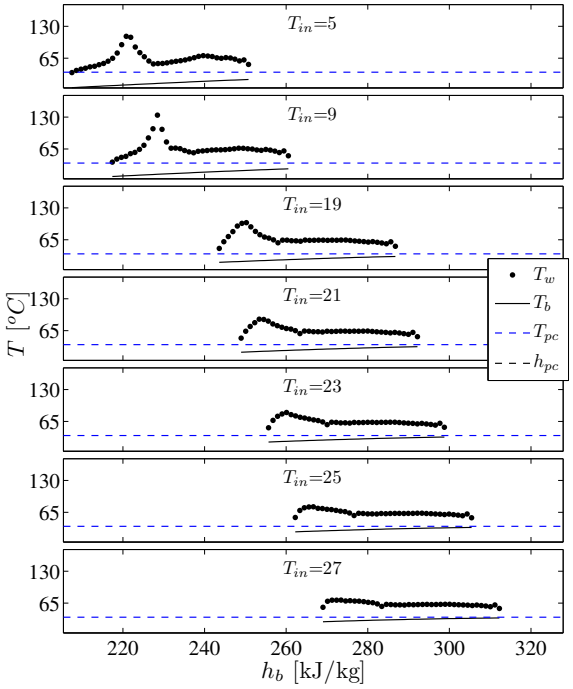


(b) Select cases

Figure A.134: Temperature profiles for $P/P_c = 1.13$, $G = 700$ kg/m^{2}s, $q = 83$ kW/m^2; units of T_{in} are °C.

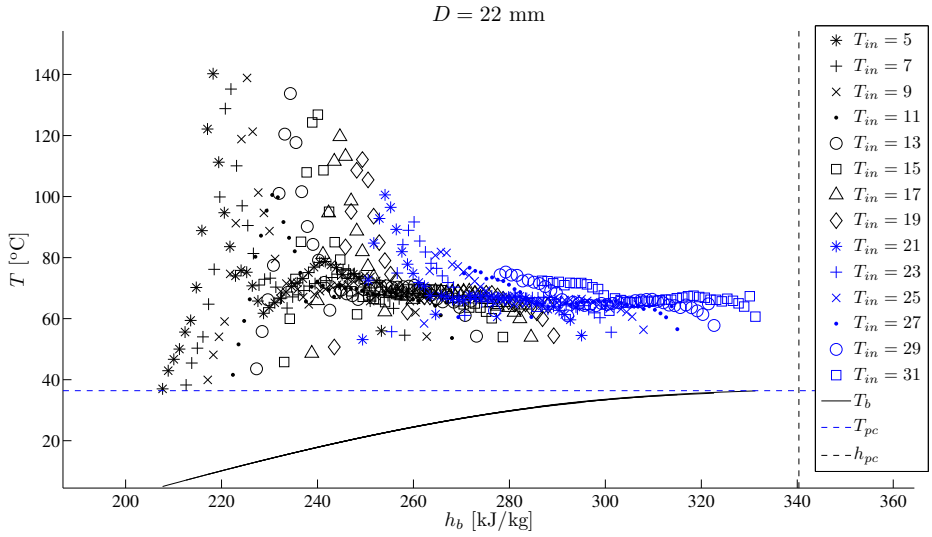


(a) All cases

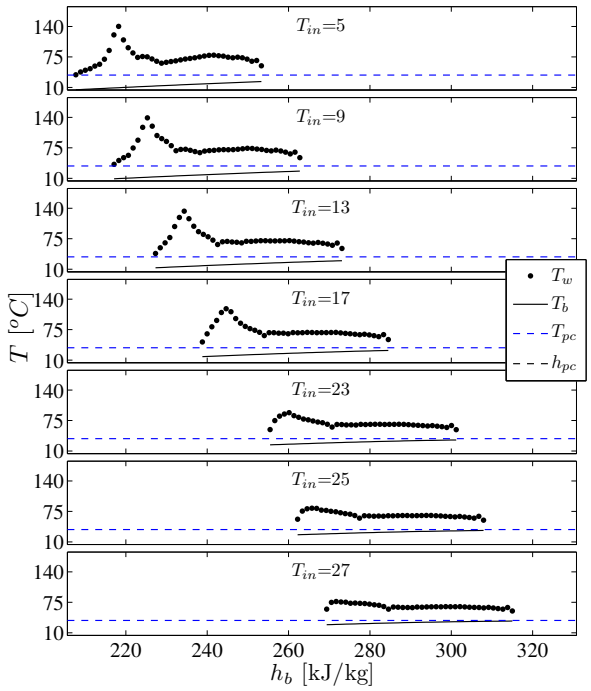


(b) Select cases

Figure A.135: Temperature profiles for $P/P_c = 1.13$, $G = 700$ kg/m^{2}s, $q = 85$ kW/m^2; units of T_{in} are °C.



(a) All cases



(b) Select cases

Figure A.136: Temperature profiles for $P/P_c = 1.13$, $G = 700$ kg/m^{2}s, $q = 90$ kW/m^2; units of T_{in} are °C.

Appendix B

Comparisons of $\mathbf{Nu}_{exp}$ with $\mathbf{Nu}_{NHT}$

B.1 4.6 mm test section

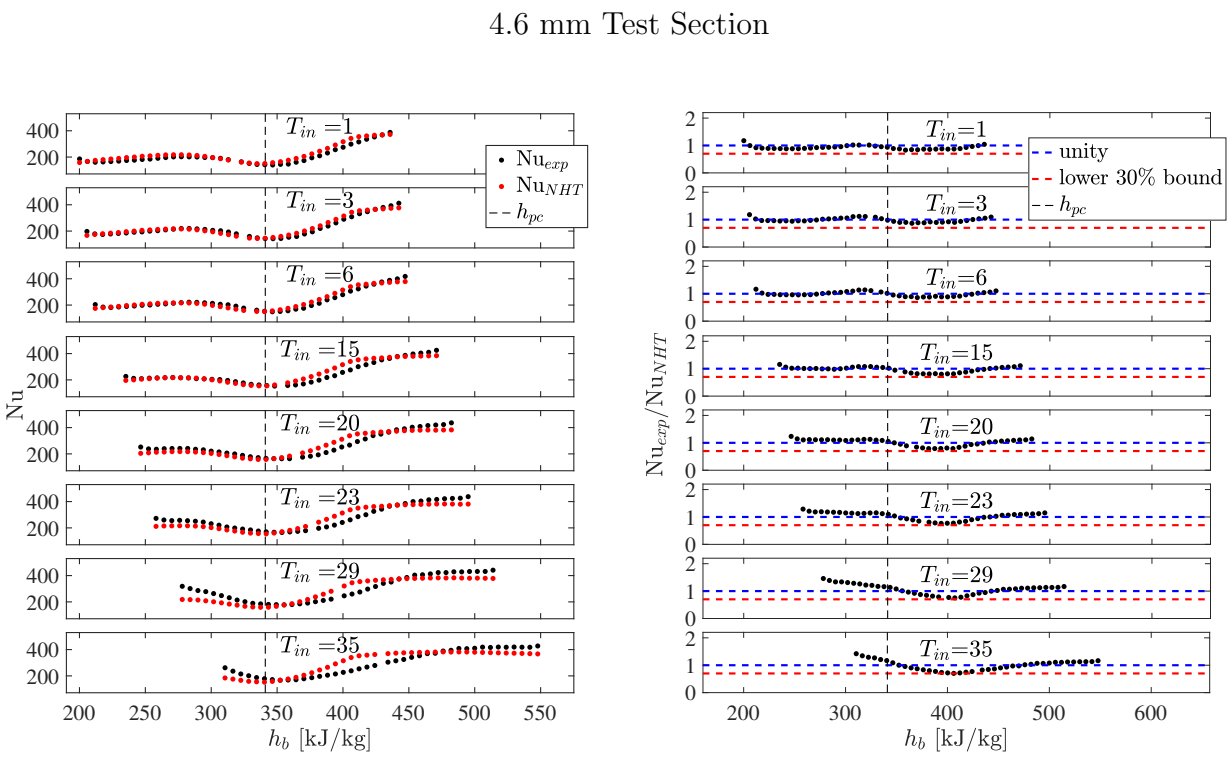


Figure B.1: Nu$_{exp}$ compared to Nu$_{NHT}$ for $P/P_c = 1.13$, $G = 1000$ kg/m^{2}s, $q = 225$ kW/m^2; units of T_{in} are in °C.

4.6 mm Test Section

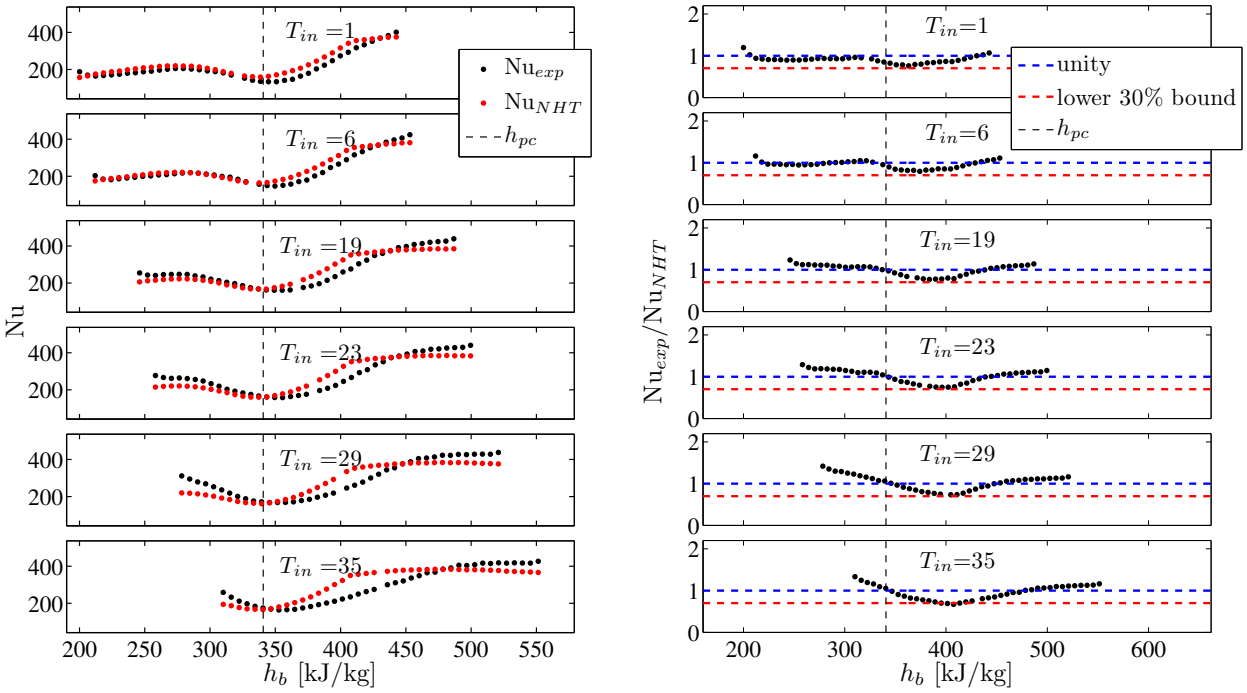


Figure B.2: Nu_{exp} compared to Nu_{NHT} for $P/P_c = 1.13$, $G = 1000$ kg/m^{2}s, $q = 230$ kW/m^2; units of T_{in} are in °C.

4.6 mm Test Section

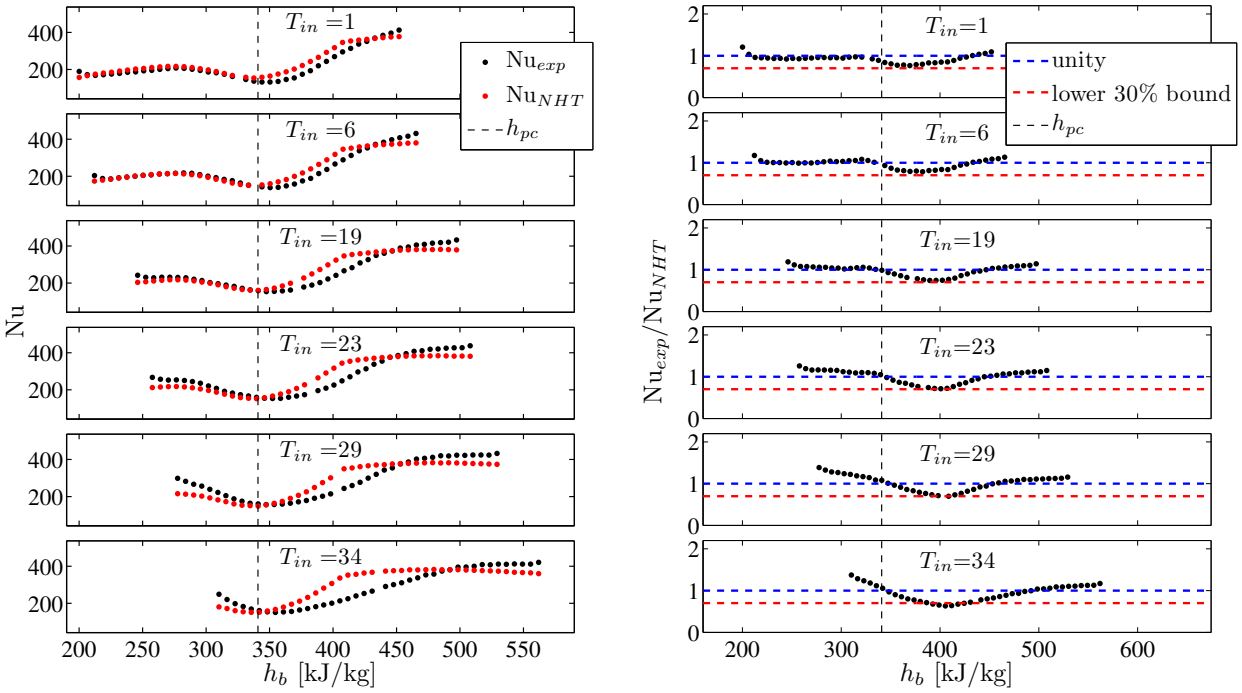


Figure B.3: Nu_{exp} compared to Nu_{NHT} for $P/P_c = 1.13$, $G = 1000$ kg/m^{2}s, $q = 240$ kW/m^2; units of T_{in} are in °C.

4.6 mm Test Section

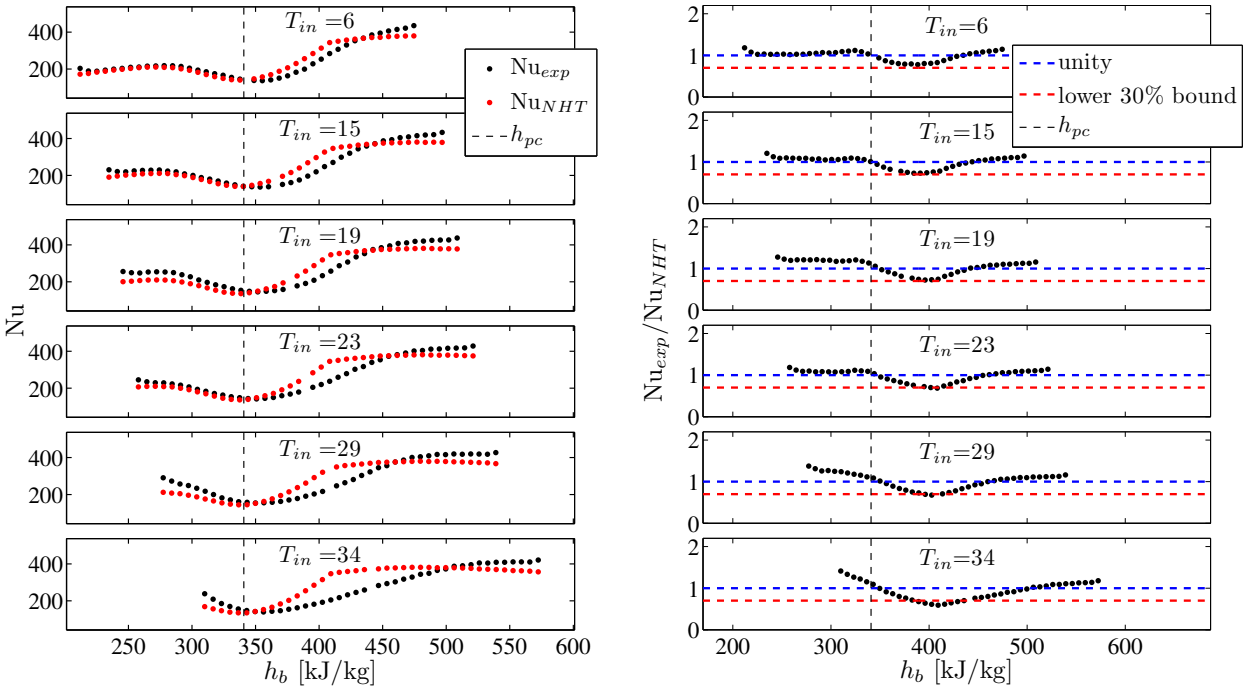


Figure B.4: Nu$_{exp}$ compared to Nu$_{NHT}$ for $P/P_c = 1.13$, $G = 1000$ kg/m^{2}s, $q = 250$ kW/m^2; units of T_{in} are in °C.

4.6 mm Test Section

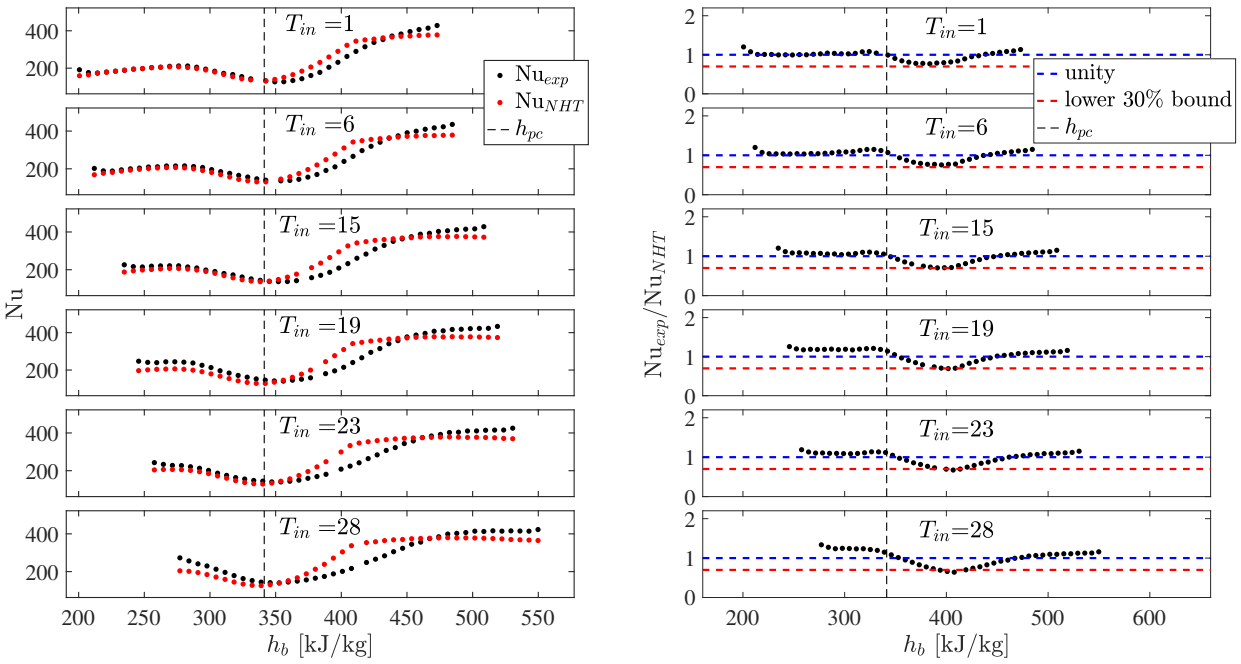


Figure B.5: Nu_{exp} compared to Nu_{NHT} for $P/P_c = 1.13$, $G = 1000$ kg/m^{2}s, $q = 260$ kW/m^2; units of T_{in} are in °C.

4.6 mm Test Section

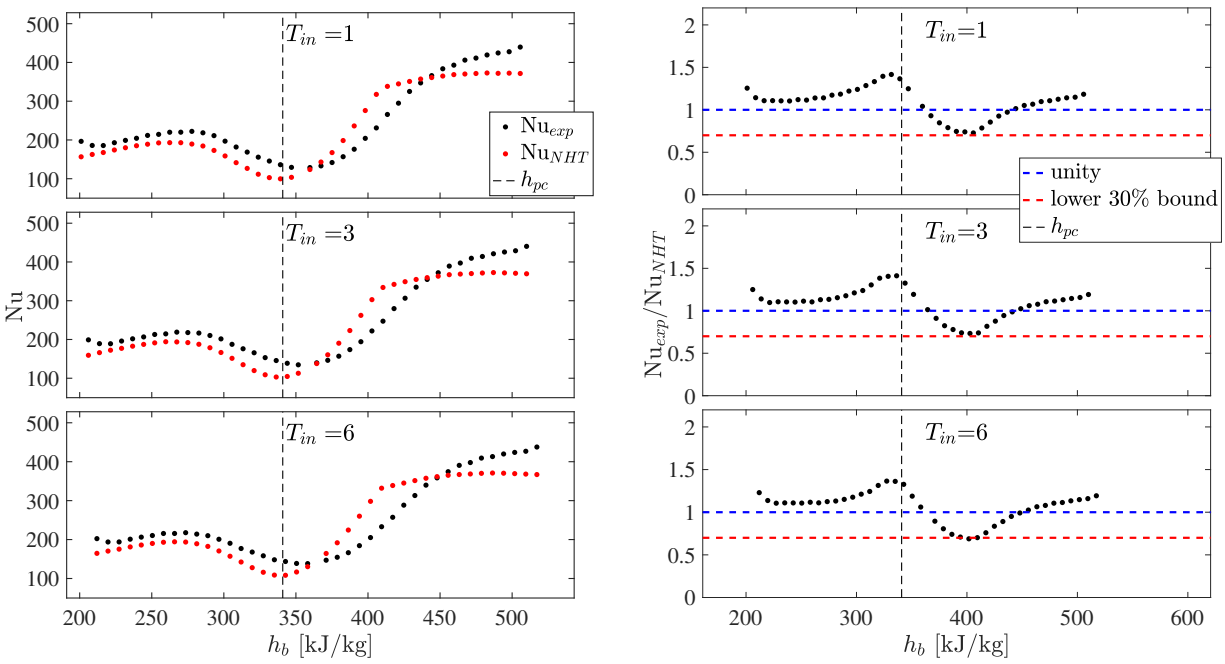


Figure B.6: Nu_{exp} compared to Nu_{NHT} for $P/P_c = 1.13$, $G = 1000$ kg/m^{2}s, $q = 290$ kW/m^2; units of T_{in} are in °C.

4.6 mm Test Section

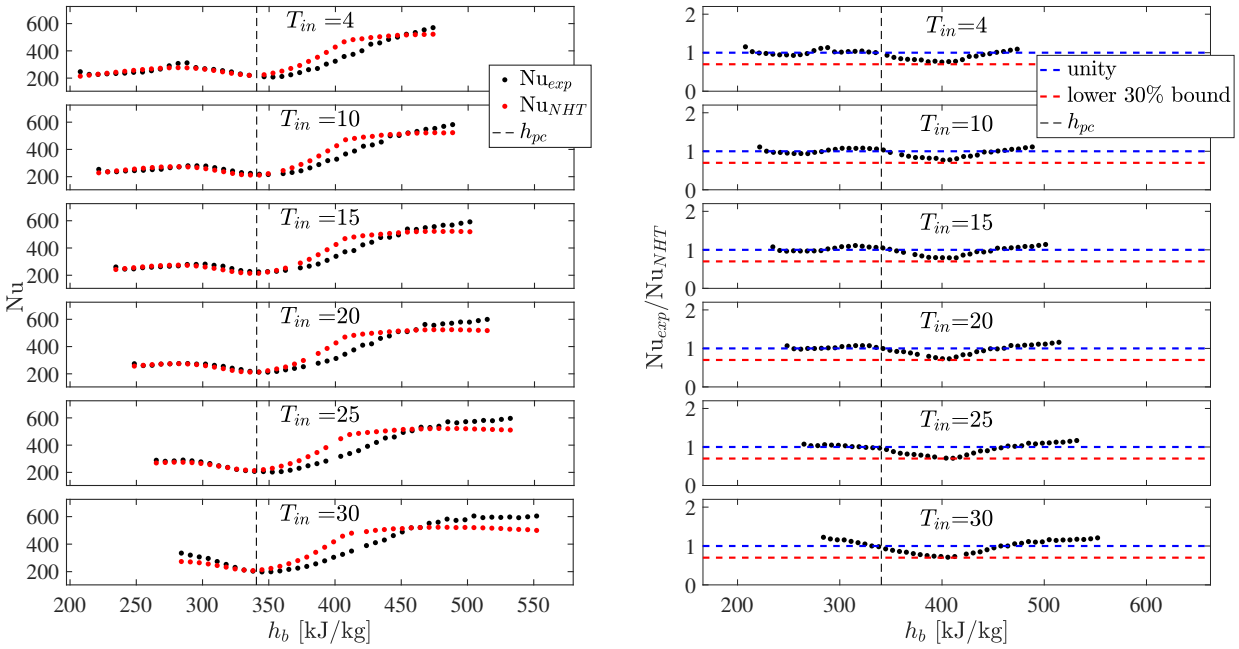


Figure B.7: Nu_{exp} compared to Nu_{NHT} for $P/P_c = 1.13$, $G = 1500$ kg/m^{2}s, $q = 380$ kW/m^2; units of T_{in} are in °C.

4.6 mm Test Section

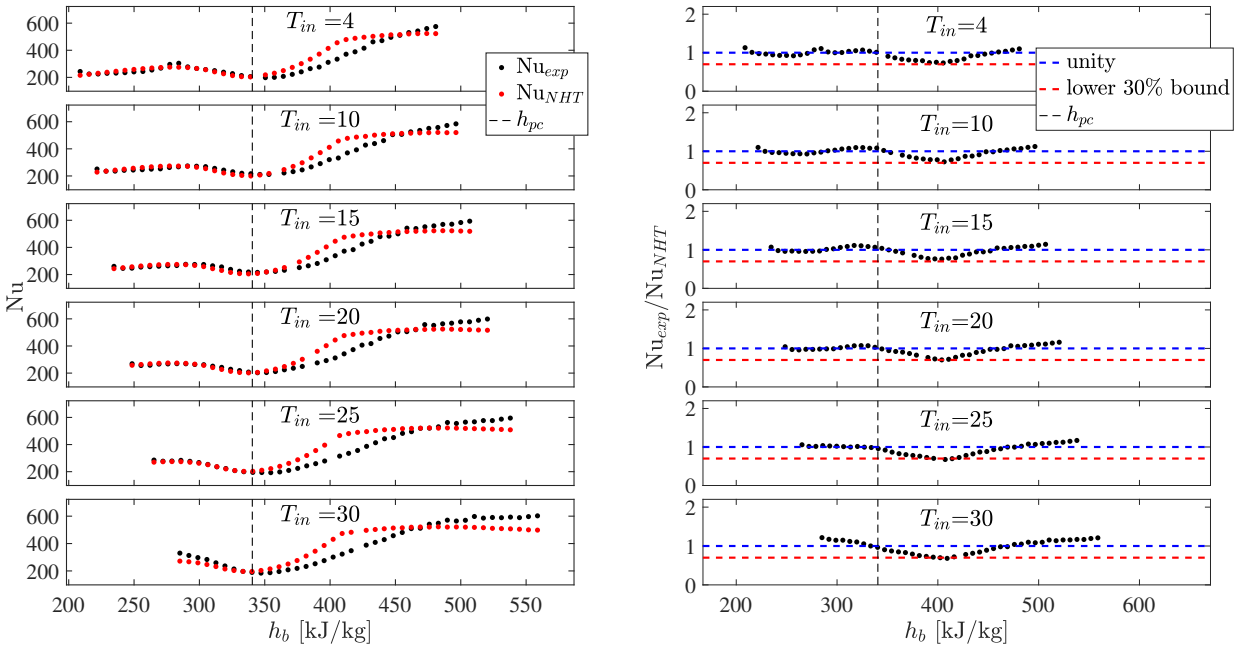


Figure B.8: Nu_{exp} compared to Nu_{NHT} for $P/P_c = 1.13$, $G = 1500$ kg/m^{2}s, $q = 390$ kW/m^2; units of T_{in} are in °C.

4.6 mm Test Section

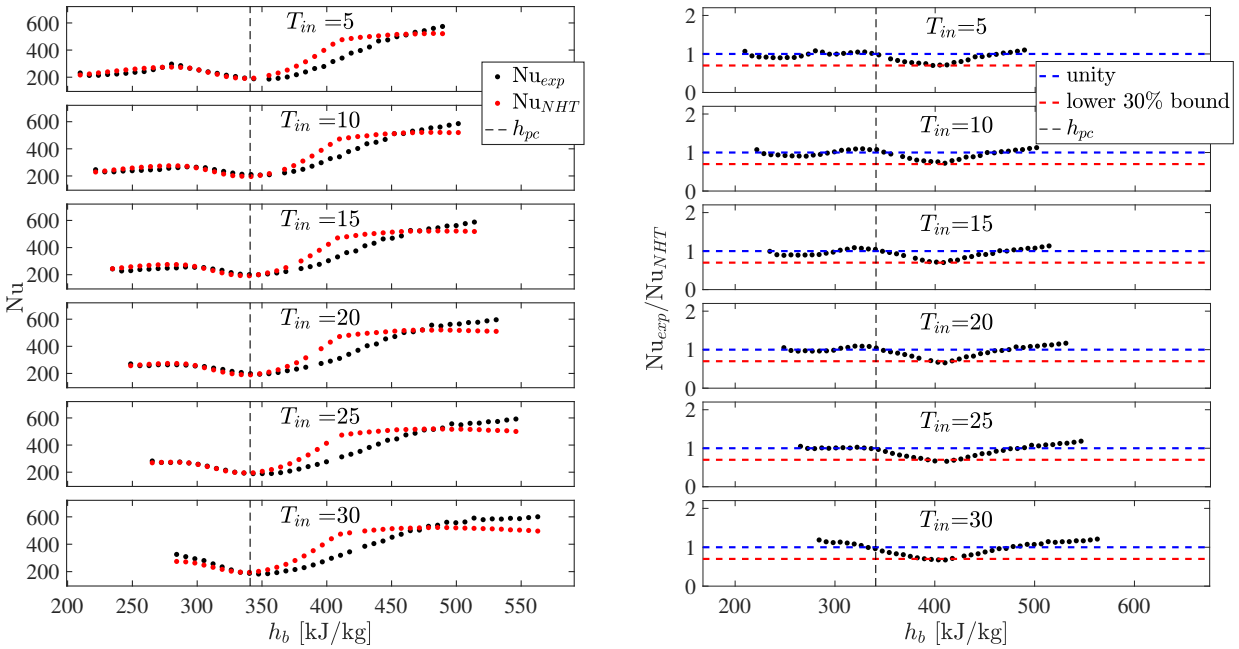


Figure B.9: Nu_{exp} compared to Nu_{NHT} for $P/P_c = 1.13$, $G = 1500$ kg/m^{2}s, $q = 400$ kW/m^2; units of T_{in} are in °C.

4.6 mm Test Section

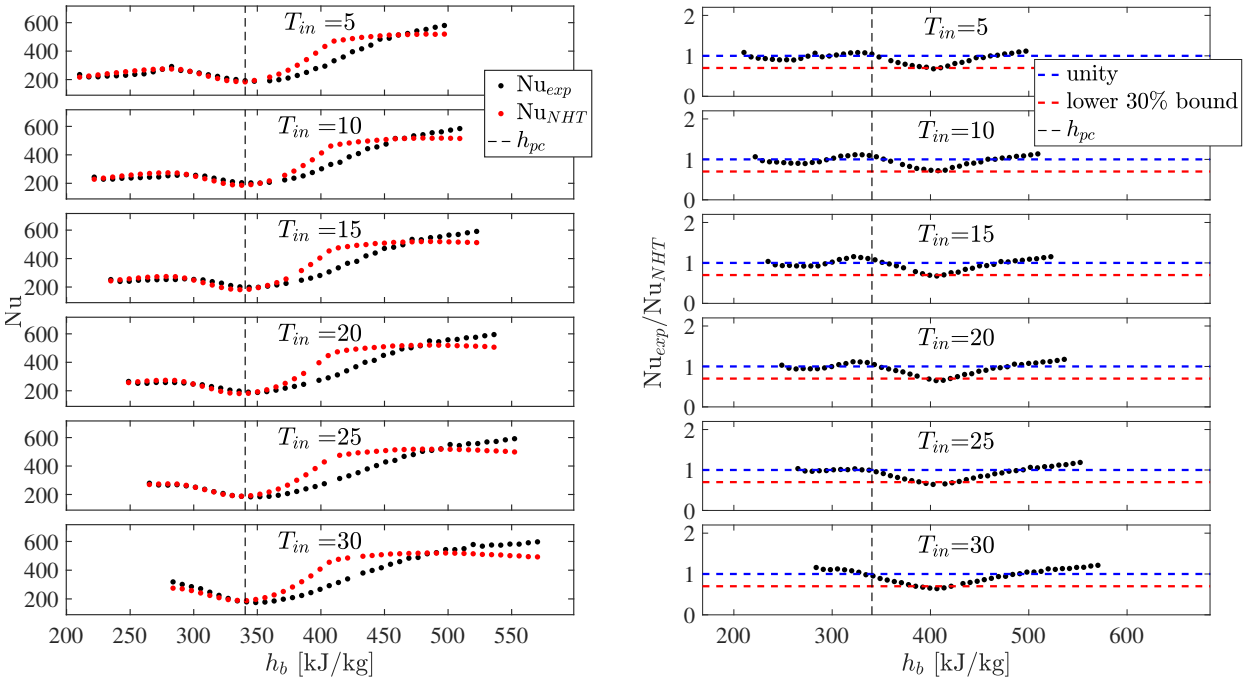


Figure B.10: Nu$_{exp}$ compared to Nu$_{NHT}$ for $P/P_c = 1.13$, $G = 1500\,\mathrm{kg/m^2s}$, $q = 410\,\mathrm{kW/m^2}$; units of T_{in} are in °C.

4.6 mm Test Section

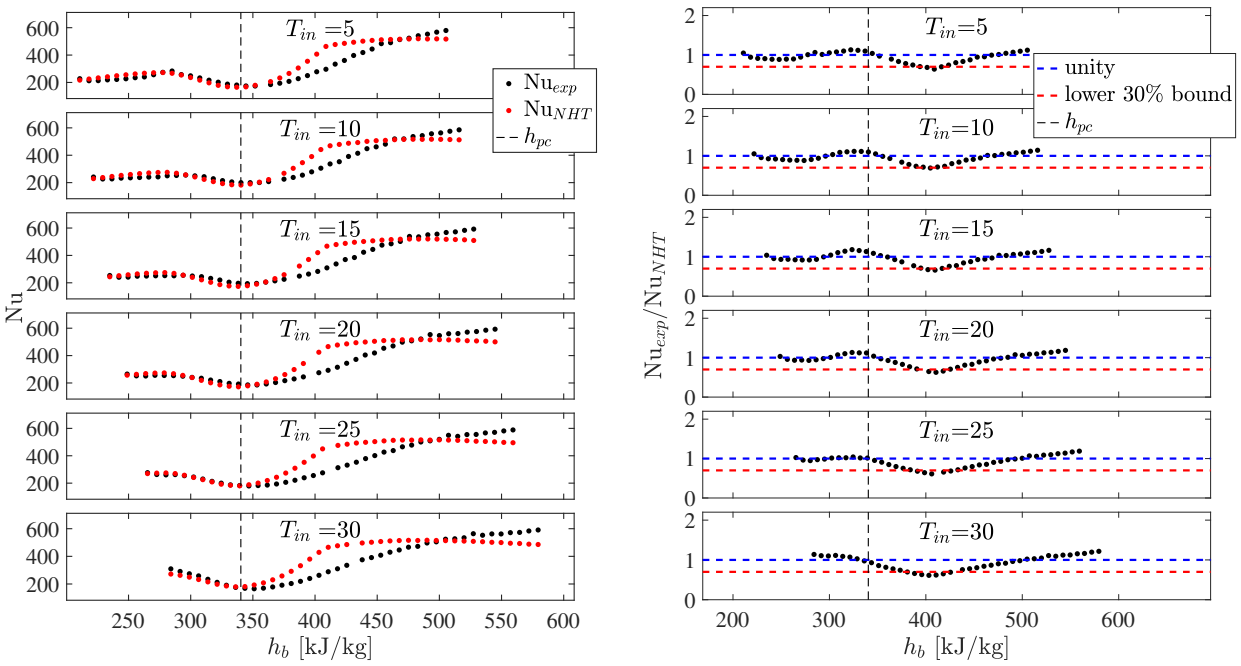


Figure B.11: Nu_{exp} compared to Nu_{NHT} for $P/P_c = 1.13$, $G = 1500\,\mathrm{kg/m^2s}$, $q = 420\,\mathrm{kW/m^2}$; units of T_{in} are in °C.

4.6 mm Test Section

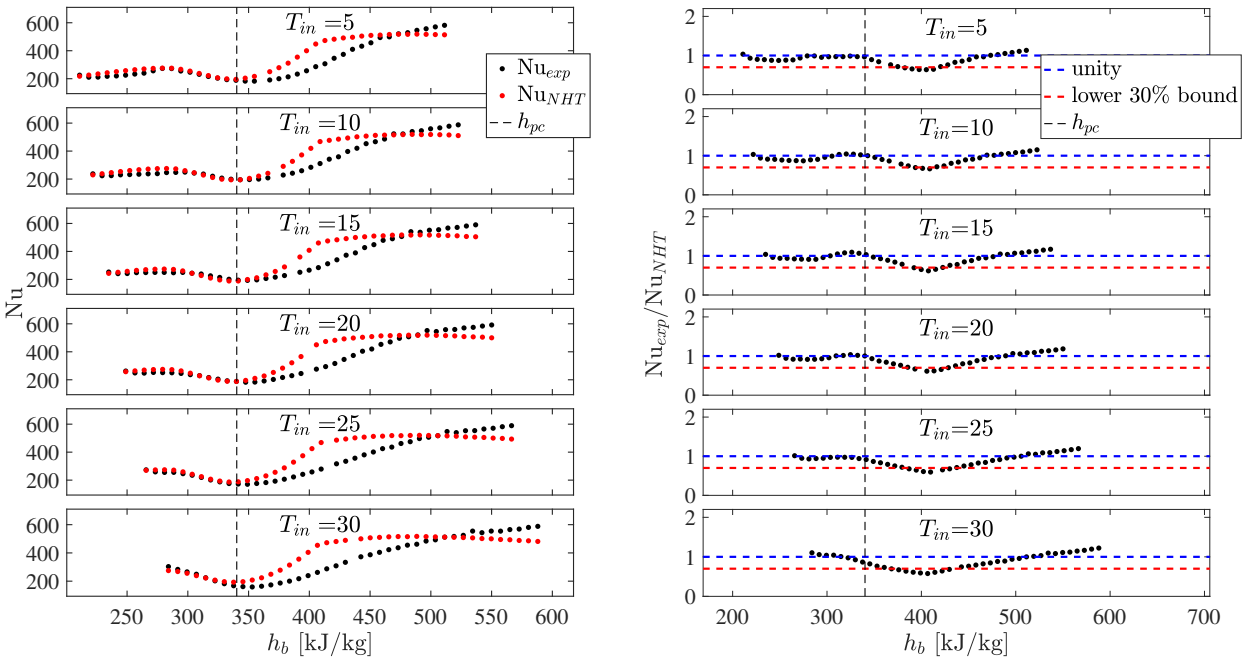


Figure B.12: Nu$_{exp}$ compared to Nu$_{NHT}$ for $P/P_c = 1.13$, $G = 1500\,\mathrm{kg/m^2s}$, $q = 430\,\mathrm{kW/m^2}$; units of T_{in} are in °C.

4.6 mm Test Section

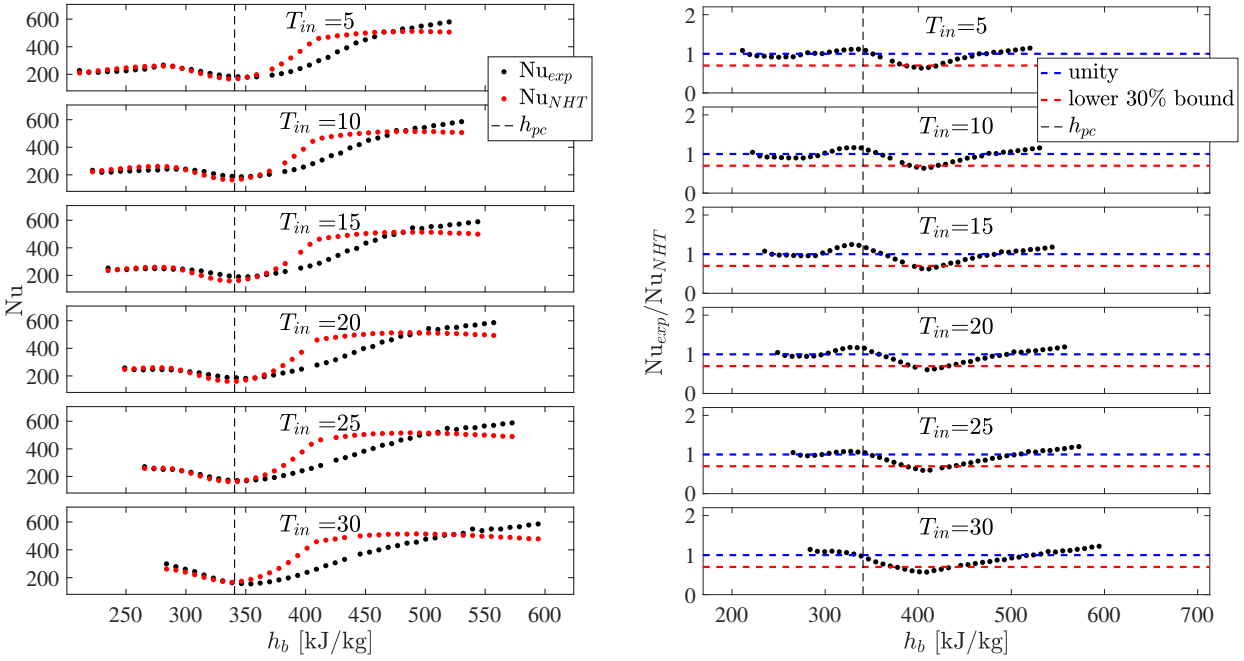


Figure B.13: Nu$_{exp}$ compared to Nu$_{NHT}$ for $P/P_c = 1.13$, $G = 1500\,\mathrm{kg/m^2s}$, $q = 440\,\mathrm{kW/m^2}$; units of T_{in} are in °C.

4.6 mm Test Section

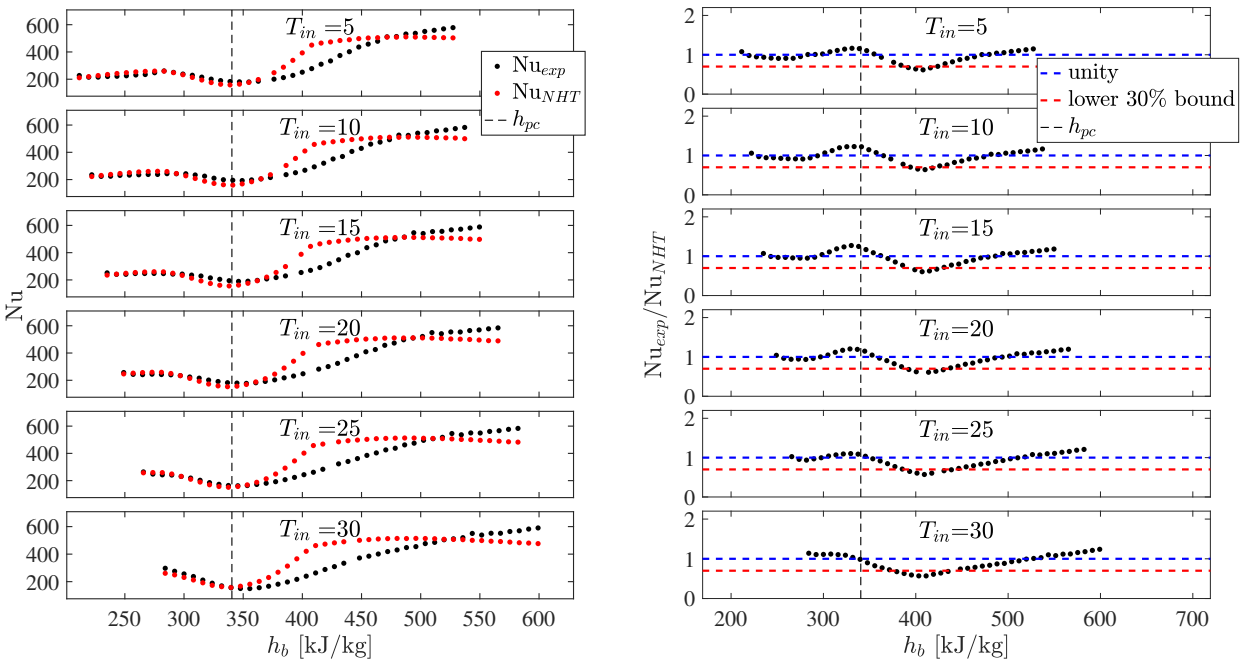


Figure B.14: Nu_{exp} compared to Nu_{NHT} for $P/P_c = 1.13$, $G = 1500\,\mathrm{kg/m^2s}$, $q = 450\,\mathrm{kW/m^2}$; units of T_{in} are in °C.

B.2 8 mm test section

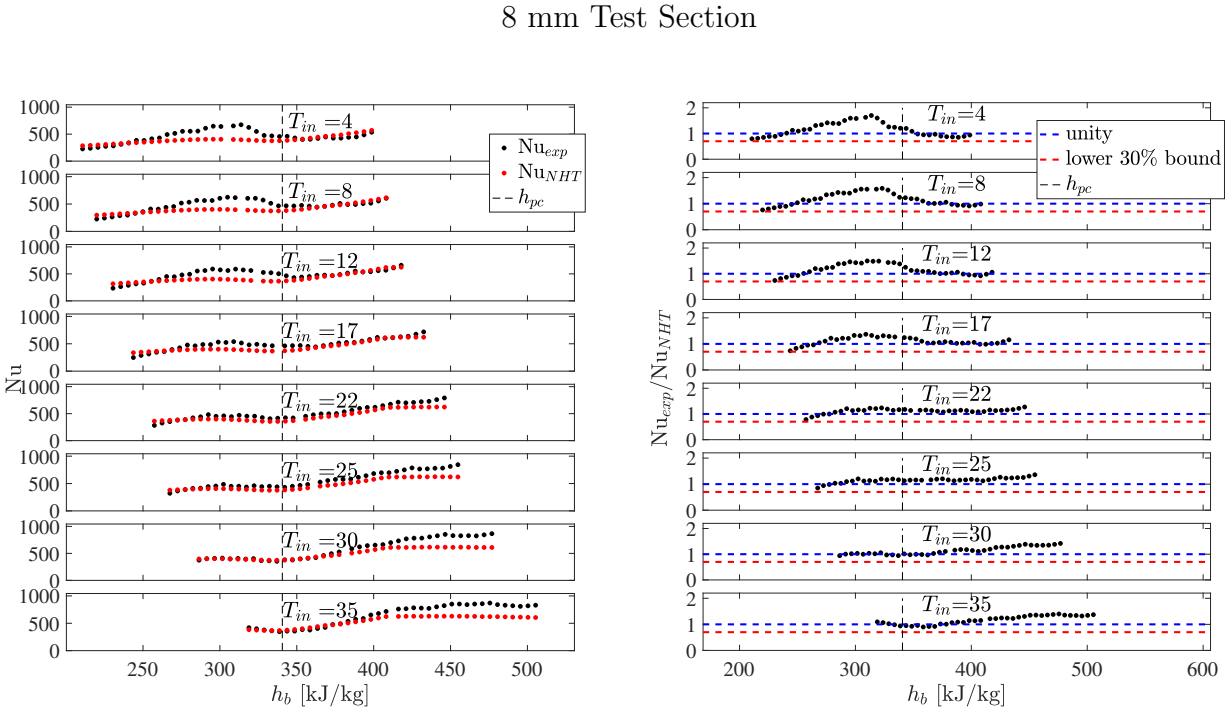


Figure B.15: Nu$_{exp}$ compared to Nu$_{NHT}$ for $P/P_c = 1.13$, $G = 1000\,\mathrm{kg/m^2s}$, $q = 200\,\mathrm{kW/m^2}$; units of T_{in} are in °C.

8 mm Test Section

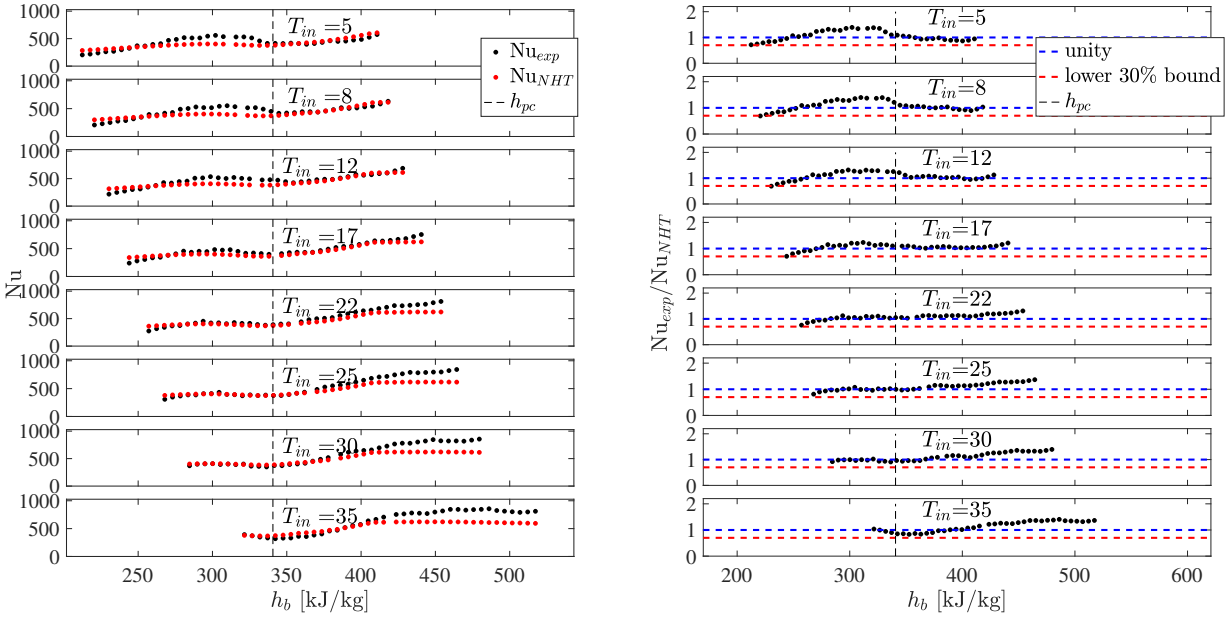


Figure B.16: Nu_{exp} compared to Nu_{NHT} for $P/P_c = 1.13$, $G = 1000\,\mathrm{kg/m^2s}$, $q = 210\,\mathrm{kW/m^2}$; units of T_{in} are in °C.

8 mm Test Section

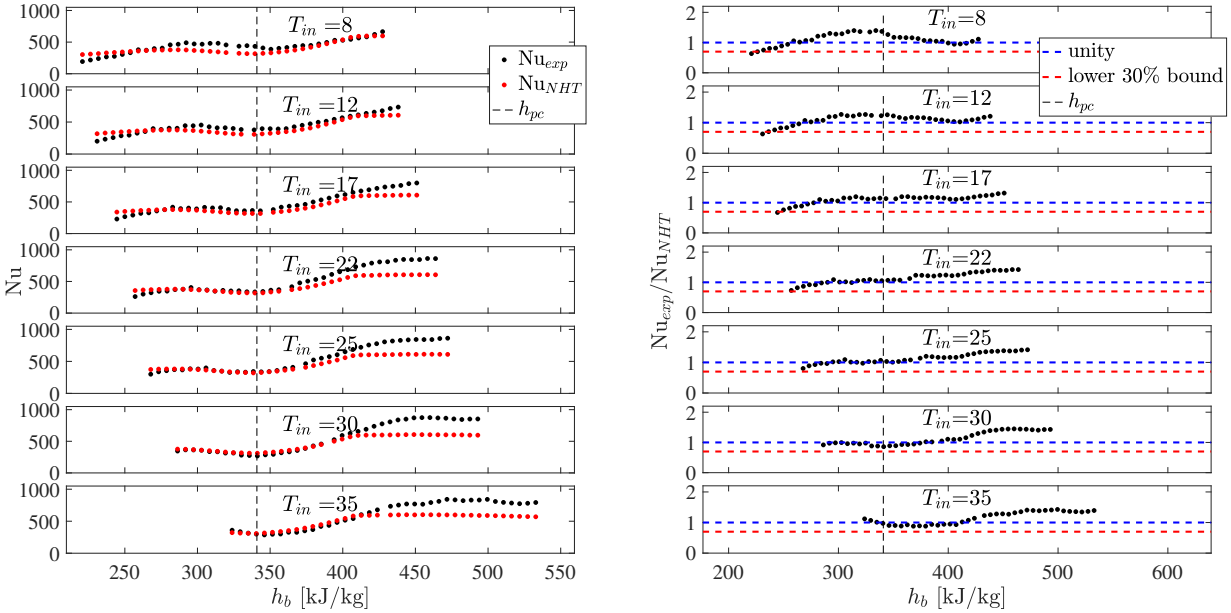


Figure B.17: Nu_{exp} compared to Nu_{NHT} for $P/P_c = 1.13$, $G = 1000\,\mathrm{kg/m^2s}$, $q = 220\,\mathrm{kW/m^2}$; units of T_{in} are in °C.

8 mm Test Section

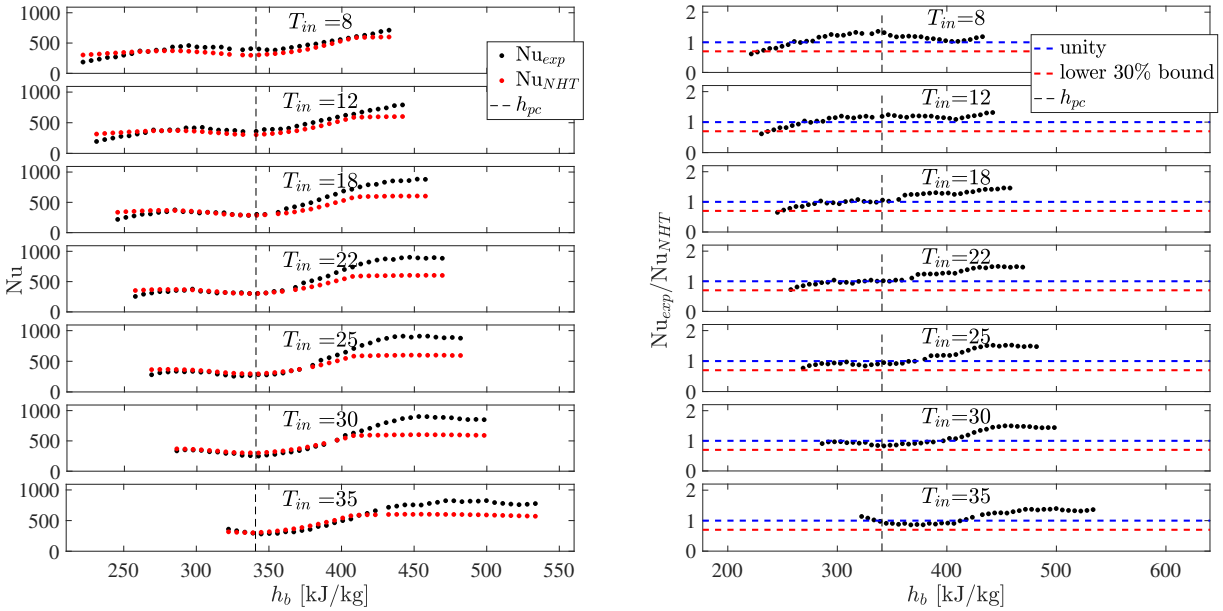


Figure B.18: Nu_{exp} compared to Nu_{NHT} for $P/P_c = 1.13$, $G = 1000\,\mathrm{kg/m^2s}$, $q = 225\,\mathrm{kW/m^2}$; units of T_{in} are in °C.

8 mm Test Section

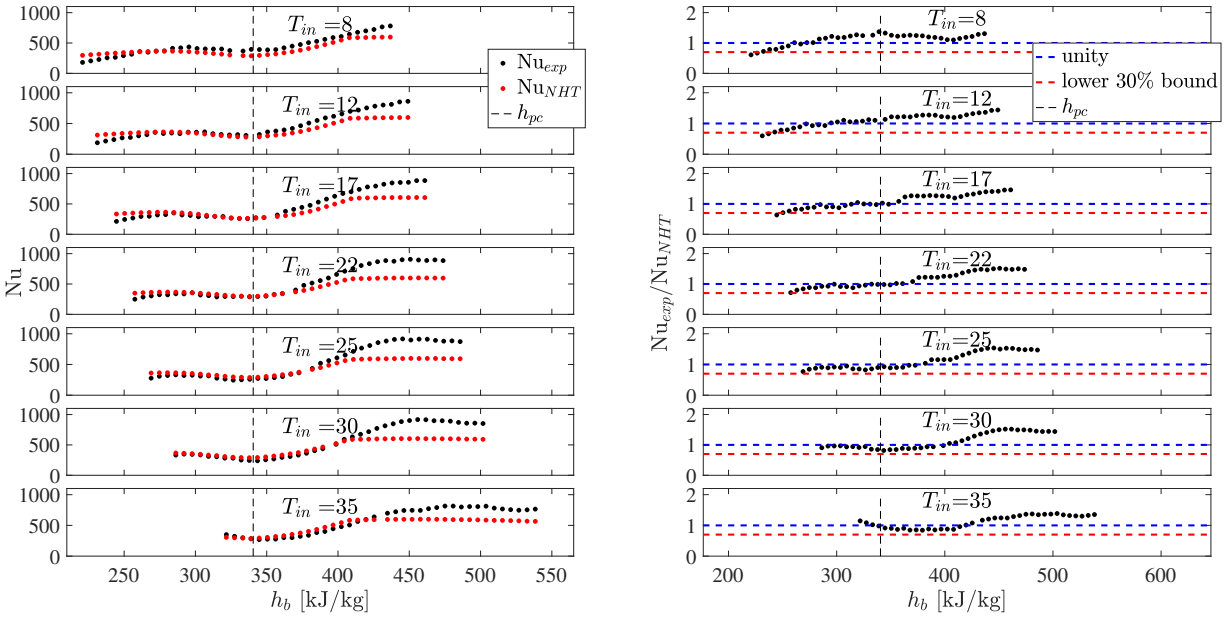


Figure B.19: Nu$_{exp}$ compared to Nu$_{NHT}$ for $P/P_c = 1.13$, $G = 1000\,\mathrm{kg/m^2s}$, $q = 230\,\mathrm{kW/m^2}$; units of T_{in} are in °C.

8 mm Test Section

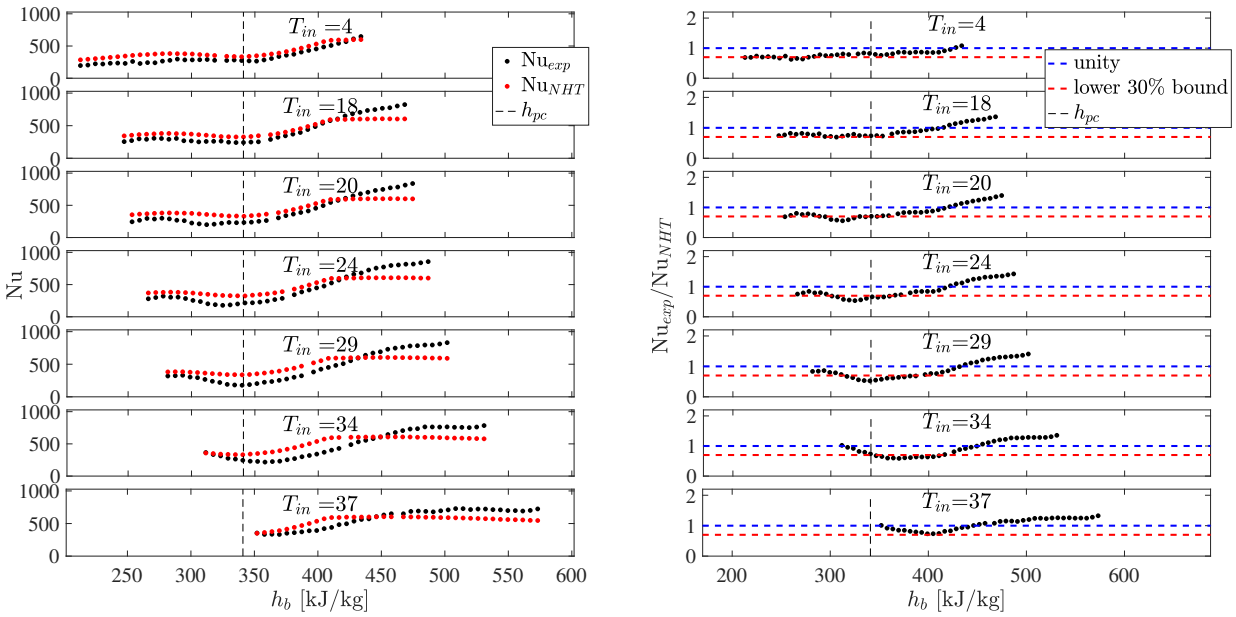


Figure B.20: Nu_{exp} compared to Nu_{NHT} for $P/P_c = 1.13$, $G = 1000\,\mathrm{kg/m^2s}$, $q = 235\,\mathrm{kW/m^2}$; units of T_{in} are in °C.

8 mm Test Section

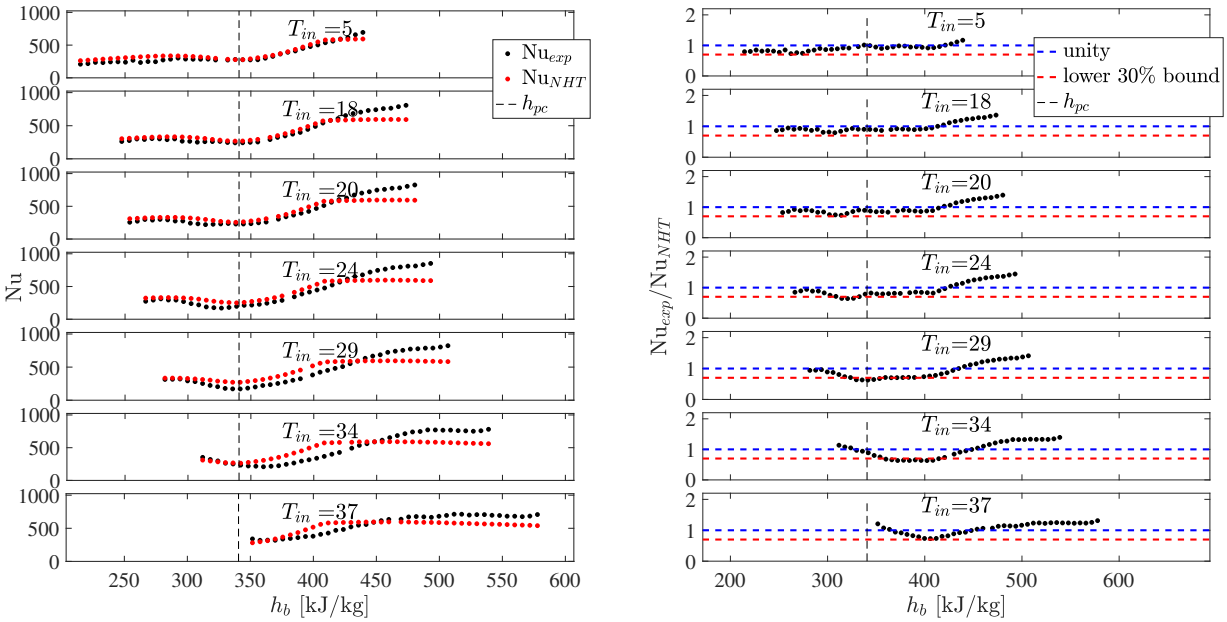


Figure B.21: Nu_{exp} compared to Nu_{NHT} for $P/P_c = 1.13$, $G = 1000\,\mathrm{kg/m^2s}$, $q = 240\,\mathrm{kW/m^2}$; units of T_{in} are in °C.

8 mm Test Section

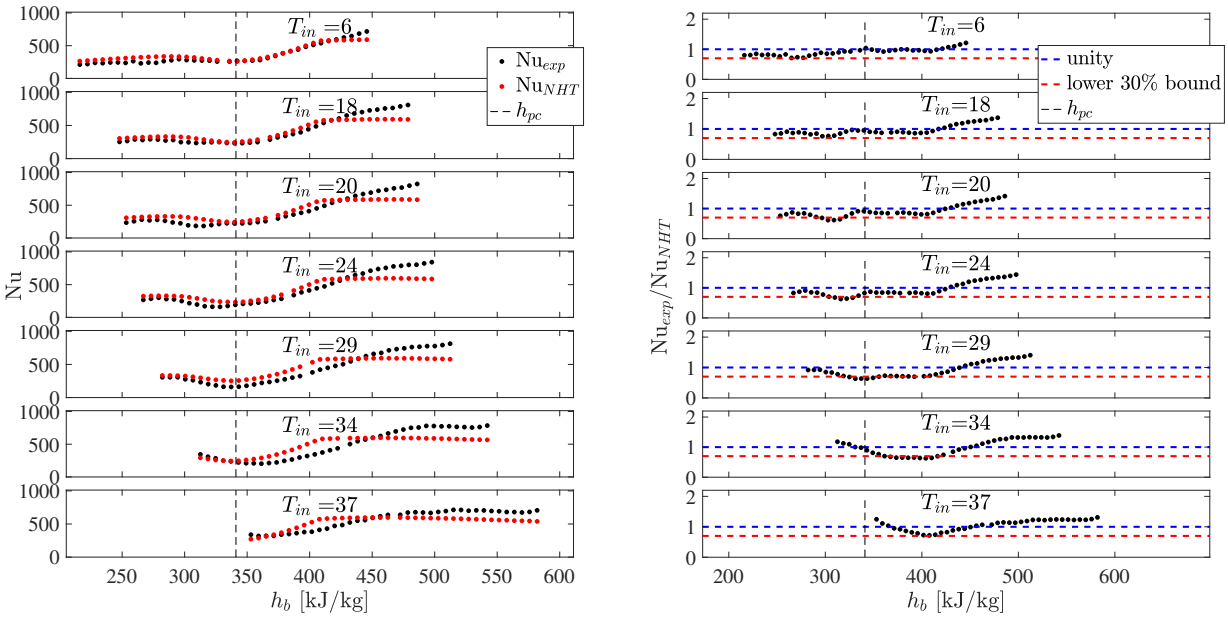


Figure B.22: Nu$_{exp}$ compared to Nu$_{NHT}$ for $P/P_c = 1.13$, $G = 1000\,\mathrm{kg/m^2s}$, $q = 245\,\mathrm{kW/m^2}$; units of T_{in} are in °C.

8 mm Test Section

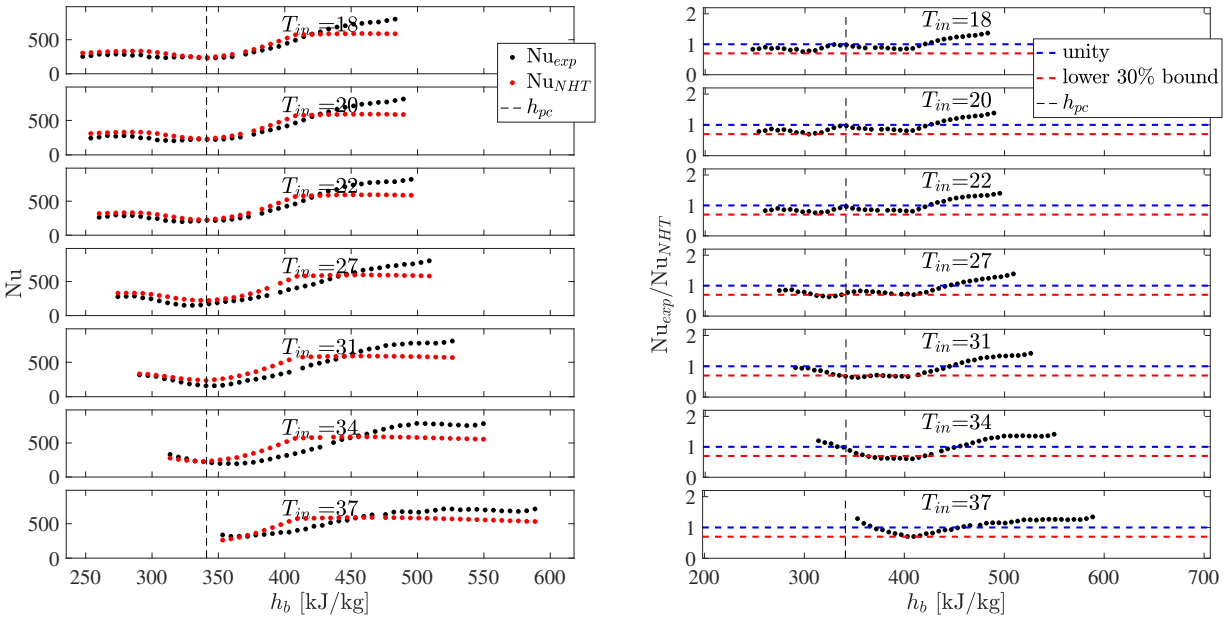


Figure B.23: Nu_{exp} compared to Nu_{NHT} for $P/P_c = 1.13$, $G = 1000\ \mathrm{kg/m^2s}$, $q = 250\ \mathrm{kW/m^2}$; units of T_{in} are in °C.

8 mm Test Section

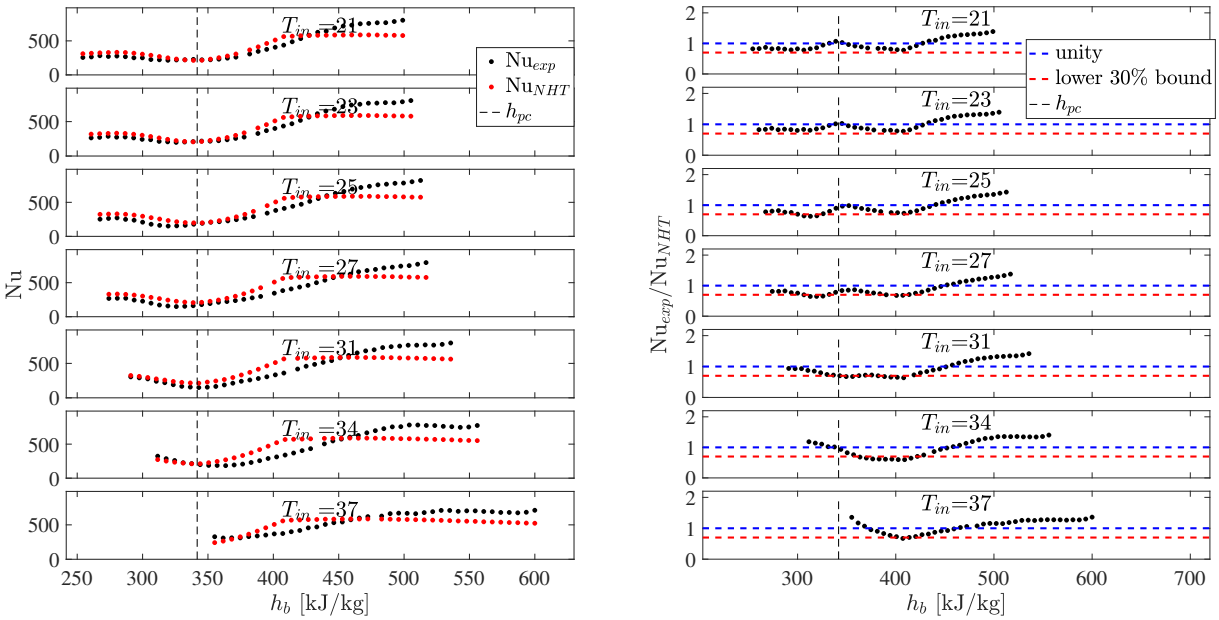


Figure B.24: Nu_{exp} compared to Nu_{NHT} for $P/P_c = 1.13$, $G = 1000\,\mathrm{kg/m^2s}$, $q = 260\,\mathrm{kW/m^2}$; units of T_{in} are in °C.

8 mm Test Section

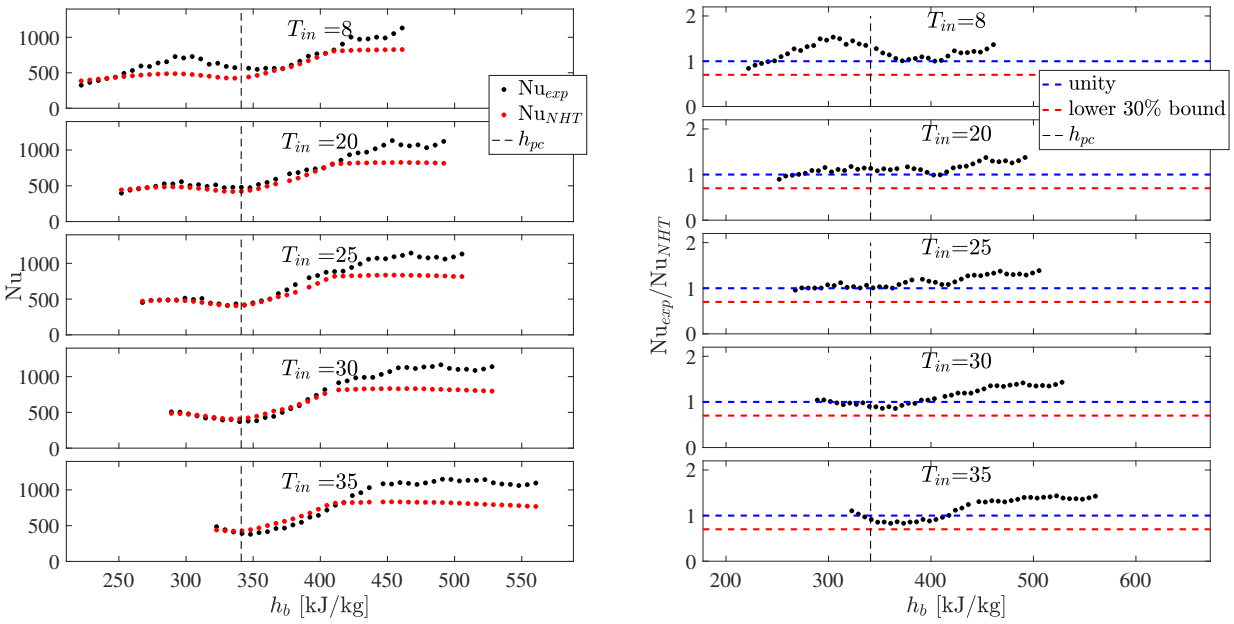


Figure B.25: Nu_{exp} compared to Nu_{NHT} for $P/P_c = 1.13$, $G = 1500\,\mathrm{kg/m^2s}$, $q = 380\,\mathrm{kW/m^2}$; units of T_{in} are in °C.

8 mm Test Section

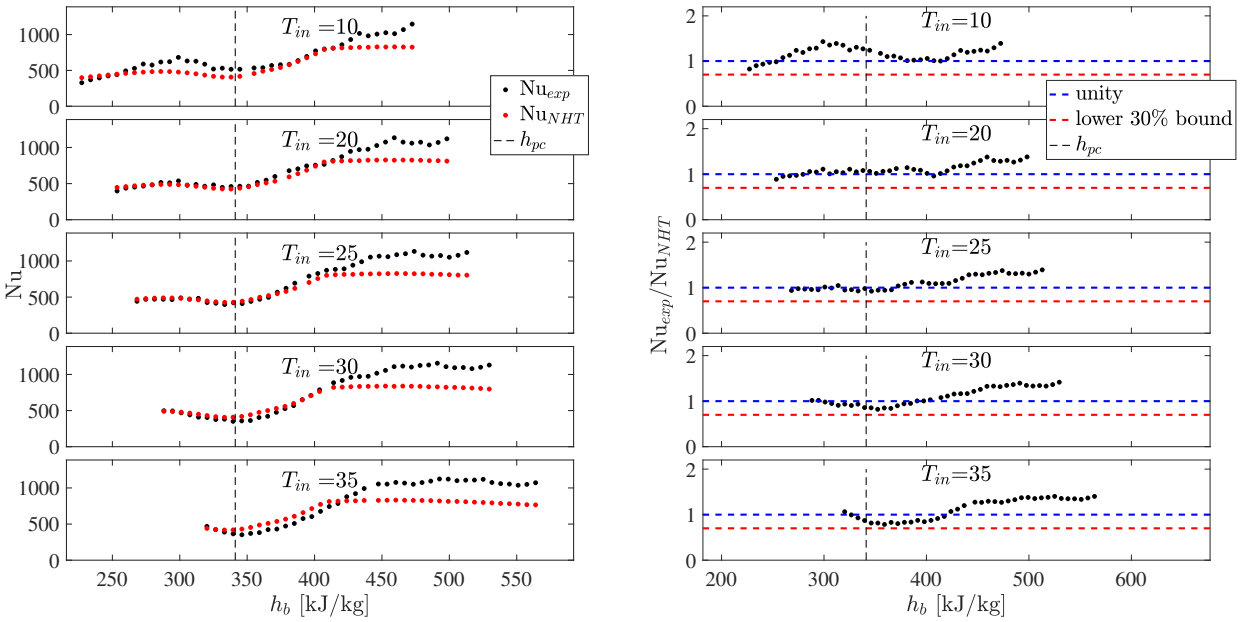


Figure B.26: Nu_{exp} compared to Nu_{NHT} for $P/P_c = 1.13$, $G = 1500\,\mathrm{kg/m^2s}$, $q = 380\,\mathrm{kW/m^2}$; units of T_{in} are in °C.

8 mm Test Section

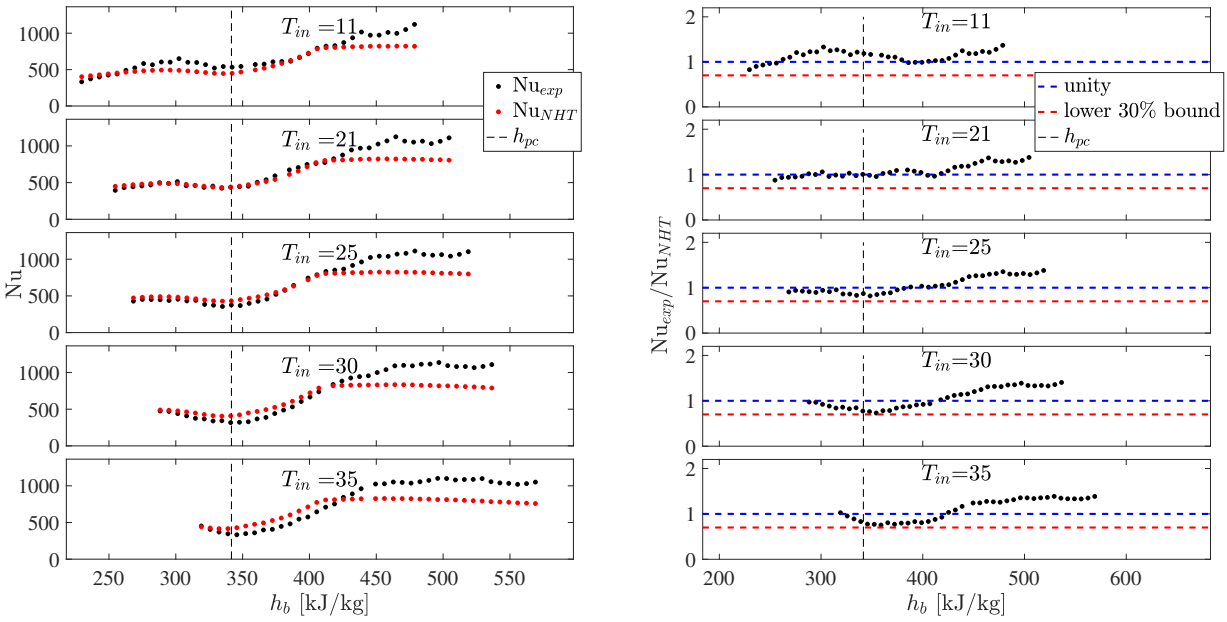


Figure B.27: Nu_{exp} compared to Nu_{NHT} for $P/P_c = 1.13$, $G = 1500\,\mathrm{kg/m^2s}$, $q = 400\,\mathrm{kW/m^2}$; units of T_{in} are in °C.

8 mm Test Section

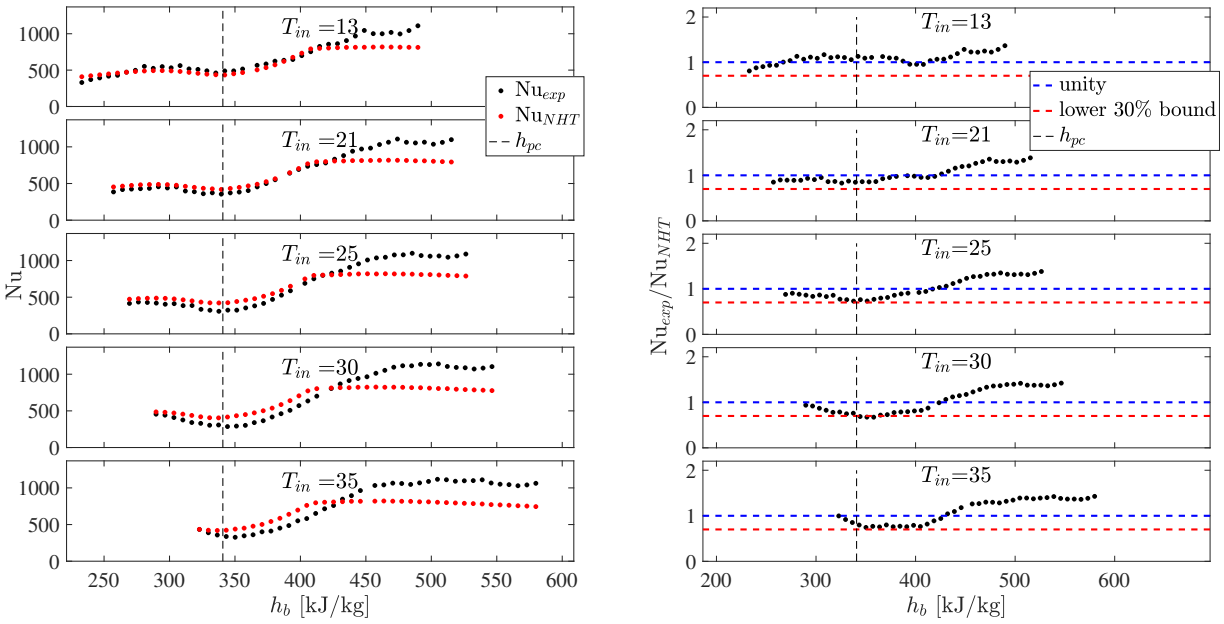


Figure B.28: Nu_{exp} compared to Nu_{NHT} for $P/P_c = 1.13$, $G = 1500\,\mathrm{kg/m^2s}$, $q = 410\,\mathrm{kW/m^2}$; units of T_{in} are in °C.

8 mm Test Section

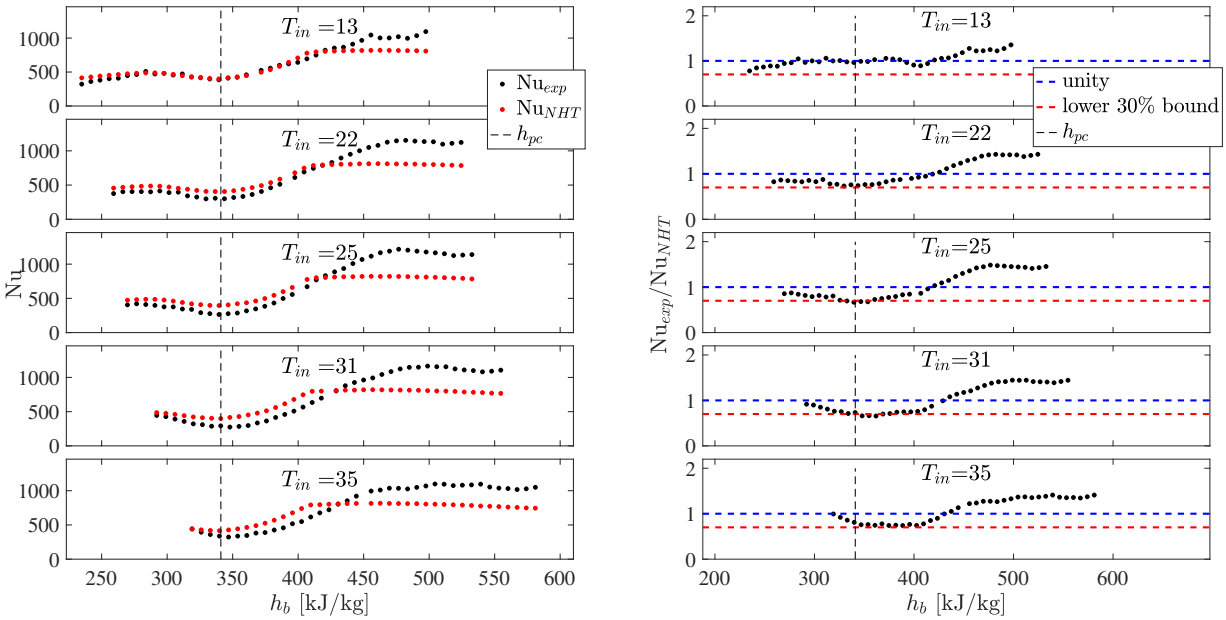


Figure B.29: Nu_{exp} compared to Nu_{NHT} for $P/P_c = 1.13$, $G = 1500\,\mathrm{kg/m^2s}$, $q = 420\,\mathrm{kW/m^2}$; units of T_{in} are in °C.

8 mm Test Section

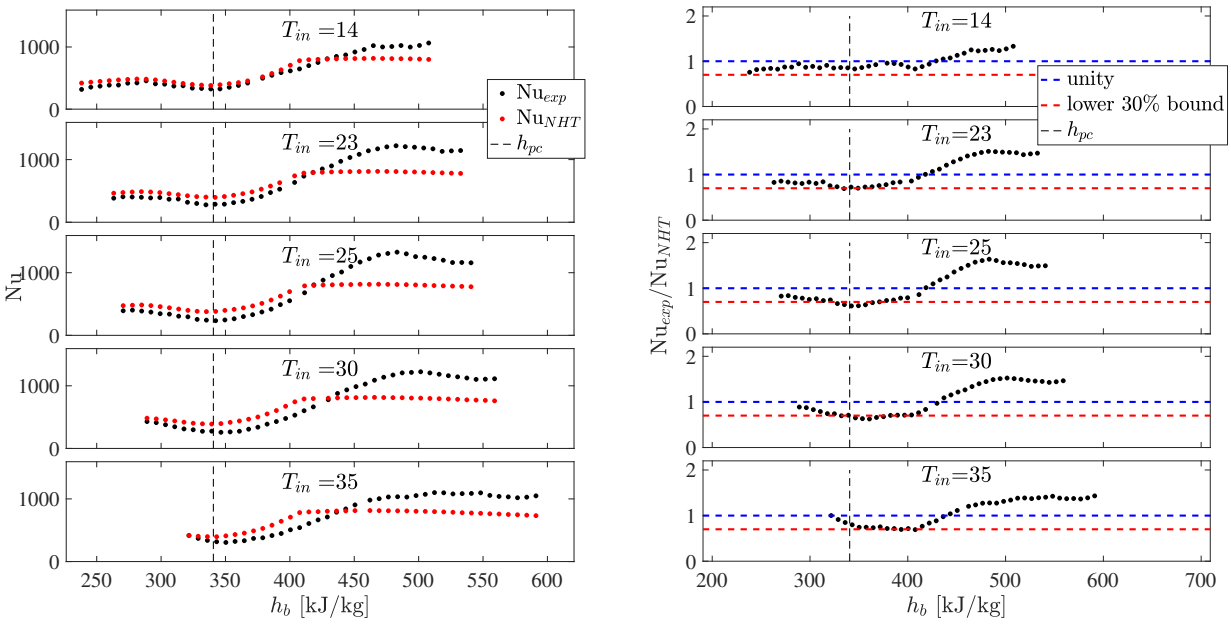


Figure B.30: Nu_{exp} compared to Nu_{NHT} for $P/P_c = 1.13$, $G = 1500\,\mathrm{kg/m^2s}$, $q = 430\,\mathrm{kW/m^2}$; units of T_{in} are in °C.

8 mm Test Section

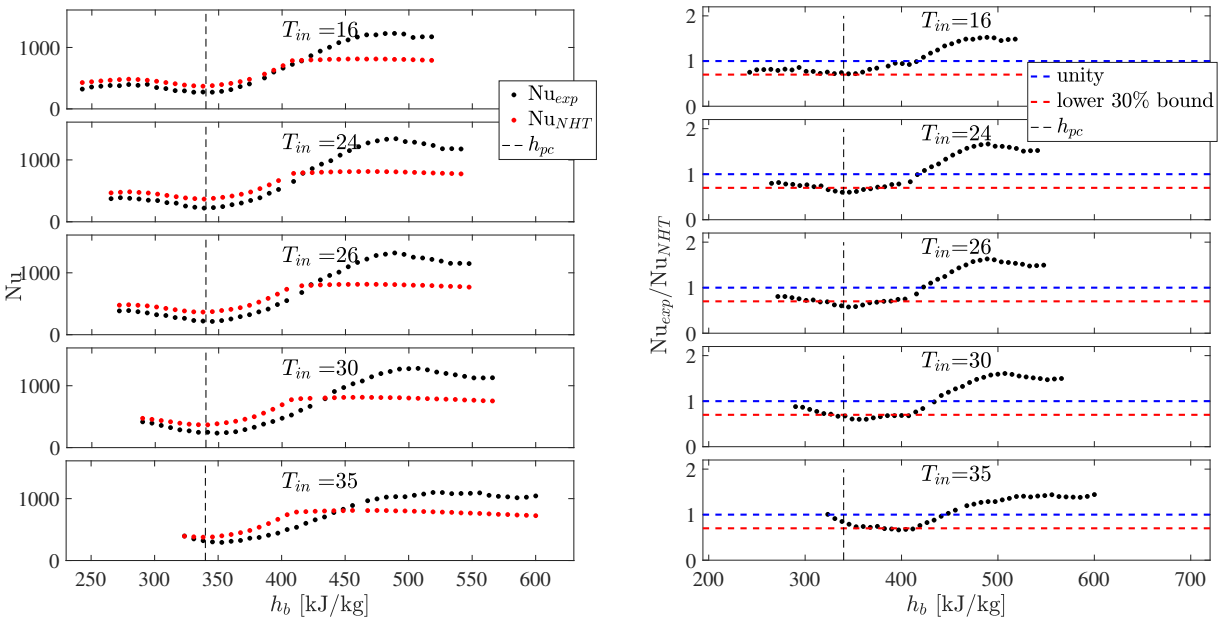


Figure B.31: Nu_{exp} compared to Nu_{NHT} for $P/P_c = 1.13$, $G = 1500\,\mathrm{kg/m^2s}$, $q = 440\,\mathrm{kW/m^2}$; units of T_{in} are in °C.

8 mm Test Section

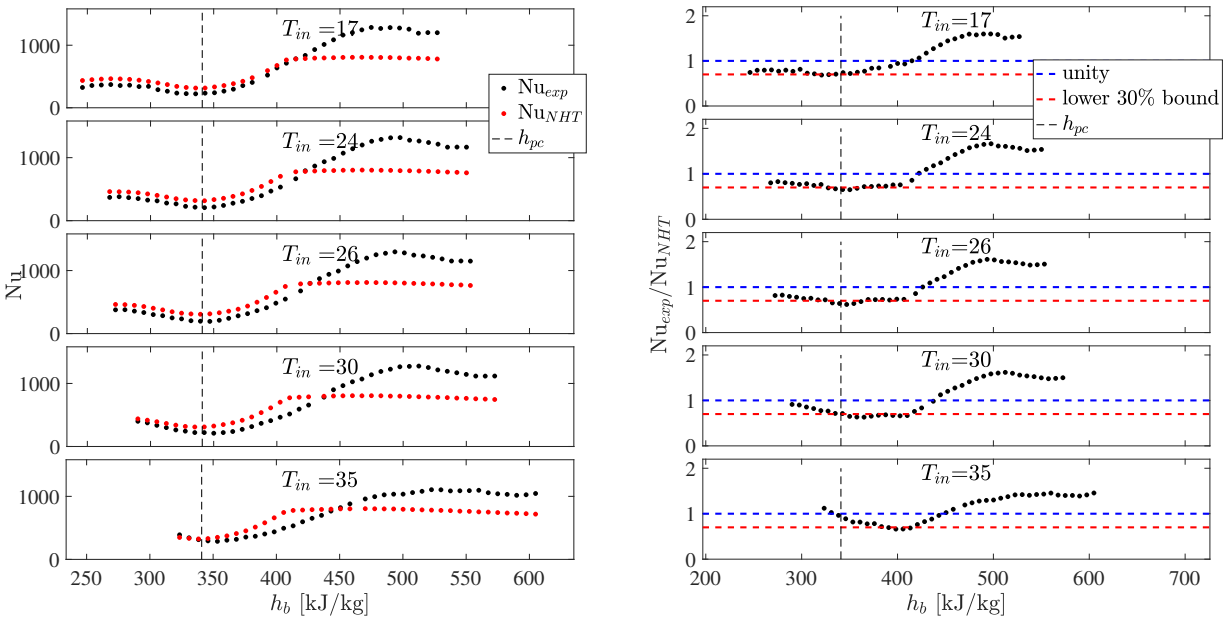
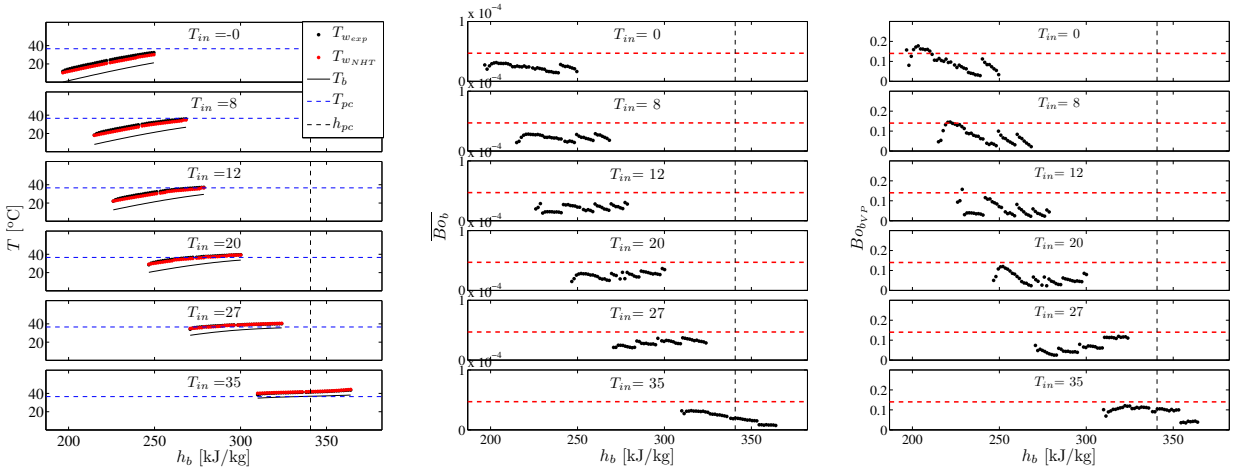


Figure B.32: Nu$_{exp}$ compared to Nu$_{NHT}$ for $P/P_c = 1.13$, $G = 1500\,\mathrm{kg/m^2s}$, $q = 450\,\mathrm{kW/m^2}$; units of T_{in} are in °C.

Appendix C

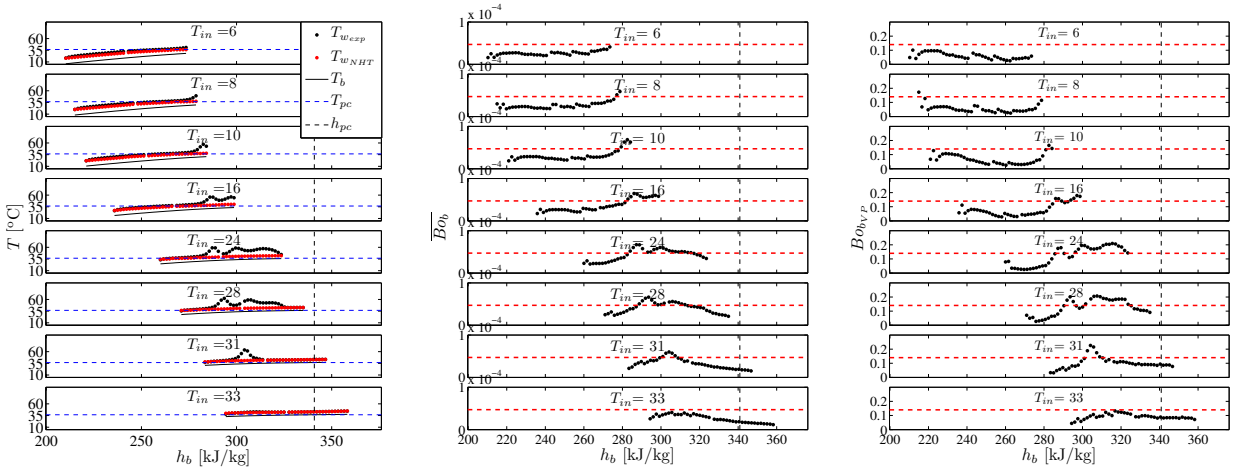
Buoyancy parameter estimates

C.1 4.6 mm test section



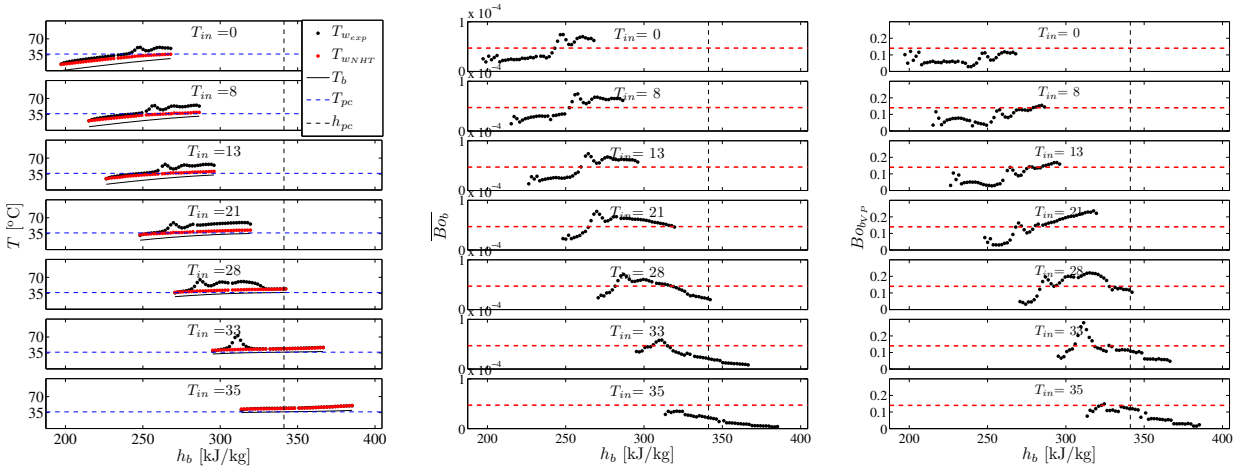
(a) T_w profiles (b) $\overline{Bo_b}$ profiles (c) $Bo_{b_{VP}}$ profiles

Figure C.1: $\overline{Bo_b}$, $Bo_{b_{VP}}$, and T_w profiles for $P/P_c = 1.13$, $D = 4.6$ mm, $G = 300$ kg/m^{2}s, $q = 15$ kW/m^2; dashed red lines represent suggested thresholds; T_{in} is in °C.



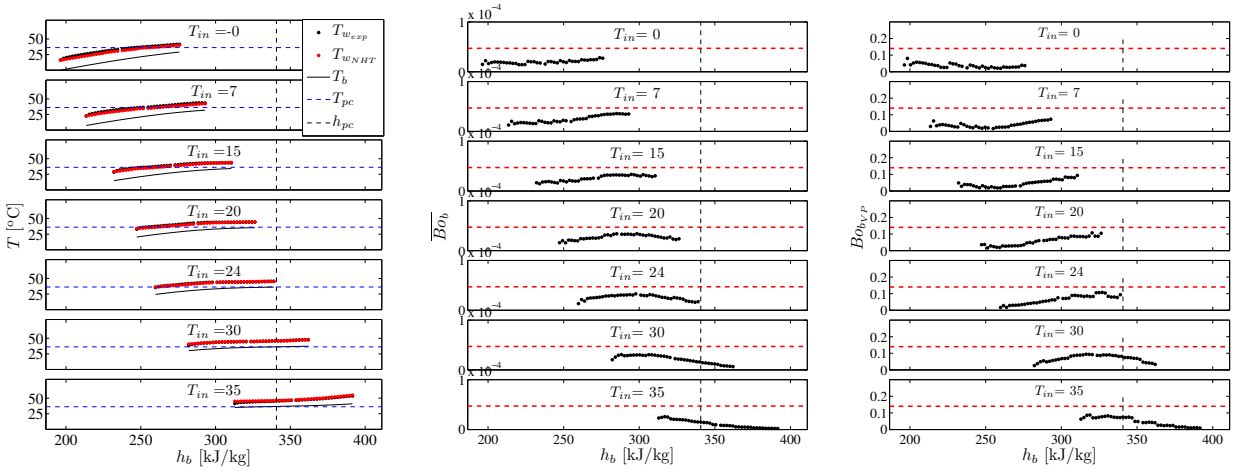
(a) T_w profiles (b) $\overline{Bo_b}$ profiles (c) $Bo_{b_{VP}}$ profiles

Figure C.2: $\overline{Bo_b}$, $Bo_{b_{VP}}$, and T_w profiles for $P/P_c = 1.13$, $D = 4.6$ mm, $G = 300$ kg/m^{2}s, $q = 18$ kW/m^2; dashed red lines represent suggested thresholds; T_{in} is in °C.



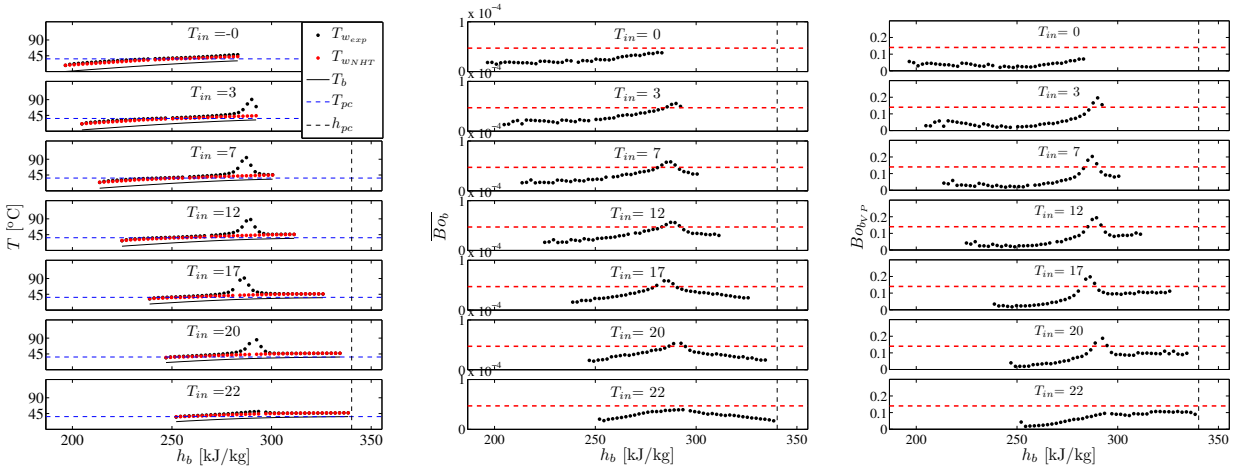
(a) T_w profiles (b) $\overline{Bo_b}$ profiles (c) $Bo_{b_{VP}}$ profiles

Figure C.3: $\overline{Bo_b}$, $Bo_{b_{VP}}$, and T_w profiles for $P/P_c = 1.13$, $D = 4.6$ mm, $G = 300$ kg/m^{2}s, $q = 20$ kW/m^2; dashed red lines represent suggested thresholds; T_{in} is in °C.



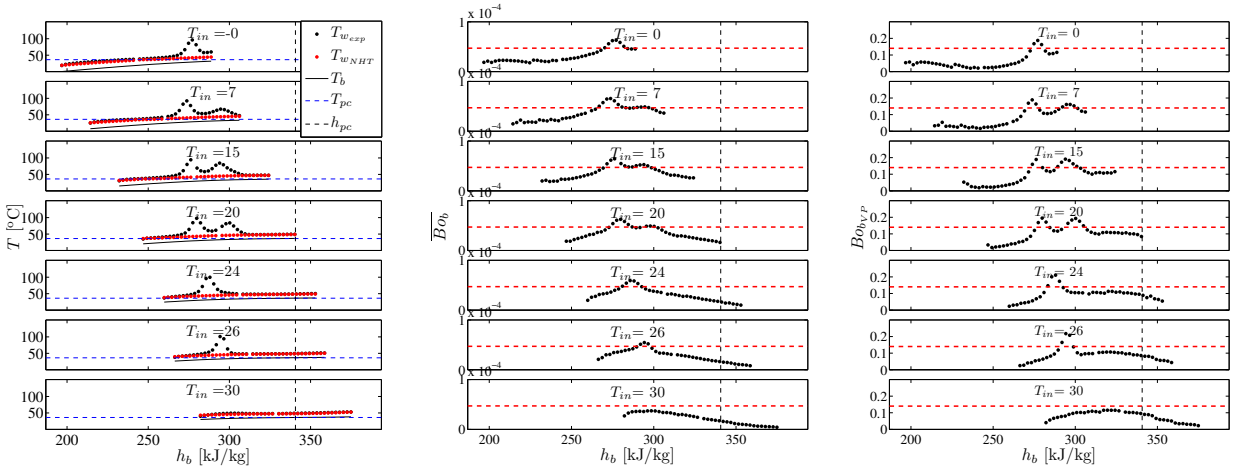
(a) T_w profiles (b) $\overline{Bo_b}$ profiles (c) $Bo_{b_{VP}}$ profiles

Figure C.4: $\overline{Bo_b}$, $Bo_{b_{VP}}$, and T_w profiles for $P/P_c = 1.13$, $D = 4.6$ mm, $G = 400$ kg/m^{2}s, $q = 30$ kW/m^2; dashed red lines represent suggested thresholds; T_{in} is in °C.



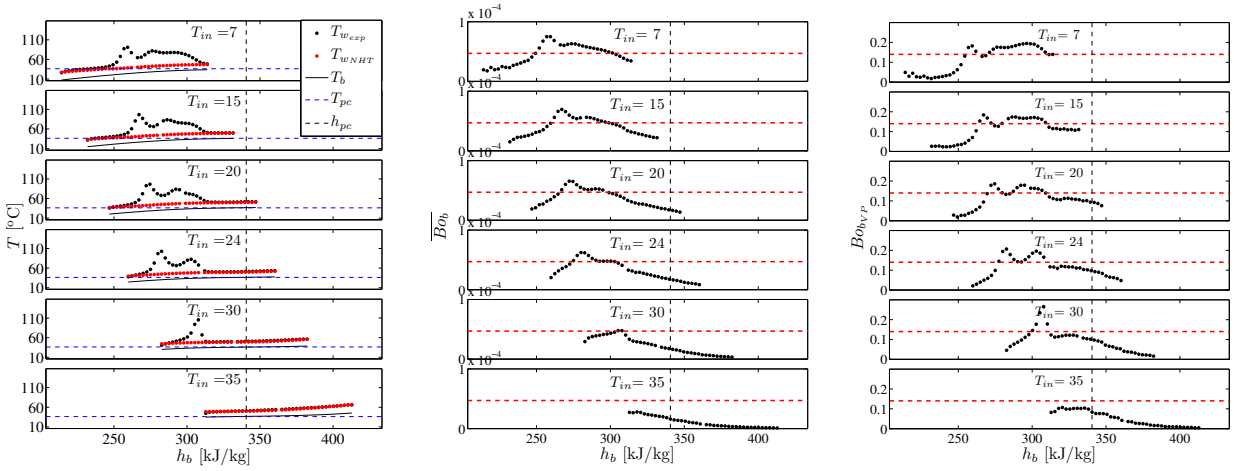
(a) T_w profiles (b) $\overline{Bo_b}$ profiles (c) $Bo_{b_{VP}}$ profiles

Figure C.5: $\overline{Bo_b}$, $Bo_{b_{VP}}$, and T_w profiles for $P/P_c = 1.13$, $D = 4.6$ mm, $G = 400$ kg/m^{2}s, $q = 33$ kW/m^2; dashed red lines represent suggested thresholds; T_{in} is in °C.



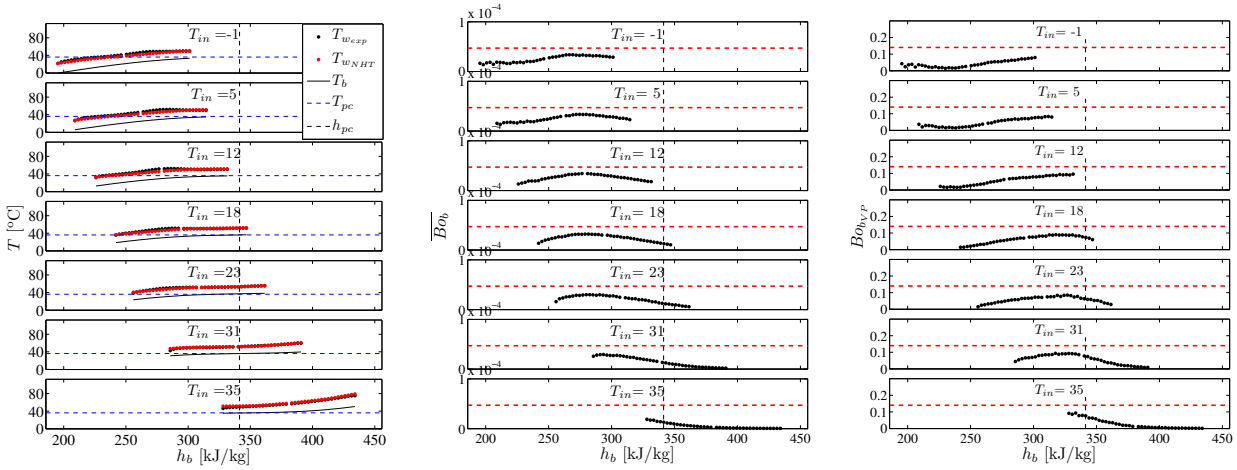
(a) T_w profiles (b) $\overline{Bo_b}$ profiles (c) $Bo_{b_{VP}}$ profiles

Figure C.6: $\overline{Bo_b}$, $Bo_{b_{VP}}$, and T_w profiles for $P/P_c = 1.13$, $D = 4.6$ mm, $G = 400$ kg/m^{2}s, $q = 35$ kW/m^2; dashed red lines represent suggested thresholds; T_{in} is in °C.



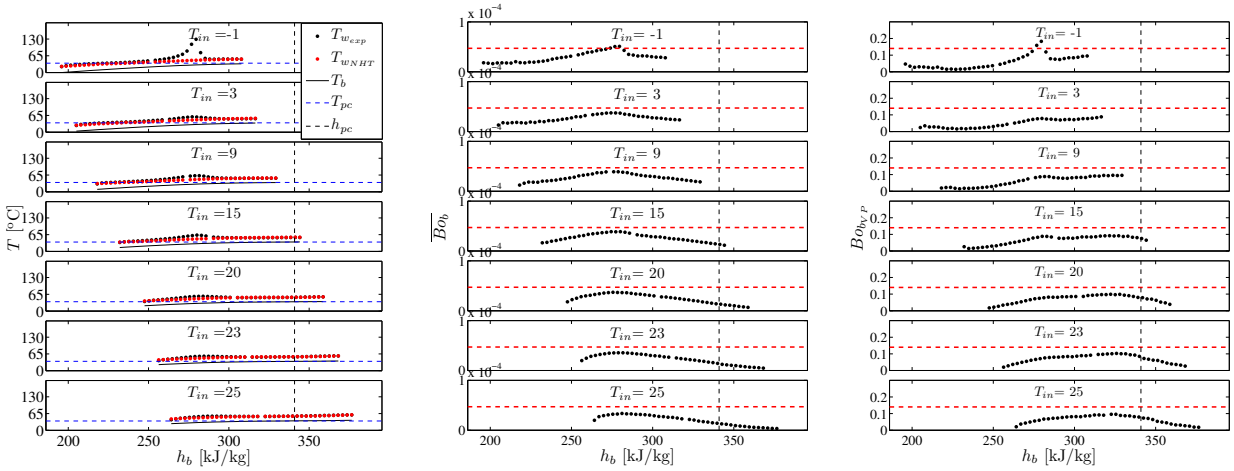
(a) T_w profiles (b) $\overline{Bo_b}$ profiles (c) $Bo_{b_{VP}}$ profiles

Figure C.7: $\overline{Bo_b}$, $Bo_{b_{VP}}$, and T_w profiles for $P/P_c = 1.13$, $D = 4.6$ mm, $G = 400$ kg/m^{2}s, $q = 38$ kW/m^2; dashed red lines represent suggested thresholds; T_{in} is in °C.



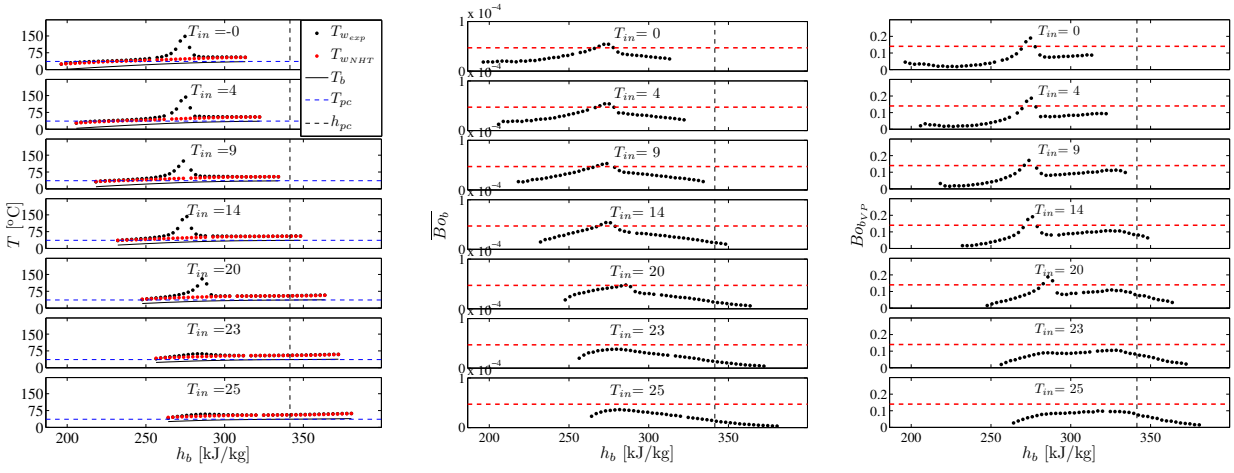
(a) T_w profiles (b) $\overline{Bo_b}$ profiles (c) $Bo_{b_{VP}}$ profiles

Figure C.8: $\overline{Bo_b}$, $Bo_{b_{VP}}$, and T_w profiles for $P/P_c = 1.13$, $D = 4.6$ mm, $G = 500$ kg/m^{2}s, $q = 50$ kW/m^2; dashed red lines represent suggested thresholds; T_{in} is in °C.



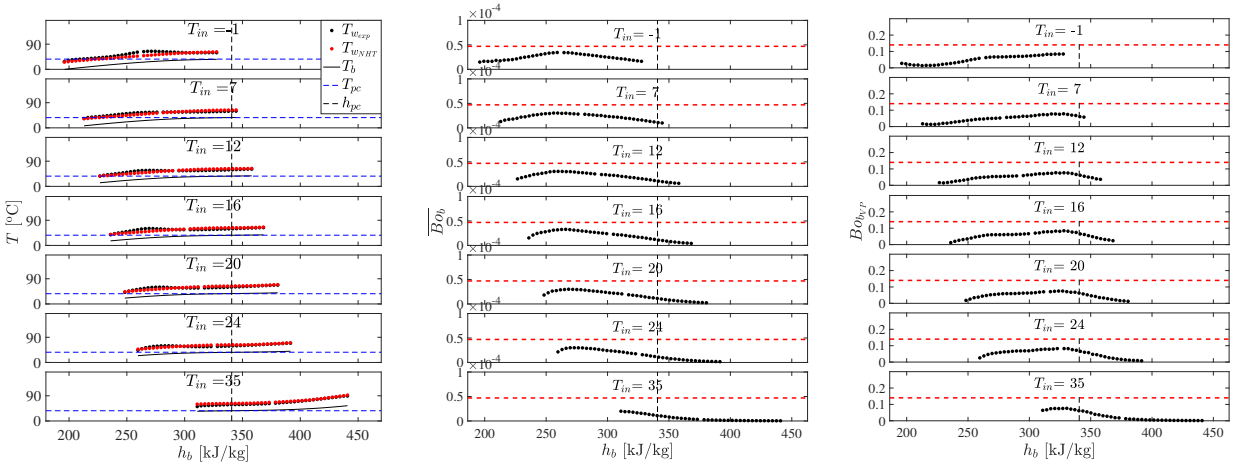
(a) T_w profiles (b) $\overline{Bo_b}$ profiles (c) $Bo_{b_{VP}}$ profiles

Figure C.9: $\overline{Bo_b}$, $Bo_{b_{VP}}$, and T_w profiles for $P/P_c = 1.13$, $D = 4.6$ mm, $G = 500$ kg/m^{2}s, $q = 53$ kW/m^2; dashed red lines represent suggested thresholds; T_{in} is in °C.



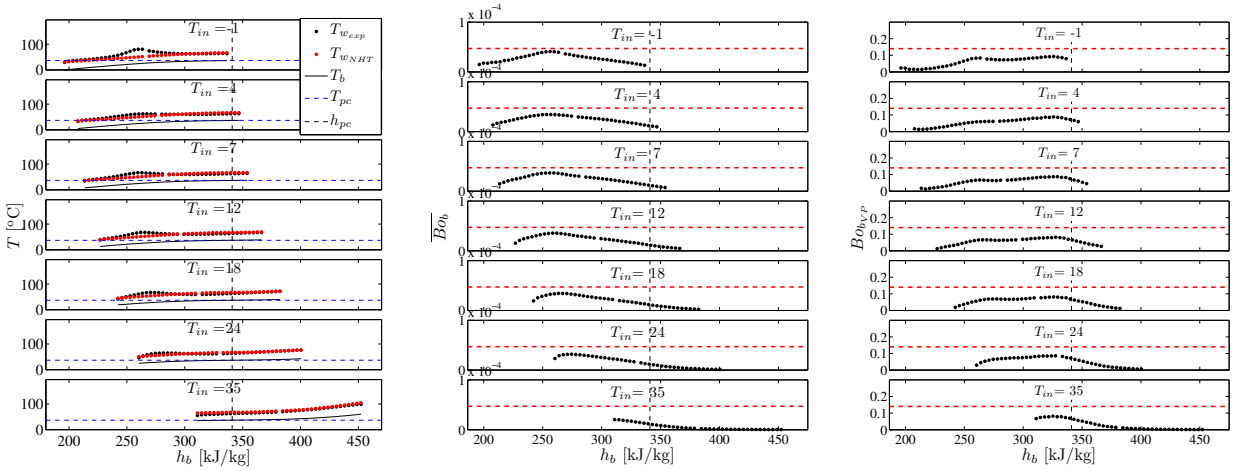
(a) T_w profiles (b) $\overline{Bo_b}$ profiles (c) $Bo_{b_{VP}}$ profiles

Figure C.10: $\overline{Bo_b}$, $Bo_{b_{VP}}$, and T_w profiles for $P/P_c = 1.13$, $D = 4.6$ mm, $G = 500$ kg/m^{2}s, $q = 55$ kW/m^2; dashed red lines represent suggested thresholds; T_{in} is in °C.



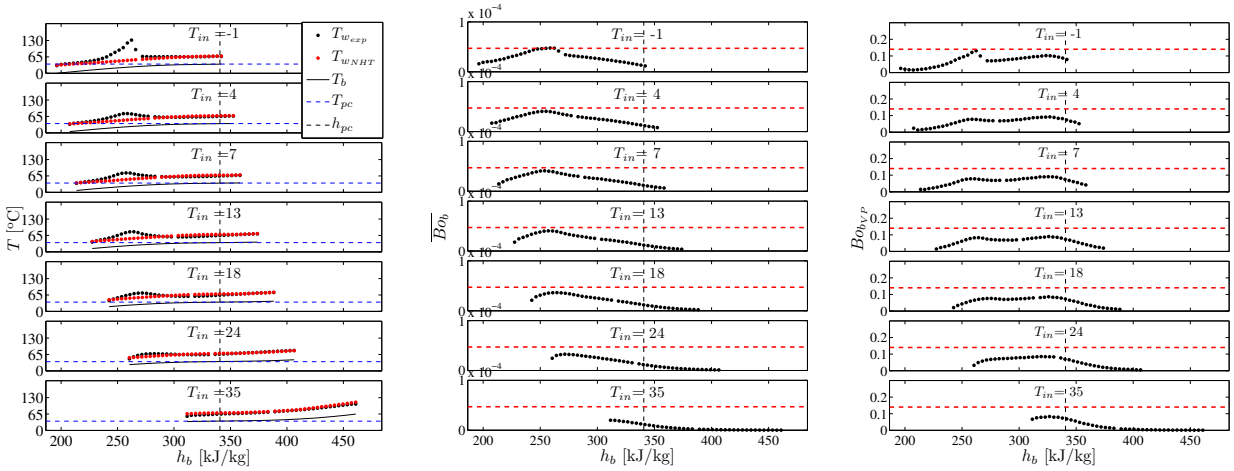
(a) T_w profiles (b) $\overline{Bo_b}$ profiles (c) $Bo_{b_{VP}}$ profiles

Figure C.11: $\overline{Bo_b}$, $Bo_{b_{VP}}$, and T_w profiles for $P/P_c = 1.13$, $D = 4.6$ mm, $G = 600$ kg/m^{2}s, $q = 75$ kW/m^2; dashed red lines represent suggested thresholds; T_{in} is in °C.



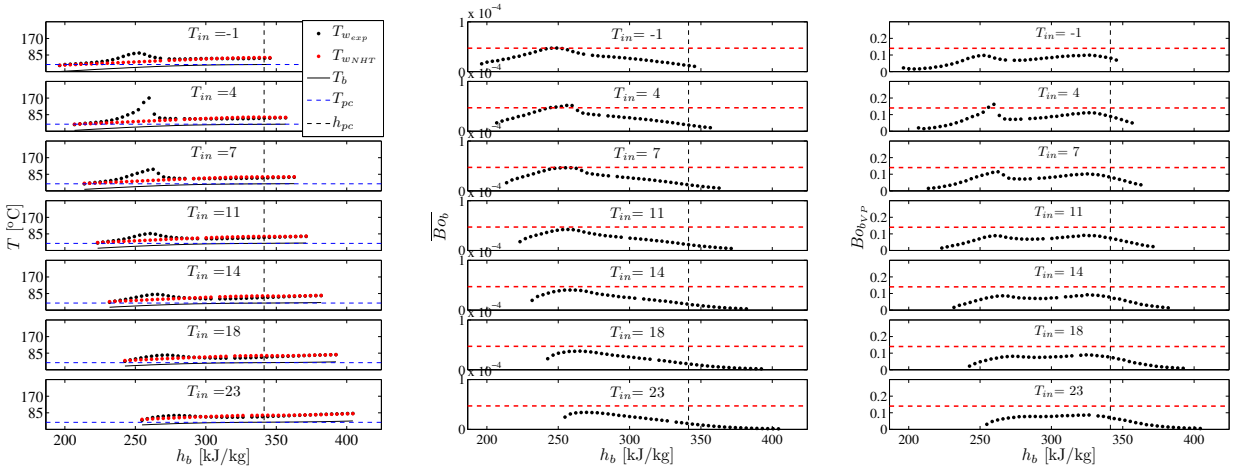
(a) T_w profiles (b) $\overline{Bo_b}$ profiles (c) $Bo_{b_{VP}}$ profiles

Figure C.12: $\overline{Bo_b}$, $Bo_{b_{VP}}$, and T_w profiles for $P/P_c = 1.13$, $D = 4.6$ mm, $G = 600$ kg/m^{2}s, $q = 80$ kW/m^2; dashed red lines represent suggested thresholds; T_{in} is in °C.



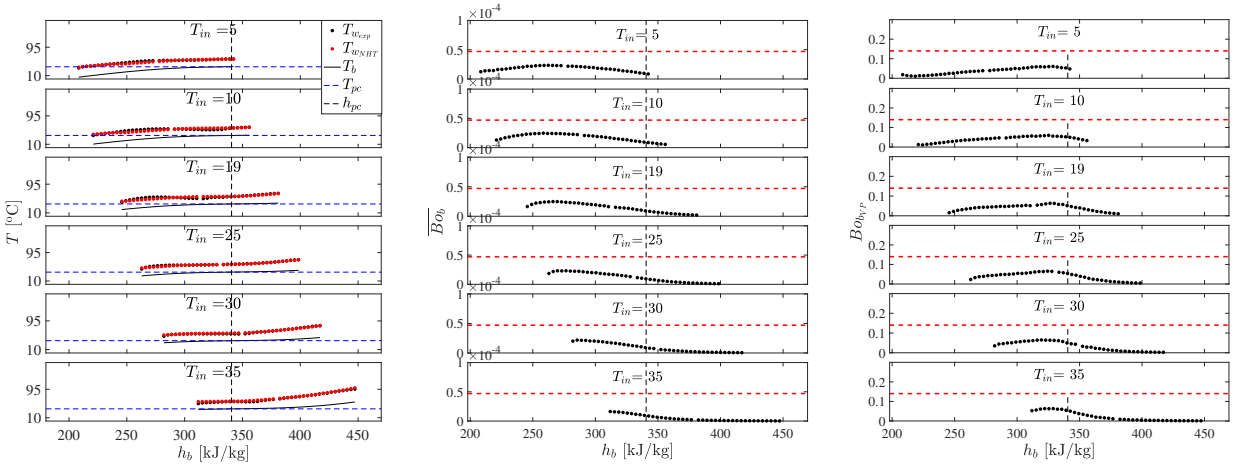
(a) T_w profiles (b) $\overline{Bo_b}$ profiles (c) $Bo_{b_{VP}}$ profiles

Figure C.13: $\overline{Bo_b}$, $Bo_{b_{VP}}$, and T_w profiles for $P/P_c = 1.13$, $D = 4.6$ mm, $G = 600$ kg/m^{2}s, $q = 83$ kW/m^2; dashed red lines represent suggested thresholds; T_{in} is in °C.



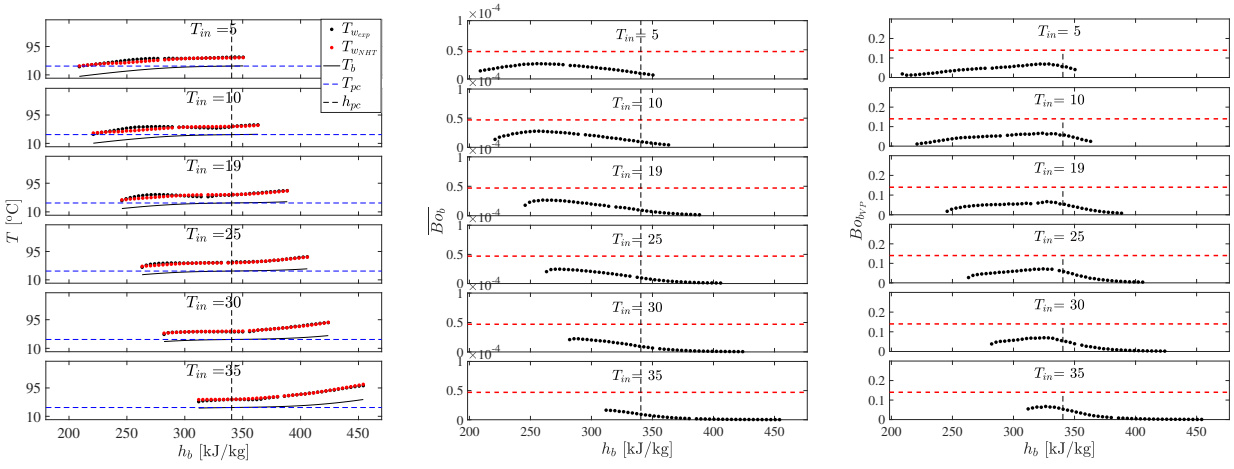
(a) T_w profiles (b) $\overline{Bo_b}$ profiles (c) $Bo_{b_{VP}}$ profiles

Figure C.14: $\overline{Bo_b}$, $Bo_{b_{VP}}$, and T_w profiles for $P/P_c = 1.13$, $D = 4.6$ mm, $G = 600$ kg/m^{2}s, $q = 85$ kW/m^2; dashed red lines represent suggested thresholds; T_{in} is in °C.



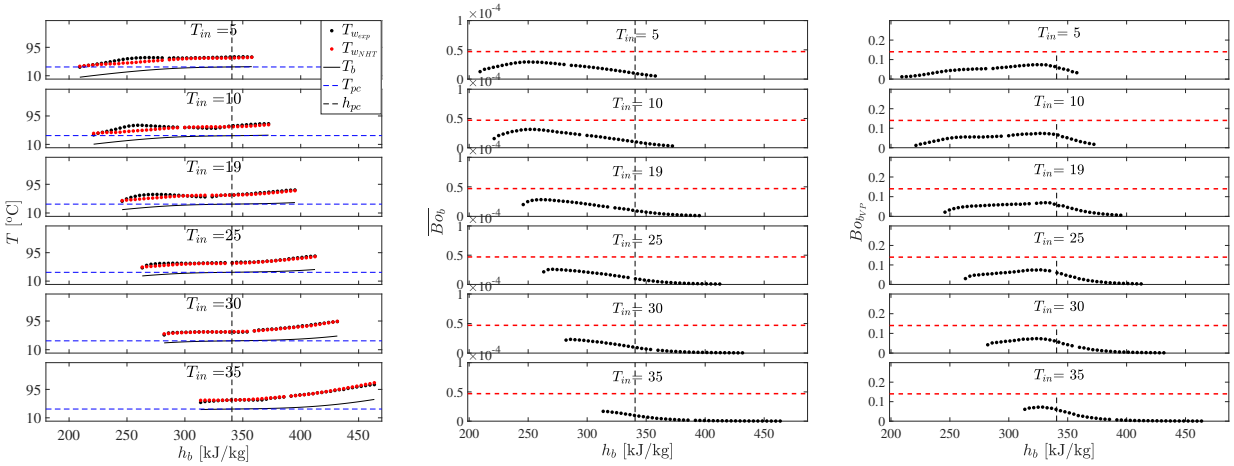
(a) T_w profiles (b) $\overline{Bo_b}$ profiles (c) $Bo_{b_{VP}}$ profiles

Figure C.15: $\overline{Bo_b}$, $Bo_{b_{VP}}$, and T_w profiles for $P/P_c = 1.13$, $D = 4.6$ mm, $G = 700$ kg/m^{2}s, $q = 90$ kW/m^2; dashed red lines represent suggested thresholds; T_{in} is in °C.



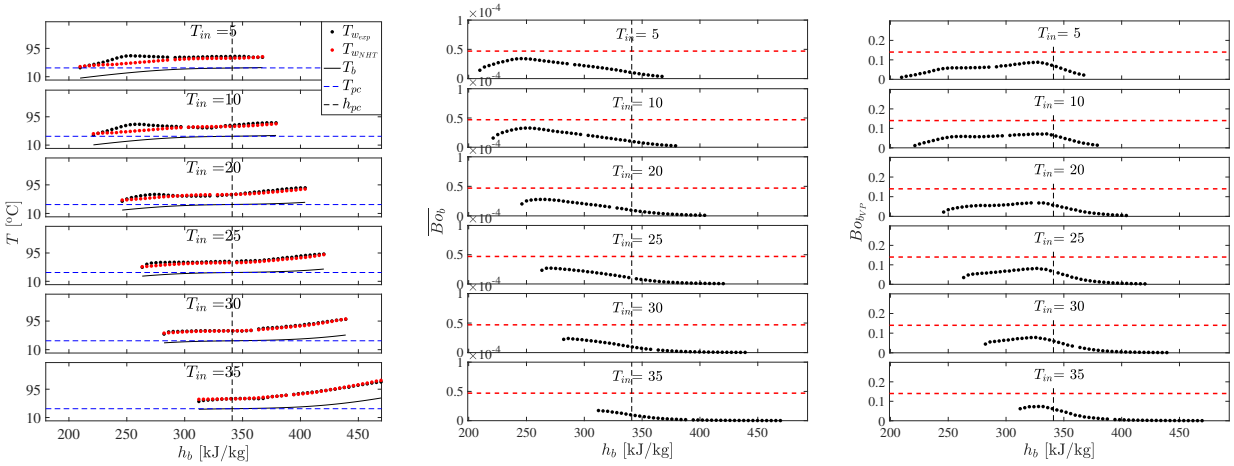
(a) T_w profiles (b) $\overline{Bo_b}$ profiles (c) $Bo_{b_{VP}}$ profiles

Figure C.16: $\overline{Bo_b}$, $Bo_{b_{VP}}$, and T_w profiles for $P/P_c = 1.13$, $D = 4.6$ mm, $G = 700$ kg/m^{2}s, $q = 95$ kW/m^2; dashed red lines represent suggested thresholds; T_{in} is in °C.



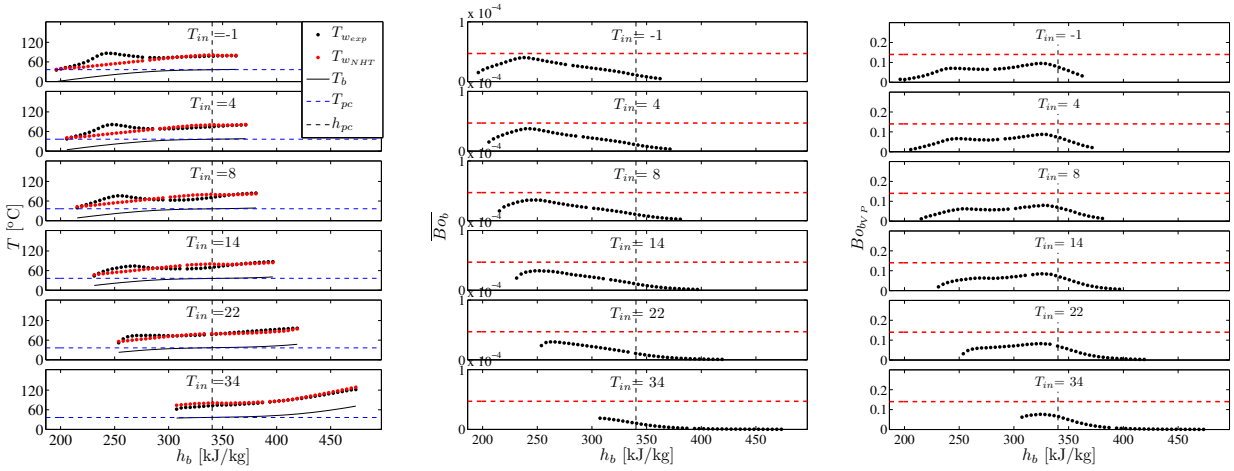
(a) T_w profiles (b) $\overline{Bo_b}$ profiles (c) $Bo_{b_{VP}}$ profiles

Figure C.17: $\overline{Bo_b}$, $Bo_{b_{VP}}$, and T_w profiles for $P/P_c = 1.13$, $D = 4.6$ mm, $G = 700$ kg/m^{2}s, $q = 100$ kW/m^2; dashed red lines represent suggested thresholds; T_{in} is in °C.



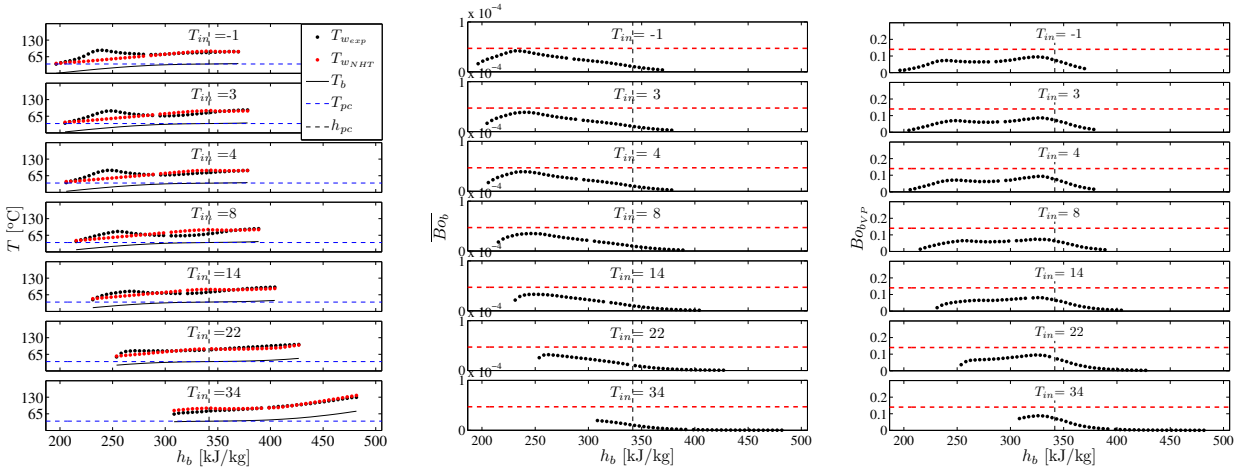
(a) T_w profiles (b) $\overline{Bo_b}$ profiles (c) $Bo_{b_{VP}}$ profiles

Figure C.18: $\overline{Bo_b}$, $Bo_{b_{VP}}$, and T_w profiles for $P/P_c = 1.13$, $D = 4.6$ mm, $G = 700$ kg/m^{2}s, $q = 105$ kW/m^2; dashed red lines represent suggested thresholds; T_{in} is in °C.



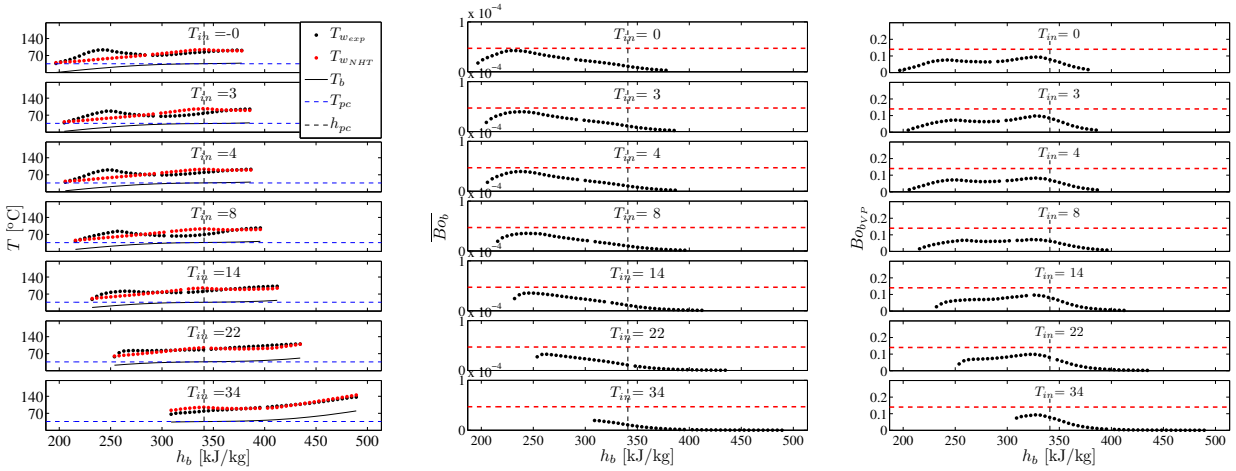
(a) T_w profiles (b) $\overline{Bo_b}$ profiles (c) $Bo_{b_{VP}}$ profiles

Figure C.19: $\overline{Bo_b}$, $Bo_{b_{VP}}$, and T_w profiles for $P/P_c = 1.13$, $D = 4.6$ mm, $G = 700$ kg/m^{2}s, $q = 110$ kW/m^2; dashed red lines represent suggested thresholds; T_{in} is in °C.



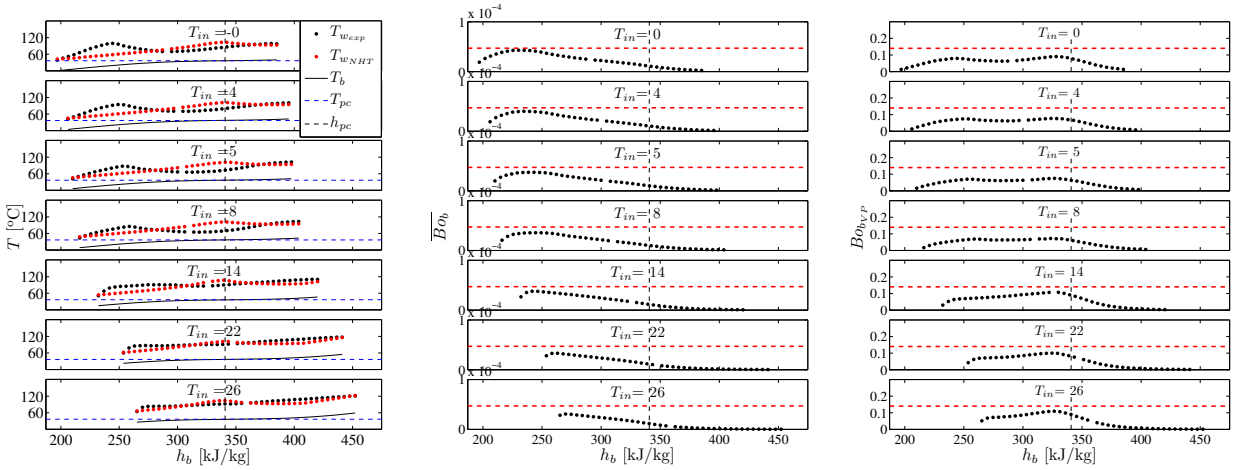
(a) T_w profiles (b) $\overline{Bo_b}$ profiles (c) $Bo_{b_{VP}}$ profiles

Figure C.20: $\overline{Bo_b}$, $Bo_{b_{VP}}$, and T_w profiles for $P/P_c = 1.13$, $D = 4.6$ mm, $G = 700$ kg/m^{2}s, $q = 115$ kW/m^2; dashed red lines represent suggested thresholds; T_{in} is in °C.



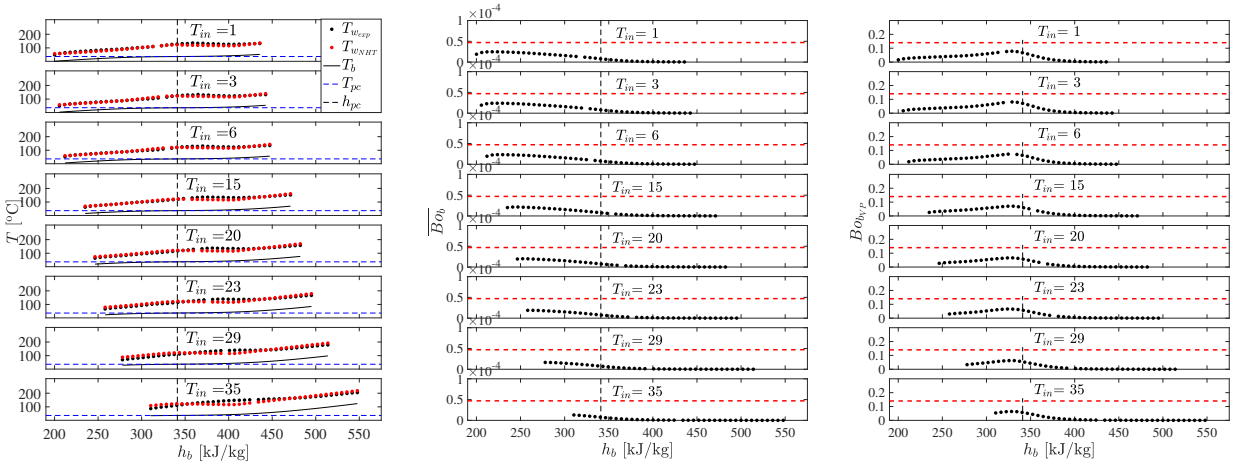
(a) T_w profiles (b) $\overline{Bo_b}$ profiles (c) $Bo_{b_{VP}}$ profiles

Figure C.21: $\overline{Bo_b}$, $Bo_{b_{VP}}$, and T_w profiles for $P/P_c = 1.13$, $D = 4.6$ mm, $G = 700$ kg/m^{2}s, $q = 120$ kW/m^2; dashed red lines represent suggested thresholds; T_{in} is in °C.



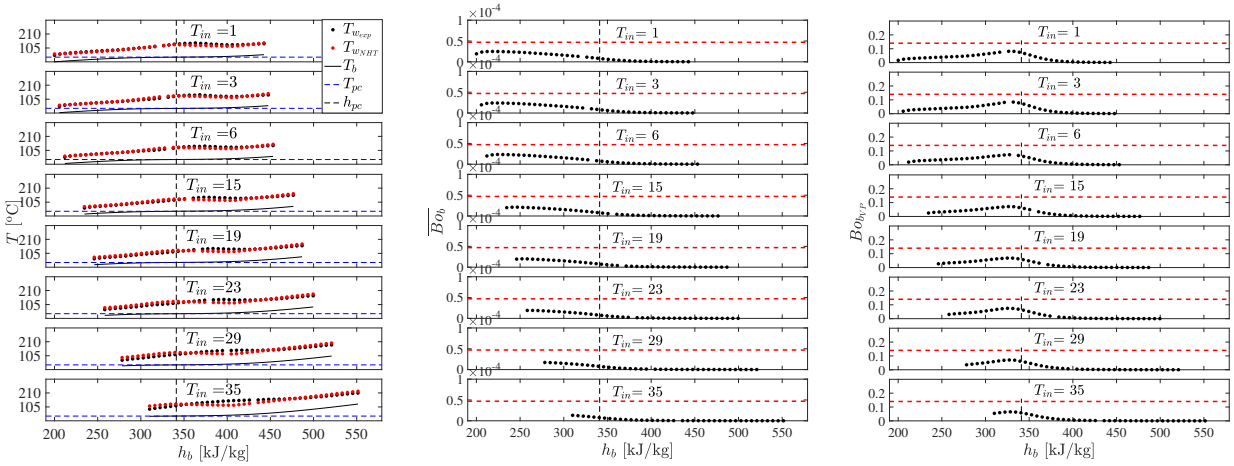
(a) T_w profiles (b) $\overline{Bo_b}$ profiles (c) $Bo_{b_{VP}}$ profiles

Figure C.22: $\overline{Bo_b}$, $Bo_{b_{VP}}$, and T_w profiles for $P/P_c = 1.13$, $D = 4.6$ mm, $G = 700$ kg/m^{2}s, $q = 125$ kW/m^2; dashed red lines represent suggested thresholds; T_{in} is in °C.



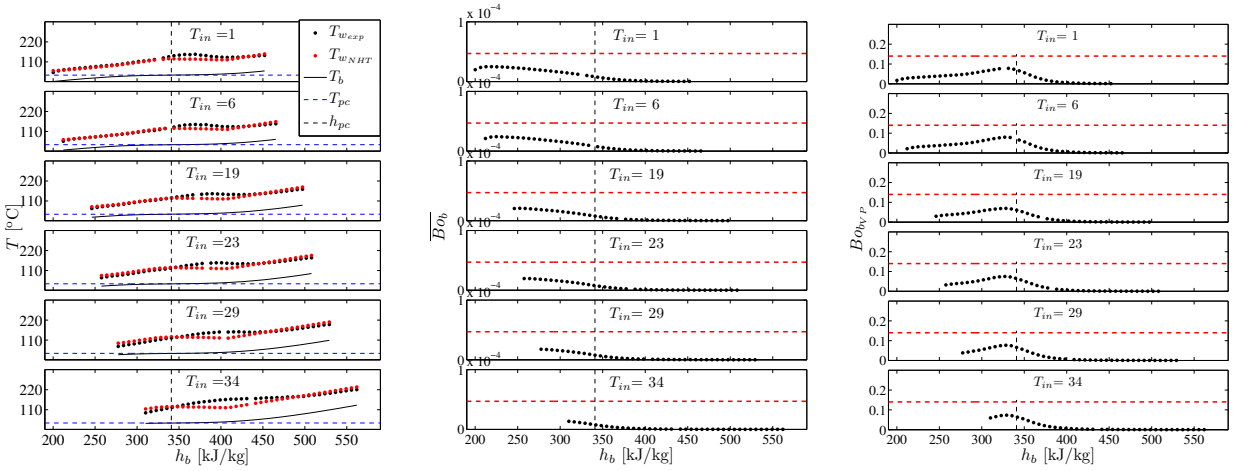
(a) T_w profiles (b) $\overline{Bo_b}$ profiles (c) $Bo_{b_{VP}}$ profiles

Figure C.23: $\overline{Bo_b}$, $Bo_{b_{VP}}$, and T_w profiles for $P/P_c = 1.13$, $D = 4.6$ mm, $G = 1000$ kg/m^{2}s, $q = 225$ kW/m^2; dashed red lines represent suggested thresholds; T_{in} is in °C.



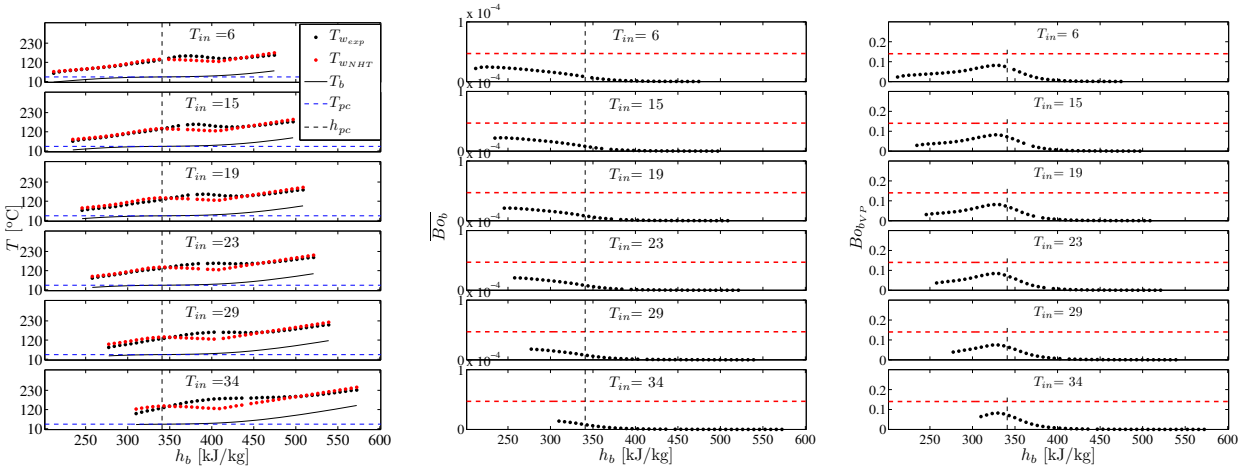
(a) T_w profiles (b) $\overline{Bo_b}$ profiles (c) $Bo_{b_{VP}}$ profiles

Figure C.24: $\overline{Bo_b}$, $Bo_{b_{VP}}$, and T_w profiles for $P/P_c = 1.13$, $D = 4.6$ mm, $G = 1000$ kg/m^{2}s, $q = 230$ kW/m^2; dashed red lines represent suggested thresholds; T_{in} is in °C.



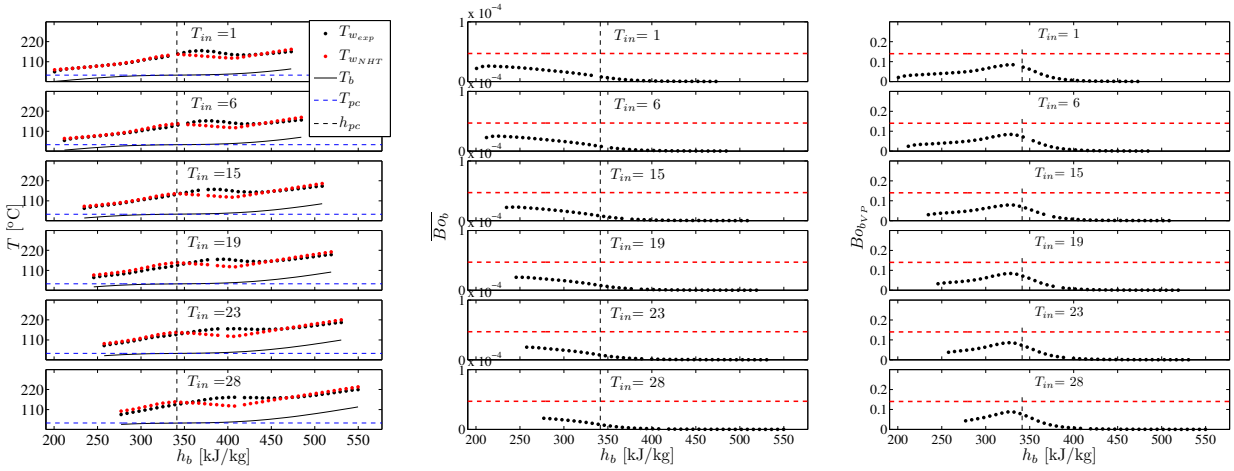
(a) T_w profiles (b) $\overline{Bo_b}$ profiles (c) $Bo_{b_{VP}}$ profiles

Figure C.25: $\overline{Bo_b}$, $Bo_{b_{VP}}$, and T_w profiles for $P/P_c = 1.13$, $D = 4.6$ mm, $G = 1000$ kg/m^{2}s, $q = 240$ kW/m^2; dashed red lines represent suggested thresholds; T_{in} is in °C.



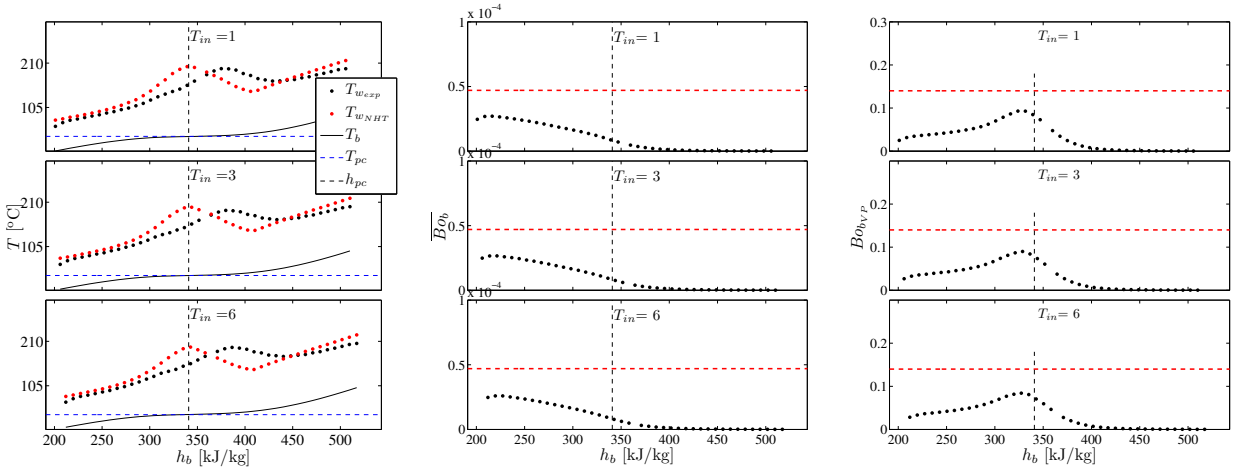
(a) T_w profiles (b) $\overline{Bo_b}$ profiles (c) $Bo_{b_{VP}}$ profiles

Figure C.26: $\overline{Bo_b}$, $Bo_{b_{VP}}$, and T_w profiles for $P/P_c = 1.13$, $D = 4.6$ mm, $G = 1000$ kg/m^{2}s, $q = 250$ kW/m^2; dashed red lines represent suggested thresholds; T_{in} is in °C.



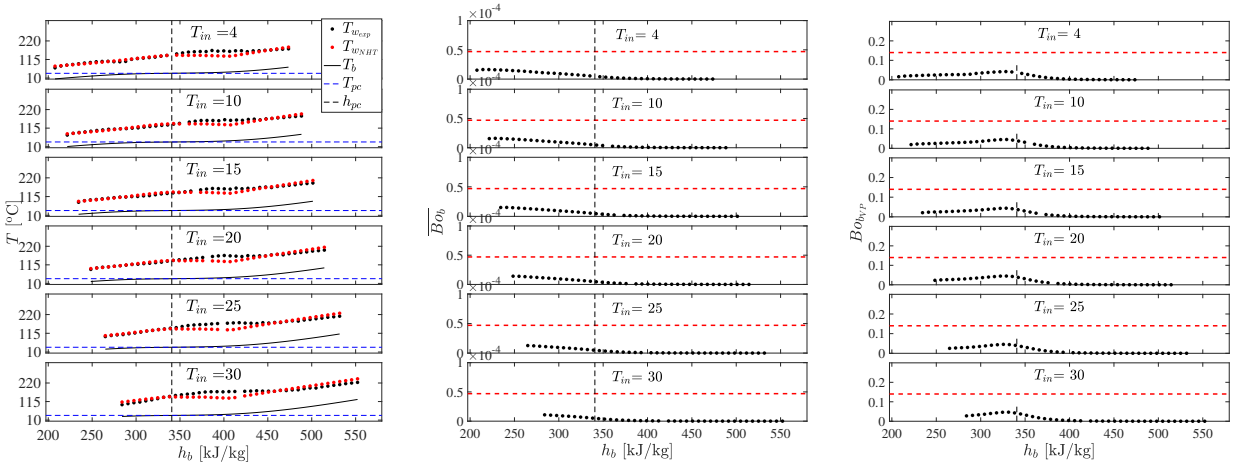
(a) T_w profiles (b) $\overline{Bo_b}$ profiles (c) $Bo_{b_{VP}}$ profiles

Figure C.27: $\overline{Bo_b}$, $Bo_{b_{VP}}$, and T_w profiles for $P/P_c = 1.13$, $D = 4.6$ mm, $G = 1000$ kg/m^{2}s, $q = 260$ kW/m^2; dashed red lines represent suggested thresholds; T_{in} is in °C.



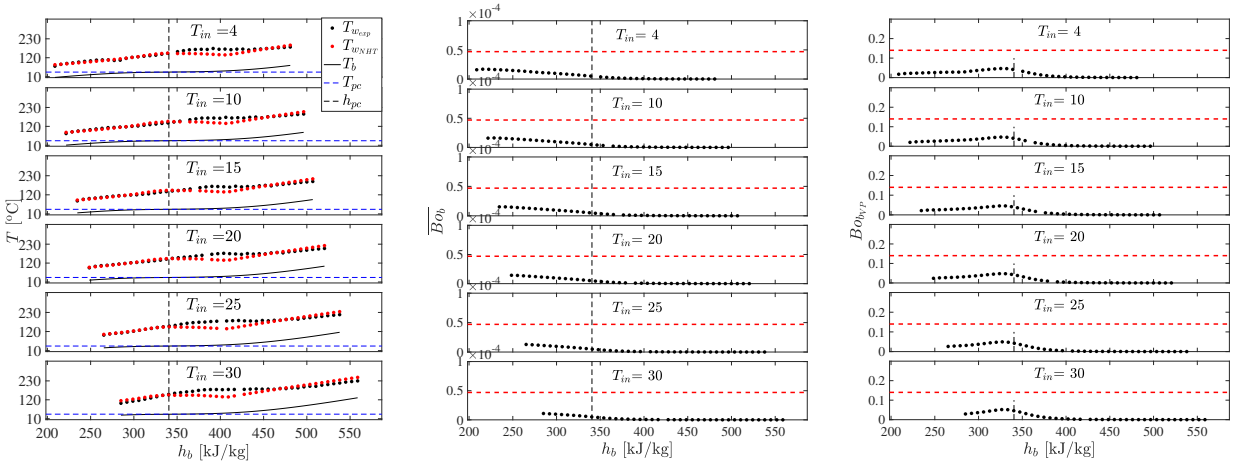
(a) T_w profiles (b) $\overline{Bo_b}$ profiles (c) $Bo_{b_{VP}}$ profiles

Figure C.28: $\overline{Bo_b}$, $Bo_{b_{VP}}$, and T_w profiles for $P/P_c = 1.13$, $D = 4.6$ mm, $G = 1000$ kg/m^{2}s, $q = 290$ kW/m^2; dashed red lines represent suggested thresholds; T_{in} is in °C.



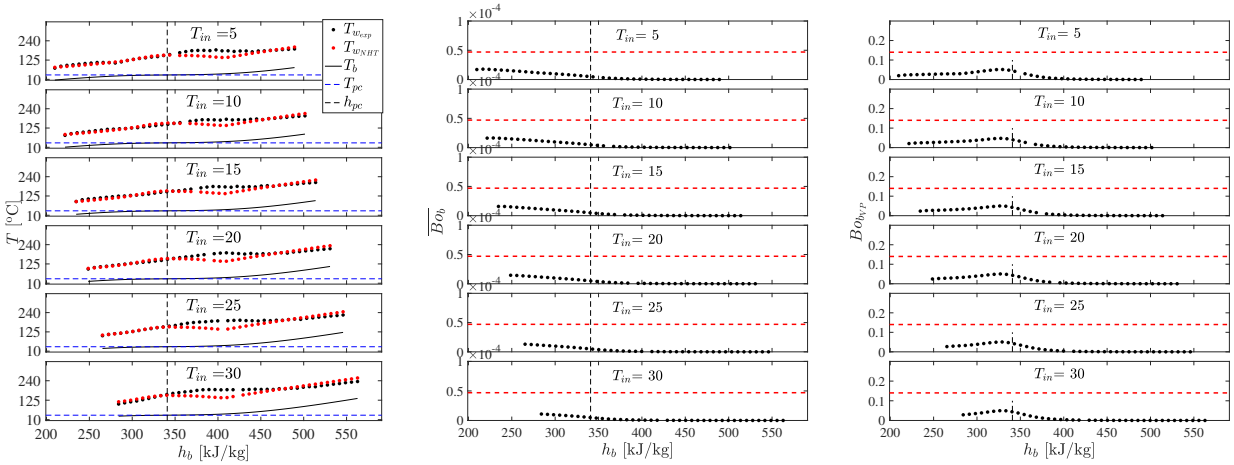
(a) T_w profiles (b) $\overline{Bo_b}$ profiles (c) $Bo_{b_{VP}}$ profiles

Figure C.29: $\overline{Bo_b}$, $Bo_{b_{VP}}$, and T_w profiles for $P/P_c = 1.13$, $D = 4.6$ mm, $G = 1500$ kg/m^{2}s, $q = 380$ kW/m^2; dashed red lines represent suggested thresholds; T_{in} is in °C.



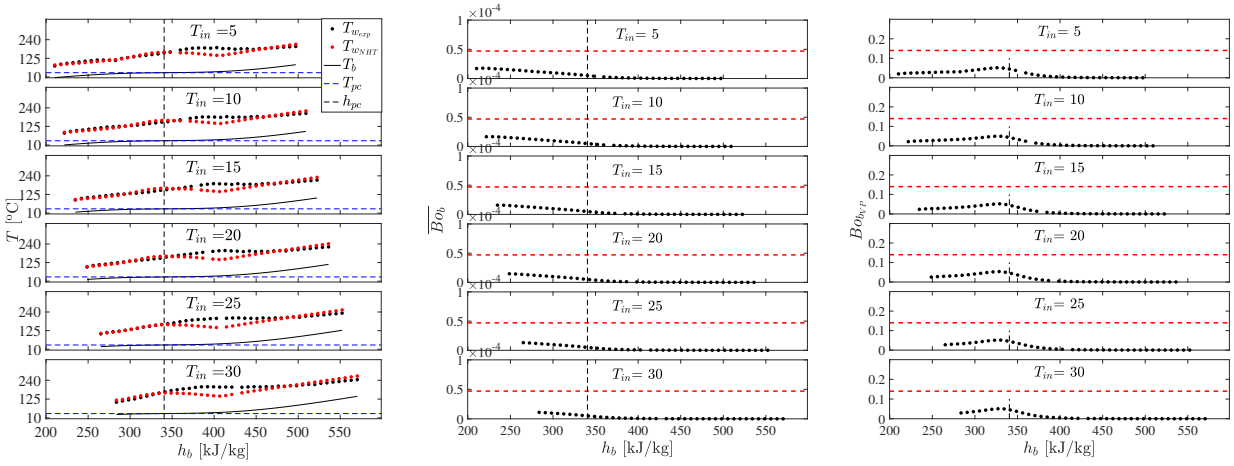
(a) T_w profiles (b) $\overline{Bo_b}$ profiles (c) $Bo_{b_{VP}}$ profiles

Figure C.30: $\overline{Bo_b}$, $Bo_{b_{VP}}$, and T_w profiles for $P/P_c = 1.13$, $D = 4.6$ mm, $G = 1500$ kg/m^{2}s, $q = 390$ kW/m^2; dashed red lines represent suggested thresholds; T_{in} is in °C.



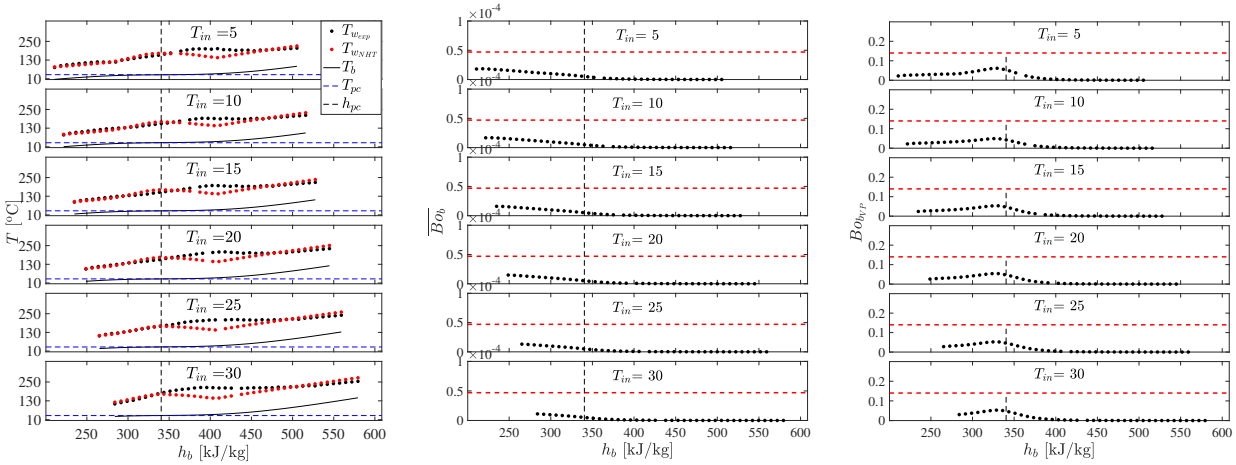
(a) T_w profiles (b) $\overline{Bo_b}$ profiles (c) $Bo_{b_{VP}}$ profiles

Figure C.31: $\overline{Bo_b}$, $Bo_{b_{VP}}$, and T_w profiles for $P/P_c = 1.13$, $D = 4.6$ mm, $G = 1500$ kg/m^{2}s, $q = 400$ kW/m^2; dashed red lines represent suggested thresholds; T_{in} is in °C.



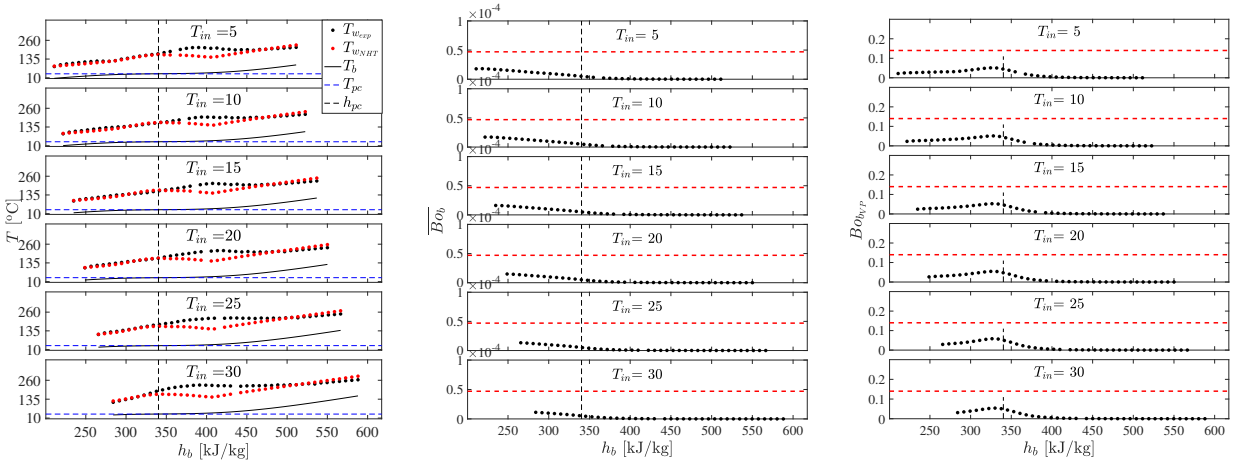
(a) T_w profiles (b) $\overline{Bo_b}$ profiles (c) $Bo_{b_{VP}}$ profiles

Figure C.32: $\overline{Bo_b}$, $Bo_{b_{VP}}$, and T_w profiles for $P/P_c = 1.13$, $D = 4.6$ mm, $G = 1500$ kg/m^{2}s, $q = 410$ kW/m^2; dashed red lines represent suggested thresholds; T_{in} is in °C.



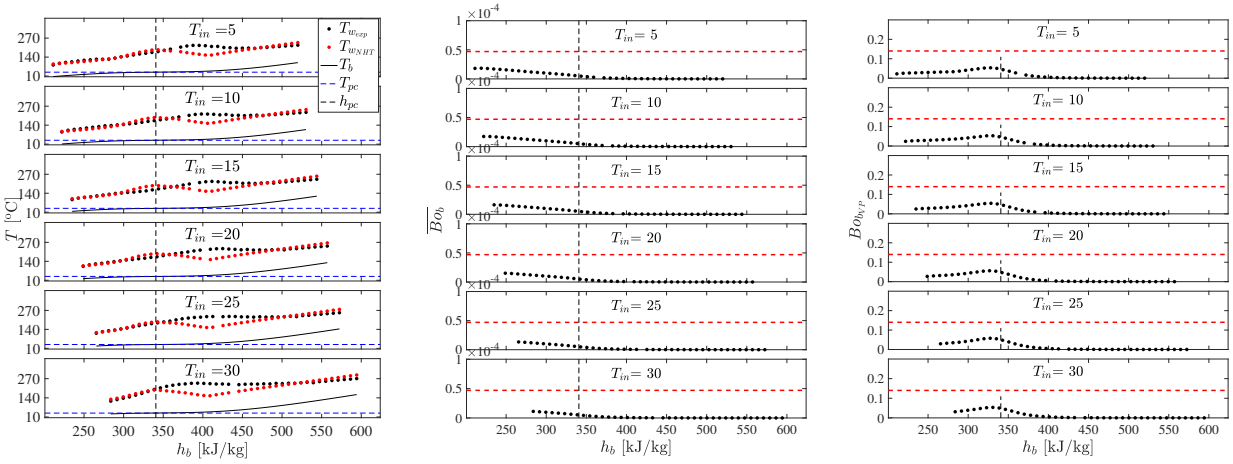
(a) T_w profiles (b) $\overline{Bo_b}$ profiles (c) $Bo_{b_{VP}}$ profiles

Figure C.33: $\overline{Bo_b}$, $Bo_{b_{VP}}$, and T_w profiles for $P/P_c = 1.13$, $D = 4.6$ mm, $G = 1500$ kg/m^{2}s, $q = 420$ kW/m^2; dashed red lines represent suggested thresholds; T_{in} is in °C.



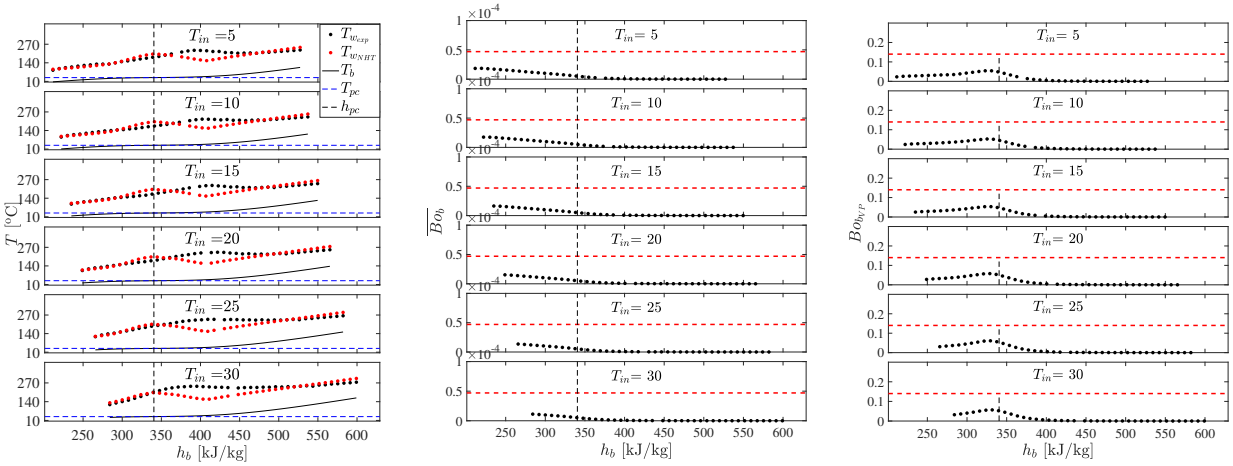
(a) T_w profiles (b) $\overline{Bo_b}$ profiles (c) $Bo_{b_{VP}}$ profiles

Figure C.34: $\overline{Bo_b}$, $Bo_{b_{VP}}$, and T_w profiles for $P/P_c = 1.13$, $D = 4.6$ mm, $G = 1500$ kg/m^{2}s, $q = 430$ kW/m^2; dashed red lines represent suggested thresholds; T_{in} is in °C.



(a) T_w profiles (b) $\overline{Bo_b}$ profiles (c) $Bo_{b_{VP}}$ profiles

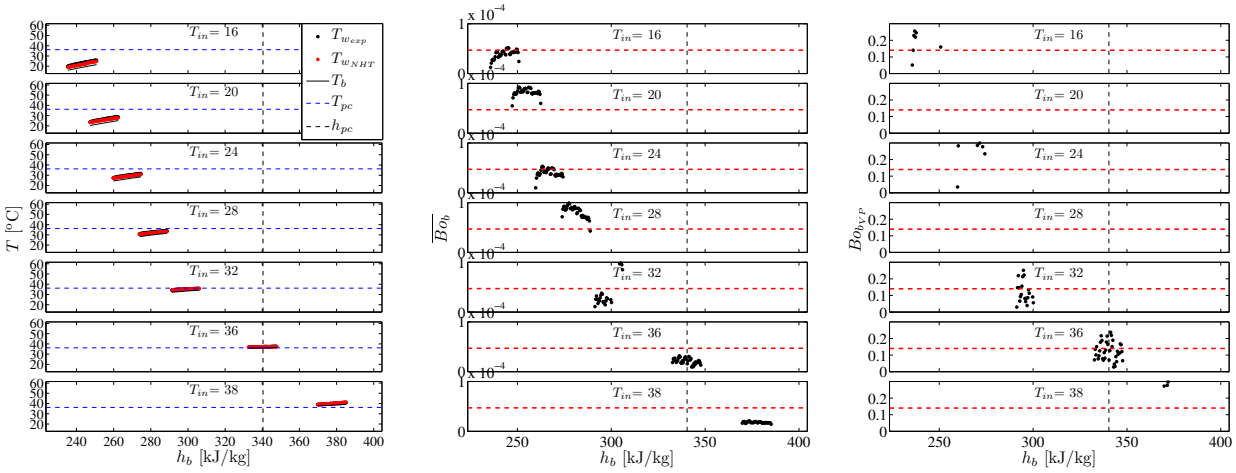
Figure C.35: $\overline{Bo_b}$, $Bo_{b_{VP}}$, and T_w profiles for $P/P_c = 1.13$, $D = 4.6$ mm, $G = 1500$ kg/m^{2}s, $q = 440$ kW/m^2; dashed red lines represent suggested thresholds; T_{in} is in °C.



(a) T_w profiles (b) $\overline{Bo_b}$ profiles (c) $Bo_{b_{VP}}$ profiles

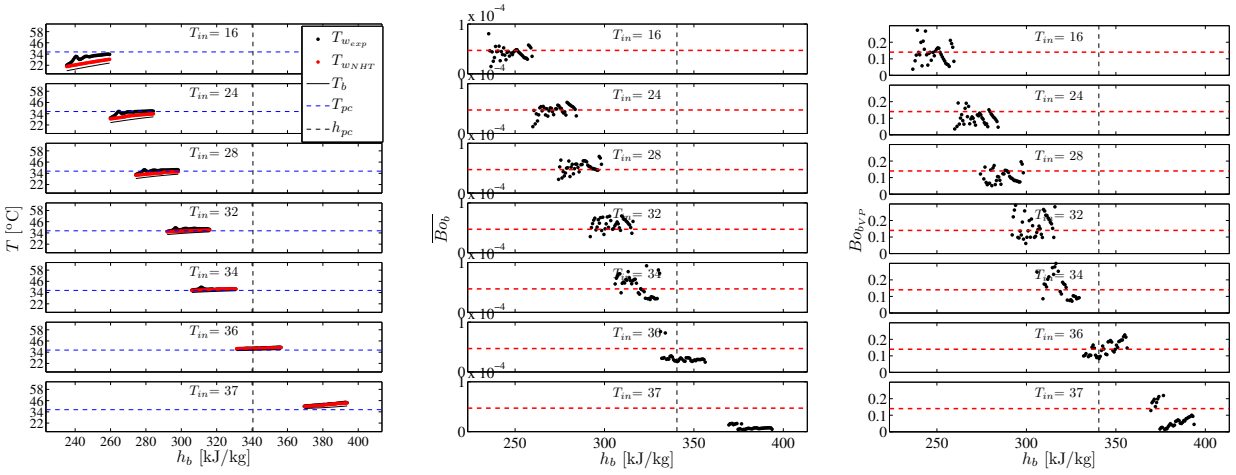
Figure C.36: $\overline{Bo_b}$, $Bo_{b_{VP}}$, and T_w profiles for $P/P_c = 1.13$, $D = 4.6$ mm, $G = 1500$ kg/m^{2}s, $q = 450$ kW/m^2; dashed red lines represent suggested thresholds; T_{in} is in °C.

C.2 8 mm test section



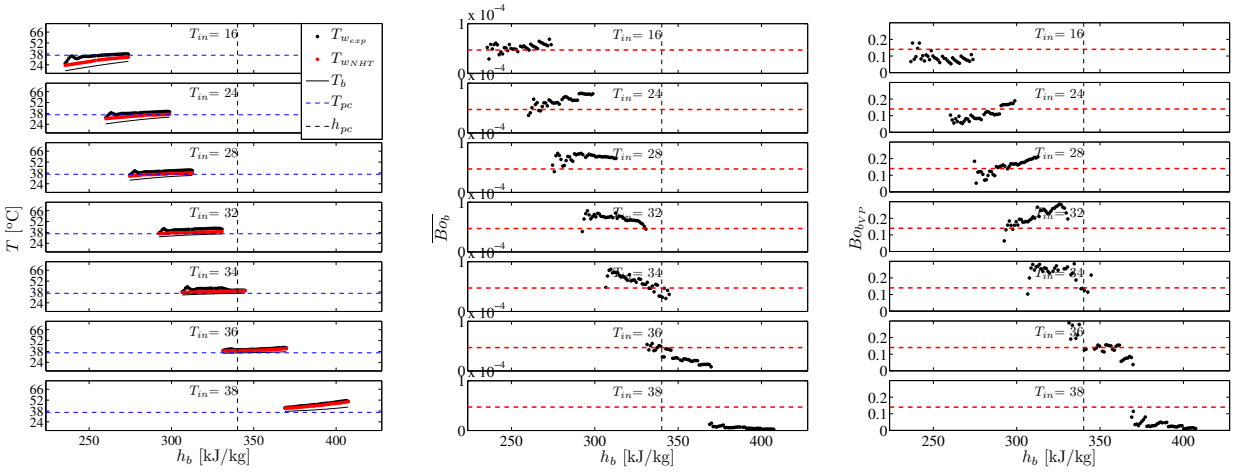
(a) T_w profiles (b) $\overline{Bo_b}$ profiles (c) $Bo_{b_{VP}}$ profiles

Figure C.37: $\overline{Bo_b}$, $Bo_{b_{VP}}$, and T_w profiles for $P/P_c = 1.13$, $D = 8$ mm, $G = 200$ kg/m^{2}s, $q = 3$ kW/m^2; dashed red lines represent suggested thresholds; T_{in} is in °C.



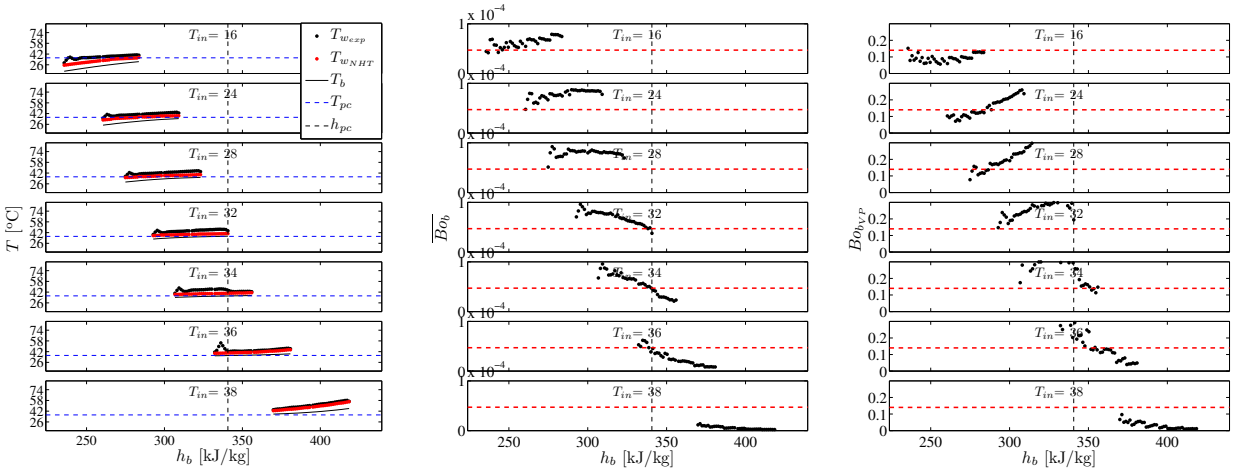
(a) T_w profiles (b) $\overline{Bo_b}$ profiles (c) $Bo_{b_{VP}}$ profiles

Figure C.38: $\overline{Bo_b}$, $Bo_{b_{VP}}$, and T_w profiles for $P/P_c = 1.13$, $D = 8$ mm, $G = 200$ kg/m^{2}s, $q = 5$ kW/m^2; dashed red lines represent suggested thresholds; T_{in} is in °C.



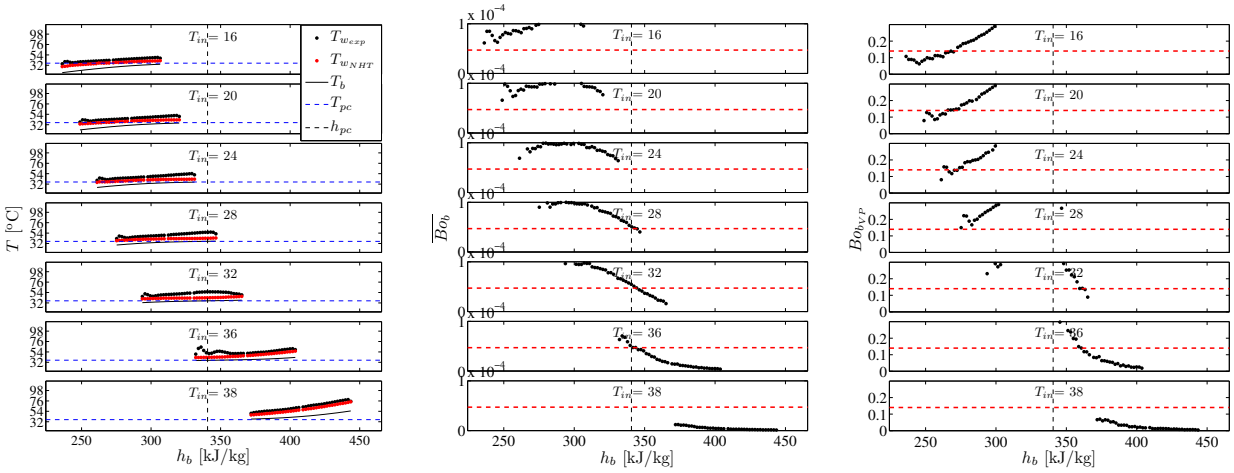
(a) T_w profiles (b) $\overline{Bo_b}$ profiles (c) $Bo_{b_{VP}}$ profiles

Figure C.39: $\overline{Bo_b}$, $Bo_{b_{VP}}$, and T_w profiles for $P/P_c = 1.13$, $D = 8$ mm, $G = 200$ kg/m^{2}s, $q = 8$ kW/m^2; dashed red lines represent suggested thresholds; T_{in} is in °C.



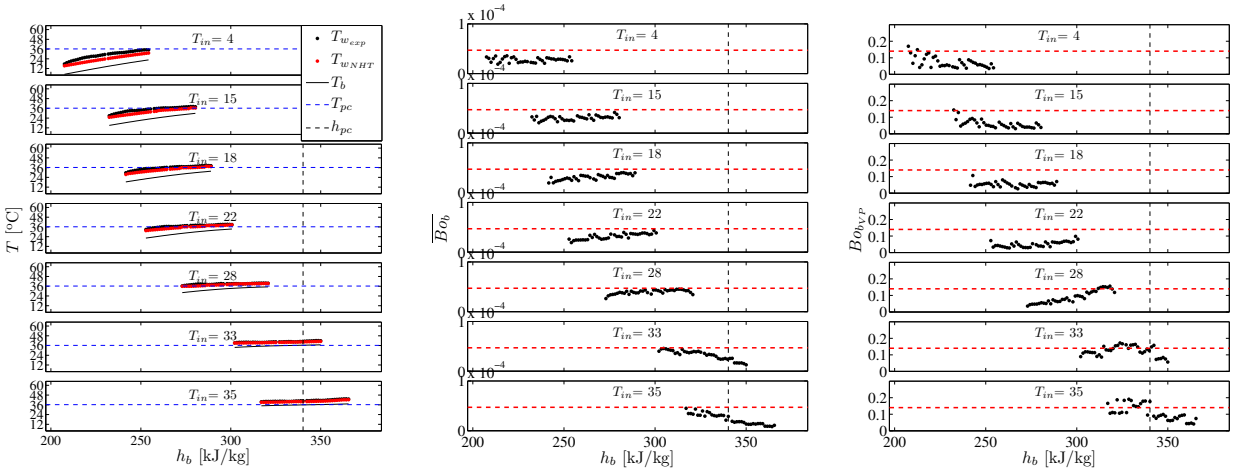
(a) T_w profiles (b) $\overline{Bo_b}$ profiles (c) $Bo_{b_{VP}}$ profiles

Figure C.40: $\overline{Bo_b}$, $Bo_{b_{VP}}$, and T_w profiles for $P/P_c = 1.13$, $D = 8$ mm, $G = 200$ kg/m^{2}s, $q = 10$ kW/m^2; dashed red lines represent suggested thresholds; T_{in} is in °C.



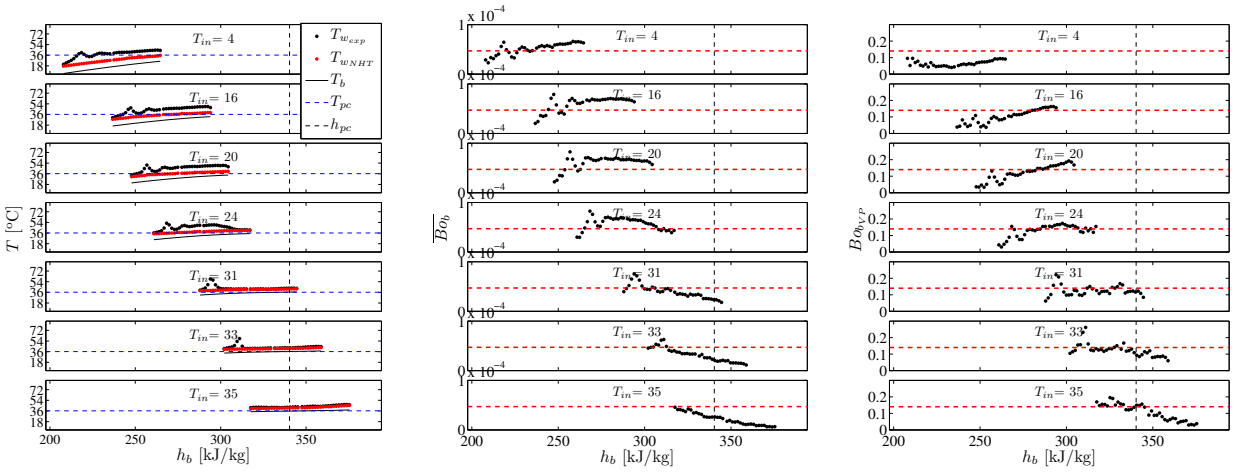
(a) T_w profiles (b) $\overline{Bo_b}$ profiles (c) $Bo_{b_{VP}}$ profiles

Figure C.41: $\overline{Bo_b}$, $Bo_{b_{VP}}$, and T_w profiles for $P/P_c = 1.13$, $D = 8$ mm, $G = 200$ kg/m^{2}s, $q = 15$ kW/m^2; dashed red lines represent suggested thresholds; T_{in} is in °C.



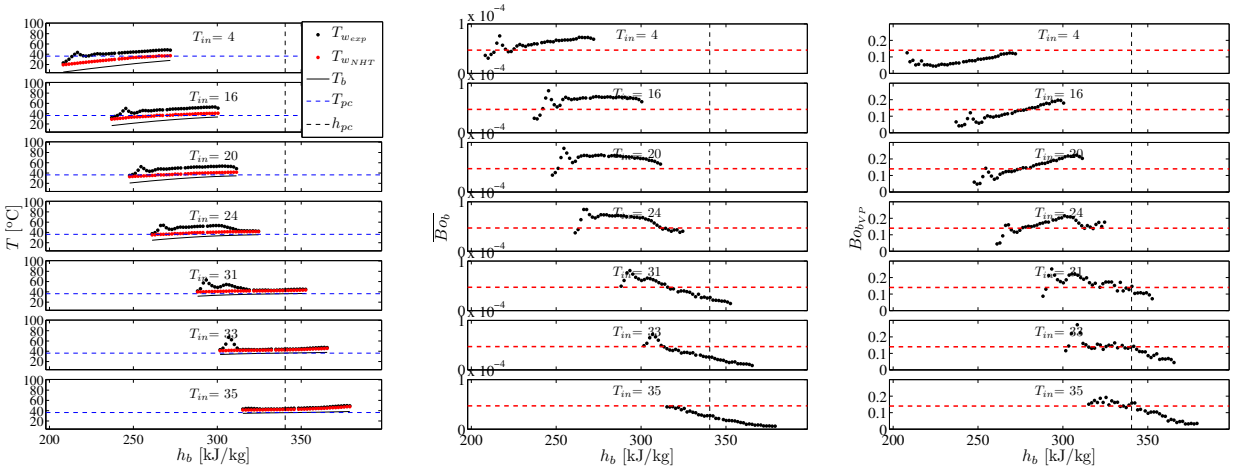
(a) T_w profiles (b) $\overline{Bo_b}$ profiles (c) $Bo_{b_{VP}}$ profiles

Figure C.42: $\overline{Bo_b}$, $Bo_{b_{VP}}$, and T_w profiles for $P/P_c = 1.13$, $D = 8$ mm, $G = 300$ kg/m^{2}s, $q = 15$ kW/m^2; dashed red lines represent suggested thresholds; T_{in} is in °C.



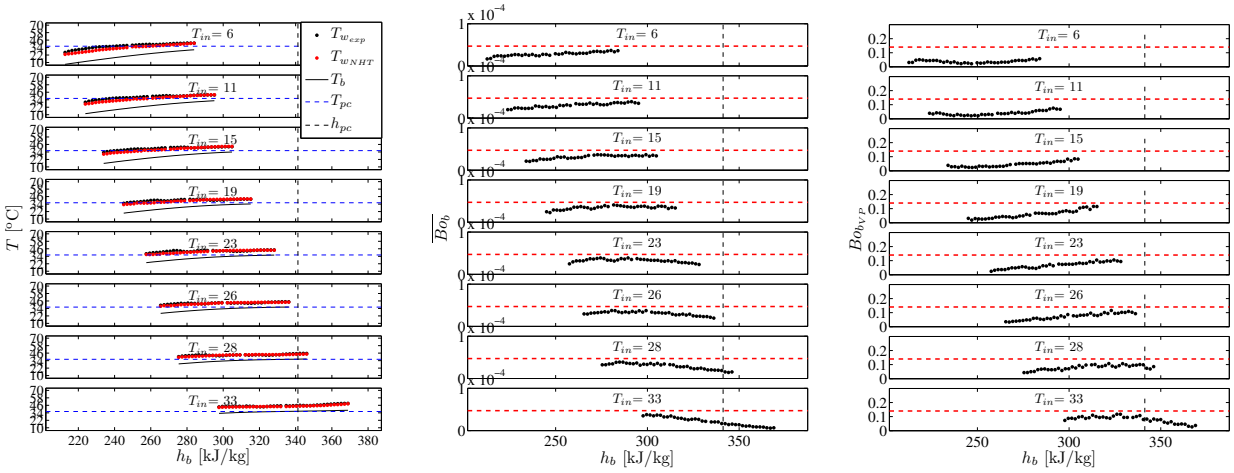
(a) T_w profiles (b) $\overline{Bo_b}$ profiles (c) $Bo_{b_{VP}}$ profiles

Figure C.43: $\overline{Bo_b}$, $Bo_{b_{VP}}$, and T_w profiles for $P/P_c = 1.13$, $D = 8$ mm, $G = 300$ kg/m^{2}s, $q = 18$ kW/m^2; dashed red lines represent suggested thresholds; T_{in} is in °C.



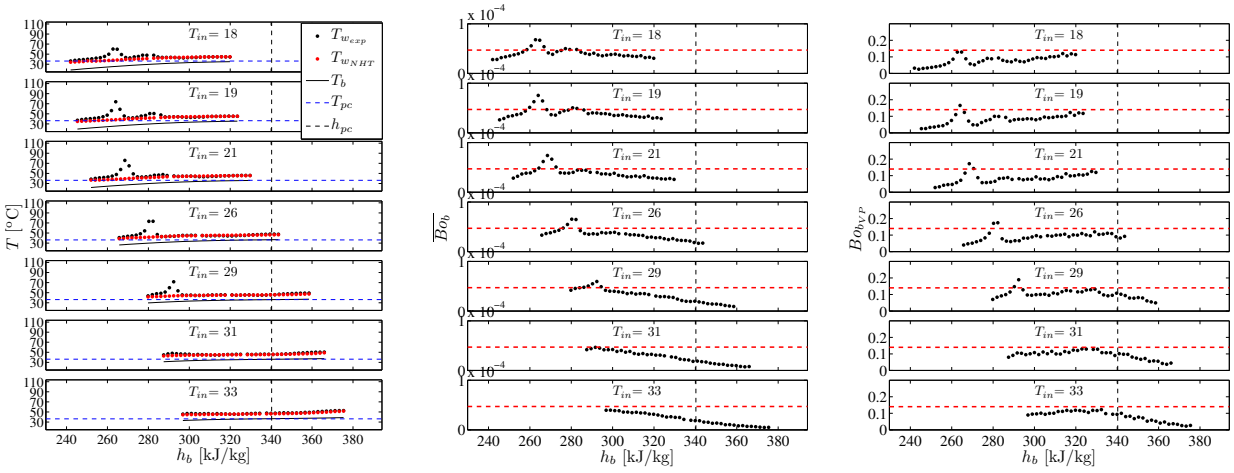
(a) T_w profiles (b) $\overline{Bo_b}$ profiles (c) $Bo_{b_{VP}}$ profiles

Figure C.44: $\overline{Bo_b}$, $Bo_{b_{VP}}$, and T_w profiles for $P/P_c = 1.13$, $D = 8$ mm, $G = 300$ kg/m^{2}s, $q = 20$ kW/m^2; dashed red lines represent suggested thresholds; T_{in} is in °C.



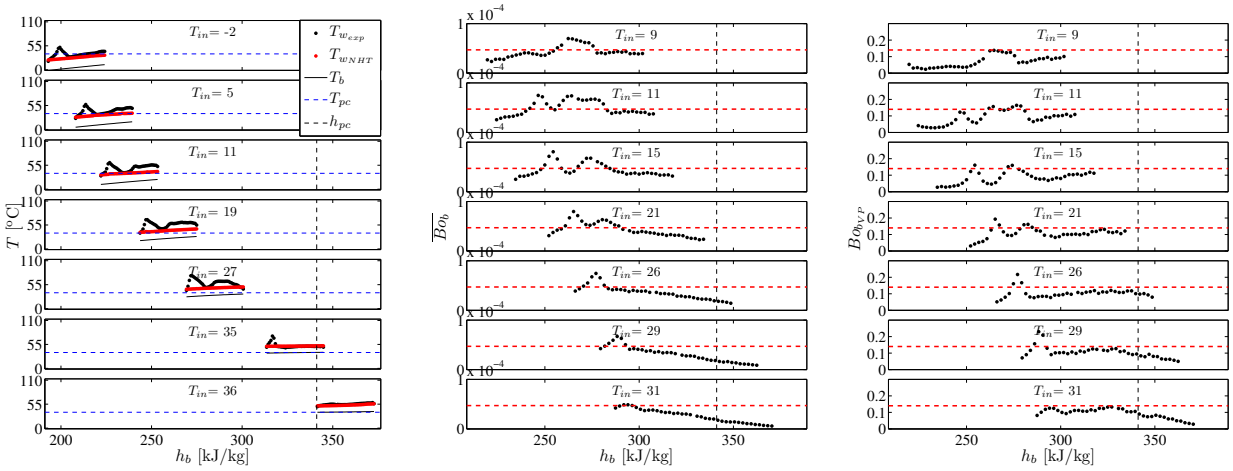
(a) T_w profiles (b) $\overline{Bo_b}$ profiles (c) $Bo_{b_{VP}}$ profiles

Figure C.45: $\overline{Bo_b}$, $Bo_{b_{VP}}$, and T_w profiles for $P/P_c = 1.13$, $D = 8$ mm, $G = 400$ kg/m^{2}s, $q = 30$ kW/m^2; dashed red lines represent suggested thresholds; T_{in} is in °C.



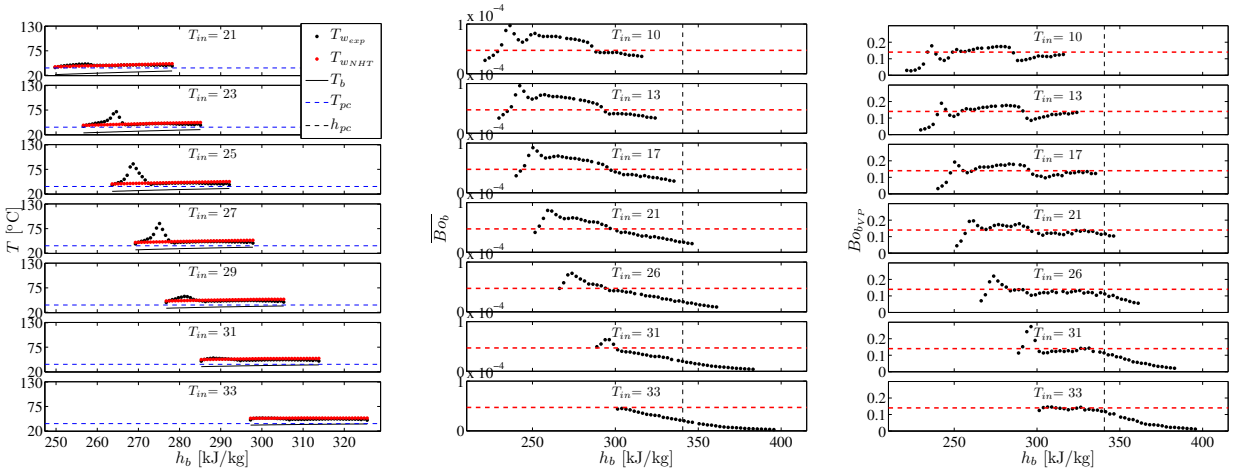
(a) T_w profiles (b) $\overline{Bo_b}$ profiles (c) $Bo_{b_{VP}}$ profiles

Figure C.46: $\overline{Bo_b}$, $Bo_{b_{VP}}$, and T_w profiles for $P/P_c = 1.13$, $D = 8$ mm, $G = 400$ kg/m^{2}s, $q = 33$ kW/m^2; dashed red lines represent suggested thresholds; T_{in} is in °C.



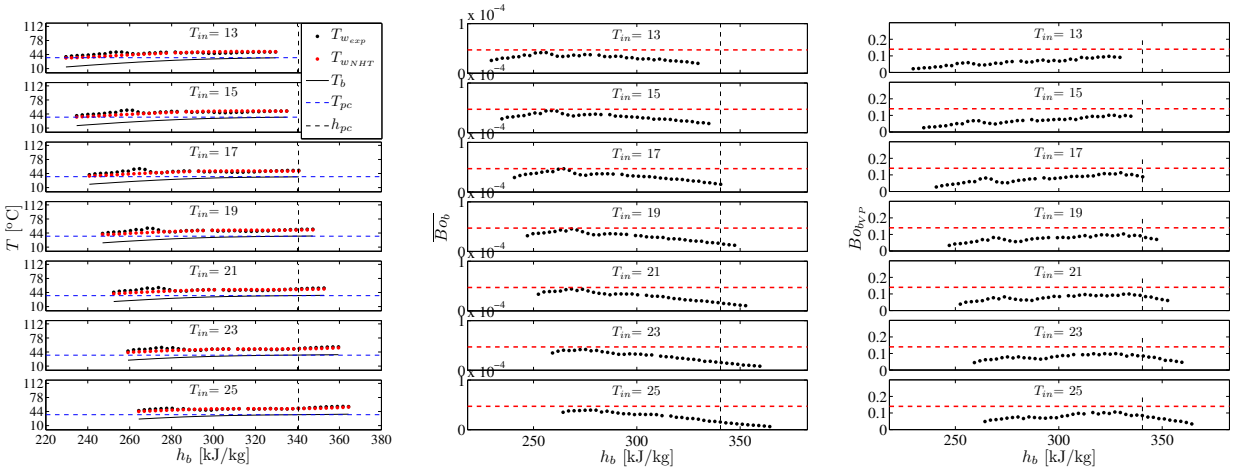
(a) T_w profiles (b) $\overline{Bo_b}$ profiles (c) $Bo_{b_{VP}}$ profiles

Figure C.47: $\overline{Bo_b}$, $Bo_{b_{VP}}$, and T_w profiles for $P/P_c = 1.13$, $D = 8$ mm, $G = 400$ kg/m^{2}s, $q = 35$ kW/m^2; dashed red lines represent suggested thresholds; T_{in} is in °C.



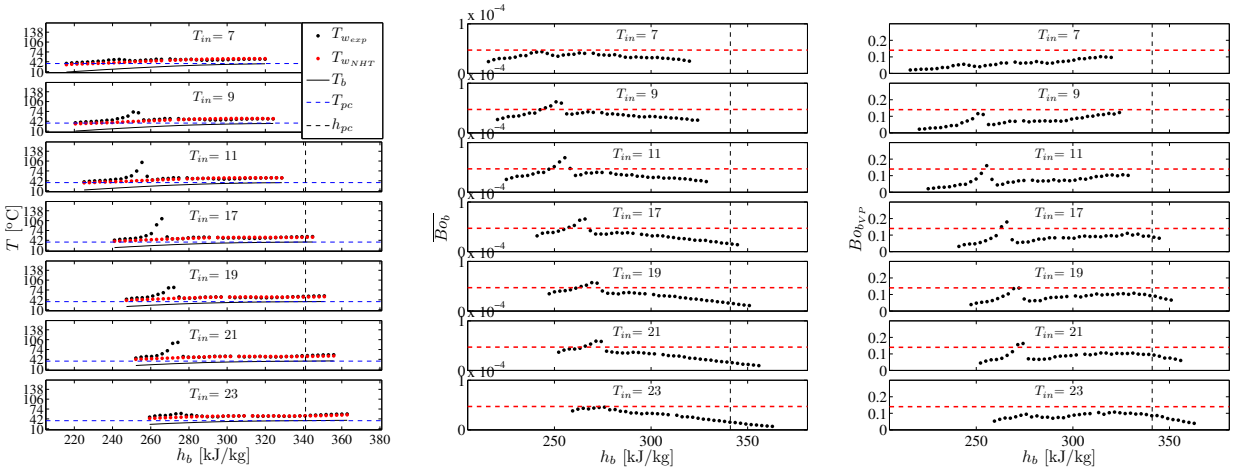
(a) T_w profiles (b) $\overline{Bo_b}$ profiles (c) $Bo_{b_{VP}}$ profiles

Figure C.48: $\overline{Bo_b}$, $Bo_{b_{VP}}$, and T_w profiles for $P/P_c = 1.13$, $D = 8$ mm, $G = 400$ kg/m^{2}s, $q = 40$ kW/m^2; dashed red lines represent suggested thresholds; T_{in} is in °C.



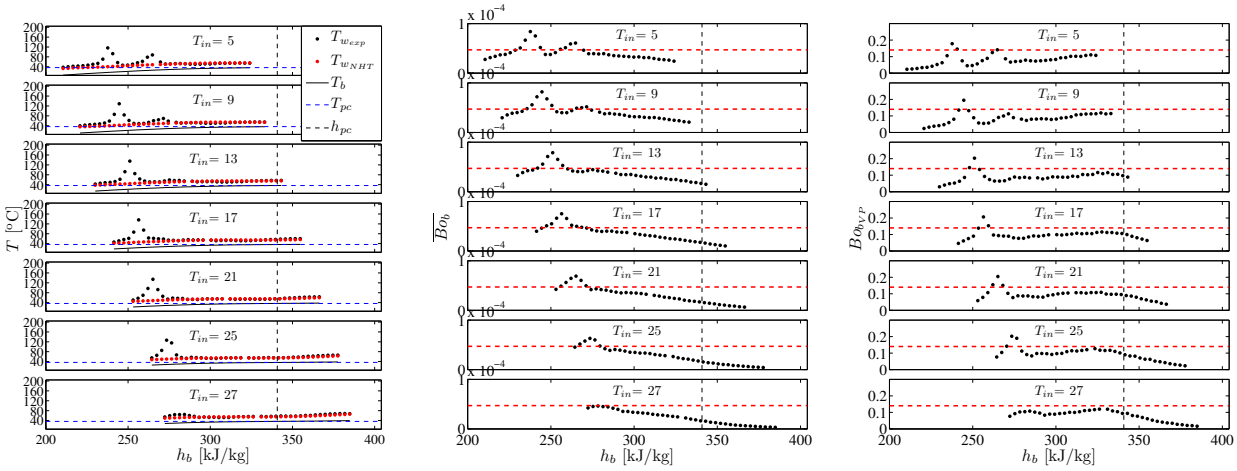
(a) T_w profiles (b) $\overline{Bo_b}$ profiles (c) $Bo_{b_{VP}}$ profiles

Figure C.49: $\overline{Bo_b}$, $Bo_{b_{VP}}$, and T_w profiles for $P/P_c = 1.13$, $D = 8$ mm, $G = 500$ kg/m^{2}s, $q = 53$ kW/m^2; dashed red lines represent suggested thresholds; T_{in} is in °C.



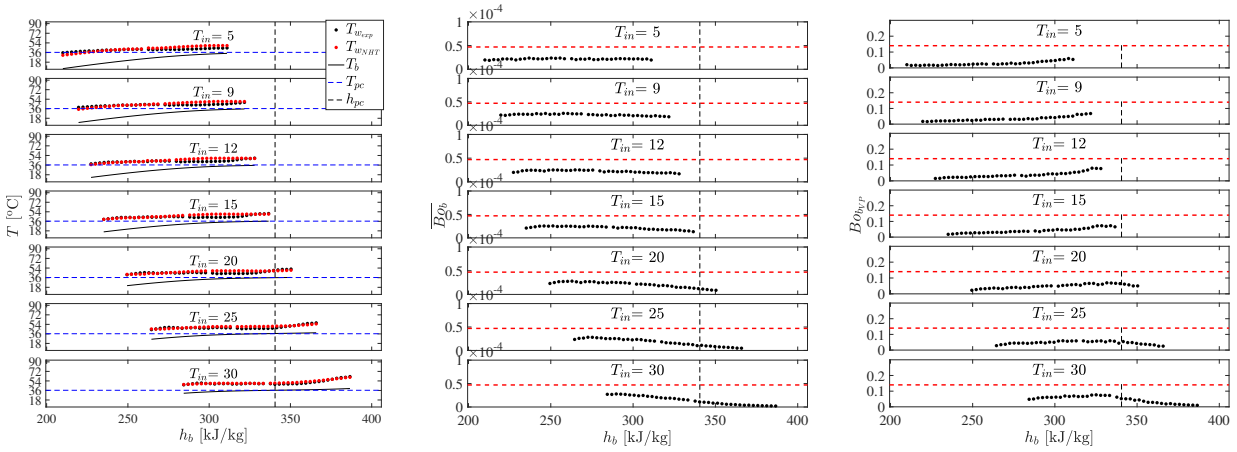
(a) T_w profiles (b) $\overline{Bo_b}$ profiles (c) $Bo_{b_{VP}}$ profiles

Figure C.50: $\overline{Bo_b}$, $Bo_{b_{VP}}$, and T_w profiles for $P/P_c = 1.13$, $D = 8$ mm, $G = 500$ kg/m^{2}s, $q = 55$ kW/m^2; dashed red lines represent suggested thresholds; T_{in} is in °C.



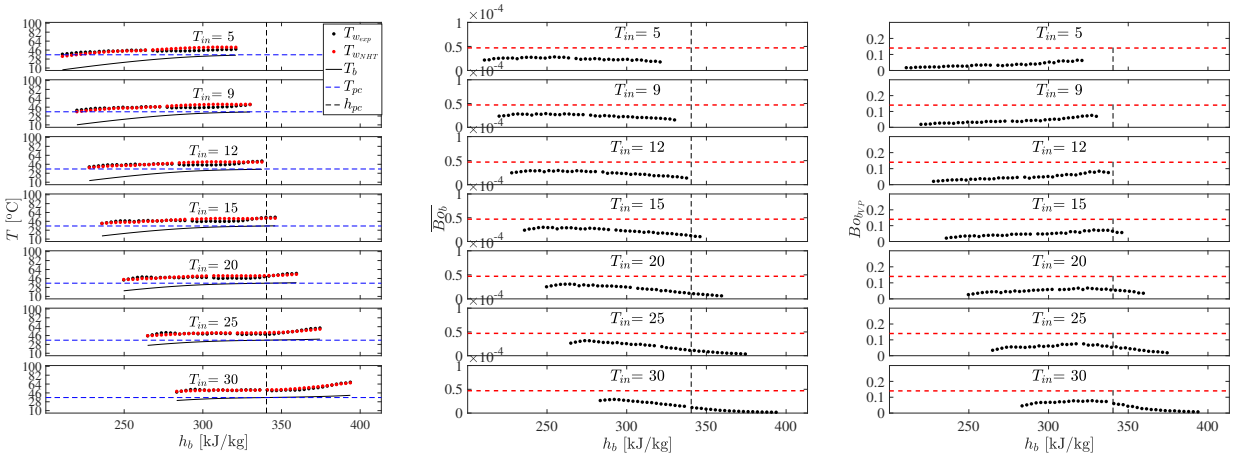
(a) T_w profiles (b) $\overline{Bo_b}$ profiles (c) $Bo_{b_{VP}}$ profiles

Figure C.51: $\overline{Bo_b}$, $Bo_{b_{VP}}$, and T_w profiles for $P/P_c = 1.13$, $D = 8$ mm, $G = 500$ kg/m^{2}s, $q = 60$ kW/m^2; dashed red lines represent suggested thresholds; T_{in} is in °C.



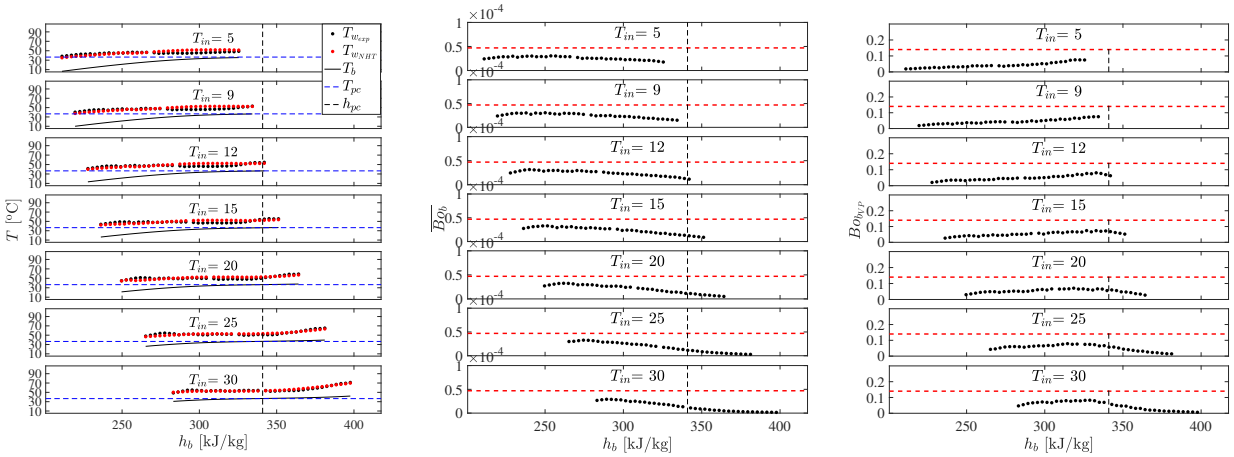
(a) T_w profiles (b) $\overline{Bo_b}$ profiles (c) $Bo_{b_{VP}}$ profiles

Figure C.52: $\overline{Bo_b}$, $Bo_{b_{VP}}$, and T_w profiles for $P/P_c = 1.13$, $D = 8$ mm, $G = 600$ kg/m^{2}s, $q = 65$ kW/m^2; dashed red lines represent suggested thresholds; T_{in} is in °C.



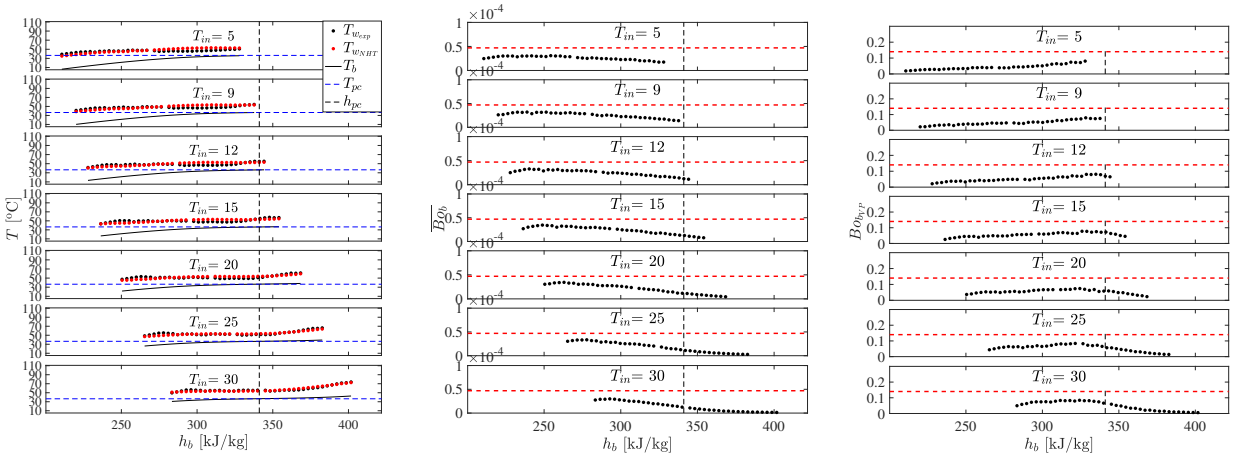
(a) T_w profiles (b) $\overline{Bo_b}$ profiles (c) $Bo_{b_{VP}}$ profiles

Figure C.53: $\overline{Bo_b}$, $Bo_{b_{VP}}$, and T_w profiles for $P/P_c = 1.13$, $D = 8$ mm, $G = 600$ kg/m^{2}s, $q = 70$ kW/m^2; dashed red lines represent suggested thresholds; T_{in} is in °C.



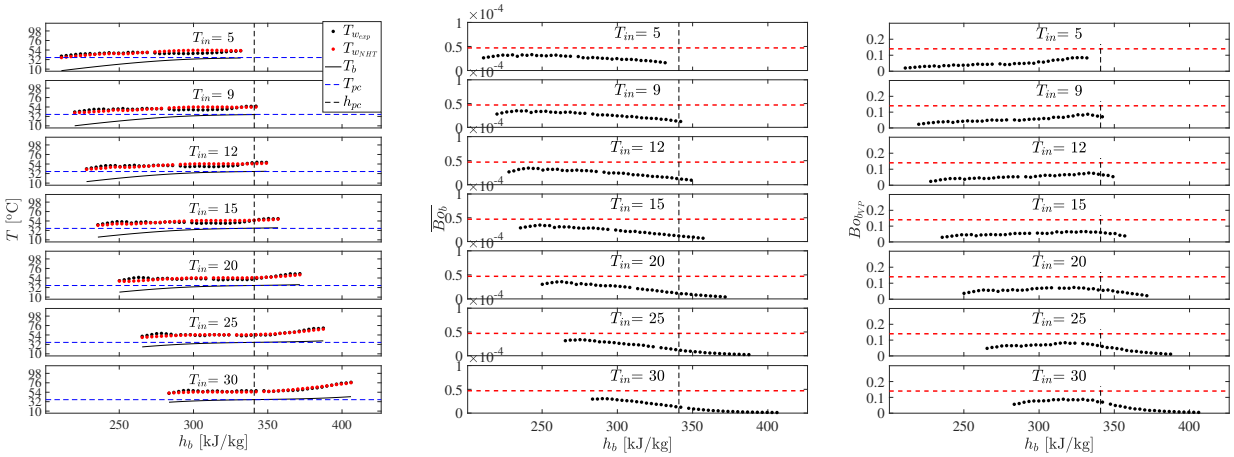
(a) T_w profiles (b) $\overline{Bo_b}$ profiles (c) $Bo_{b_{VP}}$ profiles

Figure C.54: $\overline{Bo_b}$, $Bo_{b_{VP}}$, and T_w profiles for $P/P_c = 1.13$, $D = 8$ mm, $G = 600$ kg/m^{2}s, $q = 73$ kW/m^2; dashed red lines represent suggested thresholds; T_{in} is in °C.



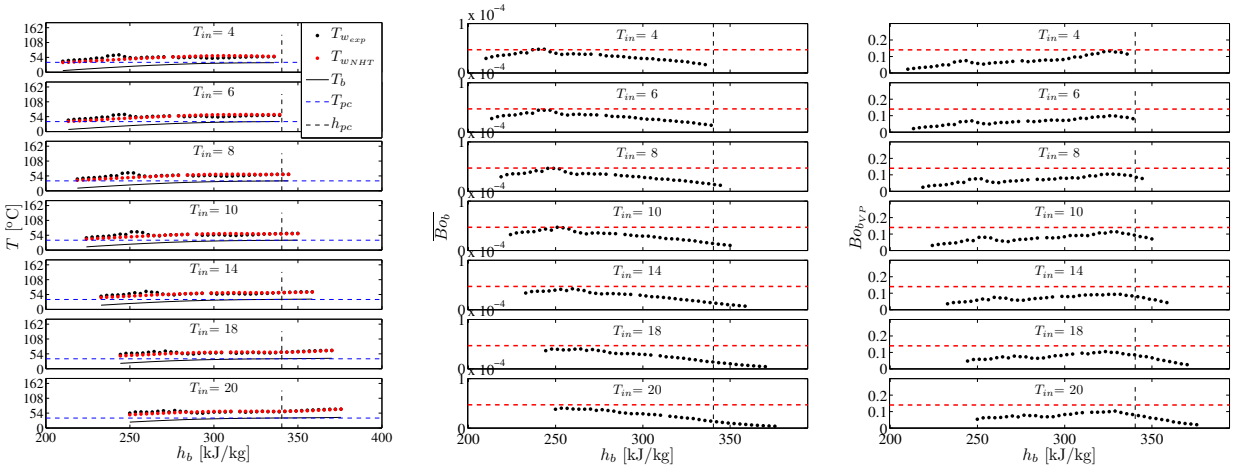
(a) T_w profiles (b) $\overline{Bo_b}$ profiles (c) $Bo_{b_{VP}}$ profiles

Figure C.55: $\overline{Bo_b}$, $Bo_{b_{VP}}$, and T_w profiles for $P/P_c = 1.13$, $D = 8$ mm, $G = 600$ kg/m^{2}s, $q = 75$ kW/m^2; dashed red lines represent suggested thresholds; T_{in} is in °C.



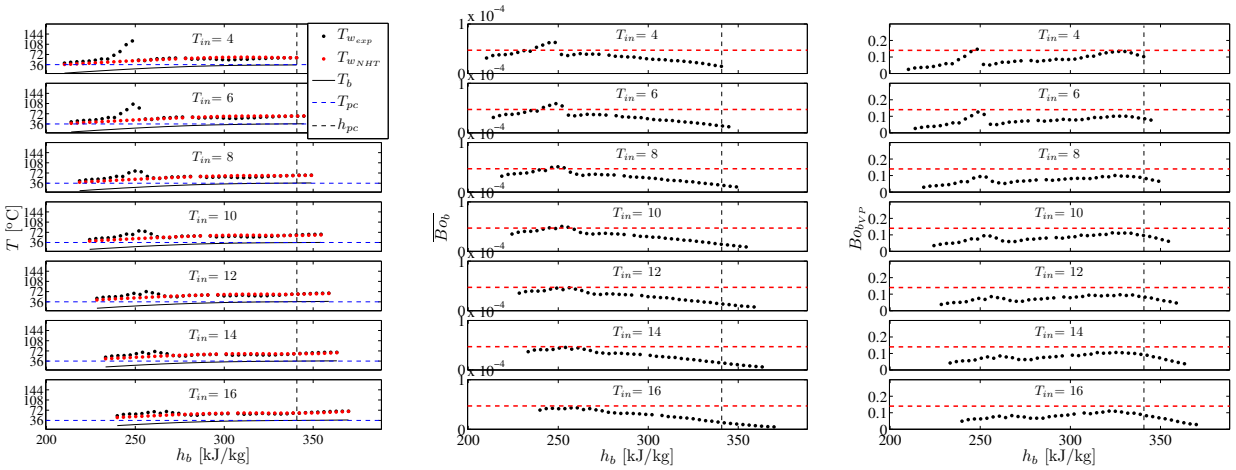
(a) T_w profiles (b) $\overline{Bo_b}$ profiles (c) $Bo_{b_{VP}}$ profiles

Figure C.56: $\overline{Bo_b}$, $Bo_{b_{VP}}$, and T_w profiles for $P/P_c = 1.13$, $D = 8$ mm, $G = 600$ kg/m^{2}s, $q = 78$ kW/m^2; dashed red lines represent suggested thresholds; T_{in} is in °C.



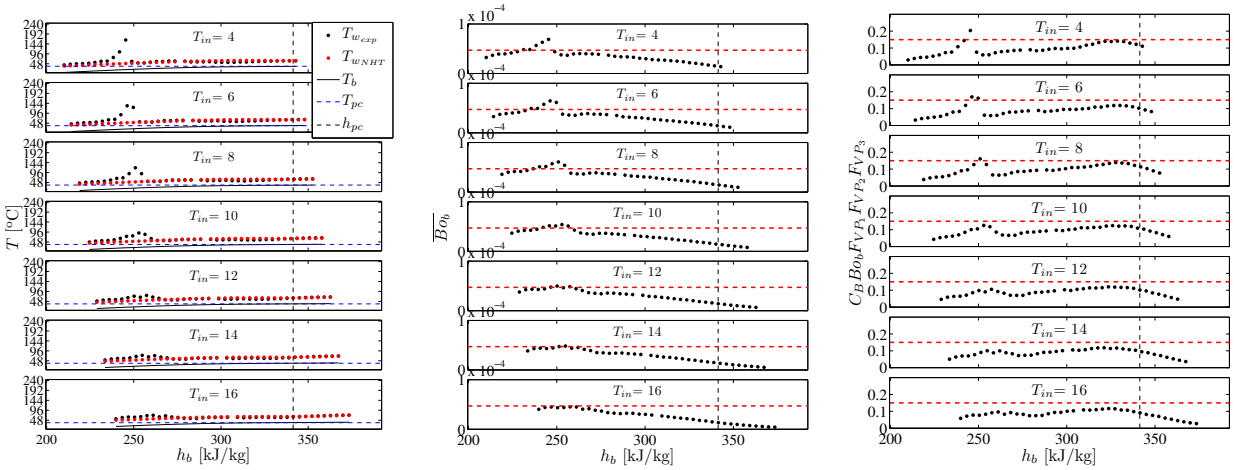
(a) T_w profiles (b) $\overline{Bo_b}$ profiles (c) $Bo_{b_{VP}}$ profiles

Figure C.57: $\overline{Bo_b}$, $Bo_{b_{VP}}$, and T_w profiles for $P/P_c = 1.13$, $D = 8$ mm, $G = 600$ kg/m^{2}s, $q = 80$ kW/m^2; dashed red lines represent suggested thresholds; T_{in} is in °C.



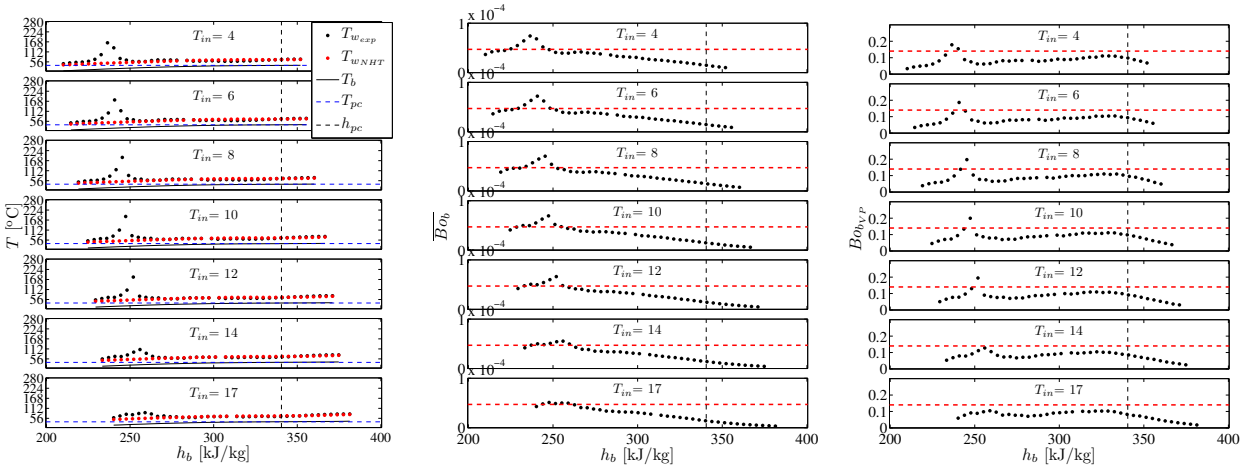
(a) T_w profiles (b) $\overline{Bo_b}$ profiles (c) $Bo_{b_{VP}}$ profiles

Figure C.58: $\overline{Bo_b}$, $Bo_{b_{VP}}$, and T_w profiles for $P/P_c = 1.13$, $D = 8$ mm, $G = 600$ kg/m^{2}s, $q = 83$ kW/m^2; dashed red lines represent suggested thresholds; T_{in} is in °C.



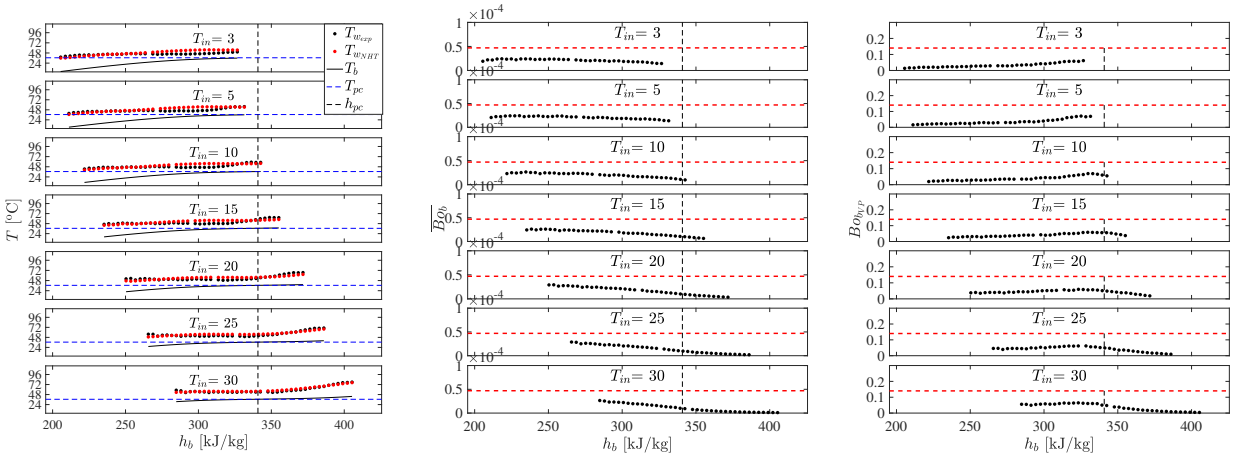
(a) T_w profiles (b) $\overline{Bo_b}$ profiles (c) $Bo_{b_{VP}}$ profiles

Figure C.59: $\overline{Bo_b}$, $Bo_{b_{VP}}$, and T_w profiles for $P/P_c = 1.13$, $D = 8$ mm, $G = 600$ kg/m^{2}s, $q = 85$ kW/m^2; dashed red lines represent suggested thresholds; T_{in} is in °C.



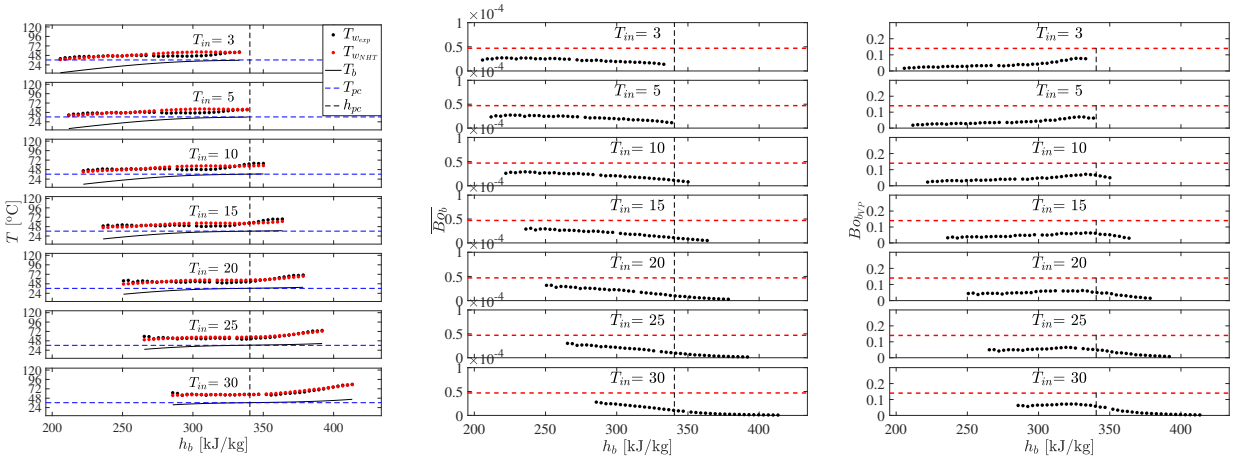
(a) T_w profiles (b) $\overline{Bo_b}$ profiles (c) $Bo_{b_{VP}}$ profiles

Figure C.60: $\overline{Bo_b}$, $Bo_{b_{VP}}$, and T_w profiles for $P/P_c = 1.13$, $D = 8$ mm, $G = 600$ kg/m^{2}s, $q = 90$ kW/m^2; dashed red lines represent suggested thresholds; T_{in} is in °C.



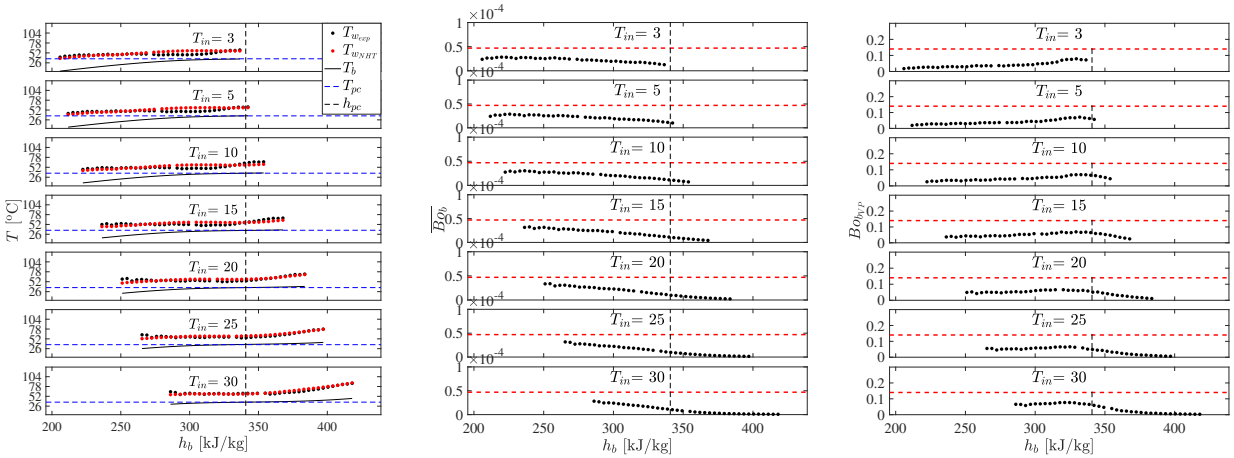
(a) T_w profiles (b) $\overline{Bo_b}$ profiles (c) $Bo_{b_{VP}}$ profiles

Figure C.61: $\overline{Bo_b}$, $Bo_{b_{VP}}$, and T_w profiles for $P/P_c = 1.13$, $D = 8$ mm, $G = 700$ kg/m^{2}s, $q = 90$ kW/m^2; dashed red lines represent suggested thresholds; T_{in} is in °C.



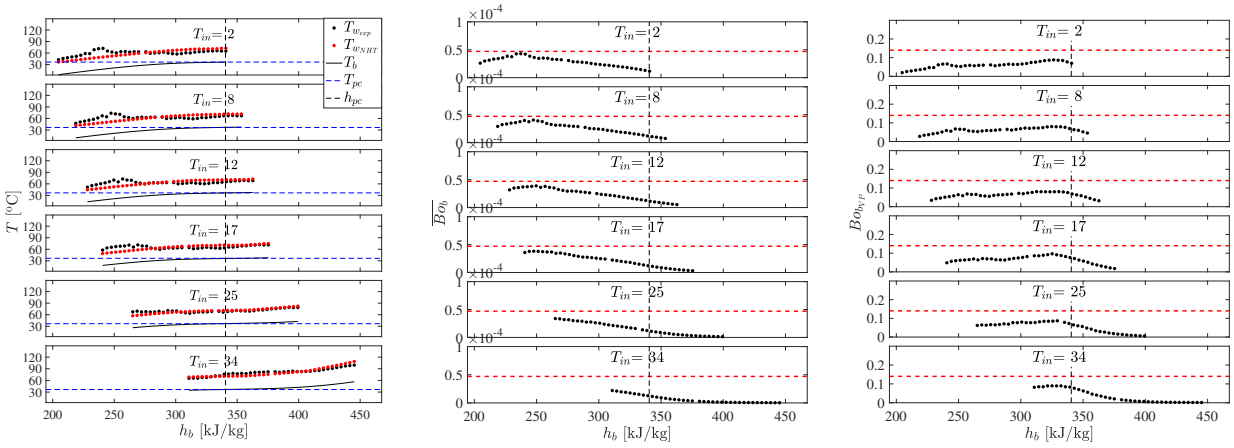
(a) T_w profiles (b) $\overline{Bo_b}$ profiles (c) $Bo_{b_{VP}}$ profiles

Figure C.62: $\overline{Bo_b}$, $Bo_{b_{VP}}$, and T_w profiles for $P/P_c = 1.13$, $D = 8$ mm, $G = 700$ kg/m^{2}s, $q = 95$ kW/m^2; dashed red lines represent suggested thresholds; T_{in} is in °C.



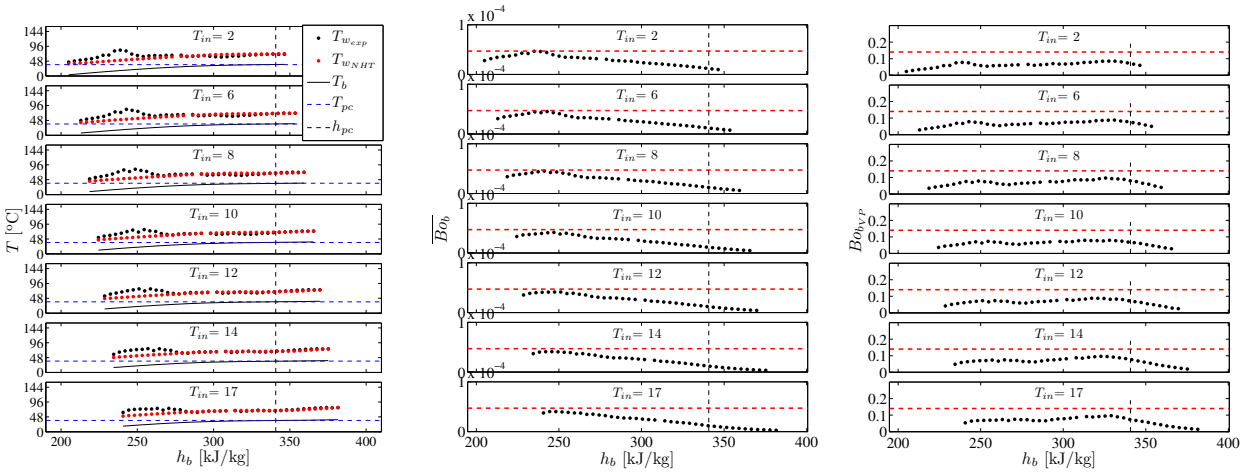
(a) T_w profiles (b) $\overline{Bo_b}$ profiles (c) $Bo_{b_{VP}}$ profiles

Figure C.63: $\overline{Bo_b}$, $Bo_{b_{VP}}$, and T_w profiles for $P/P_c = 1.13$, $D = 8$ mm, $G = 700$ kg/m^{2}s, $q = 98$ kW/m^2; dashed red lines represent suggested thresholds; T_{in} is in °C.



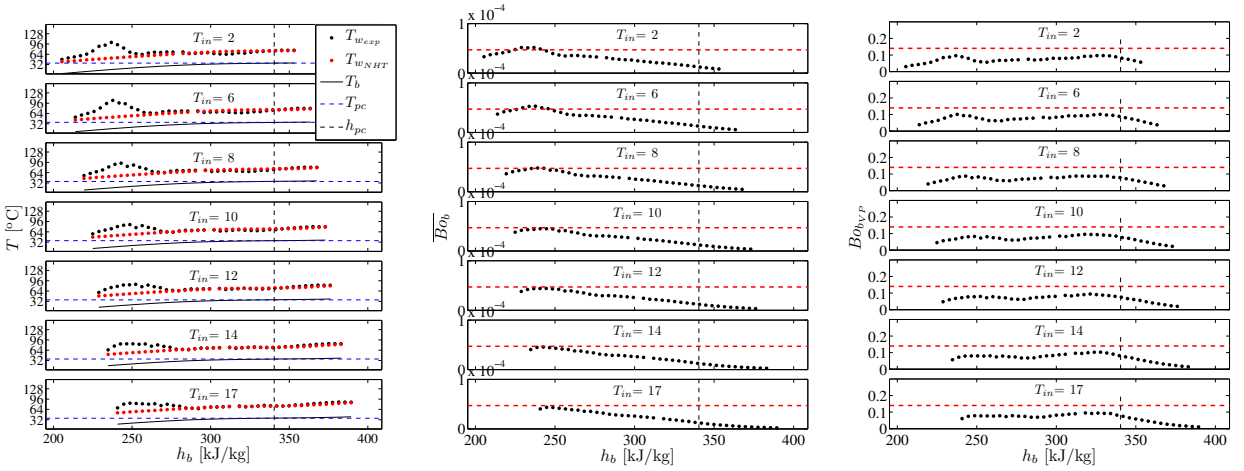
(a) T_w profiles (b) $\overline{Bo_b}$ profiles (c) $Bo_{b_{VP}}$ profiles

Figure C.64: $\overline{Bo_b}$, $Bo_{b_{VP}}$, and T_w profiles for $P/P_c = 1.13$, $D = 8$ mm, $G = 700$ kg/m^{2}s, $q = 100$ kW/m^2; dashed red lines represent suggested thresholds; T_{in} is in °C.



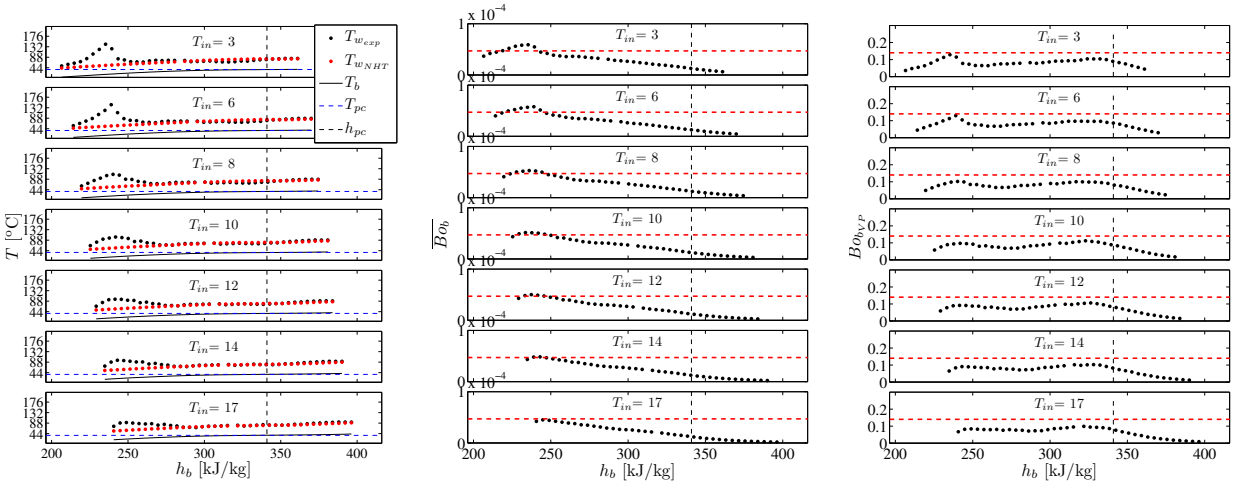
(a) T_w profiles (b) $\overline{Bo_b}$ profiles (c) $Bo_{b_{VP}}$ profiles

Figure C.65: $\overline{Bo_b}$, $Bo_{b_{VP}}$, and T_w profiles for $P/P_c = 1.13$, $D = 8$ mm, $G = 700$ kg/m^{2}s, $q = 105$ kW/m^2; dashed red lines represent suggested thresholds; T_{in} is in °C.



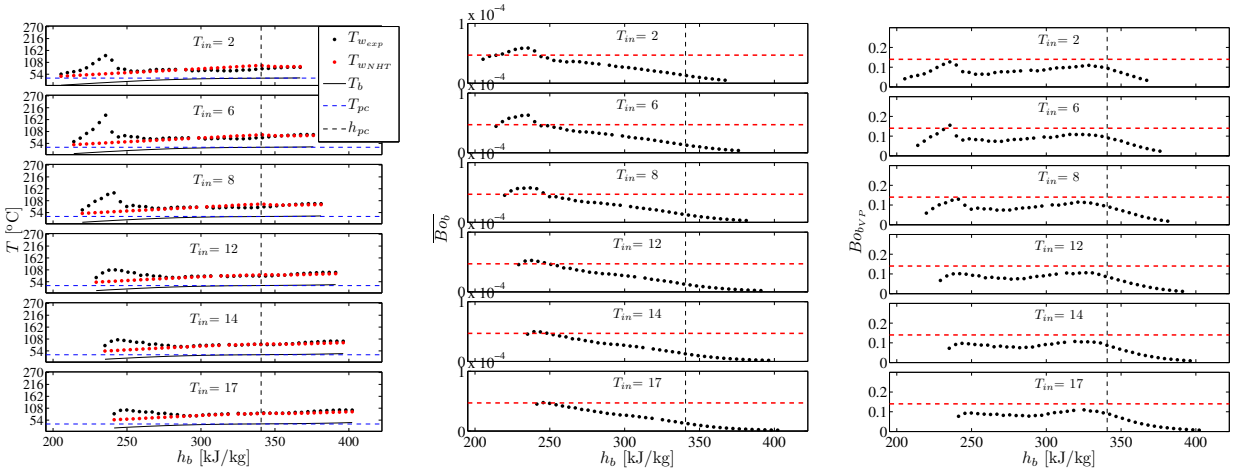
(a) T_w profiles (b) $\overline{Bo_b}$ profiles (c) $Bo_{b_{VP}}$ profiles

Figure C.66: $\overline{Bo_b}$, $Bo_{b_{VP}}$, and T_w profiles for $P/P_c = 1.13$, $D = 8$ mm, $G = 700$ kg/m^{2}s, $q = 110$ kW/m^2; dashed red lines represent suggested thresholds; T_{in} is in °C.



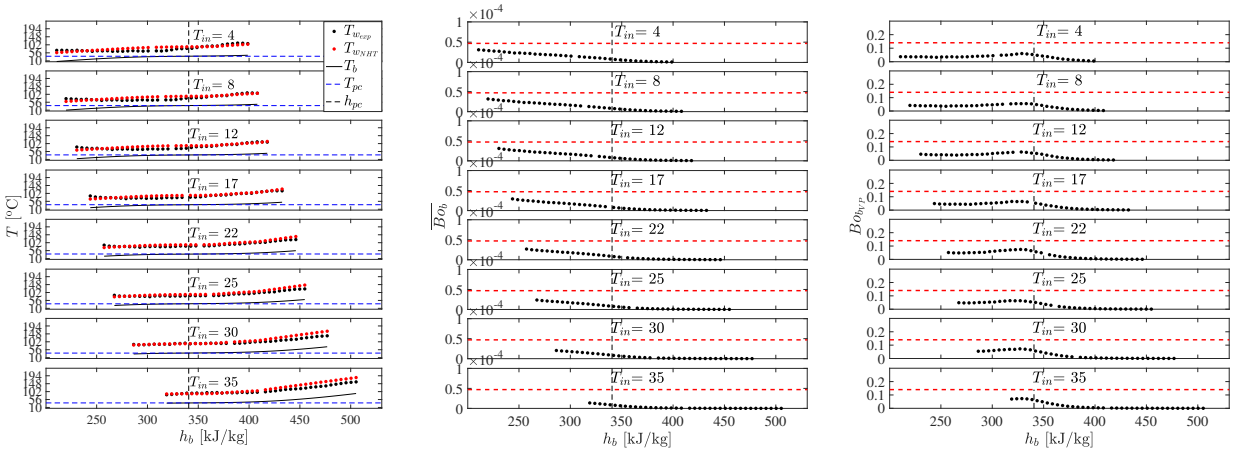
(a) T_w profiles (b) $\overline{Bo_b}$ profiles (c) $Bo_{b_{VP}}$ profiles

Figure C.67: $\overline{Bo_b}$, $Bo_{b_{VP}}$, and T_w profiles for $P/P_c = 1.13$, $D = 8$ mm, $G = 700$ kg/m^{2}s, $q = 115$ kW/m^2; dashed red lines represent suggested thresholds; T_{in} is in °C.



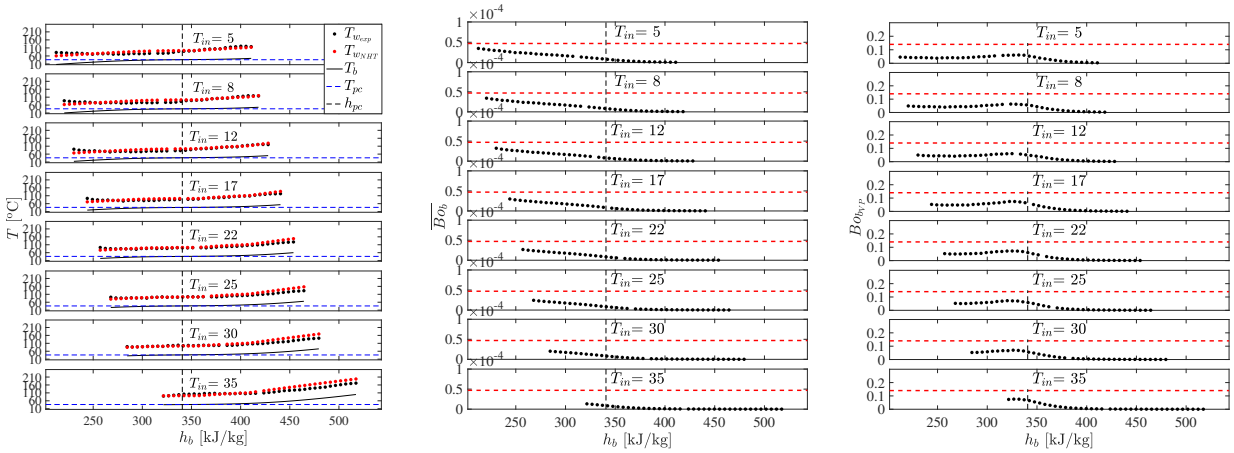
(a) T_w profiles (b) $\overline{Bo_b}$ profiles (c) $Bo_{b_{VP}}$ profiles

Figure C.68: $\overline{Bo_b}$, $Bo_{b_{VP}}$, and T_w profiles for $P/P_c = 1.13$, $D = 8$ mm, $G = 700$ kg/m^{2}s, $q = 120$ kW/m^2; dashed red lines represent suggested thresholds; T_{in} is in °C.



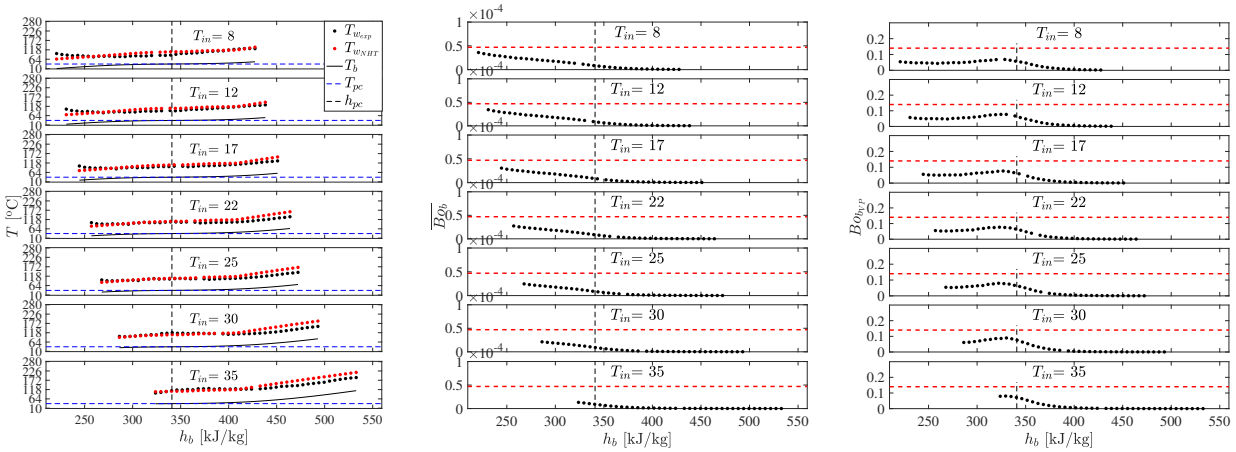
(a) T_w profiles (b) $\overline{Bo_b}$ profiles (c) $Bo_{b_{VP}}$ profiles

Figure C.69: $\overline{Bo_b}$, $Bo_{b_{VP}}$, and T_w profiles for $P/P_c = 1.13$, $D = 8$ mm, $G = 1000$ kg/m^{2}s, $q = 200$ kW/m^2; dashed red lines represent suggested thresholds; T_{in} is in °C.



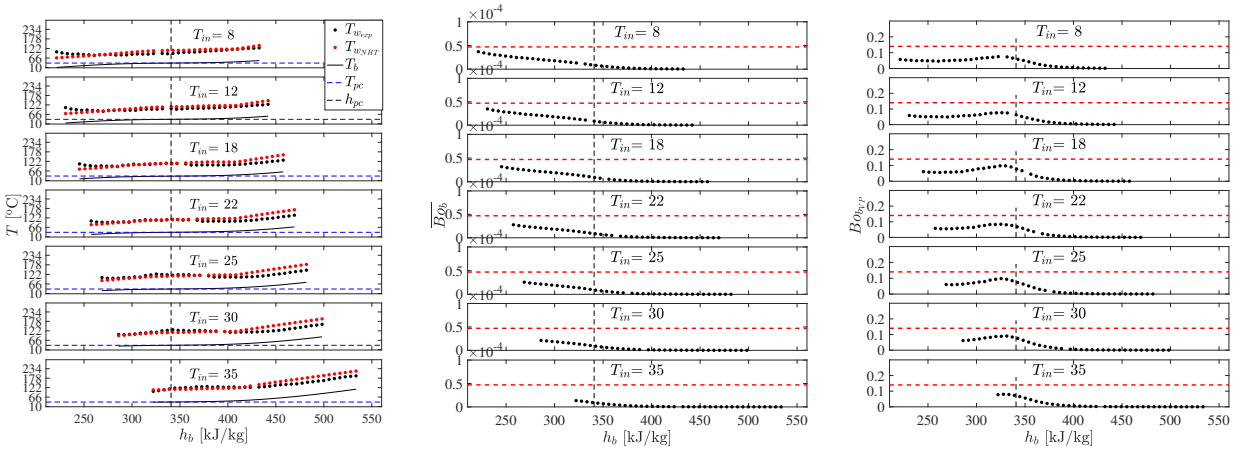
(a) T_w profiles (b) $\overline{Bo_b}$ profiles (c) $Bo_{b_{VP}}$ profiles

Figure C.70: $\overline{Bo_b}$, $Bo_{b_{VP}}$, and T_w profiles for $P/P_c = 1.13$, $D = 8$ mm, $G = 1000$ kg/m^{2}s, $q = 210$ kW/m^2; dashed red lines represent suggested thresholds; T_{in} is in °C.



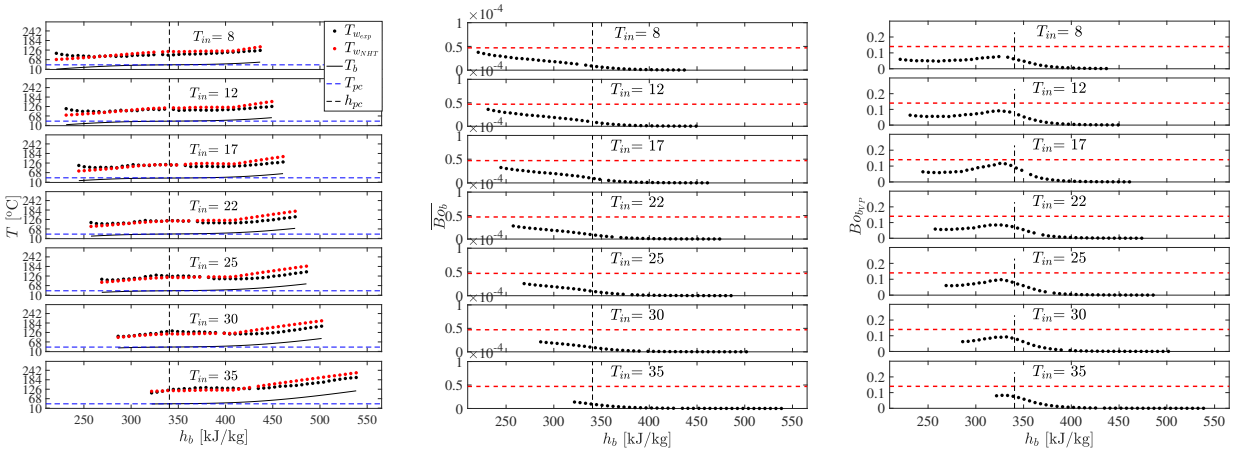
(a) T_w profiles (b) $\overline{Bo_b}$ profiles (c) $Bo_{b_{VP}}$ profiles

Figure C.71: $\overline{Bo_b}$, $Bo_{b_{VP}}$, and T_w profiles for $P/P_c = 1.13$, $D = 8$ mm, $G = 1000$ kg/m^{2}s, $q = 220$ kW/m^2; dashed red lines represent suggested thresholds; T_{in} is in °C.



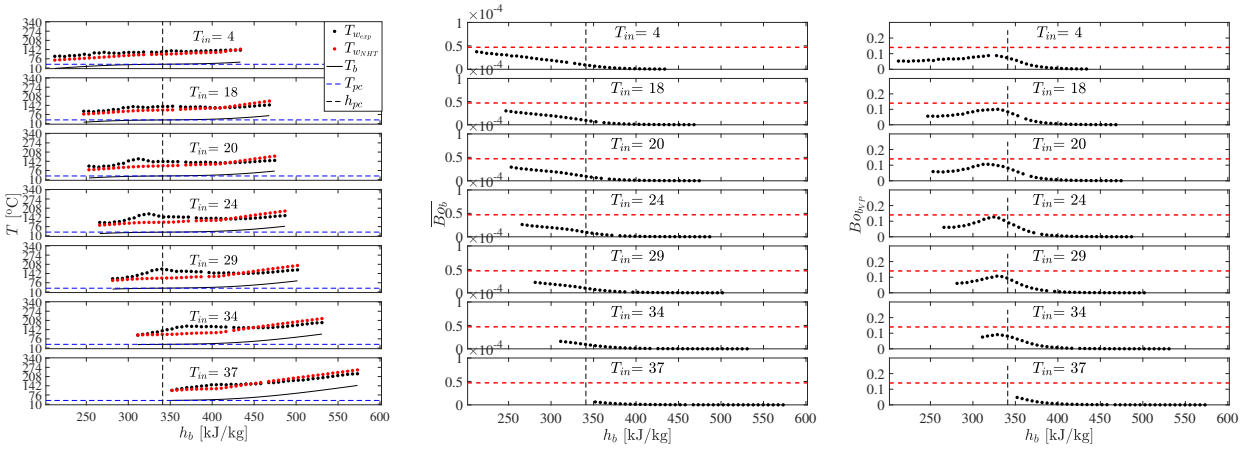
(a) T_w profiles (b) $\overline{Bo_b}$ profiles (c) $Bo_{b_{VP}}$ profiles

Figure C.72: $\overline{Bo_b}$, $Bo_{b_{VP}}$, and T_w profiles for $P/P_c = 1.13$, $D = 8$ mm, $G = 1000$ kg/m^{2}s, $q = 225$ kW/m^2; dashed red lines represent suggested thresholds; T_{in} is in °C.



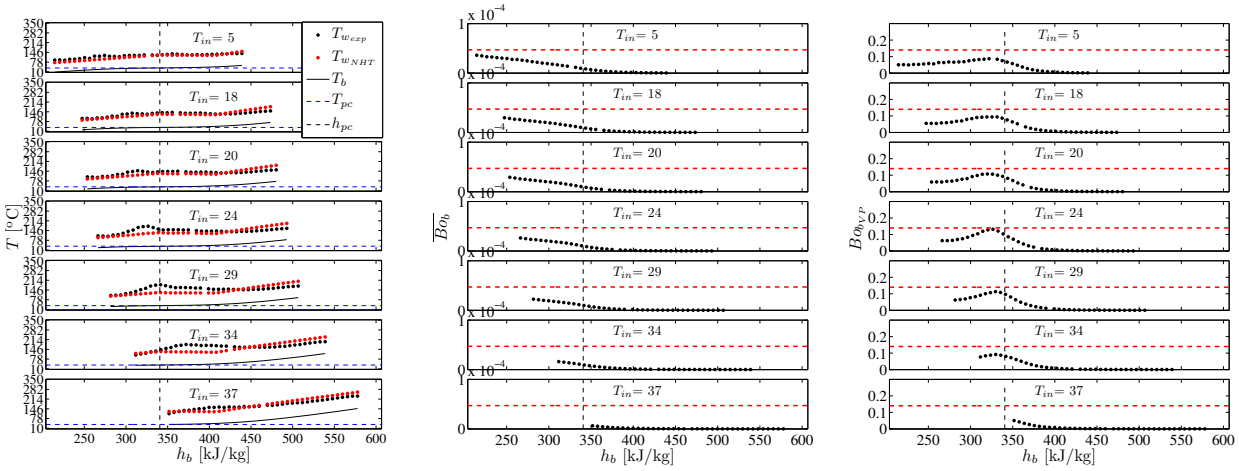
(a) T_w profiles (b) $\overline{Bo_b}$ profiles (c) $Bo_{b_{VP}}$ profiles

Figure C.73: $\overline{Bo_b}$, $Bo_{b_{VP}}$, and T_w profiles for $P/P_c = 1.13$, $D = 8$ mm, $G = 1000$ kg/m^{2}s, $q = 230$ kW/m^2; dashed red lines represent suggested thresholds; T_{in} is in °C.



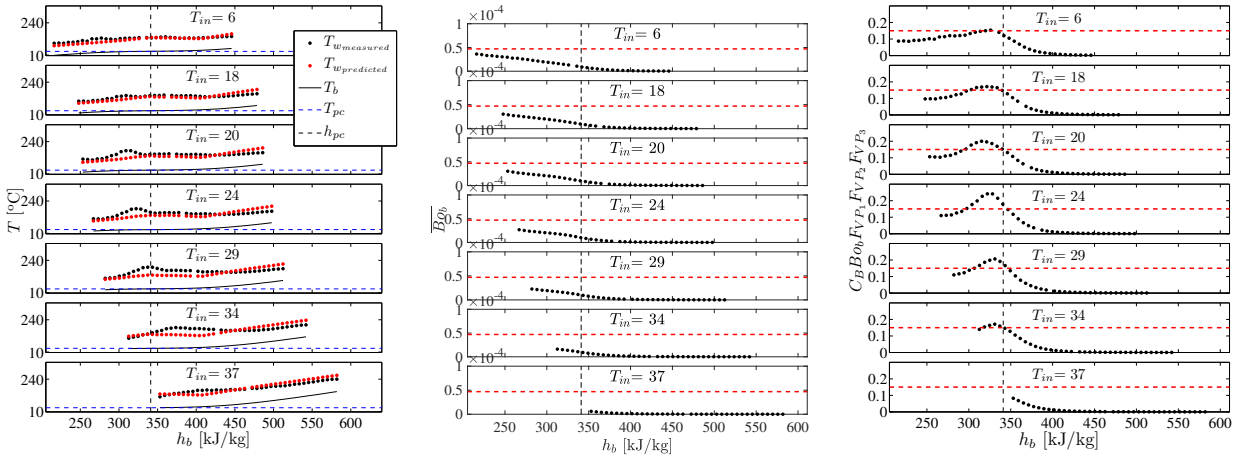
(a) T_w profiles (b) $\overline{Bo_b}$ profiles (c) $Bo_{b_{VP}}$ profiles

Figure C.74: $\overline{Bo_b}$, $Bo_{b_{VP}}$, and T_w profiles for $P/P_c = 1.13$, $D = 8$ mm, $G = 1000$ kg/m^{2}s, $q = 235$ kW/m^2; dashed red lines represent suggested thresholds; T_{in} is in °C.



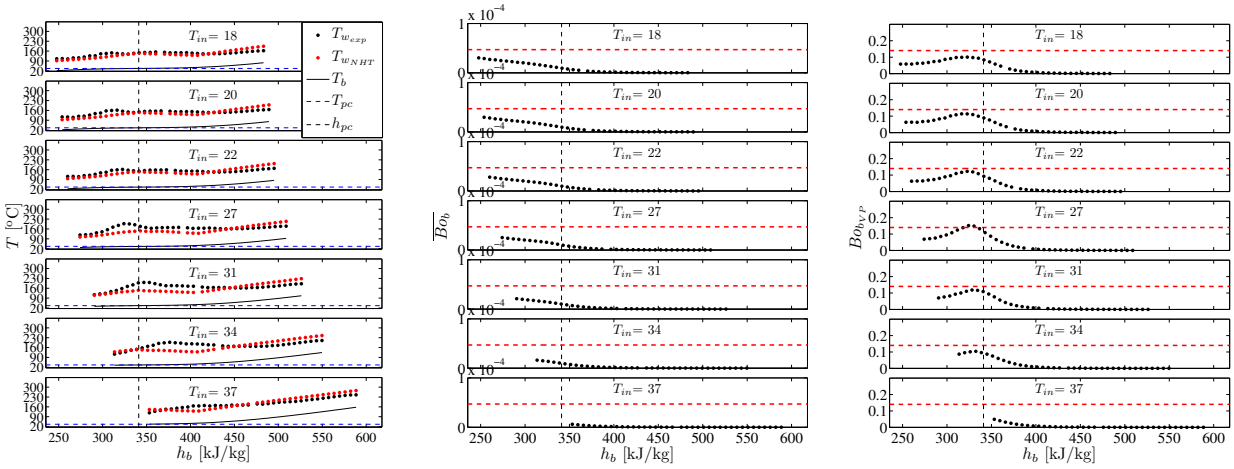
(a) T_w profiles (b) $\overline{Bo_b}$ profiles (c) $Bo_{b_{VP}}$ profiles

Figure C.75: $\overline{Bo_b}$, $Bo_{b_{VP}}$, and T_w profiles for $P/P_c = 1.13$, $D = 8$ mm, $G = 1000$ kg/m^{2}s, $q = 240$ kW/m^2; dashed red lines represent suggested thresholds; T_{in} is in °C.



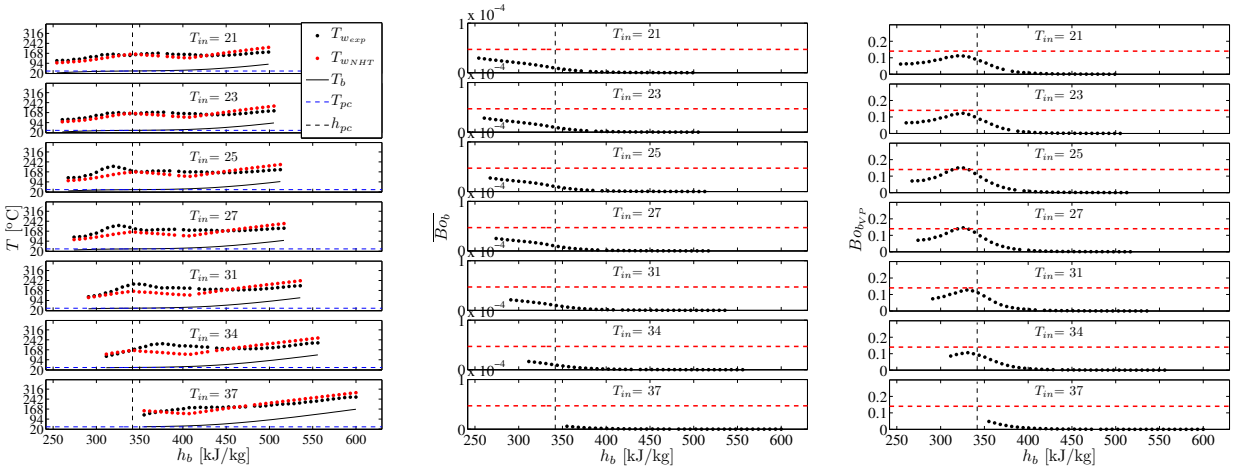
(a) T_w profiles (b) $\overline{Bo_b}$ profiles (c) $Bo_{b_{VP}}$ profiles

Figure C.76: $\overline{Bo_b}$, $Bo_{b_{VP}}$, and T_w profiles for $P/P_c = 1.13$, $D = 8$ mm, $G = 1000$ kg/m^{2}s, $q = 245$ kW/m^2; dashed red lines represent suggested thresholds; T_{in} is in °C.



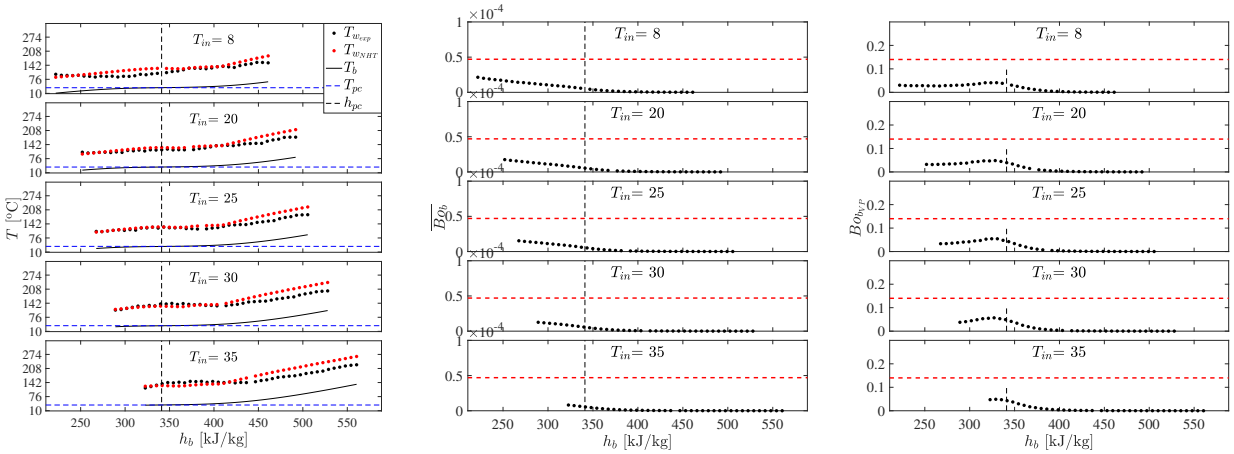
(a) T_w profiles (b) $\overline{Bo_b}$ profiles (c) $Bo_{b_{VP}}$ profiles

Figure C.77: $\overline{Bo_b}$, $Bo_{b_{VP}}$, and T_w profiles for $P/P_c = 1.13$, $D = 8$ mm, $G = 1000$ kg/m^{2}s, $q = 250$ kW/m^2; dashed red lines represent suggested thresholds; T_{in} is in °C.



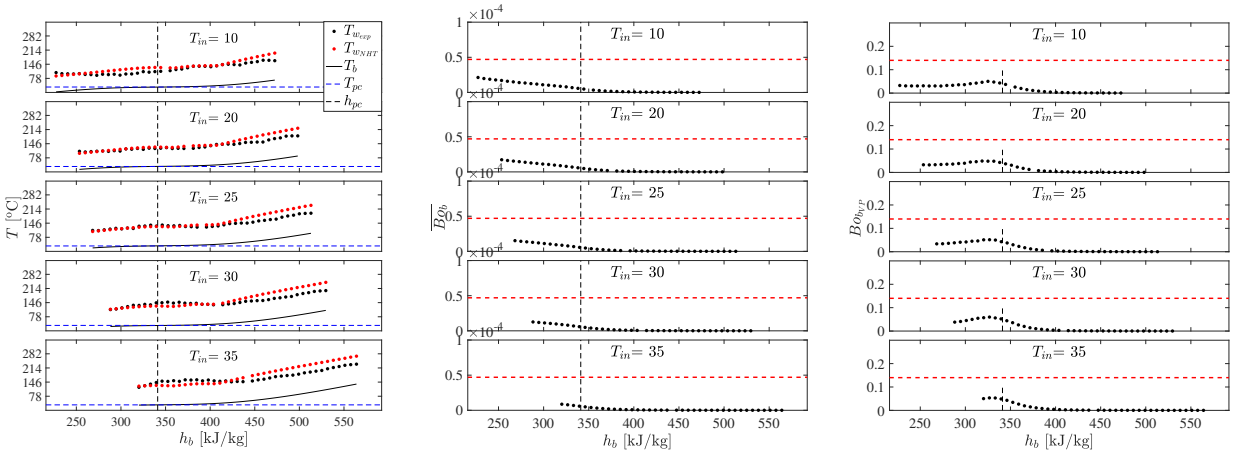
(a) T_w profiles (b) $\overline{Bo_b}$ profiles (c) $Bo_{b_{VP}}$ profiles

Figure C.78: $\overline{Bo_b}$, $Bo_{b_{VP}}$, and T_w profiles for $P/P_c = 1.13$, $D = 8$ mm, $G = 1000$ kg/m^{2}s, $q = 260$ kW/m^2; dashed red lines represent suggested thresholds; T_{in} is in °C.



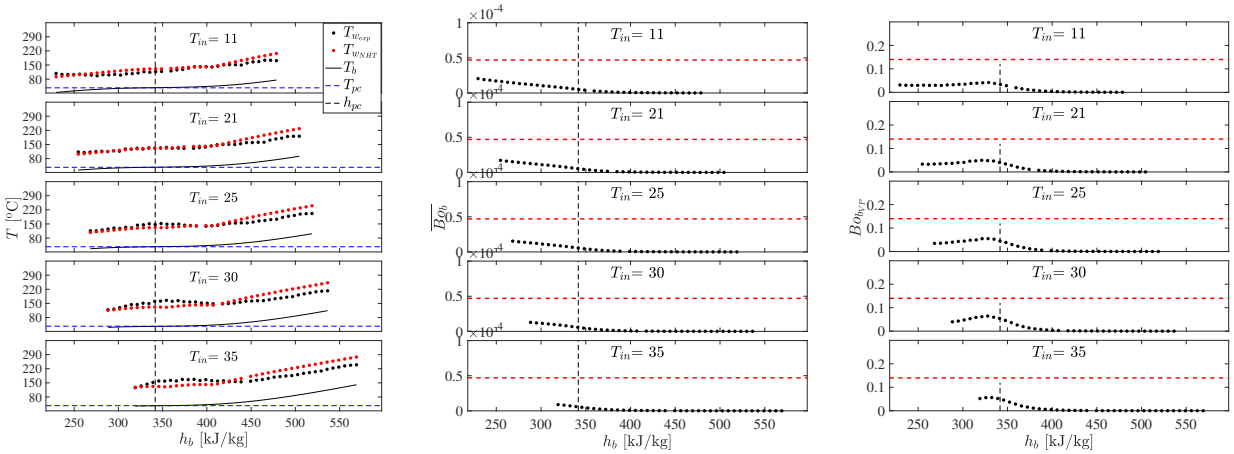
(a) T_w profiles (b) $\overline{Bo_b}$ profiles (c) $Bo_{b_{VP}}$ profiles

Figure C.79: $\overline{Bo_b}$, $Bo_{b_{VP}}$, and T_w profiles for $P/P_c = 1.13$, $D = 8$ mm, $G = 1500$ kg/m^{2}s, $q = 380$ kW/m^2; dashed red lines represent suggested thresholds; T_{in} is in °C.



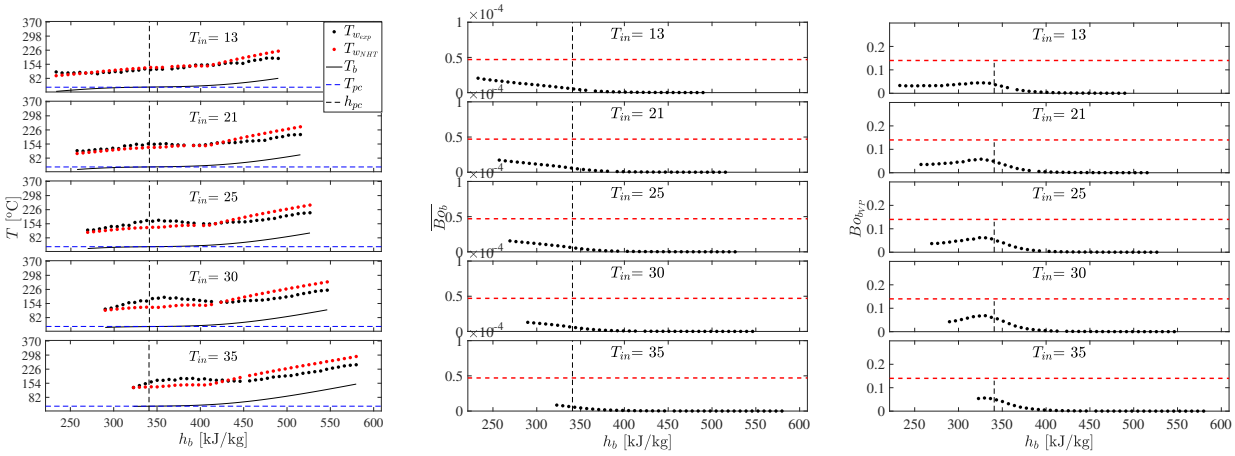
(a) T_w profiles (b) $\overline{Bo_b}$ profiles (c) $Bo_{b_{VP}}$ profiles

Figure C.80: $\overline{Bo_b}$, $Bo_{b_{VP}}$, and T_w profiles for $P/P_c = 1.13$, $D = 8$ mm, $G = 1500$ kg/m^{2}s, $q = 390$ kW/m^2; dashed red lines represent suggested thresholds; T_{in} is in °C.



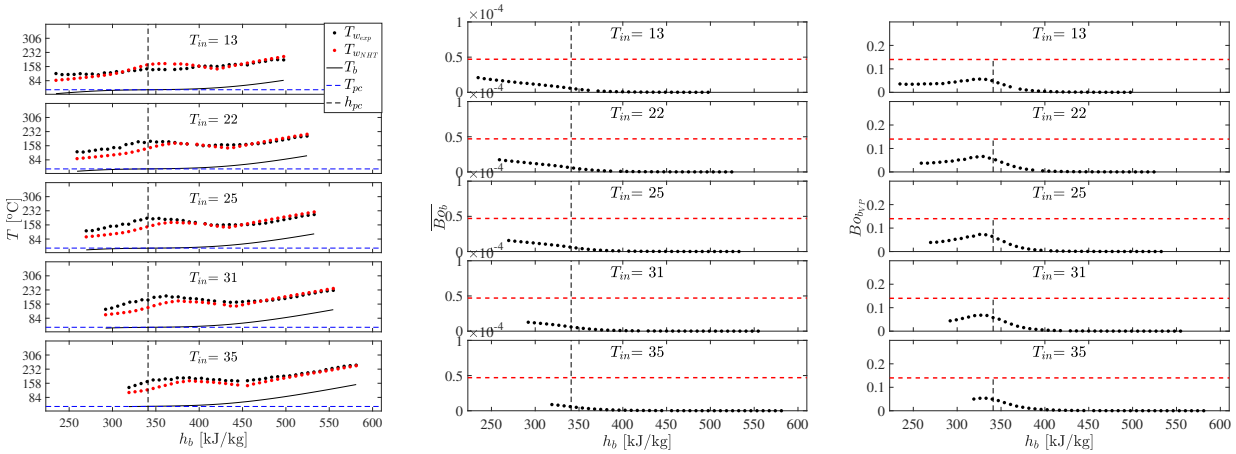
(a) T_w profiles (b) $\overline{Bo_b}$ profiles (c) $Bo_{b_{VP}}$ profiles

Figure C.81: $\overline{Bo_b}$, $Bo_{b_{VP}}$, and T_w profiles for $P/P_c = 1.13$, $D = 8$ mm, $G = 1500$ kg/m^{2}s, $q = 400$ kW/m^2; dashed red lines represent suggested thresholds; T_{in} is in °C.



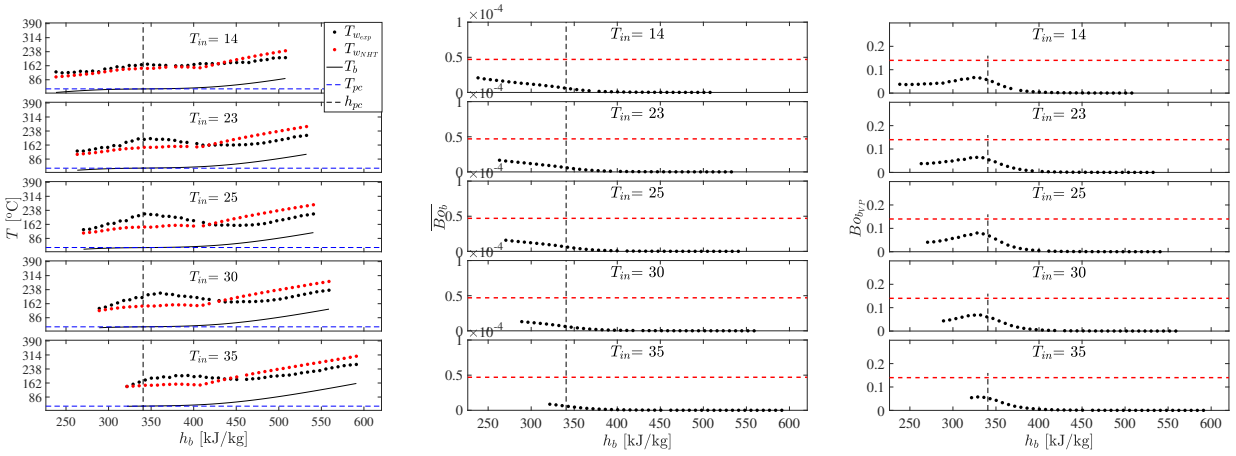
(a) T_w profiles (b) $\overline{Bo_b}$ profiles (c) $Bo_{b_{VP}}$ profiles

Figure C.82: $\overline{Bo_b}$, $Bo_{b_{VP}}$, and T_w profiles for $P/P_c = 1.13$, $D = 8$ mm, $G = 1500$ kg/m^{2}s, $q = 410$ kW/m^2; dashed red lines represent suggested thresholds; T_{in} is in °C.



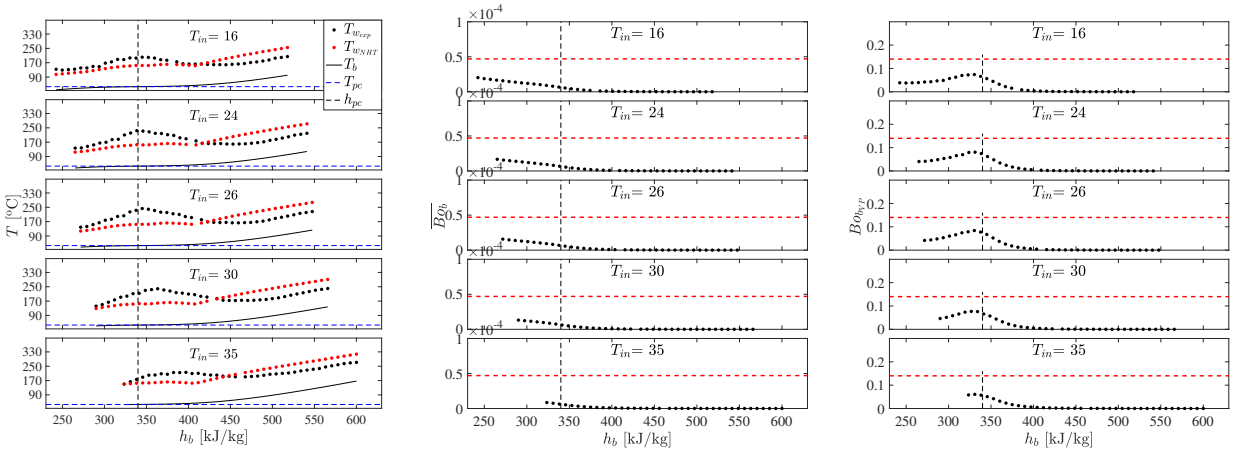
(a) T_w profiles (b) $\overline{Bo_b}$ profiles (c) $Bo_{b_{VP}}$ profiles

Figure C.83: $\overline{Bo_b}$, $Bo_{b_{VP}}$, and T_w profiles for $P/P_c = 1.13$, $D = 8$ mm, $G = 1500$ kg/m^{2}s, $q = 420$ kW/m^2; dashed red lines represent suggested thresholds; T_{in} is in °C.



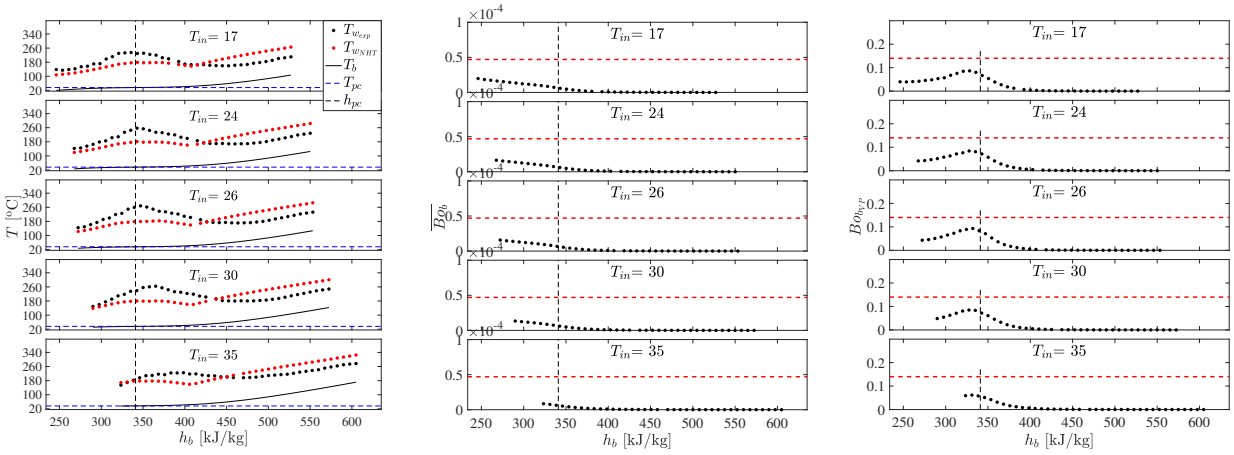
(a) T_w profiles (b) $\overline{Bo_b}$ profiles (c) $Bo_{b_{VP}}$ profiles

Figure C.84: $\overline{Bo_b}$, $Bo_{b_{VP}}$, and T_w profiles for $P/P_c = 1.13$, $D = 8$ mm, $G = 1500$ kg/m^{2}s, $q = 430$ kW/m^2; dashed red lines represent suggested thresholds; T_{in} is in °C.



(a) T_w profiles (b) $\overline{Bo_b}$ profiles (c) $Bo_{b_{VP}}$ profiles

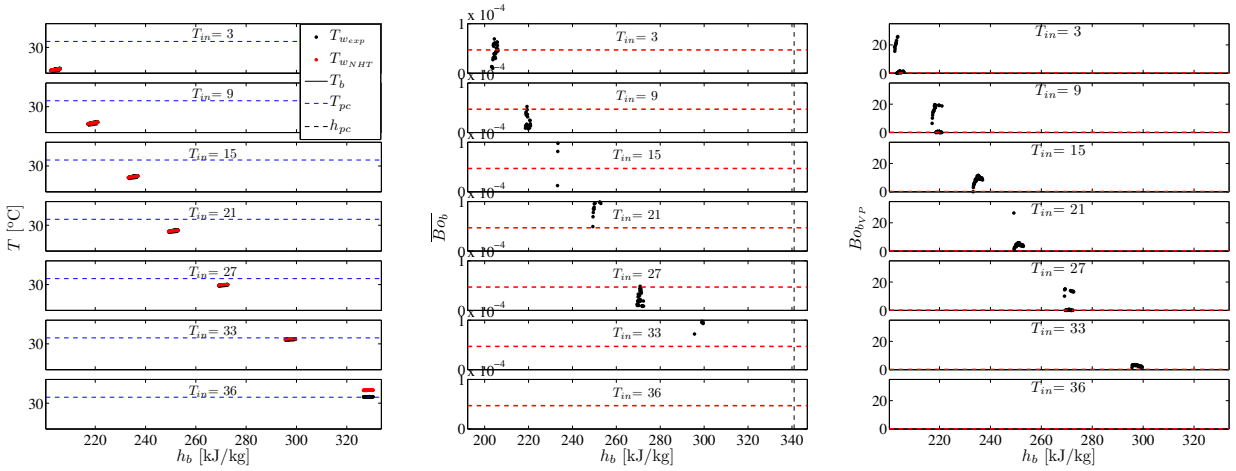
Figure C.85: $\overline{Bo_b}$, $Bo_{b_{VP}}$, and T_w profiles for $P/P_c = 1.13$, $D = 8$ mm, $G = 1500$ kg/m^{2}s, $q = 440$ kW/m^2; dashed red lines represent suggested thresholds; T_{in} is in °C.



(a) T_w profiles (b) $\overline{Bo_b}$ profiles (c) $Bo_{b_{VP}}$ profiles

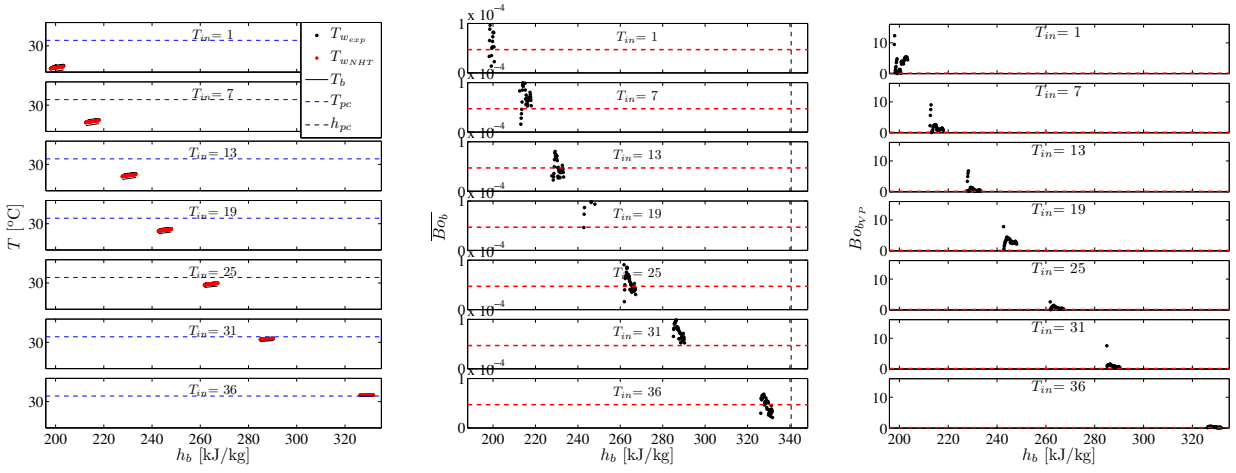
Figure C.86: $\overline{Bo_b}$, $Bo_{b_{VP}}$, and T_w profiles for $P/P_c = 1.13$, $D = 8$ mm, $G = 1500$ kg/m^{2}s, $q = 450$ kW/m^2; dashed red lines represent suggested thresholds; T_{in} is in °C.

C.3 22 mm test section



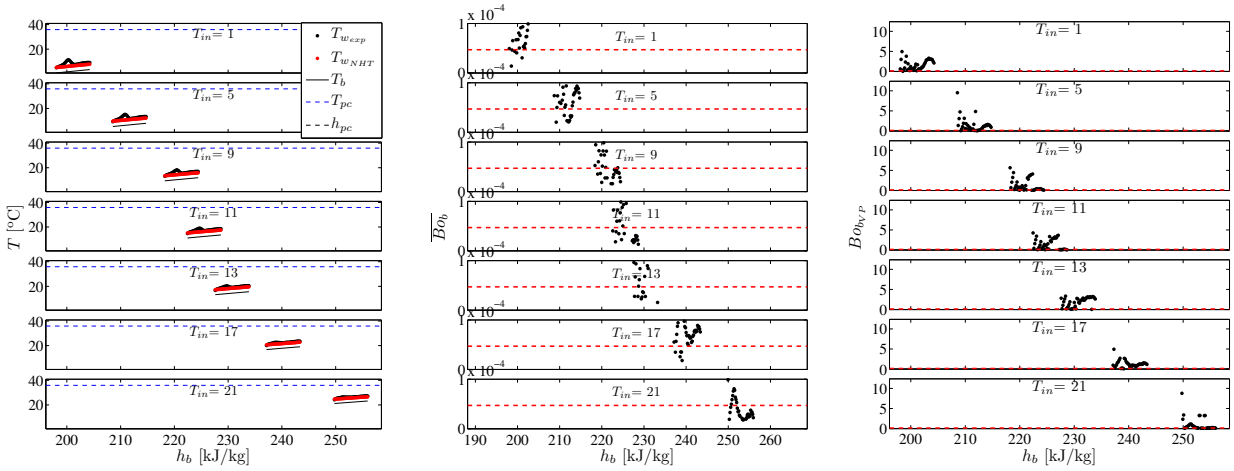
(a) T_w profiles (b) $\overline{Bo_b}$ profiles (c) $Bo_{b_{VP}}$ profiles

Figure C.87: $\overline{Bo_b}$, $Bo_{b_{VP}}$, and T_w profiles for $P/P_c = 1.13$, $D = 22$ mm, $G = 200$ kg/m^{2}s, $q = 2$ kW/m^2; dashed red lines represent suggested thresholds; T_{in} is in °C.



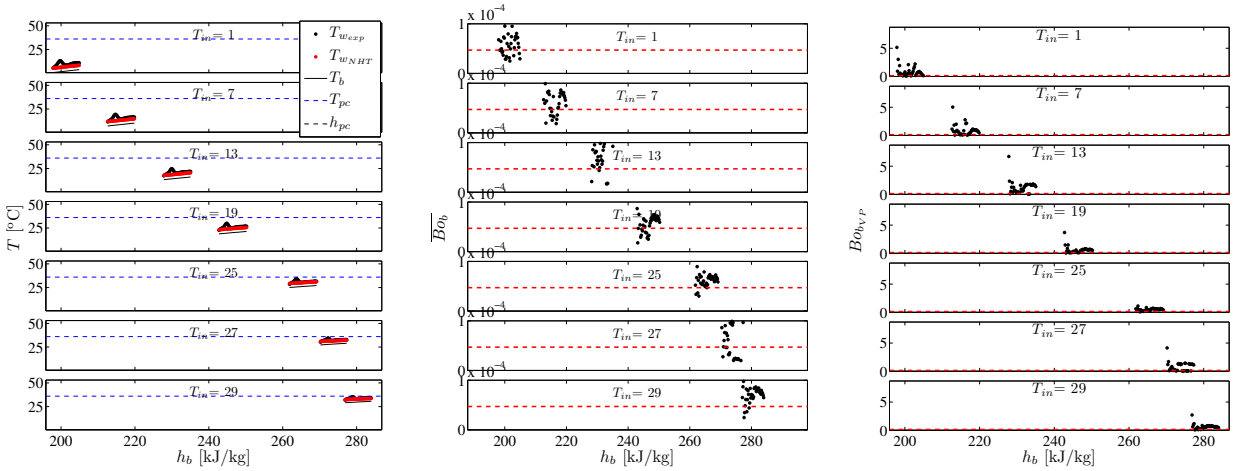
(a) T_w profiles (b) $\overline{Bo_b}$ profiles (c) $Bo_{b_{VP}}$ profiles

Figure C.88: $\overline{Bo_b}$, $Bo_{b_{VP}}$, and T_w profiles for $P/P_c = 1.13$, $D = 22$ mm, $G = 200$ kg/m^{2}s, $q = 3$ kW/m^2; dashed red lines represent suggested thresholds; T_{in} is in °C.



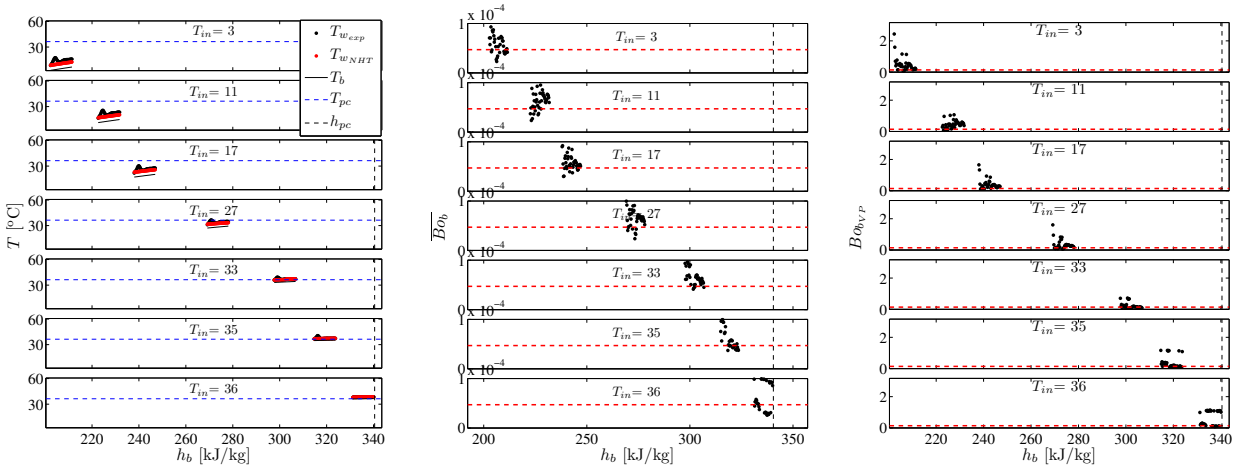
(a) T_w profiles (b) $\overline{Bo_b}$ profiles (c) $Bo_{b_{VP}}$ profiles

Figure C.89: $\overline{Bo_b}$, $Bo_{b_{VP}}$, and T_w profiles for $P/P_c = 1.13$, $D = 22$ mm, $G = 200$ kg/m^{2}s, $q = 3.5$ kW/m^2; dashed red lines represent suggested thresholds; T_{in} is in °C.



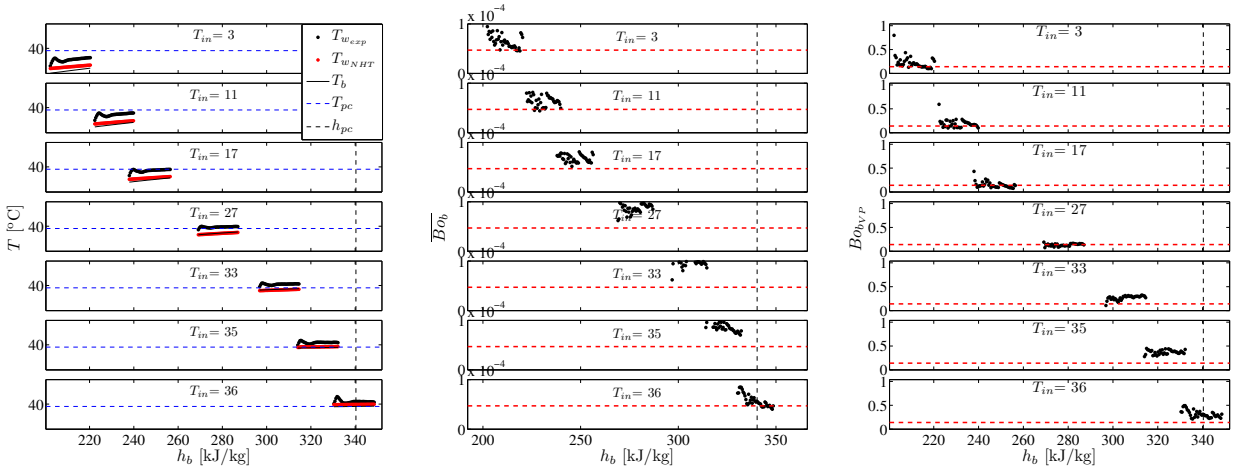
(a) T_w profiles (b) $\overline{Bo_b}$ profiles (c) $Bo_{b_{VP}}$ profiles

Figure C.90: $\overline{Bo_b}$, $Bo_{b_{VP}}$, and T_w profiles for $P/P_c = 1.13$, $D = 22$ mm, $G = 200$ kg/m^{2}s, $q = 4$ kW/m^2; dashed red lines represent suggested thresholds; T_{in} is in °C.



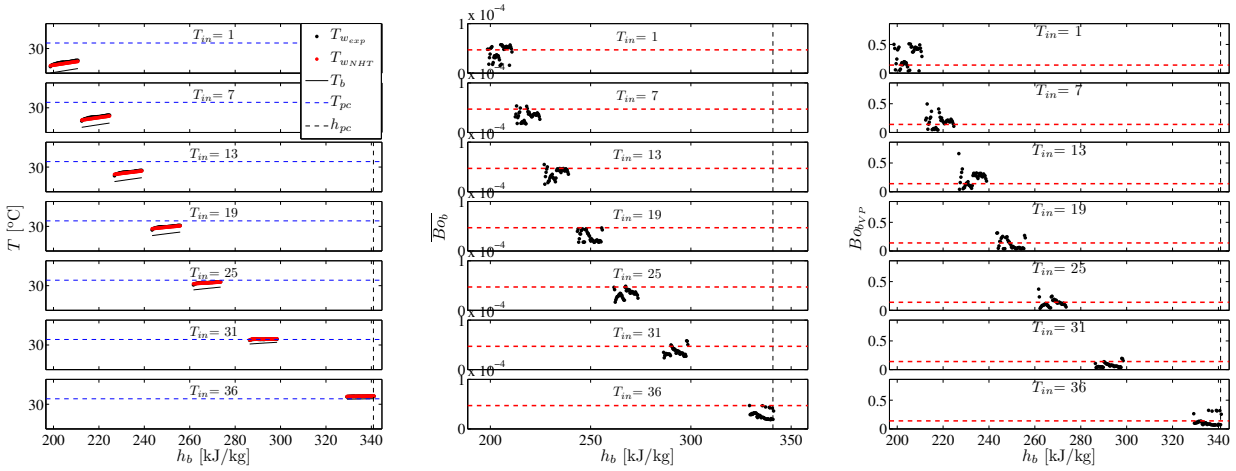
(a) T_w profiles (b) $\overline{Bo_b}$ profiles (c) $Bo_{b_{VP}}$ profiles

Figure C.91: $\overline{Bo_b}$, $Bo_{b_{VP}}$, and T_w profiles for $P/P_c = 1.13$, $D = 22$ mm, $G = 200$ kg/m^{2}s, $q = 5$ kW/m^2; dashed red lines represent suggested thresholds; T_{in} is in °C.



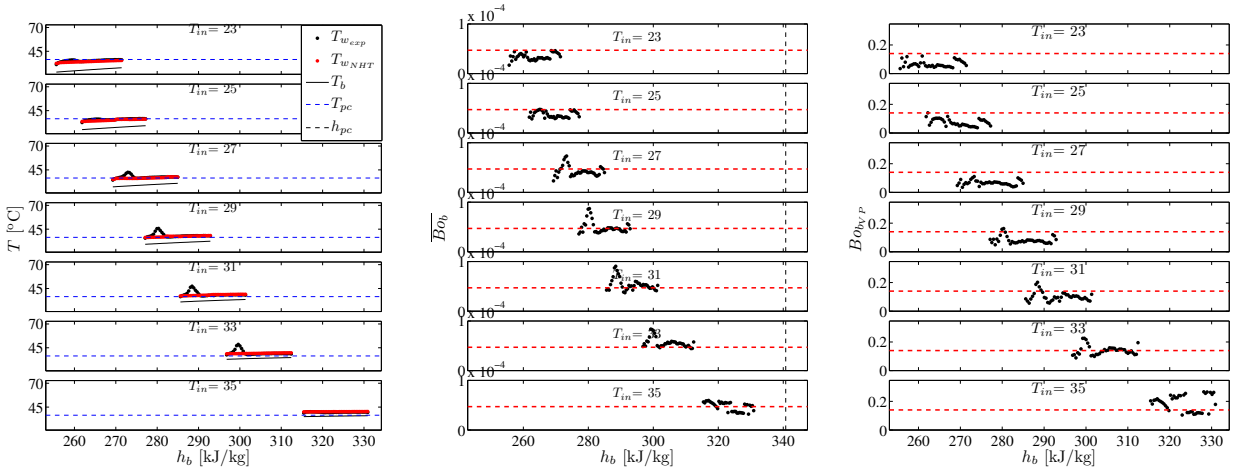
(a) T_w profiles (b) $\overline{Bo_b}$ profiles (c) $Bo_{b_{VP}}$ profiles

Figure C.92: $\overline{Bo_b}$, $Bo_{b_{VP}}$, and T_w profiles for $P/P_c = 1.13$, $D = 22$ mm, $G = 200$ kg/m^{2}s, $q = 10$ kW/m^2; dashed red lines represent suggested thresholds; T_{in} is in °C.



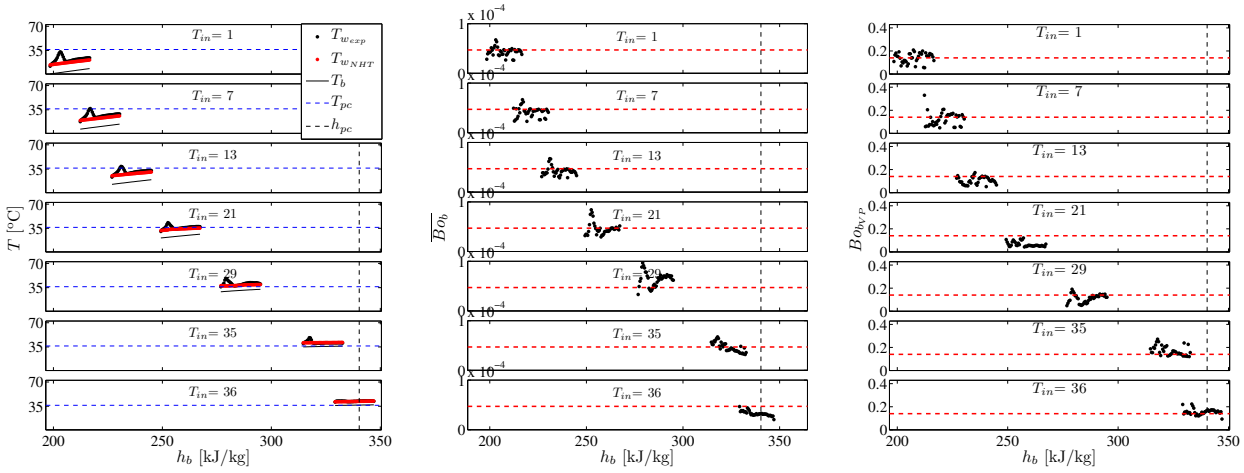
(a) T_w profiles (b) $\overline{Bo_b}$ profiles (c) $Bo_{b_{VP}}$ profiles

Figure C.93: $\overline{Bo_b}$, $Bo_{b_{VP}}$, and T_w profiles for $P/P_c = 1.13$, $D = 22$ mm, $G = 300$ kg/m^{2}s, $q = 10$ kW/m^2; dashed red lines represent suggested thresholds; T_{in} is in °C.



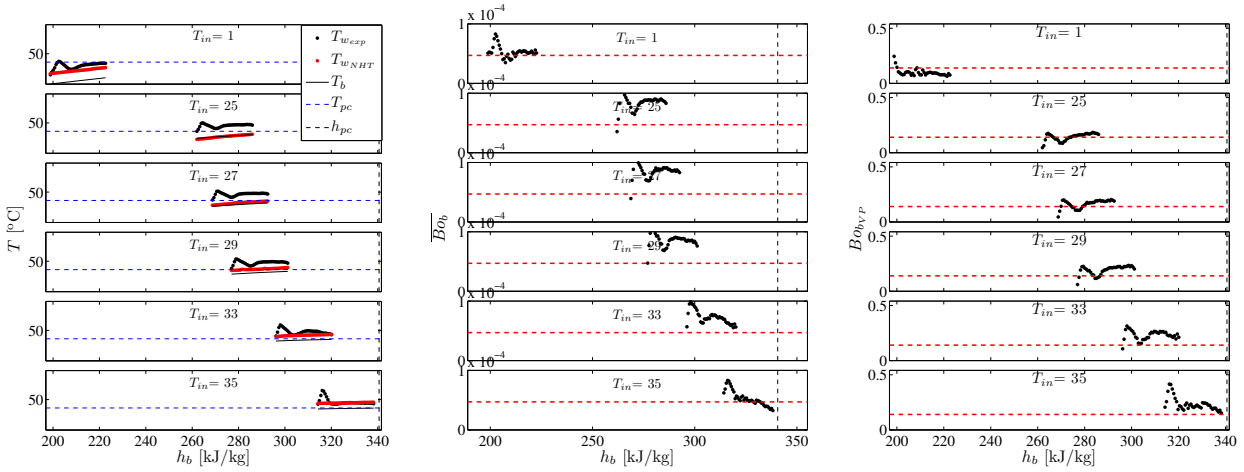
(a) T_w profiles (b) $\overline{Bo_b}$ profiles (c) $Bo_{b_{VP}}$ profiles

Figure C.94: $\overline{Bo_b}$, $Bo_{b_{VP}}$, and T_w profiles for $P/P_c = 1.13$, $D = 22$ mm, $G = 300$ kg/m^{2}s, $q = 13$ kW/m^2; dashed red lines represent suggested thresholds; T_{in} is in °C.



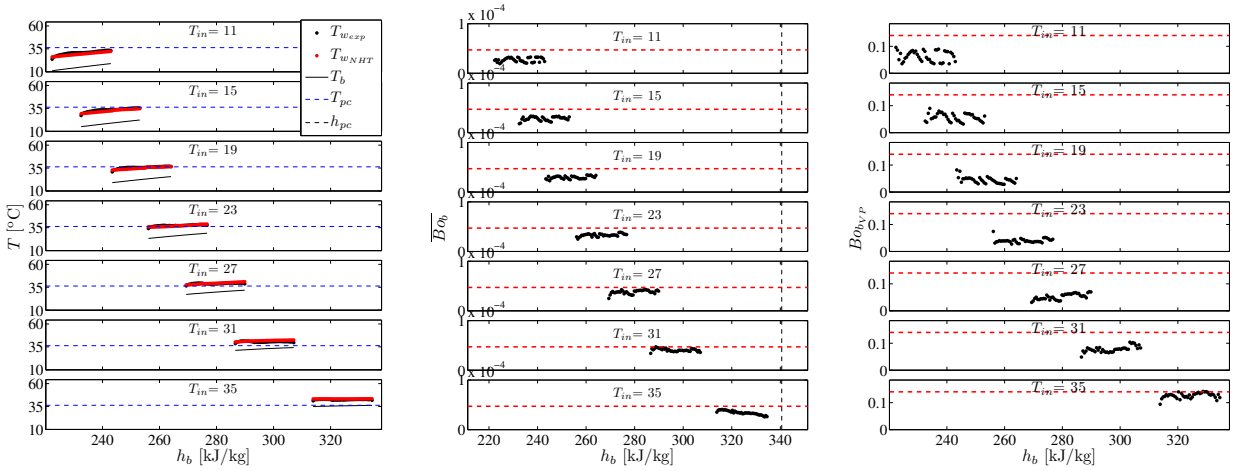
(a) T_w profiles (b) $\overline{Bo_b}$ profiles (c) $Bo_{b_{VP}}$ profiles

Figure C.95: $\overline{Bo_b}$, $Bo_{b_{VP}}$, and T_w profiles for $P/P_c = 1.13$, $D = 22$ mm, $G = 300$ kg/m^{2}s, $q = 15$ kW/m^2; dashed red lines represent suggested thresholds; T_{in} is in °C.



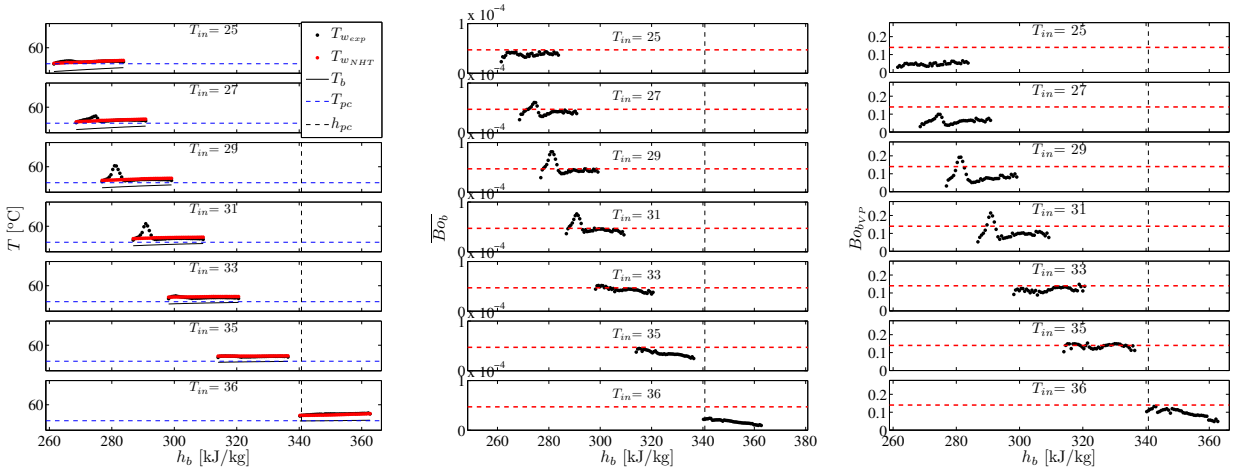
(a) T_w profiles (b) $\overline{Bo_b}$ profiles (c) $Bo_{b_{VP}}$ profiles

Figure C.96: $\overline{Bo_b}$, $Bo_{b_{VP}}$, and T_w profiles for $P/P_c = 1.13$, $D = 22$ mm, $G = 300$ kg/m^{2}s, $q = 20$ kW/m^2; dashed red lines represent suggested thresholds; T_{in} is in °C.



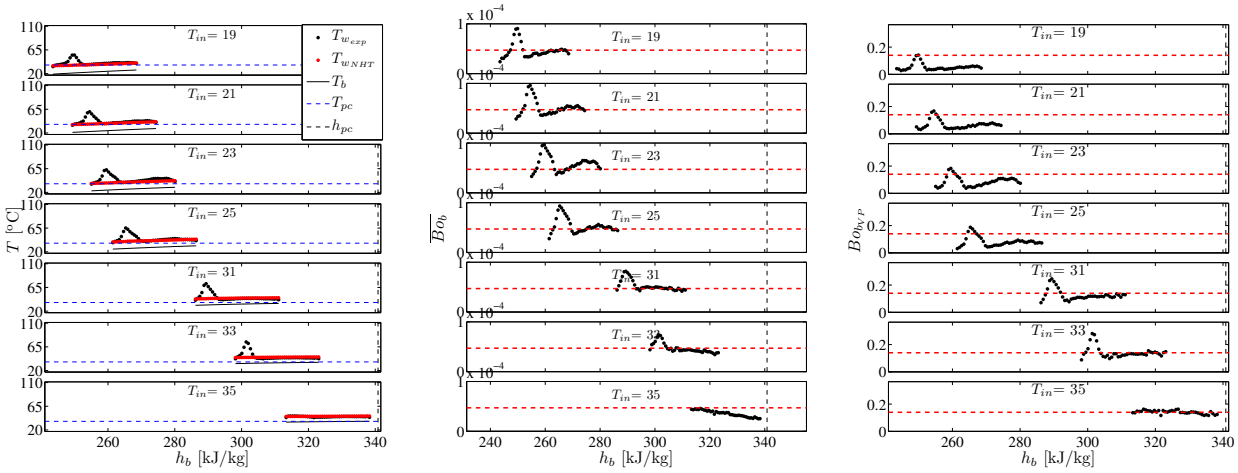
(a) T_w profiles (b) $\overline{Bo_b}$ profiles (c) $Bo_{b_{VP}}$ profiles

Figure C.97: $\overline{Bo_b}$, $Bo_{b_{VP}}$, and T_w profiles for $P/P_c = 1.13$, $D = 22$ mm, $G = 400$ kg/m^{2}s, $q = 23$ kW/m^2; dashed red lines represent suggested thresholds; T_{in} is in °C.



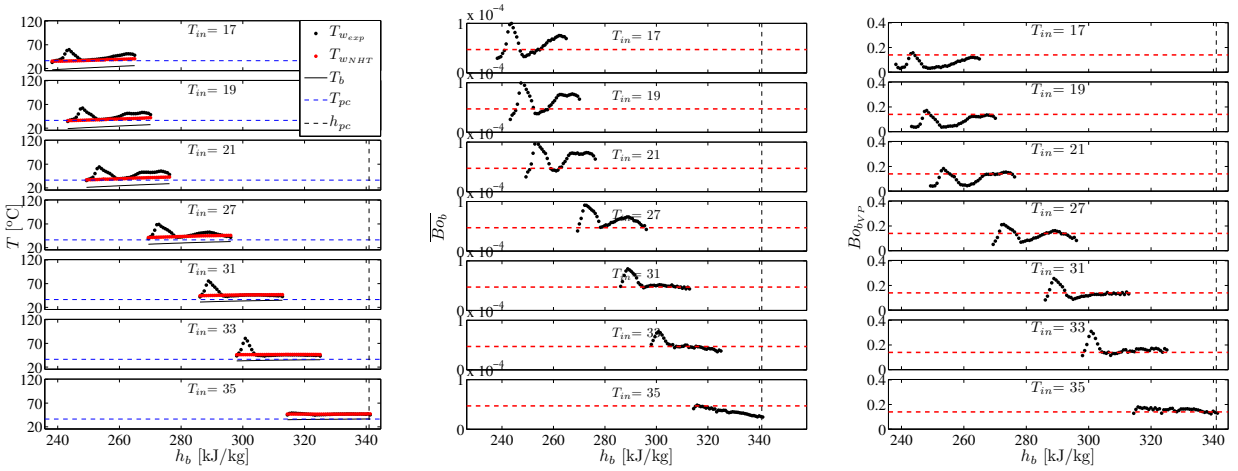
(a) T_w profiles (b) $\overline{Bo_b}$ profiles (c) $Bo_{b_{VP}}$ profiles

Figure C.98: $\overline{Bo_b}$, $Bo_{b_{VP}}$, and T_w profiles for $P/P_c = 1.13$, $D = 22$ mm, $G = 400$ kg/m^{2}s, $q = 25$ kW/m^2; dashed red lines represent suggested thresholds; T_{in} is in °C.



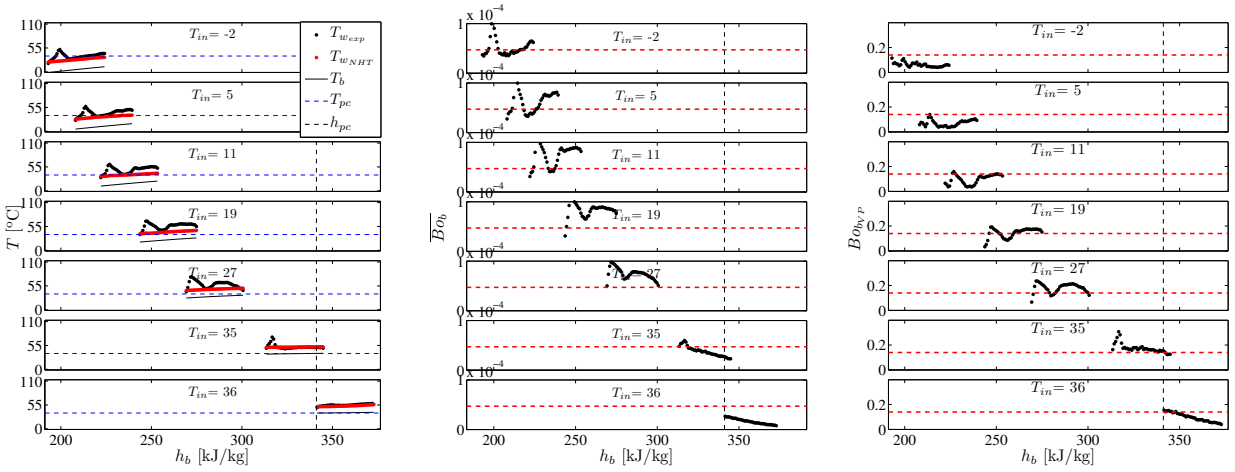
(a) T_w profiles (b) $\overline{Bo_b}$ profiles (c) $Bo_{b_{VP}}$ profiles

Figure C.99: $\overline{Bo_b}$, $Bo_{b_{VP}}$, and T_w profiles for $P/P_c = 1.13$, $D = 22$ mm, $G = 400$ kg/m^{2}s, $q = 28$ kW/m^2; dashed red lines represent suggested thresholds; T_{in} is in °C.



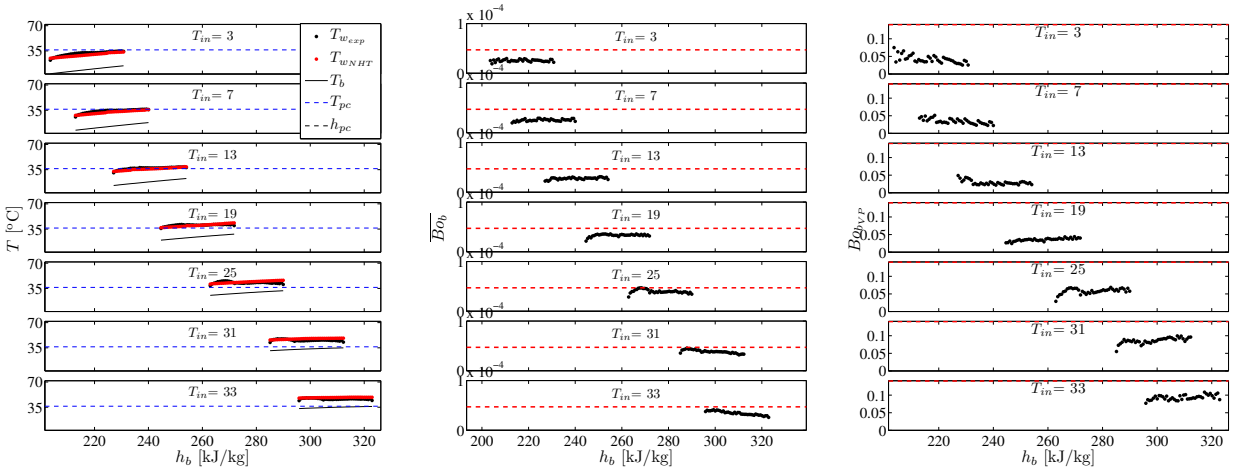
(a) T_w profiles (b) $\overline{Bo_b}$ profiles (c) $Bo_{b_{VP}}$ profiles

Figure C.100: $\overline{Bo_b}$, $Bo_{b_{VP}}$, and T_w profiles for $P/P_c = 1.13$, $D = 22$ mm, $G = 400$ kg/m^{2}s, $q = 30$ kW/m^2; dashed red lines represent suggested thresholds; T_{in} is in °C.



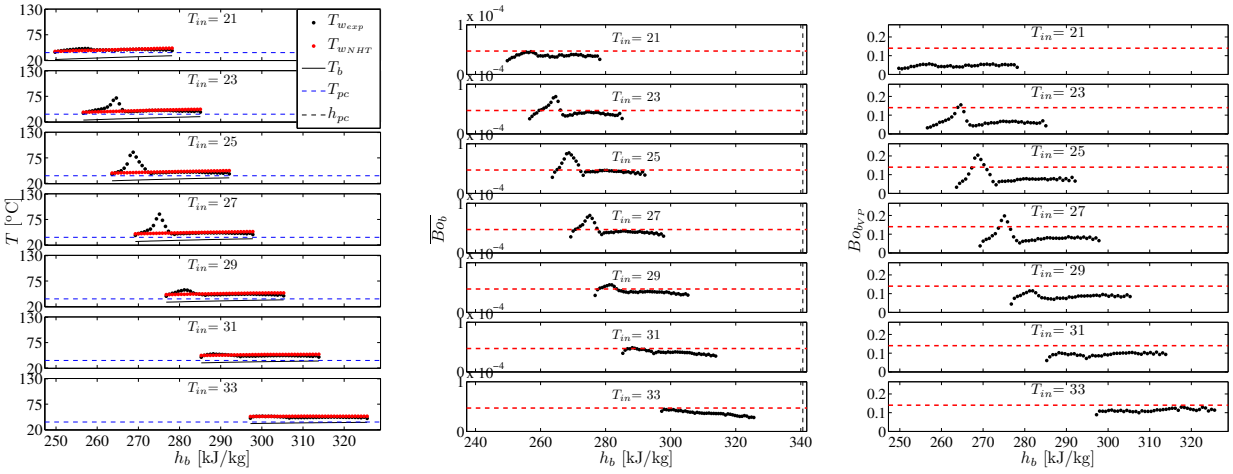
(a) T_w profiles (b) $\overline{Bo_b}$ profiles (c) $Bo_{b_{VP}}$ profiles

Figure C.101: $\overline{Bo_b}$, $Bo_{b_{VP}}$, and T_w profiles for $P/P_c = 1.13$, $D = 22$ mm, $G = 400$ kg/m^{2}s, $q = 35$ kW/m^2; dashed red lines represent suggested thresholds; T_{in} is in °C.



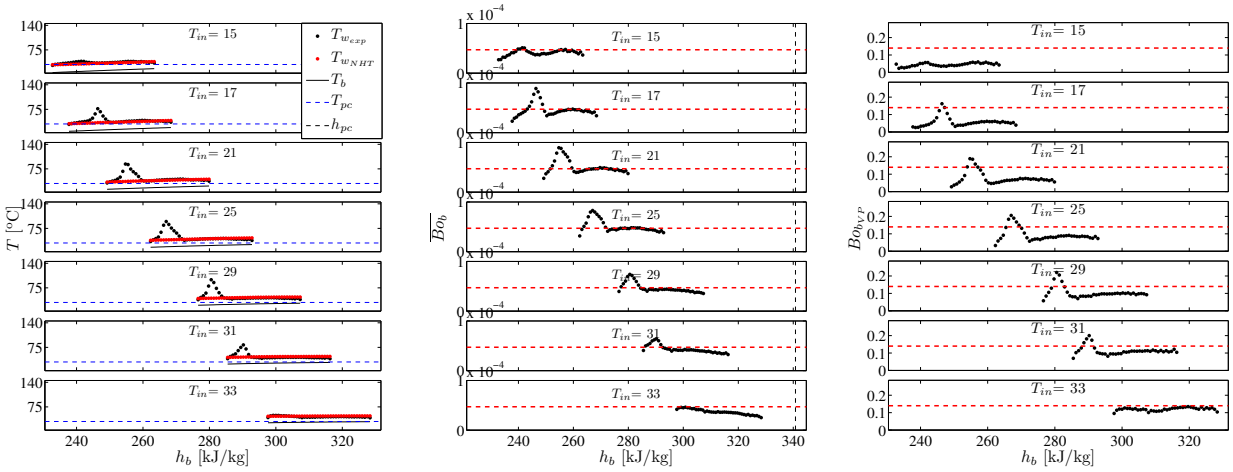
(a) T_w profiles (b) $\overline{Bo_b}$ profiles (c) $Bo_{b_{VP}}$ profiles

Figure C.102: $\overline{Bo_b}$, $Bo_{b_{VP}}$, and T_w profiles for $P/P_c = 1.13$, $D = 22$ mm, $G = 500$ kg/m^{2}s, $q = 38$ kW/m^2; dashed red lines represent suggested thresholds; T_{in} is in °C.



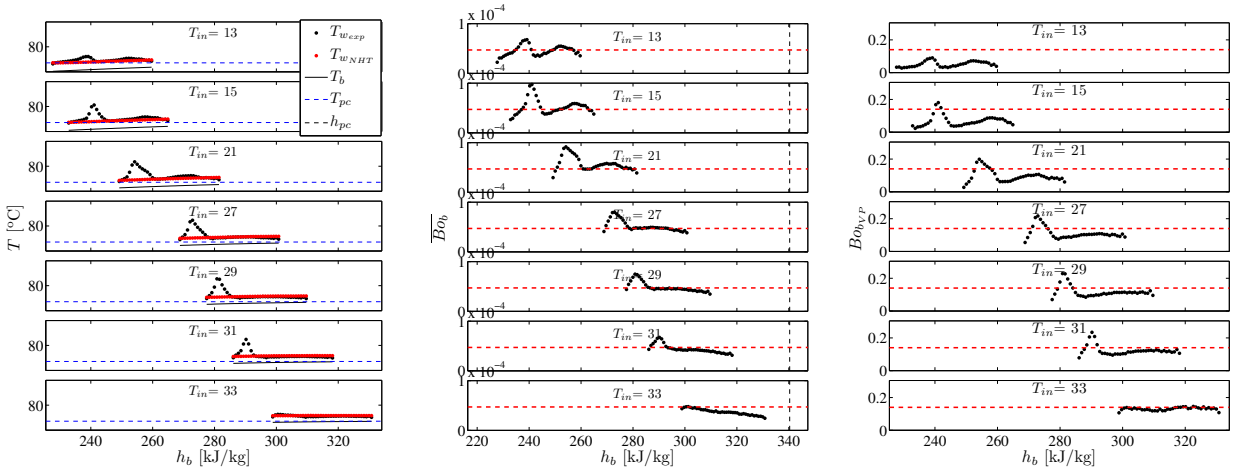
(a) T_w profiles (b) $\overline{Bo_b}$ profiles (c) $Bo_{b_{VP}}$ profiles

Figure C.103: $\overline{Bo_b}$, $Bo_{b_{VP}}$, and T_w profiles for $P/P_c = 1.13$, $D = 22$ mm, $G = 500$ kg/m^{2}s, $q = 40$ kW/m^2; dashed red lines represent suggested thresholds; T_{in} is in °C.



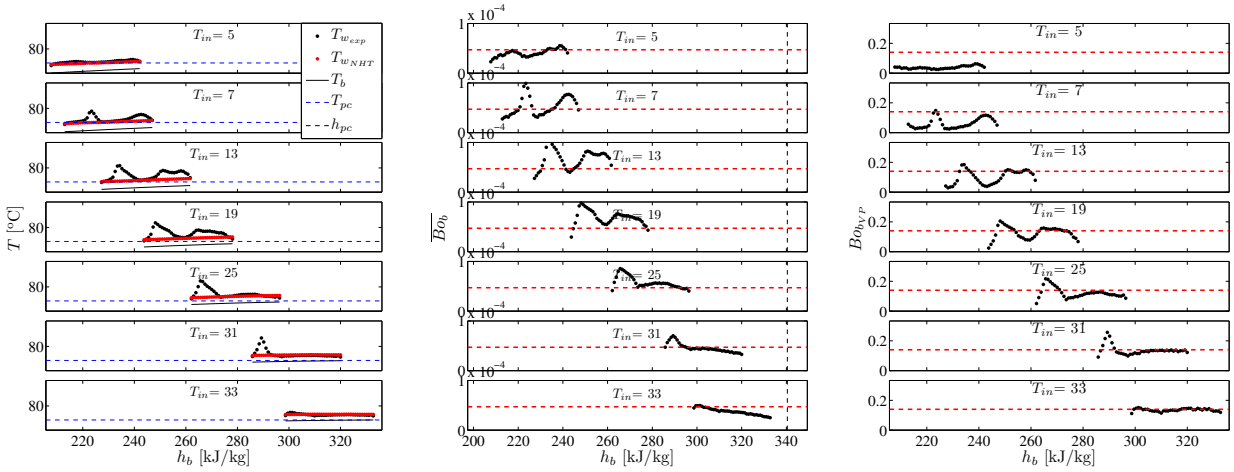
(a) T_w profiles (b) $\overline{Bo_b}$ profiles (c) $Bo_{b_{VP}}$ profiles

Figure C.104: $\overline{Bo_b}$, $Bo_{b_{VP}}$, and T_w profiles for $P/P_c = 1.13$, $D = 22$ mm, $G = 500$ kg/m^{2}s, $q = 43$ kW/m^2; dashed red lines represent suggested thresholds; T_{in} is in °C.



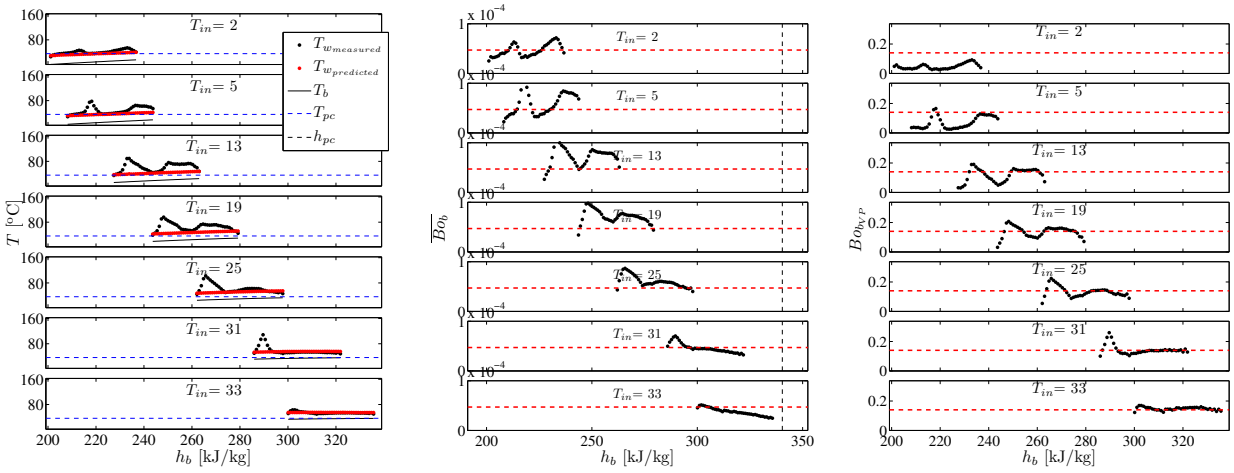
(a) T_w profiles (b) $\overline{Bo_b}$ profiles (c) $Bo_{b_{VP}}$ profiles

Figure C.105: $\overline{Bo_b}$, $Bo_{b_{VP}}$, and T_w profiles for $P/P_c = 1.13$, $D = 22$ mm, $G = 500$ kg/m^{2}s, $q = 45$ kW/m^2; dashed red lines represent suggested thresholds; T_{in} is in °C.



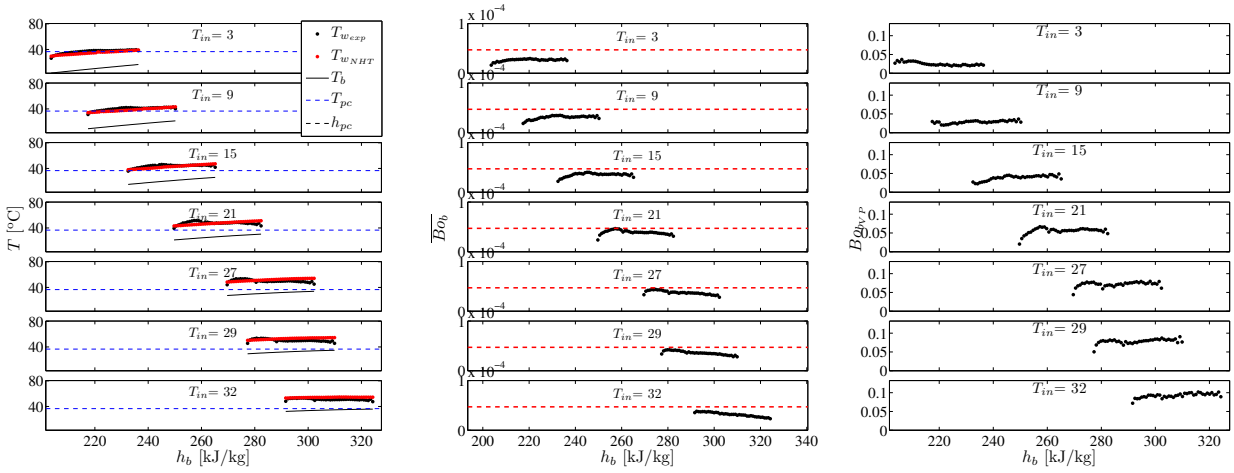
(a) T_w profiles (b) $\overline{Bo_b}$ profiles (c) $Bo_{b_{VP}}$ profiles

Figure C.106: $\overline{Bo_b}$, $Bo_{b_{VP}}$, and T_w profiles for $P/P_c = 1.13$, $D = 22$ mm, $G = 500$ kg/m^{2}s, $q = 48$ kW/m^2; dashed red lines represent suggested thresholds; T_{in} is in °C.



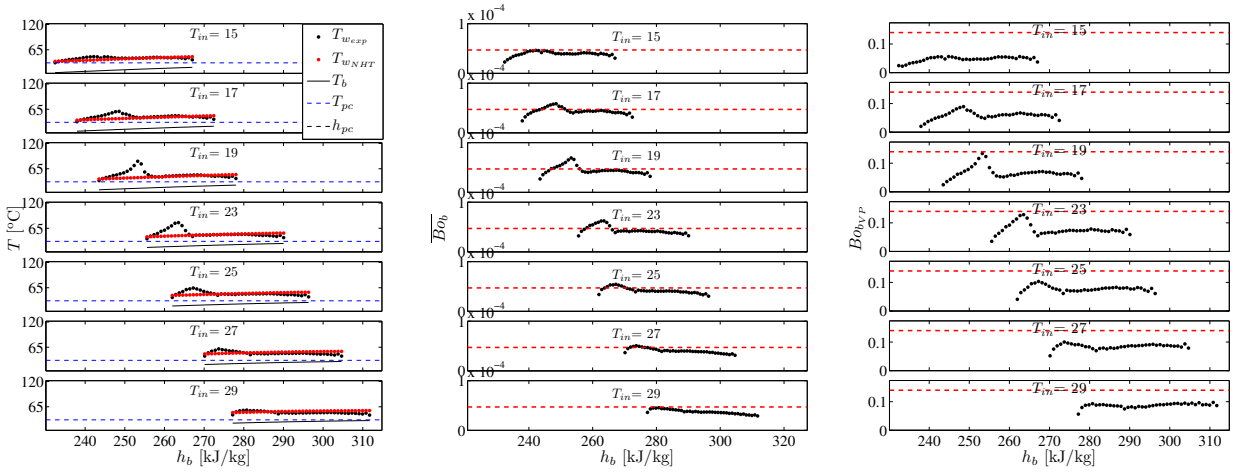
(a) T_w profiles (b) $\overline{Bo_b}$ profiles (c) $Bo_{b_{VP}}$ profiles

Figure C.107: $\overline{Bo_b}$, $Bo_{b_{VP}}$, and T_w profiles for $P/P_c = 1.13$, $D = 22$ mm, $G = 500$ kg/m^{2}s, $q = 50$ kW/m^2; dashed red lines represent suggested thresholds; T_{in} is in °C.



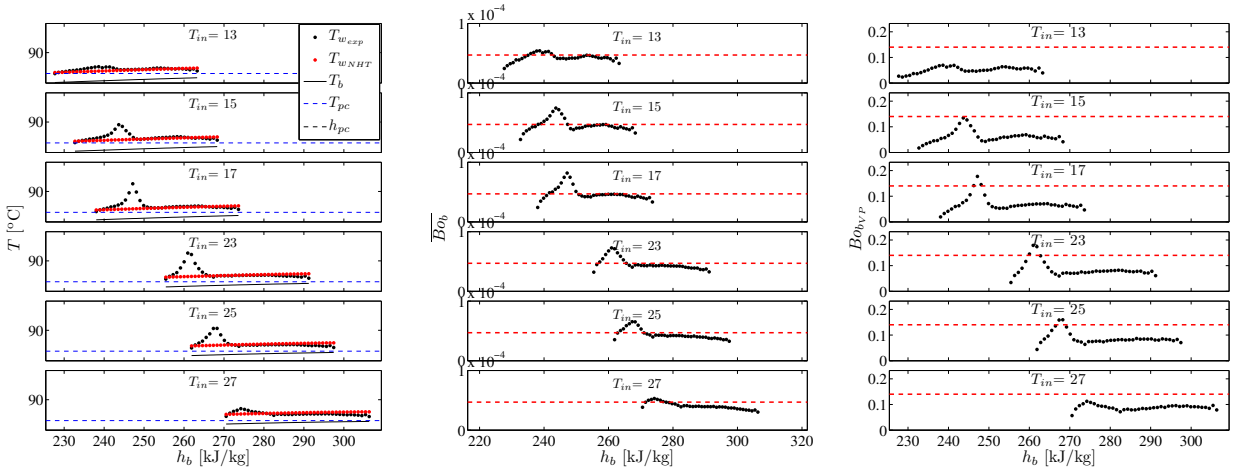
(a) T_w profiles (b) $\overline{Bo_b}$ profiles (c) $Bo_{b_{VP}}$ profiles

Figure C.108: $\overline{Bo_b}$, $Bo_{b_{VP}}$, and T_w profiles for $P/P_c = 1.13$, $D = 22$ mm, $G = 600$ kg/m^{2}s, $q = 55$ kW/m^2; dashed red lines represent suggested thresholds; T_{in} is in °C.



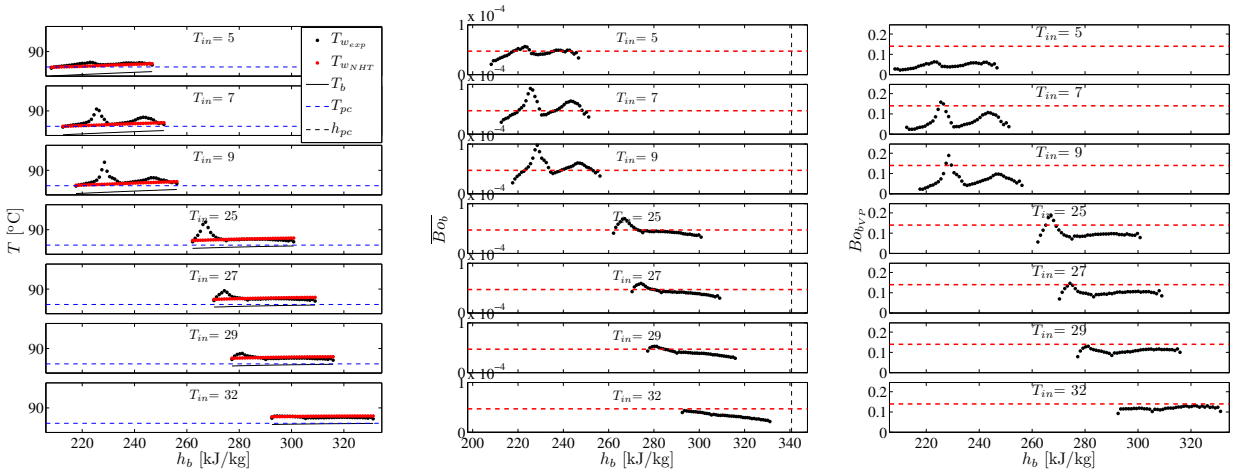
(a) T_w profiles (b) $\overline{Bo_b}$ profiles (c) $Bo_{b_{VP}}$ profiles

Figure C.109: $\overline{Bo_b}$, $Bo_{b_{VP}}$, and T_w profiles for $P/P_c = 1.13$, $D = 22$ mm, $G = 600$ kg/m^{2}s, $q = 58$ kW/m^2; dashed red lines represent suggested thresholds; T_{in} is in °C.



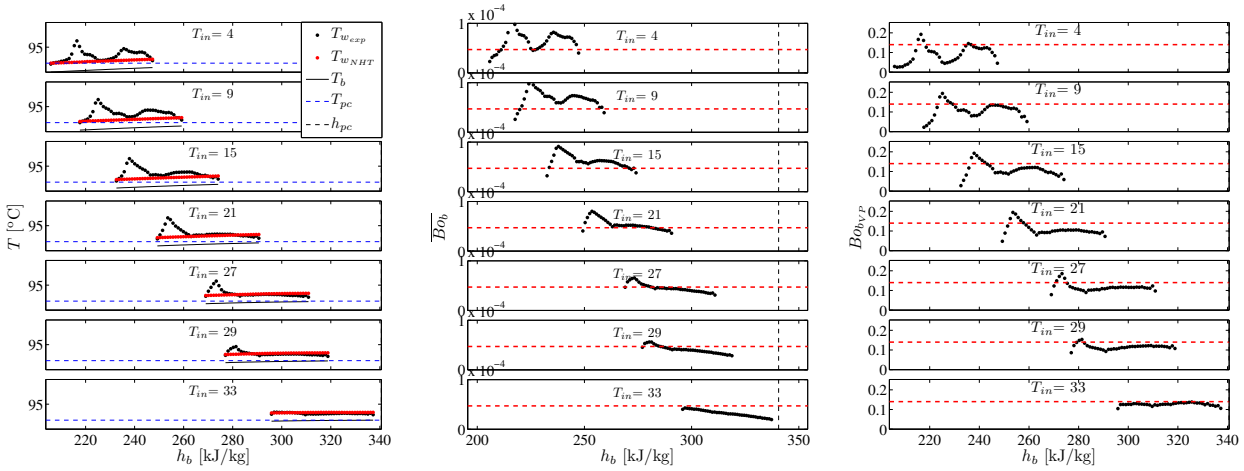
(a) T_w profiles (b) $\overline{Bo_b}$ profiles (c) $Bo_{b_{VP}}$ profiles

Figure C.110: $\overline{Bo_b}$, $Bo_{b_{VP}}$, and T_w profiles for $P/P_c = 1.13$, $D = 22$ mm, $G = 600$ kg/m^{2}s, $q = 60$ kW/m^2; dashed red lines represent suggested thresholds; T_{in} is in °C.



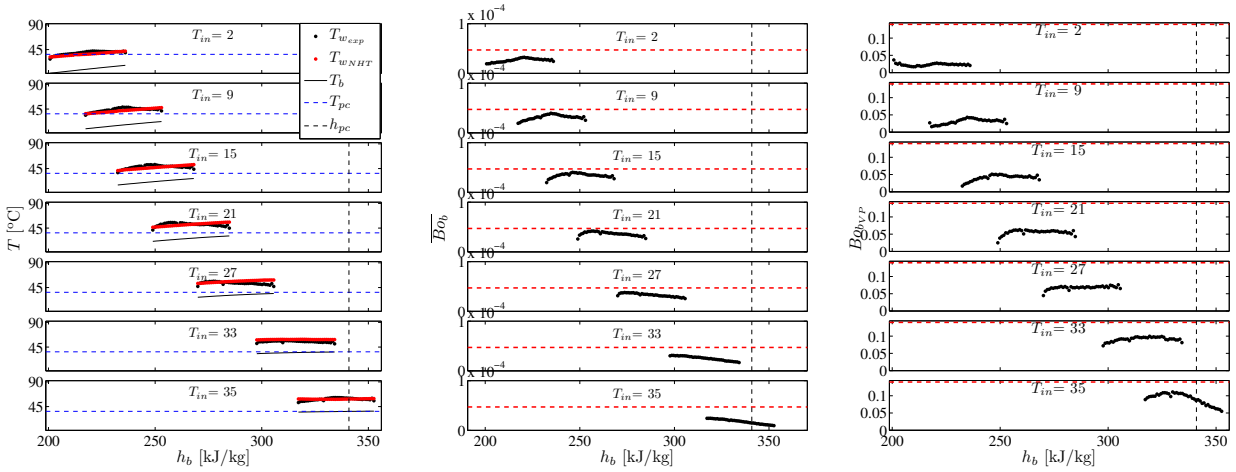
(a) T_w profiles (b) $\overline{Bo_b}$ profiles (c) $Bo_{b_{VP}}$ profiles

Figure C.111: $\overline{Bo_b}$, $Bo_{b_{VP}}$, and T_w profiles for $P/P_c = 1.13$, $D = 22$ mm, $G = 600$ kg/m^{2}s, $q = 65$ kW/m^2; dashed red lines represent suggested thresholds; T_{in} is in °C.



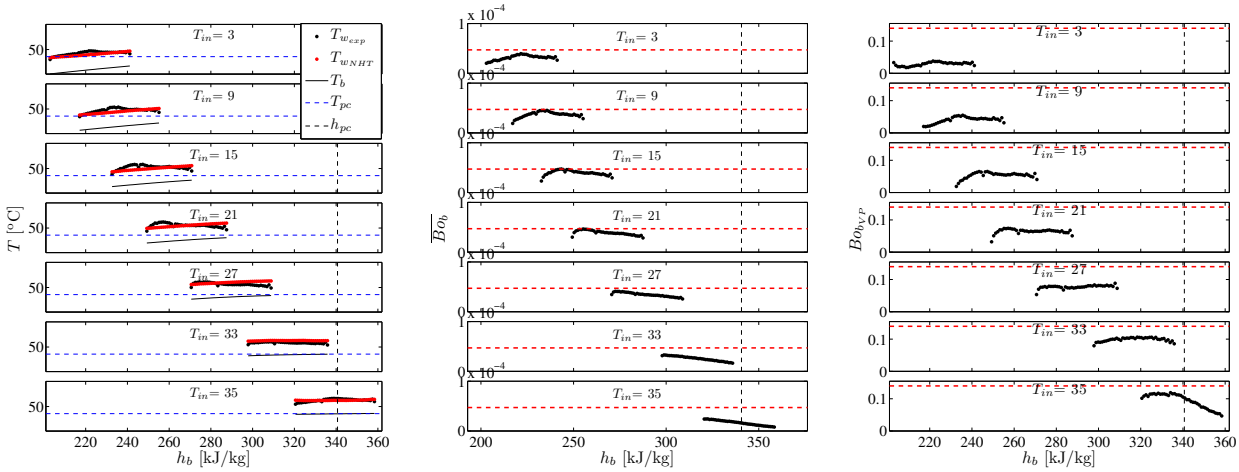
(a) T_w profiles (b) $\overline{Bo_b}$ profiles (c) $Bo_{b_{VP}}$ profiles

Figure C.112: $\overline{Bo_b}$, $Bo_{b_{VP}}$, and T_w profiles for $P/P_c = 1.13$, $D = 22$ mm, $G = 600$ kg/m^{2}s, $q = 70$ kW/m^2; dashed red lines represent suggested thresholds; T_{in} is in °C.



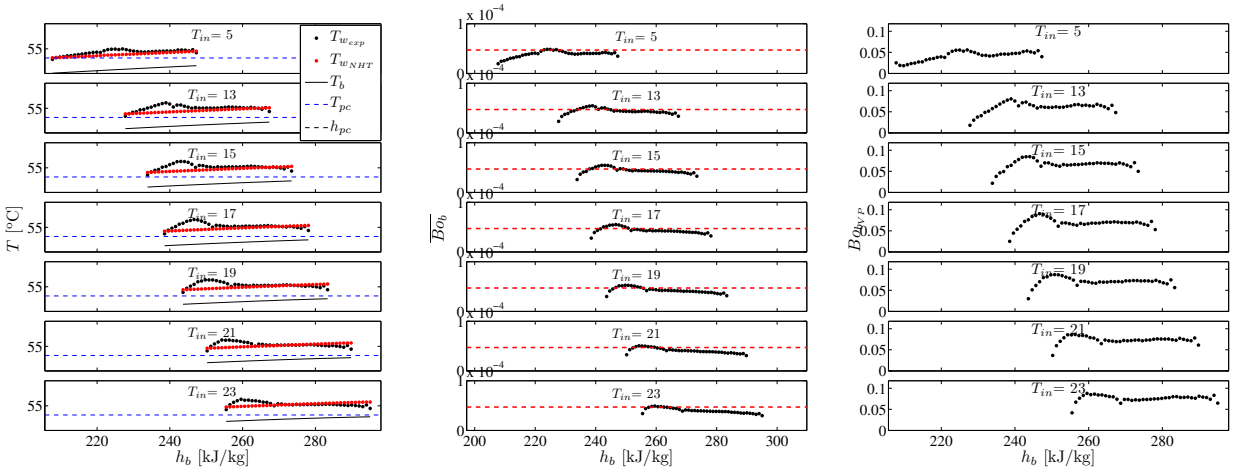
(a) T_w profiles (b) $\overline{Bo_b}$ profiles (c) $Bo_{b_{VP}}$ profiles

Figure C.113: $\overline{Bo_b}$, $Bo_{b_{VP}}$, and T_w profiles for $P/P_c = 1.13$, $D = 22$ mm, $G = 700$ kg/m^{2}s, $q = 70$ kW/m^2; dashed red lines represent suggested thresholds; T_{in} is in °C.



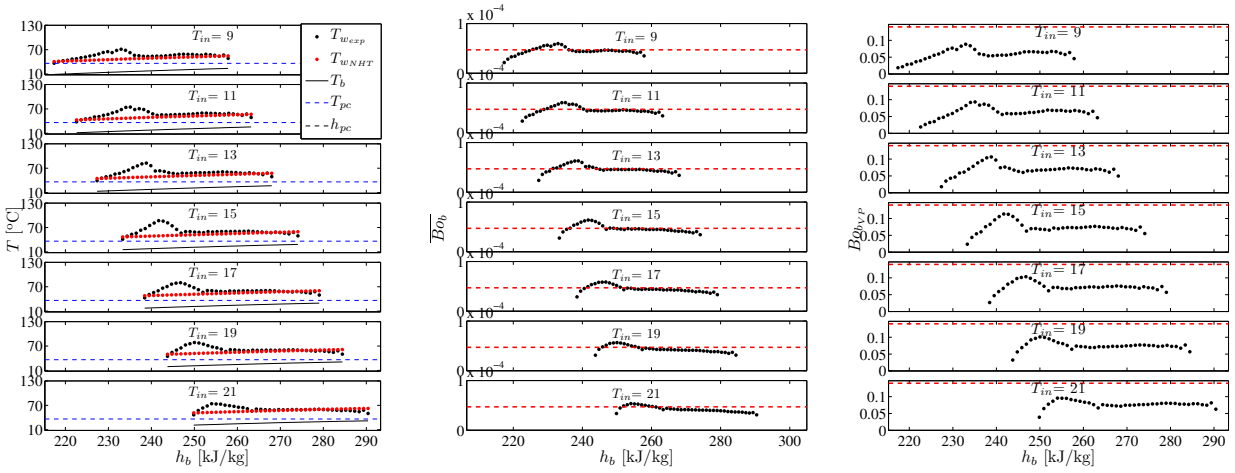
(a) T_w profiles (b) $\overline{Bo_b}$ profiles (c) $Bo_{b_{VP}}$ profiles

Figure C.114: $\overline{Bo_b}$, $Bo_{b_{VP}}$, and T_w profiles for $P/P_c = 1.13$, $D = 22$ mm, $G = 700$ kg/m^{2}s, $q = 75$ kW/m^2; dashed red lines represent suggested thresholds; T_{in} is in °C.



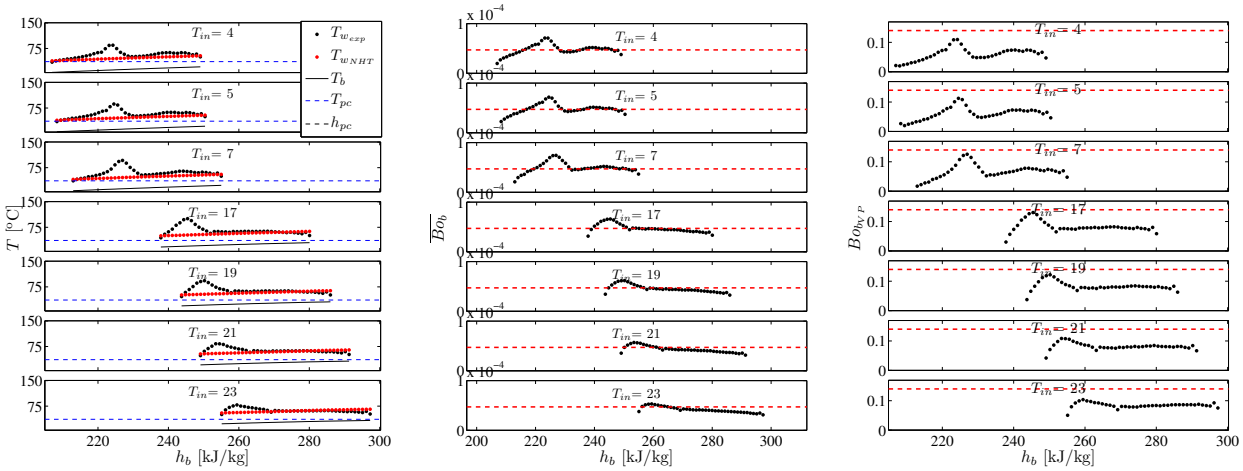
(a) T_w profiles (b) $\overline{Bo_b}$ profiles (c) $Bo_{b_{VP}}$ profiles

Figure C.115: $\overline{Bo_b}$, $Bo_{b_{VP}}$, and T_w profiles for $P/P_c = 1.13$, $D = 22$ mm, $G = 700$ kg/m^{2}s, $q = 78$ kW/m^2; dashed red lines represent suggested thresholds; T_{in} is in °C.



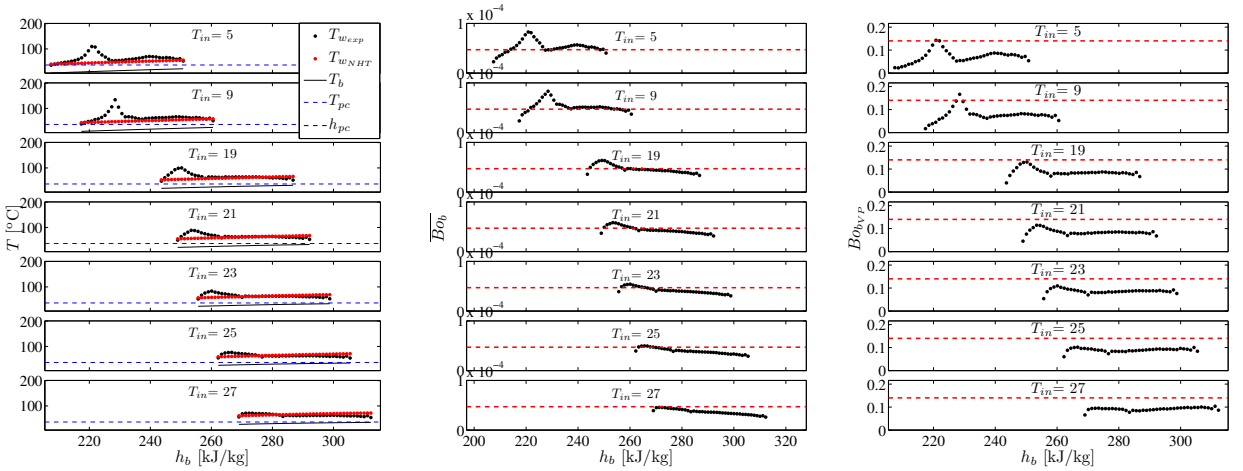
(a) T_w profiles (b) $\overline{Bo_b}$ profiles (c) $Bo_{b_{VP}}$ profiles

Figure C.116: $\overline{Bo_b}$, $Bo_{b_{VP}}$, and T_w profiles for $P/P_c = 1.13$, $D = 22$ mm, $G = 700$ kg/m^{2}s, $q = 80$ kW/m^2; dashed red lines represent suggested thresholds; T_{in} is in °C.



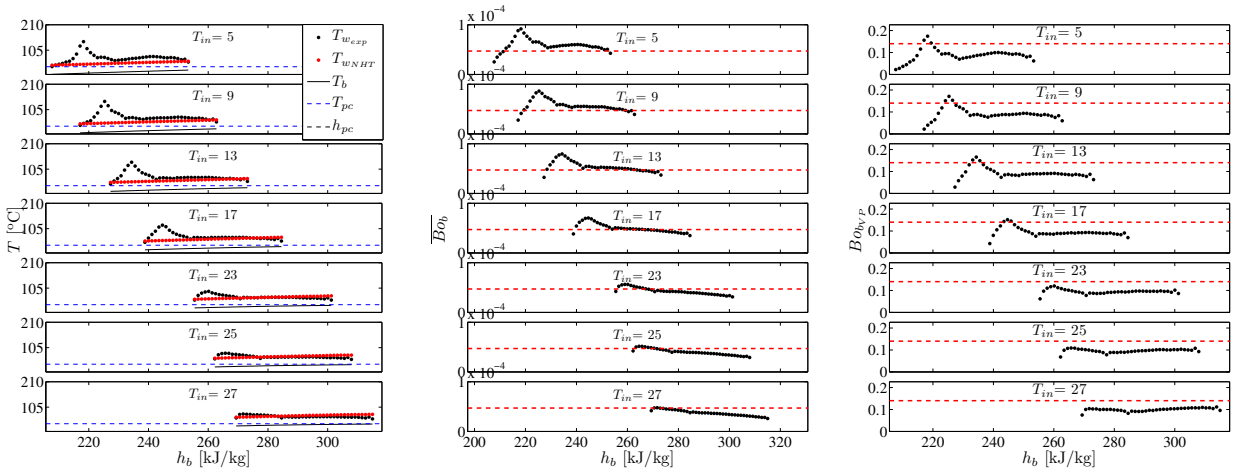
(a) T_w profiles (b) $\overline{Bo_b}$ profiles (c) $Bo_{b_{VP}}$ profiles

Figure C.117: $\overline{Bo_b}$, $Bo_{b_{VP}}$, and T_w profiles for $P/P_c = 1.13$, $D = 22$ mm, $G = 700$ kg/m^{2}s, $q = 83$ kW/m^2; dashed red lines represent suggested thresholds; T_{in} is in °C.



(a) T_w profiles (b) $\overline{Bo_b}$ profiles (c) $Bo_{b_{VP}}$ profiles

Figure C.118: $\overline{Bo_b}$, $Bo_{b_{VP}}$, and T_w profiles for $P/P_c = 1.13$, $D = 22$ mm, $G = 700$ kg/m^{2}s, $q = 85$ kW/m^2; dashed red lines represent suggested thresholds; T_{in} is in °C.



(a) T_w profiles (b) $\overline{Bo_b}$ profiles (c) $Bo_{b_{VP}}$ profiles

Figure C.119: $\overline{Bo_b}$, $Bo_{b_{VP}}$, and T_w profiles for $P/P_c = 1.13$, $D = 22$ mm, $G = 700$ kg/m^{2}s, $q = 90$ kW/m^2; dashed red lines represent suggested thresholds; T_{in} is in °C.

Appendix D

List of experimental conditions for all runs

Table D.1: List of all measured conditions with severe HTD cases in red

D [mm]	P/P_c [ ]	G [kg/m^{2}s]	q [kW/m^2]	T_{in} [°C]
4.6	1.13	300	13	8, 10, 12, 16, 20, 24, 27, 30, 32, 35
4.6	1.13	300	15	0, 6, 8, 10, 12, 16, 20, 24, 27, 30, 32, 35
4.6	1.13	300	18	0, 6, 8, 10, 12, 16, 20, 24, 27, 30, 32, 35
4.6	1.13	300	20	0, 6, 8, 10, 12, 16, 20, 24, 27, 30, 32, 35
4.6	1.13	400	30	0, 4, 7, 11, 15, 17, 20, 22, 24, 26, 30, 35
4.6	1.13	400	33	0, 4, 7, 11, 15, 17, 20, 22, 24, 26, 30, 35
4.6	1.13	400	35	0, 4, 7, 11, 15, 17, 20, 22, 24, 26, 30, 35
4.6	1.13	400	38	7, 12, 15, 17, 20, 22, 24, 26, 30, 35
4.6	1.13	400	40	7, 11, 15, 17, 20, 22, 24, 26, 30, 35
4.6	1.13	500	45	-1, 3, 5, 9, 12, 14, 18, 20, 23, 25, 31, 35
4.6	1.13	500	48	-1, 3, 5, 9, 12, 14, 18, 20, 23, 25, 31, 35
4.6	1.13	500	50	-1, 3, 5, 9, 12, 14, 18, 20, 23, 25, 31, 35
4.6	1.13	500	53	-1, 3, 5, 9, 12, 14, 18, 20, 23, 25, 31, 35
4.6	1.13	500	55	0, 4, 5, 9, 12, 14, 18, 20, 23, 25, 31, 35
4.6	1.13	600	75	-1, 4, 7, 10, 12, 14, 16, 18, 20, 22, 24, 26, 30, 35
4.6	1.13	600	80	-1, 4, 7, 11, 12, 14, 16, 18, 21, 22, 24, 26, 30, 35
4.6	1.13	600	83	-1, 4, 7, 11, 13, 14, 16, 18, 21, 23, 24, 26, 30, 35
4.6	1.13	600	85	-1, 4, 7, 11, 12, 14, 16, 18, 21, 22, 24, 26, 30, 35
4.6	1.13	700	90	5, 10, 19, 25, 30, 35
4.6	1.13	700	95	5, 10, 19, 25, 30, 35
4.6	1.13	700	100	5, 10, 19, 25, 30, 35
4.6	1.13	700	105	5,10, 20, 25, 30, 35

Table D.1: List of all measured conditions with severe HTD cases in red (Cont'd)

D [mm]	P/P_c [ ]	G [kg/m^{2}s]	q [kW/m^2]	T_{in} [°C]
4.6	1.13	700	110	-1, 3, 4, 5, 8, 11, 14, 18, 22, 26, 34
4.6	1.13	700	115	-1, 3, 4, 5, 8, 11, 14, 18, 22, 26, 34
4.6	1.13	700	120	0, 3, 4, 5, 8, 11, 14, 18, 22, 26, 34
4.6	1.13	700	125	0, 4, 5, 8, 11, 14, 18, 22, 26
4.6	1.13	1000	225	1, 3, 6, 15, 20, 23, 29, 35
4.6	1.13	1000	230	1, 3, 6, 15, 19, 23, 29, 35
4.6	1.13	1000	240	1, 3, 6, 15, 19, 23, 29, 35
4.6	1.13	1000	245	1, 3, 6, 15, 19, 23, 29, 35
4.6	1.13	1000	250	1, 3, 6, 15, 19, 23, 29, 34
4.6	1.13	1000	260	1, 3, 6, 15, 19, 23, 28
4.6	1.13	1500	380	4, 10, 15, 20, 25, 30
4.6	1.13	1500	390	4, 10, 15, 20, 25, 30
4.6	1.13	1500	400	5, 10, 15, 20, 25, 30
4.6	1.13	1500	410	5, 10, 15, 20, 25, 30
4.6	1.13	1500	420	5, 10, 15, 20, 25, 30
4.6	1.13	1500	430	5, 10, 15, 20, 25, 30
4.6	1.13	1500	440	5, 10, 15, 20, 25, 30
4.6	1.13	1500	450	5, 10, 15, 20, 25, 30
8	1.13	200	3	16, 18, 20, 22, 24, 26, 28, 30, 32, 34, 36, 38
8	1.13	200	5	16, 18, 20, 22, 24, 26, 28, 30, 32, 34, 36, 37
8	1.13	200	8	16, 18, 20, 22, 24, 26, 28, 30, 32, 34, 36, 38
8	1.13	200	10	16, 18, 20, 22, 24, 26, 28, 30, 32, 34, 36, 38
8	1.13	200	15	16, 18, 20, 22, 24, 26, 28, 30, 32, 34, 36, 38
8	1.13	300	10	4, 8, 11, 14, 16, 18, 20, 22, 24, 28, 31, 33, 35
8	1.13	300	13	14, 16, 18, 20, 22, 24, 28, 31, 33, 35

Table D.1: List of all measured conditions with severe HTD cases in red (Cont'd)

D [mm]	P/P_c [ ]	G [kg/m^{2}s]	q [kW/m^2]	T_{in} [°C]
8	1.13	300	15	4, 15, 16, 18, 20, 22, 24, 28, 31, 33, 35
8	1.13	300	18	4, 8, 11, 15, 16, 18, 20, 22, 24, 28, 31, 33, 35
8	1.13	300	20	4, 8, 11, 15, 16, 18, 20, 22, 24, 28, 31, 33, 35
8	1.13	400	25	8, 9, 11, 13, 15, 17, 19, 21, 23, 26, 28, 31
8	1.13	400	30	6, 9, 11, 13, 15, 18, 19, 21, 23, 25, 26, 27, 28, 31, 33
8	1.13	400	33	7, 9, 11, 13, 15, 18, 19, 21, 23, 25, 26, 27, 28, 29, 31, 33
8	1.13	400	35	7, 9, 11, 13, 15, 18, 19, 21, 23, 25, 26, 27, 28, 29, 31, 33
8	1.13	400	40	10, 11, 13, 15, 17, 19, 21, 23, 26, 28, 31, 33, 34
8	1.13	500	50	5, 7, 9, 11, 13, 15, 17, 19, 21, 23, 25, 27, 29, 31
8	1.13	500	53	5, 7, 9, 11, 13, 15, 17, 19, 21, 23, 25, 27, 29, 31
8	1.13	500	55	5, 7, 9, 11, 13, 15, 17, 19, 21, 23, 25, 27, 29, 31
8	1.13	500	60	5, 7, 9, 11, 13, 15, 17, 19, 21, 23, 25, 27, 29, 31
8	1.13	600	65	5, 9, 12, 15, 20, 25, 30
8	1.13	600	70	5, 9, 12, 15, 20, 25, 30
8	1.13	600	73	5, 9, 12, 15, 20, 25, 30
8	1.13	600	75	5, 9, 12, 15, 20, 25, 30
8	1.13	600	78	5, 9, 12, 15, 20, 25, 30
8	1.13	600	80	4, 6, 8, 10, 12, 14, 16, 18, 20

Table D.1: List of all measured conditions with severe HTD cases in red (Cont'd)

D [mm]	P/P_c [ ]	G [kg/m^{2}s]	q [kW/m^2]	T_{in} [°C]
8	1.13	600	83	4, 6, 8, 10, 12, 14, 16, 18, 20
8	1.13	600	85	4, 6, 8, 10, 12, 14, 16, 18, 20
8	1.13	600	90	4, 6, 8, 10, 12, 14, 17, 18, 20
8	1.13	700	90	3, 5, 10, 15, 20, 25, 30
8	1.13	700	95	3, 5, 10, 15, 20, 25, 30
8	1.13	700	98	3, 5, 10, 15, 20, 25, 30
8	1.13	700	100	2, 5, 8, 10, 12, 14, 17, 20, 25, 29, 34
8	1.13	700	105	2, 6, 8, 10, 12, 14, 17, 20, 25, 29, 34
8	1.13	700	110	2, 6, 8, 10, 12, 14, 17, 20, 25, 29, 34
8	1.13	700	115	3, 6, 8, 10, 12, 14, 17, 20, 25, 29, 34
8	1.13	700	120	2, 6, 8, 11, 12, 14, 17, 20, 25, 29, 34
8	1.13	1000	200	4, 8, 12, 17, 22, 25, 30, 35
8	1.13	1000	210	5, 8, 12, 17, 22, 25, 30, 35
8	1.13	1000	220	8, 12, 17, 22, 25, 30, 35
8	1.13	1000	225	8, 12, 17, 22, 25, 30, 35
8	1.13	1000	230	8, 12, 17, 22, 25, 30, 35
8	1.13	1000	235	4, 8, 10, 12, 14, 16, 18, 20, 22, 24, 26, 29, 31, 33, 34, 37
8	1.13	1000	240	5, 8, 10, 12, 14, 16, 18, 20, 22, 24, 26, 29, 31, 33, 34, 37
8	1.13	1000	245	6, 8, 10, 12, 14, 16, 18, 20, 22, 24, 27, 29, 31, 33, 34, 37
8	1.13	1000	250	6, 8, 10, 12, 14, 16, 18, 20, 22, 24, 27, 29, 31, 33, 34, 37

Table D.1: List of all measured conditions with severe HTD cases in red (Cont'd)

D [mm]	P/P_c [ ]	G [kg/m^{2}s]	q [kW/m^2]	T_{in} [°C]
8	1.13	1000	260	7, 8, 10, 12, 14, 16, 19, 21, 23, 25, 27, 29, 31, 32, 34, 37
8	1.13	1500	380	8, 20, 25, 30, 35
8	1.13	1500	390	10, 20, 25, 30, 35
8	1.13	1500	400	11, 21, 25, 30, 35
8	1.13	1500	410	13, 21, 25, 30, 35
8	1.13	1500	420	13, 22, 25, 31, 35
8	1.13	1500	430	14, 23, 25, 30, 35
8	1.13	1500	440	16, 24, 26, 30, 35
8	1.13	1500	450	17, 24, 26, 30, 35
22	1.13	200	2	3, 5, 7, 9, 11, 13, 15, 17, 19, 21, 23, 25, 27, 29, 31, 33, 35, 36
22	1.13	200	3	1, 3, 5, 7, 9, 11, 13, 15, 17, 19, 21, 23, 25, 27, 29, 31, 33, 35, 36
22	1.13	200	3.5	1, 3, 5, 7, 9, 11, 13, 15, 17, 19, 21, 23, 25, 27, 29, 31, 33, 35
22	1.13	200	4	1, 3, 5, 7, 9, 11, 13, 15, 17, 19, 21, 23, 25, 27, 29, 31, 33, 35, 36
22	1.13	200	5	3, 5, 7, 9, 11, 13, 15, 17, 19, 21, 23, 25, 27, 29, 31, 33, 35, 36
22	1.13	200	10	3, 5, 7, 9, 11, 13, 15, 17, 19, 21, 23, 25, 27, 29, 31, 33, 35, 36, 37
22	1.13	300	10	1, 3, 5, 7, 9, 11, 13, 15, 17, 19, 21, 23, 25, 27, 29, 31, 33, 35, 36
22	1.13	300	13	1, 3, 5, 7, 9, 11, 13, 15, 17, 19, 21, 23, 25, 27, 29, 31, 33, 35, 36

Table D.1: List of all measured conditions with severe HTD cases in red (Cont'd)

D [mm]	P/P_c [ ]	G [kg/m^{2}s]	q [kW/m^2]	T_{in} [°C]
22	1.13	300	15	1, 3, 5, 7, 9, 11, 13, 15, 17, 19, 21, 23, 25, 27, 29, 31, 33, 35, 36
22	1.13	300	20	1, 3, 5, 7, 9, 11, 13, 15, 17, 19, 21, 23, 25, 27, 29, 31, 33, 35, 36, 37
22	1.13	400	20	13, 15, 17, 19, 21, 23, 25, 27, 29, 31, 33, 35, 36
22	1.13	400	23	11, 13, 15, 17, 19, 21, 23, 25, 27, 29, 31, 33, 35
22	1.13	400	25	-2, 1, 3, 5, 7, 9, 11, 13, 15, 17, 19, 21, 23, 25, 27, 29, 31, 33, 35, 36
22	1.13	400	28	-2, 1, 3, 5, 7, 9, 11, 13, 15, 17, 19, 21, 23, 25, 27, 29, 31, 33, 35
22	1.13	400	30	-2, 1, 3, 5, 7, 9, 11, 13, 15, 17, 19, 21, 23, 25, 27, 29, 31, 33, 35, 36
22	1.13	400	35	-2, 1, 3, 5, 7, 9, 11, 13, 15, 17, 19, 21, 23, 25, 27, 29, 31, 33, 35, 36
22	1.13	500	35	3, 5, 7, 9, 11, 13, 15, 17, 19, 21, 23, 25, 27
22	1.13	500	38	3, 5, 7, 9, 11, 13, 15, 17, 19, 21, 23, 25, 27, 29, 31, 33
22	1.13	500	40	3, 5, 7, 9, 11, 13, 15, 17, 19, 21, 23, 25, 27, 29, 31, 33
22	1.13	500	43	2, 5, 7, 9, 11, 13, 15, 17, 19, 21, 23, 25, 27, 29, 31, 33
22	1.13	500	45	2, 5, 7, 9, 11, 13, 15, 17, 19, 21, 23, 25, 27, 29, 31, 33

Table D.1: List of all measured conditions with severe HTD cases in red (Cont'd)

D [mm]	P/P_c [ ]	G [kg/m^{2}s]	q [kW/m^2]	T_{in} [°C]
22	1.13	500	48	2, 5, 7, 9, 11, 13, 15, 17, 19, 21, 23, 25, 27, 29, 31, 33
22	1.13	500	50	2, 5, 7, 9, 11, 13, 15, 17, 19, 21, 23, 25, 27, 29, 31, 33
22	1.13	600	55	3, 5, 7, 9, 11, 13, 15, 17, 19, 21, 23, 25, 27, 29, 32
22	1.13	600	58	3, 5, 7, 9, 11, 13, 15, 17, 19, 21, 23, 25, 27, 29, 32
22	1.13	600	60	3, 5, 7, 9, 11, 13, 15, 17, 19, 21, 23, 25, 27, 29
22	1.13	600	65	3, 5, 7, 9, 11, 13, 15, 17, 19, 21, 23, 25, 27, 29, 32
22	1.13	600	70	4, 5, 7, 9, 11, 13, 15, 17, 19, 21, 23, 25, 27, 29, 33
22	1.13	700	70	2, 5, 7, 9, 11, 13, 15, 17, 19, 21, 23, 25, 27, 29, 31, 33, 35
22	1.13	700	73	2, 5, 7, 9, 11, 13, 15, 17, 19, 21, 23, 25, 27, 29, 31, 33, 35
22	1.13	700	75	3, 5, 7, 9, 11, 13, 15, 17, 19, 21, 23, 25, 27, 29, 31, 33, 35
22	1.13	700	78	5, 7, 9, 11, 13, 15, 17, 19, 21, 23, 25, 27, 29, 31
22	1.13	700	80	4, 5, 7, 9, 11, 13, 15, 17, 19, 21, 23, 25, 27, 29, 31
22	1.13	700	83	4, 5, 7, 9, 11, 13, 15, 17, 19, 21, 23, 25, 27, 29, 31

Table D.1: List of all measured conditions with severe HTD cases in red (Cont'd)

D [mm]	P/P_c [ ]	G [kg/m^{2}s]	q [kW/m^2]	T_{in} [°C]
22	1.13	700	85	4, 5, 7, 9, 11, 13, 15, 17, 19, 21, 23, 25, 27, 29, 31
22	1.13	700	90	5, 7, 9, 11, 13, 15, 17, 19, 21, 23, 25, 27, 29, 31

Appendix E

Iteration method for evaluating $\mathbf{Nu}_{NHT}$

In section 5.4.2, we compared the measured local wall temperature T_w and a hypothetical wall temperature T_{wNHT} that was computed with the use of Equation (5.5), which was our chosen correlation Nu_{NHT} for normal heat transfer. However, the properties ρ_w and $\overline{C_p}$ as well as the exponent n (Equation 5.2) on the right side of this equation depend on the value of wall temperature and it is not possible to solve this equation analytically for T_{wNHT}. For this reason, we estimated T_{wNHT} with the use of an iterative method, programmed in Matlab®. The main steps were as follows.

1. Equation (5.5) was separated into a left side and a right side:

$$\mathrm{LS} = \frac{qD}{k_b(T_w - T_b)} \ , \tag{E.1}$$

$$\mathrm{RS} = \mathrm{Nu}_{DB} \left(\frac{\rho_w}{\rho_b}\right)^{0.3} \left(\frac{\overline{C_p}}{C_{p_b}}\right)^{n} \ . \tag{E.2}$$

2. A convergence threshold CT for the calculation of Nu_{NHT} was chosen by trial and error. This was the smallest value that ensured convergence for all data points for each profile tested and was approximately equal to 10% of the corresponding maximum experimental value Nu_{exp}. As a result, cases with higher mass fluxes required larger values of CT.

3. A data point with specified values of D, P, q, G and T_b was chosen. T_{pc} was calculated from NIST tables. The value of the correlation Nu_{DB} (Dittus and Boelter, 1930) was calculated from Equation (5.1); this only requires the values of properties at T_b.

4. A starting value of wall temperature was set as equal to T_b+ 1 °C. We avoided choosing a larger starting value to ensure convergence of the iteration.

5. The values of LS and RS were calculated. The iteration was terminated if

$$|\mathrm{LS} - \mathrm{RS}| \leq \mathrm{CT} \ . \tag{E.3}$$

   If this was not the case, the value of wall temperature was incremented by ΔT = 0.1 °C and this step was repeated until convergence was achieved. This choice of ΔT was found to be optimal, as smaller increments did not result in visible changes of the calculated values, whereas larger increments reduced the accuracy of the solution.

6. Once convergence was reached, the desired value T_{wNHT} was calculated as

$$T_{w_{NHT}} = \frac{qD}{k_b \mathrm{RS}} + T_b \ , \tag{E.4}$$

because it was found that, when LS was used instead of RS in this expression, the predictions were offset from the experimental values by approximately 10%.

Previous researchers have noted that iterative calculations of wall temperature from supercritical heat transfer correlations may, under certain conditions, produce multiple values, which depend on the starting point. We have not encountered such problems for the present set of conditions.

References

Ackerman, J. (1970). Pseudoboiling heat transfer to supercritical pressure water in smooth and ribbed tubes. *J. Heat Transfer*, 92(3):490–497.

Aksan, N., Ambrosini, W., Ammirabile, L., Anderson, M., Bae, Y., Chen, Y., Churkin, A., Haenninen, M., Jackson, J., Kirillov, P., Leung, L., Novog, D., Pioro, I., Razumovski, V., Vijayan, P., Xiaojing, L., and Yamada, K. (2014). Heat transfer behaviour and thermohydraulics code testing for supercritical water cooled reactors (SCWRs). Technical Report IAEA-TECDOC-1746, International Atomic Energy Agency.

Alferov, N., Rybin, R., and Balunov, B. (1969). Heat transfer with turbulent water flow in a vertical tube under conditions of appreciable influence of free convection. *Therm. Eng.*, 16:90–95.

Bae, Y., Kim, H., and Kang, D. (2010). Forced and mixed convection heat transfer to supercritical carbon dioxide vertically flowing in a uniformly-heated circular tube. *Exp. Therm. Fluid Sci.*, 34(8):1295–1308.

Bourke, P. and Pulling, D. (1972). Experimental explanation of deterioration in heat transfer to supercrtitical carbon dioxide. In *Proceedings of the ASME-AIChE Heat Transfer Conference*, number 71-HT-24 in 1, pages 2–7, Tulsa, Oklahoma. ASME.

Bourke, P., Pulling, D., Gill, L., and Denton, W. (1970). Forced convective heat transfer to turbulent carbon dioxide in the supercritical region. *Int. J. Heat Mass Tran.*, 13(8):1339–1348.

Cheng, X., Yang, Y., and Huang, S. (2009). A simplified method for heat transfer prediction of supercritical fluids in circular tubes. *Ann. Nucl. Energy*, 36(8):1120–1128.

Dittus, F. and Boelter, L. (1930). Heat transfer in automobile radiators of the tubular type. *Int. Commun. Heat Mass Transfer*, 12(1):3–22.

Fewster, J. and Jackson, J. (2004). Experiments on supercritical pressure convective heat transfer having relevance to SPWR. In *Proceedings of the 2004 International Congress on Advances in Nuclear Power Plants - ICAPP'04*, number 4342 in 1, pages 537–551, Pittsburgh, USA. American Nuclear Society.

Giarratano, P. and Jones, M. (1975). Deterioration of heat transfer to supercritical helium at 2.5 atmospheres. *Int. J. Heat Mass Tran.*, 18(5):649–653.

Glushchenko, L., Kalachev, S., and Gandzyuk, O. (1972). Determining the conditions of existence of deteriorated heat transfer at supercritical pressures of the medium. *Therm. Eng.*, 19(2):69–72.

Goldman, K. (1961). Heat transfer to supercritical water at 5000 psi flowing at high mass flow rates through round tubes. In *Proceedings of the International Developments in Heat Transfer Conference*, Part III, pages 561–568. ASME.

Grabezhnaya, V. and Kirillov, P. (2006). Heat transfer under supercritical pressures and heat transfer deterioration boundaries. *Therm. Eng.*, 53(4):296–301.

Hall, W. and Jackson, J. (1969). Laminarization of a turbulent pipe flow by buoyancy forces. In *Proceedings of the ASME-AIChE Heat Transfer Conference*, number 69-HT-55 in 1, pages 2–8, Minneapolis, Minnesota, USA. ASME.

Jackson, J. (2013). Fluid flow and convective heat transfer to fluids at supercritical pressure. *Nucl. Eng. Des.*, 264(1):24–40.

Jackson, J. (2015). Screening and correlating data on heat transfer to fluids at supercritical pressure. *ASME J. of Nuclear Rad. Sci.*, 2(1):1–7.

Jackson, J., Cotton, M., and Axcell, B. (1989). Studies of mixed convection in vertical tubes. *Int. J. Heat Fluid Fl.*, 10(1):2–15.

Jackson, J. and Hall, W. (1978). *Influence of Buoyancy on Heat Transfer to Fluids Flowing in Vertical Tubes Under Turbulent Conditions*, volume 2 of *Turbulent Forced Convection in Channels and Bundles*. McGraw-Hill International Book Company, New York, NY.

Jiang, K. (2015). An Experimental Facility for Studying Heat Transfer in Supercritical Fluids. Master's thesis, University of Ottawa, Ottawa, Canada.

Kays, W. (1966). *Convective Heat and Mass Transfer*. McGraw-Hill Series in Mechanical Engineering. McGraw-Hill International Book Company, New York, NY.

Kim, H., Kim, H., Song, J., and Bae, Y. (2008). Heat transfer to supercritical pressure carbon dioxide flowing upward through tubes and a narrow annulus passage. *Prog. Nucl. Energ.*, 50(2-6):518–525.

Kim, H. Y., Kim, H., Song, J. H., Cho, B. H., and Bae, Y. Y. (2007). Heat transfer test in a vertical tube using CO_2 at supercritical pressures. *J. Nucl. Sci. Technol.*, 44(3):285–293.

Krasnoshchekov, E. and Protopopov, V. (1966). Experimental study of heat exchange in carbon dioxide in the supercritical range at high temperature drops. *High Temp.*, 4(3):375–382.

Kurganov, V., Zeigarnik, Y., and Maslakova, I. (2012). Heat transfer and hydraulic resistance of supercritical-pressure coolants. Part I: Specifics of thermophysical properties of supercrticial pressure fluids and turbulent heat transfer under heating conditions in round tubes (state fo the art). *Int. J. Heat Mass Tran.*, 55(11-12):3061–3075.

Kurganov, V. A., Zeigarnik, Y. A., and Maslakova, I. V. (2016). On caculating heat transfer and pressure drop of supercritical-pressure coolants. *ASME J. of Nuclear Rad. Sci.*, 2(3):1–14.

Lemmon, E., McLinden, M., and Huber, M. (2002). Thermophysical properties of fluid systems. National Institute of Standards and Technology (NIST) Standard Reference Database Number 69, Reference Fluid Properties (REFPROP): Version 7.0.

Li, Z., Jiang, P., Zhao, C., and Zhang, Y. (2010). Experimental investigation of convection heat transfer of carbon dioxide at supercrtitical pressures in a vertical circular tube. *Exp. Therm. Fluid Sci.*, 34(8):1162–1171.

McEligot, D. and Jackson, J. (2004). "Deterioration" criteria for convective heat transfer in gas flow through non-circular ducts. *Nucl. Eng. Des.*, 232(3):327–333.

Mokry, S., Pioro, I., Farah, A., King, K., Gupta, S., Peiman, W., and Kirillov, P. (2011). Development of supercritical water heat-transfer correlation for vertial bare tubes. *Nucl. Eng. Des.*, 241(4):1126–1136.

Pioro, I., Mokry, S., and Draper, S. (2011). Specifics of thermophysical properties and forced-convective heat transfer at critical and supercritical pressures. *Rev. Chem. Eng.*, 27(3-4):191–214.

Polyakov, A. (1975). Mechanism and limits on the formation of conditions for impaired heat transfer at a superctitical coolant pressure. *High Temp.*, 13(1):1119–1126.

Protopopov, V. and Sharma, G. (1976). Experimental investigation of heat transfer from a vertical surface to carbon dioxide with natural convection in the supercritical region of the parameters of state. *High Temp.*, 14(4):693–698.

Schatte, G., Kohlhepp, A., Wieland, C., and Spliethoff, H. (2016). Development of a new empirical correlation for the prediction of the onset of the deterioration of heat transfer to supercritical water in vertical tubes. *Int. J. Heat Mass Tran.*, 102(1):133–141.

Shiralkar, B. and Griffith, P. (1969). The deterioration in heat transfer to fluids at supercritical pressure and high heat fluxes. *J. Heat Transfer*, 91(1):27–36.

Shiralkar, B. and Griffith, P. (1970). The effect of swirl, inlet conditions, flow direction, and tube diameter on the heat transfer to fluids at supercritical pressure. *J. Heat Transfer*, 92(3):465–471.

Shitsman, M. E. (1963). Impairment of the heat transmission at supercritical pressures. *High Temp.*, 1(2):237–244.

Song, J., Kim, H., Kim, H., and Bae, Y. (2008). Heat transfer characteristics of a supercritical fluid flow in a vertical pipe. *J. Supercrit. Fluid*, 44(2):164–171.

Vikhrev, Y., Barulin, Y., and Konkov, A. (1967). A study of heat transfer in vertical tubes at supercritical pressures. *Therm. Eng.*, 14(9):116–119.

Vikrev, Y. V. and Lokshin, V. A. (1964). An experimental study of temperature conditions in horizontal steam-generating tubes at supercritical pressures. *Therm. Eng.*, 11(12):105–109.

Watts, M. and Chou, C. (1982). Mixed convection heat transfer to superctitical pressure water. In *Proceedings of the Seventh International Heat Transfer Conference (IHTC)*, volume 3, pages 495–500. International Heat Transfer Conference.

Yamagata, K., Nishikawa, K., Hasegawa, S., Fujii, T., and Yoshida, S. (1972). Forced convective heat transfer to supercritical water flowing in tubes. *Int. J. Heat Mass Tran.*, 15(12):2575–2593.

Yamashita, T., Yoshida, S., Mori, H., Morooka, S., Komita, H., and Nishida, K. (2003). Heat transfer study under supercritical pressure conditions. In *Proceedings of the GENES4/ANP2003 International Conference on Global Environment and Advanced Nuclear Power Plants*, volume 35, Kyoto, Japan. International Atomic Energy Agency.

Yildiz, S. and Groeneveld, D. (2014). Diameter effect on supercritical heat transfer. *Int. Commun. Heat Mass*, 54(1):27–32.

Zahlan, H., Groeneveld, D., and Tavoularis, S. (2014). Fluid-to-fluid scaling for convective heat transfer in tubes at supercritical and high pressures. *Int. J. Heat Mass Tran.*, 73(1):274–283.

Zahlan, H., Groeneveld, D., and Tavoularis, S. (2015). Measurements of convective heat transfer to vertical upwad flows of CO_2 in circular tubes at near-critical and supercritical pressures. *Nucl. Eng. Des.*, 289(1):92–107.